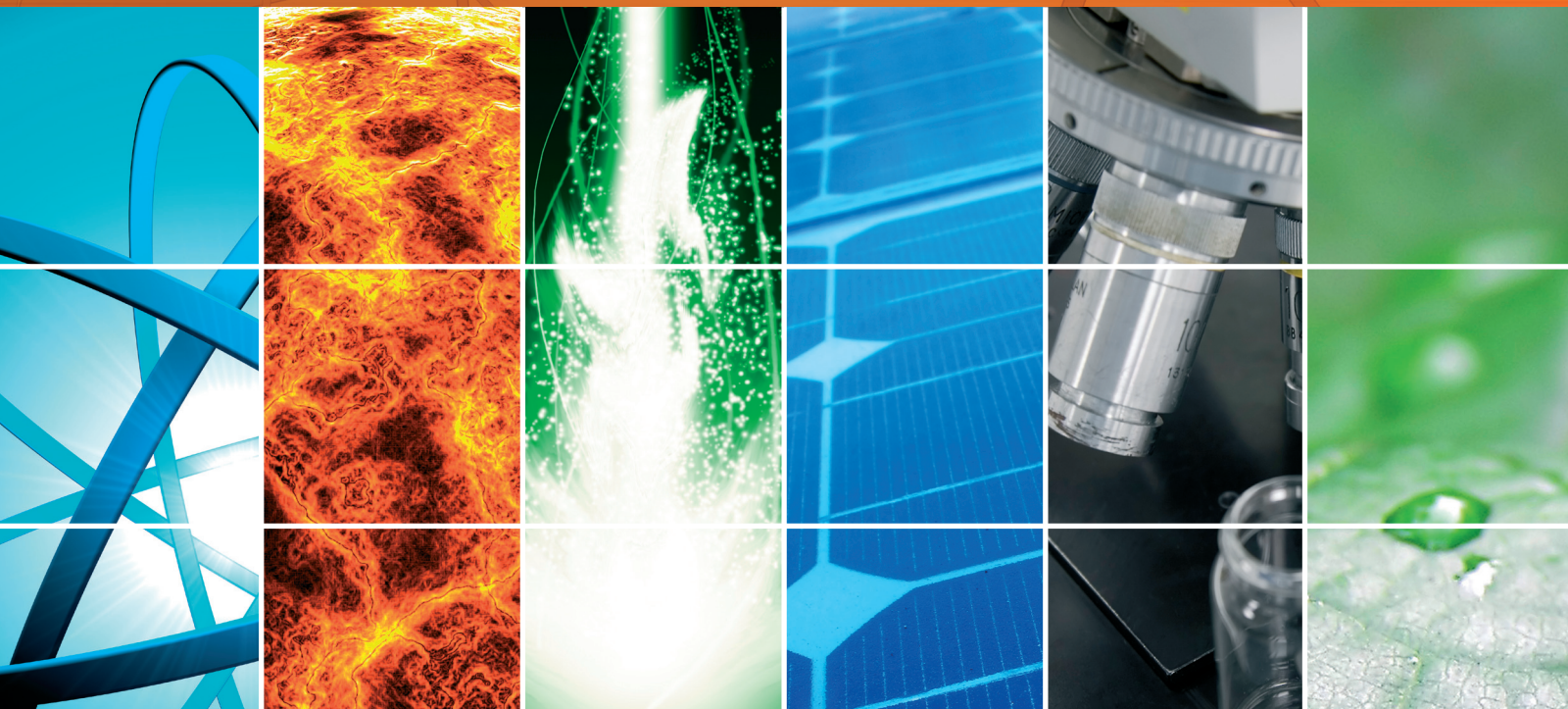


# Photovoltaic Materials and Devices 2013

Guest Editors: Bhushan Sopori, Keith Emery, Peter Rupnowski,  
and Sudhakar Shet





---

# **Photovoltaic Materials and Devices 2013**

International Journal of Photoenergy

---

## **Photovoltaic Materials and Devices 2013**

Guest Editors: Bhushan Sopori, Keith Emery, Peter Rupnowski,  
and Sudhakar Shet



---

Copyright © 2013 Hindawi Publishing Corporation. All rights reserved.

This is a special issue published in "International Journal of Photoenergy." All articles are open access articles distributed under the Creative Commons Attribution License, which permits unrestricted use, distribution, and reproduction in any medium, provided the original work is properly cited.

## Editorial Board

- M. Sabry Abdel-Mottaleb, Egypt  
Nihal Ahmad, USA  
Nicolas Alonso-Vante, France  
Wayne A. Anderson, USA  
Vincenzo Augugliaro, Italy  
Detlef W. Bahnemann, Germany  
Mohammad A. Behnajady, Iran  
Ignazio Renato Bellobono, Italy  
Raghu N. Bhattacharya, USA  
Gion Calzaferri, Switzerland  
Adriana G. Casas, Argentina  
Wonyong Choi, Korea  
Věra Cimrova, Czech Republic  
Vikram L. Dalal, USA  
D. Demetriou Dionysiou, USA  
Mahmoud M. El-Nahass, Egypt  
Ahmed Ennaoui, Germany  
Chris Ferekides, USA  
David Ginley, USA  
Beverley Glass, Australia  
Shinya Higashimoto, Japan  
Chun-Sheng Jiang, USA  
Yadong Jiang, China
- Shahed Khan, USA  
Cooper H. Langford, Canada  
Yuexiang Li, China  
Stefan Lis, Poland  
N. M. Mahmoodi, Iran  
Dionissios Mantzavinos, Greece  
Ugo Mazzucato, Italy  
Jacek Miller, Poland  
Kazuhiko Mizuno, Japan  
Jarugu N. Moorthy, India  
Franca Morazzoni, Italy  
Fabrice Morlet-Savary, France  
Ebinazar B. Namdas, Australia  
Maria da Graça P. Neves, Portugal  
Leonidas Palilis, Greece  
Leonardo Palmisano, Italy  
Ravindra K. Pandey, USA  
David Lee Phillips, Hong Kong  
Pierre Pichat, France  
Xie Quan, China  
Tijana Rajh, USA  
Peter Robertson, UK  
Avigdor Scherz, Israel
- Lukas Schmidt-Mende, Germany  
Panagiotis Smirniotis, USA  
Zofia Stasicka, Poland  
Juliusz Sworakowski, Poland  
Nobuyuki Tamaoki, Japan  
Gopal N. Tiwari, India  
Nikolai V. Tkachenko, Finland  
Veronica Vaida, USA  
Roel van De Krol, Germany  
Mark van Der Auweraer, Belgium  
Ezequiel Wolcan, Argentina  
Man Shing Wong, Hong Kong  
David Worrall, UK  
Fahrettin Yakuphanoglu, Turkey  
Minjoong Yoon, Korea  
Jimmy C. Yu, Hong Kong  
Hongtao Yu, USA  
Jun-Ho Yum, Switzerland  
Klaas Zachariasse, Germany  
Lizhi Zhang, China  
Jincai Zhao, China

# Contents

**Photovoltaic Materials and Devices 2013**, Bhushan Sopori, Keith Emery, Peter Rupnowski, and Sudhakar Shet  
Volume 2013, Article ID 306463, 1 page

**Solar Spectral and Module Temperature Influence on the Outdoor Performance of Thin Film PV Modules Deployed on a Sunny Inland Site**, G. Nofuentes, J. de la Casa, M. Torres-Ramírez, and M. Alonso-Abella  
Volume 2013, Article ID 620127, 12 pages

**Picosecond Photovoltaic Response in Tilted Lanthanum Doped Manganite Films**, Zhiqing Lu, Hao Ni, Jianfeng Xi, Xiaoming Li, and Kun Zhao  
Volume 2013, Article ID 436910, 4 pages

**Research on the Comparison Analyses of Three-Phase Discrete and Integrated LC Filters in Three-Phase PV Inverter**, Ying Jiang, Jianguo Li, Sanbo Pan, Xi Zhang, Peng Hu, and Haiyan Zhang  
Volume 2013, Article ID 217023, 14 pages

**Operation of TUT Solar PV Power Station Research Plant under Partial Shading Caused by Snow and Buildings**, Diego Torres Lobera, Anssi Mäki, Juha Huusari, Kari Lappalainen, Teuvo Suntio, and Seppo Valkealahti  
Volume 2013, Article ID 837310, 13 pages

**Synthesis and Characterization of Carbazole-Benzothiadiazole-Based Conjugated Polymers for Organic Photovoltaic Cells with Triazole in the Main Chain**, Eunhee Lim  
Volume 2013, Article ID 607826, 7 pages

**Multi-Input Converter with MPPT Feature for Wind-PV Power Generation System**, Chih-Lung Shen and Shih-Hsueh Yang  
Volume 2013, Article ID 129254, 13 pages

**Photovoltaic High-Frequency Pulse Charger for Lead-Acid Battery under Maximum Power Point Tracking**, Hung-I. Hsieh, Sheng-Fang Shih, Jen-Hao Hsieh, and Chi-Hao Wang  
Volume 2013, Article ID 687693, 8 pages

**Simulation and Experimental Study of Photogeneration and Recombination in Amorphous-Like Silicon Thin Films Deposited by 27.12 MHz Plasma-Enhanced Chemical Vapor Deposition**, Chia-Hsun Hsu, In-Cha Hsieh, Chia-Chi Tsou, and Shui-Yang Lien  
Volume 2013, Article ID 698026, 6 pages

**Structural and Optoelectronic Properties of CdSe Tetrapod Nanocrystals for Bulk Heterojunction Solar Cell Applications**, Nguyen Tam Nguyen Truong, Thao Phuong Ngoc Nguyen, and Chinho Park  
Volume 2013, Article ID 146582, 7 pages

**Optimization of Rear Local Contacts on High Efficiency PERC Solar Cells Structures**, Kapila Wijekoon, Fei Yan, Yi Zheng, Dapeng Wang, Hemant Mungekar, Lin Zhang, and Hari Ponnekanti  
Volume 2013, Article ID 368403, 8 pages

**Characterization of a Bifacial Photovoltaic Panel Integrated with External Diffuse and Semimirror Type Reflectors**, P. Ooshaksaraei, K. Sopian, R. Zulkifli, M. A. Alghoul, and Saleem H. Zaidi  
Volume 2013, Article ID 465837, 7 pages

**Organic Photovoltaic Cells Based on PbPc Nanocolumns Prepared by Glancing Angle Deposition,**

Yang Liu, Fujun Zhang, and Jian Wang

Volume 2013, Article ID 346818, 6 pages

**p-Type Quasi-Mono Silicon Solar Cell Fabricated by Ion Implantation,** Chien-Ming Lee, Sheng-Po Chang,

Shoou-Jinn Chang, and Ching-In Wu

Volume 2013, Article ID 171390, 8 pages

**Realization of Colored Multicrystalline Silicon Solar Cells with SiO<sub>2</sub>/SiN<sub>x</sub>:H Double Layer Antireflection Coatings,** Minghua Li, Libin Zeng, Yifeng Chen, Lin Zhuang, Xuemeng Wang, and Hui Shen

Volume 2013, Article ID 352473, 8 pages

**A New Optimization Approach for Maximizing the Photovoltaic Panel Power Based on Genetic Algorithm and Lagrange Multiplier Algorithm,** Mahdi M. M. El-Arini, Ahmed M. Othman,

and Ahmed Fathy

Volume 2013, Article ID 481468, 12 pages

**Investigation of Solar Hybrid Electric/Thermal System with Radiation Concentrator and Thermoelectric Generator,** Edgar Arturo Chávez Urbiola and Yuri Vorobiev

Volume 2013, Article ID 704087, 7 pages

**Key Success Factors and Future Perspective of Silicon-Based Solar Cells,** S. Binetti, M. Acciarri,

A. Le Donne, M. Morgano, and Y. Jestin

Volume 2013, Article ID 249502, 6 pages

**Reduction of Oxygen Impurity in Multicrystalline Silicon Production,** Bing Gao, Satoshi Nakano, and Koichi Kakimoto

Volume 2013, Article ID 908786, 6 pages

**Effect of Annealing Temperature on CuInSe<sub>2</sub>/ZnS Thin-Film Solar Cells Fabricated by Using Electron Beam Evaporation,** H. Abdullah and S. Habibi

Volume 2013, Article ID 568904, 5 pages

**Interface Study of ITO/ZnO and ITO/SnO<sub>2</sub> Complex Transparent Conductive Layers and Their Effect on CdTe Solar Cells,** Tingliang Liu, Xing Zhang, Jingquan Zhang, Wenwu Wang, Lianghuan Feng, Lili Wu,

Wei Li, Guanggen Zeng, and Bing Li

Volume 2013, Article ID 765938, 8 pages

**Forecasting the Development of Different Solar Cell Technologies,**

Arturo Morales-Acevedo and Gaspar Casados-Cruz

Volume 2013, Article ID 202747, 5 pages

**Alumina and Hafnia ALD Layers for a Niobium-Doped Titanium Oxide Photoanode,** Naji Al Dahoudi,

Qifeng Zhang, and Guozhong Cao

Volume 2012, Article ID 401393, 6 pages

## *Editorial*

# Photovoltaic Materials and Devices 2013

**Bhushan Sopori,<sup>1</sup> Keith Emery,<sup>1</sup> Peter Rupnowski,<sup>2</sup> and Sudhakar Shet<sup>3</sup>**

<sup>1</sup> National Renewable Energy Laboratory, 1617 Cole Boulevard, Golden, CO 80401, USA

<sup>2</sup> Solar Energy Consultant, Midland, MI 48686, USA

<sup>3</sup> Princeton Optronics, Trenton, NJ 08619, USA

Correspondence should be addressed to Bhushan Sopori; [bhushan.sopori@nrel.gov](mailto:bhushan.sopori@nrel.gov)

Received 14 November 2013; Accepted 14 November 2013

Copyright © 2013 Bhushan Sopori et al. This is an open access article distributed under the Creative Commons Attribution License, which permits unrestricted use, distribution, and reproduction in any medium, provided the original work is properly cited.

Photovoltaic energy has now gained acceptance from most of the electrical energy users for both the residential and the commercial applications. Concomitantly, the production of PV energy has been steadily increasing. Likewise there is an enormous expansion of the PV research community, with PV becoming a mainstream educational topic both as general course work and as research field at universities and academic institutions. While new areas of PV research are continually being fostered, the silicon manufacturing technology has retained a dominant role through availability of lower cost poly, advances in the crystal growth technologies that led to higher quality wafers, advances in the wafering technology, and new cell processing methods. Reduction in cost has placed a renewed emphasis on the development of higher efficiency devices—based on *n*-type Si and using architectures suitable for thinner, passivated devices. Likewise, growth in production volume and improvements in the module efficiencies of commercial CdTe and CIGS modules have been further lowering their costs. However, there are still many challenges in both R&D and commercialization of PV modules in areas that include new cell designs, commercial manufacturing equipment, and implementation of online monitoring technologies.

This second special issue serves as a timely publication bringing the latest results of various PV technologies. It includes a collection of 22 peer-reviewed papers encompassing all areas of PV fields. We hope that readers find them interesting as well as of help in their research work.

## **Acknowledgments**

The editors acknowledge with thanks the contributing authors for submitting their manuscripts and the reviewers for ensuring high quality of the published papers.

*Bhushan Sopori  
Keith Emery  
Peter Rupnowski  
Sudhakar Shet*

## Research Article

# Solar Spectral and Module Temperature Influence on the Outdoor Performance of Thin Film PV Modules Deployed on a Sunny Inland Site

G. Nofuentes,<sup>1</sup> J. de la Casa,<sup>1</sup> M. Torres-Ramírez,<sup>1</sup> and M. Alonso-Abella<sup>2</sup>

<sup>1</sup> Grupo de Investigación y Desarrollo de Energía Solar, IDEA, Escuela Politécnica Superior, University of Jaén, Campus de Las Lagunillas, s/n, 23071 Jaén, Spain

<sup>2</sup> CIEMAT/DER, Avenida Complutense 22, 28040 Madrid, Spain

Correspondence should be addressed to G. Nofuentes; gnofuen@ujaen.es

Received 25 January 2013; Revised 29 September 2013; Accepted 30 September 2013

Academic Editor: Keith Emery

Copyright © 2013 G. Nofuentes et al. This is an open access article distributed under the Creative Commons Attribution License, which permits unrestricted use, distribution, and reproduction in any medium, provided the original work is properly cited.

This work aims at analysing the influence of both module temperature and solar spectrum distribution on the outdoor performance of the following thin film technologies: hydrogenated amorphous silicon (a-Si:H), cadmium telluride (CdTe), copper indium gallium selenide sulfide (CIGS), and hydrogenated amorphous silicon/hydrogenated microcrystalline silicon hetero-junction (a-Si:H/ $\mu$ c-Si:H). A 12-month experimental campaign carried out in a sunny inland site in which a module of each one of these technologies was tested and measured outdoors has provided the necessary empirical data. Results show that module temperature exerts a limited influence on the performance of the tested a-Si:H, CdTe, and a-Si:H/ $\mu$ c-Si:H modules. In contrast, the outdoor behaviour of the CIGS module is the most affected by its temperature. Blue-rich spectra enhance the outdoor behaviour of the a-Si:H and a-Si:H/ $\mu$ c-Si:H modules while it is the other way round for the CIGS module. However, the CdTe specimen shows little sensitivity to the solar spectrum distribution. Anyway, spectral effects are scarcely relevant on an annual basis, ranging from gains for the CIGS module (1.5%) to losses for the a-Si:H module (1.0%). However, the seasonal impact of the spectrum shape is more noticeable in these two materials; indeed, spectral issues may cause performance gains or losses of up to some 4% when winter and summer periods are considered.

## 1. Introduction

Doubtless, crystalline silicon (c-Si) is today's photovoltaic (PV) dominating technology. Although it will likely preserve its prevalence in the near and midterm, PV designers and installers are increasingly interested in thin film technologies, still a small but noticeable share of the market. If all announced expansion plans had been completed in due time, thin film production capacity could already have reached around 17 GW—19% of the envisaged market—in 2012 [1]. Some estimates forecast thin film production capacity will rise up to 27 GW—or 24% of the reported future PV market—in 2015 [2]. In this sense, recent widely marketed modules using materials such as hydrogenated amorphous silicon (a-Si:H), cadmium telluride (CdTe), copper indium gallium selenide sulfide (CIGS), and hydrogenated amorphous silicon/hydrogenated microcrystalline silicon heterojunction

(a-Si:H/ $\mu$ c-Si:H) will certainly play a crucial role in PV system engineering over the next years due to their ceaseless declining cost and improved outdoor performance [1–3].

The estimation of the PV electricity yield from the climate conditions of a given site is essential in PV engineering. Hence, understanding the outdoor electrical behaviour of PV modules is a key issue for this electricity yield estimation. A wide variety of numerical, algebraic, and empirical methods referenced in the literature [4–12] have succeeded in estimating quite accurately the c-Si PV module outdoor performance. These methods basically state the relationship between the outdoor performance of these devices and two environmental factors: incident irradiance ( $G$ , in  $\text{W}\cdot\text{m}^{-2}$ ) and module temperature ( $T_{\text{mod}}$ , in  $^{\circ}\text{C}$ ).

However, this outdoor behaviour is not understood to such a large extent for thin film technologies [13, 14].

In fact, the peculiarities of their spectral responses make these technologies more sensitive to the spectral distribution of the irradiance than those based on c-Si. Therefore, the spectrum shape must be taken into account when modeling the power output of a thin film PV module, in addition to  $G$  and  $T_{\text{mod}}$ . Some efforts approaching this issue are worthy mention, just to give some instances. Thus, in spite of being quite accurate, the Martín and Ruiz model [15], based on equations that derive the effective responsivity of the modules from the optical air mass and the clearness index, has been solely proposed for c-Si and a-Si:H. Also, some “one-of-a-kind” complex models addressed to modelling the efficiency of a specific CIGS module have been proposed. This sort of complex models usually involve the clearness index, the optical air mass, and some empirical coefficients [16, 17], which cannot be conclusive for thin film technology, in general.

An interesting, well-proven, and useful method to predict the electricity yield for a given site has been reported for PV grid-connected systems (PVGCS) that use c-Si, a-Si:H, a-Si:H/ $\mu\text{c-Si:H}$ , and a-Si/a-SiGe/a-SiGe technologies in Kusatsu city (Japan, latitude 35°N, longitude 136°E) [18–20]. To summarise, this method is mainly based on (a) obtaining a contour graph for each technology in which the module performance ratio (PR) is depicted versus a spectral index termed average photon energy (APE, in eV, to be stated below) and  $T_{\text{mod}}$ , and (b) producing contour graphs of the collected incident irradiation versus APE and the ambient temperature ( $T_{\text{amb}}$ , in °C) of the site, which leads to a suitable characterisation of the specific site from a spectral point of view. Since  $T_{\text{mod}}$  may be derived from  $T_{\text{amb}}$  and some other environmental factors such as wind speed, a suitable combination of the diagrams obtained in (a) and (b) is the key to achieve a good estimation of the energy yield of the above PV technologies. It should be understood that values of APE depend on the measurement wavelength interval of the spectrum. Thus, in the above works, a wavelength interval ranging from 350 to 1050 nm was considered, so that APE of the AM 1.5 G spectrum equals 1.88 eV. Anyway, this issue will be dealt with more deeply in this paper.

Nevertheless, the method described above still requires a lot of research aimed at improving the understanding of the behaviour of thin film materials under natural sunlight. Thus, although CIGS and CdTe are second and third, respectively, regarding projected thin film production capacity—a-Si:H heads this rank [2]—no contour graphs depicting PR versus APE and  $T_{\text{mod}}$  for these important technologies have been produced so far. Further, these contour graphs have not been obtained for sites with inland climates, in which levels of water vapour are lower—a fact that leads to shift the solar spectrum to the red—than those of sites which have a maritime climate, in which “blue rich” solar spectra prevail. More specifically, the solar spectral influence on PV materials performance has been explored for values of APE ranging from 1.85 to 2.03 eV. Therefore, the influence exerted by a “red rich” dominating spectrum on thin film technologies still remains to be suitably ascertained; that is, the impact of solar spectra with APE lower than 1.85 eV on such technologies has not been analysed yet. Last, but not least, the works described

in the previous paragraph are supported on experimental data which were drawn from the operation monitoring of several PVGCS, whose PV fields had not been calibrated at standard test conditions (STC). This experimental setup introduces some sources of uncertainty, in principle. Thus, the values for the peak power of these PV fields used in PR calculations and its further analysis have been taken from the module manufacturers’ data sheets, which probably differ from the real calibrated peak power values. Further, uncertainty is also introduced in the maximum power point tracking of the PV fields; these errors should not be underestimated as most reported systems date their start of operation back to a time interval between 1998 and 2004. Existing inverters by then did not show such low values for error in maximum power point tracking as state-of-the-art inverters do nowadays. Besides, these works have not taken into account the impact on PR of the angle of incidence (AOI, in °) combined with dirt. Seasonal annealing experienced by the a-Si:H material has not been properly addressed, either.

This work aims at achieving a wider knowledge of the influence of module temperature and solar spectrum distribution on the outdoor performance of thin film PV materials, following the approach described above. Also, this work attempts to amend the shortcomings identified in the previous paragraph as much as possible. Thus, four thin film PV modules—a sample for each one of four considered technologies (a-Si:H, CIGS, CdTe, and a-Si:H/ $\mu\text{c-Si:H}$ )—were installed outdoors in the city of Jaén (Spain, latitude 37°N, longitude 3°W, with a Mediterranean-Continental climate). This city is spectrally characterised by enhanced levels of long wavelengths—when compared to maritime and humid sites—due to its sunny inland and dry climate. Thus, the four selected PV specimens underwent an initial calibration in STC prior to be deployed outdoors and another one after their exposure, to check their stability over time. A 12-month experimental campaign was carried out basically intended to scan current ( $I$ , in A) voltage ( $V$ , in V) curves of these specimens together with some other environmental parameters at which these curves were scanned. For each one of the tested PV modules, a contour graph was obtained in which their outdoor performance is depicted versus APE and  $T_{\text{mod}}$ , following the approach previously described [18, 21]. PR over the experimental campaign was calculated for each tested PV module. Then, the impact of some phenomena that influence the performance of each considered PV technology over the 12-month test and measurement period—including module temperature and spectral effects—is quantified. Last, some important conclusions regarding the impact of the spectral irradiance distribution and  $T_{\text{mod}}$  on the outdoor behaviour of the tested thin film PV modules are derived from the analysis of both the contour graphs and the quantified effects of these two influencing factors.

## 2. Materials and Methods

This section deals with a short tutorial focused on APE, introduced as a meaningful and convenient spectral index together with a description of the experimental setup from

TABLE 1: Module maximum power in STC (W) of the four thin film PV modules under test as provided by the manufacturer and by both the initial and final outdoor calibration.

Module technology	Manufacturer data sheet	Initial calibration (October 2011)	Final calibration (November 2012)
a-Si:H	60 $-5/+10\%$	57.4 $\pm 4\%$	56.2 $\pm 4\%$
CIGS	120 $\pm 10\%$	119.1 $\pm 4\%$	121.2 $\pm 4\%$
CdTe	70 $\pm 5\%$	67.2 $\pm 4\%$	66.5 $\pm 4\%$
a-Si:H/ $\mu\text{c-Si:H}$	121 $-5/+10\%$	109.4 $\pm 4\%$	107.6 $\pm 4\%$

which the results to be presented here were obtained. The methodology followed to achieve the targets detailed in the previous section is also described.

**2.1. The Average Photon Energy.** A suitable characterisation of different spectra is a crucial requirement to assess how the solar spectral variations influence the performance of thin film PV materials. Thus, some atmospheric parameters such as the clearness index and the optical air mass condense important information on the solar spectrum distribution [15, 17]. Nevertheless, in principle, a spectral distribution should be characterized by means of a single parameter, which could lend itself to be used just as the above environmental factors  $G$  and  $T_{\text{mod}}$ . Bearing this in mind, the data recorded using a spectroradiometer are not especially adequate to achieve this characterisation, since these data consist of a more or less large set of points within a given wavelength interval, depending on the spectral range and the resolution of the used instrument. In this sense, APE has been proposed as a single index that characterizes the shape of the incident irradiance spectrum [18, 21, 22] and, consequently, characterises its “colour.” Thus, high values of APE imply that the solar spectrum is shifted towards the blue, as depicted in Figure 1. This index is calculated by dividing the integrated incident irradiance by the integrated photon flux density:

$$\text{APE} = \frac{\int_a^b G(\lambda) d\lambda}{\int_a^b \phi(\lambda) d\lambda}, \quad (1)$$

where  $G(\lambda)$  [ $\text{W}\cdot\text{m}^{-2}\cdot\text{nm}^{-1}$ ] is the incident spectral irradiance,  $\Phi(\lambda)$  [ $\text{m}^{-2}\cdot\text{nm}^{-1}\cdot\text{s}^{-1}$ ] is the incident spectral photon flux density, and  $a$  [nm] and  $b$  [nm] are the lower and upper wavelength limits, respectively, of the interval of the spectrum to be considered. The measurement range of the spectroradiometer usually determines the values for  $a$  and  $b$ .

It stems from (1) that APE is an index that does not depend on the specific PV material under analysis. Besides, its uniqueness for the spectra measured in a particular site and climate has been raised [23]. Thus, APE is a meaningful and convenient index to determine the impact of the solar spectrum on PV devices outdoor behaviour [14, 24, 25]. Last, (1) shows that, given a specific solar spectral distribution, the value for APE highly depends on the lower and upper wavelength limits— $a$  and  $b$ , respectively—used for its calculation. Thus, APE for the AM 1.5 G reference spectrum is equal to 1.88 eV if the wavelength range 350–1050 nm is considered while this value lowers down to 1.59 eV for the range 350–1700 nm [18].

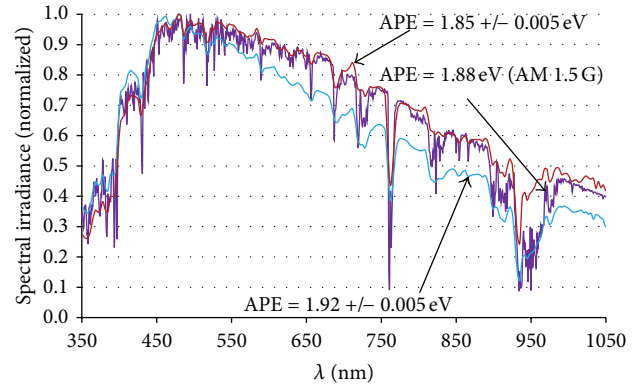


FIGURE 1: Incident spectral irradiance distributions normalized to their maxima. Redder spectra imply lower values of APE. Data corresponding to the reference AM 1.5 G spectrum have been obtained from the IEC 60904-3 standard.

**2.2. Experimental Setup.** A PV module of each considered technology (a-Si:H, CIGS, CdTe, and a-Si:H/ $\mu\text{c-Si:H}$ ) was deployed outdoors in the city of Jaén on December 2010. The outdoor calibration in STC of all the significant electrical parameters of these four thin film PV modules was carried out in the University of Jaén research facilities on October 2011, prior to the beginning of the experimental campaign to be detailed below. The most meaningful measured parameter for our purpose—the calibrated peak power ( $P_{\text{CAL}}^*$ , in W)—is shown in Table 1. The nominal peak power, as provided by the manufacturer data sheets ( $P_{\text{NOM}}^*$ , in W), is also provided in this table. A ten-month term ranging from December 2010 to October 2011 was considered a reasonable duration of the outdoor exposure to ensure the initial stabilization of the tested specimens. In fact, they underwent a new outdoor calibration in the same facilities after the completion of the aforementioned experimental campaign, in November 2012. Results gathered in Table 1 prove that this assumption was suitable for the objectives of our work. Consequently, the outdoor initial calibration values were assumed as the real peak power of each one of the CIGS, CdTe, and a-Si:H/ $\mu\text{c-Si:H}$  tested PV modules in the experimental results which are to be presented hereafter. The real peak power assumed for the a-Si:H specimen will be detailed in Section 3.3 in order to take into account the seasonal annealing which this material experiences over the year.

The used outdoor test and measurement research facilities are installed in the High Technical School building of the University of Jaén. An equator-facing open rack with a tilt angle of  $35^\circ$  is mounted and located on

the flat roof of this building. The four thin film PV modules were fixed on this open rack. The basic features of the test and measurement have been thoroughly described in some previous works [26, 27]. Thus, the  $I$ - $V$  curve tracer system is based on a PVE PVPM 2540C capacitive load which is controlled by a PC running LabView. As the tracing curve process is underway the voltage-current pairs are recorded by means of two Agilent 34411A digital multimeters. The voltage and current data acquisition is synchronized thanks to an external trigger produced by an Agilent 33220A function generator so that the  $I$ - $V$  pairs are recorded at the same time. Additionally, the above four PV modules could be tested sequentially using this setup, as four switchgear boxes of solid state relays controlled by means of a multipurpose Agilent 34970A data acquisition/data logger switch unit provide this feature. Regarding environmental parameters,  $G$  and  $G(\lambda)$  are measured by means of a Kipp & Zonnen CMP 21 pyranometer and an EKO MS700 spectroradiometer, respectively. Two four-wire resistive thermal detectors (RTD) Pt100 pasted at the back skin of each one of the PV modules aim at measuring the module temperature, while a Young 41382VC relative humidity and ambient temperature probe measures these two parameters. Finally, a Young 05305VM anemometer and a Vaisala barometric pressure sensor complete the experimental setup.

The  $I$ - $V$  curve of each PV module together with the above parameters was periodically scanned every five minutes from November 2011 to October 2012, inclusive. Incident irradiance was measured at each  $I$ - $V$  point in order to check any changes in this environmental parameter that might exceed 2%, due to transient cloud cover during measurement time. Measurements recorded in such changing environmental conditions have not been considered in the results to be presented hereafter. All these measurements have been taken during the time interval comprised between 10:00 and 14:00—the sun elevation is then higher than that of the rest of the day—so that the impact of the angle of incidence lends itself to be estimated in a simplified way, as shown in Section 3.3. Further, measurements with levels of  $G$  below  $300 \text{ W}\cdot\text{m}^{-2}$  have also been disregarded. Disregarding these measurements is justified since efficiency at low irradiance levels is hardly relevant [28, 29]. Additionally, low levels of light could turn the inverter into a net energy consumer in grid-tied systems [29]. Then, as only poor contributions to the total electricity yield can be expected below  $300 \text{ W}\cdot\text{m}^{-2}$  in sunny sites [10, 30], they have not been taken into account in this work. Additionally, this lower threshold allows omitting the performance losses of PV modules at low-light levels [31, 32].

**2.3. Methodology.** In this work, a short spectral characterisation of the collected irradiation over the experimental campaign is carried out first. Indeed, this characterisation proves to be useful to achieve a better understanding of some results shown later. Then, the influence of the module temperature and the spectral irradiance on the outdoor behaviour of the four tested PV modules is analysed in a qualitative way. This analysis is based on some contour

graphs in which the module performance is depicted versus APE and  $T_{\text{mod}}$ . In addition, PR over the experimental campaign is obtained for each tested PV module. Last, the impact of some phenomena that influence the performance of each considered PV technology over the 12-month test and measurement period—including module temperature and spectral effects—is quantified.

The output DC energy ( $E_{\text{DC}}$ , in Wh) delivered by each module during the 12-month experimental campaign was calculated by means of the integration of the maximum power obtained from each  $I$ - $V$  curve over 5-minute time intervals. The same method was also applied to stored values of  $G$ —measured by means of a pyranometer—in order to calculate the incident irradiation ( $H$ , in  $\text{Wh}\cdot\text{m}^{-2}$ ) collected during these 12 months. The lower and upper limits of the considered interval of the spectrum— $a$  and  $b$ , in (1)—were set to 350 and 1050 nm, respectively.

As commented in the previous section, data collected from November 2011 to October 2012, inclusive, have been used to produce the histogram and contour graphs to be shown next. These contour graphs depict the following, according to a colour code: (a) a matrix of  $H$  and (b) matrices of PR, for each tested module. All these matrices have APE and  $T_{\text{mod}}$  for row and column, respectively, with a grid mesh size of  $1^\circ\text{C} \times 0.005 \text{ eV}$ .

The procedure to create the above contour graphs may be summarized as follows [18].

- (1) The APE of  $G$  is determined by the spectrum shape.
- (2) The rows of both  $H$  and  $E_{\text{DC}}$  are indexed by APE.
- (3) The columns of both  $H$  and  $E_{\text{DC}}$  are indexed by  $T_{\text{mod}}$ .
- (4) The values of  $H$  and the  $E_{\text{DC}}$  are added to the corresponding grid mesh. Then, incident irradiation for each grid mesh ( $H_{\text{GM}}$ , in  $\text{Wh}\cdot\text{m}^{-2}$ ) and output DC energy for each grid mesh ( $E_{\text{DCGM}}$ , in  $\text{Wh}\cdot\text{m}^{-2}$ ) are obtained

Then, grid-mesh performance ratio ( $\text{PR}_{\text{GM}}$ ), or performance ratio for each grid mesh, is calculated as follows:

$$\text{PR}_{\text{GM}} = \frac{E_{\text{DCGM}}/P_{\text{NOM}}^*}{H_{\text{GM}}/G^*}, \quad (2)$$

where  $G^*$  is the incident irradiance at STC ( $1000 \text{ W}\cdot\text{m}^{-2}$ ). Values for  $P_{\text{NOM}}^*$  [W] were drawn from the second column of Table 1.

### 3. Results and Discussion

Over 9,500  $I$ - $V$  curves together with the same number of data corresponding to the different environmental factors listed in Section 2.2 were recorded for the tested CIGS, CdTe, and a-Si:H/ $\mu\text{c}$ -Si:H PV modules during the 12-month experimental campaign. However, only over 3,500 experimental samples like those previously described were selected from the whole data set for the tested a-Si:H PV module. These samples correspond to months ranging from December to March, inclusive (winter period, from now on). Approximately

the same amount of these samples was selected for this module corresponding to months ranging from June to September, inclusive (summer period, from now on). Presenting and discussing the experimental results obtained for the a-Si:H PV module according to the winter and summer period is key to address the effects of seasonal annealing which this PV material experiences.

**3.1. Spectral Characterisation of the Incident Irradiation Collected over the Experimental Campaign.** Figure 2 depicts a histogram in which the percentage cumulative contribution of APE classes to  $H$  collected over the 12-month experimental period is shown. Over 60% of this parameter has been generated with values of APE below 1.88 eV (AM 1.5 G). This value is much higher than those reported for Kusatsu city (Japan, latitude 35°N, longitude 136°E) and Málaga (Spain, latitude 36°N, longitude 4°W) which are below 30% for equator-facing surfaces with a tilt angle somewhat lower than the local latitude [21, 27]. This clearly indicates a higher red content of the spectral irradiance in Jaén than those of the other two sites, given the four-hour time window (10:00–14:00) within which spectra were measured. The inland location of Jaén when compared to those of Kusatsu city and Málaga should be kept in mind. The lower humidity of the atmosphere in Jaén leads to a smaller absorption by water vapour. Consequently, the fraction of spectral irradiance at longer wavelengths is increased; this causes a relative “red-rich” spectrum [25]. This spectral feature of the site will allow us to explore how incident spectral irradiance distributions with APE lower than 1.85 eV influence the tested PV specimens. It should be remembered again that previous works [18–20] have only dealt with APE values ranging from 1.85 to 2.03 eV.

Owing to the similarities found between the four contour graphs of  $H_{GM}$  collected over the experimental campaign—one for each tested PV module, produced according to the methodology described in Section 2.3—only one of them is shown in Figure 3. Indeed, the peculiarities of this contour graph can be assumed for the four modules under test. The colour related to each grid mesh—1°C × 0.005 eV in size—indicates the range of incident irradiation where the corresponding  $H_{GM}$  lies according to the colour code displayed on the right-hand side of Figure 3. The relatively low value of  $H$  collected over the experimental campaign—some 600 kWh·m<sup>-2</sup>—is due to the fact that the considered time window when data were recorded in this campaign spans from 10:00 to 14:00. It is also worth pointing out that only a negligible fraction of  $H$  impinged on the modules under test at STC (APE = 1.88 eV and  $T_{mod} = 25^\circ\text{C}$ ).

**3.2. Performance of the Tested PV Modules as a Function of the Average Photon Energy and Module Temperature.** In this context,  $PR_{GM}$  is an index that characterises the performance of a PV module at specific values of APE and  $T_{mod}$ , so that the influence of the irradiance intensity is negligible, given that measurements taken at incident irradiance levels below 300 W·m<sup>-2</sup> have been left aside [31, 32]. An expression related to  $PR_{GM}$  shown below will be most helpful in the

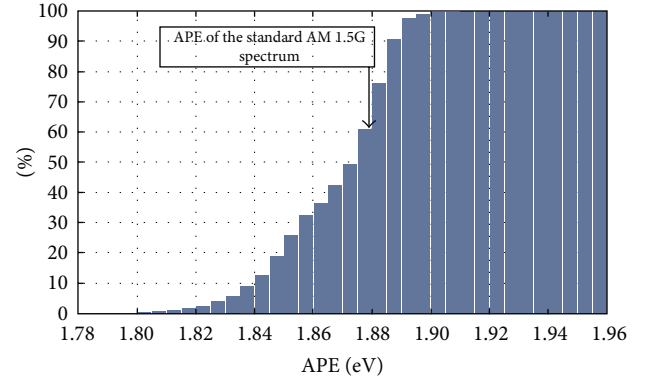


FIGURE 2: Percentage cumulative distribution of  $H$  collected over the experimental campaign as a function of APE (class width = 0.005 eV).

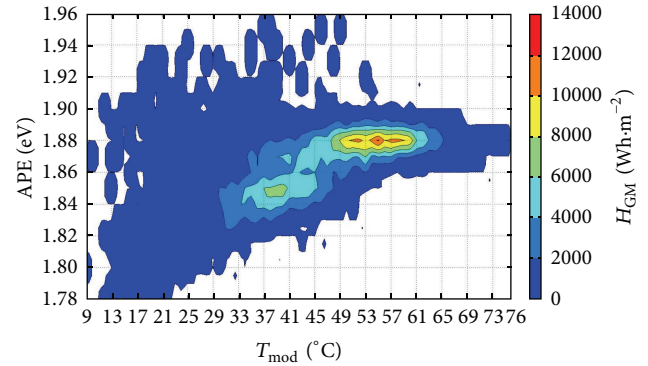


FIGURE 3: Contour graph of  $H_{GM}$  over the whole experimental campaign (November 2011–October 2012, inclusive) as a function of  $T_{mod}$  and APE for the tested a-Si:H module. Blank areas indicate no data points.

discussion of results detailed hereafter. In this expression, some second-order effects are ignored—low performance at low-light levels as this is our case, AOI combined with dirt effects, and deviations of  $P_{CAL}^*$  from  $P_{NOM}^*$ —in order to compromise accuracy in favour of simplicity. Thus, as a first approach, this index may be written as follows [33]:

$$PR_{GM} \approx (1 + \gamma(T_{mod} - T_{mod}^*)) \cdot SF^{-1}, \quad (3)$$

where  $\gamma$  [°C<sup>-1</sup>] is the maximum power temperature coefficient of the module,  $T_{mod}^*$  [°C] is the module temperature at STC, and  $SF^{-1}$  is the reciprocal of the spectral factor. The latter parameter may be written as

$$SF^{-1} = \frac{\int G(\lambda) SR(\lambda) d\lambda \cdot \int G_{AM1.5G}(\lambda) d\lambda}{\int G_{AM1.5G}(\lambda) SR(\lambda) d\lambda \cdot \int G(\lambda) d\lambda}, \quad (4)$$

where  $G_{AM1.5G}(\lambda)$  [W·m<sup>-2</sup>·nm<sup>-1</sup>] is the spectral irradiance of the standard AM 1.5 G spectrum and  $SR(\lambda)$  is the relative spectral response of the PV device.

Values of  $SF^{-1}$  above 1 imply a better performance of the considered device under the actual spectrum than that

achieved under the standard AM 1.5 G spectrum if only spectral issues are considered. Conversely, values of  $SF^{-1}$  below 1 indicate a worse performance of the PV material under the actual spectrum when compared to the standard one, also assuming only spectral issues. Obviously,  $SF^{-1}$  higher than 1 implies spectral gains while  $SF^{-1}$  lower than 1 implies spectral losses.

Figures 4–6 show the contour graphs of  $PR_{GM}$  for the tested CIGS, CdTe, and a-Si:H/ $\mu$ c-Si:H PV modules as a function of  $T_{mod}$  and APE. In these figures, some obvious spurious data points have been filtered. At first glance, these three contour graphs share a similar appearance leaving aside some differences which are to be discussed below. In fact,  $PR_{GM}$  data points appear when APE ranges from 1.79 to 1.91 eV at values of  $T_{mod}$  below 25°C, while these  $PR_{GM}$  data points only appear within a much narrower interval of APE which varies between 1.86 and 1.90 eV when  $T_{mod}$  exceeds some 55°C. Thus, some of the measured low incident irradiances—values of  $G$  in the vicinity of  $300 \text{ W}\cdot\text{m}^{-2}$ —have been recorded under cloudy conditions. Under these conditions, transmission is enhanced in both the ultraviolet and blue range of the spectrum while water vapour absorption takes place at larger wavelength ranges [34]. Consequently, spectra obtained in overcast conditions are shifted to shorter wavelengths and lead to high values of APE. On the other hand, some of the data for these low incident irradiances have been recorded in the morning of clear and cold days, when the spectrum is redder than in the afternoon [35] so that this leads to lower values of APE down to 1.79 eV and values of  $T_{mod}$  below 25°C. Measured high incident irradiances—over  $600 \text{ W}\cdot\text{m}^{-2}$ —are assumed to be related to fine weather. In such conditions, as raised by Ishii et al. [25], the Rayleigh scattering which leads to an increase/decrease of the spectral irradiance at shorter wavelengths below 700 nm is balanced by the increase/decrease of “red” light due to water vapour absorption. This “offset effect” keeps values of APE within a relatively small interval around 1.88 eV. This interval gets even narrower—it varies between some 1.87 and 1.89 eV—as incident irradiance exceeds some  $900 \text{ W}\cdot\text{m}^{-2}$ , a fact which is highly correlated with relatively high module temperatures—that is,  $T_{mod}$  above some 60°C—in hot and sunny climates such as that of Jaén.

Figures 7 and 8 depict the contour plots of  $PR_{GM}$  for the a-Si:H PV tested module in the winter and summer periods, respectively. The shape of the contour graph shown in Figure 7—winter period—resembles those of Figures 4–6. However, the values of  $PR_{GM}$  obtained in the winter period take place at APE below 1.88 eV, which indicates a prevailing red-rich spectrum in this season. Only some sixty values of  $PR_{GM}$  at APE above 1.88 eV were obtained. In fact, these values are omitted in Figure 7 due to their minor relevance, when compared to the remaining 3,500 points represented in the graph. On the other hand, the contour graph of Figure 8—summer period—shows how a sizeable number of values of  $PR_{GM}$  take place at APE above 1.88 eV. Consequently, spectra shifted to shorter wavelengths play an important role in the hot season. The “red-richness” of the solar spectra recorded in the winter period owes a good deal to the sun altitude. In fact,

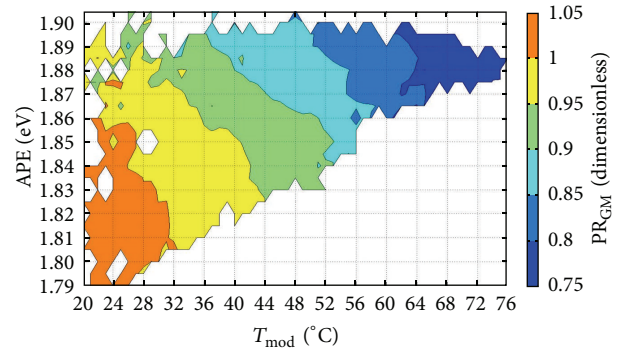


FIGURE 4: Contour graph of  $PR_{GM}$  of the tested CIGS PV module as a function of  $T_{mod}$  and APE. Blank areas indicate no data points.

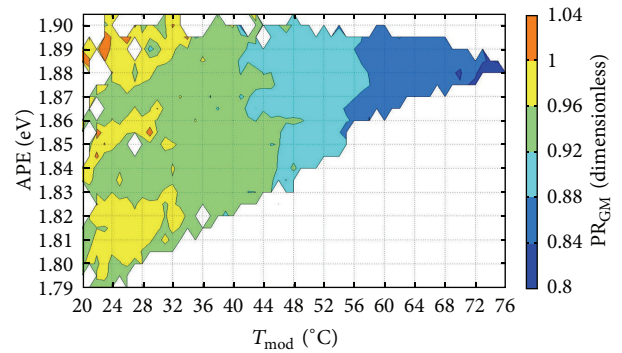


FIGURE 5: Contour graph of  $PR_{GM}$  of the tested CdTe PV module as a function of  $T_{mod}$  and APE. Blank areas indicate no data points.

the sun altitude is lower in the cold season than in the warm one, so that this fact gives rise to higher values of the optical air mass (OAM), when compared to summer ones. Hence, long wavelength light is enhanced in the winter period, so that low values of APE are obtained.

Regarding seasonal annealing, comparing some areas of Figures 7 and 8 allows identifying this phenomenon in the tested a-Si:H PV module. Thus, in Figure 7—winter period—most values of  $PR_{GM}$  vary between 0.88 and 0.92 within the stripe where APE and  $T_{mod}$  range from 1.86 to 1.87 eV and from 45 to 57°C, respectively. However, most values of  $PR_{GM}$  lie in the interval 0.92 to 0.96 within the stripe determined by the same range of APE and  $T_{mod}$  in the summer period (Figure 8).

Contour graphs depicted in Figures 4–8 provide us with some qualitative information to assess the influence of module temperature, which is first discussed below. Then, the impact of the spectral irradiance distribution by means of APE is to be analysed.

- (a) Module temperature turns out to exert a limited influence on the performance of the a-Si:H, CdTe, and a-Si:H/ $\mu$ c-Si:H modules. This stems from scanning Figures 5, 6, 7, and 8 in the horizontal direction, at a given fixed APE. According to (3), the explanation of this behaviour lies in the low maximum power

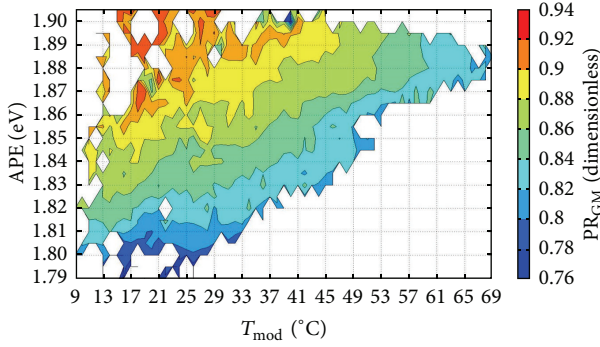


FIGURE 6: Contour graph of  $PR_{GM}$  of the tested a-Si:H/ $\mu$ c-Si:H PV module as a function of  $T_{mod}$  and APE. Blank areas indicate no data points.

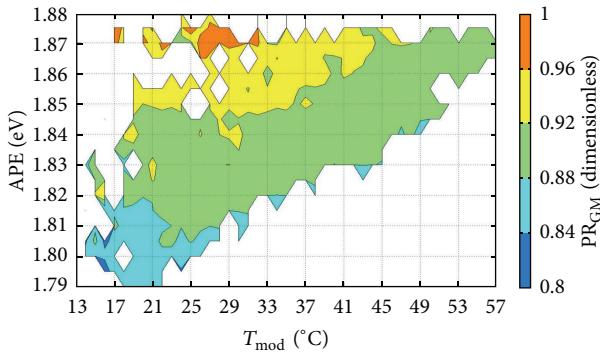


FIGURE 7: Contour graph of  $PR_{GM}$  of the tested a-Si:H PV module as a function of  $T_{mod}$  and APE for the winter period. Blank areas indicate no data points.

temperature coefficients of these modules when compared to those of modules based on c-Si technologies. Thus,  $\gamma$  equals  $-0.0023$ ,  $-0.0025$ , and  $-0.0024^{\circ}\text{C}^{-1}$  for the tested a-Si:H, CdTe, and a-Si:H/ $\mu$ c-Si:H specimens, as provided by their manufacturers' data sheets. Regarding c-Si, a typical average value of  $-0.0040^{\circ}\text{C}^{-1}$  can be assumed for  $\gamma$  [36]. However, the value provided by the CIGS module manufacturer for this parameter ( $-0.0045^{\circ}\text{C}^{-1}$ ) helps to explain the noticeable impact of  $T_{mod}$  on the outdoor performance of this module. This is also derived from scanning Figure 4 in the horizontal direction, at a given fixed APE.

- (b) Regarding the spectral incident irradiance distribution, both a-Si:H and a-Si:H/ $\mu$ c-Si:H specimens are very sensitive to variations of the shape of the spectrum. This can be easily noticed in Figures 6, 7, and 8, since increasing values of APE—given a fixed module temperature—lead to higher values of  $PR_{GM}$ , as a general trend. Doubtless, high spectral gains cause this behaviour, as values of  $SF^{-1}$  above 1.1 have been reported when the solar spectrum shifts to the blue [25]. Broadly speaking, blue-rich spectra

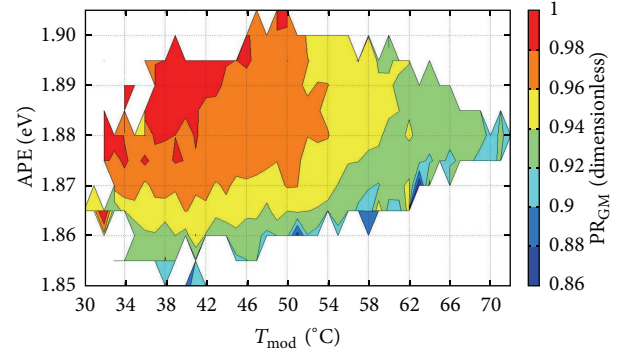


FIGURE 8: Contour graph of PR of the tested a-Si:H PV module as a function of  $T_{mod}$  and APE for the summer period. Blank areas indicate no data points.

cause spectral gains in the a-Si:H and a-Si:H/ $\mu$ c-Si:H modules, according to (3). Nevertheless, the CIGS module is also very sensitive to the spectral incident irradiance in an opposite way: decreasing values of APE—given a fixed module temperature—lead to higher values of  $PR_{GM}$ , also as a general trend. Figure 4 also shows how this performance parameter is greater than 1 within some specific areas of the contour graph where APE is lower than 1.86 eV; spectral gains doubtless explain this, together with low values of  $T_{mod}$ . Contrary to the a-Si:H and a-Si:H/ $\mu$ c-Si:H specimens—and also broadly speaking—blue-rich spectra cause spectral losses in the CIGS module performance, bearing in mind (3). Last, Figure 5 shows how the CdTe specimen is not so sensitive to APE, especially when  $T_{mod}$  exceeds a certain threshold; this can be easily checked by scanning this figure in the vertical direction at a fixed  $T_{mod}$ , when this parameter is greater than some  $35^{\circ}\text{C}$ .

**3.3. Assessment of the Impact of Phenomena Influencing Performance Ratio over the Experimental Campaign.** A qualitative analysis on the influence of the solar spectrum distribution and module temperature on the considered PV modules has been presented in Section 3.2. However, in this section, we attempt to quantitatively assess the impact of these two factors on the performance of the four tested PV modules over the experimental campaign. Thus, in general, five phenomena—which generally cause performance losses—mainly influence the outdoor behaviour of PV modules:

- low performance at low-light levels,
- AOI combined with dirt effects,
- module temperature effects,
- deviations of  $P_{CAL}^*$  from  $P_{NOM}^*$ ,
- spectral effects.

Additionally, the a-Si:H PV module is subject to seasonal annealing, which must be properly addressed.

The effects of the above phenomena overlap over time and sometimes are rather difficult to clearly be distinguished.

This is why the experimental campaign was arranged in a way that is relatively simple to quantify the impact of both module temperature and irradiance spectral distribution. Thus, since all data were recorded at incident irradiance below  $300 \text{ W}\cdot\text{m}^{-2}$ , low performance related to low-light levels is disregarded here [31, 32]. Also, the effects of dirt have been neglected in what follows; in fact, modules were cleaned manually at least once a month, except under rainy weather.

Leaving aside these two phenomena simplifies the way to make a quantitative estimation of the impact of the remaining ones on the outdoor behaviour of the tested PV specimens. Indeed, the used procedure to quantify these effects is detailed below.

If the module peak power is assumed to be equal to  $P_{\text{NOM}}^*$ , nominal energy ( $E_N$ , in Wh) is stated as the energy which the tested PV module would have delivered over the experimental campaign if the module had ideally operated without any losses, with  $T_{\text{mod}} = 25^\circ\text{C}$  and the same solar irradiation during that period of time:

$$E_N = \frac{1}{12} \cdot \frac{P_{\text{NOM}}^*}{G^*} \sum_{i=1}^N G_i \quad (\text{Wh}), \quad (5)$$

where  $G_i$  [ $\text{W}\cdot\text{m}^{-2}$ ] is the  $i$ th measured value of the incident irradiance and  $N$  is the number of measured values. Factor  $1/12$  is used to reconcile units, keeping in mind that the samples were recorded every five minutes.

The final energy ( $E_F$ , in Wh) is stated as the energy that the tested PV module actually delivered over the experimental campaign, and it may be written as

$$E_F = \frac{1}{12} \sum_{i=1}^N P_{\text{DC},i} \quad (\text{Wh}), \quad (6)$$

where  $P_{\text{DC},i}$  is the  $i$ th measured value of the maximum power delivered by the PV module.

Obviously, PR is the ratio of  $E_F$  to  $E_N$ . It is commonly accepted to express this ratio in percentage units, so that it may be written as

$$\text{PR} = \frac{E_F}{E_N} \cdot 100 \quad (\%). \quad (7)$$

Temperature losses are obtained by calculating the difference between temperature-corrected  $E_F$  and  $E_F$  itself. For convenience purposes, these temperature losses ( $L_{T_{\text{mod}}}$ ) are expressed in this work in percentage units, relative to  $E_N$ :

$$L_{T_{\text{mod}}} = \frac{1}{12} \sum_{i=1}^N P_{\text{DC},i} \left( \frac{1}{1 + \gamma(T_{\text{mod},i} - T_{\text{mod}}^*)} - 1 \right) \quad (8)$$

$$\div E_N \cdot 100 \quad (\%),$$

where  $T_{\text{mod},i}$  is the  $i$ th measured value of the module temperature. For each module, values of  $\gamma$  as provided by the manufacturer datasheets are used here.

Losses derived from differences between  $P_{\text{CAL}}^*$  and  $P_{\text{NOM}}^*$  are obtained by multiplying temperature-corrected  $E_F$  by a factor that takes into account this phenomenon. Also, for

TABLE 2: Values of the incident angle modifier for solstices and equinoxes at 10:00, 12:00, and 14:00 ( $\omega = -30^\circ, 0^\circ$ , and  $30^\circ$ , resp.).

	$\omega$ [ $^\circ$ ]	$\theta_s$ [ $^\circ$ ]	IAM ( $\theta_s$ )
Summer and winter solstices	$-30$	$37.4$	$0.98$
	$0$	$23.5$	$0.99$
	$30$	$37.4$	$0.98$
Autumn and spring equinoxes	$-30$	$30$	$0.99$
	$0^\circ$	$0$	$1$
	$30$	$30$	$0.99$

convenience purposes, these losses due to the deviation of  $P_{\text{CAL}}^*$  from  $P_{\text{NOM}}^*$  ( $L_{P_{\text{CAL}}^* \neq P_{\text{NOM}}^*}$ ) are expressed in this work in percentage units, relative to  $E_N$ :

$$L_{P_{\text{CAL}}^* \neq P_{\text{NOM}}^*} = \frac{1}{12} \sum_{i=1}^N \frac{P_{\text{DC},i}}{1 + \gamma(T_{\text{mod}} - T_{\text{mod}}^*)} \left( \frac{P_{\text{NOM}}^*}{P_{\text{CAL}}^*} - 1 \right) \quad (9)$$

$$\div E_N \cdot 100 \quad (\%).$$

Regarding the optical losses experienced by the PV modules, a popular formula for the incident angle modifier (IAM( $\theta_s$ )) or relative transmittance is widely used, normalized by the total transmittance for normal incidence, where  $\theta_s$  [ $^\circ$ ] is the angle of incidence between the rays of the sun and the normal to the surface. This is an expression [37] proposed by the American Society of Heating Refrigerating and Air Conditioning Engineers (ASHRAE):

$$\text{IAM}(\theta_s) = 1 - b_0 \left( \frac{1}{\cos \theta_s} - 1 \right), \quad (10)$$

where  $b_0$  is an empirical coefficient determined for each type of PV module. When unknown, as this is our case, a general value of  $b_0 = 0.07$  may be assumed. Equation (10) is applied to direct and circumsolar irradiances, while an approximate constant of 0.9 is used with isotropic and reflected irradiances [36].

Since the tested PV modules were deployed in the Northern Hemisphere on a south-oriented surface with a tilt angle ( $35^\circ$ ) very close to the latitude ( $37^\circ\text{N}$ ), it may be assumed that [36]

$$\cos \theta_s = \cos \delta \cos \omega, \quad (11)$$

where  $\delta$  [ $^\circ$ ] is the solar declination and  $\omega$  [ $^\circ$ ] is the true solar time:  $\omega = 0^\circ$  at noon and is counted negative in the morning and positive in the afternoon. Given that experimental data have been recorded daily at 5-minute intervals from 10:00 ( $\omega = -30^\circ$ ) to 14:00 ( $\omega = 30^\circ$ ), Table 3 gathers some relevant values related to the optical losses experienced by the tested PV modules.

From Table 2, it is clear that  $\theta_s$  varied over our experimental campaign between 0 and  $37.4^\circ$ , which correspond to values of IAM( $\theta_s$ ) ranging from 1 to 0.98, respectively. Then, a reasonable value to take into account the effects of

TABLE 3: Values of performance ratio and different performance losses experienced by the four tested PV modules over the experimental campaign.

	PR (%)	$L_{T_{\text{mod}}}$ (%)	$L_{P_{\text{CAL}}^* \neq P_{\text{NOM}}^*}$ (%)	$L_{\text{AOI}}$ (%)	$L_{\text{Spec}}$ (%)
CIGS	89.4	10.3	0.8	1.0	-1.5
CdTe	91.1	4.8	3.6	0.9	-0.4
Si: H/ $\mu\text{c-Si:H}$	85.9	3.8	8.7	1.0	0.6
a-Si: H (winter)	88.4	2.2	4.4	1.0	4.0
a-Si: H (summer)	95.4	7.0	0.7	1.0	-4.1

the AOI on an annual basis is 0.99. Indeed, albedo can be neglected in most PV calculations [36]; in our case, the flat roof ground where the PV modules are deployed has a very dark ochre colour. Besides, direct and circumsolar irradiation highly prevails in sunny climates such as that of Jaén.

Taking into account all the above considerations, the AOI losses ( $L_{\text{AOI}}$ ) are expressed in this work in percentage units, relative to  $E_N$ , too, as follows:

$$L_{\text{AOI}} = \frac{1}{12} \cdot \sum_{i=1}^N \frac{P_{\text{DC},i}}{1 + \gamma(T_{\text{mod}} - T_{\text{mod}}^*)} \cdot \frac{P_{\text{NOM}}^*}{P_{\text{CAL}}^*} \cdot \left( \frac{1}{0.99} - 1 \right) \div E_N \cdot 100 \quad (\%) . \quad (12)$$

Last, the estimation of spectral losses ( $L_{\text{Spec}}$ ) is rather straightforward, expressed in percentage units, relative to  $E_N$ , as well:

$$L_{\text{Spec}} = 100 - \text{PR} (\%) - L_{T_{\text{mod}}} - L_{P_{\text{CAL}}^* \neq P_{\text{NOM}}^*} - L_{\text{AOI}} \quad (\%) . \quad (13)$$

Table 3 gathers the values of PR,  $L_{T_{\text{mod}}}$ ,  $L_{P_{\text{CAL}}^* \neq P_{\text{NOM}}^*}$ ,  $L_{\text{AOI}}$ , and  $L_{\text{Spec}}$  derived from the experimental data collected from November 2011 to October 2012, inclusive. Values of  $P_{\text{CAL}}^*$  have been drawn from the third column of Table 1—initial calibration—in order to calculate  $L_{P_{\text{CAL}}^* \neq P_{\text{NOM}}^*}$  for the CIGS, CdTe, and a-Si:H/ $\mu\text{c-Si:H}$  PV tested modules, by means of (9). Regarding the a-Si:H specimen, seasonal annealing causes a module power variation during its outdoor exposure. Thus, the peak power of this module was calibrated at the beginning of each month during the winter and summer periods, from December to March, inclusive, and from June to September, inclusive, respectively. Accordingly, the average values of these calibrated peak power data have been used to calculate  $L_{P_{\text{CAL}}^* \neq P_{\text{NOM}}^*}$  for each season. Indeed, average values of 54.6 and 58.6 W were used for  $P_{\text{CAL}}^*$  in the winter and summer periods, respectively.

The especially noticeable deviation of  $P_{\text{CAL}}^*$  from  $P_{\text{NOM}}^*$  in the a-Si:H/ $\mu\text{c-Si:H}$  PV module—the reader is referred to Table 1—causes the high value obtained for  $L_{P_{\text{CAL}}^* \neq P_{\text{NOM}}^*}$  for this specimen. On the other hand, the seasonal annealing experienced by the a-Si:H material is reflected in the oscillation of  $L_{P_{\text{CAL}}^* \neq P_{\text{NOM}}^*}$  between 0.7%—summer period—and 7%—winter period. Besides, all the tested modules experience similar losses related to AOI (~1%).

As it could be easily anticipated due to its module maximum power temperature coefficient ( $-0.0045^\circ\text{C}^{-1}$ , according to manufacturer's data sheets), the CIGS module is the most affected by losses caused by values of  $T_{\text{mod}}$  other than  $25^\circ\text{C}$  (10.3%). The remaining modules are less sensitive to the impact of this parameter, due to their lower values of  $\gamma$ , as commented in Section 3.2.

Spectral losses are scarcely relevant, in general, for the CIGS, CdTe, and a-Si:H/ $\mu\text{c-Si:H}$  PV tested modules. Anyway, it is worth noting that spectral losses turn into gains—negative values of parameter  $L_{\text{Spec}}$ —for the CdTe and, above all, for the CIGS PV module. As commented in Section 3.2—Figure 4—the performance of this module is enhanced when the spectrum shifts to longer wavelengths. This fact, combined with the prevailing “red-richness” of the solar spectra recorded over the experimental campaign, as derived from Figure 1, is the logical explanation of the annual spectral gains (1.5%) experienced by the CIGS material. On the other hand, the a-Si:H module behaves in an opposite way from a spectral point of view. As shorter wavelengths of the spectra are enhanced in the summer period, this material experiences noticeable spectral gains (4.1%) due to its good performance under “blue-rich” spectra. These gains turn to losses in the winter period (4.0%). Anyway, it should be remembered that longer considered time intervals reduce spectral effects [38]. Thus, although not shown in Table 3,  $L_{\text{Spec}}$  calculated for the CIGS PV module from December to March, inclusive, equals  $-3.9\%$ —that is, spectral gains—while this parameter rises up to  $3.4\%$ —that is, spectral losses—when calculated from June to September, inclusive. Likewise—not shown in Table 3, either— $L_{\text{Spec}}$  equals  $1.0\%$  when calculated over the 12 months of the experimental campaign for the a-Si:H PV module.

## 4. Conclusions

The influence of module temperature and solar spectrum distribution on the outdoor performance of four thin film PV modules—a sample for each one of four considered technologies (a-Si:H, CIGS, CdTe, and a-Si:H/ $\mu\text{c-Si:H}$ )—has been explored by means of an experimental campaign arranged so that 60% of the collected incident irradiation over 12 months has been generated under solar spectra whose long wavelength light is enhanced, when compared to the AM 1.5G incident spectral irradiance distribution. In this sense, the inland climate of the site where the experimental campaign took place has allowed us to study the outdoor behaviour of the four tested modules under a “red-rich” solar

spectrum. This has paved the way to analyse this behaviour under values of APE—ranging from 1.79 to 1.91 eV—lower than those explored in previous works—ranging from 1.85 to 2.03 eV—aiming at the same direction [18–20]. For each one of these technologies, a contour graph was obtained in which the module performance is depicted versus APE and  $T_{\text{mod}}$ . Despite not being an original approach, no such contour graphs have been produced yet for CIGS and CdTe modules, as far as we know. These figures have allowed us to carry out a qualitative analysis of the impact of module temperature and the spectrum shape on the performance of the tested PV modules.

- (a) The performance of the tested a-Si:H, CdTe, and a-Si:H/ $\mu\text{c-Si:H}$  modules shows little sensitivity to  $T_{\text{mod}}$  due to their low maximum power temperature coefficients. The higher value provided for this parameter by the manufacturer of the CIGS module explains why this device performs worse as  $T_{\text{mod}}$  increases, at fixed APE.
- (b) Both the a-Si:H and a-Si:H/ $\mu\text{c-Si:H}$  modules noticeably improve their outdoor performance as APE increases—the solar spectral incident irradiance is enhanced at short wavelengths—at fixed  $T_{\text{mod}}$ . The trend is the other way round for the CIGS module; at fixed  $T_{\text{mod}}$ , its performance worsens as APE increases; that is, the solar spectral incident irradiance is enhanced at long wavelengths. Last, the CdTe PV module does not show such a strong dependence on this spectral index as the other PV specimens do.

Additionally, PR over the experimental campaign has been calculated for each tested PV module. Also, the impact of some phenomena influencing this index for each considered PV technology over the 12-month test and measurement period has been quantified and discussed.

The especially noticeable deviation of  $P_{\text{CAL}}^*$  from  $P_{\text{NOM}}^*$  in the a-Si:H/ $\mu\text{c-Si:H}$  PV module causes the most remarkable losses due to this phenomenon (8.7%). On the other hand, the seasonal annealing experienced by the a-Si:H material is reflected in the oscillation of these kinds of losses between 0.7%—summer period—and 7%—winter period. Nevertheless, all the tested modules experience similar losses related to the impact of the angle of incidence ( $\sim 1\%$ ).

As it could be easily predicted, given its module maximum power temperature coefficient, the CIGS module is the most affected by temperature losses (10.3%). The remaining modules are less sensitive to variations in module temperature, due to their lower values of  $\gamma$ .

Taking an overall view, spectral losses or gains are scarcely relevant—below 1.5%—in general, for all the tested modules when an annual basis is considered. This is not the case when the time interval of integration to calculate spectral effects is lowered down to four months.

Small annual spectral losses are experienced by the CdTe PV module (0.4%) and also small annual spectral gains are experienced by the CdTe specimen (0.6%). These gains rise up to 1.5% for the CIGS PV module; this is the consequence of the improved performance of this module

under long wavelength light, as commented above, combined with the “red-richness” of the solar spectra recorded over the experimental campaign. Since the a-Si:H PV module behaves in an opposite way from a spectral point of view, its spectral losses are equal to 1% on an annual basis.

The impact of the spectrum is more noticeable when time intervals shorter than a year are considered. Spectral gains calculated for the CIGS PV module from December to March, inclusive, equal 3.9% while these gains turn to losses (3.4%) when calculated from June to September, inclusive. On the other hand, the a-Si:H PV module experiences spectral losses of 4.0% and spectral gains of 4.1% for the winter and summer periods, respectively.

Anyway, the small size of the sample and the relatively limited amount of available data—only a module from a specific manufacturer of each one of the four studied technologies, experiencing a 12-month outdoor exposure in a specific sunny suite—suggest using the above conclusions with caution. However, it should be remembered that many valuable contributions have gathered some sound conclusions on thin film PV module outdoor performance using measurements drawn from only one specimen [13–16, 18, 24, 39–41].

## Abbreviations

### Terminology

AM:	Air mass
ASHRAE:	American Society of Heating Refrigerating and Air Conditioning Engineers
a-Si:H:	Hydrogenated amorphous silicon
a-Si:H/ $\mu\text{c-Si:H}$ :	Hydrogenated amorphous silicon/hydrogenated microcrystalline silicon hetero-Junction
CdTe:	Cadmium telluride
CIGS:	Copper indium gallium selenide sulfide
c-Si:	Crystalline silicon
IEC:	International Electrotechnical Commission
PC:	Personal computer
PV:	Photovoltaic(s)
PVGCS:	PV grid-connected system(s)
RTD:	Resistive thermal detector
STC:	Standard test conditions.

### Symbols

$a$ :	Lower wavelength limit of an interval of the spectrum [nm]
AOI:	Angle of incidence (in general) [°]
APE:	Average photon energy [eV]
$b$ :	Upper wavelength limit of an interval of the spectrum [nm]
$b_0$ :	Empirical coefficient determined for each type of PV module
$E_{\text{DC}}$ :	Output DC energy [Wh]

$E_{\text{DCGM}}$ :	Output DC energy for each grid mesh [Wh·m <sup>-2</sup> ]
$E_F$ :	Final energy [Wh]
$E_N$ :	Nominal energy [Wh]
$G$ :	Incident irradiance [W·m <sup>-2</sup> ]
$G(\lambda)$ :	Incident spectral irradiance [W·m <sup>-2</sup> ·nm <sup>-1</sup> ]
$G^*$ :	Incident irradiance at standard test conditions [1000 W·m <sup>-2</sup> ]
$G_{\text{AM1.5}}(\lambda)$ :	Incident spectral irradiance of the standard AM 1.5 G spectrum [W·m <sup>-2</sup> ·nm <sup>-1</sup> ]
$G_i$ :	The $i$ th measured value of the incident irradiance
$H$ :	Incident irradiation [Wh·m <sup>-2</sup> ]
$H_{\text{GM}}$ :	Incident irradiation for each grid mesh [Wh·m <sup>-2</sup> ]
$I$ :	Current [A]
$\text{IAM}(\theta_s)$ :	Incident angle modifier
$L_{\text{AOI}}$ :	Angle of incidence losses
$L_{P_{\text{CAL}}^* \neq P_{\text{NOM}}^*}$ :	Losses due to deviation of the calibrated peak power of a PV module from its nominal peak power
$L_{\text{Spec}}$ :	Spectral losses
$L_{T_{\text{mod}}}$ :	Temperature losses
$N$ :	Number of measured values (of incident irradiance or maximum power delivered by the PV module)
$P_{\text{CAL}}^*$ :	Calibrated peak power of a PV module [W].
$P_{\text{NOM}}^*$ :	Nominal peak power of a PV module (as provided by the manufacturer data sheets) [W]
$P_{\text{DC},i}$ :	The $i$ th measured value of the maximum power delivered by the PV module [W]
PR:	(Module) performance ratio
$\text{PR}_{\text{GM}}$ :	(Module) grid-mesh performance ratio
SF:	Spectral factor
$\text{SR}(\lambda)$ :	Relative spectral response
$T_{\text{amb}}$ :	Ambient temperature [°C]
$T_{\text{mod}}$ :	Module temperature [°C]
$T_{\text{mod}}^*$ :	Module temperature at STC [°C]
$T_{\text{mod},i}$ :	The $i$ th measured value of module temperature [°C]
$V$ :	Voltage [V]
$\gamma$ :	Module maximum power temperature coefficient [°C <sup>-1</sup> ]
$\delta$ :	Solar declination [°]
$\theta_s$ :	Angle of incidence between the rays of the sun and the normal to the surface [°]
$\Phi(\lambda)$ :	Incident spectral photon flux density [m <sup>-2</sup> ·nm <sup>-1</sup> ·s <sup>-1</sup> ]
$\omega$ :	True solar time [°].

## Acknowledgments

The authors would like to thank B. García-Domingo, F. Chenlo, J. Aguilera, M. Fuentes, and J. V. Muñoz for their

help. This work was supported by the Spanish Ministry of Education, Social Policy and Sports, within the frame of the Project under expedient code ENE200908302, the Spanish Science and Innovation Ministry and the ERDF within the frame of the Project under expedient code ENE2008-05098/ALT, and the Andalusian Research Plan within the Project under expedient code TEP- 5045M. One of the authors (M. Torres-Ramírez) greatly acknowledges *Fundación Iberdrola* for granting an “Energy for Research” Scholarship.

## References

- [1] A. Jäger-Waldau, “Research, solar cell production and market implementation of photovoltaics,” PV Status Report, European Commission, DG Joint Research Centre, Ispra, Italy, 2011.
- [2] A. Jäger-Waldau, “Thin film photovoltaics: markets and industry,” *International Journal of Photoenergy*, vol. 2012, Article ID 768368, 6 pages, 2012.
- [3] Fraunhofer Institute for Solar Energy Systems, “ISE photovoltaics report,” Tech. Rep., 2013, <http://www.ise.fraunhofer.de/en>.
- [4] G. L. Araujo and E. Sánchez, “Analytical expressions for the determination of the maximum power point and the fill factor of a solar cell,” *Solar Cells*, vol. 5, no. 4, pp. 377–386, 1982.
- [5] G. L. Araujo, E. Sánchez, and M. Martí, “Determination of the two-exponential solar cell equation parameters from empirical data,” *Solar Cells*, vol. 5, no. 2, pp. 199–204, 1982.
- [6] C. R. Osterwald, “Translation of device performance measurements to reference conditions,” *Solar Cells*, vol. 18, no. 3-4, pp. 269–279, 1986.
- [7] B. Kroposki, K. Emery, D. Myers, and L. Mrig, “A comparison of PV module performance evaluation methodologies for energy ratings,” in *Proceedings of the 1st World Conference on Photovoltaic Solar Energy Conversion*, pp. 858–862, Waikoloa, Hawaii, USA, December 1994.
- [8] B. Marion, “A method for modeling the current-voltage curve of a PV module for outdoor conditions,” *Progress in Photovoltaics*, vol. 10, no. 3, pp. 205–214, 2002.
- [9] B. Marion, S. Rummel, and A. Anderberg, “Current-voltage curve translation by bilinear interpolation,” *Progress in Photovoltaics*, vol. 12, no. 8, pp. 593–607, 2004.
- [10] M. Fuentes, G. Nofuentes, J. Aguilera, D. L. Talavera, and M. Castro, “Application and validation of algebraic methods to predict the behaviour of crystalline silicon PV modules in Mediterranean climates,” *Solar Energy*, vol. 81, no. 11, pp. 1396–1408, 2007.
- [11] W. Zhou, H. Yang, and Z. Fang, “A novel model for photovoltaic array performance prediction,” *Applied Energy*, vol. 84, no. 12, pp. 1187–1198, 2007.
- [12] F. Almonacid, C. Rus, L. Hontoria, M. Fuentes, and G. Nofuentes, “Characterisation of Si-crystalline PV modules by artificial neural networks,” *Renewable Energy*, vol. 34, no. 4, pp. 941–949, 2009.
- [13] A. Virtuani, H. Müllejans, and E. D. Dunlop, “Comparison of indoor and outdoor performance measurements of recent commercially available solar modules,” *Progress in Photovoltaics*, vol. 19, no. 1, pp. 11–20, 2011.
- [14] C. Cornaro and A. Andreotti, “Influence of Average Photon Energy index on solar irradiance characteristics and outdoor

- performance of photovoltaic modules,” *Progress in Photovoltaics*, vol. 21, no. 2, pp. 996–1003, 2013.
- [15] N. Martín and J. M. Ruiz, “A new method for the spectral characterization of PV modules,” *Progress in Photovoltaics*, vol. 7, no. 4, pp. 299–310, 1999.
- [16] K. H. Lam, J. Close, and W. Durisch, “Modelling and degradation study on a copper indium diselenide module,” *Solar Energy*, vol. 77, no. 1, pp. 121–127, 2004.
- [17] W. Durisch, B. Bitnar, J.-C. Mayor, H. Kiess, K.-H. Lam, and J. Close, “Efficiency model for photovoltaic modules and demonstration of its application to energy yield estimation,” *Solar Energy Materials and Solar Cells*, vol. 91, no. 1, pp. 79–84, 2007.
- [18] T. Minemoto, S. Nagae, and H. Takakura, “Impact of spectral irradiance distribution and temperature on the outdoor performance of amorphous Si photovoltaic modules,” *Solar Energy Materials and Solar Cells*, vol. 91, no. 10, pp. 919–923, 2007.
- [19] T. Minemoto, M. Toda, S. Nagae et al., “Effect of spectral irradiance distribution on the outdoor performance of amorphous Si//thin-film crystalline Si stacked photovoltaic modules,” *Solar Energy Materials and Solar Cells*, vol. 91, no. 2-3, pp. 120–122, 2007.
- [20] N. Katsumata, Y. Nakada, T. Minemoto, and H. Takakura, “Estimation of irradiance and outdoor performance of photovoltaic modules by meteorological data,” *Solar Energy Materials and Solar Cells*, vol. 95, no. 1, pp. 199–202, 2011.
- [21] T. Minemoto, S. Fukushige, and H. Takakura, “Difference in the outdoor performance of bulk and thin-film silicon-based photovoltaic modules,” *Solar Energy Materials and Solar Cells*, vol. 93, no. 6-7, pp. 1062–1065, 2009.
- [22] S. R. Williams, T. R. Betts, T. Helf, R. Gottschalg, H. G. Beyer, and D. G. Infield, “Modelling long-term module performance based on realistic reporting conditions with consideration to spectral effects,” in *Proceedings of the 3rd World Conference on Photovoltaic Energy Conversion*, pp. 1908–1911, Osaka, Japan, May 2003.
- [23] T. Minemoto, Y. Nakada, H. Takahashi, and H. Takakura, “Uniqueness verification of solar spectrum index of average photon energy for evaluating outdoor performance of photovoltaic modules,” *Solar Energy*, vol. 83, no. 8, pp. 1294–1299, 2009.
- [24] J. Tsutsui and K. Kurokawa, “Investigation to estimate the short circuit current by applying the solar spectrum,” *Progress in Photovoltaics*, vol. 16, no. 3, pp. 205–211, 2008.
- [25] T. Ishii, K. Otani, T. Takashima, and Y. Xue, “Solar spectral influence on the performance of photovoltaic (PV) modules under fine weather and cloudy weather conditions,” *Progress in Photovoltaics*, vol. 21, no. 4, pp. 481–489, 2013.
- [26] G. Nofuentes, M. Alonso-Abella, J. V. Muñoz et al., “Influence of spectral irradiance distribution and module temperature on the outdoor performance of some thin film PV module technologies,” in *Proceedings of the 26th European Photovoltaic Solar Energy Conference*, Hamburg, Germany, September 2011.
- [27] G. Nofuentes, B. García-Domingo, M. Fuentes et al., “Comparative analysis of the effects of spectrum and module temperature on the performance of thin film modules on different sites,” in *Proceedings of the 26th European Photovoltaic Solar Energy Conference*, Frankfurt, Germany, September 2012.
- [28] H. Wilk, “Electricity yield of PV systems in different climates and dependence of module efficiency as a function of irradiance and other factors,” in *Proceedings of the 14th European PV Solar Energy Conference*, Barcelona, Spain, July 1997.
- [29] A. Luque and S. Hegedus, *Handbook of PV Science and Engineering*, John Wiley & Sons, Chichester, UK, 2003.
- [30] G. Nofuentes, M. Fuentes, J. Aguilera, and J. V. Muñoz, “An assessment on simple modeling approaches to the electric behavior of two cis pv modules in a sunny climate,” *Journal of Solar Energy Engineering, Transactions of the ASME*, vol. 131, no. 3, Article ID 031013, 10 pages, 2009.
- [31] Y. Nakada, S. Fukushige, T. Minemoto, and H. Takakura, “Seasonal variation analysis of the outdoor performance of amorphous Si photovoltaic modules using the contour map,” *Solar Energy Materials and Solar Cells*, vol. 93, no. 3, pp. 334–337, 2009.
- [32] T. Minemoto, H. Takahashi, Y. Nakada, and H. Takakura, “Outdoor performance evaluation of photovoltaic modules using contour plots,” *Current Applied Physics*, vol. 10, no. 2, pp. S257–S260, 2010.
- [33] T. Ishii, K. Otani, and T. Takashima, “Effects of solar spectrum and module temperature on outdoor performance of photovoltaic modules in round-robin measurements in Japan,” *Progress in Photovoltaics*, vol. 19, no. 2, pp. 141–148, 2011.
- [34] S. Nann and C. Riordan, “Solar spectral irradiance under overcast skies,” in *Proceedings of the 21st IEEE Photovoltaic Specialist Conference*, pp. 1110–1115, Orlando, Fla, USA, May 1990.
- [35] F. Fabero and F. Chenlo, “Variance in the solar spectrum with the position of the receiver surface during the day for PV applications,” in *Proceedings of the 22nd IEEE Photovoltaic Specialist Conference*, pp. 812–817, Las Vegas, Nev, USA, October 1991.
- [36] A. Luque and S. Hegedus, *Handbook of PV Science and Engineering*, John Wiley & Sons, Chichester, UK, 2nd edition, 2011.
- [37] Standard ASHRAE 93-77, *Methods of Testing to Determine the Thermal Performance of Solar Collectors*, American Society of Heating, Refrigeration, and Air Conditioning Engineers, New York, NY, USA, 1977.
- [38] S. Nann and K. Emery, “Spectral effects on PV-device rating,” *Solar Energy Materials and Solar Cells*, vol. 27, no. 3, pp. 189–216, 1992.
- [39] E. E. Van Dyk, A. R. Gxasheka, and E. L. Meyer, “Monitoring current-voltage characteristics and energy output of silicon photovoltaic modules,” *Renewable Energy*, vol. 30, no. 3, pp. 399–411, 2005.
- [40] A. J. Carr and T. L. Pryor, “A comparison of the performance of different PV module types in temperate climates,” *Solar Energy*, vol. 76, no. 1–3, pp. 285–294, 2004.
- [41] E. E. van Dyk and E. L. Meyer, “Analysis of the effect of parasitic resistances on the performance of photovoltaic modules,” *Renewable Energy*, vol. 29, no. 3, pp. 333–344, 2004.

## Research Article

# Picosecond Photovoltaic Response in Tilted Lanthanum Doped Manganite Films

Zhiqing Lu,<sup>1</sup> Hao Ni,<sup>1</sup> Jianfeng Xi,<sup>1</sup> Xiaoming Li,<sup>2</sup> and Kun Zhao<sup>1</sup>

<sup>1</sup> College of Science, China University of Petroleum, Beijing 102249, China

<sup>2</sup> Department of Physics, The Chinese University of Hong Kong, Hong Kong

Correspondence should be addressed to Hao Ni; nihona@163.com

Received 24 January 2013; Revised 7 August 2013; Accepted 9 September 2013

Academic Editor: Bhushan Sopori

Copyright © 2013 Zhiqing Lu et al. This is an open access article distributed under the Creative Commons Attribution License, which permits unrestricted use, distribution, and reproduction in any medium, provided the original work is properly cited.

Anisotropic picosecond photovoltaic responses were observed in lanthanum doped manganite  $\text{La}_x\text{Ca}_{1-x}\text{MnO}_3$  ( $x = 0.67$  and  $0.4$ ) thin films, which were deposited on miscut  $\text{LaSrAlO}_4$  substrates under ultraviolet pulsed laser irradiation without external bias. The 10%–90% rise time and the full width at half maximum of  $\text{La}_{0.67}\text{Ca}_{0.33}\text{MnO}_3$  were 470 and 585 ps, respectively, and those of  $\text{La}_{0.4}\text{Ca}_{0.6}\text{MnO}_3$  were 220 and 515 ps. The photovoltage sensitivities of  $\text{La}_{0.67}\text{Ca}_{0.33}\text{MnO}_3$  and  $\text{La}_{0.4}\text{Ca}_{0.6}\text{MnO}_3$ , which are sensitive to the concentrations of lanthanum of the samples, are 0.28 V/mJ and 3.47 V/mJ, respectively. The photosensitivity in the films deposited on MgO is higher than that in those deposited on  $\text{LaSrAlO}_4$  substrates, for it has a big lattice mismatch. These results should open a route for the application of lanthanum doped manganite as an ultrafast photodetector material.

## 1. Introduction

Previously, the photovoltaic effect was reported in the perovskite-based p-n junctions, thin films, and single crystals [1–6]. The charge carriers of p-n junctions are separated by the electric field in the space charge region, and the photovoltage can be observed. However, as a typical photodetector structure, p-n junction detectors cannot normally have ultrafast responses, which would limit the applications in nanosecond and picosecond pulse laser detections. Recently, focus on tilted structures in lanthanide doped perovskite oxides which present ultrafast photoresponses and high sensitivities in photodetection [7–9]. Theoretical researches demonstrated that ultrafast photoresponse processes should be attributed to anisotropy diffusion and Seebeck effect. Researches also demonstrated that the concentrations of lanthanide of the samples could modulate the photoresponse signals in nanometer size domain tilted thin films, which indicate a new type nanometer scale photosensitive source.

In the present study, we deposited different concentrations of lanthanum doped manganite thin films,  $\text{La}_{0.67}\text{Ca}_{0.33}\text{MnO}_3$  (LCMO1) and  $\text{La}_{0.4}\text{Ca}_{0.6}\text{MnO}_3$  (LCMO2), on miscut  $\text{LaSrAlO}_4$  (LSAO) substrates, and observed picosecond ultraviolet (UV) photovoltaic effect under pulsed laser irradiations

without external bias. The photoresponse signals are sensitive to the measurement circuit input impedance. A small paralleling resistance with thin film can effectively improve the response speed. When the  $\text{La}_x\text{Ca}_{1-x}\text{MnO}_3$  (LCMO) thin film is connected in parallel with a  $0.5\ \Omega$  resistance, the 10%–90% rise time (RT) and the full width at half maximum (FWHM) decrease to 470 ps and 585 ps for LCMO1, and 220 ps and 515 ps for LCMO2. The voltage sensitivities can reach 0.28 V/mJ for LCMO1 and 3.47 V/mJ for LCMO2, respectively. Correspondingly, the current sensitivities are 0.21 A/mJ for LCMO1 and 3.44 A/mJ for LCMO2. The comparative experiments on LCMO film deposited on miscut MgO substrates prove that the photo sensitivity is higher in a big lattice mismatch system. All these experimental results reveal that the lanthanum doped manganite films on miscut substrates can be used as ultrafast photodetective materials.

## 2. Experimental

The 100 nm thick LCMO thin films were deposited on miscut LSAO substrates with (001)<sub>LSAO</sub> plane tilted to the surface wafer at an angle  $\alpha$  of  $10^\circ$  by facing-target sputtering technique from stoichiometry targets [10]. During the deposition, the substrates were kept at  $680^\circ\text{C}$ , with oxygen partial pressure of

30 mTorr. The film thickness, controlled by sputtering time with the deposition rate, is 100 nm. After the deposition, the vacuum chamber was immediately backfilled with 1 atm oxygen gas to improve the oxygen stoichiometry. X-ray diffraction (XRD) was adopted to characterize the structure of the as-deposited products.

For the photovoltaic measurements, two Ag electrodes ( $1 \times 5 \text{ mm}^2$  in size) separated by 3 mm were prepared on the surface of the LCMO, as shown in Figure 2(b). Electrodes "A" and "B" are parallel to the tilted direction, while "C" and "D" are perpendicular to the tilted direction. Thus, the photovoltage of the "AB" and "CD" can be investigated and characterized, and  $V_{AB}$  and  $V_{CD}$  can represent the photovoltage of tilted direction and untilted direction, respectively. The third harmonic of an actively and passively mode-locked Nd: yttrium-aluminum-garnet laser was used as the source at room temperature. The laser was operated at the wavelength of 355 nm (3.49 eV photon energy) with 25 ps duration at 10 Hz repetition rate, and the energy density was  $0.0127 \text{ mJ/mm}^2$ . Thus, the on-sample energy was 0.435 mJ. The photovoltaic signals were monitored by a Tektronix sampling oscilloscope with a 2.5 GHz bandwidth terminated into  $1 \text{ M}\Omega$  and  $50 \Omega$ .

### 3. Results and Discussion

The microstructure of LCMO/LSAO sample with different lanthanum component was checked with X-ray diffraction (XRD)  $\theta$ - $2\theta$  scan as shown in Figure 1(a), where the [001] axis was aligned carefully and the offset point was set by  $10^\circ$  to satisfy Bragg's diffraction. Except for the (00 $l$ ) LSAO substrate and the ( $h0h$ ) LCMO film reflections, there was no diffraction peak from impurity phase or randomly oriented grain, indicating the epitaxial growth of the sample. In LCMO thin epitaxial film, the decrease of lanthanum component led to a consequence of lattice contraction due to the transition from  $\text{Mn}^{3+}$  to  $\text{Mn}^{4+}$ . Therefore, the diffraction peak moved to a higher angle.

The linear current-voltage ( $I$ - $V$ ) characteristics, shown in Figure 2(a), of the LCMO films indicated ohmic contacts between the films and Ag electrodes. And the resistivity of the LCMO1 film is larger than that of the LCMO2 film. The open-circuit photovoltaic pulses between the two electrodes which were painted on the surface of the LCMO were observed without any applied bias when the LCMO surfaces were irradiated by the pulse laser directly. Figure 3 shows typical photovoltaic responses of LCMO thin films along the tilted direction, recorded by the oscilloscope terminated into  $1 \text{ M}\Omega$  and  $50 \Omega$ . When the impedance of the oscilloscope was set as  $1 \text{ M}\Omega$ , the peak voltages  $V^P$  was 0.053 V for the LCMO1 and 0.661 V for the LCMO2, respectively. However, it should be noted that the responses are composed of a fast rise time, several oscillations, and a slow decay. The RC constant in the circuit and the impedance mismatch should be responsible for these phenomena. In order to reduce the influence of the RC effect in the measurement, we changed the import impedance of the oscilloscope from  $1 \text{ M}\Omega$  to  $50 \Omega$ . As shown in Figure 3, the RT and the FWHM decreased to 870 ps and 2435 ps for the LCMO1, and 278 ps and 1624 ps for

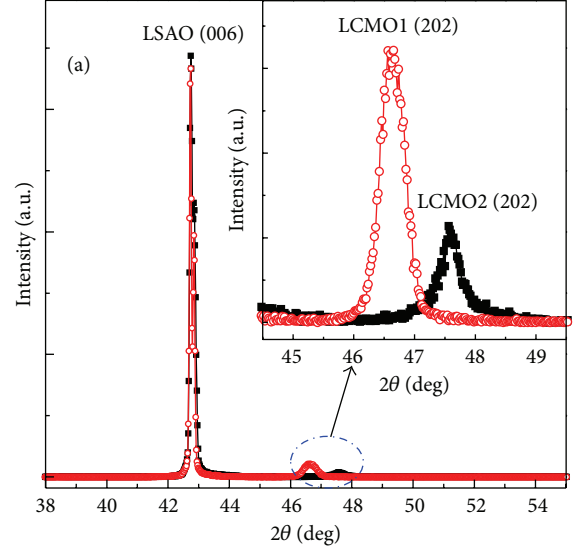


FIGURE 1: XRD patterns of LCMO films on miscut LSAO substrates. The inset shows the details of the LCMO peaks. Except for the (00 $l$ ) LSAO substrate and the ( $h0h$ ) LCMO film reflections, there was no diffraction peak.

the LCMO2. In addition, a  $0.5 \Omega$  resistance was connected in parallel with the LCMO thin film, and the RT and the FWHM are 470 ps and 585 ps for LCMO1, and 220 ps and 515 ps for LCMO2, indicating that the photovoltaic response of the LCMO thin film is a picosecond process.

The anisotropic photoelectric effect was systematically investigated along the tilted direction and untilted direction. And the waveforms which were recorded by the oscilloscope with the input impedance of  $50 \Omega$  were shown in Figures 3 and 4. For the titled direction, the peak photovoltage  $V_{AB}^P$  in LCMO1, which is exhibited in Figure 3(a), is 0.0294 V when the film surface was irradiated directly. At the untilted direction,  $V_{CD}^P$  (shown in Figure 4(a)) in LCMO1 is 0.002 V, which is 14 times smaller than  $V_{AB}^P$ . In LCMO2, the peak photovoltages  $V_{AB}^P$  and  $V_{CD}^P$  are 0.542 V and 0.0308 V, respectively, shown in Figures 3(b) and 4(b). It is noteworthy that the photovoltaic response was reversed when the LSAO substrate was irradiated. Therefore, the whole photoresponse process can be understood as follows. The ultrafast laser pulses irradiated the LCMO film surface uniformly and generated photoinduced charge carriers (electron and hole pairs) with gradient distribution ( $dn_i/dz$ ) perpendicular to the film surface [9]. Due to anisotropy and the large ratio of  $\rho_{[10\bar{1}]}/\rho_{[101]}$ , the diffusion current along  $[10\bar{1}]$  axis is much larger than that along the  $[101]$  axis. In carriers' diffusion process, the mobility of electrons is much larger than that of holes ( $\mu_n - \mu_p > 0$ ), and electron-hole pairs were separated and generated the diffusion current density

$$J_y \approx J_{[10\bar{1}]} \cos \alpha \approx k_0 T \Delta \mu_{[10\bar{1}]} \sin 2\alpha \frac{(dn_i/dz)}{2}. \quad (1)$$

From Figure 3, we can deduce that the voltage sensitivities are 0.28 V/mJ for tilting LCMO1 and 3.47 V/mJ for tilting

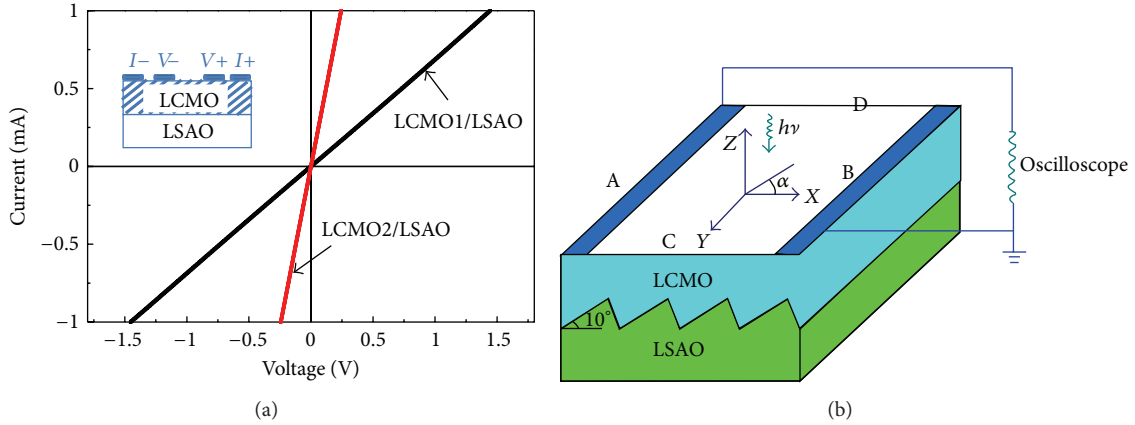


FIGURE 2: (a)  $I$ - $V$  characteristics of the LCMO1 and LCMO2 films along tilted directions (AB) at room temperature. (b) Schematic illustration of the samples, electrodes structure, and the circuit of the measurements. Electrodes A and B are along the tilted direction ( $x$  is the “tilted direction” of the film) and electrodes C and D are along the untilted direction ( $y$  is the “untilted direction” of the film).

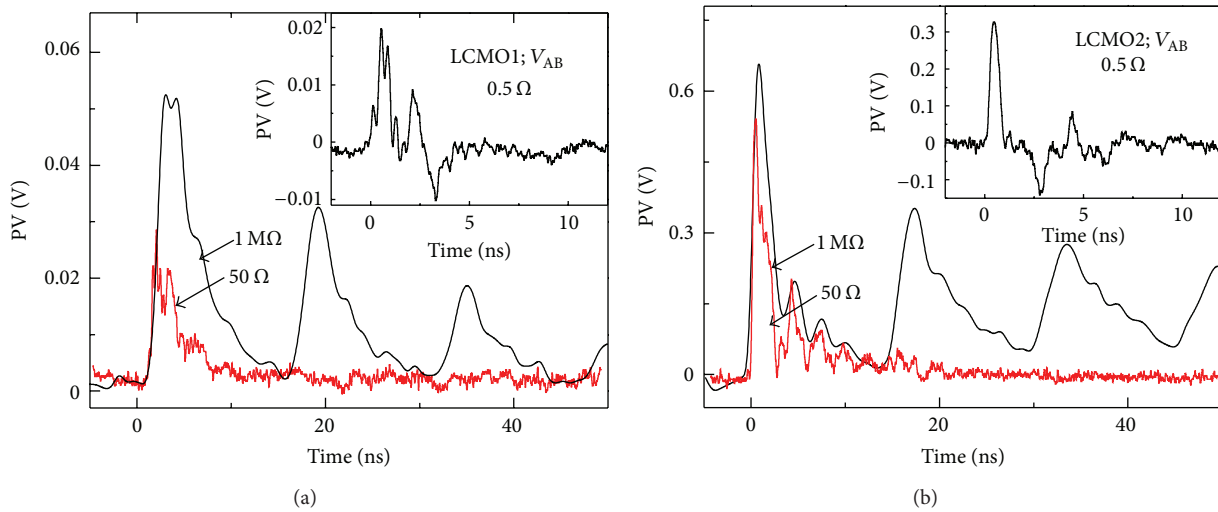


FIGURE 3: Photovoltaic response of (a) LCMO1 film and (b) LCMO2 film, under the illumination of a 355 nm laser pulse in duration of 25 ps along the tilted direction, recorded by an oscilloscope terminated into 1 M $\Omega$  and 50  $\Omega$ . The inset shows the photovoltaic response with a 0.5  $\Omega$  resistance which was connected in parallel with the LCMO thin film.

LCMO2. Similarly, we can get the current sensitivities which are 0.21 A/mJ for tilting LCMO1 and 3.44 A/mJ for tilting LCMO2. These experimental results show that the photoinduced voltage effect in the tilting LCMO films is not only an ultrafast process but also highly sensitive to the UV laser pulse. The photosensitivity of LCMO2 was higher than that of LCMO1. In further study, we also deposited LCMO1 and LCMO2 films on miscut MgO substrates (at a tilt angle of 10°) and observed the ultrafast photovoltaic responses in LCMO/MgO samples [9]. All the experiment conditions were the same as before. We can see clearly that the photosensitivity in LCMO2/MgO was higher than that in LCMO1/MgO. And the LCMO films on MgO substrates showed much higher photosensitivity than the same component content LCMO films on LSAO substrates.

To understand the mechanism, high resolution transmission electron microscope (HRTEM) analysis of the interface of the LCMO/LSAO and LCMO/MgO has been done. From

the images by HRTEM, we can clearly see that there is a good epitaxial growth in the LCMO/LSAO sample, due to the small lattice mismatch [11]. However, there exist a lot of dislocations and domains in LCMO/MgO, due to the larger lattice mismatch. Dislocations and domain boundaries consist of a lot of dangling bonds, which can create a lot of carriers under UV irradiation. Thus, LCMO deposited on MgO substrates with large lattice mismatch shows higher photovoltaic sensitivity.

#### 4. Conclusion

In summary, we deposited lanthanum doped manganite thin films on miscut LSAO substrates and observed anisotropic picosecond UV photovoltaic responses under pulsed laser irradiation without external bias. A 0.5  $\Omega$  resistance was connected in parallel with the La<sub>1-x</sub>Ca<sub>x</sub>MnO<sub>3</sub> (LCMO) thin film. And the RT and the FWHM decreased to 470 ps and 585 ps for LCMO1, and 220 ps and 515 ps for LCMO2. The voltage

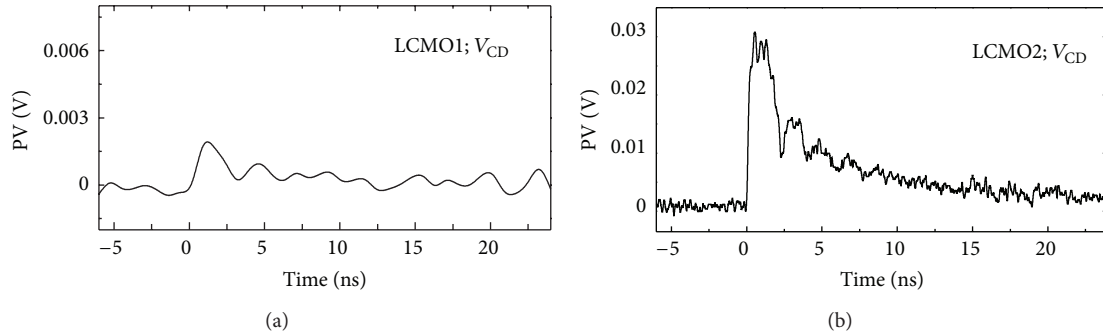


FIGURE 4: Photovoltaic responses of (a) the LCMO1 film (b) the LCMO2 film, under the illumination of a 355 nm laser pulse along the untilted direction ( $V_{CD}$ ), recorded by the oscilloscope terminated into  $50 \Omega$ .

sensitivities reached  $0.28 \text{ V/mJ}$  for LCMO1 and  $3.47 \text{ V/mJ}$  for LCMO2. The current sensitivities are  $0.21 \text{ A/mJ}$  for LCMO1 and  $3.44 \text{ A/mJ}$  for LCMO2. From the above experiments, we can see several significant characteristics of the photovoltaic effect of the lanthanum doped manganite thin film: (I) the photovoltage along the tilted direction ( $V_{AB}^P$ ) is larger than that along the untilted direction ( $V_{CD}^P$ ); (II) the peak value of photoresponse in LCMO2 is higher than that in LCMO1; (III) the photosensitivity in LCMO films deposited on MgO is higher than that deposited on LSAO substrates, for the LCMO films deposited on MgO have a big lattice mismatch. These results should carve out a new way for the application of LCMO as an ultrafast photodetector material.

## Acknowledgments

This paper has been supported by National Key Basic Research Program of China (2013CB328706), special-funded program on national key scientific instruments and equipment development (2012YQ14005), Beijing National Science Foundation (4122064), and Science Foundation of China University of Petroleum (Beijing) (QZDX-2010-01 and KYJJ2012-06-27). The authors express their thanks for the samples prepared by Professor. Hong-Kuen Wong and Mr. Yu-Chau Kong in The Chinese University of Hong Kong.

## References

- [1] Y. G. Zhao, J. J. Li, R. Shreekala et al., "Ultrafast laser induced conductive and resistive transients in  $\text{La}_{0.7}\text{Ca}_{0.3}\text{MnO}_3$ : charge transfer and relaxation dynamics," *Physical Review Letters*, vol. 81, no. 6, pp. 1310–1313, 1998.
- [2] M. Rajeswari, C. H. Chen, A. Goyal et al., "Low-frequency optical response in epitaxial thin films of  $\text{La}_{0.67}\text{Ca}_{0.33}\text{MnO}_3$  exhibiting colossal magnetoresistance," *Applied Physics Letters*, vol. 68, no. 25, pp. 3555–3557, 1996.
- [3] J. R. Sun, C. M. Xiong, B. G. Shen, P. Y. Wang, and Y. X. Weng, "Manganite-based heterojunction and its photovoltaic effects," *Applied Physics Letters*, vol. 84, no. 14, pp. 2611–2613, 2004.
- [4] H.-B. Lu, K.-J. Jin, Y.-H. Huang et al., "Picosecond photoelectric characteristic in  $\text{La}_{0.7}\text{Sr}_{0.3}\text{MnO}_3/\text{Si}$  p-n junctions," *Applied Physics Letters*, vol. 86, no. 24, Article ID 241915, 3 pages, 2005.
- [5] H. Katsu, H. Tanaka, and T. Kawai, "Photocarrier injection effect on double exchange ferromagnetism in  $(\text{La,Sr})\text{MnO}_3/\text{SrTiO}_3$  heterostructure," *Applied Physics Letters*, vol. 76, no. 22, pp. 3245–3247, 2000.
- [6] H.-U. Habermeyer, X. H. Li, P. X. Zhang, and B. Leibold, "Anisotropy of thermoelectric properties in  $\text{La}_{2/3}\text{Ca}_{1/3}\text{MnO}_3$  thin films studied by laser-induced transient voltages," *Solid State Communications*, vol. 110, no. 9, pp. 473–478, 1999.
- [7] K. Zhao, K.-J. Jin, H. Lu et al., "Transient lateral photovoltaic effect in p-n heterojunctions of  $\text{La}_{0.7}\text{Sr}_{0.3}\text{MnO}_3$  and Si," *Applied Physics Letters*, vol. 88, no. 14, Article ID 141914, 2006.
- [8] H. Ni, D. Yu, K. Zhao et al., "Oxygen content dependence of the photovoltaic characteristic of miscut manganite thin films," *Journal of Applied Physics*, vol. 110, no. 3, Article ID 033112, 2001.
- [9] H. Ni, K. Zhao, K. J. Jin et al., "Nano-domain orientation modulation of photoresponse based on anisotropic transport in manganite films," *Europhysics Letters*, vol. 97, no. 4, Article ID 46005, 2012.
- [10] X. T. Zeng and H. K. Wong, "Epitaxial growth of single-crystal  $(\text{La, Ca})\text{MnO}_3$  thin films," *Applied Physics Letters*, vol. 66, no. 24, pp. 3371–3373, 1995.
- [11] X. M. Li, K. Zhao, H. Ni et al., "Voltage tunable photodetecting properties of  $\text{La}_{0.4}\text{Ca}_{0.6}\text{MnO}_3$  films grown on miscut  $\text{LaSrAlO}_4$  substrates," *Applied Physics Letters*, vol. 97, no. 4, Article ID 044104, 2010.

## Research Article

# Research on the Comparison Analyses of Three-Phase Discrete and Integrated LC Filters in Three-Phase PV Inverter

Ying Jiang,<sup>1</sup> Jianguo Li,<sup>1</sup> Sanbo Pan,<sup>1</sup> Xi Zhang,<sup>2</sup> Peng Hu,<sup>1</sup> and Haiyan Zhang<sup>1</sup>

<sup>1</sup> College of Electrical Engineering, Shanghai Dianji University, Shanghai 200240, China

<sup>2</sup> College of Mechanical Engineering, Shanghai Jiao Tong University, Shanghai 200240, China

Correspondence should be addressed to Ying Jiang; [abjiangying@gmail.com](mailto:abjiangying@gmail.com)

Received 25 January 2013; Revised 25 June 2013; Accepted 11 July 2013

Academic Editor: Keith Emery

Copyright © 2013 Ying Jiang et al. This is an open access article distributed under the Creative Commons Attribution License, which permits unrestricted use, distribution, and reproduction in any medium, provided the original work is properly cited.

In three-phase photovoltaic (PV) system, three-phase filter inductors are important part for the output electrical power quality. The comparison analyses of three-phase discrete filter inductors and two kinds of three-phase integrated filter inductors in three-phase PV inverter are proposed. Firstly, the three-phase PV inverter operation with discrete filter inductors is analyzed, and the design of discrete filter inductors is given; then operation of the three-phase PV inverter with three-phase integrated five-limb magnetic core filter inductors is analyzed, the design of integrated filter inductors with five-limb magnetic core is given, then the operation of three-phase PV inverter with three-phase integrated three-limb magnetic core filter inductors is analyzed, and the design of integrated filter inductors with three limbs magnetic core is given. The conclusion of comparison between three-phase discrete filter inductors and two kinds of three-phase integrated filter inductors is done; it means that the three-phase discrete filter inductors can achieve better output electrical power quality with lower power density and three-phase integrated filter inductors can achieve higher power density with lower output electrical power quality. Finally, the experiment results are given to compare the volume and filter effect of three kinds of filter inductors in three-phase PV inverter.

## 1. Introduction

Photovoltaic (PV) system is becoming increasingly more interesting among all renewable energy [1–4]. Three-phase inverter is widely used in PV system, and the output electrical power quality is a very important part for the inverter no matter for the grid or the local load [5–7]. In order to achieve better output electrical power quality, the switching harmonics generated by the power inverters must be properly filtered out reaching a compromise between the cost and the weight of the filter and a fulfillment of international standards. Therefore, the PV inverter requires an output low-pass filter to interface with the grid or local load. Nowadays, L filter, LC filter, and LCL filter are widely used in PV system [8–10]. For L filter, a single inductor L filter is popular and simple to use. Due to causing a long-time response, the system dynamics is poor, but the L filter has the lowest cost among the three filters. The LC filter is very commonly used with most applications, and its output electrical power quality is better than L filter. For LCL filter, it has the best output

electrical power quality, but the stability of the system may be compromised by the resonances of the LCL filter, so that several authors have recently studied these issues [11–13]. For example, in [14–16] some control techniques to actively damp the resonances of the filter have been presented.

The demands for PV inverter are not only the good electrical performance but also the high power density, high reliability, and low cost. Among the L filter, LC filter, and LCL filter, most papers pay attention to the electrical performance, and most applications are the single phase PV inverter [17–21]. There are seldom papers of filters about the combination of the electrical performance and the power density, especially in the three-phase PV inverter. However, the three-phase filters are very important factor for the electrical performance, power density, and cost. Therefore, this paper takes the most used LC filter, for example, to research the relation between the output electrical power quality and the volume of three-phase inductors with discrete magnetic core and integrated magnetic core in three-phase PV inverter.

In this paper, the comparison analyses of three-phase discrete filter inductors and two kinds of three-phase integrated filter inductors of LC filter in three-phase PV inverter are proposed, and the design of three-phase is analyzed including the method how to integrate the three-phase filter inductors into five-limb magnetic core and three-limb magnetic core. The main works are done as below: according to the volume of filter inductor from large to small, the operation of three-phase PV inverter with discrete magnetic filter inductor is analyzed firstly, and the design of magnetic core is given; then according to the deduced mathematic expression formula of filter inductor with five-limb magnetic core, the operation of three-phase PV inverter with five-limb magnetic core filter inductor is analyzed, and the design of inductance and magnetic core is given, and then according to the deduced mathematic expression formula of filter inductor with three-limb magnetic core, the operation of three-phase PV inverter with three-limb magnetic core filter inductor is analyzed, and the design of inductance and magnetic core is given. Finally, the experiment results are given to compare the volume and filter effect of three kinds of filter inductors.

## 2. The Three-Phase Discrete Filter Inductors in Three-Phase Inverter

*2.1. The Operational Principle of Three-Phase Discrete Filter Inductors in Three-Phase LC Filter.* The three-phase discrete filter inductors in three-phase inverter are shown in Figure 1. Every filter inductor has its own magnetic core. Therefore, the volumes of inductors are large and the costs are high. Before the analyses, several assumptions are made as follows:

- (1) the input voltage source is  $V_{in}$  which come from the PV panel;
- (2) switches  $Q_{1-6}$  are ideal, diode  $D_{1-6}$  is the antiparallel diode of  $Q_{1-6}$ , and the voltages  $V_a$ ,  $V_b$ , and  $V_c$  are the output voltage of three bridge arms;
- (3)  $L_{f1}$ ,  $L_{f2}$ , and  $L_{f3}$  are three filter inductors,  $C_1$ ,  $C_2$ , and  $C_3$  are three filter capacitors, and  $V_{Lf1}$ ,  $V_{Lf2}$ , and  $V_{Lf3}$  are voltages of three inductors;
- (4)  $R_a$ ,  $R_b$ , and  $R_c$  are three-phase resistance load,  $e_a$ ,  $e_b$ , and  $e_c$  are three-phase voltage,  $i_a$ ,  $i_b$ , and  $i_c$  are three-phase current, and  $e_o$  is the voltage of the three-phase load neutral point;
- (5) the switch signals can be defined as follows:

$$\begin{aligned} S_a &= \begin{cases} 1 & Q_1 \text{ is turned on, } Q_4 \text{ is turned off;} \\ 0 & Q_4 \text{ is turned on, } Q_1 \text{ is turned off;} \end{cases} \\ S_b &= \begin{cases} 1 & Q_3 \text{ is turned on, } Q_6 \text{ is turned off;} \\ 0 & Q_6 \text{ is turned on, } Q_3 \text{ is turned off;} \end{cases} \\ S_c &= \begin{cases} 1 & Q_5 \text{ is turned on, } Q_2 \text{ is turned off;} \\ 0 & Q_2 \text{ is turned on, } Q_5 \text{ is turned off.} \end{cases} \end{aligned} \quad (1)$$

According to Figure 1,  $V_{Lf1}$ ,  $V_{Lf2}$ , and  $V_{Lf3}$  can be described as follows:

$$\begin{aligned} V_{Lf1} &= V_a - e_a - e_o = L_{f1} \frac{di_a}{dt}, \\ V_{Lf2} &= V_b - e_b - e_o = L_{f2} \frac{di_b}{dt}, \\ V_{Lf3} &= V_c - e_c - e_o = L_{f3} \frac{di_c}{dt}. \end{aligned} \quad (2)$$

In three-phase system, the amplitude of current and voltage of every phase are the same, and the  $120^\circ$  phase difference between every two phase, and then it can be got as

$$\begin{aligned} e_a + e_b + e_c &= 0, \\ i_a + i_b + i_c &= 0. \end{aligned} \quad (3)$$

According to (2) and (3), neutral point voltage  $e_o$  can be got as follows:

$$e_o = \frac{V_a + V_b + V_c}{3}. \quad (4)$$

Also,  $V_a$ ,  $V_b$ , and  $V_c$  can be described as follows:

$$\begin{aligned} V_a &= S_a V_{in}, \\ V_b &= S_b V_{in}, \\ V_c &= S_c V_{in}. \end{aligned} \quad (5)$$

Therefore, finally  $V_{Lf1}$ ,  $V_{Lf2}$ , and  $V_{Lf3}$  can be simplified as follows:

$$\begin{aligned} V_{Lf1} &= L_{f1} \frac{di_a}{dt} = \frac{2S_a - S_b - S_c}{3} V_{in} - e_a, \\ V_{Lf2} &= L_{f2} \frac{di_b}{dt} = \frac{2S_b - S_a - S_c}{3} V_{in} - e_b, \\ V_{Lf3} &= L_{f3} \frac{di_c}{dt} = \frac{2S_c - S_a - S_b}{3} V_{in} - e_c. \end{aligned} \quad (6)$$

The above formula is the basic expression of three-phase discrete inductors. The main functions of three-phase inductors are to reduce the harmonic by limiting the ripple current.

*2.2. The SPWM Control Method of Three-Phase Inverter.* In this paper, the sine-wave pulse-width modulation (SPWM) control method is adopted. The SPWM control method is widely used in the inverter due to its simple and easy realizing, and it is has been a mature technology. Though there are some advantaged control methods such as space voltage vector pulse-width modulation (SVPWM), the SPWM control method is enough to verify the basic function of LC filter, and the SPWM control method is shown in Figure 2. Through the comparison between the high frequency triangular wave signal  $u_o$  and three-phase line frequency sine wave signal  $u_{ga}$ ,  $u_{gb}$ , and  $u_{gc}$ , the control signals  $u_{Q1-6}$  for switches  $Q_{1-6}$  are got.

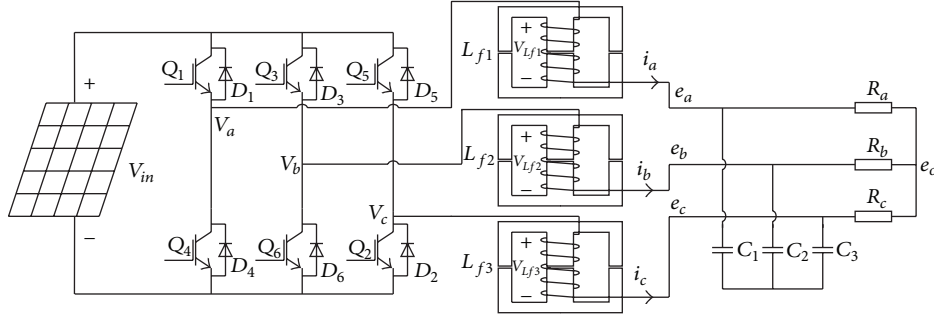


FIGURE 1: The three-phase discrete filter inductors in three-phase inverter.

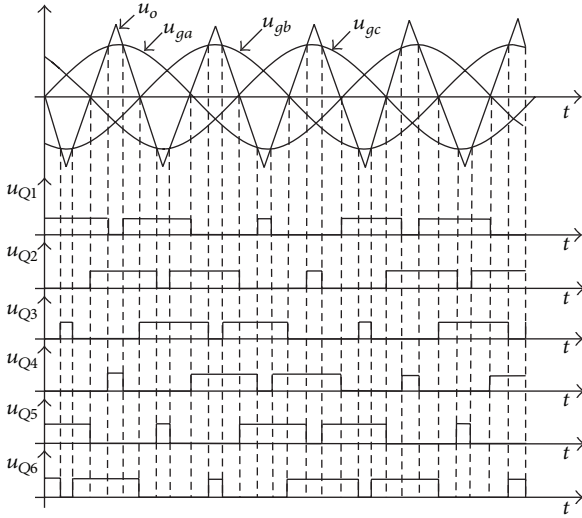


FIGURE 2: The three-phase SPWM control method.

**2.3. The Ripple Current of Three-Phase Discrete Filter Inductors.** In order to get better output electrical power quality, smaller ripple current of inductor should be achieved. Besides, the ripple current also decides the volume and the value of inductor. Therefore, the ripple current of filter inductor is an important parameter.

According to (6), take the ripple current of  $L_{f1}$ , for example, to analyze, it can be got that

$$V_{L_{f1}} = L_{f1} \frac{\Delta i_a}{\Delta t} = \frac{2S_a - S_b - S_c}{3} V_{dc} - e_a \quad (7)$$

$\Delta i_a$  is the ripple current of  $L_{f1}$ , and it can be got as follows:

$$\Delta i_a = \left( \frac{2S_a - S_b - S_c}{3} V_{dc} - e_a \right) \frac{D_{on} T}{L_{f1}}, \quad (8)$$

where  $T$  is cycle and  $D_{on}$  is duty cycle when the ripple current increases. Since the current ripple directly decides the harmonic, the ripple current  $\Delta i_a$  is always selected as the (10–20)% of the max value of  $i_a$ . Based on the selected ripple current  $\Delta i_a$ , the value of inductor  $L_{f1}$  can also be selected. Since the three-phase inductors have three discrete magnetic cores, every inductor does not affect each other; then the

demanded filter effect can be achieved and the design of inductor is not very complicated. The three-phase discrete inductors can achieve wide application, but the volume, weight, and cost are their disadvantage.

**2.4. The Max Flux Density of Discrete Filter Inductors.** In order to design the magnetic core of the discrete filter inductor, the flux density should be analyzed. Take the  $L_{f1}$  for example, to analyze, and the other  $L_{f2}$  and  $L_{f3}$  have the same analyzed method. The  $L_{f1}$  filter inductor with magnetic core is shown in Figure 3(a).  $\phi_a$  is the flux generated by  $L_{f1}$  winding;  $\mathfrak{R}_{01}$  are the magnetic resistance of the middle limb, and  $\mathfrak{R}_{02}$  are the magnetic resistance of the other two limbs;  $N_{L_{f1}}$  is the number of turns of  $L_{f1}$  winding. According to the magnetic circuit which is shown in Figure 3(b),  $\phi_a$  can be described as follows:

$$\phi_a = \frac{N_{L_{f1}} i_a}{\mathfrak{R}_{01} + \mathfrak{R}_{02} // \mathfrak{R}_{02}} = \frac{2N_{L_{f1}} i_a}{2\mathfrak{R}_{01} + \mathfrak{R}_{02}}. \quad (9)$$

Therefore, the voltage of inductors  $V_{L_{f1}}$  can be described as follows:

$$V_{L_{f1}} = N_{L_{f1}} \frac{d\phi_a}{dt}. \quad (10)$$

According to (10),  $V_{L_{f1}}$  can be described as follows:

$$V_{L_{f1}} = L_{f1} \frac{di_a}{dt}, \quad (11)$$

where  $L_{f1}$  is self-inductor and can be described as follows:

$$L_{f1} = \frac{2N_{L_{f1}}^2}{2\mathfrak{R}_{01} + \mathfrak{R}_{02}}. \quad (12)$$

The magnetic resistance can be got as follows:

$$\mathfrak{R}_{0i} = \frac{l_{gi}}{\mu_0 A_i}, \quad i = 1, 2, \quad (13)$$

where  $l_{gi}$  and  $A_i$  are, respectively, the air gap and cross section area of  $\mathfrak{R}_{0i}$ ,  $\mu_0$  is air permeability, and for the EE type magnetic core, the cross section area of middle limb is two times of that of the other two limbs. Then, when make the air gap of three limbs are the same, it can be got that  $2\mathfrak{R}_{01} = \mathfrak{R}_{02}$ .

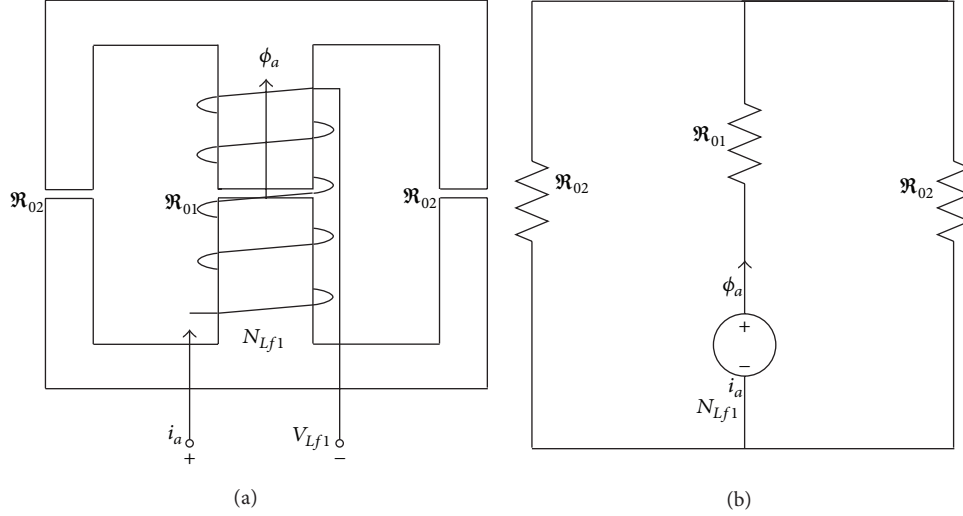


FIGURE 3: Three-phase discrete inductor: (a) magnetic core, (b) magnetic circuit.

The three-phase current  $i_a$  can be described as follows:

$$i_a = \sqrt{2}I_m \sin(\omega t), \quad (14)$$

where  $I_m$  is the effective value of current.

Therefore, when  $\phi_a$  achieves its max value  $\phi_{a\max}$ , the max flux density  $B_{a\max}$  of middle limb can be described as follows:

$$B_{a\max} = \frac{\phi_{a\max}}{A_2} = \frac{L_{f1} \sqrt{2}I_m}{A_2 N_{Lf1}} = \frac{\sqrt{2}I_m N_{Lf1} \mu_0}{l_{g2}}. \quad (15)$$

Then, the magnetic core can be selected according to the  $B_{a\max}$ .

### 3. The Three-Phase Integrated Filter Inductors with One Five-Limb Magnetic Core in Three-Phase Inverter

The three-phase integrated filter inductors with one five-limb magnetic core in three-phase inverter are shown in Figure 4. The three filter inductors have one magnetic core with five limbs, and the magnetic core consists of two EE magnetic cores. The three filter inductors are on the middle three limbs, and the cross section area of three middle limbs is twice than that of the other two limbs.

**3.1. The Expression of Three-Phase Integrated Filter Inductors with Five Magnetic Limbs.** The three-phase integrated filter inductors with five magnetic limbs are shown in Figure 5(a).  $\phi_a$ ,  $\phi_b$ , and  $\phi_c$  are, respectively, the fluxes generated by  $L_{f1}$  winding,  $L_{f2}$  winding, and  $L_{f3}$  winding;  $\mathfrak{R}_{01}$  are the magnetic resistance of three middle limbs, and  $\mathfrak{R}_{02}$  are the magnetic resistance of the other two limbs;  $N_{Lf1}$ ,  $N_{Lf2}$ , and  $N_{Lf3}$  are, respectively, the number of turns of  $L_{f1}$  winding,  $L_{f2}$  winding, and  $L_{f3}$  winding. According to the magnetic circuit which is shown in Figure 5(b),  $\phi_a$  is the flux generated by  $L_{f1}$  winding,  $\phi_{ab}$  is the flux generated by  $L_{f1}$  winding flows through  $L_{f2}$  winding, and  $\phi_{ac}$  is the flux generated by

$L_{f1}$  winding flows through  $L_{f3}$  winding, and they can be described as follows:

$$\begin{aligned} \phi_a &= \frac{N_{Lf1} i_a}{\mathfrak{R}_{01} + \mathfrak{R}_{01} // \mathfrak{R}_{01} // \mathfrak{R}_{02} // \mathfrak{R}_{02}} = \frac{2N_{Lf1} i_a (\mathfrak{R}_{01} + \mathfrak{R}_{02})}{2\mathfrak{R}_{01}^2 + 3\mathfrak{R}_{01} \mathfrak{R}_{02}}, \\ \phi_{ab} = \phi_{ac} &= \frac{2N_{Lf1} i_a (\mathfrak{R}_{01} + \mathfrak{R}_{02})}{2\mathfrak{R}_{01}^2 + 3\mathfrak{R}_{01} \mathfrak{R}_{02}} \frac{\mathfrak{R}_{02}}{2(\mathfrak{R}_{01} + \mathfrak{R}_{02})} \\ &= \frac{N_{Lf1} i_a \mathfrak{R}_{02}}{2\mathfrak{R}_{01}^2 + 3\mathfrak{R}_{01} \mathfrak{R}_{02}} \end{aligned} \quad (16)$$

$\phi_b$  is the flux generated by  $L_{f2}$  winding,  $\phi_{ba}$  is the flux generated by  $L_{f2}$  winding flows through  $L_{f1}$  winding, and  $\phi_{bc}$  is the flux generated by  $L_{f2}$  winding flows through  $L_{f3}$  winding, and they can be described as follows:

$$\begin{aligned} \phi_b &= \frac{N_{Lf2} i_b}{\mathfrak{R}_{01} + \mathfrak{R}_{01} // \mathfrak{R}_{01} // \mathfrak{R}_{02} // \mathfrak{R}_{02}} \\ &= \frac{2N_{Lf2} i_b (\mathfrak{R}_{01} + \mathfrak{R}_{02})}{2\mathfrak{R}_{01}^2 + 3\mathfrak{R}_{01} \mathfrak{R}_{02}}, \\ \phi_{ba} = \phi_{bc} &= \frac{2N_{Lf2} i_b (\mathfrak{R}_{01} + \mathfrak{R}_{02})}{2\mathfrak{R}_{01}^2 + 3\mathfrak{R}_{01} \mathfrak{R}_{02}} \frac{\mathfrak{R}_{02}}{2(\mathfrak{R}_{01} + \mathfrak{R}_{02})} \\ &= \frac{N_{Lf2} i_b \mathfrak{R}_{02}}{2\mathfrak{R}_{01}^2 + 3\mathfrak{R}_{01} \mathfrak{R}_{02}} \end{aligned} \quad (17)$$

$\phi_c$  is the flux generated by  $L_{f3}$  winding,  $\phi_{ca}$  is the flux generated by  $L_{f3}$  winding flows through  $L_{f1}$  winding, and  $\phi_{cb}$  is the flux generated by  $L_{f3}$  winding flows through  $L_{f2}$  winding, and they can be described as follows:

$$\begin{aligned} \phi_c &= \frac{N_{Lf3} i_c}{\mathfrak{R}_{01} + \mathfrak{R}_{01} // \mathfrak{R}_{01} // \mathfrak{R}_{02} // \mathfrak{R}_{02}} \\ &= \frac{2N_{Lf3} i_c (\mathfrak{R}_{01} + \mathfrak{R}_{02})}{2\mathfrak{R}_{01}^2 + 3\mathfrak{R}_{01} \mathfrak{R}_{02}}, \end{aligned}$$

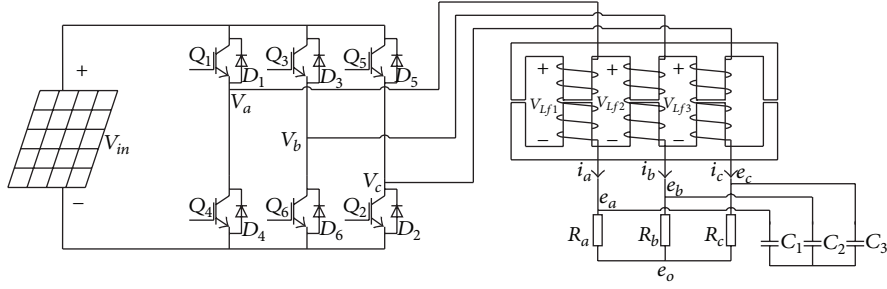


FIGURE 4: The three-phase integrated filter inductors with five magnetic limbs in three-phase inverter.

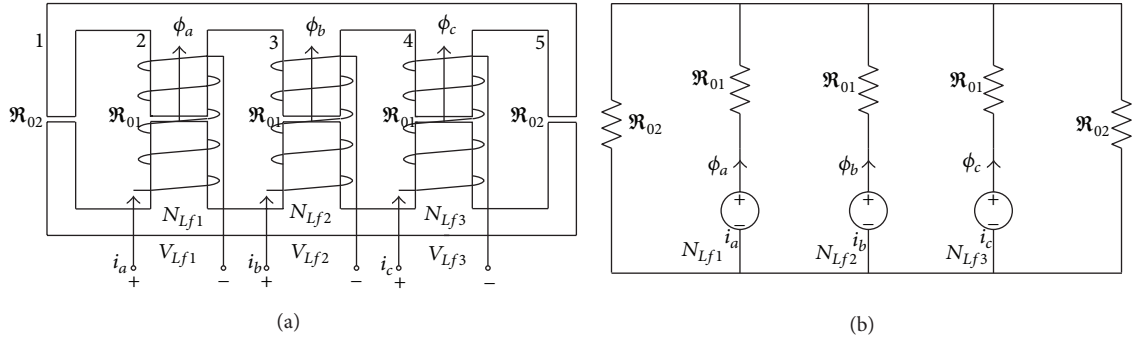


FIGURE 5: Three-phase integrated inductors with five magnetic limbs: (a) three-phase magnetic core with five limbs, (b) magnetic circuit.

$$\begin{aligned} \phi_{ca} = \phi_{cb} &= \frac{2N_{Lf3}i_c(\mathfrak{R}_{01} + \mathfrak{R}_{02})}{2\mathfrak{R}_{01}^2 + 3\mathfrak{R}_{01}\mathfrak{R}_{02}} \frac{\mathfrak{R}_{02}}{2(\mathfrak{R}_{01} + \mathfrak{R}_{02})} \\ &= \frac{N_{Lf3}i_c\mathfrak{R}_{02}}{2\mathfrak{R}_{01}^2 + 3\mathfrak{R}_{01}\mathfrak{R}_{02}}. \end{aligned} \quad (18)$$

Every total flux of inductor winding consists of three parts: one is the self-flux and the others are generated by the other two inductor windings. Therefore, the voltages of inductors  $V_{Lf1}$ ,  $V_{Lf2}$ , and  $V_{Lf3}$  can be described as follows:

$$\begin{aligned} V_{Lf1} &= N_{Lf1} \frac{d}{dt} (\phi_a + \phi_{ba} + \phi_{ca}), \\ V_{Lf2} &= N_{Lf2} \frac{d}{dt} (\phi_b + \phi_{ab} + \phi_{cb}), \\ V_{Lf3} &= N_{Lf3} \frac{d}{dt} (\phi_c + \phi_{ac} + \phi_{bc}). \end{aligned} \quad (19)$$

According to (16), (17), (18), and (19),  $V_{Lf1}$ ,  $V_{Lf2}$ , and  $V_{Lf3}$  also can be described as follows:

$$\begin{pmatrix} V_{Lf1} \\ V_{Lf2} \\ V_{Lf3} \end{pmatrix} = \begin{pmatrix} L_{f1} & M_{ab} & M_{ac} \\ M_{ab} & L_{f2} & M_{bc} \\ M_{ac} & M_{bc} & L_{f3} \end{pmatrix} \begin{pmatrix} \frac{di_a}{dt} \\ \frac{di_b}{dt} \\ \frac{di_c}{dt} \end{pmatrix}, \quad (20)$$

where  $L_{f1}$ ,  $L_{f2}$ , and  $L_{f3}$  are self-inductor and can be described as follows:

$$\begin{aligned} L_{f1} &= \frac{2N_{Lf1}^2(\mathfrak{R}_{01} + \mathfrak{R}_{02})}{2\mathfrak{R}_{01}^2 + 3\mathfrak{R}_{01}\mathfrak{R}_{02}}, \\ L_{f2} &= \frac{2N_{Lf2}^2(\mathfrak{R}_{01} + \mathfrak{R}_{02})}{2\mathfrak{R}_{01}^2 + 3\mathfrak{R}_{01}\mathfrak{R}_{02}}, \\ L_{f3} &= \frac{2N_{Lf3}^2(\mathfrak{R}_{01} + \mathfrak{R}_{02})}{2\mathfrak{R}_{01}^2 + 3\mathfrak{R}_{01}\mathfrak{R}_{02}}. \end{aligned} \quad (21)$$

$M_{ab}$ ,  $M_{ac}$ , and  $M_{bc}$  are mutual inductance and can be described as follows:

$$\begin{aligned} M_{ab} &= \frac{N_{Lf1}N_{Lf2}\mathfrak{R}_{02}}{2\mathfrak{R}_{01}^2 + 3\mathfrak{R}_{01}\mathfrak{R}_{02}}, \\ M_{ac} &= \frac{N_{Lf1}N_{Lf3}\mathfrak{R}_{02}}{2\mathfrak{R}_{01}^2 + 3\mathfrak{R}_{01}\mathfrak{R}_{02}}, \\ M_{bc} &= \frac{N_{Lf2}N_{Lf3}\mathfrak{R}_{02}}{2\mathfrak{R}_{01}^2 + 3\mathfrak{R}_{01}\mathfrak{R}_{02}}. \end{aligned} \quad (22)$$

In order to make the three-phases balanced, the number of turns of three-phase inductor is the same; it means that  $N_{Lf1} = N_{Lf2} = N_{Lf3}$ . Therefore, it can be got that  $L_{f1} = L_{f2} = L_{f3} = L_f$ , and  $M_{ab} = M_{ac} = M_{bc} = M$ . Then, finally

the expression of three-phase integrated inductors with five magnetic limbs can be described as follows:

$$\begin{pmatrix} V_{Lf1} \\ V_{Lf2} \\ V_{Lf3} \end{pmatrix} = \begin{pmatrix} L_f & M & M \\ M & L_f & M \\ M & M & L_f \end{pmatrix} \begin{pmatrix} \frac{di_a}{dt} \\ \frac{di_b}{dt} \\ \frac{di_c}{dt} \end{pmatrix}. \quad (23)$$

Based on (23), it can be got that the three-phase inductors couple with each other, and then the current ripple can be analyzed.

**3.2. The Ripple Current of Three-Phase Integrated Filter Inductors with Five-Limb Magnetic Core.** In order to achieve the demanded filter effect of three-phase integrated filter inductors with five magnetic limbs, the current ripples should be analyzed. According to (23),  $V_{Lf1}$ ,  $V_{Lf2}$ , and  $V_{Lf3}$  can be described as follows:

$$\begin{aligned} V_{Lf1} &= V_a - e_a - e_o = L_{f1} \frac{di_a}{dt} + M \frac{di_b}{dt} + M \frac{di_c}{dt}, \\ V_{Lf2} &= V_b - e_b - e_o = L_{f2} \frac{di_b}{dt} + M \frac{di_a}{dt} + M \frac{di_c}{dt}, \\ V_{Lf3} &= V_c - e_c - e_o = L_{f3} \frac{di_c}{dt} + M \frac{di_b}{dt} + M \frac{di_a}{dt}. \end{aligned} \quad (24)$$

Furthermore, it can be simplified as follows:

$$\begin{aligned} V_{Lf1} &= \frac{2S_a - S_b - S_c}{3} V_{in} - e_a = L_{f1} \frac{di_a}{dt} + M \frac{di_b}{dt} + M \frac{di_c}{dt}, \\ V_{Lf2} &= \frac{2S_b - S_a - S_c}{3} V_{in} - e_b = L_{f2} \frac{di_b}{dt} + M \frac{di_a}{dt} + M \frac{di_c}{dt}, \\ V_{Lf3} &= \frac{2S_c - S_a - S_b}{3} V_{in} - e_c = L_{f3} \frac{di_c}{dt} + M \frac{di_b}{dt} + M \frac{di_a}{dt}. \end{aligned} \quad (25)$$

Take the ripple current  $\Delta i_a$  of  $L_{f1}$ , for example, to analyze, it can be got that

$$\begin{aligned} \Delta i_a &= \left( \frac{2S_a - S_b - S_c}{3} V_{dc} - e_a - M \frac{di_b}{dt} - M \frac{di_c}{dt} \right) \\ &\quad \times \frac{D_{on} T}{L_{f1}}. \end{aligned} \quad (26)$$

It can be got that the ripple current  $\Delta i_a$  are influenced by switching signals  $S_a$ ,  $S_b$ , and  $S_c$  which are decided by control method, and the mutual inductors and currents of the other two phases. Since the ripple currents are coupled with each other, it is complicated to design the ideal value of ripple current for fulfilling the demand of harmonic. In order to reduce the influence by other two phases, the mutual inductors can be eliminated. According to (22), the mutual inductor is described as follows:

$$M = \frac{N_{Lf}^2 \mathfrak{R}_{02}}{2\mathfrak{R}_{01}^2 + 3\mathfrak{R}_{01} \mathfrak{R}_{02}}. \quad (27)$$

The magnetic resistance can be got as follows:

$$\mathfrak{R}_{0i} = \frac{l_{gi}}{\mu_0 A_i}, \quad i = 1, 2, \quad (28)$$

where  $l_{gi}$  and  $A_i$  are, respectively, the air gap and cross section area of  $\mathfrak{R}_{0i}$  and  $\mu_0$  is air permeability.

In order to reduce the mutual inductor, according to (27), when the magnetic resistance  $\mathfrak{R}_{02}$  is zero, the mutual inductor  $M$  can be eliminated. Therefore, the air gap  $l_{g2}$  of  $\mathfrak{R}_{02}$  can be adjusted to zero to reduce the mutual inductor. Then, (26) can be simplified as follows:

$$\begin{aligned} \Delta i_a &= \left( \frac{2S_a - S_b - S_c}{3} V_{dc} - e_a \right) \\ &\quad \times \frac{D_{on} T}{L_{f1}}. \end{aligned} \quad (29)$$

Based on (22), it can be got that the ripple currents of three-phase integrated filter inductors with five limbs are the same as those of three-phase discrete filter inductors. It means that the two kinds of three-phase inductors have the same filter effect, but the volume of integrated filter inductors with five limbs is less than that of discrete filter inductors.

**3.3. The Max Flux Density of Integrated Filter Inductors with Five Magnetic Limbs.** In order to design the magnetic core of the three-phase integrated filter inductors with five limbs, the flux density of every limb should be analyzed. There are five limbs of the magnetic core of integrated filter inductor, and the middle three limbs have the windings of three-phase filter inductors. In order to reduce the mutual inductor, the middle three limbs have the same air gaps; the other two limbs have no air gaps; it means that the middle three limbs have the magnetic resistances and the other two limbs have no magnetic resistances. Therefore, the fluxes generated by the three inductor windings of middle three limbs all flow through the other two limbs and donot flow through each other. Taking the flux  $\phi_a$  generated by  $L_{f1}$  winding of second limb for example,  $\phi_a$  can be got as follows:

$$\phi_a = \frac{L_{f1} i_a}{N_{Lf1}}. \quad (30)$$

Since the magnetic resistance  $\mathfrak{R}_{02}$  is zero, and according to (28), then  $L_{f1}$  can be got as follows:

$$\begin{aligned} L_{f1} &= \frac{2N_{Lf1}^2 (\mathfrak{R}_{01} + \mathfrak{R}_{02})}{2\mathfrak{R}_{01}^2 + 3\mathfrak{R}_{01} \mathfrak{R}_{02}} \\ &= \frac{N_{Lf1}^2}{\mathfrak{R}_{01}} = \frac{N_{Lf1}^2 \mu_0 A_2}{l_{g2}}. \end{aligned} \quad (31)$$

The three-phase current  $i_a$ ,  $i_b$ , and  $i_c$  can be described as follows:

$$\begin{aligned} i_a &= \sqrt{2}I_m \sin(\omega t), \\ i_b &= \sqrt{2}I_m \sin\left(\omega t + \frac{2\pi}{3}\right), \\ i_c &= \sqrt{2}I_m \sin\left(\omega t - \frac{2\pi}{3}\right), \end{aligned} \quad (32)$$

where  $I_m$  is the effective value of current.

Therefore, when  $\phi_a$  achieves its max value  $\phi_{a\max}$ , the max flux density  $B_{2\max}$  of second limb can be described as follows:

$$\begin{aligned} B_{2\max} &= \frac{\phi_{a\max}}{A_2} \\ &= \frac{L_{f1} \sqrt{2}I_m}{A_2 N_{L_{f1}}} = \frac{\sqrt{2}I_m N_{L_{f1}} \mu_0}{l_{g2}}. \end{aligned} \quad (33)$$

Also, the max flux densities  $B_{3\max}$  and  $B_{4\max}$  of the third and fourth limbs can be described as follows:

$$\begin{aligned} B_{3\max} &= \frac{\sqrt{2}I_m N_{L_{f2}} \mu_0}{l_{g3}}, \\ B_{4\max} &= \frac{\sqrt{2}I_m N_{L_{f3}} \mu_0}{l_{g4}}. \end{aligned} \quad (34)$$

The fluxes of the first and fifth limbs consist of three parts of fluxes which are generated by the middle three limbs. Taking the flux  $\phi_1$  of the first limb, for example,  $\phi_1$  consists of  $\phi_{a1}$  generated by  $L_{f1}$  winding,  $\phi_{b1}$  generated by  $L_{f2}$  winding, and  $\phi_{c1}$  generated by  $L_{f3}$  winding.  $\phi_{a1}$ ,  $\phi_{b1}$ , and  $\phi_{c1}$  can be described as follows:

$$\begin{aligned} \phi_{a1} &= \frac{N_{L_{f1}} i_a \mathfrak{R}_{01}}{2\mathfrak{R}_{01}^2 + 3\mathfrak{R}_{01} \mathfrak{R}_{02}}, \\ \phi_{b1} &= \frac{N_{L_{f2}} i_b \mathfrak{R}_{01}}{2\mathfrak{R}_{01}^2 + 3\mathfrak{R}_{01} \mathfrak{R}_{02}}, \\ \phi_{c1} &= \frac{N_{L_{f3}} i_c \mathfrak{R}_{01}}{2\mathfrak{R}_{01}^2 + 3\mathfrak{R}_{01} \mathfrak{R}_{02}}. \end{aligned} \quad (35)$$

Therefore,  $\phi_1$  can be got as follows:

$$\begin{aligned} \phi_1 &= \phi_{a1} + \phi_{b1} + \phi_{c1} \\ &= \frac{N_{L_{f1}} \mathfrak{R}_{01} (i_a + i_b + i_c)}{2\mathfrak{R}_{01}^2 + 3\mathfrak{R}_{01} \mathfrak{R}_{02}}. \end{aligned} \quad (36)$$

Since in three-phase system,  $i_a + i_b + i_c = 0$ . Therefore, the total flux  $\phi_1$  is zero. The main functions of the first and fifth limbs are to adjust the mutual inductors.

#### 4. The Integrated Three-Phase Filter Inductors with Five-Limb Magnetic Core in Three-Phase Inverter

In order to further decrease the volume of three-phase filter inductor, the five magnetic limbs can be simplified to three

magnetic limbs which are shown in Figure 6. In Figure 6, one EE magnetic core is adopted, and the cross section area of middle limb is twice than that of the other two limbs. Since, compared with the above two kinds of three-phase filter inductors, this kind of three-phase integrated filter inductor can achieve the least volume.

*4.1. The Expression of Three-Phase Integrated Filter Inductors with Three Magnetic Limbs.* The integrated three-phase filter inductors with three-limb magnetic core are shown in Figure 7(a).  $\phi_a$ ,  $\phi_b$ , and  $\phi_c$  are, respectively, the fluxes generated by  $L_{f1}$  winding,  $L_{f2}$  winding, and  $L_{f3}$  winding;  $\mathfrak{R}_1$ ,  $\mathfrak{R}_2$ , and  $\mathfrak{R}_3$  are, respectively, the magnetic resistance of three limbs. According to the magnetic circuit which is shown in Figure 7(b),  $\phi_a$  is the flux generated by  $L_{f1}$  winding,  $\phi_{ab}$  is the flux generated by  $L_{f1}$  winding flows through  $L_{f2}$  winding, and  $\phi_{ac}$  is the flux generated by  $L_{f1}$  winding flows through  $L_{f3}$  winding, and they can be described as follows:

$$\begin{aligned} \phi_a &= \frac{N_{L_{f1}} i_a}{\mathfrak{R}_1 + \mathfrak{R}_2 // \mathfrak{R}_3} = \frac{N_{L_{f1}} i_a (\mathfrak{R}_3 + \mathfrak{R}_2)}{\mathfrak{R}_1 \mathfrak{R}_2 + \mathfrak{R}_1 \mathfrak{R}_3 + \mathfrak{R}_2 \mathfrak{R}_3}, \\ \phi_{ab} &= \frac{N_{L_{f1}} i_a (\mathfrak{R}_3 + \mathfrak{R}_2)}{\mathfrak{R}_1 \mathfrak{R}_2 + \mathfrak{R}_1 \mathfrak{R}_3 + \mathfrak{R}_2 \mathfrak{R}_3} \frac{\mathfrak{R}_3}{\mathfrak{R}_3 + \mathfrak{R}_2} \\ &= \frac{N_{L_{f1}} i_a \mathfrak{R}_3}{\mathfrak{R}_1 \mathfrak{R}_2 + \mathfrak{R}_1 \mathfrak{R}_3 + \mathfrak{R}_2 \mathfrak{R}_3}, \\ \phi_{ac} &= \frac{N_{L_{f1}} i_a (\mathfrak{R}_3 + \mathfrak{R}_2)}{\mathfrak{R}_1 \mathfrak{R}_2 + \mathfrak{R}_1 \mathfrak{R}_3 + \mathfrak{R}_2 \mathfrak{R}_3} \frac{\mathfrak{R}_2}{\mathfrak{R}_3 + \mathfrak{R}_2} \\ &= \frac{N_{L_{f1}} i_a \mathfrak{R}_2}{\mathfrak{R}_1 \mathfrak{R}_2 + \mathfrak{R}_1 \mathfrak{R}_3 + \mathfrak{R}_2 \mathfrak{R}_3}. \end{aligned} \quad (37)$$

Also,  $\phi_b$  is the flux generated by  $L_{f2}$  winding,  $\phi_{ba}$  is the flux generated by  $L_{f2}$  winding flows through  $L_{f1}$  winding, and  $\phi_{bc}$  is the flux generated by  $L_{f2}$  winding flows through  $L_{f3}$  winding, and they can be described as follows:

$$\begin{aligned} \phi_b &= \frac{N_{L_{f2}} i_{L_{f2}}}{\mathfrak{R}_2 + \mathfrak{R}_1 // \mathfrak{R}_3} = \frac{N_{L_{f2}} i_{L_{f2}} (\mathfrak{R}_1 + \mathfrak{R}_3)}{\mathfrak{R}_1 \mathfrak{R}_2 + \mathfrak{R}_1 \mathfrak{R}_3 + \mathfrak{R}_2 \mathfrak{R}_3}, \\ \phi_{ba} &= \frac{N_{L_{f2}} i_b (\mathfrak{R}_1 + \mathfrak{R}_3)}{\mathfrak{R}_1 \mathfrak{R}_2 + \mathfrak{R}_1 \mathfrak{R}_3 + \mathfrak{R}_2 \mathfrak{R}_3} \frac{\mathfrak{R}_3}{\mathfrak{R}_1 + \mathfrak{R}_3} \\ &= \frac{N_{L_{f2}} i_b \mathfrak{R}_3}{\mathfrak{R}_1 \mathfrak{R}_2 + \mathfrak{R}_1 \mathfrak{R}_3 + \mathfrak{R}_2 \mathfrak{R}_3}, \\ \phi_{bc} &= \frac{N_{L_{f2}} i_b (\mathfrak{R}_1 + \mathfrak{R}_3)}{\mathfrak{R}_1 \mathfrak{R}_2 + \mathfrak{R}_1 \mathfrak{R}_3 + \mathfrak{R}_2 \mathfrak{R}_3} \frac{\mathfrak{R}_2}{\mathfrak{R}_1 + \mathfrak{R}_3} \\ &= \frac{N_{L_{f2}} i_b \mathfrak{R}_1}{\mathfrak{R}_1 \mathfrak{R}_2 + \mathfrak{R}_1 \mathfrak{R}_3 + \mathfrak{R}_2 \mathfrak{R}_3}. \end{aligned} \quad (38)$$

$\phi_c$  is the flux generated by  $L_{f3}$  winding,  $\phi_{ca}$  is the flux generated by  $L_{f3}$  winding flows through  $L_{f1}$  winding, and

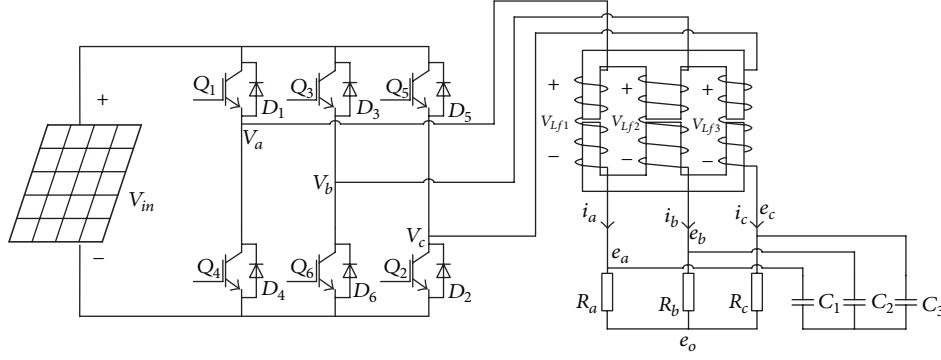


FIGURE 6: The three-phase integrated filter inductors with three magnetic limbs in three-phase inverter.

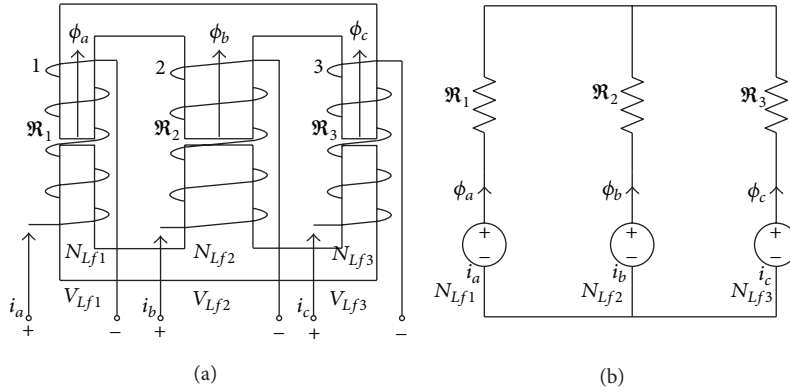


FIGURE 7: Three-phase integrated inductors with five magnetic limbs: (a) three-phase magnetic core with five limbs, (b) magnetic circuit.

$\phi_{cb}$  is the flux generated by  $L_{f3}$  winding flows through  $L_{f2}$  winding, and they can be described as follows:

$$\begin{aligned}\phi_c &= \frac{N_{Lf3}i_c}{\mathfrak{R}_3 + \mathfrak{R}_1 // \mathfrak{R}_2} = \frac{N_{Lf2}i_c (\mathfrak{R}_1 + \mathfrak{R}_2)}{\mathfrak{R}_1\mathfrak{R}_2 + \mathfrak{R}_1\mathfrak{R}_3 + \mathfrak{R}_2\mathfrak{R}_3}, \\ \phi_{ca} &= \frac{N_{Lf3}i_c (\mathfrak{R}_1 + \mathfrak{R}_2)}{\mathfrak{R}_1\mathfrak{R}_2 + \mathfrak{R}_1\mathfrak{R}_3 + \mathfrak{R}_2\mathfrak{R}_3} \frac{\mathfrak{R}_2}{\mathfrak{R}_1 + \mathfrak{R}_2} \\ &= \frac{N_{Lf3}i_c \mathfrak{R}_2}{\mathfrak{R}_1\mathfrak{R}_2 + \mathfrak{R}_1\mathfrak{R}_3 + \mathfrak{R}_2\mathfrak{R}_3}, \\ \phi_{cb} &= \frac{N_{Lf3}i_c (\mathfrak{R}_1 + \mathfrak{R}_2)}{\mathfrak{R}_1\mathfrak{R}_2 + \mathfrak{R}_1\mathfrak{R}_3 + \mathfrak{R}_2\mathfrak{R}_3} \frac{\mathfrak{R}_1}{\mathfrak{R}_1 + \mathfrak{R}_2} \\ &= \frac{N_{Lf3}i_c \mathfrak{R}_1}{\mathfrak{R}_1\mathfrak{R}_2 + \mathfrak{R}_1\mathfrak{R}_3 + \mathfrak{R}_2\mathfrak{R}_3}.\end{aligned}\quad (39)$$

Furthermore,  $V_{Lf1}$ ,  $V_{Lf2}$ , and  $V_{Lf3}$  can be represented as follows:

$$\begin{aligned}V_{Lf1} &= N_{Lf1} \frac{d}{dt} (\phi_a + \phi_{ba} + \phi_{ca}), \\ V_{Lf2} &= N_{Lf2} \frac{d}{dt} (\phi_b + \phi_{ab} + \phi_{cb}), \\ V_{Lf3} &= N_{Lf3} \frac{d}{dt} (\phi_c + \phi_{ac} + \phi_{bc}).\end{aligned}\quad (40)$$

Based on the above formulas, the expression of integrated three-phase filter inductors with three magnetic limbs can be represented as follows:

$$\begin{pmatrix} V_{Lf1} \\ V_{Lf2} \\ V_{Lf3} \end{pmatrix} = \begin{pmatrix} L_{f1} & M_{ab} & M_{ac} \\ M_{ab} & L_{f2} & M_{bc} \\ M_{ac} & M_{bc} & L_{f3} \end{pmatrix} \begin{pmatrix} \frac{di_a}{dt} \\ \frac{di_b}{dt} \\ \frac{di_c}{dt} \end{pmatrix}, \quad (41)$$

where  $L_{f1}$ ,  $L_{f2}$ , and  $L_{f3}$  can be represented as follows:

$$\begin{aligned}L_{f1} &= \frac{N_{Lf1}^2 (\mathfrak{R}_3 + \mathfrak{R}_2)}{\mathfrak{R}_1\mathfrak{R}_2 + \mathfrak{R}_1\mathfrak{R}_3 + \mathfrak{R}_2\mathfrak{R}_3}, \\ L_{f2} &= \frac{N_{Lf2}^2 (\mathfrak{R}_1 + \mathfrak{R}_3)}{\mathfrak{R}_1\mathfrak{R}_2 + \mathfrak{R}_1\mathfrak{R}_3 + \mathfrak{R}_2\mathfrak{R}_3}, \\ L_{f3} &= \frac{N_{Lf3}^2 (\mathfrak{R}_1 + \mathfrak{R}_2)}{\mathfrak{R}_1\mathfrak{R}_2 + \mathfrak{R}_1\mathfrak{R}_3 + \mathfrak{R}_2\mathfrak{R}_3}.\end{aligned}\quad (42)$$

$M_{ab}$ ,  $M_{ac}$ , and  $M_{bc}$  are mutual inductors and can be represented as follows:

$$M_{ab} = \frac{N_{Lf1}N_{Lf2}\mathfrak{R}_3}{\mathfrak{R}_1\mathfrak{R}_2 + \mathfrak{R}_1\mathfrak{R}_3 + \mathfrak{R}_2\mathfrak{R}_3},$$

$$M_{ac} = \frac{N_{Lf1}N_{Lf3}\mathfrak{R}_2}{\mathfrak{R}_1\mathfrak{R}_2 + \mathfrak{R}_1\mathfrak{R}_3 + \mathfrak{R}_2\mathfrak{R}_3},$$

$$M_{bc} = \frac{N_{Lf2}N_{Lf3}\mathfrak{R}_1}{\mathfrak{R}_1\mathfrak{R}_2 + \mathfrak{R}_1\mathfrak{R}_3 + \mathfrak{R}_2\mathfrak{R}_3}. \quad (43)$$

Based on (43), it can be got that the three inductors couple with each other, and then the current ripple can be analyzed.

**4.2. The Ripple Current of Three-Phase Integrated Filter Inductors with Three-Limb Magnetic Core.** According to (43),  $V_{Lf1}$ ,  $V_{Lf2}$ , and  $V_{Lf3}$  can be described as follows:

$$V_{Lf1} = V_a - e_a - e_o = L_{f1} \frac{di_a}{dt} + M_{ab} \frac{di_b}{dt} + M_{ac} \frac{di_c}{dt},$$

$$V_{Lf2} = V_b - e_b - e_o = L_{f2} \frac{di_b}{dt} + M_{ab} \frac{di_a}{dt} + M_{bc} \frac{di_c}{dt}, \quad (44)$$

$$V_{Lf3} = V_c - e_c - e_o = L_{f3} \frac{di_c}{dt} + M_{bc} \frac{di_b}{dt} + M_{ac} \frac{di_a}{dt}.$$

Based on (42) and (43), the self-inductors and mutual inductors are decided by magnetic resistors. The magnetic resistor can be got as follows:

$$\mathfrak{R}_i = \frac{l_{gi}}{\mu_0 A_i}, \quad i = 1, 2, 3, \quad (45)$$

where  $l_{gi}$  and  $A_i$  are respectively, the air gap and cross section area of  $\mathfrak{R}_{oi}$  and  $\mu_0$  is air permeability.

Since one EE magnetic core is adopted in this paper, the cross section area of middle limb is twice than that of the other two limbs. Then, it makes the self-inductors and mutual inductors not the same. In order to make the three-phases balanced, the air gaps can be adjusted to make the magnetic resistors of three limbs the same. Therefore, it can be got that  $l_{g2} = 2l_{g1} = 2l_{g3}$ . Furthermore, when  $N_{Lf1} = N_{Lf2} = N_{Lf3}$ , it can be got that  $L_{f1} = L_{f2} = L_{f3} = L_f$  and  $M_{ab} = M_{ac} = M_{bc} = M$ . Therefore, (44) can be simplified as follows:

$$V_{Lf1} = \frac{2S_a - S_b - S_c}{3} V_{in} - e_a = L_f \frac{di_a}{dt} + M \frac{di_b}{dt} + M \frac{di_c}{dt},$$

$$V_{Lf2} = \frac{2S_b - S_a - S_c}{3} V_{in} - e_b = L_f \frac{di_b}{dt} + M \frac{di_a}{dt} + M \frac{di_c}{dt},$$

$$V_{Lf3} = \frac{2S_c - S_a - S_b}{3} V_{in} - e_c = L_f \frac{di_c}{dt} + M \frac{di_b}{dt} + M \frac{di_a}{dt}. \quad (46)$$

In order to analyze conveniently, take the one-phase ripple current  $\Delta i_a$  of  $L_{f1}$ , for example, to analyze, it can be got that

$$\Delta i_a = \left( \frac{2S_a - S_b - S_c}{3} V_{dc} - e_a - M \frac{di_b}{dt} - M \frac{di_c}{dt} \right) \times \frac{D_{on} T}{L_{f1}}. \quad (47)$$

In three-phase system, the three-phase current  $i_a$ ,  $i_b$ , and  $i_c$  can be described as follows:

$$i_a = \sqrt{2} I_m \sin(\omega t),$$

$$i_b = \sqrt{2} I_m \sin\left(\omega t + \frac{2\pi}{3}\right), \quad (48)$$

$$i_c = \sqrt{2} I_m \sin\left(\omega t - \frac{2\pi}{3}\right),$$

where  $I_m$  is the effective value of current and  $\omega$  is the line angular frequency.

According to (48), the ripple current  $\Delta i_a$  can be simplified as follows:

$$\Delta i_a = \left( \frac{2S_a - S_b - S_c}{3} V_{dc} - e_a + \sqrt{2} M I_m \omega \cos(\omega t) \right) \times \frac{D_{on} T}{L_{f1}}. \quad (49)$$

Compared with the ripple current of discrete inductors and integrated inductors with five limbs, it can be got that the ripple current with three limbs is influenced by additional  $\sqrt{2} M I_m \omega \cos(\omega t)$ . Therefore, mutual inductor  $M$ , current  $I_m$ , and angular frequency  $\omega$  should be designed to fulfill the demand of current ripple. Then the value of  $\sqrt{2} M I_m \omega \cos(\omega t)$  can be designed to be less than 10% ( $(2S_a - S_b - S_c) V_{in} / 3 - e_a$ ), and then the influence of  $\sqrt{2} M I_m \omega \cos(\omega t)$  can be omitted. When the three-phase integrated inductors with three limbs operate in high frequency, large current, and large mutual inductor, the influence cannot be omitted and the harmonic cannot meet the demand. Therefore, when the value of  $\sqrt{2} M I_m \omega \cos(\omega t)$  can be omitted, three-phase integrated inductors with three limbs can save more volume and achieve better power density.

**4.3. The Max Flux Density of Integrated Filter Inductors with Three Magnetic Limbs.** Since there are only three magnetic limbs in one magnetic core, the three-phase fluxes are coupled with each other. Take the first limb, for example, which is shown in Figure 7(a), the total flux  $\phi_1$  of first limb consists of the flux  $\phi_a$  generated by  $L_{f1}$  winding, the flux  $\phi_{ba}$  generated by  $L_{f2}$  winding flows through the first limb, and flux  $\phi_{ca}$  generated by  $L_{f3}$  winding flows through the first limb; then it can be got that

$$\phi_1 = \phi_a + \phi_{ba} + \phi_{ca}. \quad (50)$$

The total flux can be further simplified as follows:

$$\phi_1 = \frac{1}{N_{Lf1}} (L_{f1} - M) \sqrt{2} I_m \sin(\omega t). \quad (51)$$

Since the three-phase magnetic resistors and the number of turns of three-phase inductor are the same, it can be got

that  $\mathfrak{R}_1 = \mathfrak{R}_2 = \mathfrak{R}_3 = \mathfrak{R}_0$ , and  $N_{Lf1} = N_{Lf2} = N_{Lf3} = N_{Lf}$ ; then  $L_{f1}$  and  $M$  can be described as follows:

$$\begin{aligned} L_{f1} &= \frac{2N_{Lf}^2 \mu_0 A_1}{3l_{g1}}, \\ M &= \frac{N_{Lf}^2 \mu_0 A_1}{3l_{g1}}. \end{aligned} \quad (52)$$

When  $\phi_1$  achieves its max value  $\phi_{1\max}$ , the max flux density  $B_{1\max}$  of second limb can be described as follows:

$$B_{1\max} = \frac{\phi_{1\max}}{A_1} = \frac{N_{Lf} \mu_0 \sqrt{2} I_m}{3l_{g1}}. \quad (53)$$

Also the max flux density  $B_{2\max}$  of second limb and the max flux density  $B_{3\max}$  of third limb can be described as follows:

$$\begin{aligned} B_{2\max} &= \frac{N_{Lf} \mu_0 \sqrt{2} I_m}{3l_{g2}}, \\ B_{3\max} &= \frac{N_{Lf} \mu_0 \sqrt{2} I_m}{3l_{g3}}. \end{aligned} \quad (54)$$

## 5. The Comparison between Discrete Filter Inductors and Integrated Filter Inductors

According to the above analyses, the comparison of the discrete filter inductors and integrated filter inductors is shown in Table 1. Then, based on the different demands of the PV inverter, different LC filter can be selected to fulfill the demands for the power density and the electrical performance.

## 6. Experimental Results

The parameters of three-phase inverter are shown as follows: the input voltage is  $V_{in} = 700$  VDC, the three-phase output voltages are  $e_a = e_b = e_c = 220$  VAC, the load frequency is 50 Hz, load power is 3 kW, three filter capacitors are 9  $\mu$ F, the control method is SPWM, switching frequency is 15 kHz, the max duty cycle  $D_{on\max}$  is 0.85, and the max value of every phase current is 7A. In this paper, three-phase discrete filter inductors, three-phase integrated filter inductors with five magnetic limbs, and three-phase integrated filter inductors with three magnetic limbs are, respectively, adopted to fulfill the demanded filter effect. In particular, the Three-phase integrated filter inductors can save more volume and achieve more power density.

*6.1. The Volume Comparison of Three Kinds of Three-Phase Filter Inductors.* In this paper, all the magnetic cores of three kinds of three-phase filter inductors are composed by power ferrite EE96/48/32 whose saturated flux density is 0.5 T and the cross section area of middle limb is 1024 mm<sup>2</sup>. The parameters of three kinds of filter inductors are shown in Table 2, the

three-phase discrete filter inductors adopt three power ferrite EE96/48/32 cores, the three-phase integrated filter inductors with five limbs adopt two power ferrite EE96/48/32 cores, and the three-phase integrated filter inductors with three limbs adopt one power ferrite EE96/48/32 core. The self-inductance of three kinds of three filter inductors is 3.8 mH, and the number of turns is 80. For the three-phase integrated filter inductors with three limbs; the cross section area of middle limb is twice than that of the other two limbs; then the air gap of middle limb is twice than that of the other two limbs to make the three-phases balanced. According to the analyses of flux density, it can be calculated that the max flux densities of three discrete filter inductors are 0.33 T, the max flux densities of three middle limbs of integrated filter inductors with five limbs are 0.33 T and that of the other two limbs are zero, and the max flux densities of middle limb of integrated filter inductors with three limbs are 0.17 T and that of the other two limbs are 0.33 T.

The magnetic cores of the discrete filter inductors, integrated filter inductors with five limbs and three limbs magnetics are shown in Figure 8. In Figure 8(a), three power ferrite EE96/48/32 cores are adopted in three-phase discrete filter inductors, and compared with the other two kinds of three-phase filter inductors, the volume of the three-phase discrete filter inductors is the largest. In Figure 8(b), three power ferrite EE96/48/32 cores are adopted in three-phase integrated filter inductors with five magnetic limbs; the middle three limbs have three-phase inductor's windings; the air gaps of the other two limbs can be adjusted to eliminate the three-phase flux coupling; therefore, this kind of three-phase integrated filter inductors can achieve wild application and the volume is smaller than that of the three-phase discrete filter inductors. In Figure 8(c), one power ferrite EE96/48/32 cores is adopted in three-phase integrated filter inductors with three magnetic limbs, and compared with the other two kinds of three-phase filter inductors, all the three limbs have three-phase inductor's windings and the three-phase fluxes couple with each other, and then the application area is a little limited due to the coupling, but the advantage is that this kind of three-phase integrated filter inductors achieves the minimum volume.

*6.2. The Filter Effect Comparison of Three Kinds of Three-Phase Filter Inductors.* The SPWM control method is adopted in the three-phase inverter due to its simple and easy realizing, and it can be easily used to testify the three kinds of LC filters. The switching process of switch  $Q_1$  and the control voltages  $u_{Q1}$  and  $u_{Q4}$  for the switch  $Q_1$  and  $Q_4$  are shown in Figure 9. The other control voltages are similar to  $u_{Q1}$  and  $u_{Q4}$ .

Furthermore, in order to testify the filter effects of the three kinds of three-phase filter inductors, the current THD (total harmonic distortion) of three kinds of three-phase filter inductors is compared. The three-phase load currents of three-phase discrete filter inductors are shown in Figure 10, and the THD of A phase, B phase, and C phase is, respectively, 4.5%, 4.7%, and 4.1%, and all can achieve the demand. The three-phase load currents of three-phase integrated filter inductors with five limbs are shown in Figure 11, and the THD of A phase, B phase, and C phase is, respectively, 4.4%, 4.6%,

TABLE 1: The comparison of the discrete filter inductors and integrated filter inductors.

	The volume of magnetic core	The cost	The three phase coupling	Current ripple influenced by the other two phases
Discrete filter inductor	Large	Large	Decoupling	Not influenced
Integrated filter inductor (five limbs)	Medium	Medium	Can be adjusted to decoupling	Can be adjusted to not influenced
Integrated filter inductor (three limbs)	Small	Small	Coupling	Influenced

TABLE 2: The comparison of the discrete magnetics, five-limb magnetics, and three-limb magnetics.

	The number of magnetic core	The cross section area of middle limb	Air gap distribution	Inductance	The number of turns	The max flux density
Discrete filter inductor	Three EE96/48/32	1024 mm <sup>2</sup>	The air gap of middle limb is 2.0 mm; the air gaps of the other limbs are zero	Self-inductance is 3.8 mH	80	0.33 T
Integrated filter inductor (five limbs)	Two EE96/48/32	1024 mm <sup>2</sup>	The air gaps of middle three limbs are 2.0 mm; the air gaps of the other two limbs are zero	Self-inductance is 3.8 mH	80	0.33 T
Integrated filter inductor (three limbs)	One EE96/48/32	1024 mm <sup>2</sup>	The air gap of middle limb is 1.4 mm; the air gaps of the other limbs are 0.7 mm	Self-inductance is 3.8 mH; mutual inductance is 1.9 mH	80	Middle limb is 0.17 T; the other two limbs are 0.33 T

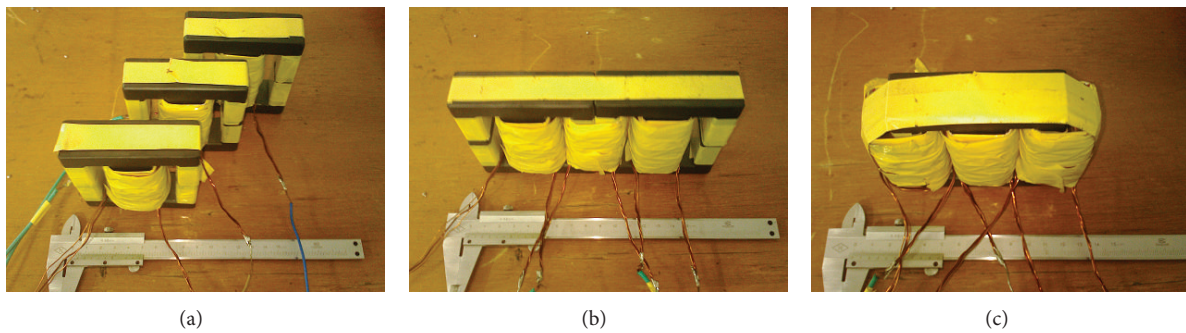


FIGURE 8: The comparison of discrete magnetics, five-limb magnetics, and three-limb magnetics: (a) discrete magnetic cores, (b) integrated magnetic core with five limbs, and (c) integrated magnetic core with three limbs.

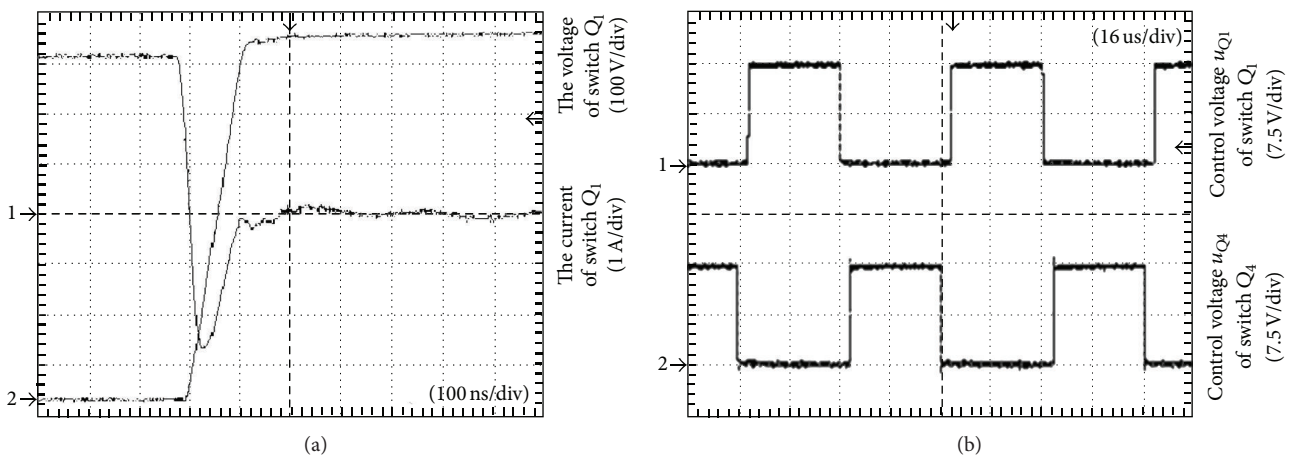


FIGURE 9: The waveforms of switching process and control voltages: (a) the switching process of switch  $Q_1$ , (b) the control voltages for the switch  $Q_1$  and  $Q_4$ . The voltage measured in CH2 by the voltage transformer; the proportion is 1 V = 100 V; in CH1, 1 V = 1 A; the time per DIV is 100 ns. In CH1, the voltage per DIV is 7.5 V; in CH2, the voltage per DIV is 7.5 V; the time per DIV is 16.6 us.

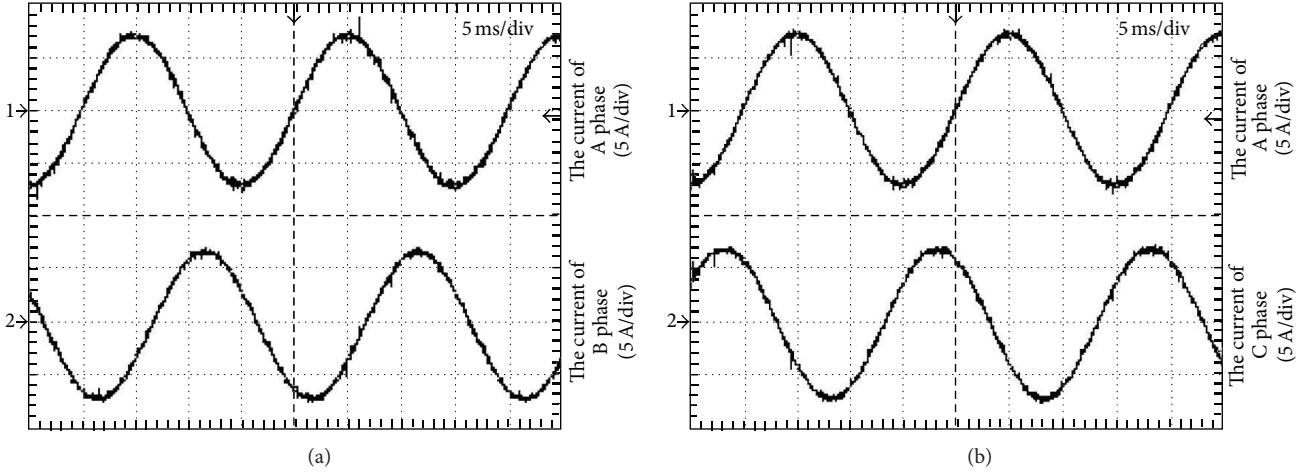


FIGURE 10: The three-phase load current with discrete filter inductor: (a) the current of A phase and B phase, (b) the current of A phase and C phase. In CH1, the current comes from the current transformer and the proportion is  $1\text{ V} = 5\text{ A}$ ; it means that the current per DIV is  $5\text{ A}$ ; in CH2, the current per DIV is  $5\text{ A}$ ; the time per DIV is  $5\text{ ms}$ .

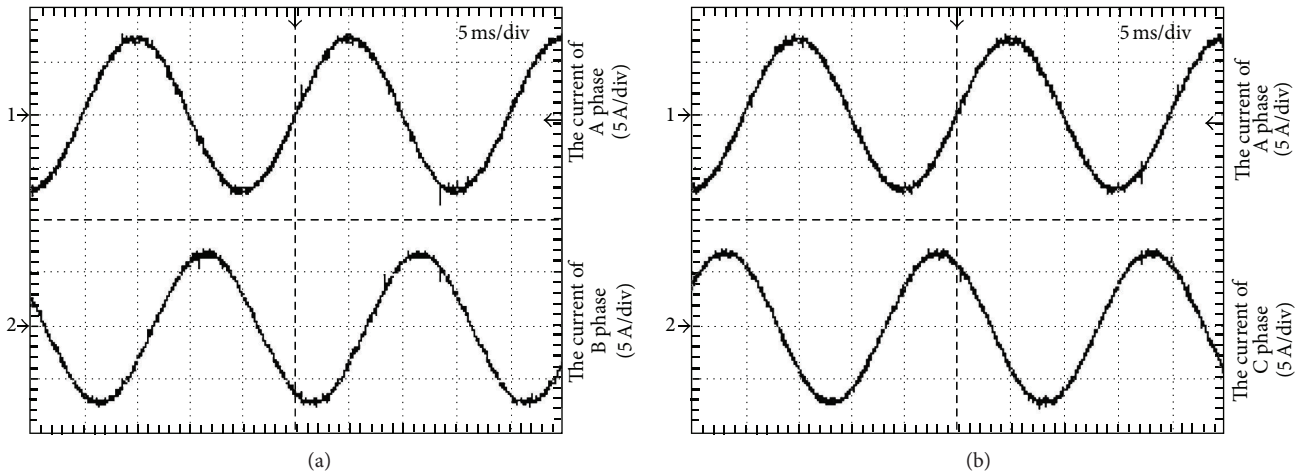


FIGURE 11: The three-phase load current with integrated filter inductor with five limbs: (a) the current of A phase and B phase, (b) the current of A phase and C phase. In CH1, the current comes from the current transformer and the proportion is  $1\text{ V} = 5\text{ A}$ ; it means that the current per DIV is  $5\text{ A}$ ; in CH2, the current per DIV is  $5\text{ A}$ ; the time per DIV is  $5\text{ ms}$ .

and 4.4%, and all can achieve the demand. The three-phase load currents of three-phase integrated filter inductors with three limbs are shown in Figure 12, and the THD of A phase, B phase, and C phase is, respectively, 4.5%, 4.4%, and 4.1%, and all can achieve the demand. Therefore, all three kinds of three-phase filter inductors can fulfill the demand of the current THD. For the low and medium power application, the three-phase coupling in the integrated filter inductors with three limbs can be omitted, and then the integrated filter inductors with three limbs can be chosen due to the minimum volume. Take A phase current of three-phase integrated filter inductors with three limbs, for example, based on formula (42),  $\sqrt{2}MI_m\omega\cos(\omega t)$  is caused by coupling, and its max value is  $\sqrt{2}MI_m\omega$ . In this paper,  $M = 1.9\text{ mH}$ ,  $I_m = 5\text{ A}$ ,  $\omega = 2\pi f = 314$ , and then it can be calculated that  $\sqrt{2}MI_m\omega = 4.2\text{ V}$ . Compared with  $V_{in}$  (700 VDC) and  $e_a$  (220 VAC), the coupling voltage  $\sqrt{2}MI_m\omega = 4.2\text{ V}$  is very small and can be

omitted. But for the large power application, load current  $I_m$  is large and the coupling cannot be omitted; then it is difficult to achieve the ideal effect. Therefore, for the large power application, the integrated filter inductors with five limbs can be chosen. The coupling of the integrated filter inductors with five limbs can be eliminated by adjusting the air gap of two side limbs, and then the filter effect is the same as the discrete filter inductors and the volume is less than the discrete filter inductors.

## 7. Conclusion

In this paper, the comparison analyses of three-phase discrete filter inductors and two kinds of three-phase integrated filter inductors in three-phase PV inverter are proposed. The experiment results show that the volumes of three-phase integrated filter inductors are reduced obviously. Compared

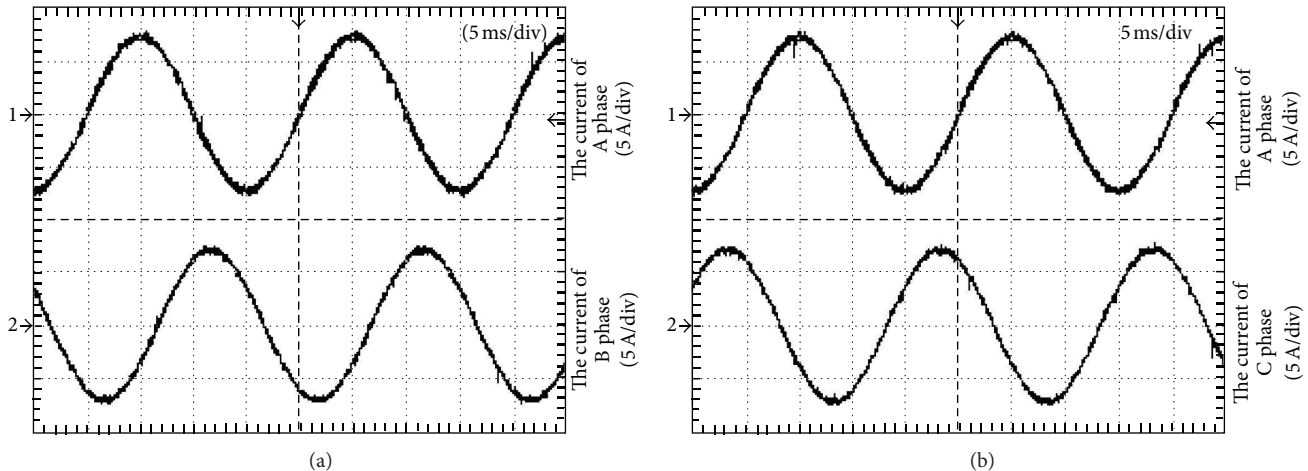


FIGURE 12: The three-phase load current with integrated filter inductor with three limbs: (a) the current of A phase and B phase, (b) the current of A phase and C phase. In CH1, the current comes from the current transformer and the proportion is  $1\text{ V} = 5\text{ A}$ ; it means that the current per DIV is  $5\text{ A}$ ; in CH2, the current per DIV is  $5\text{ A}$ ; the time per DIV is  $5\text{ ms}$ .

with three-phase discrete filter inductors, the volumes of the five-limb integrated filter inductors are reduced third, the three-limb integrated filter inductors are reduced two-thirds, and the filter effects of three kinds of filter inductors are almost the same; all can achieve the good filter effect. Based on the different demands of the PV inverter, different LC filter can be selected to fulfill the demands for the power density and the electrical performance. The analyzed method also can be used in three-phase LCL filter.

## Acknowledgments

This work was supported in part by the National Natural Science Foundation of China (51277121), in part by the National Natural Science Foundation of China (U1204515), in part by the Key Subject Research Program of Education Commission of Shanghai (J51901), in part by the Shanghai Young College Teacher Training and Finance Assistance Scheme (SDJ12001), in part by the Key Cultivation Program of Shanghai Dianji University (12C103), and in part by the Starting Research Fund of Shanghai Dianji University (11C418).

## References

- [1] S. B. Kjaer, J. K. Pedersen, and F. Blaabjerg, "Power inverter topologies for photovoltaic modules: a review," in *Proceedings of the 37th Conference Record of the Industry Applications (IAS'02)*, pp. 782–788, 2002.
- [2] M. Meinhardt and G. Cramer, "Past, present and future of grid connected photovoltaic- and hybrid-power-systems," in *Proceedings of the Power Engineering Society Summer Meeting*, vol. 2, pp. 1283–1288, July 2000.
- [3] Q. Li and P. Wolfs, "A review of the single phase photovoltaic module integrated converter topologies with three different DC link configurations," *IEEE Transactions on Power Electronics*, vol. 23, no. 3, pp. 1320–1333, 2008.
- [4] S. B. Kjaer and F. Blaabjerg, "Design optimization of a single phase inverter for photovoltaic applications," in *Proceedings of the Power Electronics Specialist Conference (PESC'03)*, pp. 1183–1190, 2003.
- [5] E. Figueres, G. Garcerá, J. Sandia, F. González-Espín, and J. C. Rubio, "Sensitivity study of the dynamics of three-phase photovoltaic inverters with an LCL grid filter," *IEEE Transactions on Industrial Electronics*, vol. 56, no. 3, pp. 706–717, 2009.
- [6] M. C. Cavalcanti, K. C. de Oliveira, A. M. de Farias, F. A. S. Neves, G. M. S. Azevedo, and F. C. Camboim, "Modulation techniques to eliminate leakage currents in transformerless three-phase photovoltaic systems," *IEEE Transactions on Industrial Electronics*, vol. 57, no. 4, pp. 1360–1368, 2010.
- [7] S. M. Moosavian, N. A. Rahim, and J. Selvaraj, "Photovoltaic power generation: a review," in *Proceedings of the 1st Conference on Clean Energy and Technology (CET '11)*, pp. 359–363, June 2011.
- [8] H. Kim and K.-H. Kim, "Filter design for grid connected PV inverters," in *Proceedings of the IEEE International Conference on Sustainable Energy Technologies (ICSET '08)*, pp. 1070–1075, November 2008.
- [9] Y. Lang, D. Xu, S. R. Hadianamrei, and H. Ma, "A novel design method of LCL type utility interface for three-phase voltage source rectifier," in *Proceedings of the Power Electronics Specialists Conference (PESC '05)*, pp. 313–317, 2005.
- [10] H. Cha and S. Lee, "Design and implementation of photovoltaic power conditioning system using a current based maximum power point tracking," in *Proceedings of the IEEE Industry Applications Society Annual Meeting (IAS '08)*, pp. 1–5, October 2008.
- [11] M. Liserre, F. Blaabjerg, and S. Hansen, "Design and control of an LCL-filter-based three-phase active rectifier," *IEEE Transactions on Industry Applications*, vol. 41, no. 5, pp. 1281–1291, 2005.
- [12] L. A. Serpa, S. Ponnaluri, P. M. Barbosa, and J. W. Kolar, "A modified direct power control strategy allowing the connection of three-phase inverters to the grid through LCL filters," *IEEE Transactions on Industry Applications*, vol. 43, no. 5, pp. 1388–1400, 2007.
- [13] E. Twining and D. G. Holmes, "Grid current regulation of a three-phase voltage source inverter with an LCL input filter," *IEEE Transactions on Power Electronics*, vol. 18, no. 3, pp. 888–895, 2003.

- [14] M. Liserre, A. Dell'Aquila, and F. Blaabjerg, "Genetic algorithm-based design of the active damping for an LCL-filter three-phase active rectifier," *IEEE Transactions on Power Electronics*, vol. 19, no. 1, pp. 76–86, 2004.
- [15] M. Liserre, R. Teodorescu, and F. Blaabjerg, "Stability of photovoltaic and wind turbine grid-connected inverters for a large set of grid impedance values," *IEEE Transactions on Power Electronics*, vol. 21, no. 1, pp. 263–271, 2006.
- [16] M. Malinowski and S. Bernet, "A simple voltage sensorless active damping scheme for three-phase PWM converters with an LCL filter," *IEEE Transactions on Industrial Electronics*, vol. 55, no. 4, pp. 1876–1880, 2008.
- [17] Y. Jiang, Z. Chen, and J. Pan, "Zero-voltage switching phase shift full-bridge step-up converter with integrated magnetic structure," *IET Power Electronics*, vol. 3, no. 5, pp. 732–739, 2010.
- [18] Q. Li and P. Wolfs, "A current fed two-inductor boost converter with an integrated magnetic structure and passive lossless snubbers for photovoltaic module integrated converter applications," *IEEE Transactions on Power Electronics*, vol. 22, no. 1, pp. 309–321, 2007.
- [19] R. C. Variath, M. A. E. Andersen, O. N. Nielsen, and A. Hyldgård, "A review of module inverter topologies suitable for photovoltaic systems," in *Proceedings of the 9th International Power and Energy Conference (IPEC '10)*, pp. 310–316, October 2010.
- [20] J.-P. Lee, B.-D. Min, T.-J. Kim, D.-W. Yoo, and J.-Y. Yoo, "A novel topology for photovoltaic DC/DC full-bridge converter with flat efficiency under wide PV module voltage and load range," *IEEE Transactions on Industrial Electronics*, vol. 55, no. 7, pp. 2602–2609, 2008.
- [21] M. Fortunato, A. Giustiniani, G. Petrone, G. Spagnuolo, and M. Vitelli, "Maximum power point tracking in a one-cycle-controlled single-stage photovoltaic inverter," *IEEE Transactions on Industrial Electronics*, vol. 55, no. 7, pp. 2684–2693, 2008.

## Research Article

# Operation of TUT Solar PV Power Station Research Plant under Partial Shading Caused by Snow and Buildings

**Diego Torres Lobera,<sup>1</sup> Anssi Mäki,<sup>1</sup> Juha Huusari,<sup>2</sup> Kari Lappalainen,<sup>1</sup>  
Teuvo Suntio,<sup>1</sup> and Seppo Valkealahti<sup>1</sup>**

<sup>1</sup> Department of Electrical Engineering, Tampere University of Technology, P.O. Box 692, 33101 Tampere, Finland

<sup>2</sup> ABB Corporate Research, Segelhofstrasse 1K, Baden-Dättwil, 5405 Aargau, Switzerland

Correspondence should be addressed to Diego Torres Lobera; [diego.torres@tut.fi](mailto:diego.torres@tut.fi)

Received 22 January 2013; Accepted 11 June 2013

Academic Editor: Keith Emery

Copyright © 2013 Diego Torres Lobera et al. This is an open access article distributed under the Creative Commons Attribution License, which permits unrestricted use, distribution, and reproduction in any medium, provided the original work is properly cited.

A grid connected solar photovoltaic (PV) research facility equipped with comprehensive climatic and electric measuring systems has been designed and built in the Department of Electrical Engineering of the Tampere University of Technology (TUT). The climatic measuring system is composed of an accurate weather station, solar radiation measurements, and a mesh of irradiance and PV module temperature measurements located throughout the solar PV facility. Furthermore, electrical measurements can be taken from single PV modules and strings of modules synchronized with the climatic data. All measured parameters are sampled continuously at 10 Hz with a data-acquisition system based on swappable I/O card technology and stored in a database for later analysis. The used sampling frequency was defined by thorough analyses of the PV system time dependence. Climatic and electrical measurements of the first operation year of the research facility are analyzed in this paper. Moreover, operation of PV systems under partial shading conditions caused by snow and building structures is studied by means of the measured current and power characteristics of PV modules and strings.

## 1. Introduction

The cost of photovoltaic (PV) power systems is decreasing with evolving technology, and PV power plants are approaching grid parity in several market areas [1] and heading for an era of market competition without subsidies. Main research and development efforts have been at the component level, such as improving the efficiency of PV cells and grid interfacing devices. Therefore, major progress in the energy efficiency of basic components is not expected in the near future, and more competition will be set to decrease production costs of components. Due to this and the competition without subsidies, system vendors face increasing pressure to provide more value for customers. One way of doing that is to improve the overall system efficiency and the amount of actual power produced under installation site conditions. Improvements in the design and operation of PV power plants are one evident and feasible way to substantially increase the produced power [2].

Accurate modeling of the electric behavior of PV modules and systems will be a key element in improving system operation and efficiency [3]. For instance, accurate modeling of the operation of PV generators under varying environmental conditions improves their performance control and assists the design of PV converters and their maximum power point tracking (MPPT). PV power plants are composed of PV modules connected in series and parallel to reach adequate voltage and power levels. Furthermore, PV modules are composed of PV cells connected in series. It has been shown that environmental effects causing nonuniform operating conditions can lead to power losses of the order of 10% in typical PV power plants [2]. These nonuniform operating conditions can be due to various reasons, such as partial shading of the PV generator by built structures, and clouds. For example, climatic effects influence the electrical characteristics of PV cells directly via incident irradiance and indirectly via module temperature, which depends on ambient temperature, incident irradiance, relative humidity,

TABLE 1: Electrical performance of the NP190GKg PV module under STC.

$P_{MPP}$ (W)	$U_{MPP}$ (V)	$I_{MPP}$ (A)	$U_{OC}$ (V)	$I_{SC}$ (A)
190.00	25.80	7.36	33.00	8.00

and wind speed and direction, among others [4]. These variables must be taken into account when modeling the dynamic operation of photovoltaic systems [5–8].

Under partial shading conditions, PV cells connected in series experience different irradiance levels. The resulting electrical characteristics deviate from their standard form, depending on the shading pattern and intensity. Extensive research exists on the effects of partial shading on the operation of PV modules and systems [9–14]. For PV modules with more than one bypass diode, the  $P$ - $U$  characteristic curves turn into multipeak curves which impede maximum power point tracking operation [15]. Significant energy losses can take place, and the overall system performance reduces [16].

The TUT solar PV power station research plant has been designed to enable systematic and thorough analysis of the dynamic phenomena in energy conversion processes in solar PV power systems. In this paper, we justify the built PV solar power research plant and measuring system, such as the selected sampling frequency of climatic and environmental data. We also demonstrate the applicability of the research facility by analyzing the climatic and electrical measurements of the first operational year. Additionally, operation of PV systems operating under partial shading conditions caused by snow and building structures is analyzed in this paper.

## 2. TUT Solar PV Power Station Research Plant

**2.1. PV Generator.** The research plant consists of 69 NP190-GKg PV modules with a total peak power of 13.1 kWp. Each PV module consists of 54 polycrystalline silicon solar cells connected in series, physically located as 6 horizontal rows and encapsulated in EVA with a 4 mm iron tempered glass as top cover. Table 1 includes the PV module's electrical performance under standard test conditions (STC).

The PV modules, designed for grid connected PV applications, include 3 protection bypass diodes connected in parallel to the cells. Each diode protects a group of 18 PV cells (2 horizontal rows) preventing them from hot spotting by driving the current if any of the cells is shaded. However, PV modules protected with bypass diodes can generate several maximum power points (MPPs), when operating under partial shading conditions [17].

In the basic configuration, the TUT PV system is composed of 3 series-connected strings of 17 PV modules and 3 strings of 6 modules with MPP voltages of 440 V and 155 V at STC, respectively. Actually, all possible electrical configurations with the 69 modules can be set and utilized. The location of PV strings has been carefully selected to avoid complete shading of strings during any time of the day or year. However, several groups of modules are partially shaded during different seasons of the year at different times of the day as seen in Figure 1. This characteristic permits us to



FIGURE 1: Example of partial shading of a PV string due to a building structure on a sunny day during spring 2012.

undertake research on different environmental aspects such as MPPT in cases of partial shading due to building structures [17].

The layout of the TUT solar power station research plant is illustrated in Figure 2. It shows the PV strings and modules located through most of the rooftop of the Department as well as the location of the different sensors of the measuring systems, which will be further described in the next chapter.

**2.2. Climate Measuring System and Data Acquisition.** The climatic measuring system is composed of an inclusive state of the art weather station and a mesh of irradiance and PV module temperature measurements. The sensor mesh is positioned throughout the PV power facility and records the operating conditions of every PV module string of the plant. The novelty of the climatic measuring systems comes from the data-acquisition system, which collects measurements continuously from all sensors with a 10 Hz sampling frequency. This means that even the fastest dynamical phenomena affecting the operation of the PV power plant are noticed.

The automatic weather station [18] measures the global atmospheric conditions under which the PV facility is operating. It includes measurements of ambient temperature and relative humidity, and wind speed and wind direction, as well as incoming global and diffuse solar radiations on the horizontal plane. The weather station measures global solar radiation with the pyranometer CMP22 (Kipp&Zonen) and diffuse component of the radiation with the pyranometer CMP21 (Kipp&Zonen) combined with a shadow ring CMC121 (Kipp&Zonen), blocking the direct solar radiation. Wind speed and direction are measured with an ultrasonic wind sensor WS425 (Vaisala), and ambient temperature and humidity are measured with the sensor HMP155 (Vaisala).

The weather station comprises equipment in two different locations of the roof. The CMP21 pyranometer mounted with the shadow ring, the HMP155<sub>T</sub> ambient temperature sensor, and the HMP155<sub>H</sub> relative humidity sensor are located on the lower rooftop for accessibility and safer adjustment of the shadow ring, especially during winter when the roof is covered with snow and ice. The CMP22 pyranometer and the WS425 wind sensor are located at the highest point of the

rooftop to measure the overall solar radiation and the wind profile at the power plant with minimum disturbance due to the building structures.

The mesh of irradiance and module temperature sensors is composed of 21 pairs of SPLite2 photodiodes (Kipp&Zonen) and Pt100 temperature sensors. These pairs are located at the ends of every PV module string, thus providing detailed information on the operating condition at string and module levels. The photodiodes are mounted with the same tilt angle as the PV modules, and the Pt100 sensors are attached to the back plates of the solar modules. Location of these sensors in the PV plant is shown in Figure 2, and installation is shown in Figure 3.

All the climatic data are acquired, transmitted, and recorded continuously in a database making them accessible for later analysis. The data-acquisition system is based on CompactRio data-acquisition cards from National Instruments enabling a flexible and economical system that uses specific swappable I/O modules to connect the sensor outputs. After collecting the data from the sensors, these cards transmit the data to a PC through Ethernet cable without interference or noise problems.

The database is based on PostgreSQL system, an open-source database management system available for several platforms including Linux, Mac OS X, or Microsoft Windows. This system enables information modification and extraction without blocking the storage process. The data is accessed using SQL queries from any computer connected to local area network of the department.

The sampling frequency of climatic measurements is a key parameter since the database will continuously store data acquired from 48 sensors. It has to be fast enough to detect even the fastest phenomena affecting the electrical operation of the PV system, but simultaneously be as long as possible because of the vast amount of data to be processed, as well as the storage needs. Among the climatic variables to be acquired, the solar radiation has the highest and fastest variations; for example, there can be changes of over  $700 \text{ W/m}^2$  within seconds in days with moving clouds. Therefore, it was essential to find out the sampling frequency required to detect even the fastest phenomena related to power generation with PV power plants. The simplest way to achieve this was to use a PV module as a solar radiation sensor and evaluate the effect of sampling frequency from the measurements.

Figure 4 illustrates the measured short-circuit current  $I_{SC}$  of a single PV-module during 7 hours on July 1st, 2010, with a sampling frequency of 25 Hz. When the PV module is short-circuited it acts as a solar radiation sensor with its output current linearly changing with the incoming irradiance. A sampling frequency of 25 Hz was considered to be high enough to detect even the fastest changes in irradiance causing an effect on the PV module. A partially cloudy day with moving clouds was chosen to provide the climatic conditions needed to evaluate such effects.

Figure 4 shows values of  $I_{SC}$  from 1.05 to 10.06 A, which correspond to irradiance levels between  $131$  and  $1255 \text{ W/m}^2$ , respectively. Changes of  $I_{SC}$  up to  $0.56 \text{ A}$  ( $71 \text{ W/m}^2$ ) happened between 2 consecutive measurements, which are roughly 5%

of the maximum current during the measurement period. A change of 5% might not yet have a drastic effect on the electrical characteristic of the PV module, but with this rate of change the current goes easily from minimum to maximum value in a second or vice versa. Such fast climatic changes demonstrate the need of sampling frequency higher than 1 Hz.

Taking the 25 Hz measurements as reference and down-sampling the acquisition frequency permit us to evaluate the effect of sampling frequency on the accuracy of the solar radiation measurements. Figure 5 presents the standard deviation error of the measured solar radiation as a function of the sampling frequency.

Figure 5 shows inverse exponential behavior of the standard deviation error with increasing sampling rate at low sampling rates as expected. The standard deviation error starts to grow considerably, when sampling frequency goes below 5 Hz, and increases up to  $48.7 \text{ W/m}^2$  at 0.125 Hz. Sampling frequencies over 5 Hz result in small standard deviation of incoming radiation below  $1 \text{ W/m}^2$ . Therefore, sampling frequency of 10 Hz was considered to be sufficient for detecting even the fastest phenomena related to power generation with PV power plants.

### 3. *I-U* Curve Tracer to Measure Electrical Characteristics

The experimental setup for measuring the *I-U* characteristics of the PV generator is composed of four parallel-connected high-power IGBT modules ( $1200 \text{ V}/200 \text{ A}$ ), the gate drive circuitry, and a high-speed oscilloscope to record the current and voltage data. The setup was designed to enable an *I-U* sweep from a string of 17 PV modules with a peak power of 3.2 kW. The measuring setup operates as follows: the IGBT modules act as regulating resistors (the channel resistance), which are used to realize an adjustable load resistor for the PV generator. Using an external microprocessor, a variable-duty PWM signal is generated and fed to the gate drivers, which are then low-pass filtered to supply linear gate voltage ramps to the IGBTs. As the filtered gate voltages exceed the threshold voltage of the IGBTs, the conductivities of the channels increase, forcing the operation point of the PV generator from open circuit to short circuit, and thereby enable the *I-U* curve measurement. Figure 6 shows (a) the *I-U* curve tracer scheme and (b) the designed tracer prototype.

### 4. Climatic Measurements

The large amount of data recorded continuously to the database from the climatic and radiation sensors can be utilized in various ways. As is commonly known, the available output power of a PV generator depends not only on the received solar radiation, but also on the operation temperature of the modules with a thermal coefficient on the order of  $-0.5\%/^{\circ}\text{C}$ . PV module temperature follows radiation changes with delay depending on various heat transfer processes. It also depends on various climatic variables [5].

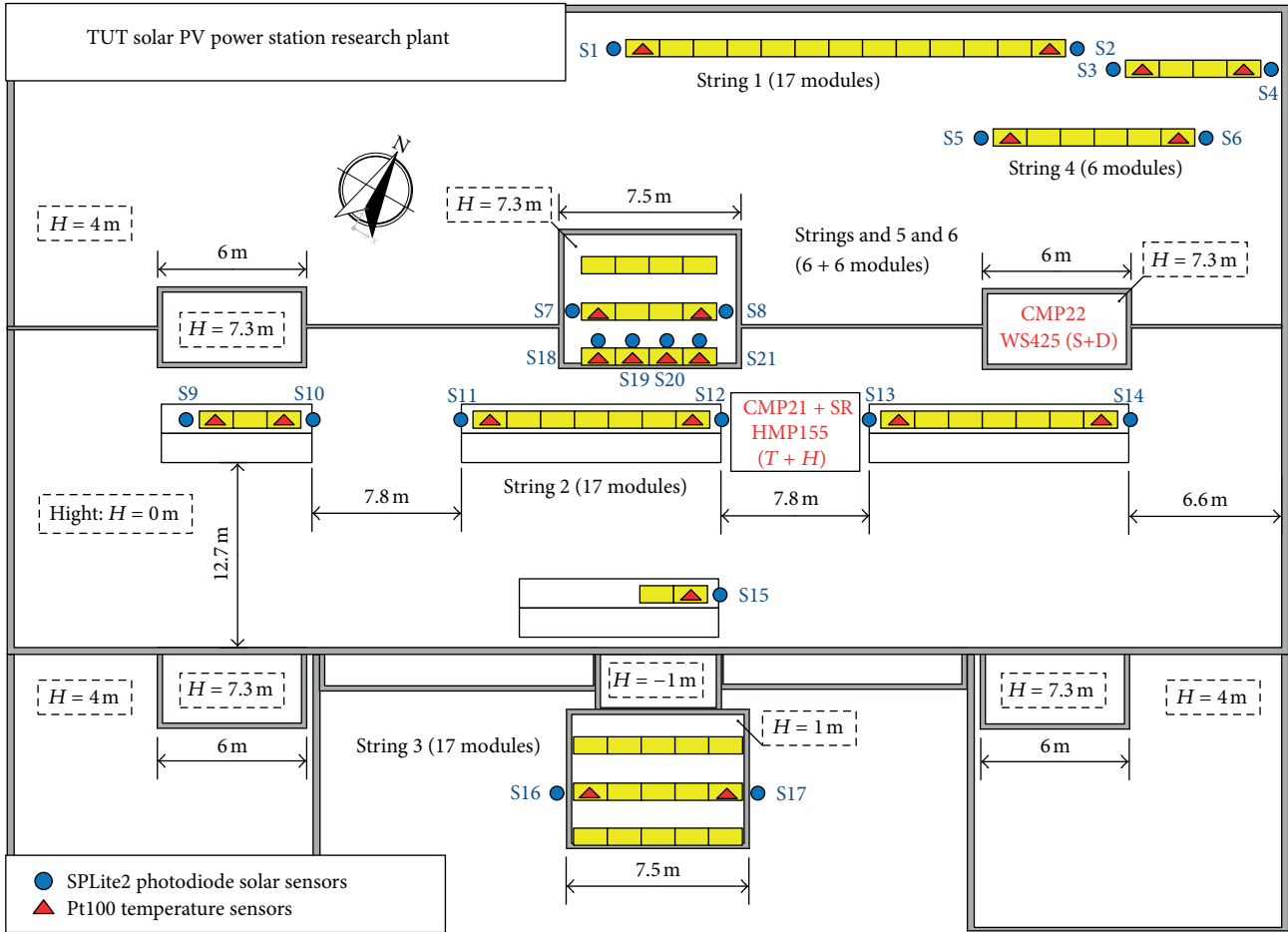


FIGURE 2: Layout scheme of the TUT solar PV power station research plant including its climatic measuring system.

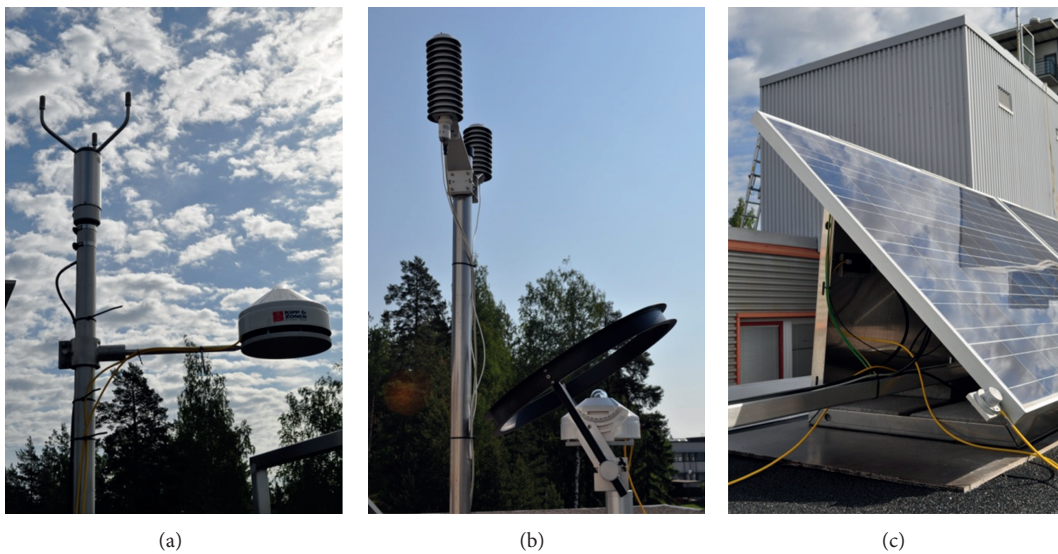


FIGURE 3: (a) WS425 wind sensor and CMP22 pyranometer, (b) HMP155 sensors with temperature and humidity probes equipped with radiation shields and CMP21 pyranometer combined with the CMC121 shadow ring, and (c) SPLite2 photodiode sensor attached to a PV module.

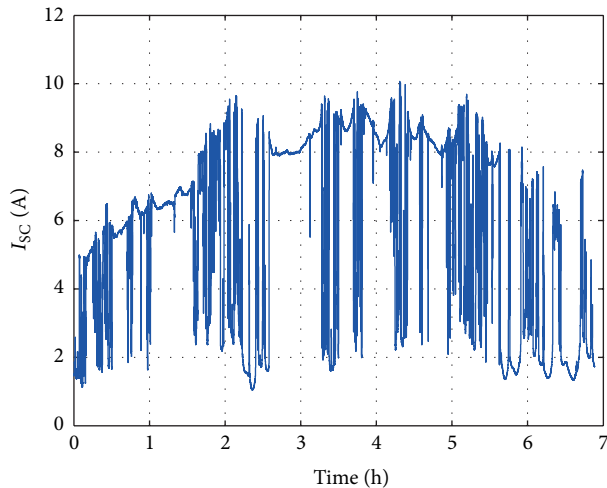


FIGURE 4: Measured  $I_{sc}$  of a single PV module on July 1st, 2010, with a sampling frequency of 25 Hz.

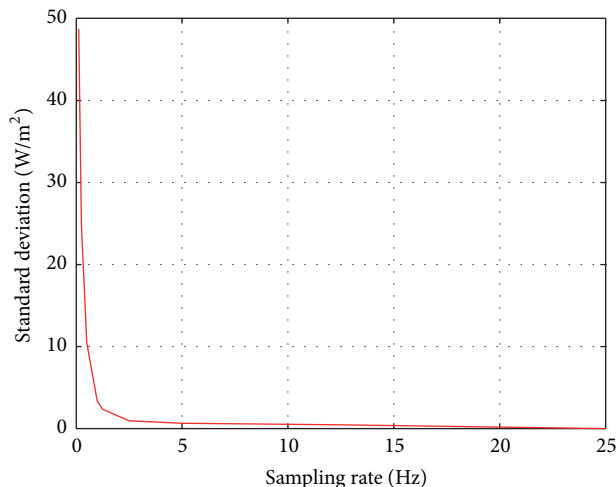


FIGURE 5: Standard deviation error of the incoming solar radiation as a function of the sampling frequency on a single PV module during a period of 7 hours on July 1st, 2010.

Figure 7 shows the measured environmental parameters during a clear sunny day on February 2nd, 2012, for two PV modules of the power plant to illustrate the applicability of the measurements system. A typical strong overall correlation exists between the module temperature and the incoming irradiance. The PV module equipped with sensors S13 (Figure 2) receives solar radiation during the whole day without any major shading, and the module temperature follows radiation changes with certain delay. This delay is directly related to the heat capacity of the module and to the heat transfer between the module and the environment. The PV module equipped with sensors S10 receives solar radiation after sunrise and before sunset, but is shaded by a building structure in the middle of the day so that only diffuse radiation is received. Although incident radiation changes rapidly, changes in temperature are slow due to the thermal

mass of the modules. The ambient temperature changed only slightly during the day, having minimal effect on changes in the module temperature. Also humidity stayed practically constant during the day.

Changes in temperature primarily follow changes in irradiance as shown in Figure 7, but temperature fluctuations around eleven o'clock and at half past one do not directly correlate with irradiances. This demonstrates that also other environmental variables affect the module temperature in addition to solar radiation. The higher wind speed before eleven o'clock obviously cools down the modules more effectively on the morning than at noon. On the afternoon around half past one o'clock, there is a period of low wind speed causing the heating up of the modules before two o'clock. Also sensor 13 seems to have a better shelter from the wind than sensor 10 during this day due to building structure. Overall, the measured PV module temperature deviates up to  $10^{\circ}\text{C}$  from an assumed module temperature based on direct correlation with the incident radiation. Accordingly, an error of 5% in the estimated electric energy yield of the module can be expected, if only incident solar radiation is used to estimate the module temperature. Therefore, to model the electrical behavior of PV modules and generators reliably, a more advanced dynamic thermal model is needed [5–8].

Sun rises only slightly above the horizon in southern parts of Finland in the midwinter. Therefore, PV modules with a tilt angle of  $45^{\circ}$  receive much higher irradiance than pyranometers measuring irradiances on a horizontal surface (Figure 7). Irradiance received by the PV modules increases sharply after the sun is visible for them and decreases as sharply on the afternoon during sunset. Before the sunrise and after the sunset there is a two-hour period of considerable diffuse irradiance. Even on the midday, diffuse radiation constitutes nearly 40% of global radiation. This is mostly due to reflection of solar radiation from snow. It also explains part of the high irradiance received by the PV modules because they are more exposed to diffuse radiation from the snow than the pyranometers facing the sky.

During summer, the sun sets in Finland only slightly below the horizon for few hours, leaving a weak intensity of light. Daytime solar irradiance is of course higher than that in winter time, but the difference is not dramatic. On the other hand, daytime in summer is up to 20 hours, leading to much higher daily energy yield than that in the winter time. Both global and direct solar radiations received by the PV modules are considerable high in summer during periods of clear sky. Also diffuse component of radiation is considerable during long periods from sunrise until the sun faces the PV modules and, accordingly, in the evening until sun sets again.

An example of partial shading caused by a building structure on String 2 containing 17 PV modules is shown in Figure 8. The irradiance profile received by the string indicates that 2 of the 3 PV modules located between sensors S9 and S10 (see Figure 2) are completely shaded by the building structure at 10:30 because sensor S9 (blue line) is shaded all the time and S10 (dashed red line) starts to be shaded after 10:37. The modules located between sensors S11 and S12 are illuminated all the time at a level of  $430\text{ W/m}^2$ . Finally, sensor S13 is illuminated at the same level as sensors

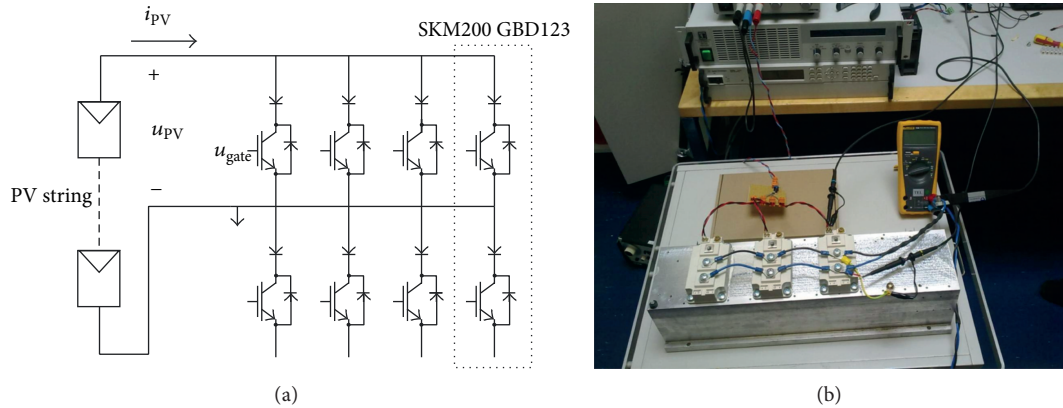


FIGURE 6: (a) Scheme of the  $I$ - $U$  curve measurement tracer for PV power systems. (b) Picture of the IGBT modules, cooler and power measuring connections.

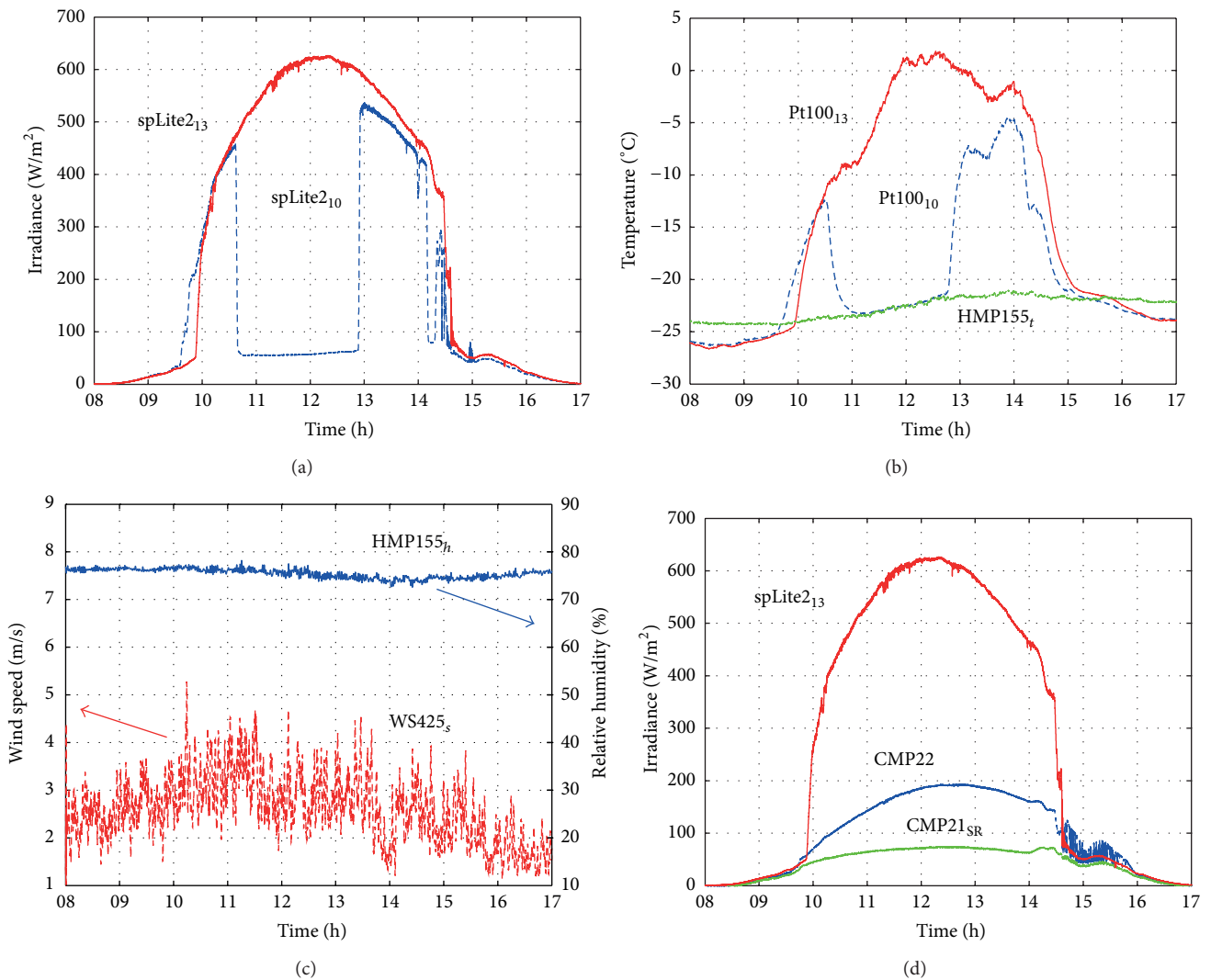


FIGURE 7: Irradiance and climatic data measured on a sunny day of February 2nd, 2012: (a) irradiances received by two PV modules equipped with irradiance and temperature sensors S10 and S13 (see Figure 2), (b) corresponding module temperatures together with the ambient temperature measured with sensor  $HMP155_T$ , (c) wind speed and relative humidity measured by sensors  $WS425_s$  and  $HMP155_H$ , respectively, (d) irradiance received by the PV module equipped with sensor S13 together with the global and diffuse irradiances at the research plant measured by pyranometers  $CMP22$  and  $CMP21$ , respectively.

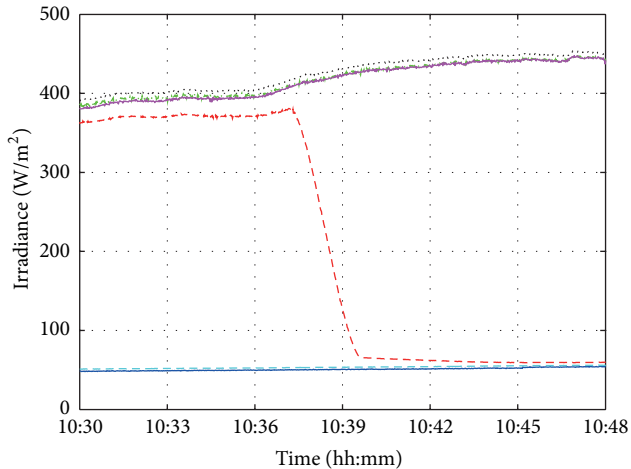


FIGURE 8: Irradiance profile received by String 2 on February 2nd, 2012, during a period of 18 minutes and measured with sensors from S9 to S14 (see Figure 2). Sensors from S9 to S14 correspond to the lines as follows: blue, red dashed, green dash-dotted, black dotted, magenta, and cyan dashed.

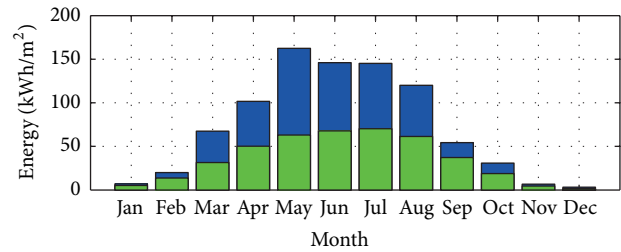
S11 and S12, but sensor S14 is shaded all the time. This indicates that parts of the PV modules located between sensors S13 and S14 are shaded due to another building.

The irradiance profile illustrated in Figure 8 demonstrates that the data measured by the climatic measurement system can be used to study systematically the effects of partial shading conditions on the operation of PV generators caused by static building structures. Furthermore, it can be used to discern between the effects due to building structure and moving clouds and to evaluate the energy losses generated by these different shading causes.

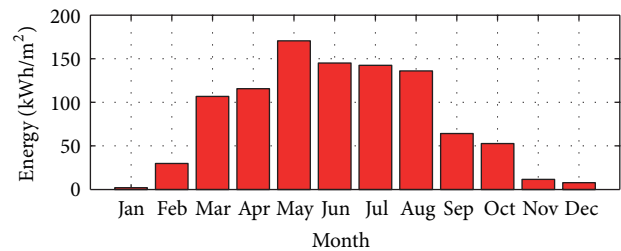
## 5. Solar Energy Received at TUT Solar PV Power Station Research Plant

The amount of solar energy collected by a PV module is a function of the incoming solar radiation, the surrounding characteristics, and the module properties, mounting tilt and orientation. In fact, the mounting orientation and tilt of a solar panel strongly affect the amount of collected yield. Therefore, PV modules must be slanted and oriented at the optimum angles to collect the maximum solar energy available in a specific location. The best method to optimize the tilt and orientation of a solar panel is by applying an active sun tracker [19].

Countries in the northern latitudes, for example, Finland, are characterized by low ambient temperatures during most part of the year and high variability of solar radiation levels and trajectory of the sun from summer to winter, which hinders the sizing and optimization of PV generators. Extreme ambient temperatures during winter, snow cover, and ice formation damage mobile parts of trackers, preventing their use. On the other hand, fixed PV module installations will result in overall power losses through the year compared to systems with sun trackers.



(a)



(b)

FIGURE 9: Monthly solar energy received at the TUT solar PV power station research plant during its first year of operation (August 2011 to July 2012): the blue bars on top graph correspond to the global solar energy received on the horizontal plane (measured by pyranometer CMP22), the green bars on top graph represent the diffuse solar energy on the horizontal plane (measured by pyranometer CMP21 combined with the shadow ring) and the red bars at the bottom graph correspond to the global solar energy received on the plane of modules (measured by the SPLite2 sensor S13).

TUT solar PV power station research plant is a fixed installation optimized for overall operation during the year. PV modules are mounted in line with the buildings oriented  $26^\circ$  east of due south with a tilt angle of  $45^\circ$  from the horizontal plane. The optimal module inclination angles by month for locations with Tampere latitude are included in Table 2. Figure 9 illustrates the monthly global and diffuse solar energy received on a horizontal plane and the monthly global solar energy on PV modules from August 2011 to July 2012.

In the top graph of Figure 9, the levels of monthly global solar energy received on the horizontal plane in Tampere vary from  $3.14 \text{ kWh/m}^2$ , in December, to  $160.50 \text{ kWh/m}^2$ , in May, in line with [20]. The year 2012 has been particularly overcast with small amount of days with clear sky in spring and summer. This can be confirmed by comparing yearly average of  $909.35 \text{ kWh/m}^2$  by [20] with the  $864.64 \text{ kWh/m}^2$  measured in TUT's research plant during its first year of operation. Nonetheless, such levels of yearly solar energy do not diverge excessively with respect to the radiation levels received in northern Germany. The diffuse component of solar radiation on the horizontal plane indicates that months from September to February are mostly cloudy as they present large ratios of diffuse to global solar radiation. The remaining months from March to August show higher values of global solar energy received on the horizontal plane

TABLE 2: Optimal monthly module inclination angles from the horizontal plane for TUT location according to [20].

Jan	Feb	Mar	Apr	May	Jun	Jul	Aug	Sep	Oct	Nov	Dec
78°	73°	59°	44°	30°	22°	25°	35°	50°	63°	72°	80°

having maximum on summer time due to the wider path of sun through the sky. In Tampere, on December, March, and June 21sts the sun rises at 38°, 92°, and 148° east of due south and sets at 38°, 92°, and 148° west of due south, respectively, resulting in much longer daytimes in summer than in winter. Also the relative part of diffuse radiation in the global radiation is smaller during summer months than that in winter, and sunny days are more common.

The bottom graph of Figure 9 illustrates the global solar energy received on a plane in line with the PV modules. The levels of solar energy measured from November to February are particularly low, especially in January when the received solar energy on the modules is lower than that on the horizontal plane. This phenomenon is caused by the snow covering the PV modules and photodiode-based SPLite2 sensors attached to them during most of this period. The pyranometers CMP22 and CMP21 were clear from snow since they are heated to prevent snow piling on the domes. Additionally, both pyranometers are located at a higher level than the PV modules (see Figure 3), ensuring that they were not covered by snow piles during the measuring period. The months of March, April, September, and October present higher values of solar energy received on the plane of modules with respect to values on the horizontal plane. This is consistent with the fact that the modules tilt is closer to the optimum angles for those months (Table 2). The summer months, May, June, July, and August, present the largest values of solar energy received. However, in June and July solar energy received on the tilted plane was 1.02 and 2.85 kWh/m<sup>2</sup> less than that on the horizontal plane, respectively. This can be explained by the wide path of the sun through the sky during summer. Figure 10 demonstrates this matter explicitly. The PV modules receive much higher solar radiation levels in the middle of the day than the horizontal plane. However, the irradiance received by the PV modules decreases rapidly after three o'clock, while the global irradiance on the horizontal plane decreases more smoothly until nine o'clock in the evening.

Figures 9 and 10 imply that the use of sun-tracking systems adjusting both inclination and orientation of PV modules would highly enhance the power produced by PV generators located in northern latitudes. Actually part of the direct solar radiation is lost totally on summer time with fixed installations because in the morning after sunrise and in the evening before sunset sun shines only on the backsides of the modules. TUT PV modules are oriented 26° east of due south, and, therefore, PV modules lose the direct part of solar radiation during evening hours. In fact, extrapolation of the solar energy levels received using a sun-tracking system suggests that they would reach the levels of solar energy received by fixed PV systems in southern Germany.

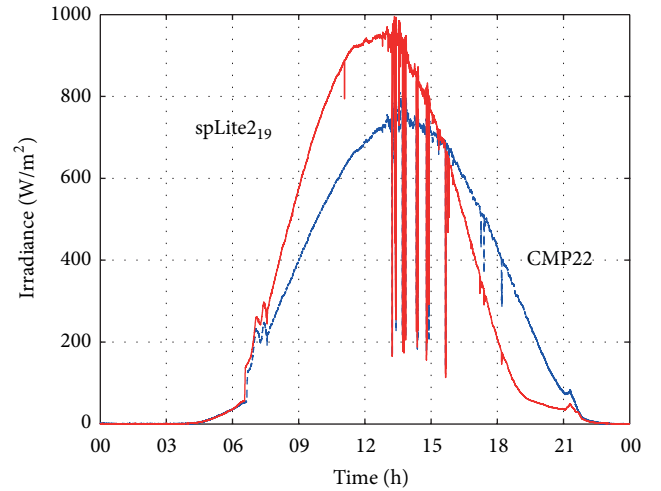


FIGURE 10: Solar radiation on the plane of PV modules measured by sensor S19 (red line) and on the horizontal plane measured by pyranometer CMP22 (blue dashed line) on July 22nd, 2011.

## 6. Effects of Partial Shading and Reflections Caused by Building Structures and Snow

The TUT solar PV power station research plant provides excellent conditions to study the operation PV power plants under varying climatic and environmental conditions. Especially the comprehensive measurements around the power plant with high sampling frequency make it possible to study even the fastest phenomena affection to the electrical operation of the plant. To demonstrate these abilities the effects of partial shading and reflections of solar radiation due to building structures and snow on PV modules and strings have been analyzed by means of the measured electrical  $I-U$  and  $P-U$  characteristics (Figures 11 and 12).

The effect of partial shading on the electrical characteristics of a single PV module is clearly seen in Figure 11, where the operation under partial shading conditions on February 3rd, 2012, is compared to the operation under homogeneous conditions on August 31st, 2011. Table 3 includes the most important environmental parameter values at the instant when the electrical measurements were taken. In this case, the partial shading is caused by a thin layer of ice covering the lower row of PV cells and, thereby, filtering the solar radiation received by them. While the rest of cells on upper rows receive sunlight directly at an irradiance level of 430 W/m<sup>2</sup>, the row of cells covered by ice received approximately two-thirds of the incoming irradiance.

Operation of the PV module under 2 different irradiance levels leads to two local MPPs in contrast with the typical

TABLE 3: Environmental conditions of the PV module equipped with radiation and temperature sensors S19 at the moments, when curves in Figure 11 were measured.

Date	Time	Irradiance (W/m <sup>2</sup> )	Mod. temp. (°C)
August 31st, 2011	12:04	450.8	32.42
February 3rd, 2012	11:19	429.5	-12.10

operation under homogeneous irradiance level, which produces one unique global MPP as can be seen in Figure 11. Disparity between the open circuit voltages of the two measurements is due to the different operating temperatures. This textbook level example demonstrates how simple partial shading condition and difference in ambient temperature are seen on a module level in real measurements. This kind of shading is typically caused also by building structures, whose cases can be analyzed systematically from the measured data.

To provide a more realistic view on the effects of partial shading on the operation of PV power plants, the operation of strings of 6 series-connected PV modules during autumn on September 28th, 2011, and in winter on February 3rd, 2012, is shown in Figure 12. Table 4 includes the most important environmental parameter values at the instant when the electrical measurements were taken. The measured  $I-U$  and  $P-U$  characteristics of String 4 (see Figure 2) are measured under homogeneous irradiance conditions during the autumn day at 09:36. Thus the electrical characteristics of the PV string are smooth with one global MPP. The electrical characteristics of String 5 (see Figure 2) are measured under varying irradiance conditions during the winter day at 12:08. They clearly show several local MPPs which could lead to incorrect operation of a MPPT algorithm in a PV inverter. The reason behind these multiple local MPPs is, again, a thin layer of ice formed in the lower part of the PV modules, as well as reflections off the snow.

In the PV modules, a bypass diode is connected in parallel with a string of 18 PV cells (2 horizontal rows of cells) to protect them from overheating. String 5 consists of 6 PV modules, which had ice covering at least part of their lower rows of cells on February 3rd 2012. Based on Figure 12, one-third of PV cells seem to be shaded by ice receiving the same irradiance of approximately 290 W/m<sup>2</sup> and producing a current of 2 A (see the  $I-U$  curve in Figure 13). Accordingly, another one-third of PV cells are nonshaded receiving an irradiance of approximately 450 W/m<sup>2</sup> and producing a current close to 3.5 A. These cells are most probably on the upper parts of the modules. The last one-third of PV cells receive varying amounts of irradiance between 290 and 450 W/m<sup>2</sup> due to smaller shading than the lower rows of cells. Therefore, several local MPPs are observed in the  $P-U$  curve in Figure 12 at voltages between 90 and 130 V. These kinds of conditions can cause major problems to the proper operation of PV inverters.

As a third demonstration on the potential of the TUT solar PV power station research plant, the operation of PV strings was analyzed under partial shading conditions caused by building structures. As explained in Section 2, the location

of the PV modules and strings in the research plant was carefully selected for permitting this type of measurements. However, this phenomenon only takes place during clear sky days in periods of the year in which the trajectory of the sun is only slightly above the horizon, that is, late autumn, winter, and early spring in Finland. Therefore, measurements on December 4th, 2012, for string 4 were used in this study.

String 4, which is composed of 6 PV modules connected in series in a row, was cleaned from snow, and electrical measurements were taken for 5 different partial shading conditions. Table 5 comprises the irradiances and module temperatures at both ends of String 4 measured by sensors S5 and S6 at the moments when the electrical measurements were taken. Measurements 1 to 4 correspond to operation under partial shading conditions of the PV string with 2, 3, 4, and 5 nonshaded modules, respectively. Measurement 5 shows the operation of the string under homogenous conditions. The operational conditions of String 4 during measurements 1 and 4 with 2 and 5 nonshaded PV modules are shown in Figure 13.

Irradiances measured at both ends of String 4 around the noon in December 4th 2012 are shown in Figure 14. Irradiances measured by sensor S5 are typical clear sky values for that time of year in Finland showing that the left end of String 4 is nonshaded during the whole measurement period. On the other hand, irradiance value measured by sensor S6 stays constant around 32 W/m<sup>2</sup> under the shadow of the building until 12:55 h. After that the whole string is nonshaded for a while and measurement 5 can be considered to be done under homogenous irradiance condition for the whole string. Solar radiation measured by sensors S5 and S6 during measurement 5 can be considered to correspond to homogenous irradiance conditions, in practice, since the small difference between them can be due to, for example, slightly different mounting angles of the irradiance sensors. The smooth shapes of  $I-U$  and  $P-U$  curves of measurement 5 in Figure 15 support this assumption.

The module temperatures measured by the temperature sensors S5 and S6 are in line with the measured irradiance trends (Table 5). Solar radiation is heating up the PV modules by almost 20°C according to the temperature difference of PV modules at both ends of the string during partial shading. Temperature of the last PV module on the left in Figure 13 measured by sensor S6 rose over 10°C before it was fully nonshaded at the time of measurement 5. It took almost half an hour for the edge of the shadow to pass the module. During this time the direct solar radiation heated the PV module gradually, before it was fully under direct solar radiation.

The effect of partial shading on String 4 is illustrated in Figure 15 by the  $I-U$  and  $P-U$  characteristics for 4 partial shading conditions along with one homogenous irradiance condition. Under partial shading conditions caused by building structures, each of the shaded  $I-U$  and  $P-U$  curves can be divided in two different areas. In the first area, bypass diodes protecting groups of shaded cells are conducting and shorting out the circuits of groups of 18 PV cells and thus eliminating effects of shading like possible hot spots. In the second area, higher voltages appear since the bypass diodes

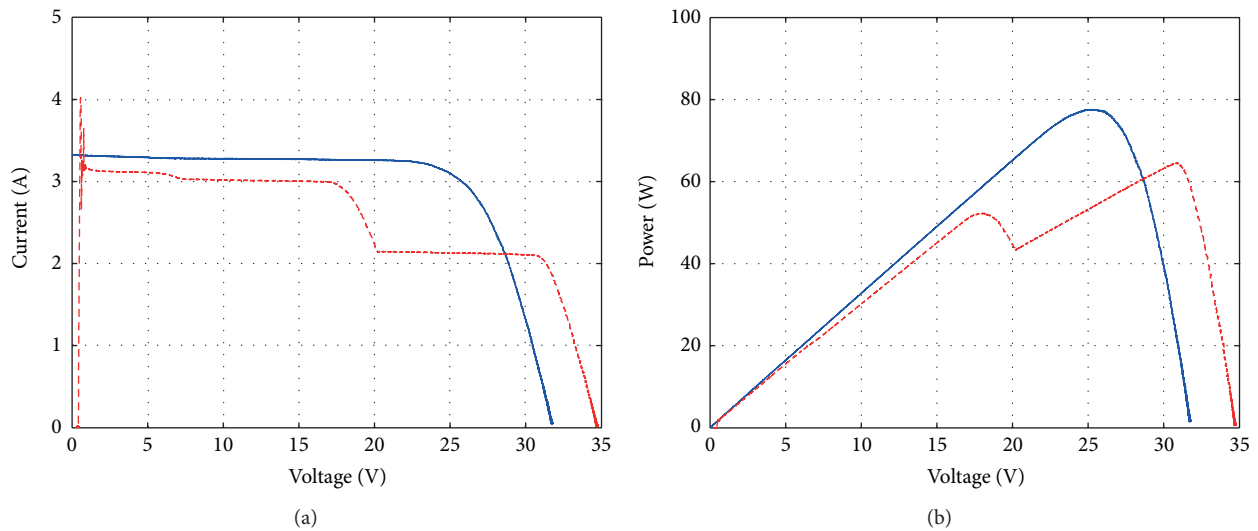


FIGURE 11: Measured (a)  $I$ - $U$  and (b)  $P$ - $U$  characteristics of the PV module equipped with irradiance and temperature sensor S19 under homogeneous irradiance on August 31st, 2011, at 12:04 (blue lines) and under partial shading conditions on February 3rd, 2012, at 11:19 (red-dashed lines).

TABLE 4: Environmental conditions of the PV strings on September 28th, 2011, measured with sensors S5 and S6 located at both ends of String 4, and on February 3rd, 2012, measured with sensors S7 and S8 located at both ends of String 5 at the moments when the curves in Figure 12 were measured.

September 28th 2011				February 3rd 2012			
Sensor	Time	Irradiance ( $W/m^2$ )	Mod. temp. ( $^{\circ}C$ )	Sensor	Time	Irradiance ( $W/m^2$ )	Mod. temp. ( $^{\circ}C$ )
S5	09:36 h	568.1	25.09	S7	12:08 h	436.7	-5.70
S6	09:36 h	594.9	26.58	S8	12:08 h	443.4	-6.50

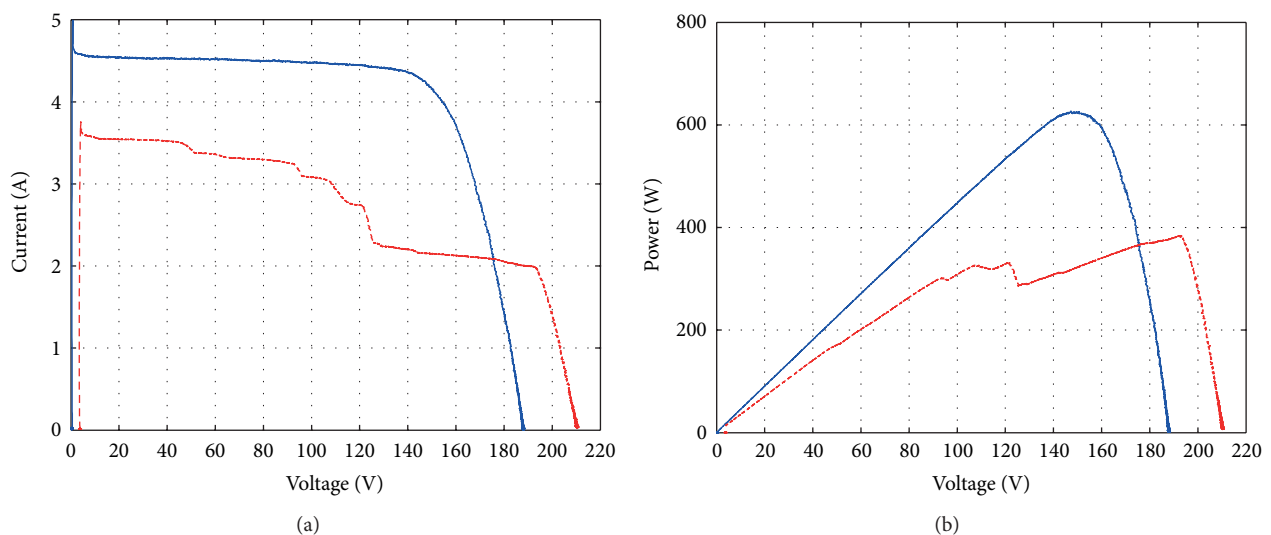


FIGURE 12: (a)  $I$ - $U$  and (b)  $P$ - $U$  characteristics of PV strings of 6 series-connected PV modules. Characteristics of String 4 were measured on September 28th, 2011, under homogeneous irradiance conditions at 09:36 (blue lines) and of String 5 on February 3rd, 2012, under partial shading conditions at 12:08 (red dashed lines).



FIGURE 13: Figures of the operational conditions of String 4 under partial shading conditions caused by a building structure during the electrical measurements on December 4th, 2012: (a) conditions of measurement 1 with 2 nonshaded PV modules and 4 fully or partially shaded PV modules, (b) conditions of measurement 4 with 5 nonshaded PV modules and 1 partially-shaded PV module.

TABLE 5: Irradiances received by the PV string and module temperatures on December 4th, 2012, measured with sensors S5 and S6 located at both ends of String 4 at the moments when curves in Figure 15 were measured.

Measurement	Time	Sensor			
		S5		S6	
		Irradiance	Mod. temp.	Irradiance	Mod. temp.
		(W/m <sup>2</sup> )	(°C)	(W/m <sup>2</sup> )	(°C)
1	11:24 h	425.9	-1.58	30.5	-17.42
2	11:37 h	439.9	0.73	31.2	-17.37
3	12:05 h	438.4	3.71	32.5	-16.97
4	12:31 h	424.0	3.19	33.3	-16.48
5	12:57 h	386.6	1.93	353.8	-5.85

protecting the groups of nonshaded cells are reverse biased and the characteristic of the string is dominated by the series-connected shaded cells. The voltage levels at the local maximum power points at low voltages in measurements 1, 2, 3, and 4 are approximately 50, 80, 105, and 140 V, respectively. The voltages of the local MPPs at high voltages are roughly between 170 and 195 V for the studied partial shading conditions.

Several maximum power point tracking algorithms search for MPPs around 80% of open-circuit voltage, that is, around 160 V under the studied operating conditions. It would result in incorrect operation of the PV inverter in the local MPP at high voltages instead of the global MPP at lower voltages leading to major power losses. Maximum power of local MPPs at high voltages is between 50 and 70 W, but the power of the local MPP at low voltages goes up to 400 W or so. In the studied case the partial shading condition leading to the occurrence of two local maxima in  $P$ - $U$  characteristics lasts for close to 2.5 hours. If an inverter has operated the whole period in the local MPP at high voltages due to a simple voltage reference, as described above, losses of produced power could have been close to 0.5 kWh for the

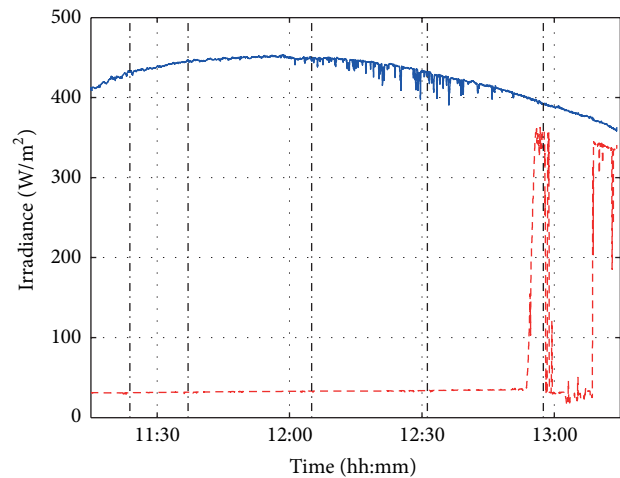


FIGURE 14: Irradiance profile received by String 4 during the electrical measurements of Figure 15 measured by sensors S5 (blue line) and S6 (red-dashed line) on December 4th, 2012. The moments when the electrical measurements were taken are marked with vertical dash-dotted lines.

studied string of only 6 PV modules. The produced power would have been just over 0.1 kWh.

The collected data from the environmental measurement system of the PV power plant enables systematic studies of the electrical behavior of the power plant, for example, under shading due to building or clouds. Simulation tools are under development to analyze these kinds of issues during periods up to years.

## 7. Conclusions

This paper describes the TUT Solar PV Power Station Research Plant installed on the rooftop of the Department of Electrical Engineering at the Tampere University of Technology jointly with its climatic, electrical, and data-acquisition systems. The layout of the PV modules and strings, climatic measurements, data acquisition, and database are designed

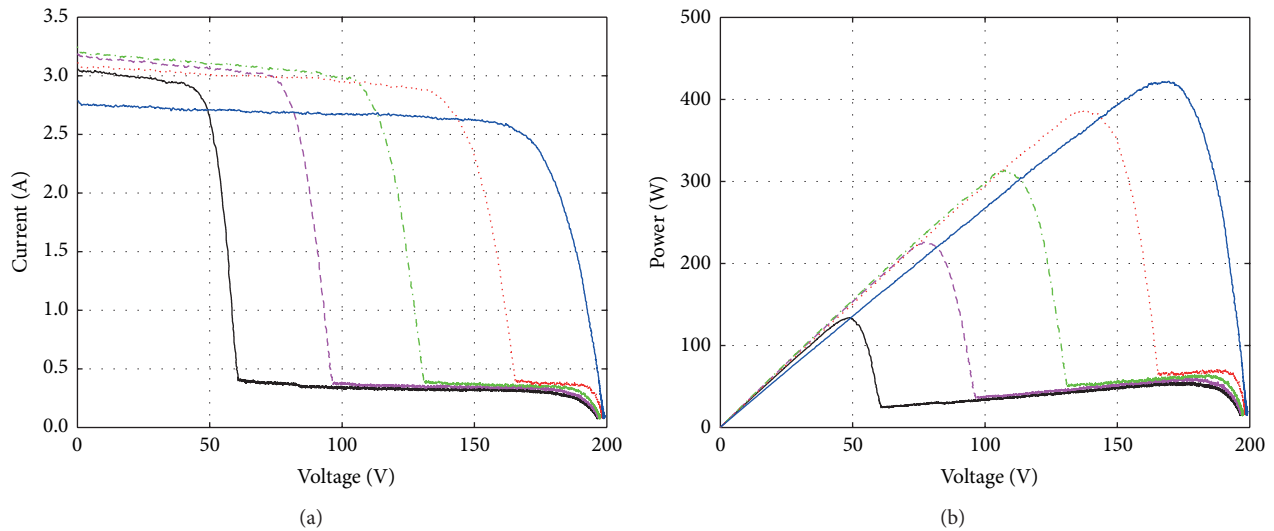


FIGURE 15: (a)  $I$ - $U$  and (b)  $P$ - $U$  characteristics of String 4 (see Figure 2) of 6 series-connected PV modules measured under partial shading conditions on December 4th, 2012. Irradiances and module temperatures measured with sensors S5 and S6 at the corresponding moments are presented in Table 4. Measurements from 1 to 5 correspond to the lines as follows: black, magenta dashed, green dash-dotted, red dotted, and blue.

for studying the operation of PV systems under nonuniform and rapidly varying operational conditions. Sampling frequency of 10 Hz is shown to be sufficient to detect even the fastest phenomena being related to power generation with PV power plants.

Strong overall correlation between the PV module temperature and the incoming irradiance has been observed in the measurements, as expected. However, the experimental results also demonstrate that irradiance does not alone describe adequately the thermal behavior of PV modules. There is a need to develop a more advanced dynamic thermal model for predicting module temperature more accurately than is possible by existing models. It was shown that ice covering part of the PV modules and reflections due to the snow surrounding the modules had a major effect on the electrical behavior of PV strings. They created multiple local maximum power points in measured electrical characteristics of PV modules and strings of series-connected modules. Operation of PV strings under partial shading caused by a building structure generates power characteristic curves with two local maximum power points in good agreement with earlier theoretical findings. These kinds of shading conditions will cause major problems to conventional maximum power point tracking algorithms.

## References

- [1] European Photovoltaic Industry Association (EPIA), "Solar photovoltaics competing in the energy sector—on the road to competitiveness," September 2011, [http://www.epia.org/index.php?eID=tx\\_nawsecuredl&u=0&file=/uploads/tx\\_eipiublications/Competing\\_Full\\_Report.pdf&t=1377285583&hash=c740-00f30f1171e54ff12bbe83caaf5396006f1dcaaf5396006f1d](http://www.epia.org/index.php?eID=tx_nawsecuredl&u=0&file=/uploads/tx_eipiublications/Competing_Full_Report.pdf&t=1377285583&hash=c740-00f30f1171e54ff12bbe83caaf5396006f1dcaaf5396006f1d).
- [2] A. Mäki and S. Valkealahti, "Operation of long series connected silicon-based photovoltaic module strings and parallel connected short strings under partial shading conditions," in *Proceedings of the 26th European Photovoltaic Solar Energy Conference and Exhibition (EUPVSEC '11)*, pp. 4227–4232, 2011.
- [3] L. Sandrolini, M. Artioli, and U. Reggiani, "Numerical method for the extraction of photovoltaic module double-diode model parameters through cluster analysis," *Applied Energy*, vol. 87, no. 2, pp. 442–451, 2010.
- [4] S. Nagae, M. Toda, T. Minemoto, H. Takakura, and Y. Hamakawa, "Evaluation of the impact of solar spectrum and temperature variations on output power of silicon-based photovoltaic modules," *Solar Energy Materials and Solar Cells*, vol. 90, no. 20, pp. 3568–3575, 2006.
- [5] A. D. Jones and C. P. Underwood, "A thermal model for photovoltaic systems," *Solar Energy*, vol. 70, no. 4, pp. 349–359, 2001.
- [6] M. Mattei, G. Notton, C. Cristofari, M. Muselli, and P. Poggi, "Calculation of the polycrystalline PV module temperature using a simple method of energy balance," *Renewable Energy*, vol. 31, no. 4, pp. 553–567, 2006.
- [7] E. Skoplaki, A. G. Boudouvis, and J. A. Palyvos, "A simple correlation for the operating temperature of photovoltaic modules of arbitrary mounting," *Solar Energy Materials and Solar Cells*, vol. 92, no. 11, pp. 1393–1402, 2008.
- [8] S. Armstrong and W. G. Hurley, "A thermal model for photovoltaic panels under varying atmospheric conditions," *Applied Thermal Engineering*, vol. 30, no. 11–12, pp. 1488–1495, 2010.
- [9] A. Woyte, J. Nijs, and R. Belmans, "Partial shadowing of photovoltaic arrays with different system configurations: literature review and field test results," *Solar Energy*, vol. 74, no. 3, pp. 217–233, 2003.
- [10] M. García, J. M. Maruri, L. Marroyo, E. Lorenzo, and M. Pérez, "Partial shadowing, MPPT performance and inverter configurations: observations at tracking PV plants," *Progress in Photovoltaics: Research and Applications*, vol. 16, no. 6, pp. 529–536, 2008.

- [11] C. E. Chamberlin, P. Lehman, J. Zoellick, and G. Pauletto, "Effects of mismatch losses in photovoltaic arrays," *Solar Energy*, vol. 54, no. 3, pp. 165–171, 1995.
- [12] N. D. Kaushika and A. K. Rai, "An investigation of mismatch losses in solar photovoltaic cell networks," *Energy*, vol. 32, no. 5, pp. 755–759, 2007.
- [13] E. Karatepe, M. Boztepe, and M. Çolak, "Development of a suitable model for characterizing photovoltaic arrays with shaded solar cells," *Solar Energy*, vol. 81, no. 8, pp. 977–992, 2007.
- [14] G. Walker, "Evaluating MPPT converter topologies using a matlab PV model," *Journal of Electrical and Electronics Engineering*, vol. 21, no. 1, pp. 49–55, 2001.
- [15] A. Mäki, S. Valkealahti, and J. Leppäaho, "Operation of series-connected silicon-based photovoltaic modules under partial shading conditions," *Progress in Photovoltaics: Research and Applications*, vol. 20, no. 3, pp. 298–309, 2012.
- [16] E. V. Paraskevadaki and S. A. Papathanassiou, "Evaluation of MPP voltage and power of mc-Si PV modules in partial shading conditions," *IEEE Transactions on Energy Conversion*, vol. 26, no. 3, pp. 923–932, 2011.
- [17] A. Mäki and S. Valkealahti, "Power losses in long string and parallel-connected short strings of series-connected silicon-based photovoltaic modules due to partial shading conditions," *IEEE Transactions on Energy Conversion*, vol. 27, no. 1, pp. 173–183, 2012.
- [18] World Meteorological Organization (WMO), *Guide to Meteorological Instruments and Methods of Observation*, 2008, <http://www.wmo.int/pages/prog/www/IMOP/CIMO-Guide.html>.
- [19] T. Khatib, A. Mohamed, and K. Sopian, "Optimization of a PV/wind micro-grid for rural housing electrification using a hybrid iterative/genetic algorithm: case study of Kuala Terengganu, Malaysia," *Energy and Buildings*, vol. 47, pp. 321–331, 2012.
- [20] "Free Online Estimation of the Solar Irradiance and Ambient Temperature in Any European and African Location," February 2012, <http://re.jrc.ec.europa.eu/pvgis/apps4/pvest.php>.

## Research Article

# Synthesis and Characterization of Carbazole-Benzothiadiazole-Based Conjugated Polymers for Organic Photovoltaic Cells with Triazole in the Main Chain

Eunhee Lim

Department of Chemistry, Kyonggi University, San 94-6, Iui-dong, Yeongtong-gu, Suwon-si, Gyeonggi 443-760, Republic of Korea

Correspondence should be addressed to Eunhee Lim; [ehlim@kyonggi.ac.kr](mailto:ehlim@kyonggi.ac.kr)

Received 24 February 2013; Accepted 11 June 2013

Academic Editor: Przemyslaw Rupnowski

Copyright © 2013 Eunhee Lim. This is an open access article distributed under the Creative Commons Attribution License, which permits unrestricted use, distribution, and reproduction in any medium, provided the original work is properly cited.

We have synthesized a series of carbazole-benzothiadiazole-triazole based copolymers, poly[(*N*-9'-heptadecanyl-2,7-carbazole)-*co*-(5,5-(4',7'-di-2-thienyl-2',1',3'-benzothiadiazole))-*co*-((4-(4-butylphenyl)-3,5-diphenyl-4*H*-1,2,4]triazole))] (**PCz3TBTz**) by Suzuki coupling polymerization. The optical and electrochemical properties of the copolymers could be tuned by changing the comonomer unit of triazole from 0% to 80%. Organic photovoltaic (OPV) cells were fabricated by blending the synthesized polymers as a donor and PCBM as an acceptor. The material solubility and film morphology were improved by introducing the triazole unit in the main chain. Improved OPV device performance of 1.74% was achieved in the presence of an optimal amount of triazole moieties.

## 1. Introduction

Organic photovoltaic (OPV) cells are promising sources of electrical power that have attracted considerable attention because of their efficiency, low cost, and potential renewable energy applications. The prototypical material system consisting of poly(3-hexylthiophene) (P3HT) and [6,6]-phenyl-C<sub>61</sub> butyric acid methylester (PCBM) normally gives power conversion efficiencies (PCEs) in a range of about 4-5% [2]. New conjugated polymers with low band gaps that can efficiently harvest solar energy over a broader spectrum are being actively developed. To enhance OPV performance, low-band-gap conjugated materials with appropriate energy levels are required for efficient charge transfer [3]. One successful approach to enhance OPV performance is to arrange electron-donating and electron-accepting units alternately along the conjugated backbone for the use of donor materials in OPVs [1, 4-6]. Many electron-accepting units such as benzothiadiazole (BT) and diketopyrrolopyrrole (DPP) have been synthesized and utilized in OPVs [7, 8].

In organic light-emitting diode (OLED) applications, highly electron-deficient groups such as oxadiazole and

triazole (Tz) units have been introduced into the polymer backbone or as the side group as electron transporting units to adjust the charge-injecting and transporting properties of the copolymers [9-11]. More recently, several reports have described improvements in PCE by incorporating electron deficient moieties into the polymer backbone or as side chains [12-16]. The incorporation of electron deficient groups such as thiadiazole or oxadiazole can improve the performance of OPVs by enhancing electron transfer in comparison to the parent polymer. Previously, we reported on polyfluorenes containing various electron transporting units such as benzothiadiazole (BT), oxadiazole, and triazole (Tz) in the main chain [17, 18]. Interestingly, the photovoltaic properties of the polymers were varied by the introduced electron transporting units and the polymer containing triazole (Tz) showed the improved performance. In this work, we introduce electron-transporting triazole (Tz) units into the well-known carbazole-benzothiadiazole-based copolymer (**PCz3TB**) by Suzuki polymerization to be used as donors for OPVs. The copolymers were designed to have different feed ratios of comonomer units (benzothiadiazole and triazole). The optical properties, film morphology, and

photovoltaic characteristics of the polymers are investigated to establish the relationship between molecular structure and device performance.

## 2. Experimental

**2.1. Materials.** 2,7-Bis(4',4',5',5'-tetramethyl-1',3',2'-dioxaborolan-2'-yl)-N-9''-heptadecanyl-carbazole, 4,7-bis(5-bromothiophen-2-yl)benzo[c][1,2,5]thiadiazole, and 3,5-bis-(4-bromophenyl)-4-(4-butylphenyl)-4H-[1,2,4]triazole were prepared according to a procedure mentioned in the literature [19]. Aliquat 336, tetrakis(triphenylphosphine)palladium(0) (Pd(PPh<sub>3</sub>)<sub>4</sub>), and sodium carbonate were purchased from Aldrich. All reagents purchased commercially were used without further purification, except for the toluene used as a solvent, which was distilled.

**2.2. Measurements.** Thermal gravimetric analysis (TGA) was performed under a nitrogen atmosphere at a heating rate of 10°C/min using a Perkin Elmer TGA7 thermogravimetric analyzer. UV-Vis spectra were obtained using a Shimadzu UV/vis spectrometer. The polymer films used in the UV-Vis absorption measurements were prepared by spin coating of polymer solution in chlorobenzene. The optical energy band gaps ( $E_g$ ) were estimated from the absorption onset wavelengths ( $E_g = 1240/\lambda_{\text{onset}}$  (eV)) of the polymer films. The electrochemical properties of the polymers were characterized by cyclic voltammetry (CV). The films were prepared by dip coating the polymer solution onto Pt wire, and the measurements were calibrated using the ferrocene value of -4.8 eV as the standard [20]. Film thicknesses were measured using a TENCOR surface profiler.

**2.3. Synthesis.** The syntheses of the copolymers, poly[(N-9'-heptadecanyl-2,7-carbazole)-*alt*-(5,5-(4',7'-di-2-thienyl-2',1',3'-benzothiadiazole))] (**PCz3TB**), and three poly[(N-9'-heptadecanyl-2,7-carbazole)-*co*-(5,5-(4',7'-di-2-thienyl-2',1',3'-benzothiadiazole))-*co*-(3,5-bis-(4-4-phenyl-[1,2,4]triazole))] (**PCz3BTz**) were carried out using the Suzuki coupling reaction between the diborolanyl compound, 2,7-bis(4',4',5',5'-tetramethyl-1',3',2'-dioxaborolan-2'-yl)-N-9''-heptadecanyl-carbazole (**Cz**), and the dibromoaryl compounds, 4,7-bis(5-bromothiophen-2-yl)benzo[c][1,2,5]thiadiazole (**3TB**) and 3,5-bis-(4-bromophenyl)-4-(4-butylphenyl)-4H-[1,2,4]triazole (**Tz**).

**2.3.1. Synthesis of PCz3TB.** Two comonomers, **Cz** (0.25 g, 0.38 mmol) and **3TB** (0.12 g, 0.38 mmol), were dissolved in distilled toluene (4.5 mL) with the air-sensitive Pd(0) complex, Pd(PPh<sub>3</sub>)<sub>4</sub> (0.004 g, 0.004 mmol). Aliquat336 (0.015 g, 0.037 mmol) and 2 M *aq.* sodium carbonate (0.18 g, 1.74 mmol) were added to the mixture. After being refluxed for 48 h, the reaction mixture was cooled to about 50°C and added slowly to a vigorously stirred mixture consisting of 230 mL of methanol and 15 mL of 1 M *aq.* HCl. The polymer fibers were collected by filtration and reprecipitation from methanol. The polymer was purified by a Soxhlet extraction in acetone for 2 days to remove oligomers and catalyst residues. The reprecipitation procedure in dichloromethane/methanol was then repeated several times. The final

product, a yellow polymer, was obtained after drying in vacuum at 60°C, with a yield of 0.42 g (64.4%). Anal. Calcd. for (C<sub>43</sub>H<sub>47</sub>N<sub>3</sub>S<sub>3</sub>)<sub>n</sub>: C: 73.56, H: 6.75, N: 5.99, S: 13.70. Found: C: 65.48, H: 5.97, N: 5.34, S: 11.01.

**2.3.2. Synthesis of PCz3BTz-1.** **PCz3BTz-1** was prepared as for **PCz3TB**, using three comonomers, **Cz** (0.55 g, 0.84 mmol), **3TB** (0.30 g, 0.65 mmol), and **Tz** (0.08 g, 0.16 mmol), resulting in purple solid with a yield of 0.20 g (34.0%). Anal. Calcd. for (C<sub>225</sub>H<sub>250</sub>N<sub>16</sub>S<sub>12</sub>)<sub>n</sub>: C: 75.71, H: 7.06, N: 6.28, S: 10.96. Found: C: 74.23, H: 7.41, N: 5.69, S: 10.94.

**2.3.3. Synthesis of PCz3BTz-2.** **PCz3BTz-2** was prepared as for **PCz3BTz-1**, using **Cz** (0.26 g, 0.39 mmol), **3TB** (0.085 g, 0.19 mmol), and **Tz** (0.095 g, 0.19 mmol), resulting in purple solid with a yield of 0.14 g (51.1%). Anal. Calcd. for (C<sub>96</sub>H<sub>109</sub>N<sub>7</sub>S<sub>3</sub>)<sub>n</sub>: C: 78.93, H: 7.52, N: 6.71, S: 6.85. Found: C: 72.50, H: 6.81, N: 5.83, S: 6.99.

**2.3.4. Synthesis of PCz3BTz-3.** **PCz3BTz-3** was prepared as for **PCz3BTz-1** using **Cz** (0.26 g, 0.39 mmol), **3TB** (0.034 g, 0.074 mmol), and **Tz** (0.15 g, 0.30 mmol), resulting in purple solid with a yield of 0.18 g (64.3%). Anal. Calcd. for (C<sub>255</sub>H<sub>295</sub>N<sub>19</sub>S<sub>3</sub>)<sub>n</sub>: C: 82.15, H: 7.97, N: 7.13, S: 2.74. Found: C: 79.19, H: 7.86, N: 6.85, S: 3.03.

**2.4. Fabrication of OPV Device.** The organic photovoltaic devices were fabricated with the configuration ITO/PEDOT:PSS (40 nm)/polymer:PC<sub>71</sub>BM (60 nm)/LiF (1 nm)/Al (100 nm). The ITO-coated glass substrates were cleaned by ultrasonic treatment in deionized water, acetone, isopropyl alcohol, and methanol. The poly(ethylene dioxythiophene):polystyrene sulfonic acid (PEDOT:PSS) layer was spin-coated on the substrate and annealed at 140°C for 10 min. The active layer consisting of copolymers and [6,6]-phenyl-C<sub>71</sub>-butyric acid methyl ester (PC<sub>71</sub>BM) was spin-coated from a chlorobenzene solution. Prior to use, a chlorobenzene solution of polymer and PC<sub>71</sub>BM with the total concentration of 20 mg/mL was stirred at room temperature overnight to ensure complete dissolution. The polymer solutions were spin-coated onto the substrate after being filtered through a 0.45 μm polytetrafluoroethylene (PTFE) membrane syringe. Next, the LiF and Al layers were deposited as the cathode electrode. The area of the device was 4 mm<sup>2</sup>. After annealed at 100°C for 10 min, the current-voltage (*J-V*) characteristics of the polymer:PCBM films were measured with a Keithley 2400 source-measure unit in air under white light illumination of AM 1.5 (100 mW/cm<sup>2</sup>).

## 3. Results and Discussion

**3.1. Synthesis and Thermal Property.** The syntheses of the carbazole-benzothiadiazole-triazole-based copolymers (**PCz3BTz-1**, **PCz3BTz-2**, and **PCz3BTz-3**) were carried out using Suzuki coupling reaction between the diborolanyl compound, 2,7-bis(4',4',5',5'-tetramethyl-1',3',2'-dioxaborolan-2'-yl)-N-9''-heptadecanyl-carbazole and the dibromoaryl compounds, 4,7-bis(5-bromothiophen-2-yl)benzo[c][1,2,5]thiadiazole (**3BT**) and 3,5-bis-(4-bromophenyl)-4-(4-butylphenyl)-4H-[1,2,4]triazole (**Tz**). The feed

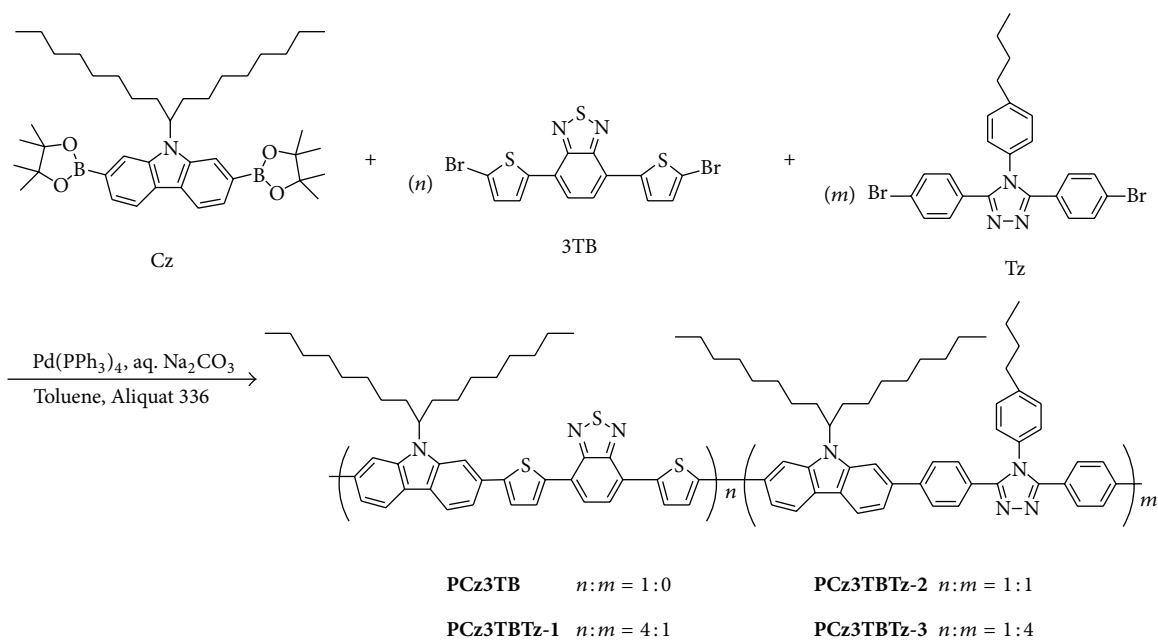
SCHEME 1: Synthetic route to the **PCz3TB** and three **PCz3TBTzs**.

TABLE 1: Physical properties of polymers.

	<b>PCz3TB</b>	<b>PCz3TBTz-1</b>	<b>PCz3TBTz-2</b>	<b>PCz3TBTz-3</b>
Ratio (Cz : 3TB : Tz)				
Feed ratio	50 : 50 : 0	50 : 40 : 10	50 : 25 : 25	50 : 10 : 40
Actual ratio <sup>a</sup>	61 : 39 : 0	62 : 35 : 3	60 : 24 : 16	56 : 10 : 34
$M_n^b$	94800	95300	77400	8300
$M_w^b$	121700	135100	110200	11700
PDI ( $M_w/M_n$ )	1.28	1.42	1.42	1.41
$T_{5d}$ (°C)	361	359	354	369
Solution ( $\lambda_{max}$ , nm) Abs.	380, 530	380, 536	380, 536	365, 528
Film ( $\lambda_{max}$ , nm) Abs.	390, 560	392, 566	383, 550	356, 539
$E_{onset}$ (V versus SCE) <sup>c</sup>	0.98	0.96	0.99	0.92
HOMO (eV) <sup>d</sup>	-5.37	-5.35	-5.38	-5.31
LUMO (eV)	-3.51	-3.49	-3.48	-3.36
$E_g$ (eV) <sup>e</sup>	1.86	1.86	1.90	1.95

<sup>a</sup> Actual ratio in polymers determined by elemental analysis.

<sup>b</sup>  $M_n$  and  $M_w$  stand for the number-average and weight-average molecular weights, respectively, determined by GPC.

<sup>c</sup>  $E_{onset}$  stands for onset potential of oxidation.

<sup>d</sup> Calculated using the empirical equation:  $I_p(\text{HOMO}) = -(E_{onset} + 4.39)$ .

<sup>e</sup> Optical band gaps ( $E_g$ ) taken as the absorption onsets in the UV-vis spectra of the polymer films ( $E_g = 1240/\lambda_{onset}$  eV).

ratios of two dibromides (**3BT** and **Tz**) were varied from 4:1, 2:2, to 1:4 to assess the effect of triazole units on the OPV performance. For comparison, the well-known OPV donor polymer, **PCz3TB**, was also synthesized at the same time. Three **PCz3TBTz** copolymers have the same polymer backbone as **PCz3TB**. In the carbazole and 4,7-bis(5-bromothiophen-2-yl)benzo[c][1,2,5]thiadiazole (**3BT**) backbone, we incorporated an electron-transporting moiety, 4-(4-butylphenyl)-4H-[1,2,4]triazole (**Tz**), as the third comonomer. The synthetic routes toward copolymers are outlined in Scheme 1. Three **PCz3TBTz** copolymers were designed

to have 10, 25, and 40% triazole unit content instead of **3TB** unit content; however, the actual ratios of the repeat units in the real copolymers could be different from the feed ratios due to the difference of reactivity between comonomers. An elemental analysis (EA) was used to calculate the actual ratio in the copolymers. **PCz3TBTz-1**, **PCz3TBTz-2**, and **PCz3TBTz-3** contained 3, 16, and 34% triazole unit content. The molecular weights, feed, and actual ratios of the repeat units in the copolymers are listed in Table 1. The number-average ( $M_n$ ) and weight-average ( $M_w$ ) molecular weights of the synthesized polymers were determined with

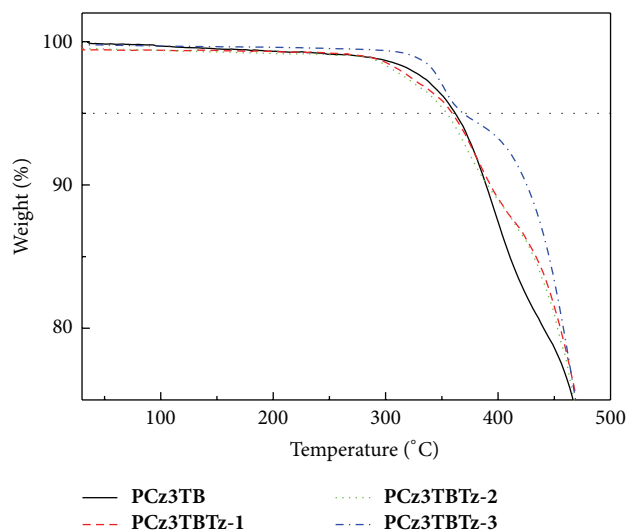


FIGURE 1: TGA thermograms of the copolymers.

gel permeation chromatography (GPC). The  $M_w$  values of **PCz3TB**, **PCz3TBTz-1**, **PCz3TBTz-2**, and **PCz3TBTz-3** were 121800, 135100, 110200, and 11700, respectively, and their polydispersity indices (PDIs) ranged from 1.28 to 1.42. The thermal stability of the copolymers was evaluated in a nitrogen atmosphere by TGA. As shown in Figure 1, the copolymers exhibited good thermal stability and the weight loss was less than 5% ( $T_{5d}$ ) upon heating to 350°C.

**3.2. Optical and Electrochemical Properties.** The UV-Vis absorption spectra of four copolymers in chlorobenzene solutions with the dilute concentration are shown in Figure 2(a), and the main optical properties are listed in Table 1. All the UV-Vis absorption spectra have two absorption peaks, which could be assigned to the  $\pi$ - $\pi^*$  transition of the conjugated backbone and intramolecular charge transfer (ICT) interactions between the thiophene donor and the benzothiadiazole/triazole acceptor units [21]. The absorption spectra of the film state are red-shifted relative to those of the solution state (see Figure 2(b)), likely due to increased intermolecular interactions between neighboring molecules in the film state. By increasing the ratio of triazole in the copolymer from **PCz3TB**, **PCz3TBTz-1**, **PCz3TBTz-2** to **PCz3TBTz-3**, the absorption intensity in the long wavelength region was gradually decreased. In other words, replacement of the benzothiadiazole moiety with the triazole moiety in the main chain exceeding 10% appeared to decrease inter- and intramolecular interactions between donor and acceptor moieties. The optical band gaps,  $E_g$ , of the copolymers are estimated from the absorption onset wavelengths of the UV-Vis spectrum of the polymer film (Table 1). The UV absorption and optical band gap of **PCz3TBTz-1** are similar to those of **PCz3TB**, and greater addition of the triazole unit into the main chain in **PCz3TBTz-2** and **PCz3TBTz-3** resulted in an increase of the band gap of copolymers as compared to that of **PCz3TB**. The electrochemical properties of the polymers were also measured to determine their highest

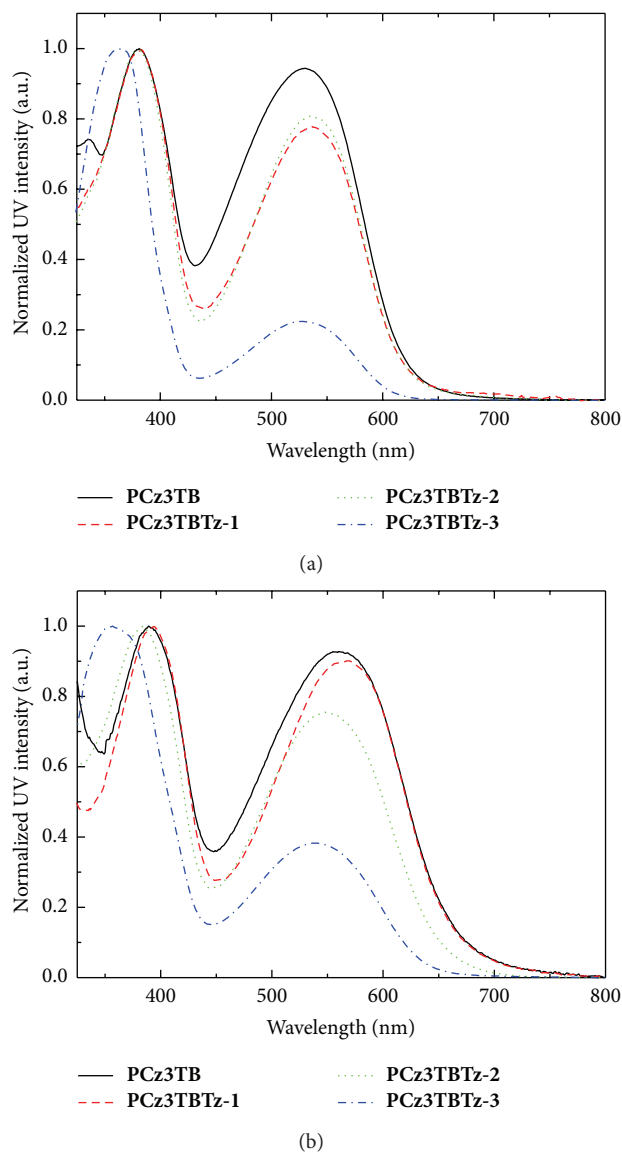


FIGURE 2: UV-Visible absorption spectra in (a) solution and (b) film.

occupied molecular orbital (HOMO) and the lowest unoccupied molecular orbital (LUMO) energy levels. Figure 3 shows the anodic scan of the CV of the copolymers. The onset of oxidation for copolymers occurred in a range of 0.92 to 0.98 V (vs SCE), which corresponds to their HOMO levels in a range of  $-5.31$  to  $-5.38$  eV (Table 1), according to the empirical relationship proposed by Leeuw et al.  $I_p(\text{HOMO}) = -(E_{\text{onset}} + 4.39)$ , where  $E_{\text{onset}}$  is the onset potential of oxidation [22]. The effects of the HOMO levels and band gaps on the photovoltaic properties are discussed below.

**3.3. Organic Photovoltaic Properties.** To investigate the current-voltage characteristics of the copolymers, devices with the configuration of ITO/PEDOT:PSS (40 nm)/polymer:PC<sub>71</sub>BM (60 nm)/LiF (1 nm)/Al (100 nm) were fabricated. The blending ratio of polymer and PCBM was adjusted

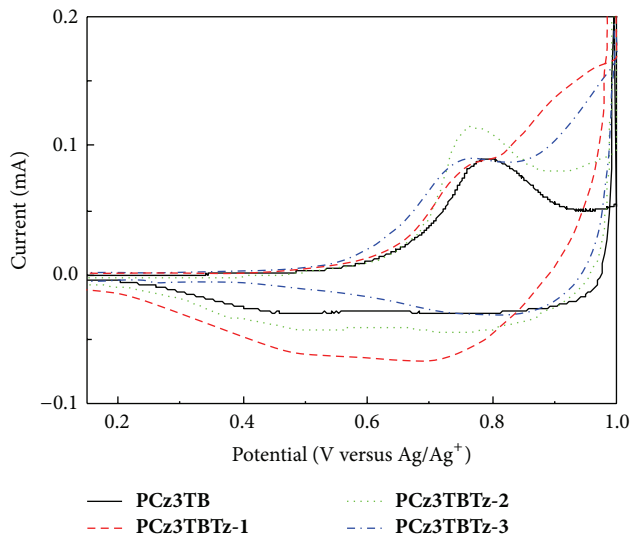
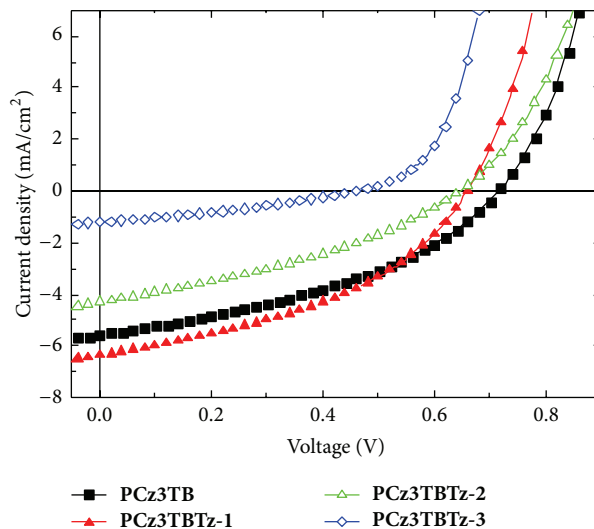


FIGURE 3: CV of the polymer films.

to be 1:3. Figure 4 shows the current density versus voltage ( $J$ - $V$ ) curves for copolymer: PCBM devices and the photovoltaic properties of the blend films are summarized in Table 2. As shown in Figure 4, **PCz3TBTz-1** showed the highest device performance, with a power conversion efficiency (PCE) of 1.74%, compared to **PCz3TB** (1.55%), **PCz3TBTz-2** (0.98%), and **PCz3TBTz-3** (0.18%). The device performances were attributed to increases of the short-circuit current ( $J_{SC}$ ) and open-circuit voltage ( $V_{OC}$ ) values. Despite a slight decrease of the  $V_{OC}$  value from 0.72 V (**PCz3TB**) to 0.66 V (**PCz3TBTz-1**), **PCz3TBTz-1** showed a higher  $J_{SC}$  value of 6.36 mA/cm<sup>2</sup> than **PCz3TB** (5.56 mA/cm<sup>2</sup>), and the  $J_{SC}$  and  $V_{OC}$  values gradually decreased by increasing the feed ratios of the triazole unit in **PCz3TBTz-2** (4.29 mA/cm<sup>2</sup>, 0.65 V) and **PCz3TBTz-3** (1.21 mA/cm<sup>2</sup>, 0.46 V). As described above, although the UV absorption and optical band gap of **PCz3TBTz-1** are similar with those of **PCz3TB**, **PCz3TBTz-2** and **PCz3TBTz-3** with more triazole units in the main chain showed lower UV absorption intensity in the long wavelength region and an increased optical band gap, compared with **PCz3TB** and **PCz3TBTz-1**. Low-band-gap conjugated materials with appropriate energy levels are required for efficient charge transfer in OPVs [23]. The gradually decreased efficiencies of **PCz3TBTz-2** and **PCz3TBTz-3** relative to **PCz3TB** can be explained by the gradually decreased UV absorption intensity in the long wavelength region and the gradually increased band gaps. In addition, the significantly low efficiency of **PCz3TBTz-3** might stem from its low molecular weight compared to the other copolymers.

In other words, the feed ratio of comonomer units of **3TB** and **Tz** was optimized and the highest PCE of 1.74% was achieved in **PCz3TBTz-1**. This increased performance of **PCz3TBTz-1** can be explained by its improved solubility and surface morphology. Figure 5 compares the surface morphologies of the **PCz3TBTz-1**:PCBM blend film with **PCz3TB**:PCBM blend film, determined from AFM measurements. The root-mean-square (RMS) roughness of the

FIGURE 4:  $J$ - $V$  curves of photovoltaic cells of copolymers.TABLE 2: OPV performances of the polymer: PC<sub>71</sub>BM OPV cells<sup>a,b</sup>.

Active layer	$J_{SC}$ (mA/cm <sup>2</sup> )	$V_{OC}$ (V)	FF (%)	PCE (%)
<b>PCz3TB</b>	5.56	0.72	0.39	1.55 (1.54)
<b>PCz3TBTz-1</b>	6.36	0.66	0.41	1.74 (1.69)
<b>PCz3TBTz-2</b>	4.29	0.65	0.35	0.98 (0.94)
<b>PCz3TBTz-3</b>	1.21	0.46	0.32	0.18 (0.17)

<sup>a</sup>Thickness of the active layer was adjusted to 60 nm (blend ratio: polymer: PCBM = 1:3).

<sup>b</sup>The values shown here are for the best device, and the average performances among three samples are also shown in parenthesis.

**PCz3TBTz-1**:PCBM film was 1.78 nm, which was nearly ten times that of the **PCz3TB**:PCBM film. Similar phenomenon was observed in our previous work with **PF3TB** and **PF3TBTz** [18]. The larger RMS value of **PCz3TBTz-1** suggests that it has rougher surface morphology, indicative of increased polymer aggregation [24]. The suitable phase separation by polymer aggregation facilitated improved charge transport and carrier collection efficiency, resulting in reduced charge recombination and an increased  $J_{SC}$  value in the device [15]. The better morphology of **PCz3TBTz-1** is ascribed to improved solubility by introduction of the alkyl-substituted triazole unit into the main chain. Further research on modification of the polymer structure is currently underway.

## 4. Conclusions

We synthesized three carbazole-benzothiadiazole-based copolymers containing different amounts of triazole into the main chains through palladium-catalyzed Suzuki polymerization. The absorption intensity of the copolymers varied according to the amount of triazole. The feed ratio of comonomer units was optimized and the highest PCE of 1.74%

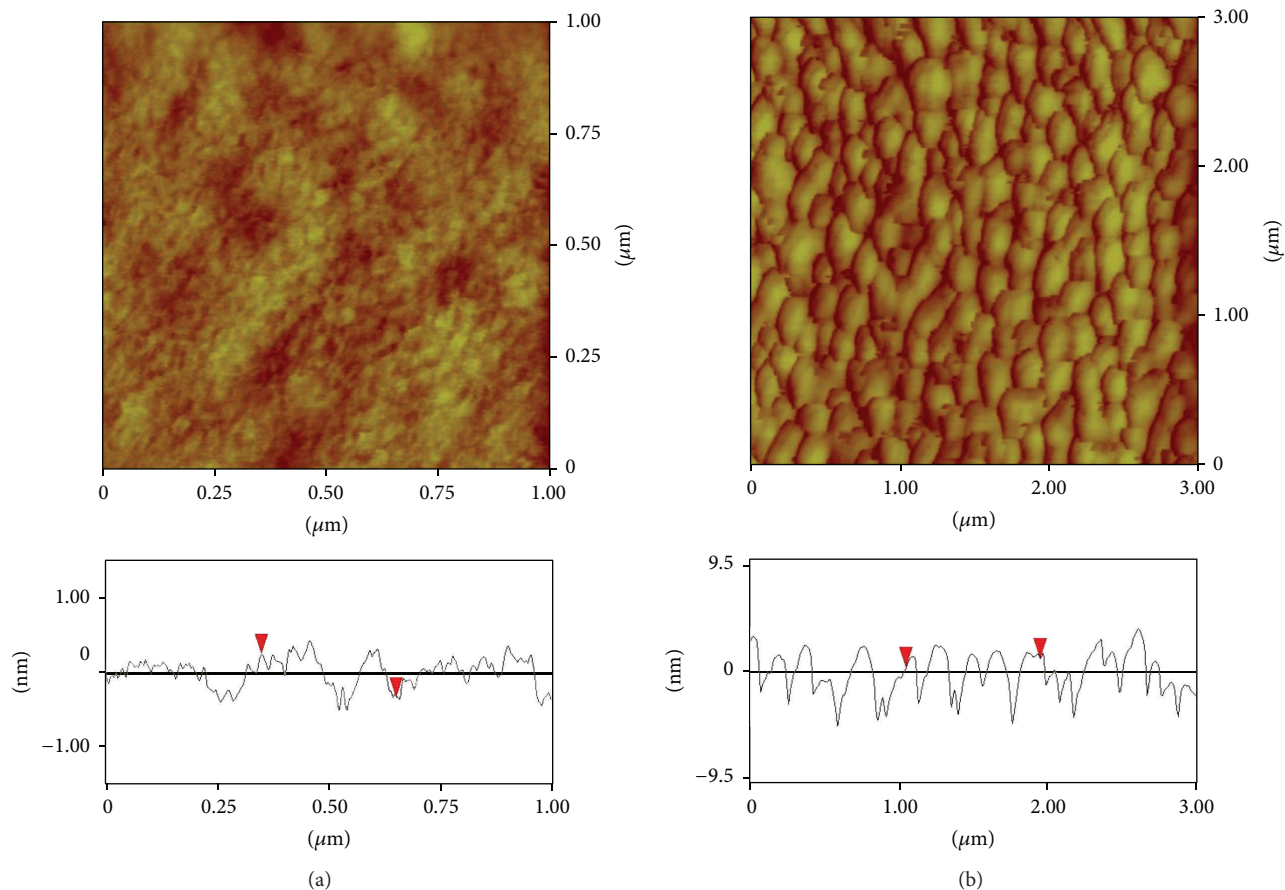


FIGURE 5: Topographic AFM images of (a) **PCz3TB:PCBM** and (b) **PCz3TBTz-1:PCBM** films.

was achieved in **PCz3TBTz-1**. This is attributed to its better morphology and solubility.

## Acknowledgment

This research was supported by Basic Science Research Program through the National Research Foundation of Korea (NRF) funded by the Ministry of Education, Science and Technology (2012R1A1A3005083).

## References

- [1] R. L. Uy, S. C. Price, and W. You, "Structure-property optimizations in donor polymers via electronics, substituents, and side chains toward high efficiency solar cells," *Macromolecular Rapid Communications*, vol. 33, no. 14, pp. 1162–1177, 2012.
- [2] G. Dennler, M. C. Scharber, and C. J. Brabec, "Polymer-fullerene bulk-heterojunction solar cells," *Advanced Materials*, vol. 21, no. 13, pp. 1323–1338, 2009.
- [3] P.-L. T. Boudreault, A. Najari, and M. Leclerc, "Processable low-bandgap polymers for photovoltaic applications," *Chemistry of Materials*, vol. 23, no. 3, pp. 456–469, 2011.
- [4] J. A. Kong, E. Lim, K. K. Lee, S. Lee, and S. H. Kim, "A benzothiadiazole-based oligothiophene for vacuum-deposited organic photovoltaic cells," *Solar Energy Materials and Solar Cells*, vol. 94, no. 12, pp. 2057–2063, 2010.
- [5] C. L. Chochos and S. A. Choulis, "How the structural deviations on the backbone of conjugated polymers influence their optoelectronic properties and photovoltaic performance," *Progress in Polymer Science*, vol. 36, no. 10, pp. 1326–1414, 2011.
- [6] J. Y. Lee, S. M. Lee, K. W. Song, and D. K. Moon, "Synthesis and photovoltaic property of polymer semiconductor with phthalimide derivative as a promising electron withdrawing material," *European Polymer Journal*, vol. 48, no. 3, pp. 532–540, 2012.
- [7] R. C. Coffin, J. Peet, J. Rogers, and G. C. Bazan, "Streamlined microwave-assisted preparation of narrow-bandgap conjugated polymers for high-performance bulk heterojunction solar cells," *Nature Chemistry*, vol. 1, no. 8, pp. 657–661, 2009.
- [8] K. H. Hendriks, W. Li, M. M. Wienk, and R. A. J. Janssen, "Band gap control in diketopyrrolopyrrole-based polymer solar cells using electron donating side chains," *Advanced Energy Materials*, vol. 3, no. 5, pp. 674–679, 2013.
- [9] S. W. Kim, S. C. Shim, B.-J. Jung, and H.-K. Shim, "Synthesis and properties of new electroluminescent polymers possessing both hole and electron-transporting units in the main chain," *Polymer*, vol. 43, no. 15, pp. 4297–4305, 2002.
- [10] E. Lim, B.-J. Jung, and H.-K. Shim, "Improved EL efficiency of fluorene-thieno[3,2-b] thiophene-based conjugated copolymers with hole-transporting or electron-transporting units in the main chain," *Journal of Polymer Science A*, vol. 44, no. 1, pp. 243–253, 2006.
- [11] H. L. Zhong, S. W. Man, H. Fukutani, and Y. Tao, "Synthesis and light-emitting properties of bipolar oligofluorenes containing

- triarylamine and 1,2,4-triazole moieties,” *Organic Letters*, vol. 8, no. 19, pp. 4271–4274, 2006.
- [12] Y.-T. Chang, S.-L. Hsu, G.-Y. Chen et al., “Intramolecular donor-acceptor regioregular poly(3-hexylthiophene)s presenting octylphenanthrenyl-imidazole moieties exhibit enhanced charge transfer for heterojunction solar cell applications,” *Advanced Functional Materials*, vol. 18, no. 16, pp. 2356–2365, 2008.
- [13] S. Wen, J. Pei, Y. Zhou et al., “Synthesis and photovoltaic properties of poly(p-phenylenevinylene) derivatives containing oxadiazole,” *Journal of Polymer Science A*, vol. 47, no. 4, pp. 1003–1012, 2009.
- [14] B. Zhao, D. Liu, L. Peng et al., “Effect of oxadiazole side chains based on alternating fluorene-thiophene copolymers for photovoltaic cells,” *European Polymer Journal*, vol. 45, no. 7, pp. 2079–2086, 2009.
- [15] H.-S. Wang, M.-S. Su, and K.-H. Wei, “Synthesis and characterization of donor-acceptor poly(3-hexylthiophene) copolymers presenting 1,3,4-oxadiazole units and their application to photovoltaic cells,” *Journal of Polymer Science A*, vol. 48, no. 15, pp. 3331–3339, 2010.
- [16] T. Higashihara, H.-C. Wu, T. Mizobe, C. Lu, M. Ueda, and W.-C. Chen, “Synthesis of thiophene-based  $\pi$ -conjugated polymers containing oxadiazole or thiadiazole moieties and their application to organic photovoltaics,” *Macromolecules*, vol. 45, no. 22, pp. 9046–9055, 2012.
- [17] E. Lim, S. Lee, and K. K. Lee, “Improved OPV efficiency of fluorene-thiophene-based copolymers with hole- and electron-transporting units in the main chain,” *Molecular Crystals and Liquid Crystals*, vol. 538, pp. 157–163, 2011.
- [18] E. Lim, K. K. Lee, and S. Lee, “Improved photovoltaic properties of fluorene-thiophene-based copolymers by an electron-transporting triazole unit in the main chain,” *Journal of Nanoscience and Nanotechnology*, vol. 12, no. 4, pp. 3483–3487, 2012.
- [19] J.-Y. Choi, D.-H. Kim, B. Lee, and J.-H. Kim, “Synthesis and electro-optical properties of  $\pi$ -conjugated polymer based on 10-hexylphenothiazine and aromatic 1,2,4-triazole,” *Bulletin of the Korean Chemical Society*, vol. 30, no. 9, pp. 1933–1938, 2009.
- [20] J. Pommerehne, H. Vestweber, W. Guss et al., “Efficient two layer LEDs on a polymer blend basis,” *Advanced Materials*, vol. 7, no. 6, pp. 551–554, 1995.
- [21] Y. Li, L. Xue, H. Li et al., “Energy level and molecular structure engineering of conjugated donor-acceptor copolymers for photovoltaic applications,” *Macromolecules*, vol. 42, no. 13, pp. 4491–4499, 2009.
- [22] D. M. de Leeuw, M. M. J. Simenon, A. R. Brown, and R. E. F. Einerhand, “Stability of n-type doped conducting polymers and consequences for polymeric microelectronic devices,” *Synthetic Metals*, vol. 87, no. 1, pp. 53–59, 1997.
- [23] B. C. Thompson and J. M. J. Fréchet, “Polymer-fullerene composite solar cells,” *Angewandte Chemie International Edition*, vol. 47, no. 1, pp. 58–77, 2007.
- [24] G. Li, V. Shrotriya, J. Huang et al., “High-efficiency solution processable polymer photovoltaic cells by self-organization of polymer blends,” *Nature Materials*, vol. 4, no. 11, pp. 864–868, 2005.

## Research Article

# Multi-Input Converter with MPPT Feature for Wind-PV Power Generation System

**Chih-Lung Shen and Shih-Hsueh Yang**

*Department of Electronic Engineering, National Kaohsiung First University of Science and Technology, Nanzih, Kaohsiung 811, Taiwan*

Correspondence should be addressed to Chih-Lung Shen; [clshen@ccms.nkfust.edu.tw](mailto:clshen@ccms.nkfust.edu.tw)

Received 16 January 2013; Revised 1 April 2013; Accepted 20 April 2013

Academic Editor: Bhushan Sopori

Copyright © 2013 C.-L. Shen and S.-H. Yang. This is an open access article distributed under the Creative Commons Attribution License, which permits unrestricted use, distribution, and reproduction in any medium, provided the original work is properly cited.

A multi-input converter (MIC) to process wind-PV power is proposed, designed, analyzed, simulated, and implemented. The MIC cannot only process solar energy but deal with wind power, of which structure is derived from forward-type DC/DC converter to step-down/up voltage for charger systems, DC distribution applications, or grid connection. The MIC comprises an upper modified double-ended forward, a lower modified double-ended forward, a common output inductor, and a DSP-based system controller. The two modified double-ended forwards can operate individually or simultaneously so as to accommodate the variation of the hybrid renewable energy under different atmospheric conditions. While the MIC operates at interleaving mode, better performance can be achieved and volume also is reduced. The proposed MIC is capable of recycling the energy stored in the leakage inductance and obtaining high step-up output voltage. In order to draw maximum power from wind turbine and PV panel, perturb-and-observe method is adopted to achieve maximum power point tracking (MPPT) feature. The MIC is constructed, analyzed, simulated, and tested. Simulations and hardware measurements have demonstrated the feasibility and functionality of the proposed multi-input converter.

## 1. Introduction

Conventionally, electric power is mainly generated from fossil fuels. However, this kind of energy resources is highly limited and will be exhausted in the near future. With the rapid requirement of electricity and the increase of worse and worse energy crisis, it is of great urgency to replace the fossil fuels with renewable energy. Among the renewable resources, solar energy and wind power attract a great deal of interest owing to their easy acquirement.

In photovoltaic (PV) or wind power generation system, a power converter is needed so as to process renewable energy. In literature [1–5] PV converters are presented while wind power converters are studied in [6–10]. However, these power converters only handle a single kind of renewable energy, that is, which cannot deal with multi-input power. Therefore, some researchers propose multi-input converters for solar-wind hybrid power generation system. As shown in Figure 1, a series double-boost converter is presented to process PV power and wind energy simultaneously [11], in which, as compared with single-boost configuration, power component

only imposes one-half power rating. Even though this boost-type converter steps up the voltage and is suitable for a high voltage supply, it cannot be applied to galvanic isolated applications. Double-input buck-boost converter shown in Figure 2 is capable of processing high-/low-voltage sources [12]. Like boost-type converter, this type of configuration is still nonisolated electrically. Instead of combining renewable energy in electricity, the concept of magnetic flux additivity is proposed to design a multi-input isolated converter, as shown in Figure 3, but its structure is complex and control low is complicated [13]. In order to simplify power-stage configuration, the forward-derived configuration is proposed. However, it cannot trap the energy in the leakage inductor and is incapable of applying to high output voltage applications [14].

In this paper, a multi-input converter (MIC) is proposed, which can not only deal with PV power and wind-turbine energy simultaneously/individually but recycles the leakage-inductance energy and steps up the input voltage. As compared with the aforementioned isolated double-input converter, the proposed one has a much simpler structure.

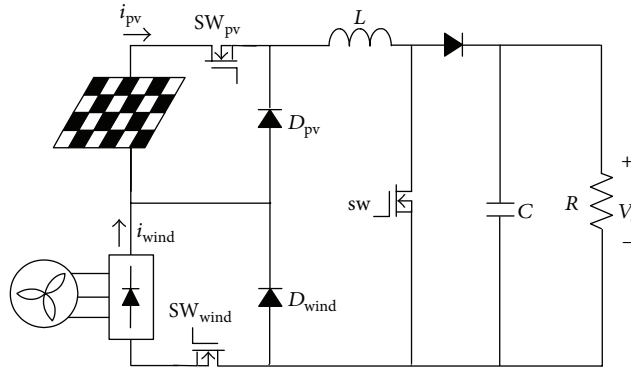


FIGURE 1: An illustration of double-boost converter for wind-PV system.

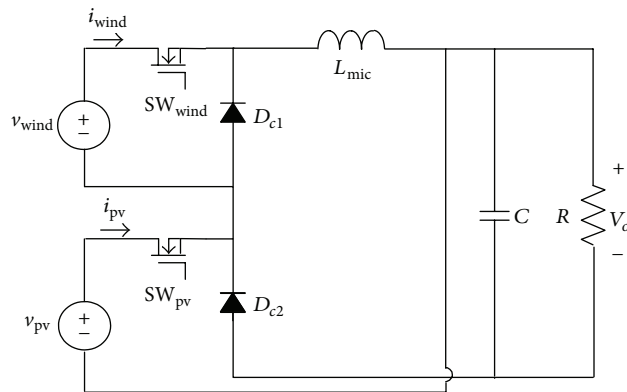


FIGURE 2: An illustration of double-input buck-boost converter.

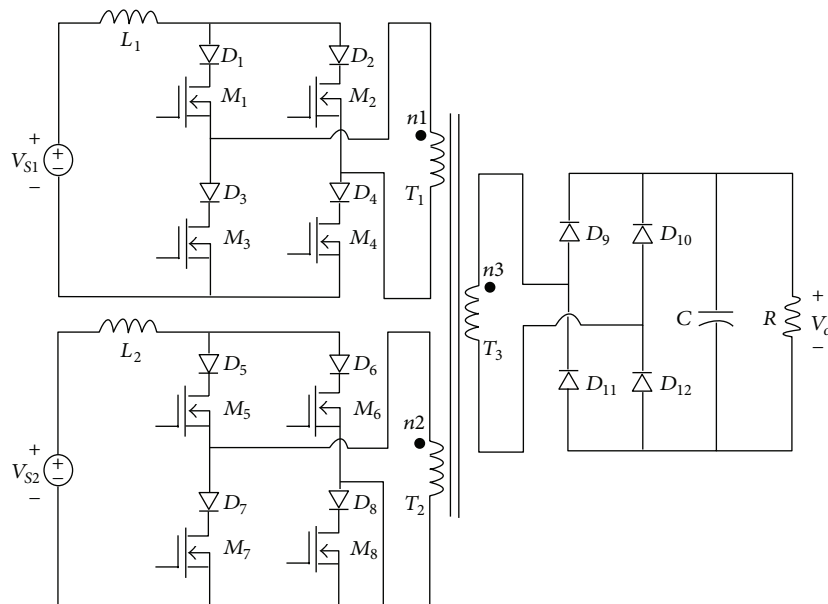


FIGURE 3: An illustration of multi-input converter based on magnetic flux additivity.

Furthermore, the proposed MIC removes the third winding from the conventional forward converter, which releases the energy stored in the magnetizing inductor to a capacitor through the second winding. As a result, its output voltage can be stepped up significantly and the efficiency is improved.

Simulated and practical results have validated the proposed PV-wind MIC.

In this paper, system architecture of the proposed MIC is described in Section 2. Section 3 presents the operational principle of the converter, while simulations and practical

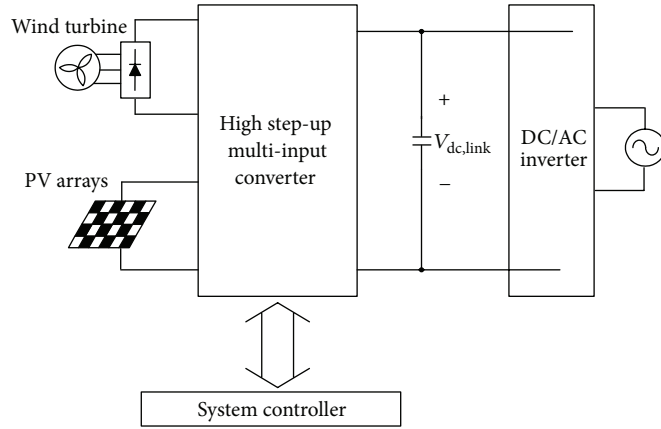


FIGURE 4: A block diagram to represent the configuration of the proposed MIC.

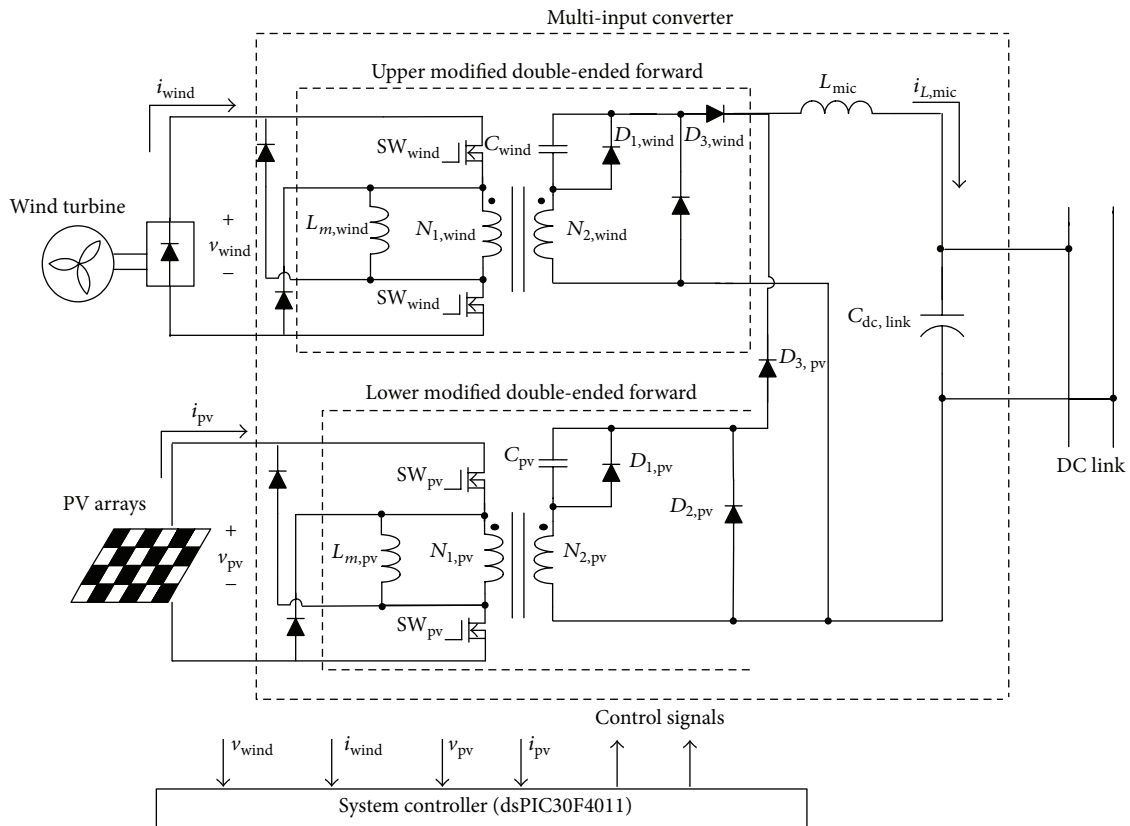


FIGURE 5: The proposed multi-input converter to process PV-wind power.

measurements to verify the feasibility of the MIC are shown in Section 4. Finally, conclusion is given in Section 5.

## 2. Configuration of the Proposed Converter

Figure 4 illustrates the block diagram of the proposed MIC, which mainly includes PV arrays, a wind turbine, a high step-up multi-input converter, and a system controller. Figure 5 shows the corresponding schematics of the main power stage of the MIC. In Figure 5, the MIC is composed of an upper

modified double-ended forward, a lower modified double-ended forward, a common output filter  $L_{mic}$ , and a system controller. The upper modified double-ended forward is in charge of dealing with wind-turbine energy while the lower one processes solar power. The both modified double-ended forwards can be operated independently, which expands the degree of control freedom. The active switches in the upper forward or in the lower one are switched synchronously so as to trap the leakage energy and to release the magnetizing inductance energy. The capacitors in the secondary windings,  $C_{wind}$  and  $C_{pv}$ , will absorb the energy of magnetizing

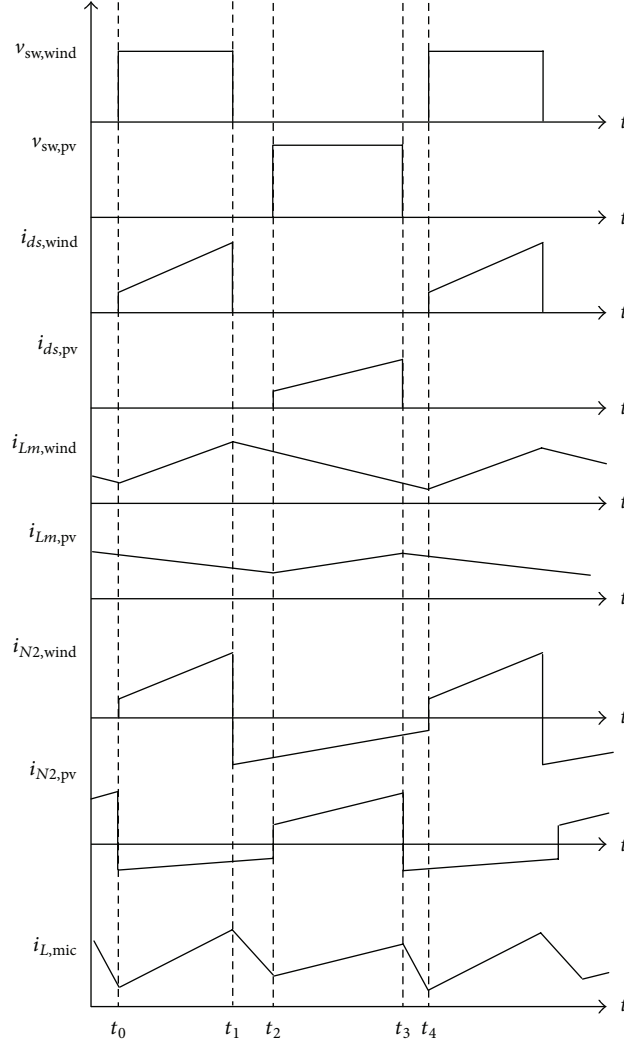


FIGURE 6: Conceptual key waveforms of the proposed MIC.

inductance and then can boost the output voltage. The system controller determines the control signals to perform output power controlling and maximum power point tracking (MPPT). In this paper, perturb-and-observe method is adopted for MPPT.

### 3. Operation Principle of the Proposed Converter

In Figure 5 the two modified double-ended forwards can operate individually to deal with PV power and wind energy. To achieve better output performance and to lower the output filter volume, the switches  $SW_{wind}$  and  $SW_{pv}$  are turned on alternatively with a duty ratio less than 0.5 at the same switching frequency. Figure 5 shows conceptual key waveforms. According to the conduction status of the switches  $SW_{wind}$  and  $SW_{pv}$ , the operation of the MIC over one switching period can be mainly divided into four modes. Corresponding equivalents are presented in Figure 6. Each operation mode is described in the following.

*Mode 1* (Figure 7(a),  $t_0 \leq t < t_1$ ). During the interval of Mode 1, the status of switches  $SW_{wind}$  is on but  $SW_{pv}$  off. While  $SW_{wind}$  conducts at  $t_0$ , this mode begins. The active switch  $SW_{pv}$  is in the off-state, and the magnetizing inductor of the lower modified forward discharges energy through the path of  $N_{2,pv}$ - $D_{2,pv}$ - $C_{pv}$ . Meanwhile, wind power is forwarded to output. Therefore,  $i_{L,mic}$  is linearly built and can be described as

$$i_{L,mic}(t) = \frac{2 \cdot N_{wind} \cdot k_{wind} \cdot v_{wind}}{L_{mic}} \cdot D_{wind} \cdot \frac{T_s}{2} + i_{L,mic}(t_0), \quad (1)$$

where  $k_{wind}$  is the coupling coefficient of the transformer in the upper forward,  $D_{wind}$  stands for duty ratio of  $SW_{wind}$ , and  $T_s$  represents the switching period. The voltage stresses of the switch  $SW_{pv}$  and diode  $D_{2,wind}$  can be found by

$$v_{DS,pv} = v_{pv}, \quad (2)$$

$$v_{D2,wind} = 2 \cdot N_{wind} \cdot k_{wind} \cdot v_{wind}.$$

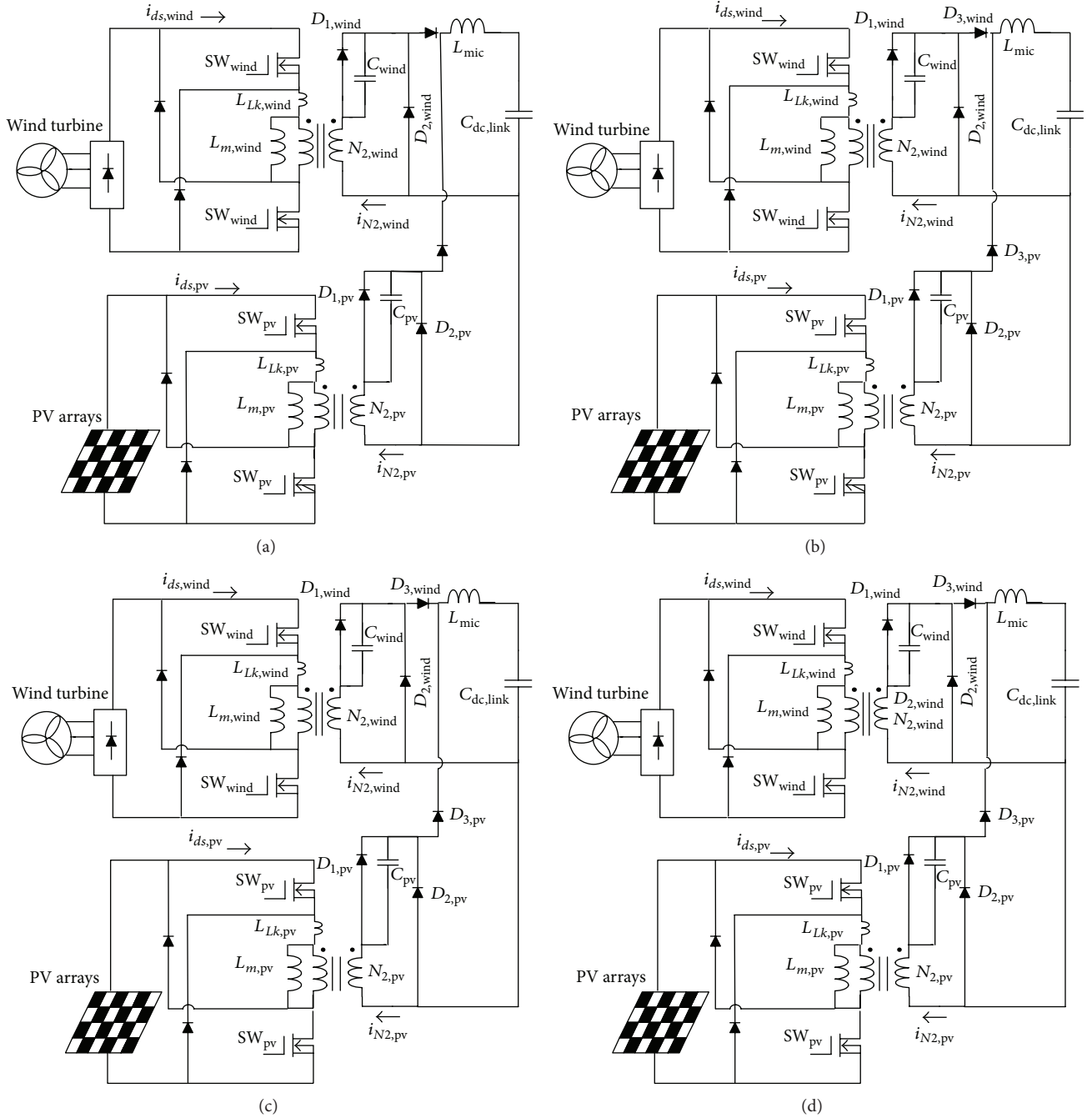


FIGURE 7: Equivalent circuits of the MIC corresponding to the four operation modes over one switching cycle: (a) Mode 1, (b) Mode 2, (c) Mode 3, and (d) Mode 4.

As the current of magnetizing inductor  $L_{m,pv}$  drops to zero, this mode ends.

**Mode 2** (Figure 7(b),  $t_1 \leq t < t_2$ ). In Mode 2, all the active switches are in off-state. At time  $t_1$ , the switch  $SW_{wind}$  is turned off and  $SW_{pv}$  in the lower forward still stays in the off-state. The magnetizing inductor in the upper modified forward  $L_{m,wind}$  discharges via the path of  $N_{2,wind}$ - $D_{2,wind}$ - $C_{wind}$ , while the energy of leakage inductor  $L_{LK,wind}$  is trapped.

The voltages across  $C_{wind}$  and  $C_{pv}$ ,  $v_{c,wind}$  and  $v_{c,pv}$ , are obtained by

$$\begin{aligned} v_{c,wind} &= N_{wind} \cdot k_{wind} \cdot v_{wind}, \\ v_{c,pv} &= N_{pv} \cdot k_{pv} \cdot v_{pv}, \end{aligned} \quad (3)$$

respectively, in which  $k_{pv}$  is the coupling coefficient of the transformer in the lower forward. In addition, the output inductor  $L_{mic}$  releases the stored energy to the load by

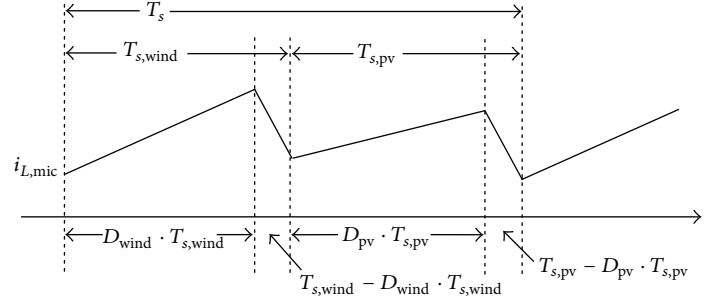


FIGURE 8: The waveform of output inductor current.

the path of  $L_{mic}-C_{dc,link}-D_{2,wind}$ , of which the current is linearly decreased and is expressed as

$$i_{L,mic}(t) = i_{L,mic}(t_1) - \frac{V_{dc,link}}{L_{mic}} \cdot D_{wind} \cdot \frac{T_s}{2} \cdot (1 - D_{wind}). \quad (4)$$

*Mode 3* (Figure 7(c),  $t_2 \leq t < t_3$ ). During this mode,  $SW_{pv}$  is in the on-state but  $SW_{wind}$  in off-state. Since the  $SW_{pv}$  is turned on at  $t_2$ , thus PV energy is dealt with by the lower modified forward. The inductor current  $i_{L,mic}$  increases linearly. The inductor  $L_{m,wind}$  releases the energy to the capacitor  $C_{wind}$  through the path of  $N_{2,wind}-D_{2,wind}-C_{wind}$ . In this interval, the current of output inductor  $L_{mic}$  is linearly built and can be described as

$$i_{L,mic}(t) = \frac{2 \cdot N_{pv} \cdot k_{pv} \cdot v_{pv}}{L_{mic}} \cdot D_{pv} \cdot \frac{T_s}{2} + i_{L,mic}(t_2), \quad (5)$$

where  $D_{pv}$  denotes the duty ratio of  $SW_{pv}$ . The voltage stresses of the switch  $SW_{pv}$  and diode  $D_{2,wind}$  can be expressed as follows:

$$\begin{aligned} v_{DS,wind} &= v_{wind}, \\ v_{D2,pv} &= 2 \cdot N_{pv} \cdot k_{pv} \cdot v_{pv}. \end{aligned} \quad (6)$$

This mode ends at the moment the current flowing through  $L_{m,wind}$  equals zero.

*Mode 4* (Figure 7(d),  $t_3 \leq t < t_4$ ). At time  $t_3$ , the switch  $SW_{pv}$  is turned off and the operation of the MIC enters into Mode 4. That is, in Mode 4 all active switches are off. During this mode, the magnetizing inductor  $L_{m,pv}$  releases energy to capacitor  $C_{pv}$  via  $N_{2,pv}$ ,  $D_{2,pv}$ , and  $C_{pv}$ . In addition, the energy stored in leakage inductance is recycled. Meanwhile, the output inductor discharges and the current  $i_{L,mic}$  decreases linearly, which can be expressed as

$$i_{L,mic}(t) = i_{L,mic}(t_3) - \frac{V_{dc,link}}{L_{mic}} \cdot D_{pv} \cdot \frac{T_s}{2} \cdot (1 - D_{pv}). \quad (7)$$

A complete switching cycle is terminated at  $t = t_4$ , at which  $SW_{wind}$  is turned on again.

While the proposed MIC operates in continuous conduction mode (CCM), the corresponding waveform of output inductor current is illustrated in Figure 8. The  $T_s$  is the switching period and can be expressed as

$$T_{s,wind} + T_{s,pv} = T_s. \quad (8)$$

In (8),  $T_{s,wind}$  stands for the intervals that the upper modified forward works, while  $T_{s,pv}$  for the lower modified forward. In the interleaved operation, the following relationship holds:

$$T_{s,pv} = T_{s,wind} = \frac{T_s}{2}. \quad (9)$$

Based on volt-second balance criterion, one can obtain the following identity:

$$\begin{aligned} &(2 \cdot N_{wind} \cdot k_{wind} \cdot v_{wind} - V_{dc,link}) \cdot D_{wind} \cdot T_{s,wind} \\ &+ (2 \cdot N_{pv} \cdot k_{pv} \cdot v_{pv} - V_{dc,link}) \cdot D_{pv} \cdot T_{s,pv} \\ &= (1 - D_{wind}) \cdot T_{s,wind} \cdot V_{dc,link} + (1 - D_{pv}) \cdot T_{s,pv} \cdot V_{dc,link}. \end{aligned} \quad (10)$$

Rearranging (10) yields

$$V_{dc,link} = N_{wind} \cdot k_{wind} \cdot v_{wind} \cdot D_{wind} + N_{pv} \cdot k_{pv} \cdot v_{pv} \cdot D_{pv}, \quad (11)$$

which reveals that the DC-link voltage can be controlled by the duty ratios of  $SW_{wind}$  and  $SW_{pv}$ .

In the MIC, perturb-and-observe method is employed to draw maximum power from wind turbine and PV arrays since it is easy to carry out. The perturb-and-observe MPPT is realized by dsPIC30F4011. The related flowchart is presented in Figure 9.

#### 4. Simulations and Practical Measurements

To demonstrate the feasibility of the proposed MIC, a prototype is constructed, simulated, and tested. Important parameters are listed as follows:

- (i) PV panel voltage:  $v_{pv} = 40-56$  V,
- (ii) wind turbine voltage:  $v_{wind} = 22-48$  V,
- (iii) dc-link voltage: 200 V,
- (iv) upper modified double-ended forward: 350 W,
- (v) lower modified double-ended forward: 350 W,
- (vi) switching frequency: 50 kHz for all active switches,
- (vii) output inductance:  $L_{mic} = 400 \mu\text{H}$ ,
- (viii) output capacitance:  $C_{dc,link} = 400 \mu\text{F}$ ,

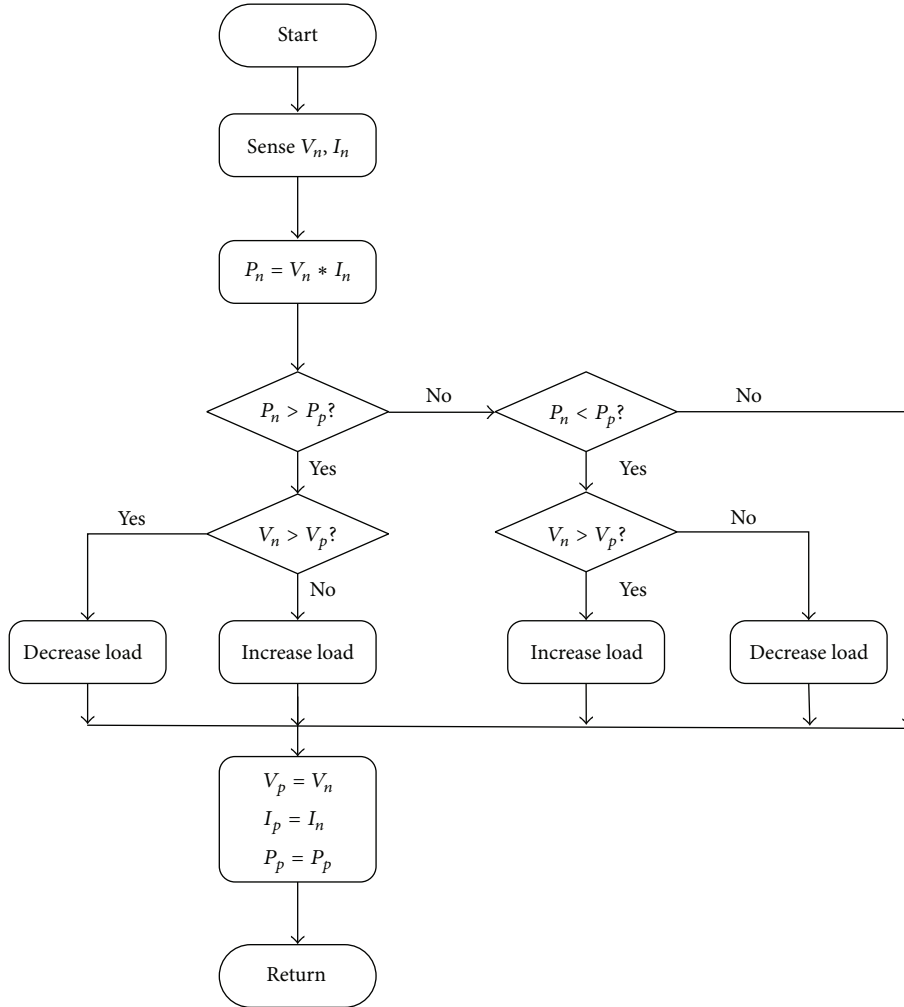


FIGURE 9: The flowchart of perturb-and-observe method to achieve MPPT feature.

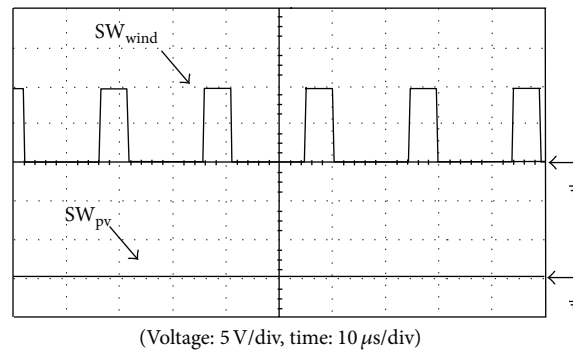


FIGURE 10: Simulated control signals while wind turbine provides 350 W.

- (ix) capacitance of upper forward:  $C_{wind} = 22 \mu\text{F}$ ,
- (x) capacitance of lower forward:  $C_{pv} = 22 \mu\text{F}$ .

In the case of only wind turbine providing 350 W, the simulated active switch signals and corresponding output inductor current are shown in Figures 10 and 11, respectively, while Figures 12 and 13 are the practical measurements. With

the perturb-and-observe method for maximum power point tracking, the measured result is shown in Figure 14, which has illustrated that the upper modified double-ended forward can draw the maximum power from wind turbine. If only 350 W PV power feeds the MIC, simulations of control signals for active switches and output inductor current are presented in Figures 15 and 16. In addition, Figures 17 and 18 are the

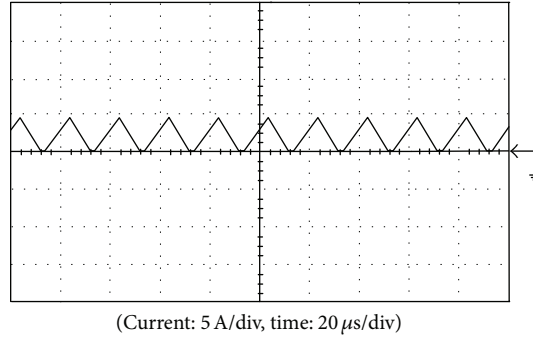


FIGURE 11: Simulated output inductor current while wind turbine provides 350 W.

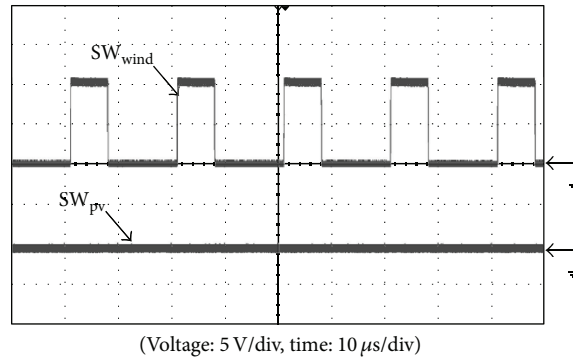


FIGURE 12: Practical measurements of control signals while wind turbine provides 350 W.

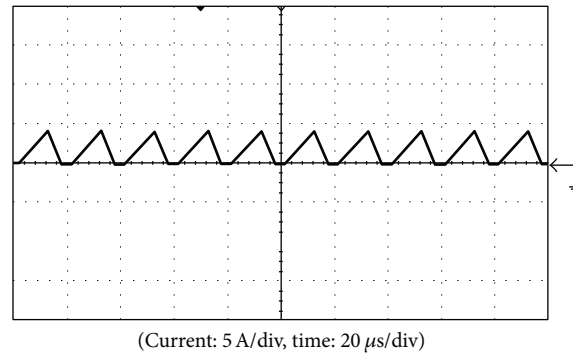


FIGURE 13: Measured output inductor current while wind turbine provides 350 W.

measured results. For MPPT feature verification, Figure 19 is the relationship between PV power and the terminal voltage of PV panel, from which it can be found that the proposed MIC is able to draw maximum power from PV panel. From Figures 10–19, it has been demonstrated that the proposed MIC is capable of dealing with individual renewable power. As the solar power and wind energy feed the MIC simultaneously, Figures 20 and 21 show the simulations of control signals and output inductor current. Then, Figures 22 and 23 present the hardware measurements. In addition, switch currents are also shown in Figure 24, in which the upper trace and the lower trace are the drain-to-source currents of  $SW_{wind}$  and  $SW_{pv}$ , respectively. Figure 25 is the hardware

measurements of the secondary currents  $i_{N2,wind}$  and  $i_{N2,pv}$ . All the experimental results correspond with the theoretical waveforms in Figure 6. From Figures 20–25, it is verified that the MIC not only can process hybrid wind-PV power but can operate in interleaved mode for current ripple suppression. Additionally, in Figures 21 and 23, the ripple of output inductor current is double the switch frequency, which results in lower volume requirement for output filter inductor. The measured efficiency of the MIC is shown in Figure 26. In the case of wind turbine shutting down from the hybrid power generation system, the output power variation of the MIC is shown in Figure 27. For converse condition, the related output power curve is shown in Figure 28.

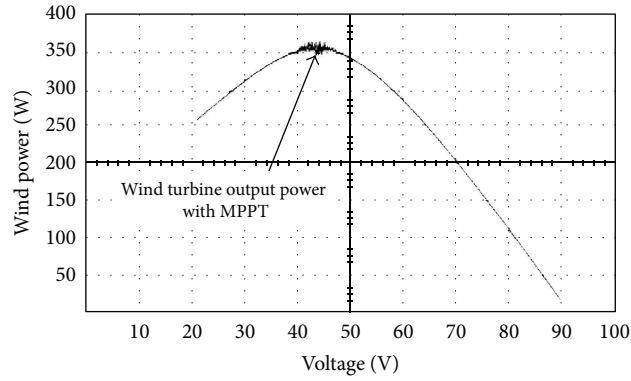


FIGURE 14: Measured result: drawn power from wind turbine with MPPT.

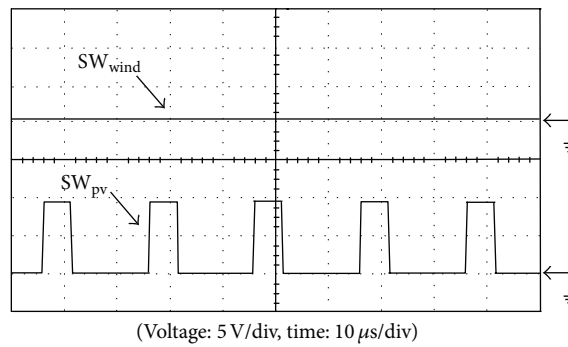


FIGURE 15: Simulated control signals while PV panel provides 350 W.

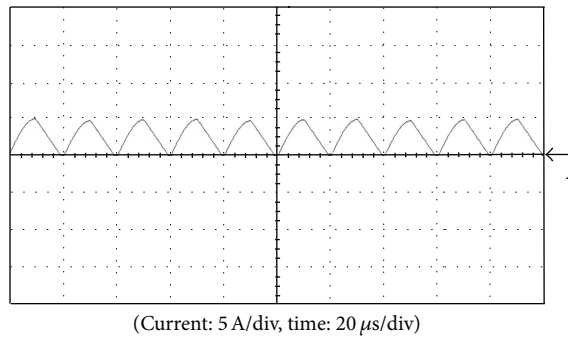


FIGURE 16: Simulated output inductor current while PV panel provides 350 W.

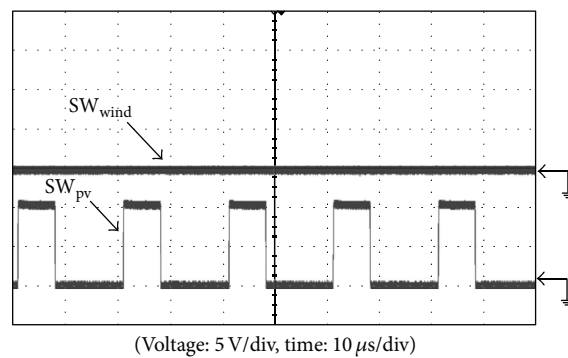


FIGURE 17: Practical measurements of control signals while PV panel provides 350 W.

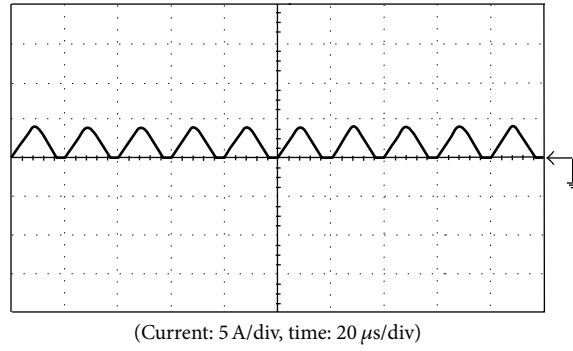


FIGURE 18: Measured output inductor current while PV panel provides 350 W.

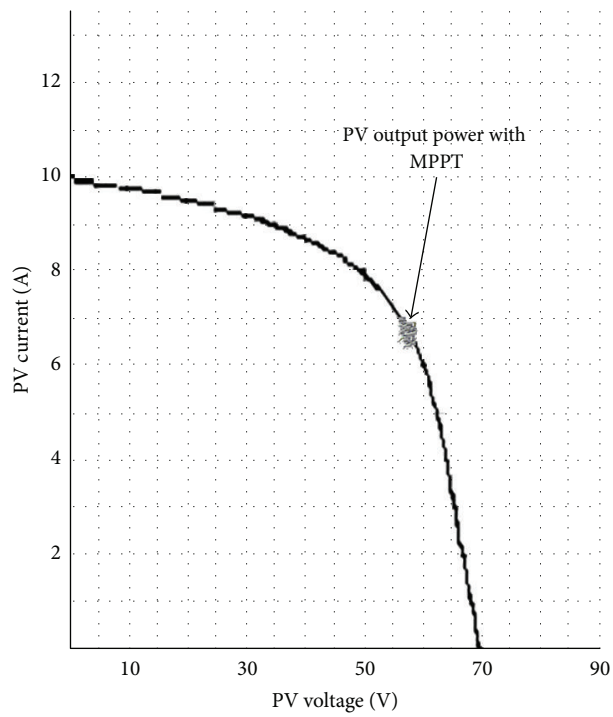


FIGURE 19: Measured result: operation point of PV panel after MPPT.

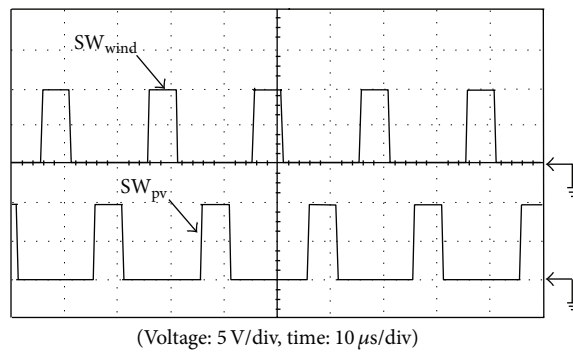
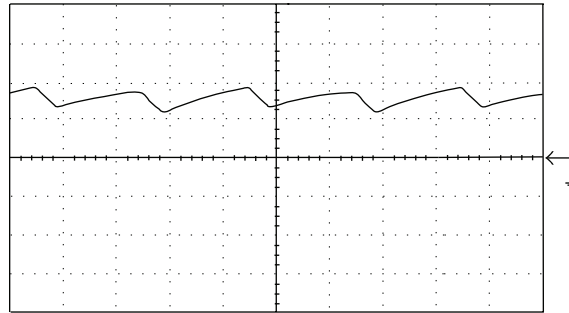
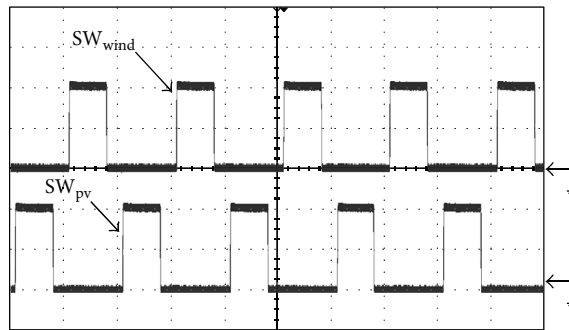


FIGURE 20: Simulated control signals while hybrid wind-PV power is 700 W.



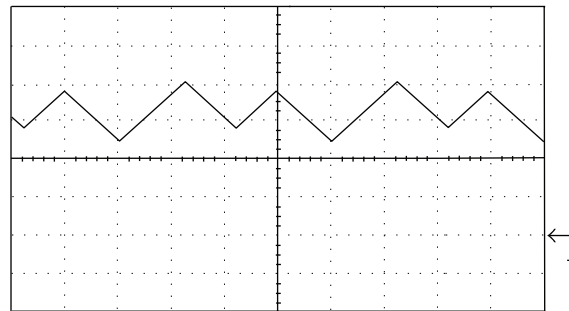
(Current: 2 A/div, time: 5  $\mu$ s/div)

FIGURE 21: Simlated output inductor current while hybrid wind-PV power is 700 W.



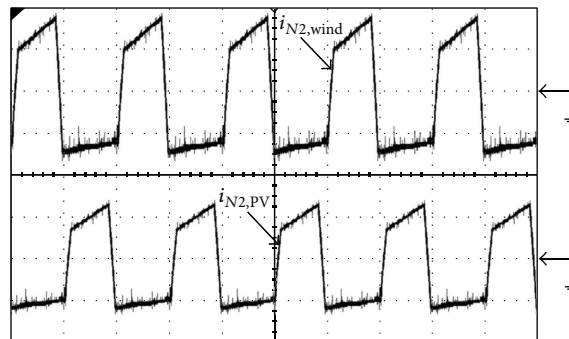
(Voltage: 5 V/div, time: 10  $\mu$ s/div)

FIGURE 22: Measured control signals while hybrid wind-PV power is 700 W.



(Current: 1 A/div, time: 5  $\mu$ s/div)

FIGURE 23: Measured output inductor current while hybrid wind-PV power is 700 W.



(Current: 2 A/div, time: 10  $\mu$ s/div)

FIGURE 24: Measured waveforms of switch currents.

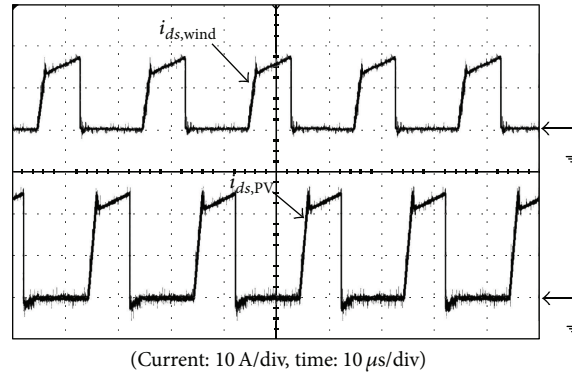


FIGURE 25: Measured current waveforms of the secondary windings in the MIC.

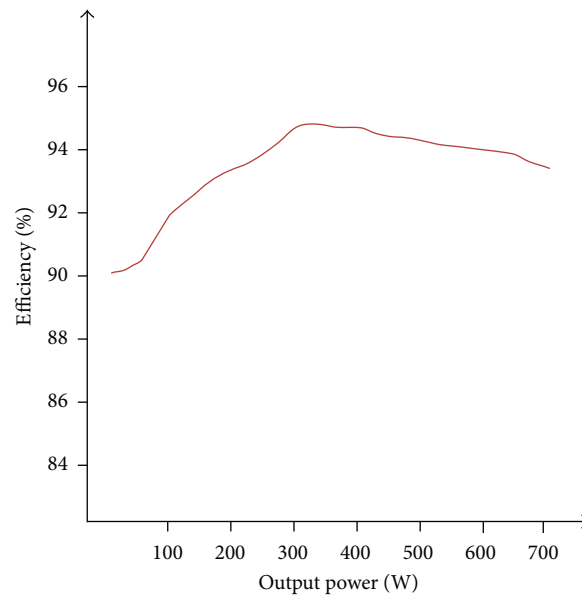


FIGURE 26: The measured efficiency of the proposed MIC.

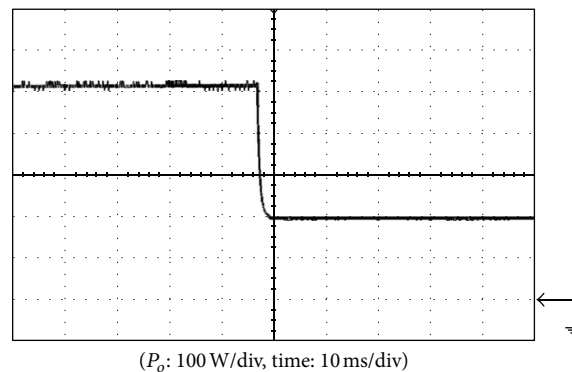


FIGURE 27: Output power variation while wind turbine shuts down from the hybrid generation system.

## 5. Conclusions

This paper proposed a galvanic isolated multi-input converter to deal with wind turbine energy and solar power with MPPT feature. The converter integrates two forward converters and

only uses one output inductor. Therefore, the structure of the proposed MIC can lower the volume of the converter. In addition, the MIC can operate in interleaved mode so that the output current ripple is suppressed significantly. The energy stored in leakage inductor can be recycled, which

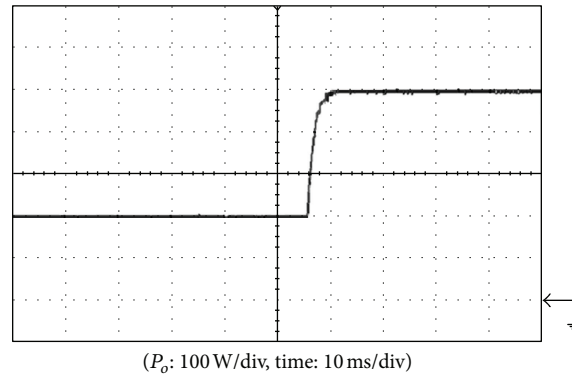


FIGURE 28: Output power variation while wind turbine incorporates into the hybrid generation system.

improves efficiency. In this paper, the proposed MIC is analyzed, simulated, and tested. Simulations and hardware measurements have validated the proposed MIC.

## References

- [1] R.-J. Wai, W.-H. Wang, and C.-Y. Lin, "High-performance stand-alone photovoltaic generation system," *IEEE Transactions on Industrial Electronics*, vol. 55, no. 1, pp. 240–250, 2008.
- [2] C.-L. Shen and J.-C. Su, "Grid-connection half-bridge PV inverter system for power flow controlling and active power filtering," *International Journal of Photoenergy*, vol. 2012, Article ID 760791, 8 pages, 2012.
- [3] R. Gules, J. D. P. Pacheco, H. L. Hey, and J. Imhoff, "A maximum power point tracking system with parallel connection for PV stand-alone applications," *IEEE Transactions on Industrial Electronics*, vol. 55, no. 7, pp. 2674–2683, 2008.
- [4] D. Meneses, O. García, P. Alou, J. A. Oliver, R. Prieto, and J. A. Cobos, "Single-stage grid-connected forward microinverter with constant off-time boundary mode control," in *Proceedings of the 27th Annual IEEE Applied Power Electronics Conference and Exposition (APEC '12)*, pp. 568–574, February 2012.
- [5] Z. Liang, R. Guo, J. Li, and A. Q. Huang, "A high-efficiency PV module-integrated DC/DC converter for PV energy harvest in FREEDM systems," *IEEE Transactions on Power Electronics*, vol. 26, no. 3, pp. 897–909, 2011.
- [6] X. Yuan, J. Chai, and Y. Li, "A transformer-less high-power converter for large permanent magnet wind generator systems," *IEEE Transactions on Sustainable Energy*, vol. 3, no. 3, pp. 318–329, 2012.
- [7] B. Singh and S. Sharma, "Design and implementation of four-leg voltage-source-converter-based VFC for autonomous wind energy conversion system," *IEEE Transactions on Industrial Electronics*, vol. 59, no. 12, pp. 4694–4703, 2012.
- [8] R. Li and D. Xu, "Parallel operation of full power converters in permanent-magnet direct-drive wind power generation system," *IEEE Transactions on Industrial Electronics*, vol. 60, no. 4, pp. 1619–1629, 2013.
- [9] F. Deng and Z. Chen, "Control of improved full-bridge three-level DC/DC converter for wind turbines in a DC grid," *IEEE Transaction on Power Electronics*, vol. 28, no. 1, pp. 314–324, 2013.
- [10] W. Chen, A. Q. Huang, C. S. Li, G. Y. Wang, and W. Gu, "Analysis and comparison of medium voltage high power DC/DC converters for offshore wind energy systems," *IEEE Transaction on Power Electronics*, vol. 28, no. 4, pp. 2014–2023, 2013.
- [11] N. Vazquez, A. Hernandez, C. Hernandez, E. Rodríguez, R. Orosco, and J. Arau, "A double input DC/DC Converter for photovoltaic/wind systems," in *Proceedings of the 39th IEEE Annual Power Electronics Specialists Conference (PESC '08)*, pp. 2460–2464, June 2008.
- [12] Y.-M. Chen, Y.-C. Liu, S.-C. Hung, and C.-S. Cheng, "Multi-input inverter for grid-connected hybrid PV/wind power system," *IEEE Transactions on Power Electronics*, vol. 22, no. 3, pp. 1070–1077, 2007.
- [13] Y.-M. Chen, Y.-C. Liu, and F.-Y. Wu, "Multi-input dc/dc converter based on the multiwinding transformer for renewable energy applications," *IEEE Transactions on Industry Applications*, vol. 38, no. 4, pp. 1096–1104, 2002.
- [14] C.-L. Shen, C.-T. Tsai, Y.-E. Wu, and C.-C. Chen, "A modified-forward multi-input power converter for solar energy and wind power generation," in *Proceedings of International Conference on Power Electronics and Drive Systems (PEDS '09)*, pp. 631–636, January 2009.

## Research Article

# Photovoltaic High-Frequency Pulse Charger for Lead-Acid Battery under Maximum Power Point Tracking

Hung-I. Hsieh,<sup>1</sup> Sheng-Fang Shih,<sup>1</sup> Jen-Hao Hsieh,<sup>2</sup> and Chi-Hao Wang<sup>2</sup>

<sup>1</sup> Department of Electrical Engineering, National Chiayi University, Chiayi 60004, Taiwan

<sup>2</sup> Department of Electrical Engineering, Chung Yuan Christian University, Chungli 320, Taiwan

Correspondence should be addressed to Hung-I. Hsieh; [hihsieh@mail.ncyu.edu.tw](mailto:hihsieh@mail.ncyu.edu.tw)

Received 30 November 2012; Accepted 30 May 2013

Academic Editor: Keith Emery

Copyright © 2013 Hung-I. Hsieh et al. This is an open access article distributed under the Creative Commons Attribution License, which permits unrestricted use, distribution, and reproduction in any medium, provided the original work is properly cited.

A photovoltaic pulse charger (PV-PC) using high-frequency pulse train for charging lead-acid battery (LAB) is proposed not only to explore the charging behavior with maximum power point tracking (MPPT) but also to delay sulfating crystallization on the electrode pores of the LAB to prolong the battery life, which is achieved due to a brief pulse break between adjacent pulses that refreshes the discharging of LAB. Maximum energy transfer between the PV module and a boost current converter (BCC) is modeled to maximize the charging energy for LAB under different solar insolation. A duty control, guided by a power-increment-aided incremental-conductance MPPT (PI-INC MPPT), is implemented to the BCC that operates at maximum power point (MPP) against the random insolation. A 250 W PV-PC system for charging a four-in-series LAB (48 V<sub>dc</sub>) is examined. The charging behavior of the PV-PC system in comparison with that of CC-CV charger is studied. Four scenarios of charging statuses of PV-BC system under different solar insolation changes are investigated and compared with that using INC MPPT.

## 1. Introduction

Renewable energy sources have become indispensable and applicable in our life in consideration to the lack of fossil fuel, especially for the photovoltaic and wind energies. As for energy storage, lead-acid battery (LAB) is always the interesting device due to low cost; even its lifecycle time is low. Fortunately, the experiment reported that, after charging the battery in 5–10 hours with a short-period large current, the sulfating crystallization covered on the plates of positive electrode area will be reduced, and the battery is without over-heat and thereby increases the discharge efficiency to extend battery life [1–3]. Thus, the pulse charge method has become one of the available charging strategies in battery management. The LAB is basically composed of two electrodes, the negative electrode made of metallic lead (Pb) and the positive one lead-oxide (PbO<sub>2</sub>), immersed in a sulphuric acid solution (H<sub>2</sub>SO<sub>4</sub>), which produces chemical reaction during charging and discharging processes. During discharge state, both the electrodes in battery will build up lead sulfate PbSO<sub>4</sub> and the electrolyte is then converted to H<sub>2</sub>O, but the opposite process

will occur in charging state. When the battery approaches 85–95% of the state of charge (SOC), the majority of the PbSO<sub>4</sub> will be converted to Pb and PbO<sub>2</sub>, in which the battery voltage might be greater than the gassing voltage. The overcharge reaction possibly results in the gas evolution of hydrogen appearing at negative electrode and of oxygen at positive electrode. This undesired phenomenon may lead to heat, increasing charging time, and shorten the battery life, even exists explosive potential if the gas is not vented. Above all, if some PbSO<sub>4</sub> is crystallized on the pores of positive electrode, the discharging current will be limited due to the reduction of effective surface area on the positive electrode. In order to prolong the battery life, a high-frequency photovoltaic pulse charger (PV-PC) system for LAB is presented, which contributes the pulsate effect for delaying the mentioned sulfating crystallization during the adjacent tiny pulse break times. In this work, a boost current converter (BCC) associated with the PV module is modeled to maximize the energy charging to LAB under maximum power transfer [4]. In order to maximize the energy pumped from PV module, a duty cycle control guided by a power-increment-aided

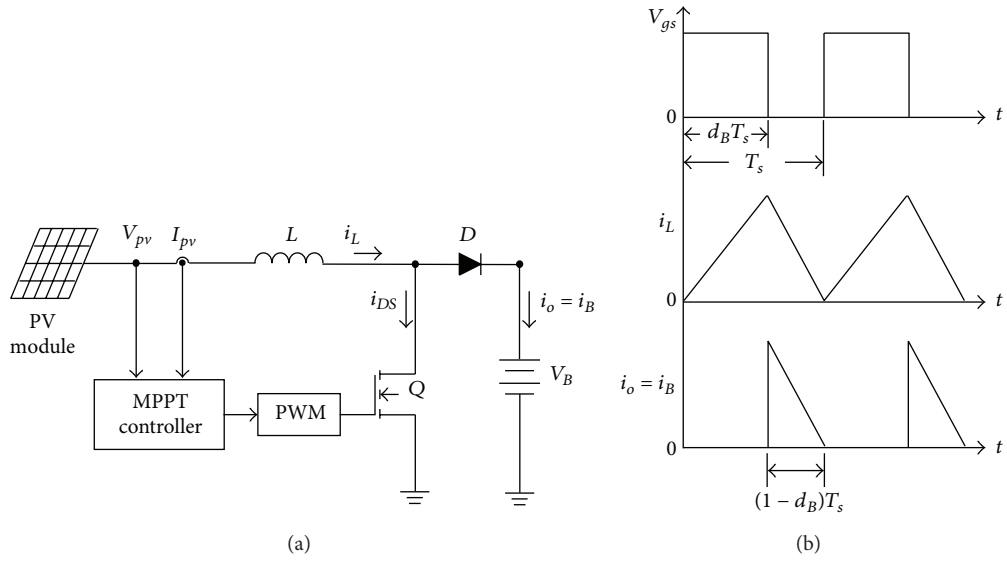


FIGURE 1: (a) Proposed PV-PC system and (b) predicted energy-pumped waveforms of PV-BCC at boundary mode.

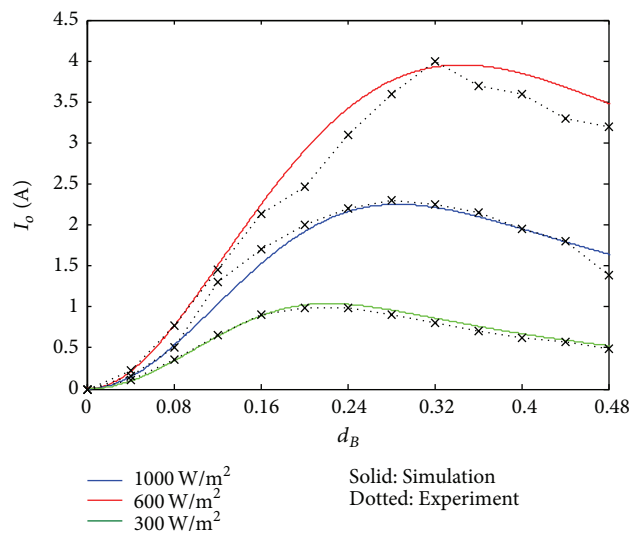
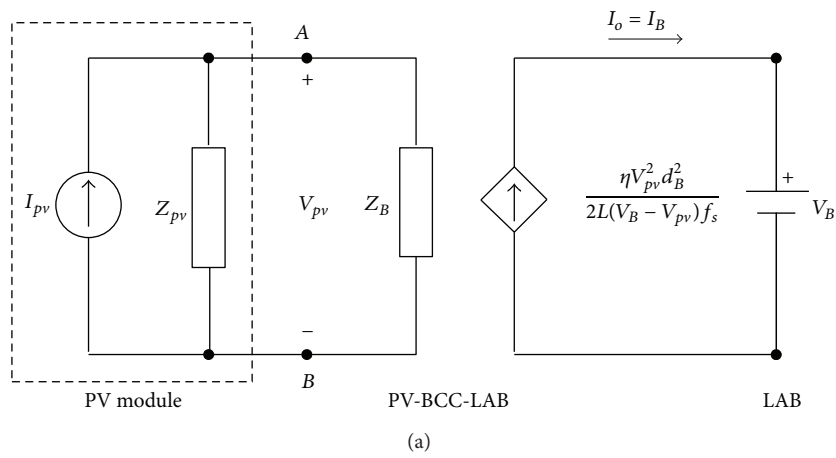


FIGURE 2: (a) The model of the proposed PV-PC and (b) simulated and experimented output-to-control responses.

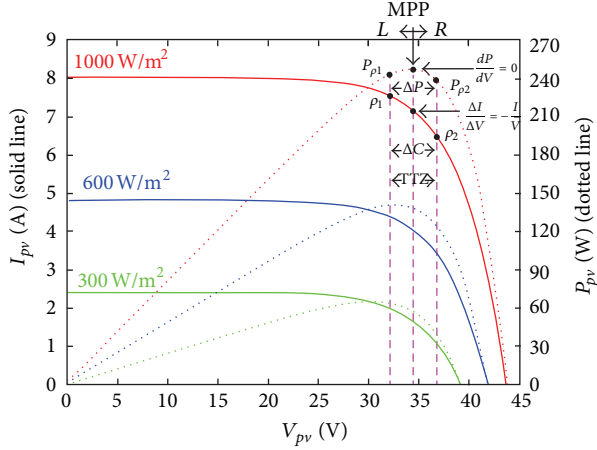


FIGURE 3:  $I_{pv}$ - $V_{pv}$  and  $P_{pv}$ - $V_{pv}$  characteristic curves for a two-in-series PV module, where a tracking threshold zone (TTZ) is indicated for distinguishing PI-coarse tracking zone and INC-fine tracking zone [6].

incremental-conductance maximum power point tracking (PI-INC MPPT), derived from the incremental-conductance maximum power point tracking (INC MPPT), is adopted to sustain the PV-BCC pumping energy from PV module that is fast and accurate against the random solar insolation [4–8]. The weakness of the INC-MPPT is its ambiguous incremental conductance occurring in the left side of the MPP, which may delay the tracking behavior of MPPT. To clearly describe the dynamic tracking behavior in charging, four scenarios of solar insolation change under the guidance of PI-INC MPPT and INC-MPPT are, respectively, investigated and compared to each other in this work. An experimental study for verifying the charging behavior of the PV-PC system with a four-in-series 45-AH (ampere hour) LABs (48 V<sub>dc</sub>) is examined. The charging characteristics of the PV-PC system in comparison with that of conventional constant-current constant-voltage (CC-CV) charger are studied. Experimental result validates that high-frequency pulse train can actually delay the sulfating crystallization on the plates of electrodes of the LAB, which prolongs the battery life.

## 2. Analysis of PV-PC System

Figure 1(a) shows the circuit diagram of the PV-PC system, which is formed by a BCC guided by a MPPT controller. Dynamic states of the BCC at boundary condition are shown in Figure 1(b), in which the output current  $i_o$  is certainly a form of pulse train that is used as a charging source. The PV BCC driven by a duty period  $d_B T_s$  from PI-INC MPPT can operate between discontinuous-conduction mode (DCM) and boundary-conduction mode (BCM) for pulse charging to the LAB.

For convenience in analysis, the steady state of PV-BCC in BCM is described. If a battery  $V_B$  greater than maximum  $V_{pv}$  is adopted and all components are presumed to be ideal,

the peak inductor current  $i_{L,pk}$  of the PV-BCC in BCM from Figure 1(b) can be represented by

$$i_{L,pk} = \frac{V_{pv}}{L} \cdot d_B T_s, \quad (1)$$

where  $L$  is the boost inductor,  $d_B$  the duty ratio, and  $T_s$  the switching period. We then have average PV current  $I_{pv}$ :

$$I_{pv} = \frac{V_B V_{pv}}{V_B - V_{pv}} \cdot \frac{d_B^2}{2L f_s}, \quad (2)$$

where switching frequency  $f_s = 1/T_s$ . If power efficiency  $\eta$  is considered, the average output current  $I_o$  ( $= I_B$ ) to LAB from (2) will be

$$I_o = \frac{\eta V_B^2 d_B^2}{2L (V_B - V_{pv}) f_s}. \quad (3)$$

Equation (3) represents the control-to-output transfer function, in which the output current  $I_o$  is proportional to square of duty ratio  $d_B$  and inversely proportional to switching frequency  $f_s$ . The model and simulation of control-to-output transfer function are presented in Figures 2(a) and 2(b), respectively. The duty ratio  $d_B$  of PV-BCC is designed associated with the PV characteristic as shown in Figure 3. The output power of PV-BCC can be obtained by

$$P_o = \frac{\eta V_B V_{pv}^2 d_B^2}{2L (V_B - V_{pv}) f_s}. \quad (4)$$

If an interleaved configuration is considered in the PV-BCC, the average output current  $I_o$  and power  $P_o$  can be easily obtained from (3) and (4) by multiplying two.

## 3. PI-INC MPPT for PV-PC System

The PV-BCC guided by PI-INC MPPT controller can draw energy from PV module fast and accurate according to the guidance specified on  $I_{pv}$ - $V_{pv}$  and  $P_{pv}$ - $V_{pv}$  characteristic curves in Figure 3, in which the tracking references for executing power-increment tracking (PI) and incremental-conductance (INC) tracking are clearly described in [6, 8]. The PI-INC MPPT can provide a PI-coarse tracking quick toward a specified threshold-tracking zone (TTZ) using  $P_{pv}$ - $V_{pv}$  curve, to avoid delay tracking that stems from some ambiguous conductance detection in the right-hand side of maximum power point (MPP) in  $I_{pv}$ - $V_{pv}$  curve by using INC MPPT method [4, 5, 9]. In Figure 3, two mutual equivalent TTZs are, respectively, defined in the  $I_{pv}$ - $V_{pv}$  and  $P_{pv}$ - $V_{pv}$  curves used to distinguish the roles of PI-INC MPPT tracking and conventional INC MPPT. A PI-coarse tracking along  $P_{pv}$ - $V_{pv}$  curve executes quick toward TTZ when the PV-BCC operates outside the TTZ. Once the detected power increment  $\Delta P$  is within TTZ, INC-fine tracking is provided toward the MPP using  $I_{pv}$ - $V_{pv}$  curve. Thus, a fast and accurate tracking performance is applicable in PI-INC MPPT in comparison to that in the conventional INC-MPPT. The MPP

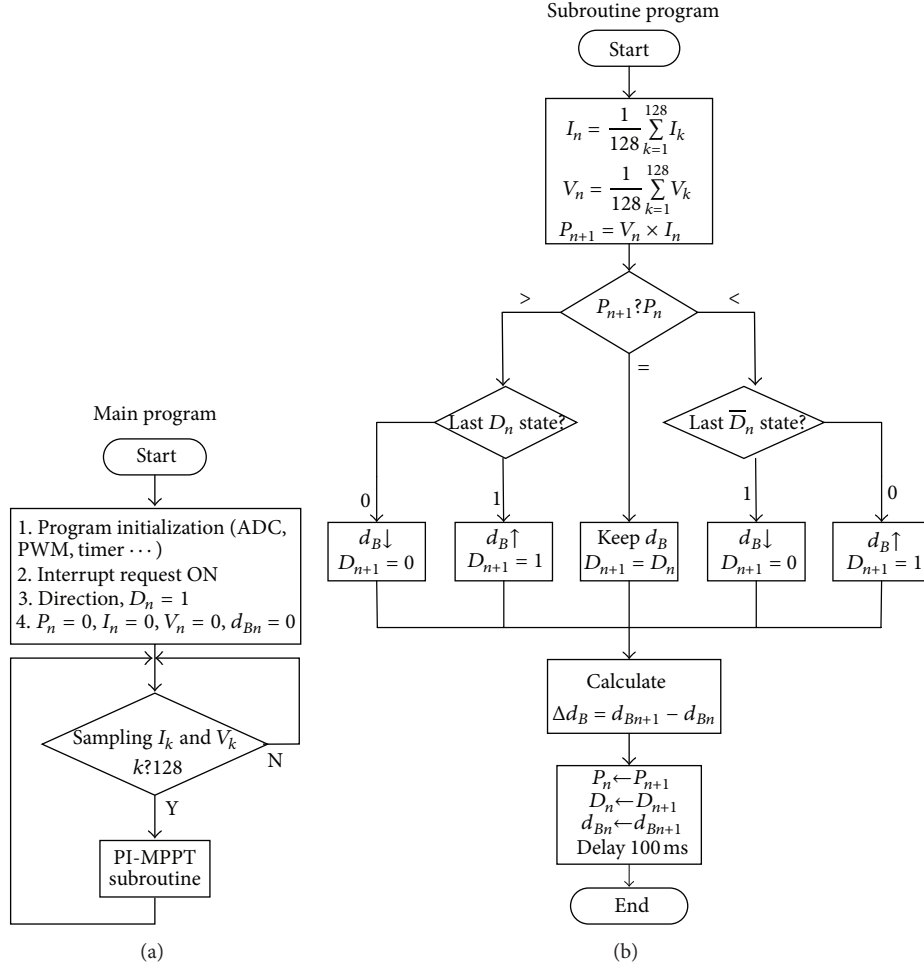


FIGURE 4: Programming of PI-INC MPPT: (a) main program and (b) subroutine program without THZ, as a simplified case of PI-INC MPPT.

for INC MPPT, reported by Wasynczuk [5], can then be given by

$$\frac{dI_{pv}}{dV_{pv}} = -\frac{I_{pv}}{V_{pv}}, \quad (5)$$

$$\frac{\Delta I_{pv}}{\Delta V_{pv}} \approx \frac{dI_{pv}}{dV_{pv}} = -\frac{I_{pv}}{V_{pv}}.$$

It is clearly shown that in Figure 3 the measure  $\Delta C$  is bounded by the two ratios  $\rho_1$  and  $\rho_2$  on the  $I_{pv}$ - $V_{pv}$  curve, and correspondingly the measure  $\Delta P$  is bounded between limits  $P_{\rho_1}$  and  $P_{\rho_2}$  on the  $P_{pv}$ - $V_{pv}$  curve, in which  $P_{\rho_1}$  and  $P_{\rho_2}$  are derived from the two ratios  $\rho_1$  and  $\rho_2$ . From the specified  $\Delta C$  on the  $I_{pv}$ - $V_{pv}$  curve, the tracking bound in TTZ will be

$$-\rho_1 \frac{I_{pv}}{V_{pv}} > \Delta C > -\rho_2 \frac{I_{pv}}{V_{pv}} \quad (6)$$

and outside the TTZ when

$$\Delta C > -\rho_1 \frac{I_{pv}}{V_{pv}} \quad (7)$$

or

$$\Delta C < -\rho_2 \frac{I_{pv}}{V_{pv}}, \quad (8)$$

where  $\Delta C$  is defined as

$$\Delta C = \frac{\Delta I_{pv}}{\Delta V_{pv}}. \quad (9)$$

The two ratios  $\rho_1$  and  $\rho_2$  are real numbers. Equation (9) is always negative because  $\Delta I_{pv}$  and  $\Delta V_{pv}$  have opposite signs. Accordingly, the corresponding relation to PI-INC MPPT derived from the specified bounds of INC MPPT will be, from (6)-(9),

$$P_{\rho_1} > \Delta P > P_{\rho_2} \quad (10)$$

within TTZ, where  $\Delta P = P_{n+1} - P_n$ ,  $\Delta V = V_{n+1} - V_n$ , and  $\Delta I = I_{n+1} - I_n$ , and

$$\Delta P > P_{\rho_1} \quad (11)$$

or

$$\Delta P < P_{\rho_2} \quad (12)$$

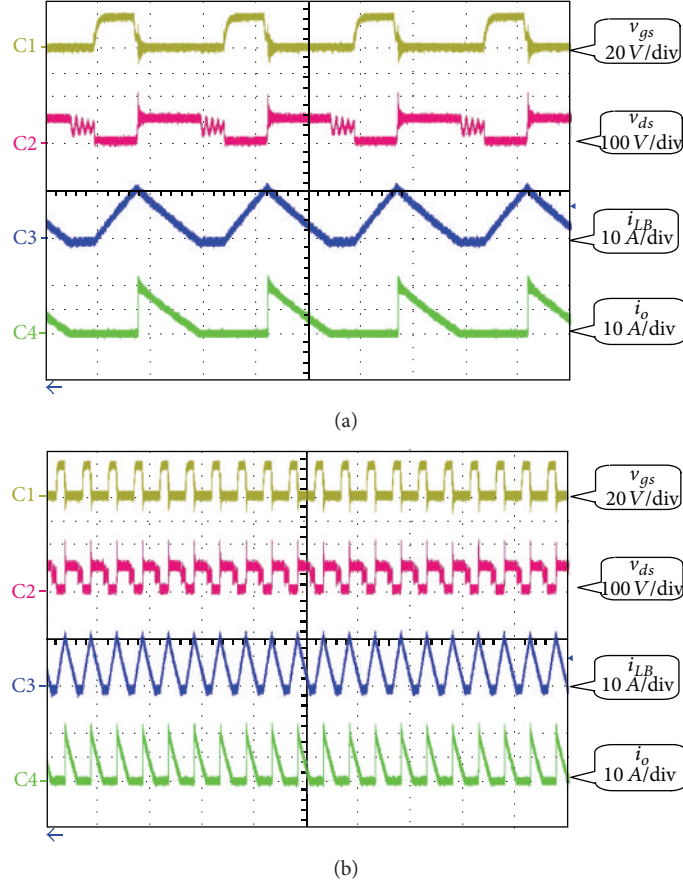


FIGURE 5: Measured waveforms of PV-BCC at  $600 \text{ W/m}^2$ , MPPT conditions:  $V_{pv} = 32.7 \text{ V}$ ,  $I_{pv} = 4.3025 \text{ A}$ ,  $f_s = 40 \text{ kHz}$ , and  $d_B = 0.29$ , (a) Hor.:  $10 \mu\text{div}$  and (b) Hor.:  $50 \mu\text{div}$ .

outside of TTZ. The two power threshold limits in (10) are defined by

$$\begin{aligned} P_{\rho_1} &\equiv (1 - \rho_1) \Delta V I_{n+1}, \\ P_{\rho_2} &\equiv (1 - \rho_2) \Delta V I_{n+1}. \end{aligned} \quad (13)$$

The flow chart of PI-INC MPPT for duty control presented in Figure 4 will enable MPPT controller adaptively providing proper duty ratio  $d_B$  for PV-BCC to pump energy from PV module at MPP in which a simplified program with  $P_{\rho_1} = P_{\rho_2} = 0$  is examined. In other words, the program is a special case of the PI-INC MPPT without TTZ.

#### 4. Design and Realization

A 250 W PV-PC system configured as in Figure 1(a) consisting of a two-in-series PV module (Kyocera KC130T), a BCC, and a four-in-series LAB (Kawasaki MF50B24,  $12 \text{ V}_{dc}$ , 45 AH, each) is designed and realized for assessing the charging behavior of LAB guided by PI-INC MPPT, and validating the feasibility in application. The PV-PC system operates at constant frequency of 40 kHz with duty varied from 0 to 0.36 under solar insolation from 0 to  $1 \text{ kW/m}^2$ , in which the duty at  $d_B = 0.36$  is when solar insolation at  $1 \text{ kW/m}^2$ , where

TABLE 1: Comparison of MPPT tracking scenarios under different insolation changes.

Scenario	Insolation jump step ( $\text{W/m}^2$ )	Initial jump location	PI-INC MPPT (sec)	INC MPPT (sec)
1	$0 \rightarrow 600$	L	9	33
2	$600 \rightarrow 1000$	R	6	13
3	$1000 \rightarrow 300$	L	15	142
4	$300 \rightarrow 1000$	R	22	32

L: Left-hand side of the MPP.  
R: Right-hand side of the MPP.

the peak charging current for LAB is 16 A. The program of PI-INC MPPT is executed by microchip dsPIC33FJ06GS202 according to the tracking guidance in Figure 4, in which a simplified case of PI-INC MPPT without THZ is presented for instance. The PI-coarse tracking along  $P_{pv}$ - $V_{pv}$  curve can perform fast and accurate tracking toward MPP in comparison with the INC tracking along  $I_{pv}$ - $V_{pv}$  curve. The waveforms of the PV-BCC working at solar insolation of  $600 \text{ W/m}^2$  and  $1000 \text{ W/m}^2$  are measured in Figures 5 and 6, respectively, in which the boost inductor current  $i_L$  is in DCM

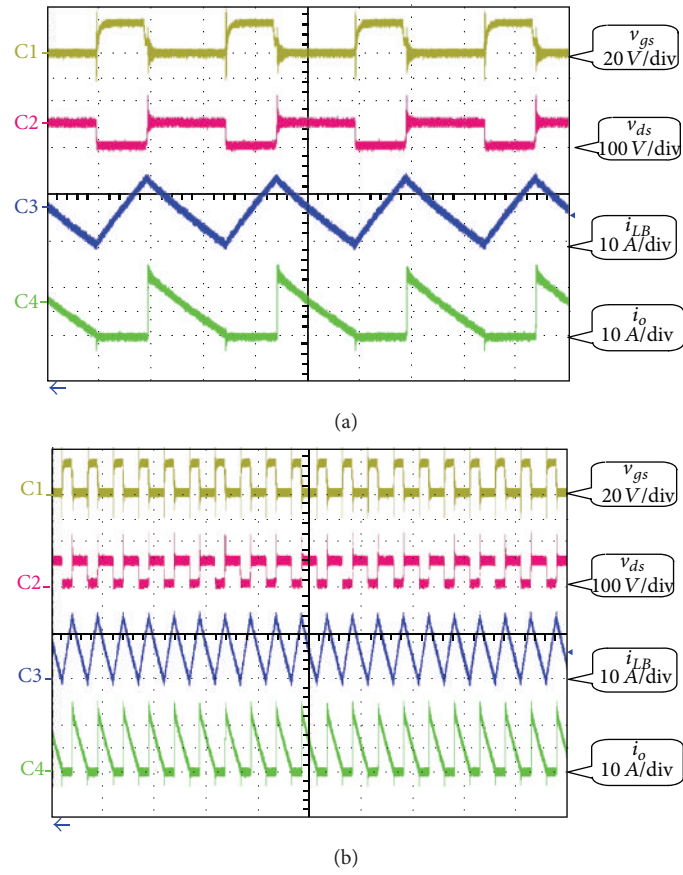


FIGURE 6: Measured waveforms of PV-BCC at  $1000 \text{ W/m}^2$ , MPPT conditions:  $V_{pv} = 34.3 \text{ V}$ ,  $I_{pv} = 47.193 \text{ A}$ ,  $f_s = 40 \text{ kHz}$ , and  $d_B = 0.36$ , (a) Hor.:  $10 \mu\text{s/div}$ . and (b) Hor.:  $50 \mu\text{s/div}$ .

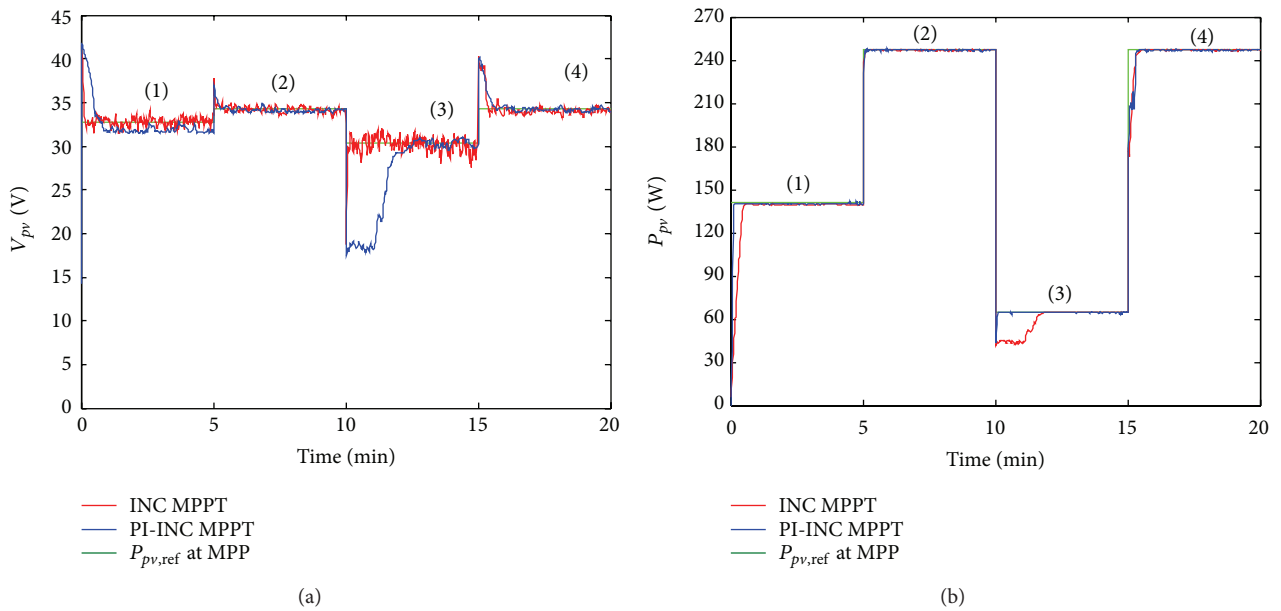


FIGURE 7: Tracking comparison of PI-INC MPPT and INC MPPT for PV-PC system under four scenarios of solar insolation change (a) voltage tracking behavior and (b) power tracking behavior.

TABLE 2: Comparison of charging statuses between CC-CV and pulse charge.

SOC (%)	CC-CV		PV pulse charge		Charging time (min.)
	Voltage (V)	Capacity (%)	Voltage (V)	Capacity (%)	
30	48.73	30	48.73	30	0
35	49.32	43.84	49.42	46.19	15
40	49.51	48.30	49.57	49.71	30
45	49.69	52.53	49.76	54.17	45
50	49.88	56.99	49.9	57.45	60
55	50	59.80	50.01	60.04	75
60	50.17	63.79	50.2	64.49	90
65	50.32	67.31	50.36	68.25	105
70	50.48	71.06	50.53	72.24	120
75	50.63	74.58	50.68	75.76	135
80	50.8	78.57	50.88	80.45	150
85	50.96	82.33	51.06	84.68	165
90	51.12	86.08	51.25	89.13	180
95	51.27	89.60	51.43	93.36	195
	51.43	93.36			210

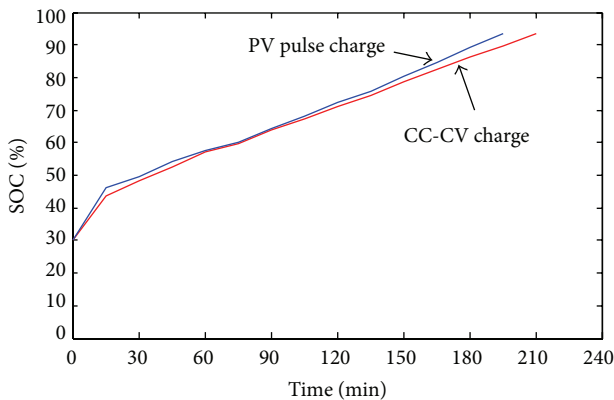


FIGURE 8: Comparison of charging behaviors between CC-CV and PV-PC.

at  $600 \text{ W/m}^2$  but in CCM at  $1000 \text{ W/m}^2$ . In spite of the state modes either DCM or CCM, the output currents  $i_o$  clearly shown in Figures 5(b) and 6(b) are always available pulse trains for charging the LABs. Figure 7 shows the comparison of the tracking behaviors of PI-INC MPPT and INC MPPT in the PV-PC system under four kinds of solar insolation scenarios. The voltage tracking in Figure 7(a) and power tracking in Figure 7(b) clearly display that the PI-INC MPPT is much more fast and accurate toward the MPP than the INC MPPT. The PI-INC MPPT can only pay few seconds to track at MPP when the solar jump step initially occurs in either side of the MPP. In other words, there is no ambiguous detection happened in PI-INC MPPT. As for the INC MPPT, it is ambiguous to detect the incremental conductance in the left-hand side of the MPP, which may lead much delay in MPPT, such behaviors as in scenarios 1 and 3; the tracking

times toward MPP should be much more over 4–10 times of the PI-INC MPPT. The measured data of tracking response shown in Table 1 show that the PI-INC MPPT is more reliable than INC MPPT in tracking process during the four scenario changes; in particularly, there is no abrupt delay response occurring in PI-INC MPPT during the insolation change, in comparison to the response of INC MPPT. The state of charge (SOC) of the PV-PC system compared with that of CC-CV charger is shown in Figure 8, and the detail charging statuses are measured in Table 2. The measured result reveals faster response of 195 min for PV-PC system than that of 210 min for CC-CV charger over about 8%, compared at SOC about 95%.

## 5. Conclusion

The PV pulse charge directly using PV energy without through a dc-to-dc converter as energy buffer enhances the utilization of renewable energy. The brief pulse break existing between adjacent high-frequency pulses can actually perform the discharge refreshing of LAB for delaying sulfate crystallization on electrodes. The charging behavior using pulse charge is faster than that using CC-CV charge, which reveals that the resulted sulfate crystallization on the positive electrode of the LAB is slow in pulse charging process, which is good for prolonging the battery life. Moreover, the PI-INC MPPT compared with INC MPPT advantages much better tracking behavior without abrupt tracking delay during solar insolation change.

## Acknowledgments

The authors would like to thank the National Science Council with the project NSC 101-2221-E-415-010 and joint project of Lien-Chang Electronics Enterprise Ltd. Co. 991206 for their financial support.

## References

- [1] L. T. Lam, H. Ozgun, O. V. Lim et al., "Pulsed-current charging of lead/acid batteries—a possible means for overcoming premature capacity loss?" *Journal of Power Sources*, vol. 53, no. 2, pp. 215–228, 1995.
- [2] J. J. A. Wilkinson and G. A. Covic, "A new pulse charging methodology for lead acid batteries," *IPENZ Transactions*, vol. 25, no. 1, pp. 1–16, 1998.
- [3] S. Minami, Y. Onishi, S. J. Hou, and A. Kozawa, "A new intense pulse-charging method for the prolongation of life in lead-acid batteries," *Journal Asian Electric Vehicles*, vol. 2, no. 1, pp. 541–544, 2004.
- [4] R. L. Mueller, M. T. Wallace, and P. Iles, "Scaling nominal solar cell impedances for array design," in *Proceedings of the 1st World Conference on Photovoltaic Energy Conversion (WCPEC '94)*, pp. 2034–2037, December 1994.
- [5] O. Wasynczuk, "Dynamic behavior of a class of photovoltaic power system," *IEEE Transactions on Power Apparatus and Systems*, vol. 102, no. 9, pp. 3031–3037, 1983.
- [6] G. C. Hsieh, C. Y. Tsai, and H. I. Hsieh, "Photovoltaic power-increment-aided incremental-conductance maximum power

- point tracking using variable frequency and duty controls,” in *Proceedings of the IEEE 3rd International Symposium on Power Electronics for Distributed Generation Systems (PEDG '12)*, pp. 542–549, Aalborg, Denmark, 2012.
- [7] H. I. Hsieh, S. F. Shih, J. H. Hsieh, and G. C. Hsieh, “A study of high-frequency photovoltaic pulse charger for lead-acid battery guided by PI-INC MPPTin,” in *Proceedings of the International Conference on Renewable Energy Research and Applications (ICRERA '12)*, pp. 283–288, Nagasaki, Japan, November 2012.
- [8] G. C. Hsieh, H. I. Hsieh, C. Y. Tsai, and C. H. Wang, “Photovoltaic power-increment-aided incremental-conductance MPPT with two-phased tracking,” *IEEE Transactions on Power Electronics*, vol. 28, no. 6, pp. 2895–22911, 2013.
- [9] K. H. Hussein, I. Muta, T. Hoshino, and M. Osakada, “Maximum photovoltaic power tracking: an algorithm for rapidly changing atmospheric conditions,” *IEE Proceedings*, vol. 142, no. 1, pp. 59–64, 1995.

## Research Article

# Simulation and Experimental Study of Photogeneration and Recombination in Amorphous-Like Silicon Thin Films Deposited by 27.12 MHz Plasma-Enhanced Chemical Vapor Deposition

Chia-Hsun Hsu,<sup>1</sup> In-Cha Hsieh,<sup>1</sup> Chia-Chi Tsou,<sup>2</sup> and Shui-Yang Lien<sup>2</sup>

<sup>1</sup> Graduate Institute of Precision Engineering, National Chung Hsing University, Taichung 402, Taiwan

<sup>2</sup> Department of Materials Science and Engineering, MingDao University, Changhua 52345, Taiwan

Correspondence should be addressed to Shui-Yang Lien; syl@mdu.edu.tw

Received 22 November 2012; Revised 3 May 2013; Accepted 16 May 2013

Academic Editor: Peter Rupnowski

Copyright © 2013 Chia-Hsun Hsu et al. This is an open access article distributed under the Creative Commons Attribution License, which permits unrestricted use, distribution, and reproduction in any medium, provided the original work is properly cited.

Amorphous-like silicon (a-Si:H-like) thin films are prepared by 27.12 MHz plasma-enhanced chemical vapor deposition technique. The films are applied to p-i-n single junction thin film solar cells with varying i-layer thickness to observe the effects on the short-circuit current density, as well as the open-circuit voltage, fill factor, and conversion efficiency. The most significant experimental result is that  $J_{sc}$  has two different behaviors with increasing the i-layer thickness, which can be related to carrier collection efficiency in the long wavelength region. Furthermore, technology computer-aided design simulation software is used to gain better insight into carrier generation and recombination of the solar cells, showing that for the i-layer thickness of 200 to 300 nm the generation dominates the carrier density and thus  $J_{sc}$ , whereas for the i-layer thickness of 300 to 400 nm the recombination becomes the leading factor. The simulation results of cell performances are in good agreement with experimental data, indicating that our simulation has great reliability. In addition, the a-Si:H-like solar cells have low light-induced degradation, which in turn can have a great potential to be used for stable and high-efficiency solar cells.

## 1. Introduction

Hydrogenated amorphous silicon (a-Si:H) thin films have been widely studied in photovoltaic technology in recent years. Because of a high-absorption coefficient of a-Si:H in the visible range of the solar spectrum, 1  $\mu\text{m}$  thick a-Si:H layer is enough to absorb 90% of usable solar energy. However, large deviations in bonding angles and bonding lengths between the neighboring atoms in a-Si:H result in the weak or strained bonds, which would easily break and thus form defects in the atomic network. As a result, a-Si:H suffers from the photoinduced problem of degradation, known as Staebler-Wronski effect, which reduces the efficiency of solar cells after light illumination. One alternative is the use of hydrogenated microcrystalline silicon ( $\mu\text{c-Si:H}$ ), in which small crystals of highly ordered material in the range of tenths of nanometers

are embedded. The amplitude of the degradation is a function of the crystallinity of the  $\mu\text{c-Si:H}$  layer: the lower the crystallinity, the higher the light-induced degradation. It is demonstrated more precisely that light-induced degradation is proportional to the ratio of the amorphous volume over the crystalline volume [1, 2]. For solar cell applications the  $\mu\text{c-Si:H}$  absorber is typically larger than 1  $\mu\text{m}$  representing an increase in production time and thus fabrication cost [3].

Recently a-Si:H-like materials, intermediate between a-Si:H and  $\mu\text{c-Si:H}$ , have been deposited [4, 5]. The films consist of silicon crystallites and/or clusters (less than 3 nm) which is difficult to be observed from the morphology of the films. Further, a-Si:H-like films have the same optical absorption coefficient as a-Si:H but the improved transport properties of  $\mu\text{c-Si:H}$ . In particular, the quantum efficiency-mobility-lifetime ( $\eta\mu\tau$ ) product of electrons can be a factor of

TABLE 1: Deposition conditions of the intrinsic and doped a-Si:H-like layers.

Deposition condition	p-type a-SiC:H	Buffer layer	Intrinsic layer	n-type layer
Power (W)	10	10	10	10
Pressure (Pa)	90	90	90	60
E/S (mm)	20	20	30	25
Temperature (°C)	200	200	200	200
SiH <sub>4</sub> flow rate (sccm)	20	20	40	40
H <sub>2</sub> flow rate (sccm)	40	40	160	80
CH <sub>4</sub> flow rate (sccm)	18	18	—	—
B <sub>2</sub> H <sub>6</sub> flow rate (sccm)	5	—	—	—
PH <sub>3</sub> flow rate (sccm)	—	—	—	5
Layer thickness (nm)	10	6	200–400	30

100 higher than that of typical a-Si:H in the as-deposited state, while  $\eta\mu\tau$  product values after light soaking are comparable to typical a-Si:H before degradation [6–8]. Furthermore, the values of the deep defect density estimated from an analysis of modulated photocurrent (MPC) are about 10 times lower than those of typical a-Si:H [9]. Although the basic properties of a-Si:H-like films have been proposed, the application in solar cell research is not well investigated [6–12].

In this study, we apply the a-Si:H-like films to fabricate p-i-n single junction solar cells and vary the i-layer thickness from 200 to 400 nm. Effects of the i-layer thickness on the device performances such as open-circuit voltage ( $V_{oc}$ ), short-circuit current density ( $J_{sc}$ ), fill factor (FF), and conversion efficiency ( $\eta$ ) are investigated. We use 27.12 MHz high-frequency plasma-enhanced chemical vapor deposition (HF-PECVD) to deposit silicon thin films, and the films almost always contain small crystalline fractions even under low H<sub>2</sub>/SiH<sub>4</sub> gas ratios. This kind of a-Si:H-like films could also be obtained by 13.56 MHz radio frequency PECVD but usually requiring a high H<sub>2</sub>/SiH<sub>4</sub> ratio which might dramatically decrease the deposition rate. Moreover, technology computer-aided design simulation software (TCAD) is used to gain better insight into charge carrier generation and recombination of the devices.

## 2. Experimental

The a-Si:H-like single junction thin film solar cells were fabricated with structure of Asahi SnO<sub>2</sub>:F-coated glass/p/buffer/i/n/ZnO:Al/Ag. All of the Si layers were prepared by HF-PECVD at a frequency of 27.12 MHz. Diborane (B<sub>2</sub>H<sub>6</sub>) and phosphine (PH<sub>3</sub>) gases were used as the doping gas to fabricate the a-Si:H-like p- and n-layers. To reduce the band offset between the energy bands of a wide band-gap p-type SiC (1.9 eV) and intrinsic layers, a buffer layer was used at the p/i interface [13, 14]. The detailed deposition conditions are summarized in Table I. Five single junction solar cells were fabricated, and the i-layer thickness was varied from 200 to 400 nm. The electrical, optical, and structural properties of the i-layer a-Si:H-like films are listed

TABLE 2: The properties of a-Si:H-like films compared to those of typical a-Si:H films.

	a-Si:H	a-Si:H-like
Crystallinity (%)	—	12
Dark conductivity ( $\Omega^{-1} \text{cm}^{-1}$ )	$1 \times 10^{-10}$	$2.3 \times 10^{-10}$
Photo conductivity ( $\Omega^{-1} \text{cm}^{-1}$ )	$1 \times 10^{-5}$	$6.1 \times 10^{-4}$
Defect density ( $\text{cm}^{-3}$ )	$\sim 10^{16}$	$10^{15}$
Hydrogen content (at.%)	15	10
Absorptivity at 400 nm ( $\text{cm}^{-1}$ )	$5 \times 10^5$	$1.3 \times 10^6$
Absorptivity at 600 nm ( $\text{cm}^{-1}$ )	$3.5 \times 10^4$	$7.5 \times 10^4$
Activation energy (eV)	0.8	0.76
Band gap (eV)	1.8	1.67

in Table 2 in comparison with a-Si:H. In Table 2, the values of the left column (a-Si:H) were obtained from [15]. The values of the right column (a-Si:H-like) were measured from our experimental films. The crystallinity was evaluated by micro-Raman spectroscopy. The dark conductivity was measured at room temperature using a source-measure unit (KEITHLEY 2400). The photoconductivity measurement was carried out under AM1.5G (100 mW/cm<sup>2</sup>) of a solar simulator. The defect density was obtained by electron spin resonance (ESR). The bonded hydrogen content was determined by Fourier transform infrared (FTIR) spectroscopy. The absorptivity was obtained by means of UV-VIS spectrophotometer. The activation energy was calculated from temperature-dependent dark conductivity measurements. The band gap was estimated by a linear fit to a Tauc plot. The area of individual solar cells was defined by the  $1 \times 1 \text{cm}^2$  sputtered ZnO:Al/Ag back contact. The film thickness was determined using an alpha-step profilometer. The solar cells were characterized by current density-voltage ( $J$ - $V$ ) measurement under 1-sun (AM1.5G, 100 mW/cm<sup>2</sup>) solar simulator irradiation and spectral response measurement from which external quantum efficiency (EQE) was obtained. The 1-sun standard light soaking test was performed in a climate chamber at 50°C for 500 h (IEC 61646).

To simulate thin film solar cells the commercially available software Silvaco TCAD, from Silvaco Inc., was used. The simulation program solved the Poisson equation coupled with the continuity equations of electrons and holes for the virtual device by dividing the whole structure into finite elements. The physical models that we used were Shockley-Read-Hall recombination model, concentration-dependent lifetimes, and low field mobility model. The photogeneration model, including a ray tracing algorithm, was used to calculate the absorption and transmission of light in the semiconductor layers. The solar cells considered here operate under the global standard solar spectrum (AM1.5G) illumination with 100 mW/cm<sup>2</sup> total incident power density. Table 3 lists the minimum set of input optical, electrical, and structural parameters used in this simulation without buffer layers between each layer. The theoretical values of the band mobility for a-Si:H-based thin films were around 1–10 cm<sup>2</sup>s<sup>-1</sup>V<sup>-1</sup>. The hole mobility was assumed to be smaller than the electron mobility. The i-layer thickness varied

TABLE 3: The minimum set of input parameters used in our simulation work.

Device parameter	Value		
Device area ( $\mu\text{m}^2$ )	1		
Average haze (%)	18		
Exterior rear reflectance (%)	95		
Light source	One sun (AM 1.5, 100 $\text{mW}/\text{cm}^2$ )		
Layer parameters	p-layer	i-layer	n-layer
Thickness (nm)	10	200–400	10
Doping concentration ( $\text{cm}^{-3}$ )	$1 \times 10^{18}$	$1 \times 10^{10}$	$1 \times 10^{19}$
Mobility gap (eV)	1.92	1.67	1.7
Electron mobility ( $\text{cm}^2/\text{Vs}$ )	8	4	8
Hole mobility ( $\text{cm}^2/\text{Vs}$ )	2	0.7	2
Effective DOS in CB ( $\text{cm}^{-3}$ )	$2.0 \times 10^{20}$	$2.0 \times 10^{20}$	$2.0 \times 10^{20}$
Effective DOS in VB ( $\text{cm}^{-3}$ )	$2.0 \times 10^{20}$	$2.0 \times 10^{20}$	$2.0 \times 10^{20}$
Dielectric constant	11.9	11.9	11.9
Electron affinity (eV)	3.9	4	4
Tail state ( $\text{cm}^{-3}$ )	$10^{20}$	$10^{20}$	$10^{20}$
Gaussian-state ( $\text{cm}^{-3}$ )	$5 \times 10^{16}$	$5 \times 10^{16}$	$5 \times 10^{16}$

between 200 and 400 nm, while both p- and n-layers were fixed to 10 nm, 30 nm, respectively. The average haze was set to be 18% for the device constructed with rough textured surfaces between layers. The distribution of states in the energy gap of a-Si:H assumed in the simulation is the general standard model of density of states (DOS), having two exponential band tails and two Gaussian distribution of states in the mobility gap [15, 16].

### 3. Results and Discussion

For each i-layer thickness, twenty solar cells were fabricated and they had very similar performances (error less than 5%). Figure 1 is a representative result of  $I$ - $V$  curves of solar cells with different a-Si:H-like i-layer thickness. It can be seen that the cell with a 300 nm i-layer has the highest  $J_{sc}$  value of 17  $\text{mA}/\text{cm}^2$ , while the other cells show  $J_{sc}$  values around 15.5–16  $\text{mA}/\text{cm}^2$ . Only little variation in  $V_{oc}$  is seen, and this may agree to that  $V_{oc}$  would rather be affected by the qualities of thin film and p/i interface [17, 18]. From this result, the best combination of  $V_{oc}$  and  $J_{sc}$  can be found for an i-layer thickness of 300 nm.

Figure 2 shows the EQE of the cells with different a-Si:H-like i-layer thickness. The result is helpful to evaluate the carrier collection efficiency at a particular wavelength. It is found that the curves remain the same in the short-wavelength region (<500 nm) for each i-layer thickness due to the good performances of the p-doped layer [19]. But the curves vary in the long-wavelength region (>500 nm) with their peaks red-shifting. At the wavelength of 600 nm, the EQE values for the thickness of 200–400 nm are 61%, 65%, 69%, 68%, and 63%, respectively. It is interesting to clarify that the EQE differences in the long-wavelength region might result from the thickness variation rather than the crystalline fractions in the a-Si:H-like films. This can also be evidenced

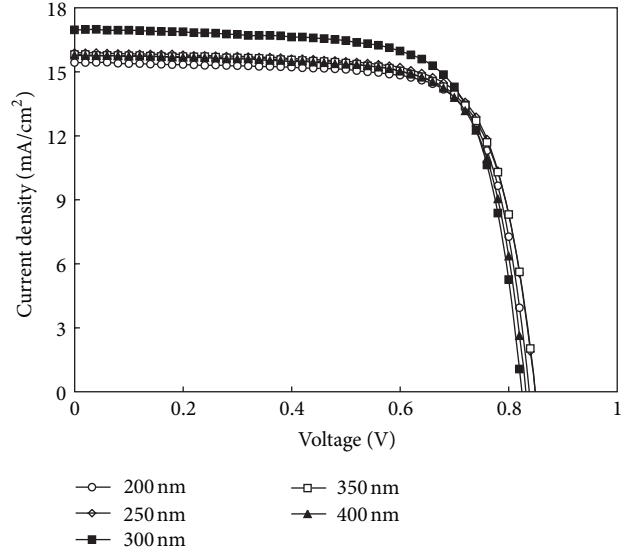
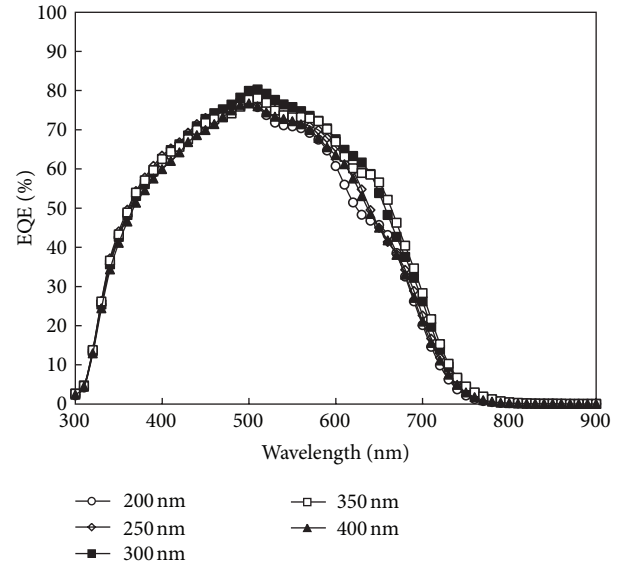
FIGURE 1: Experimental  $I$ - $V$  characteristics of a-Si:H-like solar cells with different i-layer thickness.

FIGURE 2: Experimental quantum efficiencies of a-Si:H-like solar cells with different i-layer thickness.

by the observation that the cutoff wavelength of each cell is about 800 nm, same as that of a-Si:H.

Figure 3 shows a comparison of the i-layer thickness dependences between experimental (closed symbol) and simulation (open symbol) data. The simulation results show that FF monotonously decreases with the i-layer thickness due to the longer carrier transport length and thus increased series resistance. The  $V_{oc}$  is calculated from [20]

$$V_{oc} = \frac{kt}{q} \ln \left( \frac{J_{sc}}{J_{00}} \right) + \frac{qw_d^2}{2\epsilon} \left( \frac{N_i N_p}{N_i + N_p} \right), \quad (1)$$

where  $J_{00}$  is the temperature-independent saturation current,  $w_d$  is the depletion width which usually equals to the i-layer

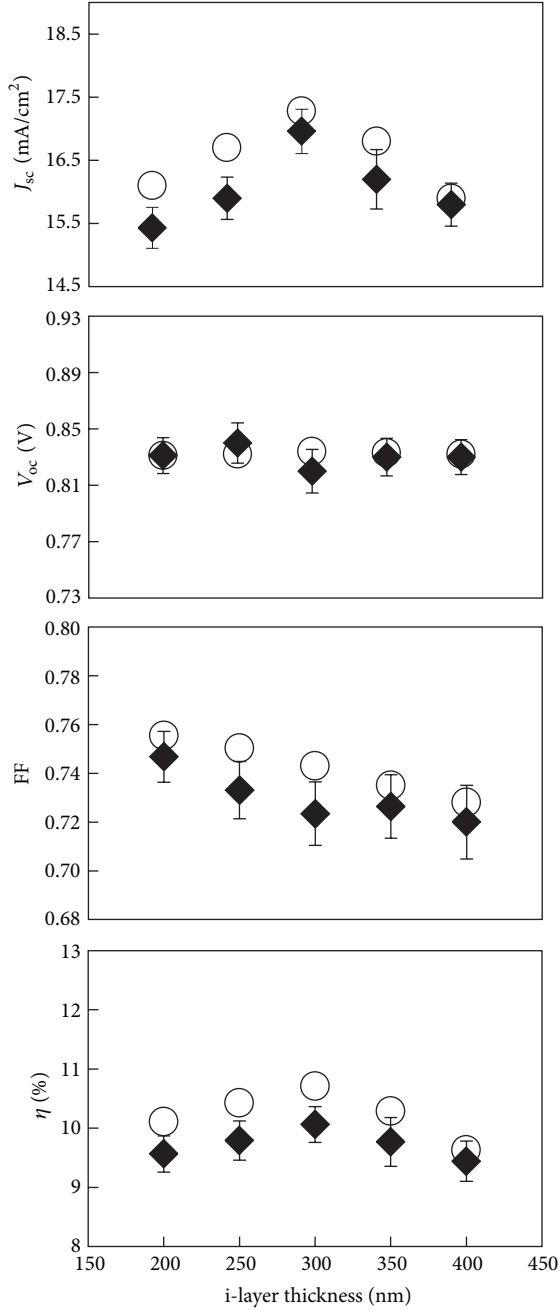


FIGURE 3: Simulated (open symbol) and experimental (closed symbol) results of external parameters of a-Si:H-like solar cells with different i-layer thickness.

thickness for a p-i-n device, and  $N_i$  and  $N_p$  are the majority carrier concentration in the i-layer and in the p-layer, respectively. The last part of the equation is the built-in voltage across the i-layer. Therefore,  $V_{oc}$  would vary depending on the values of  $w_d$  and  $J_{sc}$ . For the i-layer thickness of 300–400 nm, the loss in  $V_{oc}$  caused by the decreased  $J_{sc}$  is compensated by the increased  $w_d$ . Finally, the trend of  $\eta$  is similar to that of  $J_{sc}$  implying that the cell efficiency is mainly dominated by  $J_{sc}$ . Overall, the trends of the simulation results match well with that of experimental ones.

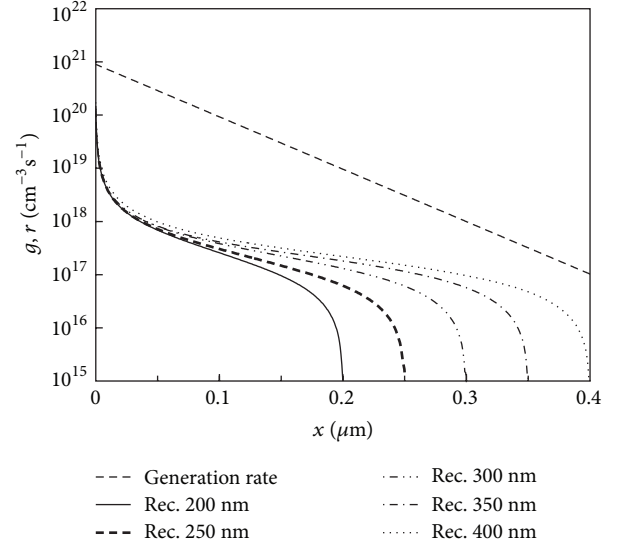


FIGURE 4: Simulated carrier generation rate and recombination rate as a function of the i-layer thickness.

Figure 4 shows the generation rate,  $g(x)$ , and the recombination rate,  $r(x)$ , of hole-electron pairs to further explain the  $J_{sc}$  behavior. In the textured i-layer,  $g(x)$  with respect to a certain point,  $x$ , is based on [21]

$$g(x) = \int [1 - R^2(\lambda)] S(\lambda) \alpha(\lambda) e^{-\alpha x} d\lambda, \quad (2)$$

where  $R(\lambda)$  is the reflectance,  $S(\lambda)$  the incident photon flux (photon  $\text{cm}^{-2}\text{s}^{-1}$ ) of the AM1.5G solar spectrum, and  $\alpha(\lambda)$  the absorption coefficient. We assume  $R$  is squared due to the textured surface that reduces the reflection. The  $y$ -axis scale is logarithmic showing that there is an enormously greater generation of electron-hole pairs near the front side of the i-layer, while further into the solar cell the generation rate exponentially decreases and finally becomes nearly constant. On the other hand, the recombination of charge carriers is assumed to be determined by Shockley-Read-Hall recombination with a recombination rate given by [22, 23]

$$r(x) = \frac{n(x)p(x) - n_i^2}{\tau_p [n(x) + n_i] + \tau_n [p(x) + n_i]}, \quad (3)$$

where  $n = n_0 + \Delta n$ ,  $p = p_0 + \Delta p$ ,  $n_0$ ,  $p_0$  are the equilibrium carrier densities,  $\Delta n$ ,  $\Delta p$  are the excess carrier densities,  $\tau_n$ ,  $\tau_p$  are the carrier lifetimes at the dangling bond state  $D^0$ , and  $n_i$  is the intrinsic carrier density. Since most of photons are absorbed in the front part of the i-layer, the regions close to p/i interface have a high recombination rate. The total generation,  $G$ , and the total recombination,  $R$ , in the i-layer can be given by

$$G = \int_0^d g(x) dx, \quad (4)$$

$$R = \int_0^d r(x) dx.$$

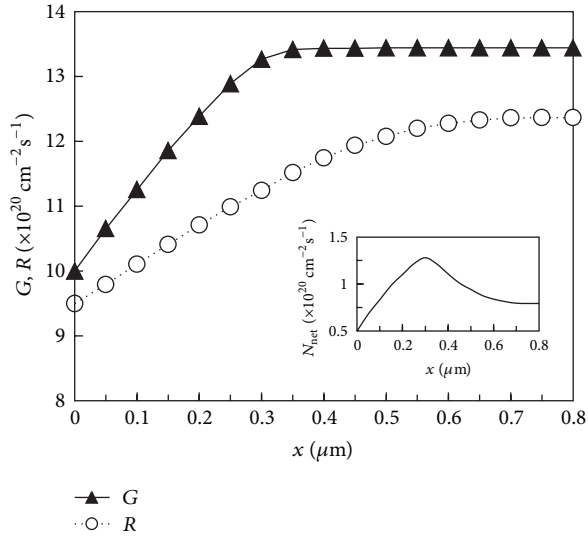


FIGURE 5: The total generation and recombination of solar cells with different i-layer thickness. The inset of Figure 6 shows the calculation result of the net charge carrier density for each i-layer thickness.

Note that the integral should be extended only from  $x = 0$  to the value of corresponding thickness,  $d$ . The calculation results are plotted in Figure 5. The total generation increases rapidly with the i-layer thickness, and a saturation occurs since the contribution at the deeper region of the i-layer can be neglected. Therefore, it is easy to obtain the net free carrier concentration,  $N_{\text{net}}$ , as given by

$$N_{\text{net}} = G - R. \quad (5)$$

The calculation result of  $N_{\text{net}}$  is illustrated as an inset in Figure 5. The trend is consistent with that of  $J_{\text{sc}}$  observed from the experimental  $I$ - $V$  measurement. However,  $N_{\text{net}}$  would finally be a constant indicating that  $J_{\text{sc}}$  would still saturate after a temporary decrease. It is interesting that if the texture is not considered, the saturation of the generation will shift to the thick region. As a consequence,  $N_{\text{net}}$  simply increases and then saturates without having a decrease.

Figure 6 shows the conversion efficiencies of the cells after 500 h exposure to  $100 \text{ mW/cm}^2$  AM1.5G light for different i-layer thickness. It can be seen that degradation increases from 8.39% to 16.96% as i-layer thickness increases. The i-layer thickness of 300 nm shows the best stabilized efficiency of 9% and a degradation of 11% smaller than the typical value (>15%) observed from a-Si:H solar cells. The 200 nm and 250 nm thick i-layers show lower initial efficiencies of 9.65% and 9.88%, respectively, but their stabilized efficiencies are close to that of the 300 nm thick i-layer. Degradation in the cells with the 350 and 400 nm thick i-layer are about 13.2% and 16.9%, respectively. Apparently, the thicker cells have a higher degradation, and this might be attributed to two reasons. First, a thick absorber leads to a weak electric field, which in turn decreases the carrier collection efficiency. Second, the total amount of the light-induced defects caused by the hydrogen out-diffusion from Si-H bonds is larger

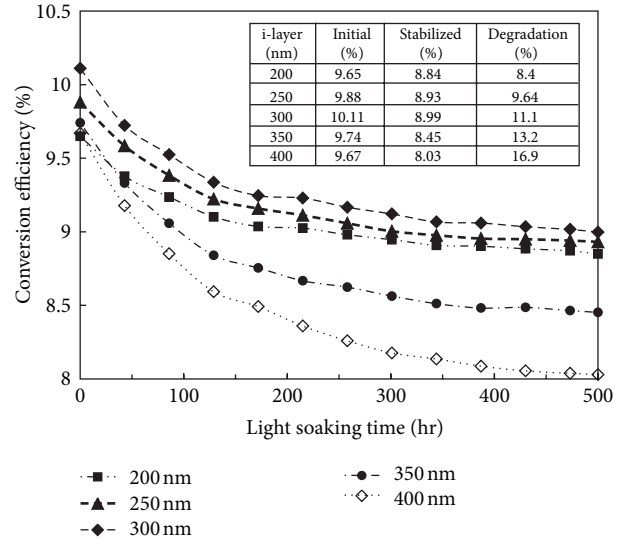


FIGURE 6: Light soaking effect for solar cells with different i-layer thickness.

for thicker absorbers. These defects will further flatten the electric field and thus increase the degradation.

## 4. Conclusions

In conclusion, the a-Si:H-like films deposited by 27.12 MHz PECVD have been applied to p-i-n single junction solar cells to investigate the influences on photovoltaic performances. The TCAD simulation result is in good agreement with the experimental data, showing great reliability. The carrier generation and recombination profiles are shown to explain the  $J_{\text{sc}}$  behavior. The generation dominates the device current density when the thin absorber is used, while for the thicker absorber the recombination begins to offset the current gain and results in a temporary reduction in  $J_{\text{sc}}$ . The i-layer thickness of 300 nm can have the optimum balance between the generation and the recombination. The solar cell with the 300 nm i-layer also has a comparable initial efficiency and a low degradation compared to that of a-Si:H cells. As a result, the thin absorber and good stability make the a-Si:H-like material suitable for solar applications.

## Acknowledgments

This work is sponsored by the BeyondPV Company and the National Science Council of the Republic of China under Contract nos. 100-2622-E-451-001-CC2, 100-2628-E-451-002-MY2, and 101-3113-E-451-001-CC2.

## References

- [1] F. Finger, R. Carius, T. Dylla, S. Klein, S. Okur, and M. Günes, "Stability of microcrystalline silicon for thin film solar cell applications," *IEE Proceedings*, vol. 150, no. 4, pp. 300–308, 2003.
- [2] Y. Wang, X. Geng, H. Stiebig, and F. Finger, "Stability of microcrystalline silicon solar cells with HWCVD buffer layer," *Thin Solid Films*, vol. 516, no. 5, pp. 733–735, 2008.

- [3] O. Vetterl, A. Lambertz, A. Dasgupta et al., "Thickness dependence of microcrystalline silicon solar cell properties," *Solar Energy Materials and Solar Cells*, vol. 66, no. 1–4, pp. 345–351, 2001.
- [4] P. Roca i Cabarrocas, S. Hamma, S. N. Sharma, J. Costa, and E. Bertran, "Nanoparticle formation in low-pressure silane plasmas: bridging the gap between a-Si:H and  $\mu\text{c-Si}$  films," *Journal of Non-Crystalline Solids*, vol. 227–230, no. 2, pp. 871–875, 1998.
- [5] A. Fontcuberta I Morral, R. Brenot, E. A. G. Hamers, R. Vanderhaghen, and P. Roca i Cabarrocas, "In situ investigation of polymorphous silicon deposition," *Journal of Non-Crystalline Solids*, vol. 266–269, pp. 48–53, 2000.
- [6] P. Roca i Cabarrocas, A. Fontcuberta i Morral, S. Lebib, and Y. Poissant, "Plasma production of nanocrystalline silicon particles and polymorphous silicon thin films for large-area electronic devices," *Pure and Applied Chemistry*, vol. 74, no. 3, pp. 359–367, 2002.
- [7] P. St'ahel, S. Hamma, P. Sladek, and P. Roca i Cabarrocas, "Metastability studies in silicon thin films: from short range ordered to medium and long range ordered materials," *Journal of Non-Crystalline Solids*, vol. 227, part 1, pp. 276–280, 1998.
- [8] P. Roca i Cabarrocas, "Plasma deposition of silicon clusters: a way to produce silicon thin films with medium-range order?" *Materials Research Society Symposium*, vol. 507, p. 855, 1998.
- [9] C. Longeaud, J. P. Kleider, P. Roca i Cabarrocas, S. Hamma, R. Meaudre, and M. Meaudre, "Properties of a new a-Si:H-like material: hydrogenated polymorphous silicon," *Journal of Non-Crystalline Solids*, vol. 227–230, no. 1, pp. 96–99, 1998.
- [10] A. Fontcuberta i Morral, R. Brenot, E. A. G. Hamers, R. Vanderhaghen, and P. Roca i Cabarrocas, "In situ investigation of polymorphous silicon deposition," *Journal of Non-Crystalline Solids*, vol. 266–269, pp. 48–53, 2000.
- [11] K. H. Kim, E. V. Johnson, and P. Roca i Cabarrocas, "Irreversible light-induced degradation and stabilization of hydrogenated polymorphous silicon solar cells," *Solar Energy Materials and Solar Cells*, vol. 105, pp. 208–212, 2012.
- [12] Y. Poissant, P. Chatterjee, and P. Roca i Cabarrocas, "No benefit from microcrystalline silicon N layers in single junction amorphous silicon p-i-n solar cells," *Journal of Applied Physics*, vol. 93, no. 1, pp. 170–174, 2003.
- [13] B. Rech, C. Beneking, and H. Wagner, "Improvement in stabilized efficiency of a-Si:H solar cells through optimized p/i-interface layers," *Solar Energy Materials and Solar Cells*, vol. 41, pp. 475–483, 1996.
- [14] S. N. Agbo, J. Krč, R. A. C. M. M. Van Swaaij, and M. Zeman, "Optimization of the pi interface properties in thin film microcrystalline silicon solar cell," *Solar Energy Materials and Solar Cells*, vol. 94, no. 11, pp. 1864–1868, 2010.
- [15] R. E. I. Schropp and M. Zeman, *Amorphous and Microcrystalline Silicon Solar Cells: Modeling, Materials and Device Technology*, Kluwer Academic Publishers, Dordrecht, The Netherlands, 1998.
- [16] R. A. Street, *Hydrogenated Amorphous Silicon*, Cambridge University, Cambridge, UK, 1991.
- [17] L. Jiang, J. H. Lyou, S. Rana, E. A. Schiff, Q. Wang, and Q. Yua, "Open-circuit voltage physics in amorphous silicon solar cells," *Materials Research Society Symposium Proceedings*, vol. 609, article A18.3, 2000.
- [18] A. Klaver and R. A. C. M. M. van Swaaij, "Modeling of light-induced degradation of amorphous silicon solar cells," *Solar Energy Materials and Solar Cells*, vol. 92, no. 1, pp. 50–60, 2008.
- [19] J. Meier, R. Fluckiger, H. Keppner, and A. Shah, "Complete microcrystalline p-i-n solar cell—Crystalline or amorphous cell behavior?" *Applied Physics Letters*, vol. 65, no. 7, pp. 860–862, 1994.
- [20] A. E. Delahoy, J. Britt, and Z. Kiss, "Annual subcontract report," NREL Report NREL/TP-413-5334, 1993.
- [21] A. Hamel and A. Chibani, "Characterization of texture surface for solar cells," *Journal of Applied Sciences*, vol. 10, no. 3, pp. 231–234, 2010.
- [22] W. Shockley and W. T. Read, "Statistics of the recombinations of holes and electrons," *Physical Review*, vol. 87, no. 5, pp. 835–842, 1952.
- [23] R. N. Hall, "Electron-hole recombination in germanium," *Physical Review Letters*, vol. 87, no. 2, p. 387, 1952.

## Research Article

# Structural and Optoelectronic Properties of CdSe Tetrapod Nanocrystals for Bulk Heterojunction Solar Cell Applications

Nguyen Tam Nguyen Truong, Thao Phuong Ngoc Nguyen, and Chinho Park

*School of Chemical Engineering, Yeungnam University, 280 Daehak-Ro, Gyeongsan, Gyeongbuk 712-749, Republic of Korea*

Correspondence should be addressed to Chinho Park; [chpark@ynu.ac.kr](mailto:chpark@ynu.ac.kr)

Received 23 December 2012; Revised 1 May 2013; Accepted 16 May 2013

Academic Editor: Peter Rupnowski

Copyright © 2013 Nguyen Tam Nguyen Truong et al. This is an open access article distributed under the Creative Commons Attribution License, which permits unrestricted use, distribution, and reproduction in any medium, provided the original work is properly cited.

Semiconducting CdSe tetrapod nanoparticles were prepared, and their structural and optical properties were examined. The surface capping molecule, octylphosphonic acid, was replaced with butylamine after the particle synthesis. The exchange of surface ligands changed the physical properties of the nanocrystals, which resulted in a slight decrease in the nanoparticles size. The effects of changing surface ligands of CdSe tetrapod nanocrystals on the structural and optoelectronic properties were investigated, and it was found that the surfactant of nanoparticles could affect the device performance by enhancing the charge carrier separation at the active layer interfaces. Power conversion efficiency of the bulk heterojunction solar cells having the structure of glass/ITO/PEDOT:PSS/(CdSe + PCPDTBT)/Al was improved from 1.21% to 1.52% with the use of ligand-exchanged nanoparticles.

## 1. Introduction

Bulk heterojunction solar cells (BHJ) based on blends of semiconducting nanocrystals (NCs) and conducting polymers have attracted considerable attention owing to their low cost, simple processing, and ability to dissolve each component to obtain composite layers optimized for solar energy conversion [1, 2]. Currently, polymer-fullerene solar cells and polymer solar cells have reached power conversion efficiencies (PCEs) of approximately 7.4% [3] and 8.62% [4], respectively. Solar cells with the fullerenes replaced with semiconducting inorganic nanoparticles (NPs) as the electron acceptors are called hybrid BHJ solar cells [5]. Although the PCEs of hybrid BHJ solar cells are lower than those of fullerene-based BHJ cells, they have the potential to show better performance, because NPs have a high absorption coefficient, high intrinsic charge mobility, and can be synthesized into various shapes (sphere, rod, elongated sphere, tetrapod, etc.) with size of 3 to 100 nm, desirable exciton dissociation characteristics, percolation pathway development, and charge transport properties [6–11]. CdSe NPs are one of the most selected materials owing to their well-established synthesis method [12, 13]. CdSe NPs also act as good electron

acceptors in combination with the commonly used semiconducting polymers [14]. The effects of the various processing conditions, shapes of the nanocrystals, and surfactants used during synthesis as well as the semiconducting polymers selected were investigated intensively [15].

The first hybrid BHJ solar cells using mixtures of semiconducting polymer and inorganic nanocrystals were reported in 1996 by Greenham et al. [1], who found that the addition of CdSe nanoparticles to polymers in devices relied on the ability of the nanoparticles to disperse within the polymer to make larger interfacial surface area for carrier transfer between the two materials and to improve continuous pathways to the contacts. Hybrid BHJ solar cells based on blends of CdSe tetrapods and polymers have been reported to show the efficiency of 3.13% (Dayal et al.) [14], and their devices contained a low-band gap polymer, poly[2,6-(4,4-bis-(2-ethylhexyl)-4H-cyclopenta[2,1-b;3,4-b']-dithiophene)-alt-4,7-(2,1,3-benzothiadiazole)] (PCPDTBT), and CdSe nanocrystals. The improved cell efficiency of this world's best CdSe hybrid BHJ solar cell was attributed to the enhanced sunlight absorption from the PCPDTBT polymer and improved charge collection by the CdSe tetrapod nanostructures. The effects of the surface ligand of CdSe

nanoparticles on the device performance have also been reported [16], which have been investigated to engineer the nanoparticle/polymer blend's morphology and phase separation behavior. Surface ligands on the nanoparticles can act as traps for charge carrier transport or can dominate the nanoparticles' electrical properties by occupying surface electronic states or acting as insulators that reduce charge transport [17]. The properties of surfactant could affect the cosolubility of CdSe/polymer blends in solvents and also affect the optoelectronic properties of the active layer.

This work discusses mainly the structural and optoelectronic properties of synthesized CdSe tetrapod nanocrystals. Furthermore, the effects of surface ligand modification on the physical properties of CdSe NPs and surface morphology of the CdSe/polymer active layer were investigated, and the improvement of the bulk heterojunction solar cell performance has been demonstrated as a result of the nanoparticles' surface ligand exchange.

## 2. Experimental

CdSe tetrapods were synthesized using the method reported elsewhere [14]. In detail, 0.7 g of cadmium oxide (CdO), 5.2 g of trioctylphosphonic acid (TOP), and 2.14 g of octylphosphonic acid (OPA) were heated to 300°C in a two-necked flask under a nitrogen ( $N_2$ ) flow. When the color of the cadmium solution turned colorless, the heat was removed and the solution was kept under a nitrogen flow. The selenium precursor was prepared by mixing 0.84 g of selenium (Se) with 2.54 g of tributylphosphine (TBP) in 0.6 mL of toluene and cooled in a refrigerator for 20 min prior to the injection. After 48 hrs, the cadmium precursor was reheated to 300°C, and the selenium precursor was injected rapidly at 300°C. The tetrapods were grown at 250°C for 50 min. The synthesized CdSe tetrapods were washed 5 times with a mixture of toluene and ethanol to remove the excess capping ligands and centrifuged 5 times. After the synthesis, the OPA ligands of as-synthesized OPA-capped CdSe tetrapods were replaced with butylamine (BA) ligands using a liquid-liquid exchange procedure.

The ultraviolet-visible spectroscopy (UV-vis), photoluminescence (PL), X-ray diffraction (XRD), and transmission electron microscopy (TEM) were used to characterize the structural and optical properties of the CdSe nanotetrapod particles. FT-IR spectra ( $450\text{--}4000\text{ cm}^{-1}$ ) were recorded on an Excalibur Series FTS 3000 spectrometer (Bio-Rad) at a resolution of 16 with 32 scans using KBr pellets. The UV-vis (Cary 5000) spectra of ligand-capped CdSe tetrapod nanoparticles were obtained using 1.0 cm path length quartz cells. The samples were prepared by dispersing the nanoparticles in ethanol before the measurements. The photoluminescence (PL) was measured using a custom-made PL system at room temperature using 488 nm (argon laser) as the excitation source. The nanocrystal structure was measured using powder X-ray diffraction (XRD) on an MPD PANalytical, using  $CuK\alpha$  radiation. The size and shape of the nanocrystals were estimated with a high-resolution transmission electron microscope (HR-TEM, H-7600).

Active layer for BHJ solar cells was formed from the blends of tetrapod NCs and semiconducting polymers.

ITO-coated glass substrates were cleaned sequentially with trichloroethylene (TCE), acetone, and methanol for 10 min in an ultrasonic bath. They were then treated in a nitrogen plasma chamber at 50 W for 10 min to improve the surface properties. A thin ( $\sim 70\text{ nm}$ ) layer of poly(ethylenedioxythiophene) doped with poly(styrene sulfonic acid) (PEDOT:PSS, Sigma Aldrich) was spin-coated on the cleaned ITO-glass substrates at 4000 rpm for 30 s and dried at 100°C for 30 min. The CdSe nanoparticles (with different surface ligands) and PCPDTBT blends were first prepared in chlorobenzene. Approximately  $150 \pm 5\text{ nm}$  thick photoactive CdSe/PCPDTBT layers were deposited by dropping the blends and spin coating them onto the substrates at 4000 rpm for 30 s. The films of (ITO/PEDOT:PSS/(CdSe+PCPDTBT)) were treated thermally for 10 min on a hot plate in a nitrogen glove box at 150°C. The structural properties and surface morphology of the active layers were investigated systematically using a range of techniques including atomic force microscopy (AFM) and scanning electron microscopy (SEM). The bulk heterojunction solar cells having glass/ITO/PEDOT:PSS/(CdSe+PCPDTBT)/Al structure were fabricated. A 100 nm thick Al electrode was added to the top of the photoactive layers by thermal evaporation to complete the device structure. The current density-voltage ( $J\text{-}V$ ) characteristics were investigated under AM1.5G illumination by a solar simulator (Keithley 69911).

## 3. Results and Discussion

Figures 1(a) and 1(b) show TEM and HR-TEM images of the as-synthesized CdSe nanocrystals (NCs). A large fraction of branches was obtained without selective precipitation, which shows that the tetrapods had been formed. The tetrapod limbs were approximately  $\sim 26\text{ nm}$  long and  $\sim 7\text{ nm}$  thick. Figure 1(b) shows the lattice fringes of the CdSe tetrapods with fringe spacing of 0.34 nm, corresponding to the (002) planes for the wurtzite structure of CdSe [18].

OPA-capped CdSe nanoparticles (NPs) were first synthesized, and the NPs' ligands were replaced from OPA to butylamine. The various cappings of the CdSe NPs with different surface ligands were confirmed by FT-IR spectroscopy as in Figure 2. The intense symmetric C-H stretching vibrations of the  $-\text{CH}_2-$  groups at 2948 and 2848  $\text{cm}^{-1}$  and a shoulder band of asymmetric stretching of the terminal  $-\text{CH}_3$  group at 2956  $\text{cm}^{-1}$  can be associated with the alkyl chain of OPA as illustrated in Figure 2(a). The IR bands at 1456 and 1402  $\text{cm}^{-1}$  can be assigned to the  $-\text{CH}_2-$  bending vibration and the C-O-H bending vibration [19, 20]. The band at 1017  $\text{cm}^{-1}$  is indicated as the P-O-H bond, which is similar to the FT-IR analysis of OPA ligand [21]. However, the peaks at 2956 and 1017  $\text{cm}^{-1}$  of the OPA ligand were non-existent in Figure 2(b), meaning that the OPA ligand was replaced by the BA ligand after the ligand exchange process. The presence of butylamine is shown by the peak at  $\sim 3700\text{--}3781\text{ cm}^{-1}$ , which corresponds to the N-H stretching vibration modes [8, 22].

The structure of CdSe tetrapods (Tpods) was confirmed by X-ray diffraction as shown in Figure 3. Comparison of the XRD patterns of as-synthesized nanocrystals with those of

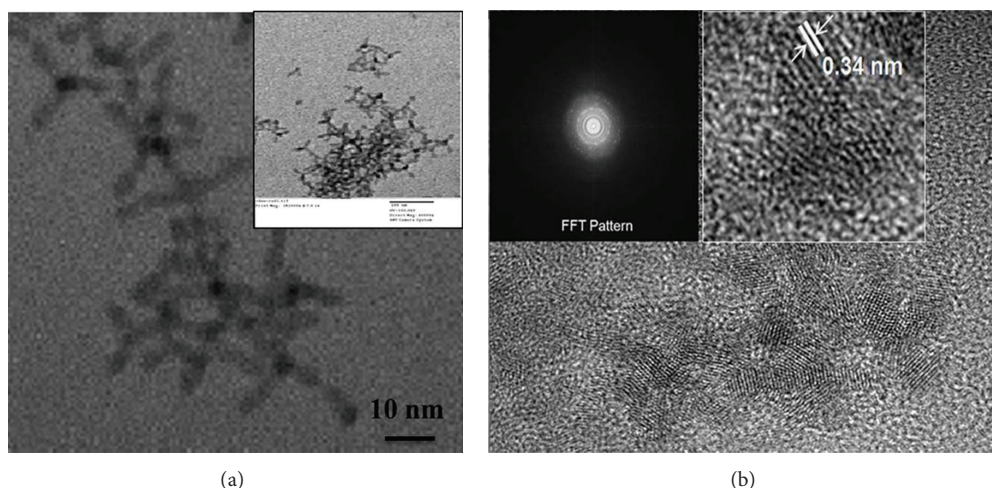


FIGURE 1: (a) Transmission electron microscopic image and (b) high-resolution transmission electron microscopic image of CdSe tetrapod nanocrystals.

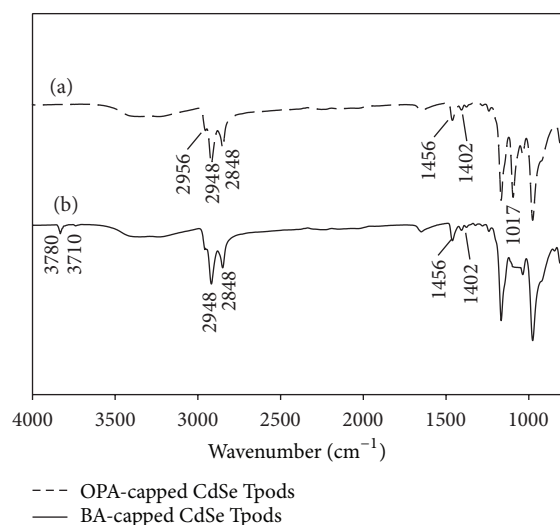


FIGURE 2: FT-IR spectra of (a) OPA-capped CdSe tetrapods (Tpods) and (b) BA-capped CdSe Tpods.

bulk CdSe crystals showed that the as-synthesized CdSe had a hexagonal wurtzite structure (ICDD-JCPDS: CdSe #00-019-0191) [23] with the arms elongated in the (002) direction. The diffraction peaks due to the reflections from (103), (100), and (101) were assigned as wurtzite phase related peaks. The (103) diffraction peak is significantly broader than the (100) and (101) peaks. This is consistent with the XRD data from the bulk tetrapod nanocrystals [24–27], which showed a more intense and narrow diffraction peak at the  $2\theta$  values of  $\sim 24$  and  $\sim 27^\circ$ , that is, consistent with the tetrapod limb in the  $c$ -axis direction of the wurtzite phase.

Figures 4(a) and 4(b) show the optical properties of the OPA-capped CdSe tetrapods determined by UV-vis and PL measurements. The CdSe nanocrystals were dispersed in ethanol prior to the spectroscopic measurements. The absorption edge of the UV-vis spectra was  $\sim 547$  nm, and

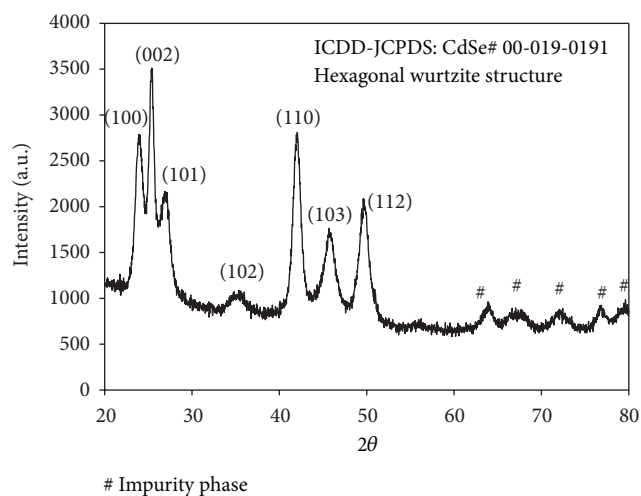


FIGURE 3: The X-ray diffraction patterns of CdSe tetrapods with the reference peak positions of bulk Wurtzite CdSe (ICDD-JCPDS: CdSe # 00-019-0191) displayed.

the emission peak of the PL spectra was  $\sim 593$  nm (band gap energy  $\sim 2.09$  eV). The effects of ligand exchange on the optical properties of the nanoparticles were investigated by UV-vis and PL, and the results are shown in Figures 5(a) and 5(b). After the ligand exchange from OPA to butylamine, the absorption edge of the UV-Vis spectra was shifted to a shorter wavelength from 547 to 542 nm, as shown in Figure 5(a), and the intensity of the emission peak of the PL spectra was decreased and shifted towards a higher energy from 2.09 to 2.14 eV, as shown in Figure 5(b). The shifting of the absorption edge and emission peak toward a shorter wavelength is often called a “blue-shift,” which may be due to the quantum confinement effect caused by the decrease in nanocrystal size [28, 29]. The luminescence intensity from the smaller nanocrystals is likely to be much stronger, because smaller-sized nanocrystals possess a larger

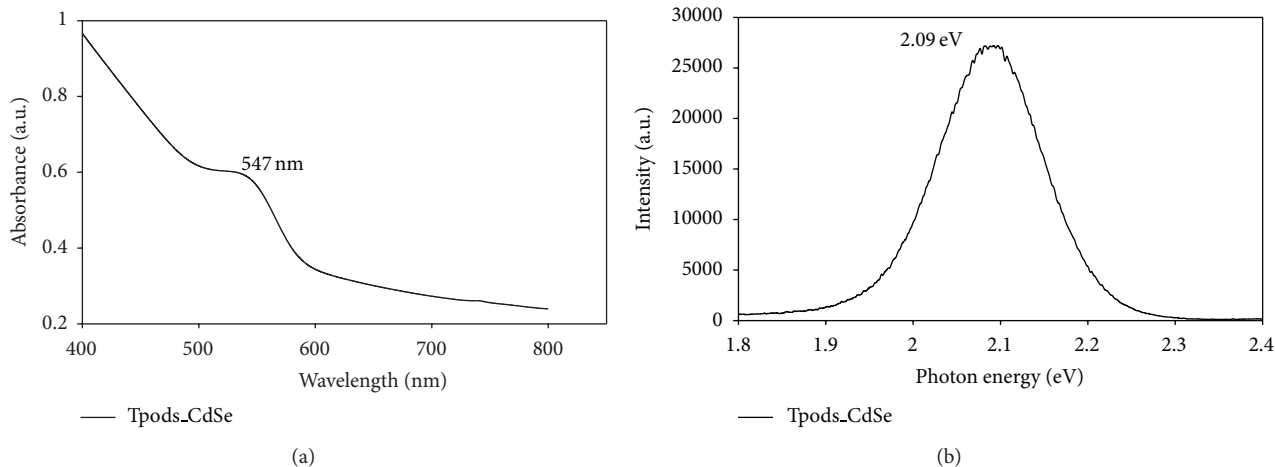


FIGURE 4: (a) Absorption and (b) photoluminescence spectra of the CdSe tetrapods capped with the OPA ligand.

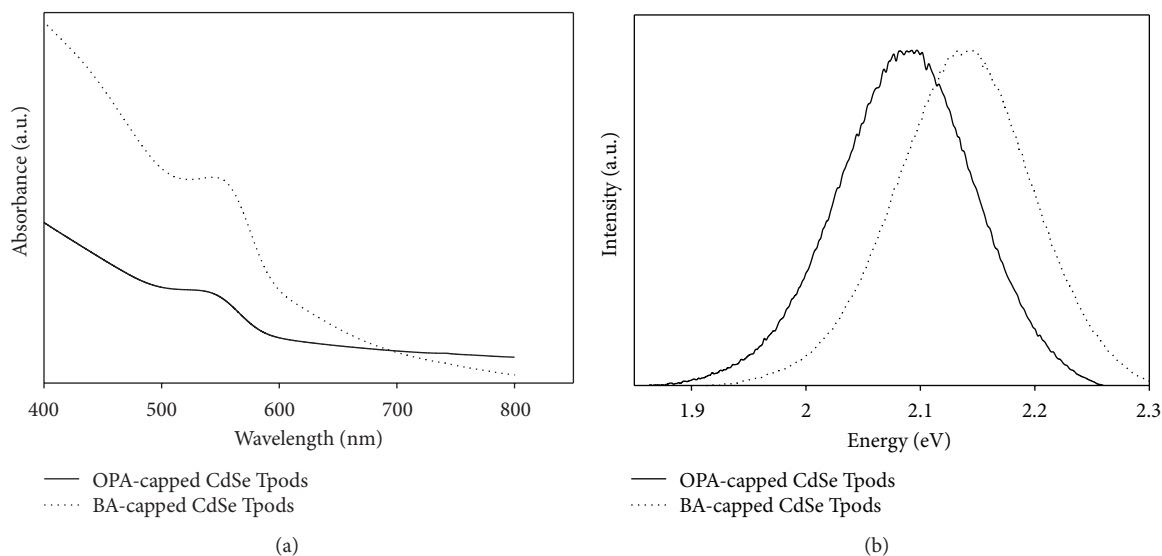


FIGURE 5: (a) Absorption and (b) photoluminescence spectra of CdSe tetrapods capped with OPA and BA ligand.

surface-to-volume ratio than larger-sized nanocrystals, and most of the photo-generated charge carriers undergo recombination at the surface vacancies. The sizes of the nanoparticles before and after the ligand exchange were measured by HR-TEM, and it was found that the size of the BA-capped CdSe tetrapods was smaller than the OPA-capped ones (data not shown here). This result is consistent with the peak shifts of UV-vis and PL spectra.

The effects of the surface ligand exchange of the CdSe tetrapods on the morphological properties of the CdSe/polymer film for bulk heterojunction solar cell applications were also investigated. The poly[2,6-(4,4-bis-(2-ethylhexyl)-4H-cyclopenta[2,1-b;3,4-b']-dithiophene)-alt-4,7-(2,1,3-benzothiazole)] (PCPDTBT) was used as a light-absorbing and electron-donating material. The semiconducting OPA- or BA-capped CdSe nanoparticles were used as electron acceptors. Figures 6(a) and 6(b) show the SEM images of the surface of a composite film of OPA- or BA-capped CdSe and

PCPDTBT with a loading of 5 mg/mL and the CdSe tetrapod concentration of 70 wt.%. The surface of the film with a BA ligand was much smoother than that with the OPA ligand. Figures 6(c) and 6(d) show the AFM images of the surface morphology of the composite films. The surface roughness of the composite films was both smooth and homogeneous, and the surface roughness of the film with BA-capped CdSe (~1.69 nm) was smoother than that of the OPA-capped CdSe (~2.52 nm). A smoother surface of the film with the BA-capped CdSe tetrapods was believed to be caused by the smaller particle size of the BA-capped CdSe tetrapods and the positive effects of butylamine in the dispersion characteristics of the nanoparticles in the solvents [30]. The rough surface was considered to be the self-organization signature of the polymer, and the solar cell devices generally showed higher efficiency on a smooth surface than on a rough surface [31].

The  $J$ - $V$  curves of BHJ solar cells fabricated by using the CdSe nanoparticles capped with various surface ligands

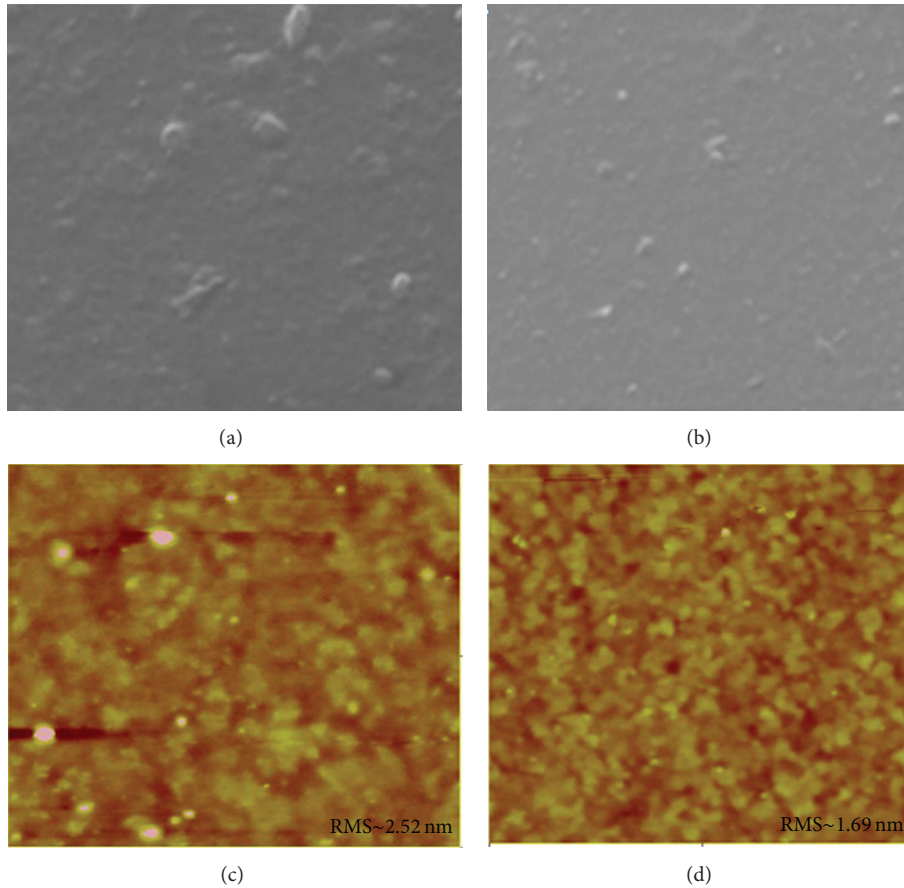


FIGURE 6: Scanning electron microscopic (SEM) image and surface roughness (RMS) of the (CdSe+PCPDTBT) (7:3) active layer annealed at 150°C with (a, c) OPA-capped and (b, d) BA-capped CdSe.

with the optimal composition of 70 wt.% CdSe in the CdSe/PCPDTBT composite layers were recorded and shown in Figure 7 along with the device parameters. Power conversion efficiency ( $\eta$ ) was improved by changing the surfactant from OPA ( $\eta \sim 1.21\%$ ) to BA ( $\eta \sim 1.52\%$ ) mainly due to the increase of current density ( $J_{sc}$ : 2.73 (OPA) to 3.41 (BA)), improvement of the surface morphology (RMS) from OPA-sample ( $\sim 2.52$  nm) to BA-sample ( $\sim 1.69$  nm), and increase of charge carrier separation at the polymer/nanoparticle interface which is observed in the quenching of photoluminescence intensity [8, 32]. Efficient separation of charge carriers prevents radiative recombination and thus quenches the photoluminescence of the nanoparticles and polymer components. The blue-shifting of the photoluminescence was also recorded when OPA was replaced by butylamine, which could be a potentially useful method of increasing charge carrier separation at polymer/nanoparticle interface in the BHJ solar cells. The BHJ solar cells made of CdSe with BA-capping ligand showed the best performance ( $J_{sc} \sim 3.41$  mA/cm<sup>2</sup>,  $V_{oc} \sim 0.72$  V, FF  $\sim 61.8\%$ , and PCE  $\sim 1.52\%$ ). The power conversion efficiency of BHJ solar cells fabricated in this study was, however, still relatively low compared with that of world record BHJ solar cells made with tetrapod-shaped

CdSe nanocrystals and PCPDTBT polymer [14]. This is possibly attributed to the poorer charge collection due to unoptimized surface morphology and thermal treatment, which might lead to poorer interfacial properties between the polymer and CdSe nanocrystals, creating a phase separation within the active layers. We thus believe that the findings of this study with the PCE values obtained open a new route to improving the BHJ solar cell performance by utilizing another kind of ligands for the CdSe nanoparticles.

#### 4. Conclusions

High-quality CdSe tetrapod nanoparticles were synthesized in this study. A large fraction of branches was obtained without selective precipitation, and the hexagonal wurtzite structure was confirmed. After the ligand exchange from OPA to the BA ligand, the size of the nanoparticles decreased, and the band gap energy increased from 2.09 up to 2.14 eV. The surface roughness of the BA-capped CdSe/PCPDTBT active layer was smoother than that of the OPA-capped CdSe one. The BHJ solar cell performance was significantly improved, showing the power conversion efficiencies of up to 1.52%

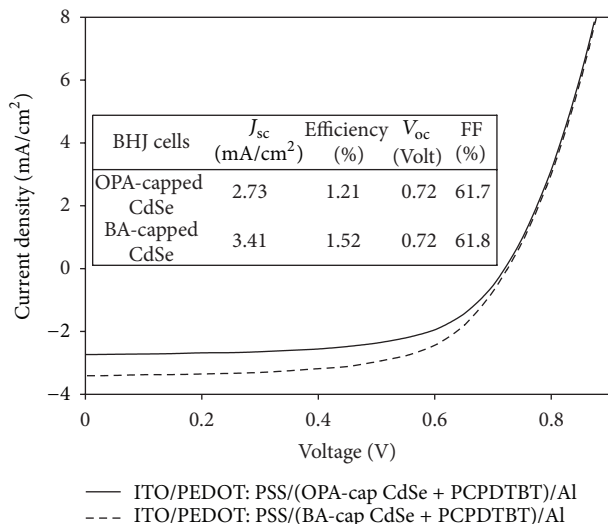


FIGURE 7:  $J$ - $V$  curves for the devices with OPA-capped and butylamine-capped CdSe tetrapod nanocrystals (CdSe/[CdSe+PCPDTBT] = 0.7).

( $J_{sc} \sim 3.41$  mA/cm<sup>2</sup>) under AM1.5G simulated solar irradiation.

## Acknowledgments

This research was supported by the Basic Science Research Program through the National Research Foundation of Korea (NRF) funded by the Ministry of Education, Science and Technology (2010-0023839) and the Human Resources Development Program of Korea Institute of Energy Technology Evaluation and Planning (KETEP) Grant (no. 20104010100580) funded by the Korean Ministry of Trade, Industry and Energy.

## References

- N. C. Greenham, X. Peng, and A. P. Alivisatos, "Charge separation and transport in conjugated-polymer/semiconductor-nanocrystal composites studied by photoluminescence quenching and photoconductivity," *Physical Review B*, vol. 54, no. 24, pp. 17628–17637, 1996.
- B. R. Saunders and M. L. Turner, "Nanoparticle-polymer photovoltaic cells," *Advances in Colloid and Interface Science*, vol. 138, no. 1, pp. 1–23, 2008.
- Y. Liang, Z. Xu, J. Xia et al., "For the bright future-bulk heterojunction polymer solar cells with power conversion efficiency of 7.4%," *Advanced Materials*, vol. 22, no. 20, pp. E135–E138, 2010.
- L. Dou, J. You, J. Yang et al., "Tandem polymer solar cells featuring a spectrally matched low-bandgap polymer," *Nature Photonics*, vol. 6, no. 3, pp. 180–185, 2012.
- W. U. Huynh, J. J. Dittmer, and A. P. Alivisatos, "Hybrid nanorod-polymer solar cells," *Science*, vol. 295, no. 5564, pp. 2425–2427, 2002.
- H. Kim, J. Y. Moon, and H. S. Lee, "Growth of ZnO nanorods on various substrates by electrodeposition," *Electronic Materials Letters*, vol. 5, no. 3, pp. 135–138, 2009.
- P. A. Chate, S. S. Patil, J. S. Patil, D. J. Sathe, and P. P. Hankare, "Nanocrystalline CdSe: structural and photoelectrochemical characterization," *Electronic Materials Letters*, vol. 8, no. 6, pp. 553–558, 2012.
- N. T. N. Truong and C. Park, "Enhancement of CdSe/poly(3-hexylthiophene) bulk hetero junction solar cell efficiency by surface ligand exchange and thermal treatment," *Japanese Journal of Applied Physics*, vol. 51, article 10NE27, 6 pages, 2012.
- H. Chen, J. Yoo, Y. Liu, and G. Zhao, "Green synthesis and characterization of se nanoparticles and nanorods," *Electronic Materials Letters*, vol. 7, no. 4, pp. 333–336, 2011.
- D. Kim, C. Hwang, D. Gwoo et al., "Synthesis and characterization of CdS nanocrystals in a novel phosphate glass," *Electronic Materials Letters*, vol. 7, no. 4, pp. 309–312, 2011.
- S. K. Mishra, R. K. Srivastava, S. G. Prakash, R. S. Yadav, and A. C. Panday, "Structural, photoconductivity and photoluminescence characterization of cadmium sulfide quantum dots prepared by a co-precipitation method," *Electronic Materials Letters*, vol. 7, no. 1, pp. 31–38, 2011.
- X. Luo, P. Liu, N. T. N. Truong, U. Farva, and C. Park, "Photoluminescence blue-shift of CdSe nanoparticles caused by exchange of surface capping layer," *Journal of Physical Chemistry C*, vol. 115, no. 43, pp. 20817–20823, 2011.
- C. S. Stan, M. S. Secula, and T. H. Oh, "Highly luminescent polystyrene embedded CdSe quantum dots obtained through a modified colloidal synthesis route," *Electronic Materials Letters*, vol. 8, pp. 275–281, 2012.
- S. Dayal, N. Kopidakis, D. C. Olson, D. S. Ginley, and G. Rumbles, "Photovoltaic devices with a low band gap polymer and CdSe nanostructures exceeding 3% efficiency," *Nano Letters*, vol. 10, no. 1, pp. 239–242, 2010.
- B. Sun, E. Marx, and N. C. Greenham, "Photovoltaic devices using blends of branched CdSe nanoparticles and conjugated polymers," *Nano Letters*, vol. 3, no. 7, pp. 961–963, 2003.
- C. Querner, P. Reiss, S. Sadki, M. Zagorska, and A. Pron, "Size and ligand effects on the electrochemical and spectroelectrochemical responses of CdSe nanocrystals," *Physical Chemistry Chemical Physics*, vol. 7, no. 17, pp. 3204–3209, 2005.
- G. Kalyuzhny and R. W. Murray, "Ligand effects on optical properties of CdSe nanocrystals," *Journal of Physical Chemistry B*, vol. 109, no. 15, pp. 7012–7021, 2005.
- H. Lee, S. W. Yoon, J. P. Ahn et al., "Synthesis of type II CdTe/CdSe heterostructure tetrapod nanocrystals for PV applications," *Solar Energy Materials and Solar Cells*, vol. 93, no. 6-7, pp. 779–782, 2009.
- J. Liu, W. Wang, H. Yu, Z. Wu, J. Peng, and Y. Cao, "Surface ligand effects in MEH-PPV/TiO<sub>2</sub> hybrid solar cells," *Solar Energy Materials and Solar Cells*, vol. 92, no. 11, pp. 1403–1409, 2008.
- G. Guerrero, P. H. Mutin, and A. Vioux, "Anchoring of phosphonate and phosphinate coupling molecules on titania particles," *Chemistry of Materials*, vol. 13, no. 11, pp. 4367–4373, 2001.
- W. Zhang, S. Ge, Y. Wang et al., "Use of functionalized WS<sub>2</sub> nanotubes to produce new polystyrene/polymethylmethacrylate nanocomposites," *Polymer*, vol. 44, no. 7, pp. 2109–2115, 2003.
- G. Ramis and G. Busca, "FTIR spectra of adsorbed n-butylamine," *Journal of Molecular Structure*, vol. 193, pp. 93–100, 1989.
- P. Chou, C. Chen, C. Cheng et al., "Spectroscopy and femtosecond dynamics of type-II CdTe/CdSe core-shell quantum dots," *ChemPhysChem*, vol. 7, no. 1, pp. 222–228, 2006.

- [24] W. W. Yu, Y. A. Wang, and X. Peng, "Formation and stability of size-, shape-, and structure-controlled CdTe nanocrystals: ligand effects on monomers and nanocrystals," *Chemistry of Materials*, vol. 15, no. 22, pp. 4300–4308, 2003.
- [25] Q. Pang, L. Zhao, Y. Cai et al., "CdSe nano-tetrapods: controllable synthesis, structure analysis, and electronic and optical properties," *Chemistry of Materials*, vol. 17, no. 21, pp. 5263–5267, 2005.
- [26] Y. Jun, S. Lee, N. Kang, and J. Cheon, "Controlled synthesis of multi-armed CdS nanorod architectures using monosurfactant system," *Journal of the American Chemical Society*, vol. 123, no. 21, pp. 5150–5151, 2001.
- [27] L. Carbone, S. Kudera, E. Carlino et al., "Multiple wurtzite twinning in CdTe nanocrystals induced by methylphosphonic acid," *Journal of the American Chemical Society*, vol. 128, no. 3, pp. 748–755, 2006.
- [28] N. Chandrasekharan and P. V. Kamat, "Tuning the properties of CdSe nanoparticles in reverse micelles," *Research on Chemical Intermediates*, vol. 28, no. 7–9, pp. 847–856, 2002.
- [29] J. H. Adair, T. Li, T. Kido et al., "Recent developments in the preparation and properties of nanometer-size spherical and platelet-shaped particles and composite particles," *Materials Science and Engineering R*, vol. 23, no. 4–5, pp. 139–242, 1998.
- [30] M. L. Monroe, Y. W. Kim, N. T. N. Truong et al., "Effect of surface modification by solvent exchange on hybrid bulk heterojunction solar cell performance," *Proceeding of Materials Research Society*, vol. 1013, 1013-Z07-10, 2007.
- [31] C. N. Hoth, P. Schilinsky, S. A. Choulis, and C. J. Brabec, "Printing highly efficient organic solar cells," *Nano Letters*, vol. 8, no. 9, pp. 2806–2813, 2008.
- [32] J. D. Olson, G. P. Gray, and S. A. Carter, "Optimizing hybrid photovoltaics through annealing and ligand choice," *Solar Energy Materials and Solar Cells*, vol. 93, no. 4, pp. 519–523, 2009.

## Research Article

# Optimization of Rear Local Contacts on High Efficiency PERC Solar Cells Structures

**Kapila Wijekoon, Fei Yan, Yi Zheng, Dapeng Wang, Hemant Mungekar, Lin Zhang, and Hari Ponnekanti**

*Applied Materials, 3535 Garrett Drive, Santa Clara, CA 95054, USA*

Correspondence should be addressed to Kapila Wijekoon; [kapila.wijekoon@amat.com](mailto:kapila.wijekoon@amat.com)

Received 1 February 2013; Revised 11 March 2013; Accepted 14 March 2013

Academic Editor: Sudhakar Shet

Copyright © 2013 Kapila Wijekoon et al. This is an open access article distributed under the Creative Commons Attribution License, which permits unrestricted use, distribution, and reproduction in any medium, provided the original work is properly cited.

A local contact formation process and integration scheme have been developed for the fabrication of rear passivated point contact solar cells. Conversion efficiency of 19.6% was achieved using  $156 \times 156$  mm, pseudo square, p-type single crystalline silicon wafers. This is a significant improvement when compared to unpassivated, full area aluminum back surface field solar cells, which exhibit only 18.9% conversion efficiency on the same wafer type. The effect of rear contact formation on cell efficiency was studied as a function of contact area and contact pitch, hence the metallization fraction. Contact shape and the thickness of Al-BSF layer were found to be heavily dependent on the laser ablation pattern and contact area. Simulated cell parameters as a function of metallization showed that there is a tradeoff between open circuit voltage and fill factor gains as the metallization fraction varies. The rear surface was passivated with an  $\text{Al}_2\text{O}_3$  layer and a  $\text{SiN}_x$  capping layer. The rear surface contact pattern was created by laser ablation and the contact geometry was optimized to obtain voids free contact filling, resulting in a uniform back surface field. The efficiency gain in rear passivated cells over the reference cells is mainly due to improved short circuit current and open circuit voltage.

## 1. Introduction

Today's industrial solar cell manufacturing process applies a full area aluminum back surface field (Al-BSF) at the rear surface of the cell. The full Al-BSF forms a good ohmic contact; however, the rear surface passivation is moderate on p-type silicon substrates [1, 2]. Another inadequacy associated with full Al-BSF is that a significant portion of infrared light reaching the rear aluminum contact is escaping the cell without being reflected back into the bulk silicon. Both the rear surface internal reflectivity and surface passivation can be significantly improved with the passivated emitter and rear cell (PERC) architectures [3]. In the PERC approach, a passivation dielectric layer is deposited on the rear surface, which not only improves the passivation quality of the rear surface, but also increases its internal reflectivity. For the fabrication of metal contacts, local areas of the passivation layer are removed before metallization, usually screen-printed aluminum paste. The localized removal of the dielectric layer is typically accomplished using either laser

ablation or chemical etching. Several different parameters, such as size of the contact opening, density of the contacts, reactivity of the aluminum paste, and thermal budget, substantially affect the formation of a robust local metal contact.

A detailed investigation of the effect of local contact geometry on the conversion efficiency of the PERC cells was performed. In this paper, the effect of the metallization factors (i.e., contact size and contact pitch) on the conversion efficiency of the PERC cells will be discussed. A thin  $\text{Al}_2\text{O}_3$  surface passivation layer with a thicker  $\text{SiN}_x$  capping layer was used as the passivation film stack. Local contact areas in the passivation layer were opened by a laser ablation process. The metallization fraction was changed by varying the number of ablation laser pulses as well as the pitch of the contact pattern. The effect of the metallization factors on the cell parameters such as open circuit voltage ( $V_{OC}$ ), short circuit current density ( $J_{SC}$ ), and fill factor (FF) was studied in fabricated PERC cells and the results are compared with numerical calculation.

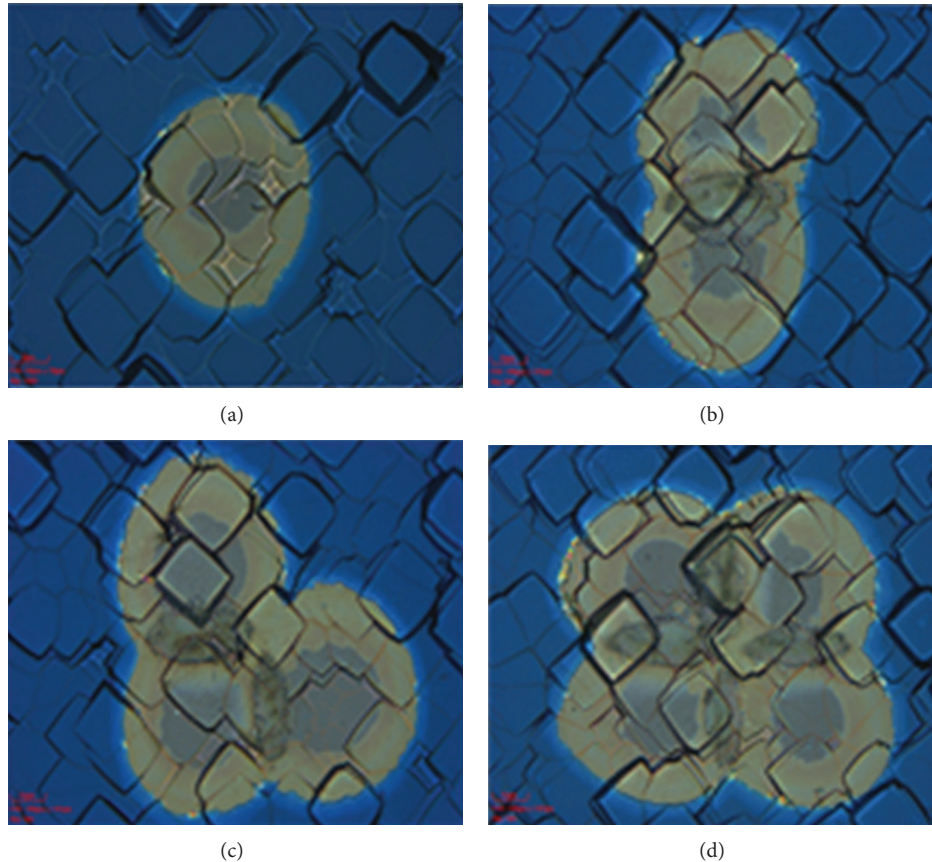


FIGURE 1: Optical microscope images of local contacts after laser ablation with one pulse (a), two pulses (b), three pulses (c), and four pulses (d).

## 2. Experimental

All wafers used in this investigation were p-type Czochralski wafers with a bulk resistivity of 1–3  $\Omega$  cm. All wafers were subjected to an IPA free texture etching process [4, 5]. After  $\text{POCl}_3$  diffusion, the rear emitter and texture were removed and a front ARC layer ( $\text{SiN}_x$ ) deposited. Front ARC layers were deposited in a PECVD thin film deposition tool. The wafers were then split into two groups. The group with no rear passivation layers was used for the fabrication of reference cells (RCs). The second group was used for fabrication of PERC cells. On wafers in this group, rear passivation films were deposited and local contacts were opened with laser ablation. The rear passivation film stack consisted of a thin  $\text{Al}_2\text{O}_3$  layer and a thicker  $\text{SiN}_x$  capping layer and was deposited using a single pass PECVD deposition system. Contact opening was performed using a high throughput laser ablation tool. The rear surface passivated wafers were subjected to several different laser ablation procedures. In one group of wafers, contact size was varied while keeping the same contact pitch. Contact size was varied with the use of multiple laser pulses. Four different ablation schemes were created using one, two, three, and four pulse sequences to make a significant change in the contact area. For the other group of wafers, the contact pitch was varied while the contact size remained constant. The same front conductor silver paste was screen printed on all wafers. Then two different

aluminum pastes, one for RC and another for PERC, were screen printed and cofired on a belt furnace. The current-voltage (IV) measurements of completed cells were made at 25°C under one-Sun illumination condition with a Newport Oriel solar simulator calibrated by using a reference cell certified by Fraunhofer ISE.

## 3. Results and Discussion

Figure 1 shows optical microscope images of local contacts formed after ablation of the dielectric film stack with different numbers of laser pulses. The laser ablation recipes were set up in such a way that with an increasing number of pulses, the ablation area increases. Consequently, the larger contact area increased the metallization fraction of the rear surface. It is important to make sure that the ablation process results in cleanly opened features without debris in the opened area. Postablation contact formation was investigated using SEM, EDX, and Auger microscopy. Only silicon was found to be present in the opened area after the completion via formation process, prior to metallization [6].

Figure 2 shows a SEM picture of local contact pattern after etching off the aluminum from the fabricated solar cell. As shown in Figure 2, the local contacts are very uniformly formed at the rear surface. The effect of contact opening on the passivation quality was monitored by measuring the lifetime of the minority carriers before and after laser

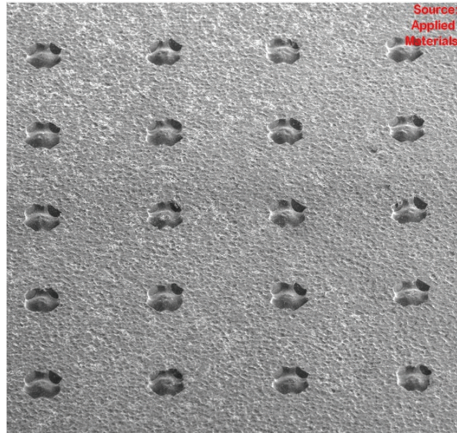


FIGURE 2: Local contact pattern fabricated using 4 laser pulses per contact point. The aluminum in the contact area has been removed with HCl.

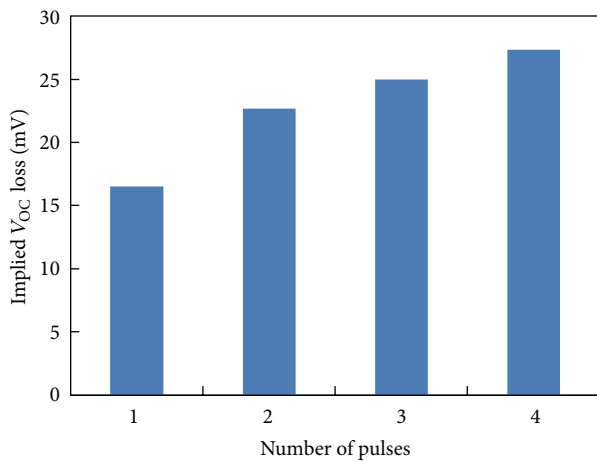


FIGURE 3: Loss in implied  $V_{OC}$  due to laser ablation as a function of number of laser pulses per contact point. Contact pitch remained constant.

ablation. All the wafers showed a decrease in lifetime after the laser ablation. Accordingly, the implied  $V_{OC}$  values decreased in all samples after the laser ablation. Figure 3 shows the loss in implied  $V_{OC}$  as a function of number of laser pulses. The loss in implied  $V_{OC}$  increased as the number of laser pulses increased. It is clear that an increasing number of laser pulses lead to a larger ablation area of contact, as shown in Figure 1. Therefore, the fraction of the passivation film removed from the surface increased as the number of laser pulses increased, leading to an increased loss in passivation quality, hence the implied  $V_{OC}$ . A similar trend in implied  $V_{OC}$  loss was observed when the contact pitch was varied (Figure 4).

When the number of pulses remained constant but contact pitch was varied, the highest implied  $V_{OC}$  loss was observed for the smallest pitch and smallest  $V_{OC}$  loss was observed for the highest pitch. This observation again can be explained in terms of the fraction of passivation layer removed. When the contact pitch was smaller, contact density was higher and the fraction of passivation layer removed during ablation was higher. Therefore, the passivation effect

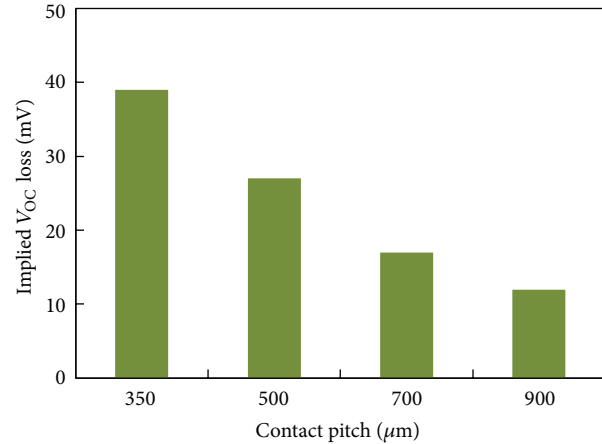


FIGURE 4: Loss in implied  $V_{OC}$  values due to laser ablation as a function of pitch of the local contact. The number of laser pulses per contact remained constant.

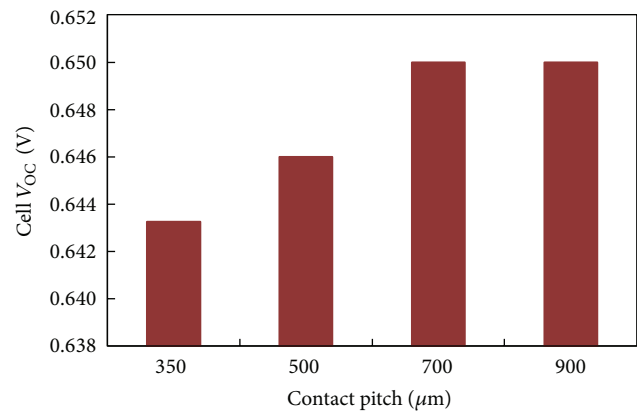


FIGURE 5:  $V_{OC}$  values of PERC cells as function of contact pitch.

was reduced. This led to a larger drop in effective lifetime and implied  $V_{OC}$ . This effect was clearly reflected on PERC cell  $V_{OC}$  values shown in Figure 5.

Figure 5 shows  $V_{OC}$  values of PERC cells fabricated by varying the contact pitch while keeping the contact size constant. When the pitch was higher, the fraction of the passivation film removed was smaller and as a consequence, the metallization fraction was smaller. The  $V_{OC}$  values of the cells gradually increased with the increased pitch and seemed to level off when the pitch was about  $700 \mu\text{m}$ . The contact pitch of  $700 \mu\text{m}$  corresponds approximately to a metallization fraction of 2.3%. Further reduction in metallization factor down to 1.4% ( $900 \mu\text{m}$  pitch) did not seem to improve the cell  $V_{OC}$  value. Nevertheless, when the metallization fraction is 1.4%, the corresponding implied  $V_{OC}$  loss (before metallization) was smaller. However, these improvements were not realized in cell efficiencies (Figure 6) due to degrading fill factor (Figure 7) values.

As indicated previously, as the area of ablated contact increased, losses in the implied  $V_{OC}$  increased (Figure 3). The  $V_{OC}$  values of the PERC cells with different contact area are shown in Figure 8. When four laser pulses were used, the metallization fraction corresponded to 4.4%. Accordingly, by

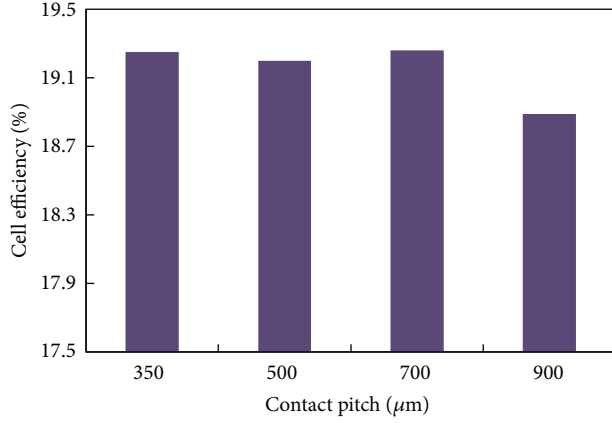


FIGURE 6: Conversion efficiencies of PERC cells as function of contact pitch.

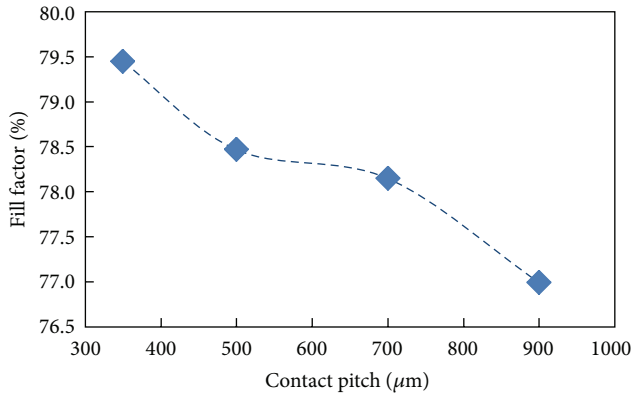


FIGURE 7: FF values of PERC cells as a function of contact pitch.

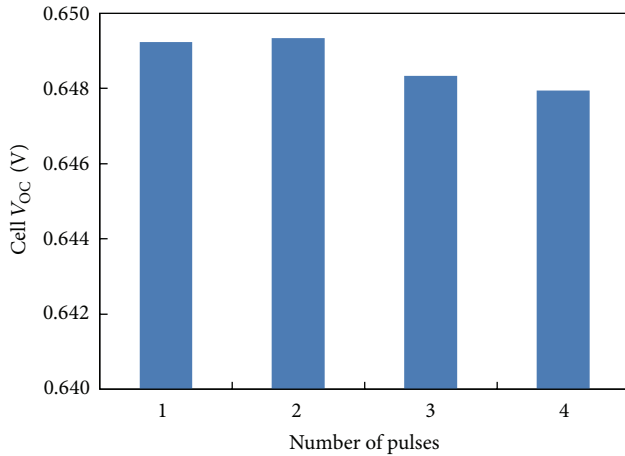


FIGURE 8: The  $V_{OC}$  values of PERC cells as function of number of laser pulses (contact area).

neglecting the change in area due to pulse overlap, single pulse ablation results in a metallization factor of 1.1%. As the metallization fraction increased, cell  $V_{OC}$  decreased gradually. However, again the  $V_{OC}$  improvement in contact with

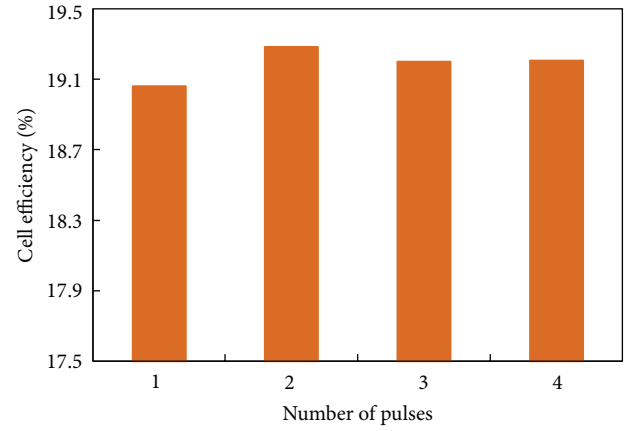


FIGURE 9: The conversion efficiencies of PERC cells as function of number of laser pulses (contact area).

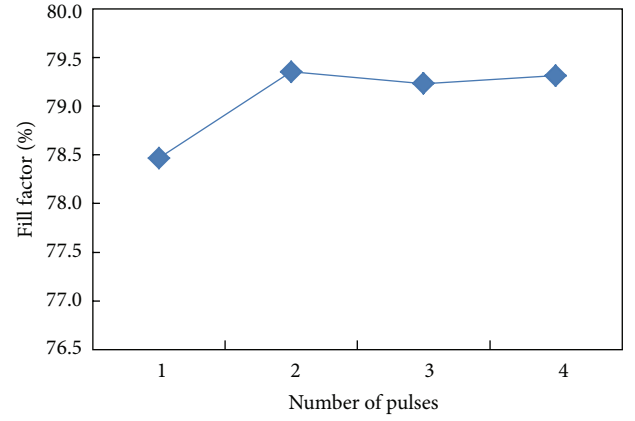


FIGURE 10: Fill factor values of PERC cells as a function of the number of laser pulses (contact size).

smaller contact area, hence smaller metallization fraction, is not reflected in cell efficiencies, as shown in Figure 9.

As shown in Figure 9, single pulse ablation (metallization fraction of 1.1%) resulted in lower conversion efficiencies in PERC cells compared to all other three ablation schemes. Again, the main factor contributing to lower conversion efficiency in PERC cells with smaller metallization fraction was found to be the low FF as shown in Figure 10. The data shown in Figure 10 clearly shows that cells with smaller contact size (metallization fraction of 1.1%) resulted in lower FF values. All other cases where metallization fractions were 2.2%, 3.3%, and 4.4% (resp., 2, 3, and 4 pulse ablation) yielded almost identical FF.

In order to gain some insight into the passivation quality of local contacts, a numerical simulation was carried out by using the theoretical formula derived by Fischer [7]. According to Fisher formula the effective rear surface recombination velocity ( $S_{eff}$ ) can be written as

$$S_{eff} = \left( \frac{R_S - \rho W}{\rho D} + \frac{1}{f S_{cont}} \right)^{-1} + \frac{S_{pass}}{1 - f}, \quad (1)$$

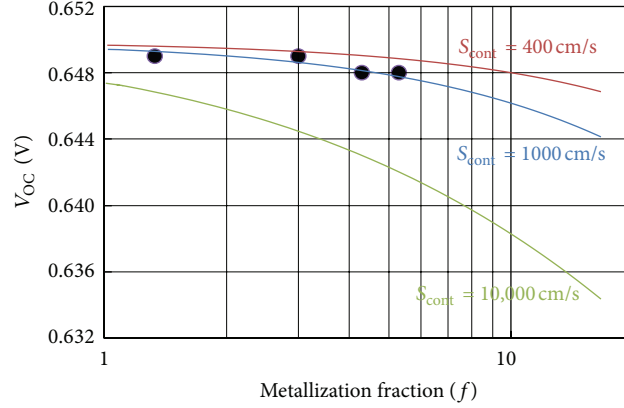


FIGURE 11: Simulated  $V_{OC}$  as a function of metallization fraction. The variation in  $V_{OC}$  for three different  $S_{cont}$  is shown. Scattered data points are the experimental values.

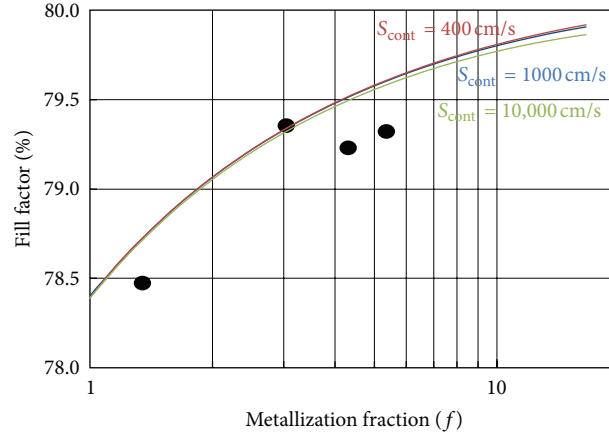


FIGURE 12: Simulated FF as function of metallization fraction. The variation of FF for three different  $S_{cont}$  is shown. Scattered data points are the experimental values.

where  $S_{pass}$  is the surface recombination velocity in passivated area, and  $S_{cont}$  is the recombination velocity at the contact,  $W$  is the substrate thickness,  $f$  is the metallization fraction,  $\rho$  is the base resistivity,  $D$  is the carrier diffusion coefficient, and  $R_S$  is the series resistance of the base. The value of  $R_S$  depends on the contact layout and can be expressed as [8]

$$R_S = p^2 \frac{\rho}{2\pi r} \arctan\left(\frac{2W}{r}\right) + \rho W \left\{1 - \exp\left(-\frac{W}{p}\right)\right\}. \quad (2)$$

Here  $r$  is the radius of the contact and  $p$  is the contact pitch. Once  $R_S$  and  $S_{eff}$  values were calculated, those values together with averaged rear surface internal reflectivity value were used as input to a calibrated device model set up in PCID simulating program [9]. This model was used to simulate the device performance for different contact size and contact pitch combinations. Passivation quality was simulated for three different  $S_{cont}$  values, namely, 400 cm/s, 1000 cm/s, and 10000 cm/s. The simulation of  $V_{OC}$ , FF values, and a comparison of corresponding experimental results are presented in Figures 11 and 12, respectively.

Simulation results presented in Figures 11 and 12 show the tradeoff between  $V_{OC}$  and FF. The FF loss at smaller

$f$  values is mainly due to resistive losses. The  $V_{OC}$ , as well as  $J_{SC}$ , losses at relatively larger  $f$  values are due to higher recombination losses ( $S_{eff}$ ) and lower internal reflectivity values. When the metallization fraction ( $f$ ) is higher, the internal reflectivity is smaller. The simulated results predicted that the highest conversion efficiency would be achieved when the metallization fraction ( $f$ ) is in the range of 2–4%.

In order to study the geometry of the contacts that were fabricated with various ablation laser pulses, aluminum paste was removed from PERC cells by dissolving it in a hydrochloric acid solution. The local contact areas were then studied with scanning electron microscopy (SEM) and confocal optical microscopy [10]. Figure 13 shows SEM images of various local contacts after aluminum removal. It is well known that, during the contact firing process, silicon dissolves into the aluminum matrix from beneath the contact area [11–14]. In the case of local contacts, only silicon underneath the opened contact areas is available for this process. Therefore, the silicon concentration is higher in liquid aluminum above the contact points compared to other areas. This concentration gradient will result in a diffusion of silicon away from contact site. As a result, recesses, which in some cases can be as deep as 30–40  $\mu\text{m}$ , formed in the bulk silicon, as shown in

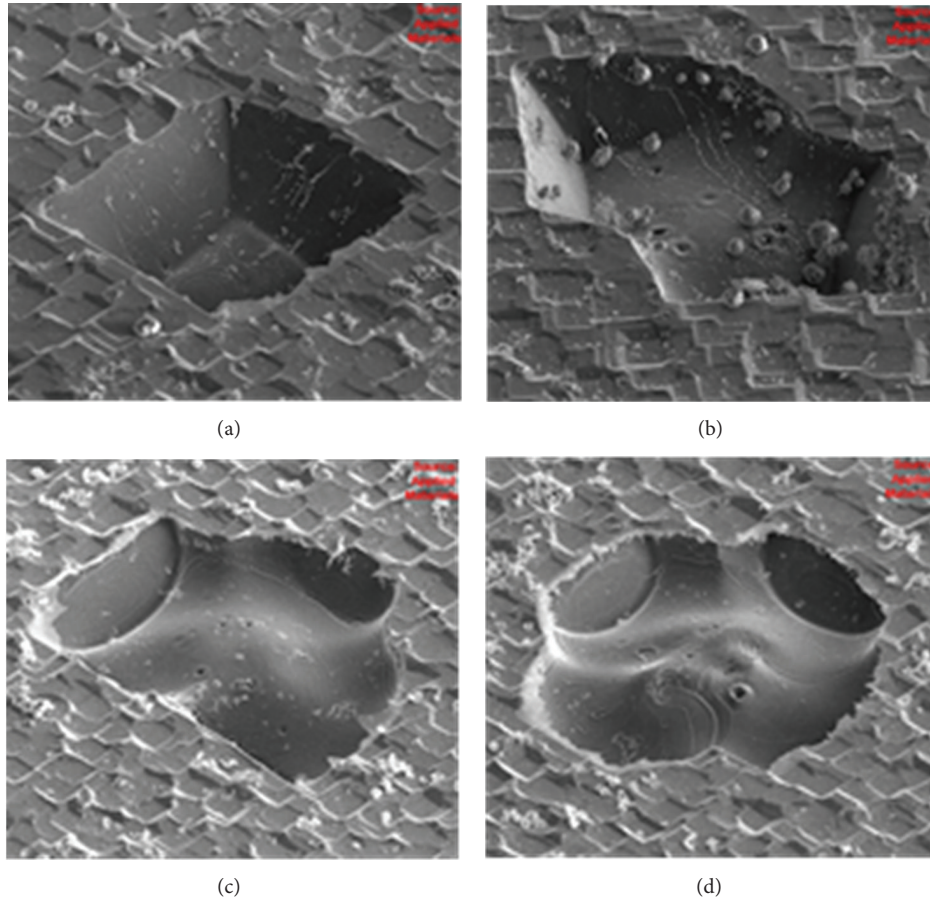


FIGURE 13: SEM images of local contacts after aluminum removal: one pulse (a), two pulses (b), three pulses (c), and four pulses (d).

Figure 13. These recesses show the characteristic shape of truncated pyramids. These truncated pyramidal structures are formed due to preferential dissolution of silicon along the (100) planes.

The aluminum etched back contacts were studied further with confocal microscopy and the results are shown in Figure 14. In many situations, it was found that the depth at the edge of the recess was larger than at the center.

The depth of the feature shown in Figure 14 was found to be about  $23\ \mu\text{m}$  at the center and about  $42\ \mu\text{m}$  at the edge. The angle between the side wall and bottom is about  $53^\circ$ , which indicates preferential dissolution of silicon along (100) planes during contact formation. In the case of an isotropic etching of silicon substrates, random pyramids are formed and the angle was found to be  $54.7^\circ$ . It was found that the depth of the recess decreased as the area of the contact increased. With smaller open contacts the area exposed to aluminum paste is smaller. For a given peak temperature, silicon dissolution into liquid aluminum takes place until the saturation limits are reached. Therefore, in the case of smaller size contacts, silicon dissolution runs deeper into the bulk silicon. During the cooling cycle, silicon re-crystallizes, creating an aluminum doped  $p^+$  (Al-BSF) layer. After further cooling, eutectic temperature is reached and the remaining Al-Si liquid phase solidifies, completing

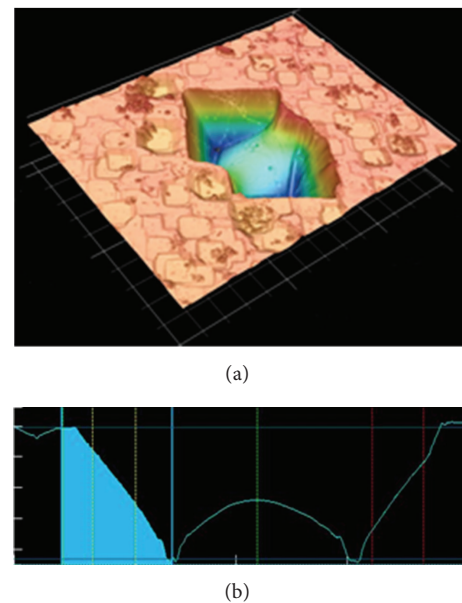


FIGURE 14: Confocal microscope image of local contacts after aluminum removal (a) and depth profile of the recess (b). In this case two laser pulses were used for ablation, as shown in Figures 1 and 13.

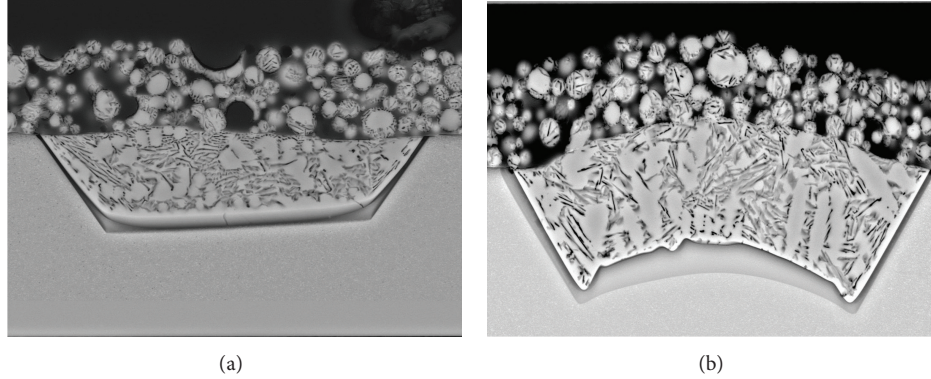


FIGURE 15: Cross sectional SEM images of fully alloyed contacts. (a) Single pulse ablation (thickness of BSF layer  $\sim 1.25 \mu\text{m}$ ), (b) three pulse ablation (thickness of BSF layer  $\sim 5.9 \mu\text{m}$ ).

the alloying process. Out-diffusion of silicon, away from the contact, will deplete the silicon concentration, which can contribute to BSF formation. In the case of smaller contacts, the extent of out-diffusion of silicon is larger, relative to larger contacts. This will result in relatively thin Al-BSF layers in smaller contacts. However, it should be noted that for a given contact geometry, these difficulties can be overcome with modifications to paste composition and optimized firing conditions [6].

Cross section SEM images of alloyed contacts fabricated with different numbers of ablation pulses are shown in Figure 15. These SEM images clearly show Al-alloyed contact with the presence of a uniform Al-BSF layers. However, as the area of the contact increased the thickness of the Al-BSF layer increased. As measured with cross sectional SEM, the thicknesses of BSF layers varied from  $1.25 \mu\text{m}$ ,  $2.45 \mu\text{m}$ , and  $5.9 \mu\text{m}$  to  $6.1 \mu\text{m}$  for contacts ablated with 1, 2, 3, and 4 laser pulses, respectively.

Based on the above findings, the contact size and the contact pitch were optimized for PERC cell development. It should be noted that all the preliminary experimental data presented in Figure 1 through Figure 10 contain the results of an average of five wafers for each data point. Once optimized process conditions were established, PERC cells and reference cells were fabricated with a larger sample size. Wafers from the same lot were divided into two groups and one group was used for the PERC cells and the other was used for fabrication of reference cells. Each group contained 12 wafers. The results of these two wafer groups are summarized in Table 1. The champion PERC cell fabricated in this study resulted in conversion efficiency of 19.6% compared to the champion RC of 18.9%. The gain in the PERC cell was due to improved  $J_{\text{SC}}$  and  $V_{\text{OC}}$ . It should be noted that, during the rear emitter removal step, the backside of the wafers was polished and texturization was removed. Therefore, both types of cells (PERC and RC) have identical rear side reflections after parasitic emitter removal. The gain in conversion efficiency in the champion PERC cell over the champion RC cell was 0.7%, as shown in Table 1. The average conversion efficiency gain was 0.6% over RC. The average  $J_{\text{SC}}$  gain in PERC cells was more than  $1 \text{ mA/cm}^2$  compared to the reference cells. The PERC cells also show significantly improved  $V_{\text{OC}}$  over the RC.

TABLE 1: Comparison of solar cell performance for PERC and RC cells.

Cell	$J_{\text{SC}}$ ( $\text{mA/cm}^2$ )	$V_{\text{OC}}$ (mV)	FF (%)	Eta (%)
Best RC	37.3	639	79.4	18.90
Best PERC	38.5	648	78.7	19.62
Average RC	37.11	638	79.52	18.82
Average PERC	38.36	646	78.69	19.49

## 4. Summary

Local contact formation in PERC cells was studied in detail with respect to contact area and pitch, hence the metallization fraction. With the optimized contact geometry, a process flow for manufacturing PERC solar cells yielding 19.6% conversion efficiency was developed for industrial applications. The efficiency gain of PERC cells over conventional solar cells was 0.7%. The efficiency gain in the PERC cells was mainly due to improved short circuit current and open circuit voltage.

## Acknowledgments

The authors thank Andie Chan, Kalyan Rapolu, Prabhat Kumar, Manoj Vellaikal, Xuesong Liu, Damanjot Kochhar, Michael Stewart, and Jeff Franklin for their contributions to this work.

## References

- [1] S. Gatz, T. Dullweber, and R. Brendel, "Evaluation of serious resistance losses in screen-printed solar cells with local rear contacts," *IEEE Journal of Photovoltaics*, vol. 1, pp. 37–42, 2011.
- [2] T. Lauermann, T. Lüder, S. Scholz, B. Raabe, G. Hahn, and B. Terheiden, "Enabling dielectric rear side passivation for industrial mass production by developing lean printing-based solar cell processes," in *Proceedings of the 35th IEEE Photovoltaic Specialists Conference (PVSC '10)*, pp. 28–33, Honolulu, Hawaii, USA, June 2010.
- [3] A. W. Blakers, A. Wang, A. M. Milne, J. Zhao, and M. A. Green, "22.8% efficient silicon solar cell," *Applied Physics Letters*, vol. 55, no. 13, pp. 1363–1365, 1989.

- [4] K. Wijekoon, T. Weidman, S. Paak, and K. MacWilliams, "Production ready noval texture etching process for fabrication of single crystalline silicon solar cells," in *Proceedings of the 35th IEEE Photovoltaic Specialists Conference (PVSC '10)*, pp. 3635–3641, Honolulu, Hawaii, USA, June 2010.
- [5] K. Wijekoon, P. Kumar, D. Tanner, H. Ponnekanti, and C. Gay, "Effect of additive and etchant concentration in surface morphology of mono-crystalline silicon solar cells textured with non-alcoholic chemical formulations," in *Proceedings of the 26th European Photovoltaic Solar Energy Conference and Exhibition (EU PVSEC '11)*, pp. 2015–2019, Hamburg, Germany, September 2011.
- [6] K. Wijekoon, H. Mungekar, M. Stewart et al., "Development of high efficiency mono-crystalline silicon solar cells: optimization of rear local contacts formation on dielectrically passivated surfaces," in *Proceedings of the 38th IEEE Photovoltaic Specialists Conference (PVSC '12)*, pp. 28–33, June 2012.
- [7] B. Fischer, *Loss analysis of crystalline silicon solar cells using photoconductance and quantum efficiency measurements [Ph.D. dissertation]*, Universität Konstanz, Konstanz, Germany, 2003.
- [8] R. H. Cox and H. Strack, "Ohmic contacts for GaAs devices," *Solid State Electronics*, vol. 10, no. 12, pp. 1213–1218, 1967.
- [9] P. Basore and D. Clugston, *PCId Version 5. 1 for Windows*, UNSW, Sydney, Australia, 1997.
- [10] M. Rauer, C. Schmiga, K. Ruhle, R. Woehl, M. Hermle, and S. Glunz, "Investigation of aluminum-alloyed local contacts for rear surface-passivated silicon solar cells," *IEEE Journal of Photovoltaics*, vol. 1, no. 1, pp. 22–28, 2011.
- [11] E. Urrejola, K. Peter, H. Plagwitz, and G. Schubert, "Silicon diffusion in aluminum for rear passivated solar cells," *Applied Physics Letters*, vol. 98, no. 15, Article ID 153508, 3 pages, 2011.
- [12] E. Urrejola, K. Peter, H. Plagwitz, and G. Schubert, "Al-Si alloy formation in narrow *p*-type Si contact areas for rear passivated solar cells," *Journal of Applied Physics*, vol. 107, no. 12, Article ID 124516, 2010.
- [13] T. Lauermann, A. Zuschlag, S. Scholz, G. Hahn, and B. Terheiden, "The influence of contact geometry and sub contact passivation on the performance of screen printed Al<sub>2</sub>O<sub>3</sub> passivated solar cells," in *Proceedings of the 26th European Photovoltaic Solar Energy Conference and Exhibition (EU PVSEC '11)*, pp. 1137–1143, Hamburg, Germany, September 2011.
- [14] J. Krause, R. Woehl, and D. Biro, "Analysis of local Al-P+ -layers for solar cells processed by small screen-printed structures," in *Proceedings of the 25th European Photovoltaic Solar Energy Conference and Exhibition (EU PVSEC '10)*, pp. 1899–1904, Valencia, Spain, September 2010.

## Research Article

# Characterization of a Bifacial Photovoltaic Panel Integrated with External Diffuse and Semimirror Type Reflectors

P. Ooshaksaraei,<sup>1,2</sup> K. Sopian,<sup>1</sup> R. Zulkifli,<sup>2</sup> M. A. Alghoul,<sup>1</sup> and Saleem H. Zaidi<sup>1</sup>

<sup>1</sup> Solar Energy Research Institute, Universiti Kebangsaan Malaysia (UKM), 43600 Bangi, Selangor, Malaysia

<sup>2</sup> Department of Mechanical & Materials Engineering, Faculty of Engineering & Built Environment, Universiti Kebangsaan Malaysia (UKM), 43600 Bangi, Selangor, Malaysia

Correspondence should be addressed to P. Ooshaksaraei; [poorya@eng.ukm.my](mailto:poorya@eng.ukm.my)

Received 25 September 2012; Revised 18 April 2013; Accepted 4 May 2013

Academic Editor: Peter Rupnowski

Copyright © 2013 P. Ooshaksaraei et al. This is an open access article distributed under the Creative Commons Attribution License, which permits unrestricted use, distribution, and reproduction in any medium, provided the original work is properly cited.

Silicon wafer accounts for almost one-half the cost of a photovoltaic (PV) panel. A bifacial silicon solar cell is attractive due to its potential of enhancing power generation from the same silicon wafer in comparison with a conventional monofacial solar cell. The bifacial PV cell is able to capture solar radiation by back surface. This ability requires a suitable reflector appropriately oriented and separated from the cell's rear surface. In order to optimize the bifacial solar cell performance with respect to an external back surface reflector, diffuse and semimirror reflectors were investigated at various angles and separations from the back surface. A simple bifacial solar panel, consisting of four  $5'' \times 5''$  monocrystalline Si solar cells, was designed and built. Reflection from the rear surface was provided by an extended semimirror and a white-painted diffuse reflector. Maximum power generation was observed at  $30^\circ$  with respect to ground for the semimirror reflector and  $10^\circ$  for diffuse reflector at an optimized reflector-panel separation of 115 mm. Output power enhancement of 20% and 15% from semimirror and diffuse reflectors, respectively, were observed. This loss from diffuse reflector is attributed to scattering of light beyond the rear surface capture cross-section of the bifacial solar panel.

## 1. Introduction

Figure 1 schematically draws conventional monofacial and bifacial silicon solar cell cross-sectional configurations [1]. In monofacial solar cells, the front surface is transparent with glass lamination, and the back surface is opaque (Figure 1(a)). Front surface of the solar cell absorbs the sunlight and converts it into electricity with a metallic grid pattern on the front surface and a blanket metal film on the rear surface. In some field applications, PV panels are installed in such a way that rear surface is able to capture diffuse reflected light from ground and other reflective surfaces surrounding the panel. In order to capture this diffuse radiation, researches in 80s led to development of a new generation of solar cells able to absorb solar radiation from rear surface [2]. This type of solar cell is referred to as a bifacial solar cell. A bifacial solar cell, in contrast with a monofacial solar cell, has identical metallic grids on both front and back surfaces (Figure 1(b)). Some modifications to conventional monofacial PV panel design are required in order to effectively utilize the bifacial

PV panel. This research is aimed at evaluating the bifacial PV panel output variation with single semimirror and diffuse reflectors.

*1.1. Bifacial Solar Cell.* Bifacial solar cell has the potential to absorb additional sunlight by rear surface, which is a significant advantage in contrast with the monofacial solar cell. Additional solar radiation absorption through the bifacial solar cell's rear surface leads to enhanced electrical power generation [3].

A key challenge in effective utilization of bifacial solar cells is in the design of appropriate rear surface reflector. The effect of external rear surface reflector for bifacial solar cells has been investigated for residential applications [4] including reflection from wall, capture of radiation reflected back by window, and terrestrial reflection in parking lot. In such applications, existence of an appropriate reflector is a critical element in order to substantially increase solar radiation incident on rear surface. However, there are many

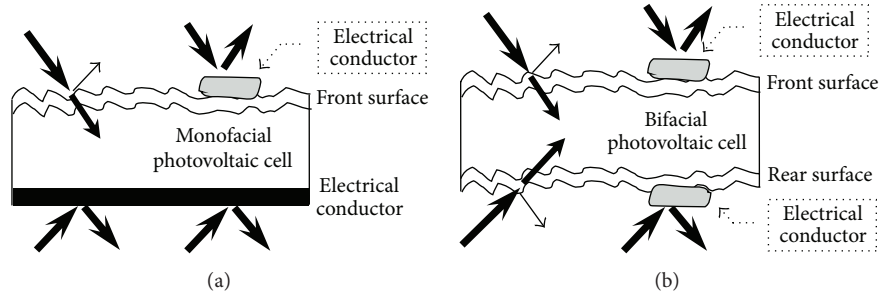


FIGURE 1: Cross-section configurations of monofacial (a) and bifacial solar cells (b).

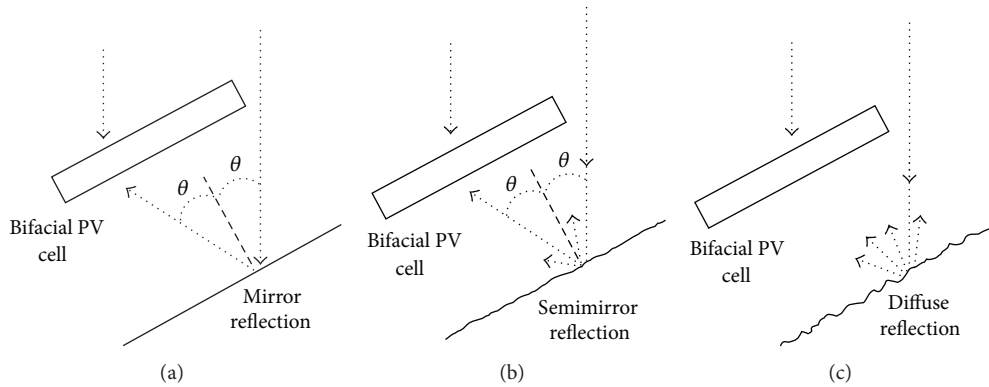


FIGURE 2: Bifacial PV panel integrated with mirror type reflector (a); semimirror type reflector (b); and diffuse type reflector (c).

cases in which bifacial solar panels are effective without the reflector [5, 6]. The slope and direction of bifacial solar panel play a significant role in maximizing the solar radiation absorption and have been investigated for bare bifacial solar panels, that is, without external reflectors, by Joge et al. [7]. Installation attitude of bare bifacial panels has been studied by Joge et al. [7], where little dependence between orientation and annual power generation was observed. This research has been followed by Uematsu et al. and proved bare bifacial panels as an orientation-free device [6].

Their work defined the bifaciality parameter as the ratio of rear surface efficiency over front surface efficiency:

$$\text{bifaciality} = \frac{\text{rear surface efficiency}}{\text{front surface efficiency}}. \quad (1)$$

This definition is based on the assumption that the same intensity of solar radiation is incident on both rear and front surfaces.

**1.2. Reflector.** In bare bifacial panel applications such as fence integration, front surface usually faces the sun, while the rear surface captures diffuse sky radiation and/or ground reflection based on panel orientation and time of the day. With two absorption surfaces, bifacial solar panels produce more electrical energy than monofacial panels especially in cloudy climates [7]. Bifacial solar panels equipped with external reflectors are expected to generate additional electrical energy depending on the materials properties of the reflector and its location. Some of the key parameters for the reflector

include its slope with respect to the panel plane, distance from the panel, and reflection efficiency.

In general, solar panels are classified either as one-sun (1X) panel or concentrator panel (multi X). For the case of bifacial panels the definition of flat panel and concentrator panel may overlap in case where the front surface receives 1X solar radiation, while the rear surface may receive additional 1X beam radiation [8]. Mirror type, diffuse type, and semitransparent reflection have been investigated for various bifacial PV panel applications [9–13]. Uematsu et al. [14] developed a flat plate bifacial panel by static V-groove concentrator to provide 1X solar radiation on rear surface of bifacial cell, which resulted in 85.6% enhancement in power.

A wide range of reflectors including diffuse, mirror, and semitransparent has been studied in the literature [4, 9, 10, 14]. Figure 2 represents a simple schematic of bifacial PV panel integrated with an external reflector. Figure 2(a) represents a mirror type reflection where only one beam of light is directed to the rear surface of the panel, while diffuse reflector scatters the reflected radiation over the rear surface of the bifacial panel/cell (Figure 2(c)).

The semimirror reflector shown in Figure 2(b) reflects back a portion of solar radiation on rear surface, like a mirror type reflector, while a portion of solar radiation is scattered.

Reflection is a function of surface roughness as well as its color [15]. Duran et al., demonstrated that variation in solar radiation intensity on rear surface leads to a corresponding variation in electricity generation [16]. Moehlecke et al., [15] studied the reflection performance of painted diffuse

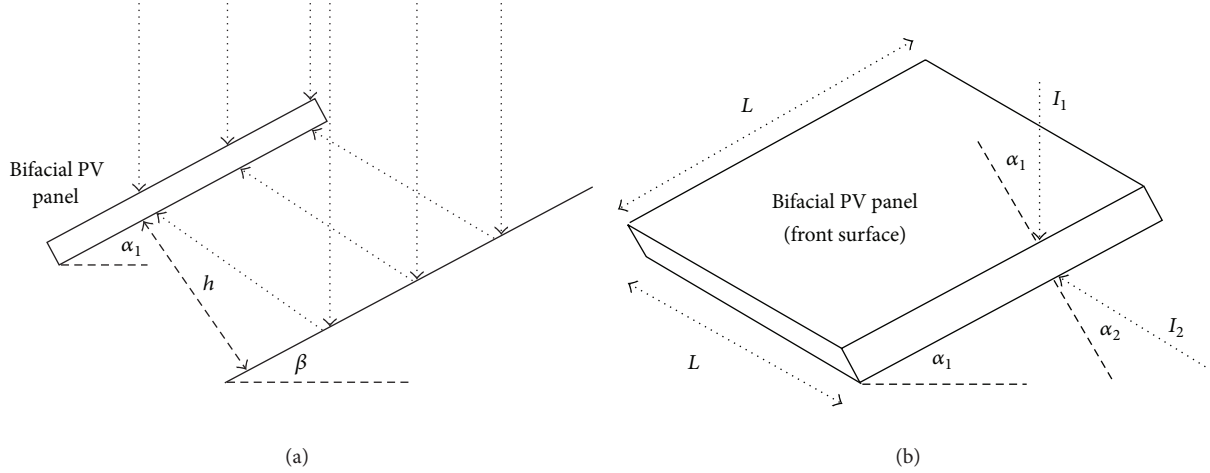


FIGURE 3: Bifacial panel integrated with an external mirror reflector (a) and schematic diagram of the incident solar radiation on front and back surfaces of bifacial solar panel of area  $L^2$  (b).

reflectors placed under bifacial solar panels. Enhancement up to 25% in solar absorption in comparison with conventional monofacial PV panel was demonstrated. Their work indicated that white color was an optimum diffuse painted reflector with approximately 75% average reflectance. Yellow color has the second best reflection performance followed by orange, red, green, blue, brown, purple, grey, dark blue, and dark green with 61%–32% reflection variation [15]. Reflection performance of a reflector is not only a function of its color but also the direction of the incident beam as well as the microstructure of the reflector.

## 2. Mathematical Formalism

Work reported in the literature suggests that a variety of reflectors can be applied to a bifacial panel. A white surface as an optimum color painted reflector and an aluminum plate as a semimirror type reflector were chosen for the work reported here. Aluminum plate was selected due to its affordability, durability, and higher reflectance.

Figure 3(a) is a graphical representation of bifacial panel integrated with an external reflector being modeled here.

The panel-reflector separation facilitates the reflection of solar radiation on rear surface of the panel. In Figure 3(b), the front surface of the panel receives the direct solar radiation  $I_1$ , while the rear surface receives the radiation reflected back from reflector  $I_2$ .  $L$  denotes the dimension of the panel.

There are three key parameters in a bifacial panel equipped with an external reflector under the panel, namely, slope of the reflector ( $\beta$ ), slope of the PV panel ( $\alpha_1$ ), and average distance between the PV panel and the reflector ( $h$ ), to be referred to as separation (Figure 3(a));  $\alpha_1$  and  $\beta$  denote the slope of bifacial panel and the slope of the reflector plate, respectively;  $I_1$  and  $I_2$  denote radiation incident on PV panel at angles  $\alpha_1$  and  $\alpha_2$  from normal to the surface (Figure 3(b)).

**2.1. Bifaciality of the Solar Panel.** Bifaciality of a bifacial solar cell only depends on the efficiency of the front and rear

surfaces and has been defined in (1), while the bifaciality of a PV panel has been defined as

$$\begin{aligned} \text{panel bifaciality} &= \frac{\text{rear surface electrical output}}{\text{front surface electrical output}} \\ &= \frac{E_{\text{rear}}}{E_{\text{front}}}, \end{aligned} \quad (2)$$

where  $E_{\text{rear}}$  and  $E_{\text{front}}$  are related to rear and front surface efficiencies as follows:

$$\begin{aligned} \eta_{\text{PV}_{\text{front}}} &= \frac{E_{\text{front}}}{I_1 \cos(\alpha_1)}, \\ \eta_{\text{PV}_{\text{rear}}} &= \frac{E_{\text{rear}}}{I_2 \cos(\alpha_2)}. \end{aligned} \quad (3)$$

From (1), the bifaciality factor of a bifacial cell has been defined as [7]

$$K_{\text{bif}} = \frac{\eta_{\text{PV}_{\text{rear}}}}{\eta_{\text{PV}_{\text{front}}}}. \quad (4)$$

Reflection performance of the reflector is a nondimensional parameter and is the ratio of intensity of reflected radiation over the intensity of radiation reaching the reflector surface:

$$\eta_{\text{reflector}} = \frac{I_2}{I_1}. \quad (5)$$

Substituting (3), (4), (5), in (2), the panel bifaciality may be redefined as

$$\text{panel bifaciality} = K_{\text{bif}} \eta_{\text{reflector}} \frac{\cos(\alpha_2)}{\cos(\alpha_1)}. \quad (6)$$

Since the rear and front surfaces represent the opposite surfaces of the same bifacial cell,  $\eta_{\text{PV}_{\text{front}}}$  and  $\eta_{\text{PV}_{\text{rear}}}$  can be measured by exposing front aperture and rear surfaces

alternatively during panel output power measurements. Both rear and front apertures must receive the same intensity of solar radiation during the measurement in order to calculate (4). Since both the rear and front surfaces have the same absorber area, (4) can be rewritten as

$$K_{\text{bif}} = \frac{\eta_{\text{PVrear}}}{\eta_{\text{PVfront}}} = \frac{E_{\text{PVrear}}}{E_{\text{PVfront}}}, \quad (7)$$

where  $E_{\text{PVfront}}$  and  $E_{\text{PVrear}}$  denote the electrical energy production by rear and front surfaces, respectively. Please note that part of incident beam radiation penetrates PV cell, during  $E_{\text{PVfront}}$  measurement, and reaches rear surfaces, which leads to additional power generation based on transmittance/absorption characteristics of front and rear surfaces of the bifacial PV cell. There is similar bias error in  $E_{\text{PVrear}}$  measurement as well. Since the cell structure is symmetric, this contribution can be ignored as it cancels out.

**2.2. Total Panel Efficiency.** The electrical energy generated by the rear surface of the bifacial solar panel strongly depends on the efficiency of the reflector placed under the cell. The total efficiency of bifacial panel is defined as

$$\eta_{\text{panel}} = \eta_{\text{PVfront}} \tau_{\text{Glass}} P + \eta_{\text{PVrear}} \tau_{\text{Glass}} \eta_{\text{Reflector}} P, \quad (8)$$

where  $\eta_{\text{PVfront}}$  and  $\eta_{\text{PVrear}}$  denote the efficiency of the front and rear surfaces of the bifacial panel, respectively.  $\tau_{\text{Glass}}$ ,  $\eta_{\text{Reflector}}$ , and “ $P$ ” denote the transmittance of the panel glazing, reflection performance of the reflector, and the packing factor of the panel, respectively.

The packing factor of a PV panel is a nondimensional factor defined as the ratio of effective absorber area of solar cells over the total panel area of the panel facing solar radiation. That is, in case of a four-cell panel, the packing factor is defined as the total area of the four cells ( $4 \times a \times b$ ) divided by the total area of the panel ( $L \times L$ ); please refer to Figure 4.

Equation (8) applies to a bifacial panel where the solar radiation is reflected back by an external reflector. In a bifacial panel with an external reflector, the dimensions of reflector are generally larger than that of the panel. A plot of (8) as a function packing factors is drawn in Figure 5.

The transparent vacant spaces between the solar cells impact the total efficiency of the panel. These transparent spaces provide open regions through which the solar radiation can pass through and reflect back to the rear surface of the panel. Therefore, the electrical energy generated by the rear surface strongly depends on the panel packing factor. The lower packing factor leads to higher solar radiation on rear aperture. Therefore, there is a tradeoff between total energy generated and the optimum packing factor, that is, a function of several factors including cost effectiveness.

Neglecting the mirror extension from panel length and considering a reflector at same size of the panel, all solar radiation captured by the rear surface originates from vacant space between cells. Therefore, total efficiency of such panel is defined as

$$\eta_{\text{panel}} = \eta_{\text{PVfront}} P + \eta_{\text{PVrear}} (1 - P) \tau_{\text{Glass}} \eta_{\text{Rear}} P, \quad (9)$$

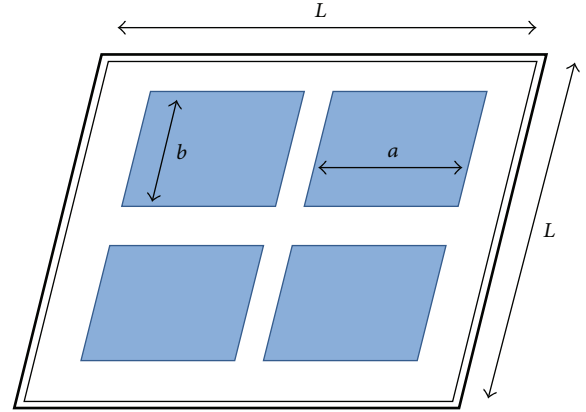


FIGURE 4: A four-cell PV panel with total absorber area of  $4ab$  and the laminated panel area of  $L^2$ .

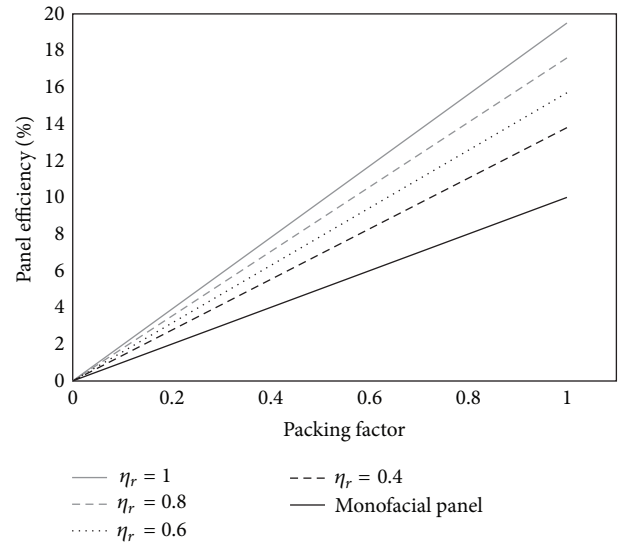


FIGURE 5: Variation of total efficiency of a bifacial panel as a function of packing factor.

where  $\eta_{\text{PVfront}}$  and  $\eta_{\text{PVrear}}$  denote the efficiency of the front and rear surfaces of the bifacial panel, respectively.  $\tau_{\text{Glass}}$ ,  $\eta_{\text{Reflector}}$ , and “ $P$ ” denote the transmittance of the panel glazing, reflection performance of the reflector, and the packing factor of the panel respectively.

A plot of the panel total efficiency (9) as a function of the packing factor in Figure 6 reveals nonlinear response. The panel efficiency represented in Figure 6 is a function of reflector efficiency and packing factor in accordance with (9).

Comparing simulations in Figures 5 and 6, benefits of external reflector are clarified in terms of enhanced power output.

### 3. Results and Discussion

Four  $5'' \times 5''$  monocrystalline bifacial cells were used to fabricate a glass to transparent Tedlar for indoor characterization.

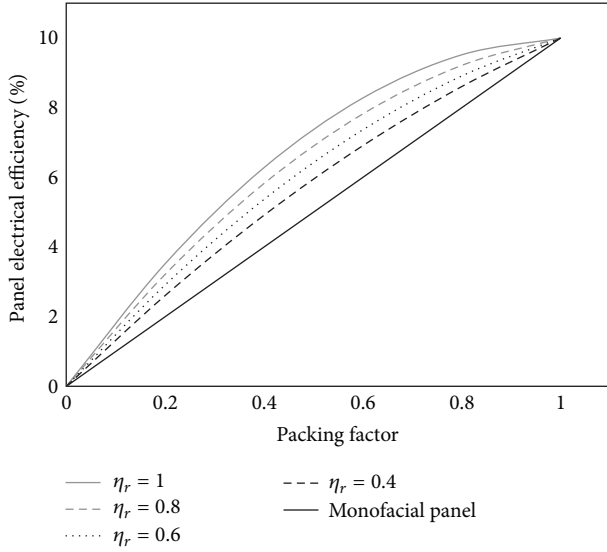


FIGURE 6: Variation of the total panel efficiency of equally sized panel and reflectors as a function packing factor.



FIGURE 7: Experimental configuration for indoor bifacial solar panel integrated with an external reflector.

The cells were manufactured by Hitachi Company with technical details as follows:

- (i) wafer thickness: 200 micrometer,
- (ii) wafer type: p type (boron doped),
- (iii) texture: inverted pyramids,
- (iv) front surface: AR film, SiN,
- (v) back surface: AR film, SiO<sub>2</sub>,
- (vi) front surface: phosphorous doped,
- (vii) back surface: boron doped.

The bifacial PV panel has packing factor of 0.69 and was integrated with a single external reflector located under the panel as shown in Figure 7. Two types of reflectors have been used for indoor characterization work: an aluminum reflector and white-painted aluminum reflector.

The efficiency of the front and rear surfaces has been measured separately. The bifaciality of the panel ( $K_{\text{bif}}$ ) has been measured under solar simulator (indoor test) as a function

TABLE 1: Bifacial factor measurements as a function of slope angle.

Panel slope (degree)	0	10	20	30	40	50	Average
$K_{\text{bif}}$	1	1	0.98	0.96	0.94	0.92	0.97

of the panel slope in zero-to-50-degree range. Measurement results have been summarized in Table 1.

There was no reflector under the panel during  $K_{\text{bif}}$  measurements. The efficiency of the front surface was measured with it facing the lamps (solar simulator) while the rear surface was protected by a black cover. Likewise, the efficiency of the rear surface was measured with the rear surface facing the lamps and front surface protected by a black cover. The bifaciality factor is reduced as the panel tilt angle increases, which may be attributed to larger reflection losses from the rear surface. Assuming identical microstructures on front and rear surfaces of the solar cell, this loss may be due to different optical response of front and rear surfaces. In the bifacial solar cells reported here, the front surface antireflection film was silicon nitride, and the back surface antireflection film was silicon dioxide. It is well known that silicon nitride has higher index of refraction and performs better than silicon dioxide.

In order to calculate the total efficiency of the bifacial panel, a reflector was placed under the panel. The panel and the reflector were parallel during the tests ( $\alpha_1 = \beta$ ), but the panel separation ( $h$ ) from the reflector was adjustable. The PV cell separation from reflector ( $h$ ) and the slope of panel ( $\alpha_1$ ) are the two key parameters. The electrical power output was measured as a function of panel slope angle in 0° to 50° range has been plotted in Figure 8; cell-reflector separation was varied from 75 mm to 215 mm.

Both diffuse and semimirror reflectors exhibit similar contribution in electrical energy generation enhancement by the bifacial panel. A panel with packing factor of 0.69 has transparent spaces in between adjacent solar cells. At least, thirty-one% of incident solar radiation (31%) passes through the gaps between the solar cells and is reflected back to the rear surface of the panel. At panel slope equal to zero, the gaps between the cells are the only source of radiation for rear surface. A panel with high packing factor strongly depends on extended reflector to achieve the optimum performance. Regardless of the panel separation, the optimum performance was observed at tilted panel (Figure 8).

The average output power of the panel tilted from zero to 50° is shown in Figure 9. In Figure 9, the “front surface” denotes the output power measured while the rear aperture is blocked and vice versa.

The bifacial panel outfitted by a semimirror type reflector represents the maximum total efficiency at the panel at panel separation 115 mm, while in case of the diffuse reflector, the maximum efficiency was observed at 75 mm and 115 mm (Figure 9). Effect of the bifacial PV panel separation from reflector on the average electrical power output of the panel is shown in Figure 9, where the output power of the front and the rear apertures is shown separately. The “semimirror” and “diffuse” denote the total electrical power generated by

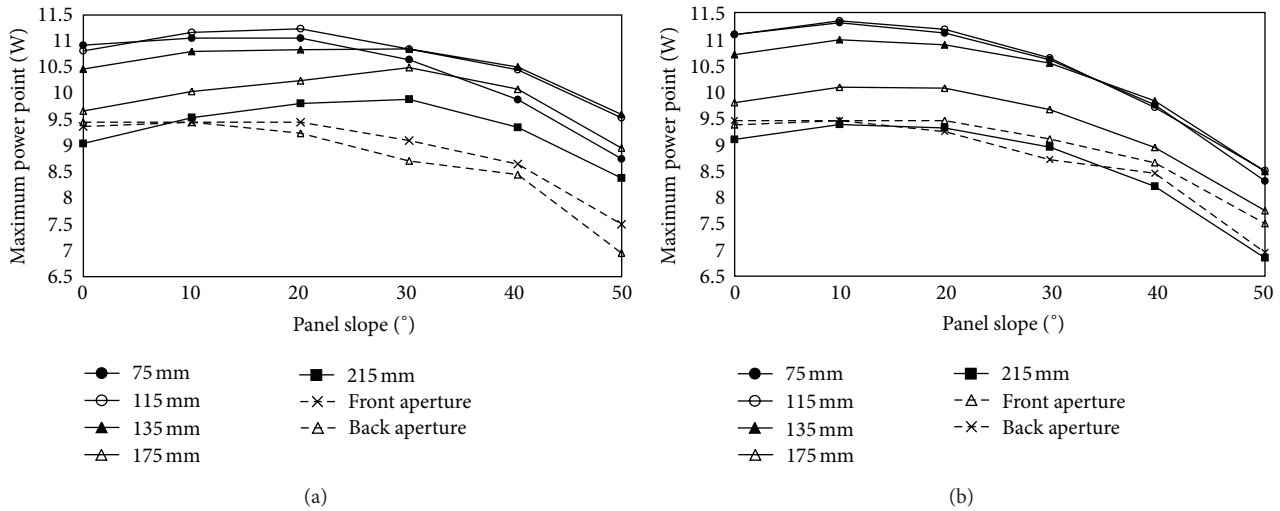


FIGURE 8: Plot of maximum power point for semimirror reflector (a) and diffuse reflector (b).

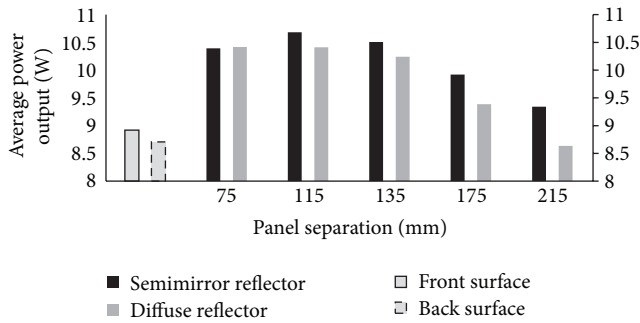


FIGURE 9: Effect of the bifacial PV panel separation from reflector on average electrical power output.

the bifacial solar cell equipped with a semimirror reflector and a diffuse reflector.

The panel adjustment variables ( $h$  and  $\beta$ ) of the maximum points of each curve from of Figure 8 have been extracted and are plotted in Figure 10. The bifacial panel integrated with a diffuse reflector reaches the maximum power production at  $10^\circ$  tilt and is relatively independent of panel separation. Meanwhile the optimum panel slope of the semimirror type reflector varies with separation of the panel.

The “maximum power point” in Figure 10 suggests the best parameters in order to achieve the maximum light to electrical energy conversion. Meanwhile, semimirror and diffuse type reflectors generate the same amount of energy at optimum adjustment.

Three distinguishable categories for semimirror reflector variation can be identified in Figure 10 and have been summarized as follow:

category (I): the majority of energy is provided by the front surface; small separation between panel and reflector does not permit significant capture of reflected light by the rear surface;

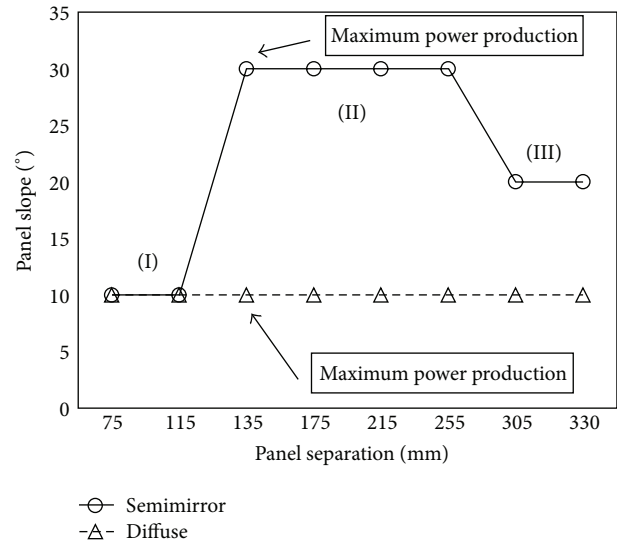


FIGURE 10: Optimum panel tilt and separation for maximum power generation as a function of panel-reflector separation.

category (II): large enough separation between the panel and the reflector leads to significant solar radiation capture by the rear surface;

category (III): For very large panel-reflector separations beyond 250 mm, diffusely reflected light can't be captured by the rear surface, hence the lower power output was observed. Therefore reducing the panel slope is necessary in order to maximize power production.

#### 4. Conclusions

Two sets of experiment have been carried out to determine optical response of bifacial solar panels with an integrated external reflector. It has been determined that in contrast with

conventional monofacial photovoltaic panels, the maximum power production does not occur at solar radiation normal to surface. There is a tradeoff between the electrical energy produced by direct solar radiation on front surface and reflected radiation on the rear surface, which depends on the properties of the reflector as well as the panel-reflector separation. In case of a bifacial panel parallel to the reflector, the maximum power is obtained at 115 mm separation from reflector and 10° slope. PV cell separation higher than 250 mm from a diffused reflector led to higher solar radiation loss, where the electrical energy produced by the front surface plays the dominant role. Integrating an external reflector with the bifacial solar panel increases the total panel power production for a semimirror type and a diffuse type reflector by 20% and 15%, respectively.

## References

- [1] A. Fahrenbruch and R. H. Bube, *Fundamentals of Solar Cells*, 1983.
- [2] A. Luque, A. Cuevas, and J. M. Ruiz, "Double-sided n<sup>+</sup>-p-n<sup>+</sup> solar cell for bifacial concentration," *Solar Cells*, vol. 2, no. 2, pp. 151–166, 1980.
- [3] A. Hubner, A. G. Aberle, and R. Hezel, "Temperature behavior of monofacial and bifacial silicon solar cells," in *Proceedings of the 26th IEEE Photovoltaic Specialists Conference (PVSC '97)*, pp. 223–226, IEEE, Anaheim, Calif, USA, September–October 1997.
- [4] R. Hezel, "Novel applications of bifacial solar cells," *Progress in Photovoltaics*, vol. 11, no. 8, pp. 549–556, 2003.
- [5] M. Libra and V. Poulek, "A very simple solar tracker for space and terrestrial applications," *Solar Energy Materials and Solar Cells*, vol. 60, no. 2, pp. 99–103, 2000.
- [6] T. Uematsu, K. Tsutsui, Y. Yazawa et al., "Development of bifacial PV cells for new applications of flat-plate modules," *Solar Energy Materials and Solar Cells*, vol. 75, no. 3–4, pp. 557–566, 2003.
- [7] T. Joge, Y. Eguchi, Y. Imazu, I. Araki, T. Uematsu, and K. Matsukuma, "Applications and field tests of bifacial solar modules," in *Proceedings of the 29th IEEE Photovoltaic Specialists Conference*, pp. 1549–1552, May 2002.
- [8] K. J. Weber, V. Everett, P. N. K. Deenapanray, E. Franklin, and A. W. Blakers, "Modeling of static concentrator modules incorporating lambertian or v-groove rear reflectors," *Solar Energy Materials and Solar Cells*, vol. 90, no. 12, pp. 1741–1749, 2006.
- [9] M. L. Vladislav Poulek and I. Persic, "Bifacial tracking concentrator TRAXLE 5X," in *Proceedings of the 2nd International Workshop on Concentrating Photovoltaic Powerplant: Optical Design and Grid Connection*, 2009.
- [10] E. Ruiz-Vasquez, B. Robles-Ocampo, H. Canseco-Sánchez et al., "Photovoltaic/thermal solar hybrid system with bifacial PV module and transparent plane collector," *Solar Energy Materials and Solar Cells*, vol. 91, no. 20, pp. 1966–1971, 2007.
- [11] M. Brogren and B. Karlsson, "Low-concentrating water-cooled PV-thermal hybrid systems for high latitudes," in *Proceedings of the 29th IEEE Photovoltaic Specialists Conference*, pp. 1733–1736, May 2002.
- [12] U. Ortabasi, K. Firor, and M. Ilyin, "Low concentration photovoltaic module design using bifacial solar cells," in *Proceedings of the 20th IEEE Photovoltaic Specialists Conference*, pp. 1324–1326, September 1988.
- [13] U. Ortabasi, "Performance of a 2X cusp concentrator PV module using bifacial solar cells," in *Proceedings of the 26th IEEE Photovoltaic Specialist Conference (PVSC '97)*, Anaheim, Calif, USA, September–October 1997.
- [14] T. Uematsu, Y. Yazawa, K. Tsutsui et al., "Design and characterization of flat-plate static-concentrator photovoltaic modules," *Solar Energy Materials and Solar Cells*, vol. 67, no. 1–4, pp. 441–448, 2001.
- [15] A. Moehlecke, I. Zanesco, A. C. Pan, T. C. Severo, and A. P. Mallmann, "Photovoltaic module with coloured diffuse reflectors," in *Proceedings of the European Photovoltaic Solar Energy Conference*, pp. 785–787, Munich, Germany, 2001.
- [16] C. Duran, H. Deuser, R. Harney, and T. Buck, "Approaches to an improved IV and QE characterization of bifacial silicon solar cells and the prediction of their module performance," *Energy Procedia*, vol. 8, pp. 88–93, 2011.

## Research Article

# Organic Photovoltaic Cells Based on PbPc Nanocolumns Prepared by Glancing Angle Deposition

Yang Liu, Fujun Zhang, and Jian Wang

Key Laboratory of Luminescence and Optical Information, Ministry of Education, Beijing Jiaotong University, Beijing 100044, China

Correspondence should be addressed to Fujun Zhang; fjzhang@bjtu.edu.cn

Received 24 January 2013; Accepted 14 March 2013

Academic Editor: Sudhakar Shet

Copyright © 2013 Yang Liu et al. This is an open access article distributed under the Creative Commons Attribution License, which permits unrestricted use, distribution, and reproduction in any medium, provided the original work is properly cited.

Organic small material lead phthalocyanine (PbPc) nanocolumns were prepared via glancing angle deposition (GLAD) on indium tin oxide (ITO) coated glass substrates. Organic electron acceptor materials fullerene ( $C_{60}$ ) was evaporated onto the nanocolumn PbPc thin films to prepare heterojunction structure ITO/PbPc/ $C_{60}$ /Bphen/Al organic photovoltaic cells (OPVs). It is worthwhile to mention that  $C_{60}$  molecules firstly fill the voids between PbPc nanocolumns and then form impact  $C_{60}$  layer. The interpenetrating electron donor/acceptor structure effectively enhances interface between electron donor and electron acceptor, which is beneficial to exciton dissociation. The short circuit current density ( $J_{sc}$ ) of organic photovoltaic devices (OPVs) based on PbPc nanocolumn was increased from 1.19 mA/cm<sup>2</sup> to 1.74 mA/cm<sup>2</sup>, which should be attributed to the increase of interface between donor and acceptor. The effect of illumination intensity on the performance of OPVs was investigated by controlling the distance between light source and sample, and the  $J_{sc}$  of two kind of OPVs was increased along with the increase of illumination intensity.

## 1. Introduction

Organic photovoltaic devices (OPVs) are potential candidates for light weight, low-cost solar energy conversion, and ease of processing [1–4]. Typical OPVs are composed of a donor (p-type semiconductor) and an acceptor (n-type semiconductor) as active layers. Photo-generated excitons are dissociated into free holes and electrons at the interface of donor-acceptor, the free charge carriers are collected by the electrodes, respectively. Two kinds of architectures with this D-A interface were developed: planar heterojunction (PHJ) and bulk heterojunction (BHJ) [5, 6]. Tang firstly reported PHJ devices based on CuPc/ $C_{60}$  as the active layer, which was considered as a milestone of OPVs development [7]. The efficiency of exciton dissociation of the PHJ cell is decreased due to the limit of the D-A interface. Some photo-generated excitons in the active layers maybe quenched when travelling a distance longer than the diffusion length to the D-A interface. The exciton dissociation efficiency could be increased in the BHJ cells, where the donor and acceptor form an interpenetrating network of structures which shortens the excitons' route to the D-A interface. However, random distribution of donor and acceptor materials in the blend

film may lead to lower charge collection due to the so-called dead ends in the conducting paths and long conducting distance from the active layers to the electrodes [4, 8]. Therefore, the key point to enhance the PCE is to form the structure which provides high interface area and good charge transport routes in the active layer. Knorr and Hoffman firstly discovered a new kind of evaporation technology, named as glancing angle deposition (GLAD). The morphology and microstructure of this kind of films prepared by GLAD could be easily controlled by changing the substrate rotating speed, the evaporation speed, the distance between substrate and evaporation source, the angle between incoming incidence flux, and the substrate surface [9–13]. Van Dijken et al. applied the GLAD technology to fabricate donor layer and then spin-coated acceptor solution onto the nanostructure donor layer for achieving a mixed heterojunction OPVs, which shows a better performance than the common bilayer heterojunction OPV [14–16]. Also this approach has been used to fabricate nanocolumn structural thin films for indium tin oxide (ITO) electrodes [17] and electron acceptor material  $C_{60}$  [18, 19], providing large interfacial area for exciton extraction and charge carrier collection. Hoppe et al. pointed out that only

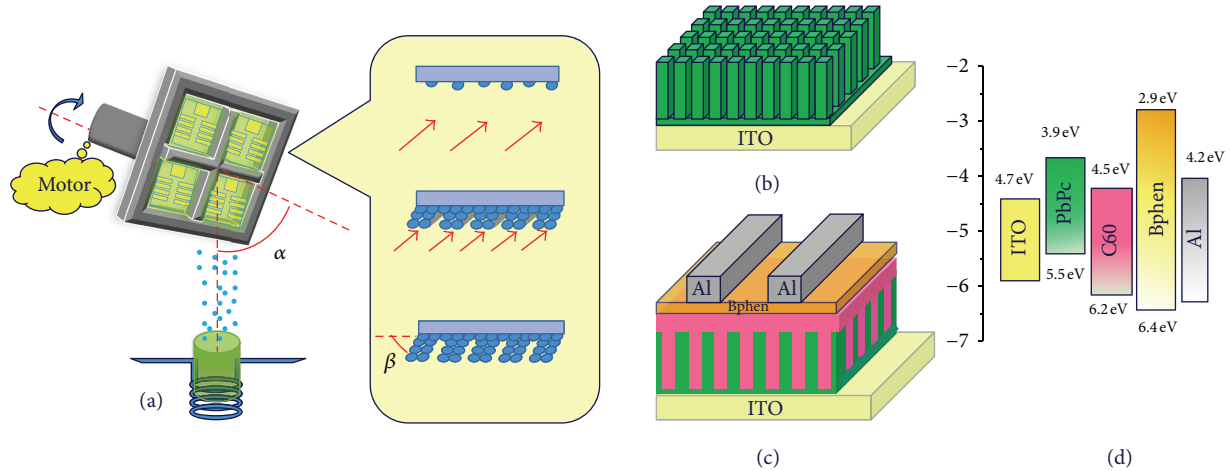


FIGURE 1: (a) Schematic diagram of GLAD installation, (b) schematic diagram of PbPc nanocolumn, (c) schematic OPV device architecture (ITO/PbPc/C<sub>60</sub>/Bphen/Al), and (d) energy level configuration of the used materials.

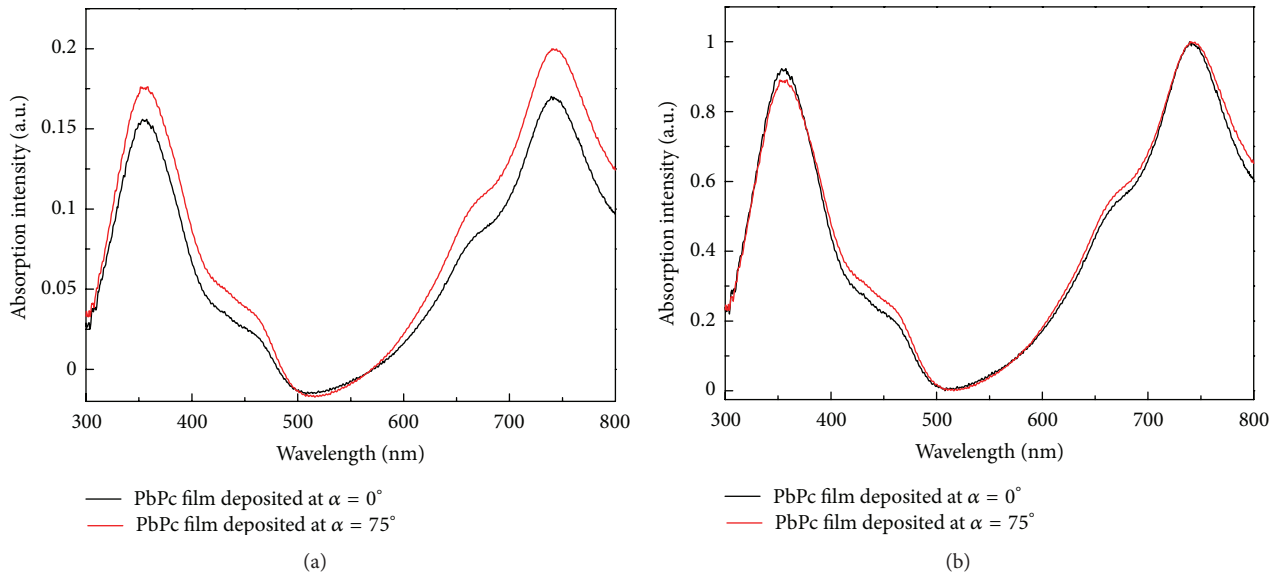


FIGURE 2: (a) The absorption spectra of PbPc films prepared by normal conditions and glancing angle deposition at 75°, (b) the normalized absorption spectra.

30% of the photons in the whole solar spectrum have energy higher than 1.9 eV [20]. Lead phthalocyanine (PbPc), as a promising small molecule donor material, has attracted more and more attention due to its near infrared absorption [21]. Organic electron acceptor materials fullerene (C<sub>60</sub>) is a proper matching for PbPc to form the heterojunction.

In this paper, two kinds of OPVs with different morphology PbPc films as the donor layer and C<sub>60</sub> films as the acceptor layer were fabricated and measured under different illumination intensities. The OPVs with PbPc films prepared by GLAD show better performance compared with the OPVs based on PbPc films prepared under normal conditions. The underlying reason for the improvement of OPVs performance was discussed from the effect of PbPc film morphology on the absorption spectra and donor/acceptor interfaces.

## 2. Experimental Details

Indium tin oxide (ITO) coated glass substrates with a sheet resistance of 15 Ω/□ (purchased from Shenzhen Jinghua Displays Co. Ltd.) were cleaned with detergent, deionized water and ethanol successively in ultrasonic baths for 15 min. All substrates were dried by nitrogen gas and were treated by UV-ozone for 10 min to improve the work function of ITO. Electron donor material PbPc (purchased from Jilin Optical and Electronic Materials Co., Ltd.) was deposited on the ITO substrates via GLAD. A computer-controlled stepper motor was used to control rotation of substrate about the substrate surface normal. The angle between the molecular flux incidence and the substrate normal was set to 75° and 0°. The substrate rotation rate was controlled about 6

rounds per minute (rpm). The deposition rate was about 0.1 ~ 0.3 nm/s, which was monitored by quartz-crystal oscillator monitor. Electron acceptor material  $C_{60}$  (purchased from Alfa Aesar) films and hole blocking material 4,7-diphenyl-1, 10-phenanthroline (Bphen, purchased from Jilin OLED Material Tech Co., Ltd) films were deposited by thermal evaporation under  $4 \times 10^{-4}$  Pa vacuum conditions successively. Al cathode of 100 nm thickness was thermally evaporated on the hole blocking layer through shadow masks. The active area of the cells was  $3 \times 3$  mm<sup>2</sup>. The schematic diagram of GLAD installation is shown in Figure 1(a) (left side): the angle between substrate normal and the incoming particle flux is defined as  $\alpha$ , and the angle between PbPc nanocolumns and substrate surface normal is defined as  $\beta$ . The schematic process of GLAD is presented in Figure 1(a) (right side): (i) a few PbPc particles arrive at the substrate at first and form some islands on the surface, (ii) the former islands block the incoming particles resulting in selective growth along the island due to the shadow effect, (iii) formed column structure. The schematic diagram of PbPc nanocolumn films and OPVs are shown in Figures 1(b) and 1(c). The energy level alignment of used materials is shown in Figure 1(d).

Morphology of PbPc films was investigated by a Hitachi S-4800 scanning electron microscope (SEM) with a secondary electron detector. The absorption spectra of films were measured via Shimadzu UV-3101PC UV-VIS. Current-voltage ( $I$ - $V$ ) curves of fabricated OPVs were measured by Keithley 4200 source measure unit under 100 mW/cm<sup>2</sup> illumination or dark conditions.

### 3. Results and Discussions

The absorption spectra of PbPc films under different preparation conditions were measured and are shown in Figure 2(a). The absorption spectrum of PbPc film prepared under normal conditions (titled angle is 0°) shows two broader absorption peaks, one at around 515 nm and the other at 350 nm, which accords with previously observed results [22]. The absorption spectrum of PbPc thin films prepared by GLAD with the tilted angle 75° is similar with that of PbPc thin film prepared under normal conditions. In order to investigate the effect of film prepared conditions on its absorption performance, the normalized absorption spectra are shown in Figure 2(b). It is worthwhile to mention that PbPc thin films prepared by GLAD have slightly strong absorption from 400 nm to 480 nm, comparing with that of PbPc films prepared under normal conditions, which should be attributed to the increased  $J_{sc}$  of OPVs (as shown in Figure 3).

Two kinds of bilayer heterojunction OPVs with different structural PbPc films as the electron donor layers were prepared, Cells A: ITO/PbPc (40 nm, prepared under normal conditions)/ $C_{60}$  (50 nm)/Bphen (8 nm)/Al (100 nm), Cells B: ITO/PbPc (40 nm, prepared by GLAD)/ $C_{60}$  (50 nm)/Bphen (8 nm)/Al (100 nm). The 8 nm Bphen layer was used as hole-blocking layer and protection layer for the active layer during metal deposition. The  $J$ - $V$  characteristics of two kinds of OPVs were measured at 100 mW/m<sup>2</sup> illumination and in dark conditions, as shown in Figure 3. The  $J_{sc}$  of Cells B is

TABLE 1: Key parameters of two kinds of OPVs under 100 mW/cm<sup>2</sup> illumination intensity.

	$J_{sc}$ (mA/cm <sup>2</sup> )	$V_{oc}$ (V)	FF (%)	PCE (%)
Cells A	1.19	0.40	35.4	0.16
Cells B	1.74	0.34	35.95	0.21

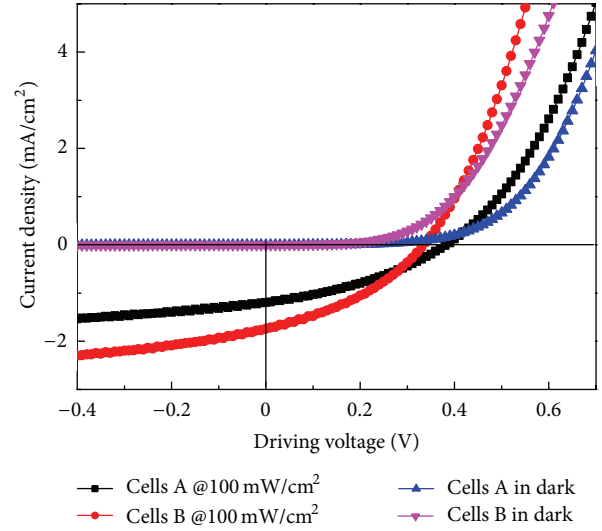


FIGURE 3:  $J$ - $V$  characteristics of two kinds of OPVs under 100 mW/cm<sup>2</sup> illumination intensity and in dark conditions.

about 1.5 times larger than that of Cells A, which may be attributed to the increase of absorption and donor/acceptor interface induced by PbPc nanocolumn structure prepared by GLAD. The open-circuit voltage ( $V_{oc}$ ) of the Cells B is about 0.34 V and lower than that (0.4 V) of Cells A, which may be induced by the leakage current of Cells B resulting from the interface between PbPc layer and ITO. According to the dark  $J$ - $V$  characteristics curves of two kinds of cells, it is apparent that both kinds of cells have good blocking characteristics in the reverse bias region, the Cells B have a lower break-over voltage in forward bias region. The power conversion efficiency (PCE) of Cells B is about 0.21%, which is larger than that (0.16%) of Cells A. The key parameters, including  $V_{oc}$ ,  $J_{sc}$ , FF and PCE of the two kinds of OPV cells are summarized in Table 1.

In order to further investigate the effect of PbPc film morphology on the performance of OPVs, the  $J$ - $V$  characteristic curves were measured under different illumination intensities. Figure 4(a) shows the  $J$ - $V$  characteristic curves of Cells A; Figure 4(b) shows the  $J$ - $V$  characteristic curves of Cells B. Both kinds of OPVs also show similar behaviors dependent on the illumination intensity. The  $J_{sc}$  is increased along with the increase of illumination intensity, and  $V_{oc}$  keeps constant under different illumination intensities. It is known that photogenerated excitons strongly depend on the incident photon numbers, which have enough energy to excite active layer materials [23, 24]. The increased  $J_{sc}$  should be well understood due to more photo-generated excitons under higher illumination intensity. It is known that  $V_{oc}$  is

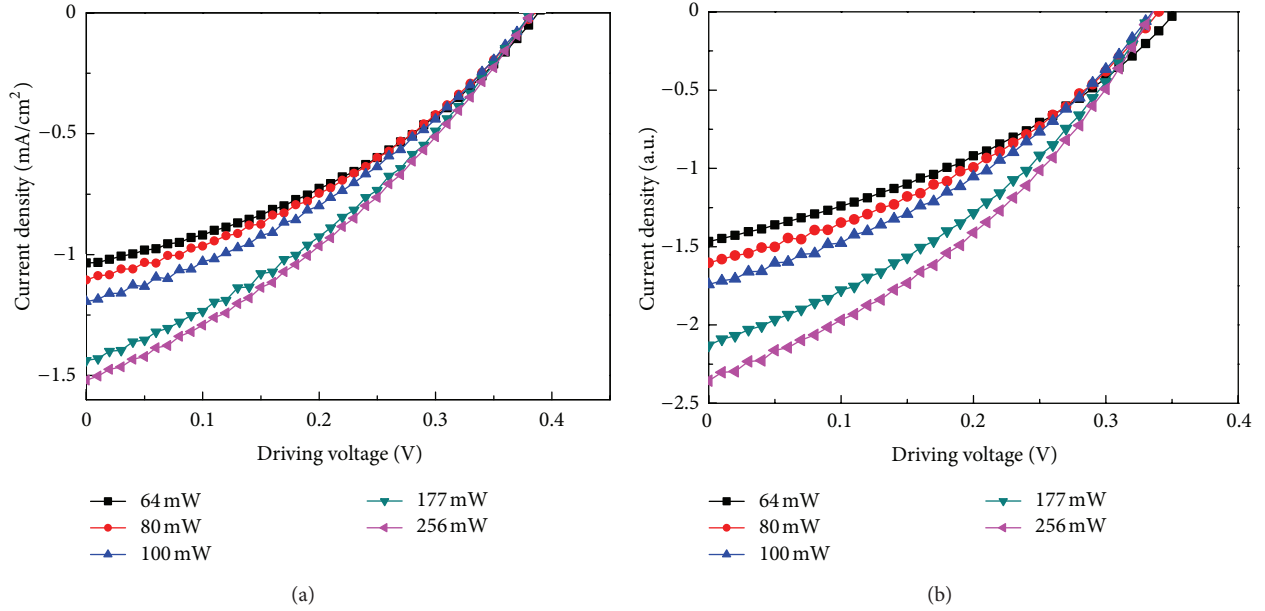


FIGURE 4:  $J$ - $V$  characteristics of two kinds of OPVs under different illumination intensities, (a) PbPc films prepared under normal conditions; (b) PbPc films prepared by GLAD.

TABLE 2: OPVs parameters of Cells A prepared under normal condition under different illumination intensities.

Input power	$J_{sc}$ (mA/cm <sup>2</sup> )	$V_{oc}$ (V)	FF (%)	PCE (%)
64 mW	1.03	0.4	37.6	0.23
80 mW	1.11	0.4	35.8	0.19
100 mW	1.19	0.4	35.4	0.16
177 mW	1.44	0.4	34.1	0.11
256 mW	1.52	0.4	33.5	0.08

determined by the difference between the highest occupied molecular orbital (HOMO) of the donor and the lowest unoccupied molecular orbital (LUMO) of the acceptor [25]. However, the large input power also increases the active layer temperature, which may induce exciton quenched in organic materials [26]. The exciton dissociation and quenching are two competitive processes, which codetermine PCE of OPVs. According to the data summarized in Tables 2 and 3, the PCE of OPVs is decreased along with the increase of illumination intensity. It means that more photo-generated excitons were quenched under higher illumination intensity, which results in the decrease of PCE. The key parameters of two kinds of OPVs are summarized in Tables 2 and 3.

From the variation of two kinds of cells' photovoltaic characteristic of OPVs, PbPc films prepared by GLAD have a positive effect on the performance of OPVs. In order to clarify the positive effect, the morphology of PbPc films prepared by normal conditions and GLAD were investigated by SEM, as shown in Figure 5. From the SEM images of Figures 5(a) and 5(b), the surface of PbPc films prepared by GLAD shows some small holes, and PbPc films prepared

TABLE 3: OPVs parameters of Cells B prepared by GLAD under different illumination intensities.

Input power	$J_{sc}$ (mA/cm <sup>2</sup> )	$V_{oc}$ (V)	FF (%)	PCE (%)
64 mW	1.47	0.35	36.40	0.30
80 mW	1.60	0.34	36.34	0.25
100 mW	1.74	0.34	35.95	0.21
177 mW	2.13	0.34	35.69	0.15
256 mW	2.36	0.34	35.34	0.11

under normal conditions look more smooth. According to Figures 5(c) and 5(d), the surface roughness of PbPc films prepared by GLAD should be larger than that of PbPc films prepared by normal condition. The similar experimental phenomenon was observed in our pervious experimental results [27, 28]. The dynamic growth process of PbPc films is described by shadow effect and atomic surface diffusion. Shadow effect implies that one given point on the surface can receive fewer particles than other points, because nearby surface features block some of the incoming particles, which results in tilted nanocolumns on the substrates [29]. Atomic scale fluctuations inevitably exist on the nominally smooth surfaces. PbPc particles arrive at the top of the surface and will migrate to other points due to their kinetic energy, leading to a smooth surface. The competition between these two factors strongly determines the morphological evolution of the growing surface. The schematic growth process is shown in Figure 1(b).

During the glancing angle deposition process, the angle ( $\beta$ ) between PbPc nanocolumns and substrate surface normal strongly depends on the angle ( $\alpha$ ) between substrate surface normal and the incoming particle flux. The angle  $\beta$  is not simply proportional to the cosine of the tilted angle  $\alpha$ , which

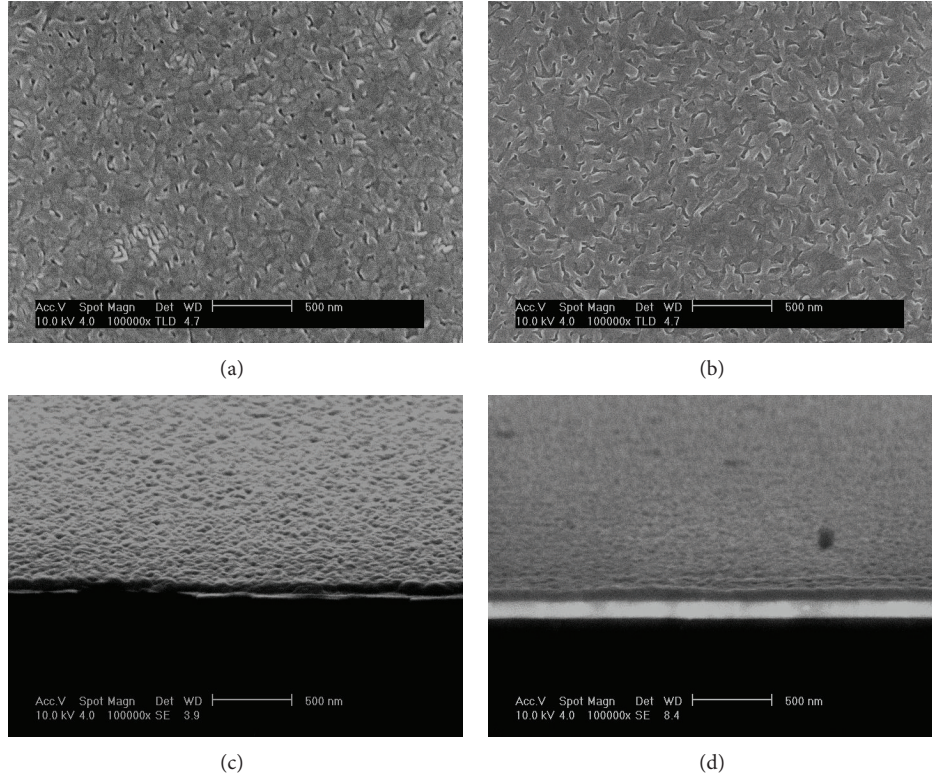


FIGURE 5: (a) SEM images of PbPc films prepared by GLAD at  $\alpha = 75^\circ$ , (b) SEM images of PbPc films prepared under normal conditions, (c) the side views of PbPc films prepared by GLAD at  $\alpha = 75^\circ$ , (d) the side views of PbPc films prepared under normal conditions.

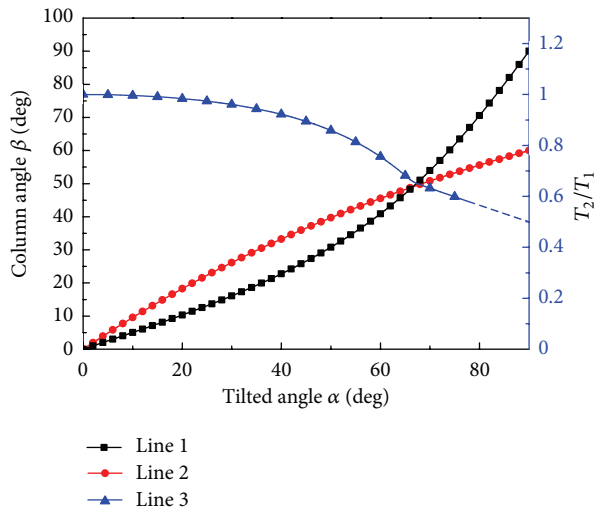


FIGURE 6: The relationship between column angle and the tilted angle, the blue line shows the ratio of actual film thickness to the thickness monitored by quartz-crystal oscillator monitor.

is given by the following formulas: (i) tangent rule ( $\tan \beta = 0.5 \tan \alpha$ ,  $\alpha < 70^\circ$ ) described by line 1 in Figure 6 and (ii) cosine rule ( $2 \sin(\alpha - \beta) = 1 - \cos \alpha$ ,  $\alpha > 70^\circ$ ), described by line 2 in Figure 6 [30]. In this work,  $\alpha$  was set to  $75^\circ$ , therefore column angle  $\beta$  was measured by formula

(II) resulting in  $45^\circ$ . In terms of the thickness of PbPc film, the actual thickness of PbPc film is defined as  $T_1$ , and the evaporation thickness monitored by quartz-crystal oscillator monitor is  $T_2$ . The relationship of the two parameters could be expressed as  $T_1 = T_2 \cos \beta$ , described by line 3 in Figure 6. In the Cells A, the thicknesses of the PbPc films prepared under normal conditions are 40 nm. For keeping PbPc films thickness constant in the two kinds of Cells, the evaporation thickness ( $T_2$ ) monitored by quartz-crystal oscillator monitor was controlled about 56.5 nm, which could keep the factual PbPc films thickness ( $T_1$ ) at 40 nm. The PbPc films prepared by GLAD show nanocolumn structures, which could increase the interfaces with  $C_{60}$ , resulting in more exciton dissociation. The PbPc nanocolumn also provides an effective charge carrier transporting road, which is beneficial to the charge carrier collection by their individual cathodes.

#### 4. Conclusion

Two kinds of OPVs based on different morphology PbPc film prepared under normal conditions or glancing angle deposition were fabricated; the OPVs based on PbPc nanocolumn prepared by GLAD obtain a larger PCE compared with OPVs based on PbPc film prepared under normal conditions. The main contribution for the increase of PCE should be due to the enhanced absorption and enlarger interface between PbPc and  $C_{60}$  layer. The effect of illumination intensity on the performance of OPVs was investigated by controlling the

distance between light source and sample, the  $J_{sc}$  of two kind of OPVs was increased along with the increase of illumination intensity.

## Acknowledgments

The authors express their thanks to the Beijing Natural Science Foundation (2122050) and Basic Research Foundation of the Central Universities (2013JBZ004). The authors also thank the supports on using synchrotron radiation light from the Beijing Synchrotron Radiation Facility. F. J. Zhang thanks the support from the State Key Laboratory of Catalysis and the Key Laboratory of Photochemical Conversion and Optoelectronic Materials, TIPC, CAS.

## References

- [1] H. Y. Chen, J. Hou, S. Zhang et al., "Polymer solar cells with enhanced open-circuit voltage and efficiency," *Nature Photonics*, vol. 3, no. 11, pp. 649–653, 2009.
- [2] Y. K. Jin, K. Lee, N. E. Coates et al., "Efficient tandem polymer solar cells fabricated by all-solution processing," *Science*, vol. 317, no. 5835, pp. 222–225, 2007.
- [3] T. D. Nielsen, C. Cruickshank, S. Foged, J. Thorsen, and F. C. Krebs, "Business, market and intellectual property analysis of polymer solar cells," *Solar Energy Materials and Solar Cells*, vol. 94, no. 10, pp. 1553–1571, 2010.
- [4] F. Yang, M. Shtein, and S. R. Forrest, "Controlled growth of a molecular bulk heterojunction photovoltaic cell," *Nature Materials*, vol. 4, no. 1, pp. 37–41, 2005.
- [5] F. J. Zhang, X. W. Xu, W. H. Tang et al., "Recent development of the inverted configuration organic solar cells," *Solar Energy Materials and Solar Cells*, vol. 95, no. 7, pp. 1785–1799, 2011.
- [6] Z. L. Zhuo, F. J. Zhang, J. Wang et al., "Efficiency improvement of polymer solar cells by iodine doping," *Solid-State Electronics*, vol. 63, pp. 83–88, 2011.
- [7] C. W. Tang, "Two-layer organic photovoltaic cell," *Applied Physics Letters*, vol. 48, no. 2, pp. 183–185, 1986.
- [8] S. Yu, C. Klimm, P. Schäfer, J. P. Rabe, B. Rech, and N. Koch, "Organic photovoltaic cells with interdigitated structures based on pentacene nanocolumn arrays," *Organic Electronics*, vol. 12, no. 12, pp. 2180–2184, 2011.
- [9] T. G. Knorr and R. W. Hoffman, "Dependence of geometric magnetic anisotropy in thin iron films," *Physical Review*, vol. 113, no. 4, pp. 1039–1046, 1959.
- [10] M. O. Jensen and M. J. Brett, "Porosity engineering in glancing angle deposition thin films," *Applied Physics A*, vol. 80, no. 4, pp. 763–768, 2005.
- [11] M. M. Hawkeye and M. J. Brett, "Glancing angle deposition: fabrication, properties, and applications of micro- and nanostructured thin films," *Journal of Vacuum Science and Technology A*, vol. 25, no. 5, pp. 1317–1335, 2007.
- [12] K. Robbie and M. J. Brett, "Sculptured thin films and glancing angle deposition: growth mechanics and applications," *Journal of Vacuum Science and Technology A*, vol. 15, no. 3, pp. 1460–1465, 1997.
- [13] K. Robbie, M. J. Brett, and A. Lakhtakia, "Chiral sculptured thin films," *Nature*, vol. 384, p. 616, 1996.
- [14] J. van Dijken, M. Fleischauer, and M. J. Brett, "Morphology control of CuPc thin films using Glancing Angle Deposition," in *Proceedings of the 33rd IEEE Photovoltaic Specialists Conference (PVSC '08)*, pp. 1–4, IEEE, 2008.
- [15] J. G. van Dijken, M. D. Fleischauer, and M. J. Brett, "Controlled nanostructuring of CuPc thin films via glancing angle deposition for idealized organic photovoltaic architectures," *Journal of Materials Chemistry*, vol. 21, no. 4, pp. 1013–1019, 2011.
- [16] J. G. van Dijken, M. D. Fleischauer, and M. J. Brett, "Solvent effects on ZnPc thin films and their role in fabrication of nanostructured organic solar cells," *Organic Electronics*, vol. 12, no. 12, pp. 2111–2119, 2011.
- [17] D. A. Rider, R. T. Tucker, B. J. Worfolk et al., "Indium tin oxide nanopillar electrodes in polymer/fullerene solar cells," *Nanotechnology*, vol. 22, no. 8, Article ID 085706, 2011.
- [18] M. Thomas, W. Li, Z. S. Bo, and M. J. Brett, "Inverted photovoltaic cells of nanocolumnar  $C_{60}$  filled with solution processed small molecule 3-Q," *Organic Electronics*, vol. 13, no. 11, pp. 2647–2652, 2012.
- [19] M. Thomas, B. J. Worfolk, D. A. Rider, M. T. Taschuk, J. M. Buriak, and M. J. Brett, " $C_{60}$  fullerene nanocolumns-polythiophene heterojunctions for inverted organic photovoltaic cells," *ACS Applied Materials & Interfaces*, vol. 3, no. 6, pp. 1887–1894, 2011.
- [20] H. Hoppe, M. Niggemann, C. Winder et al., "Nanoscale morphology of conjugated polymer/fullerene-based bulk-heterojunction solar cells," *Advanced Functional Materials*, vol. 14, no. 10, pp. 1005–1011, 2004.
- [21] H. S. Shim, H. J. Kim, J. W. Kim et al., "Enhancement of near-infrared absorption with high fill factor in lead phthalocyanine-based organic solar cells," *Journal of Materials Chemistry*, vol. 22, pp. 9077–9081, 2012.
- [22] W. Zhao, "Enhancing photovoltaic response of organic solar cells using a crystalline molecular template," *Organic Electronics*, vol. 13, no. 1, pp. 129–135, 2012.
- [23] P. Kumar, S. C. Jain, H. Kumar, S. Chand, and V. Kumar, "Effect of illumination intensity and temperature on open circuit voltage in organic solar cells," *Applied Physics Letters*, vol. 94, no. 18, Article ID 183505, 3 pages, 2009.
- [24] F. J. Zhang, F. Y. Sun, Y. Z. Shi et al., "Effect of an ultra-thin molybdenum trioxide layer and illumination intensity on the performance of organic photovoltaic devices," *Energy and Fuels*, vol. 24, no. 7, pp. 3739–3742, 2010.
- [25] C. J. Brabec, A. Cravino, D. Meissner et al., "The influence of materials work function on the open circuit voltage of plastic solar cells," *Thin Solid Films*, vol. 403–404, pp. 368–372, 2002.
- [26] V. Podzorov, E. Menard, J. A. Rogers, and M. E. Gershenson, "Hall effect in the accumulation layers on the surface of organic semiconductors," *Physical Review Letters*, vol. 95, no. 22, Article ID 226601, pp. 1–4, 2005.
- [27] L. F. Lu, Z. Xu, F. J. Zhang et al., "Preparation and transmissivity of ZnS nanocolumn thin films with glancing angle deposition technology," *Spectroscopy and Spectral Analysis*, vol. 30, no. 2, pp. 504–507, 2010.
- [28] L. F. Lu, Z. Xu, F. J. Zhang et al., "Using ZnS nanostructured thin films to enhance light extraction from organic light-emitting diodes," *Energy and Fuels*, vol. 24, no. 7, pp. 3743–3747, 2010.
- [29] A. Amassian, K. Kaminska, M. Suzuki, L. Martinu, and K. Robbie, "Onset of shadowing-dominated growth in glancing angle deposition," *Applied Physics Letters*, vol. 91, no. 17, Article ID 173114, 3 pages, 2007.
- [30] X. Xiao, G. Dong, C. Xu et al., "Structure and optical properties of  $Nb_2O_5$  sculptured thin films by glancing angle deposition," *Applied Surface Science*, vol. 255, no. 5, pp. 2192–2195, 2008.

## Research Article

# p-Type Quasi-Mono Silicon Solar Cell Fabricated by Ion Implantation

Chien-Ming Lee,<sup>1</sup> Sheng-Po Chang,<sup>1</sup> Shoou-Jinn Chang,<sup>1</sup> and Ching-In Wu<sup>2</sup>

<sup>1</sup> Institute of Microelectronics & Department of Electrical Engineering, Center for Micro/Nano Science and Technology, Advanced Optoelectronic Technology Center, National Cheng Kung University, Tainan 70101, Taiwan

<sup>2</sup> Inventec Solar Energy Corporation, Taoyuan 335, Taiwan

Correspondence should be addressed to Sheng-Po Chang; changsp@mail.ncku.edu.tw

Received 2 January 2013; Revised 3 March 2013; Accepted 13 March 2013

Academic Editor: Peter Rupnowski

Copyright © 2013 Chien-Ming Lee et al. This is an open access article distributed under the Creative Commons Attribution License, which permits unrestricted use, distribution, and reproduction in any medium, provided the original work is properly cited.

The p-type quasi-mono wafer is a novel type of silicon material that is processed using a seed directional solidification technique. This material is a promising alternative to traditional high-cost Czochralski (CZ) and float-zone (FZ) material. Here, we evaluate the application of an advanced solar cell process featuring a novel method of ion implantation on p-type quasi-mono silicon wafer. The ion implantation process has simplified the normal industrial process flow by eliminating two process steps: the removal of phosphosilicate glass (PSG) and the junction isolation process that is required after the conventional thermal POCl<sub>3</sub> diffusion process. Moreover, the good passivation performance of the ion implantation process improves  $V_{oc}$ . Our results show that, after metallization and cofiring, an average cell efficiency of 18.55% can be achieved using 156 × 156 mm p-type quasi-mono silicon wafer. Furthermore, the absolute cell efficiency obtained using this method is 0.47% higher than that for the traditional POCl<sub>3</sub> diffusion process.

## 1. Introduction

The photovoltaic (PV) industry has benefited from the policies of many successive governments that have offered incentives for power projects such as rooftop solar systems. The resulting increase in demand has grown the solar energy market by at least 20% per annum over the past ten years. The final target of the PV industry is the achievement of grid parity, and lowering manufacturing costs and increasing efficiency are very important steps in achieving this target. Reducing silicon bulk thickness and substituting alternative cheap materials are just two options available for lowering the initial cost of materials. In particular, reducing silicon bulk thickness will increase the amount of wafer per ingot or brick, thereby reducing the price per watt. However, this could produce a wafer handling issue, resulting in a higher wafer breakage rate during cell and module processing.

Substituting alternative cheap materials is one solution to reduce cost. Multicrystalline silicon (mc-Si) substrates have traditionally been used in industrial solar cells owing

to their relatively low cost, particularly compared to that of Czochralski (CZ) grown monocrystalline material. However, they can suffer from low efficiency due to defects attributed to grain boundaries. In this study, we use a p-type quasi-mono wafer as the starting material. Single-crystal silicon is produced according to a seed directional solidification technique [1] typically used for multicrystalline ingots. The p-type quasi-mono wafer produces higher cell efficiencies than those of multicrystalline silicon material with the same average minority carrier lifetime [1, 2].

Increasing solar cell efficiency will also leverage cost in the solar chain. Solar cell efficiency can be improved by various process methods, including metal-wrap-through (MWT) solar cells [3, 4], emitter-wrap-through (EWT) cells [5, 6], interdigitated backside contact (IBC) cells [7, 8], laser-fired contact cells [9, 10], and ion-implanted cells [11, 12]. Of these methods, ion implantation is one of the most attractive and cost-effective options.

In the present study, we substitute ion implantation for thermal POCl<sub>3</sub> diffusion in commercial silicon solar cells,

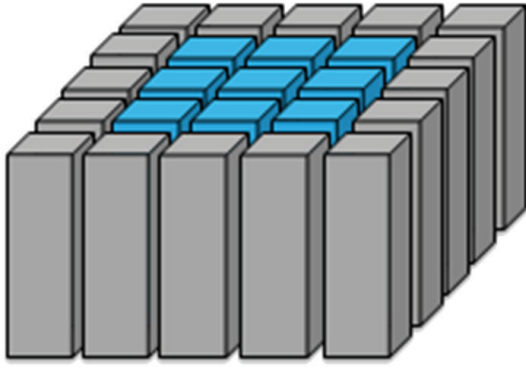


FIGURE 1: The distribution diagram for the 9 ingots used.

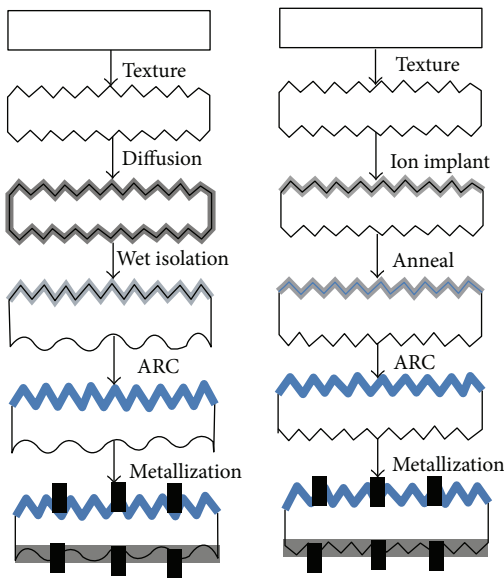


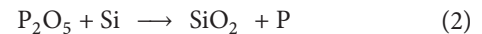
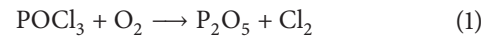
FIGURE 2: Process flow comparison of conventional and ion-implanted solar cell.

which allows us to eliminate two process steps: (1) phosphosilicate glass (PSG) removal and (2) parasitic junction isolation. In the conventional process, PSG is generated on the surface as a result of the reaction between phosphorous and oxygen during the thermal diffusion step. Accordingly, after thermal  $\text{POCl}_3$  diffusion, an isolation process is typically required to remove the PSG layer. Moreover, there are two ways to isolate the parasitic junction in the traditional process: wet isolation combined with a PSG clean step and laser isolation. However, both of these isolation processes result in a reduction of the area of the absorption surface; in particular, laser isolation damages the wafer surface and causes lower efficiency.

## 2. Experiment

Here, we used p-type quasi-mono silicon wafers (GCL-Poly Energy Holdings Limited) with resistivities of 0.5–3  $\Omega\text{cm}$ , thicknesses of 180–200  $\mu\text{m}$ , and dimensions of 156 × 156 mm.

A monocrystalline seed was placed at the bottom of a crucible, and polysilicon was then loaded on top of the seed. The underlying seed allowed quasi-mono silicon ingots to grow in the DS furnace. We selected 9 ingots from the center of the brick for use as starting material. These 9 ingots had more than 90% of their area oriented in the  $\langle 100 \rangle$  direction and less than 10% in other directions. We sliced the 9 ingots into wafers. Figure 1 illustrates the distribution of these 9 ingots within the brick. Figure 2 presents a comparison of the process flow for conventional thermal  $\text{POCl}_3$  diffusion with that for ion implantation on quasi-mono silicon wafers. Because the  $\langle 100 \rangle$  crystalline area constituted more than 90% of ingot area, an alkaline texturing method was used, and processing was conducted using a Rena alkaline machine. First, a saw damage removal step was required in order to reduce surface stress caused by the wire saw used. Wafers were dipped in a batch type system with Teflon material with a high KOH concentration (5.04 wt%) without IPA solution mixing for the saw damage removal process step. Then, anisotropic etching with a KOH : IPA :  $\text{H}_2\text{O}$  volume ratio of 1 : 1.6 : 34 was conducted to produce pyramids on the surface to absorb incoming light and increase the light path in the silicon bulk. In the commercial process, the next step would typically be thermal  $\text{POCl}_3$  diffusion to form a p-n junction. Here, a diffusion furnace (Tempress Systems, The Netherlands) was used to perform thermal  $\text{POCl}_3$  diffusion. Also, 400 wafers were placed vertically into a quartz boat; then, the boat was moved into a quartz tube and heated to 840°C. The dopant gas reacted with the silicon surface in the presence of  $\text{O}_2$  at high temperature, with the following reactions taking place:



In the ion implantation process, an inline high-throughput machine (>1000 pcs/hr) from Varian Semiconductor Equipment Associates (VSEA) was used to perform ion implantation. Ion dopant bombarded the wafer surface, subsequently penetrating into the wafer. We selected  $\text{PH}_3$  gas as the  $\text{P}^+$  ion source for implantation on the surface, with a low beam energy of 10 keV and a dose of  $3.0 \times 10^{15} \text{ P}^+/\text{cm}^2$ . However, crystal damage occurred during the ion bombardment procedure. Inclusion of a high-temperature annealing process step can recover this damage. A furnace tube from Tempress Systems was used for thermal annealing. In the annealing step, wafers were placed vertically into a quartz boat, and the boat was moved into a quartz tube. Dry oxide ( $\text{O}_2$ ) was passed into the tube, activating the dopant. Simultaneously, a thinner silicon oxide formed on the wafer surface according to the following reaction:



The dry oxide annealing step was conducted to activate the dopant and fabricate the junction. After annealing, the dopant concentration profile was different from that for  $\text{POCl}_3$  diffusion [13–16]. According to previous studies, the doping concentration profile of  $\text{POCl}_3$  typically ranges from



FIGURE 3: The appearance of quasi-mono silicon after texturing.

an error function complement (erfc) to a Gaussian distribution, with the peak dopant concentration occurring at the surface. Conversely, the profile for ion implantation occurs at a specific depth below the surface. Detailed discussions of these profiles can be found in previous studies [13–16].

After emitter formation, an isolation process was conducted to remove the parasitic junction caused by  $\text{POCl}_3$  diffusion during the industrial process flow. A chemical isolation process was performed with an inline roller type transportation system using the InOxSide instrument from Rena GmbH. In this process step, the parasitic junction was removed in an etching bath with  $\text{H}_2\text{O} : \text{HF} : \text{HNO}_3 : \text{H}_2\text{SO}_4$  volume ratio of 19 : 2 : 11 : 8.

After the isolation/annealing step,  $\text{SiN}_x$  layer was applied to act as an antireflection coating (ARC). Wafers were automatically placed into a batch type system machine from Centrotherm, and the layer was applied by direct plasma deposition. The  $\text{SiN}_x$  layer not only absorbs more light into silicon, but also passivates the silicon surface. Moreover, the thickness of silicon nitride used in the implantation process in the present study was thinner than that for the conventional  $\text{POCl}_3$  process owing to the thinner silicon oxide layer formed on the wafer surface during the annealing step in the ion implantation process.

After ARC deposition, a metal contact was formed by a Baccini belt type screen printing system and a Despatch cofiring system. During the screen printing process, frontside silver (Ag) paste, Dupont 17F, was printed on the frontside surface to form three bus bars and 83 finger lines. Dupont PV-157 was used as the backside Ag paste and Monocrystal RX-1203 as the backside aluminum (Al) paste.

Berger Lichttechnik single-pulse solar simulators were used to measure the basic parameters and  $I$ - $V$  curves of cells under standard test conditions (STCs): irradiance of  $1000 \text{ W/m}^2$ , the AM 1.5 solar spectrum, and temperature of  $25^\circ\text{C}$ . Electrical characteristics (including  $V_{\text{oc}}$ ,  $I_{\text{sc}}$ , FF,  $P_{\text{max}}$ , and cell efficiency) were obtained from the  $I$ - $V$  curves. The

shunt resistance  $R_{\text{sh}}$  was determined from the linear slope of the reverse dark current for each cell. The series resistance  $R_s$  was calculated from two  $I$ - $V$  curves measured at  $1000 \text{ W/m}^2$  and  $500 \text{ W/m}^2$ , according to IEC 891.

### 3. Results and Discussion

Here, we textured 2000 samples of p-type quasi-mono silicon simultaneously. Figure 3 shows the appearance of the quasi-mono silicon after texturing, illustrating the many different grains that appear on the surface. Figure 4 illustrates the pyramid topology revealed at different locations within the wafer for 30x (Figure 4(a)) and 550x (Figure 4(b)) SEM at the upper right of the wafer. Three different pyramid orientations are shown. Figures 4(c) and 4(d) also illustrate the pyramid topology for 95x and 350x SEM at the upper right of the wafer, respectively; these are clearly different from Figures 4(a) and 4(b). The figure indicates that quasi-mono silicon wafer exhibits a planar area after alkaline texturing. Figures 4(e) and 4(f) illustrate the pyramid topology for 30x and 550x SEM at the upper left of the wafer and indicate that scrapes have appeared on the quasi-mono silicon wafer. Such differences in topology can be seen clearly after alkaline texturing and are likely due to differences in grain boundaries.

After texturing, a Hitachi U-4100 UV-Vis-NIR spectrophotometer was used to measure the reflection. U-4100 has two light sources that can measure reflection at wavelengths of 240–2600 nm and an integrating sphere that can measure textured wafer. We selected 4 wafers randomly from each group and measured 5 points at 5 different locations within each wafer. Figure 5 illustrates a comparison of the reflection from these different locations after the alkaline texturing process.

As the figure shows, there are small differences in reflections between locations. This is likely due to the different pyramid topologies caused by different grain boundaries. To quantify the performance, we calculated the weighted reflectance  $R_w\%$  based on a previously published study [17] as follows:

$$R_w\% = \frac{\int_{\lambda_1}^{\lambda_2} F_i(\lambda) Q_i(\lambda) R(\lambda) d\lambda}{\int_{\lambda_1}^{\lambda_2} F_i(\lambda) Q_i(\lambda) d\lambda}, \quad (4)$$

where  $F_i(\lambda)$  is the photon flux and  $Q_i(\lambda)$  is the cell internal quantum efficiency [18, 19]. Table 1 presents a comparison of  $R_w\%$  for 5 different locations within the wafers and indicates that  $R_w\%$  is highest for the upper right location at 13.92%. This corresponds to an area with a shiny appearance caused by a different pyramid orientation and planar topology. Conversely, the lowest  $R_w\%$  (12.94%) was found for the center location and is thought to be due to the single-crystalline structure in the center.

After texturing, the next step in the ion implantation process was ion implantation itself. For this, 1600 wafers were automatically transferred into the chamber, and  $\text{P}^+$  ion sources were implanted onto the wafer surface from the ion source. Then, we divided the 1600 wafers into 4 groups, each with 400 wafers.

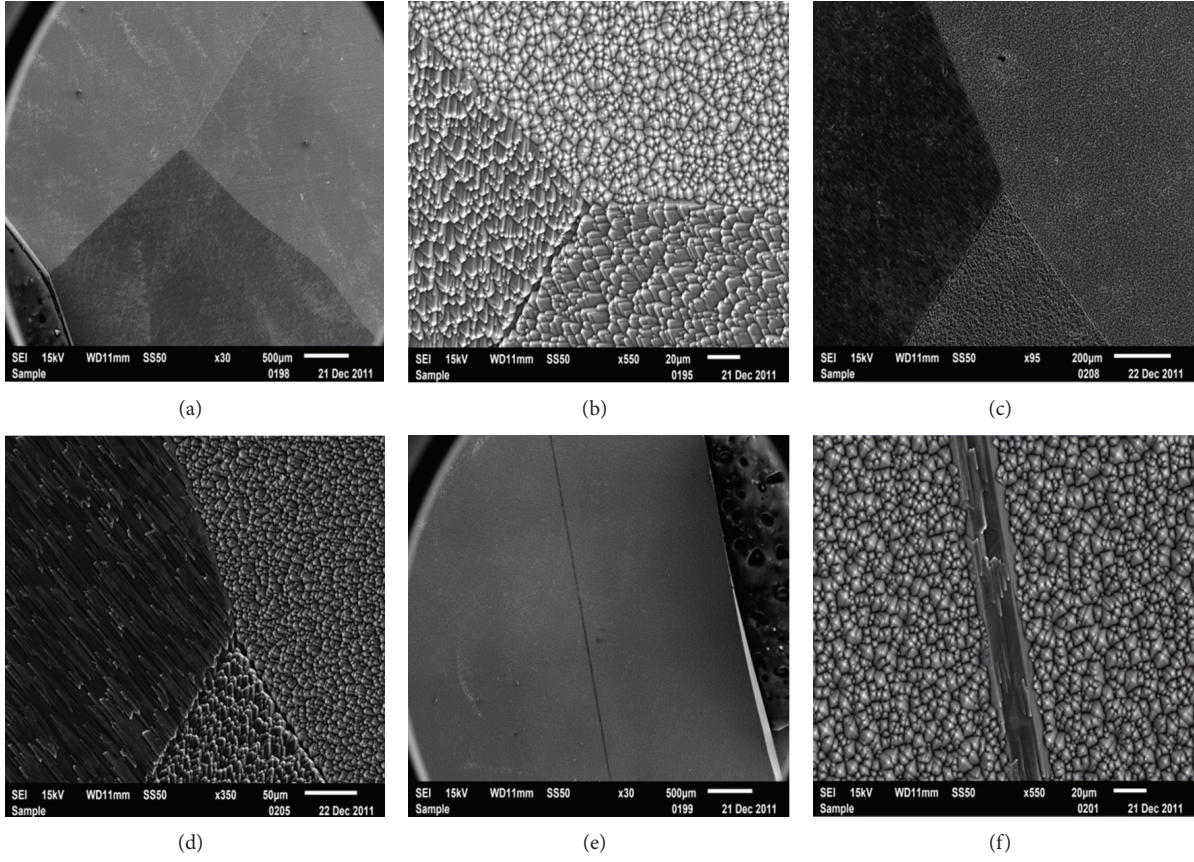


FIGURE 4: The pyramid topology shown by SEM at different locations within the wafer.

TABLE 1: Comparison of  $R_w\%$  of five different locations within the wafer.

Location	Centre	Upper right	Lower right	Upper left	Lower left
$R_w\%$	12.94	13.92	13.88	13.87	13.71

TABLE 2: Comparison of  $R_{sheet}$  and uniformity between  $POCl_3$  diffusion and 4 different anneal processes.

$R_{sheet}$ (ohm/sq)	Ave	MAX	MIN	Uniformity
$POCl_3$	64.68	67.53	61.32	4.80%
Anneal.810	70.02	73.08	68.96	2.94%
Anneal.840	65.47	67.14	63.31	2.93%
Anneal.870	61.39	63.07	59.65	2.79%
Anneal.900	57.13	59.41	56.98	2.13%

These 4 groups were processed at peak temperatures of 810, 840, 870, and 900°C during the subsequent annealing step. A four-point probe was used to measure the sheet resistance ( $R_{sheet}$ ). Table 2 presents a comparison of  $R_{sheet}$  and uniformity for  $POCl_3$  diffusion and the 4 different annealing processes; in particular, the table indicates that  $R_{sheet}$  decreased when the peak temperature was 810–900°C and the baseline  $R_{sheet}$  for the  $POCl_3$  diffusion process was 64.68  $\Omega$ /sq. The  $R_{sheet}$  uniformity for thermal  $POCl_3$

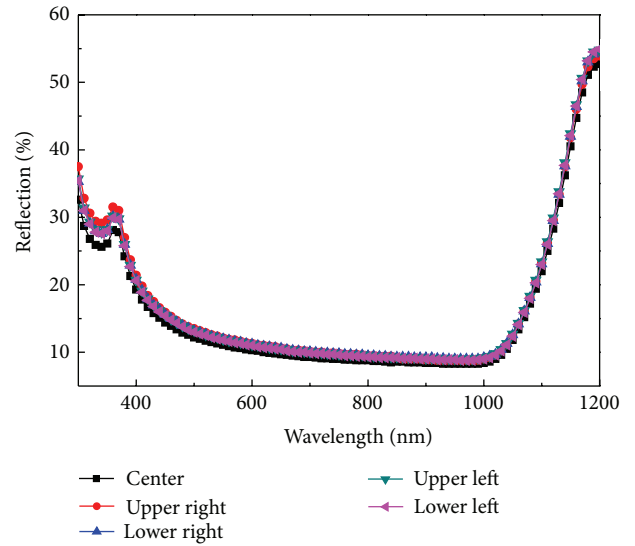


FIGURE 5: A comparison of the reflection at five different locations within the wafers after the alkaline texturing process.

diffusion was 4.80%, which was worse than that for the implantation process. In fact, the uniformity of the implantation process was below 3%, likely owing to the precise

control exercised over the dose amount by the emitter in the ion implantation apparatus. The good  $R_{\text{sheet}}$  uniformity and precise control also enabled a repeatable process for fabrication of lightly doped emitter regions [20–22].

In order to obtain the best performance from the annealing step, 5 p-type quasi-mono wafers, implanted with  $2.0 \times 10^{15}$  dopant ions at a beam energy of 10 keV on both faces of the wafer, were used to monitor the implied  $V_{\text{oc}}$  and carrier lifetime [23] for each condition. The WCT-120 tool from Sinton Instruments uses a quasi-steady-state photoconductance (QSSPC) method to measure implied  $V_{\text{oc}}$  and lifetime [24]. Table 3 presents the average implied  $V_{\text{oc}}$  and lifetime for each condition. The implied  $V_{\text{oc}}$  for wafers doped by thermal  $\text{POCl}_3$  diffusion was found to be 0.625 V at 1 sun. However, the implied  $V_{\text{oc}}$  after high-temperature annealing at  $900^\circ\text{C}$  was 0.620 V, the worst among all conditions studied. This was likely because high-temperature annealing can degrade the lifetime and reduce the  $V_{\text{oc}}$ . When the annealing temperature was decreased to  $840^\circ\text{C}$ , the implied  $V_{\text{oc}}$  reached 0.640 V; this higher implied  $V_{\text{oc}}$  was likely due to better surface passivation.

In the annealing step, a thinner  $\text{SiO}_2$  layer was grown on the wafer surface, and the ion-implanted dopant was activated. The thickness of the  $\text{SiO}_2$  was measured by a SemiLab LE-100PV ellipsometer. A single laser wavelength from a 632.8 nm He-Ne laser incident on the wafer surface was used to measure the refractive index and thickness of the dielectric layer. In this study, the  $\langle 111 \rangle$  silicon polished wafer with a dose of  $3.2 \times 10^{15}$  implanted and a beam energy of 10 keV on its surface was used as the control wafer. During the annealing process, control wafers were processed simultaneously with the experimental p-type quasi-mono silicon wafers in the same tube. Table 4 shows the resulting  $\text{SiO}_2$  thickness and uniformity for each condition. The thickness of  $\text{SiO}_2$  was found to be around 17 nm and was very similar for all the different conditions. Moreover, the uniformity of  $\text{SiO}_2$  was improved at higher annealing temperatures, and we found good  $\text{SiO}_2$  thickness uniformity (below 1.3% for each annealing condition).

After the junction formation step,  $\text{SiN}_x$  was deposited on the silicon surface by PECVD. In contrast to the industrial process, the thickness of the silicon nitride must be modulated during this process owing to the thinner oxide on the surface. In order to minimize the reflection from the frontside of the cell, a 57 nm  $\text{SiN}_x$  layer was deposited on top of the  $\text{SiO}_2$ . We selected 4 wafers for each condition after the ARC process and measured 5 points at different  $\langle 100 \rangle$  locations within each p-type quasi-mono wafer. Figure 6 illustrates the comparison of average reflection between  $\text{POCl}_3$  diffusion and the ion implantation process after deposition of the ARC. At short wavelengths, the reflection from samples treated by  $\text{POCl}_3$  diffusion was lower than that of samples treated by ion implantation. According to the Schuster diagram [25], the optimum refractive index of the inner  $n_1$  and outer  $n_2$  layers of the silicon substrate can be calculated as follows for zero reflection:

$$\frac{AB}{CD} > 0, \quad (5)$$

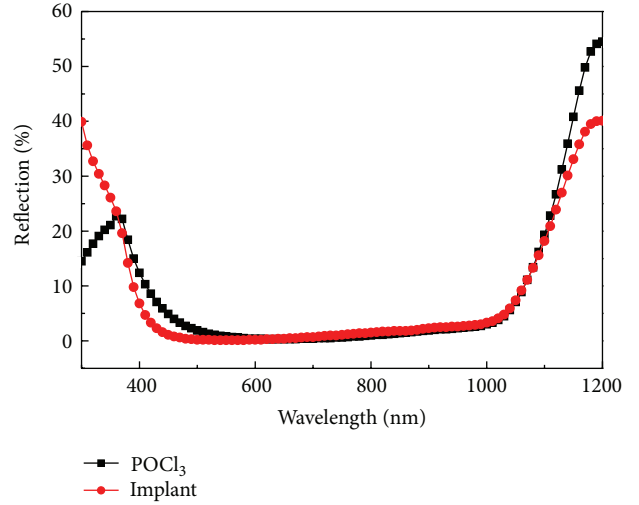


FIGURE 6: The average reflection for the  $\text{POCl}_3$  diffusion and implantation process after  $\text{SiN}_x$  deposition.

where

$$\begin{aligned} A &= n_o - n_s, & B &= n_o n_2^2 - n_s n_1^2, \\ C &= n_o n_s - n_2^2, & D &= n_1^2 - n_s n_o. \end{aligned} \quad (6)$$

As explained previously, based on detailed calculations [25], better optical performance can be achieved by using a low-high refractive index design, in which the outer layer has a low refractive index and the inner layer has a high refractive index, on the silicon substrate. However, the design of the ARC in our ion implantation process displayed the opposite characteristics; the outer  $\text{SiN}_x$  and inner  $\text{SiO}_2$  layers had refractive indexes of 2.03 and 1.46, respectively. Such high-low design tends to cause higher reflection at short wavelengths. In the long-wavelength range, the reflection following implantation was lower than that following  $\text{POCl}_3$  diffusion, because the wafer had a planar backside surface owing to the wet chemical isolation process that used  $\text{HNO}_3$  and  $\text{HF}$  to remove the backside p-n junction after  $\text{POCl}_3$  diffusion. Table 5 presents a comparison of  $R_w\%$  between  $\text{POCl}_3$  diffusion and ion implantation after  $\text{SiN}_x$  deposition. It is clear that  $R_w\%$  resulting from implantation was 4.64%, which is better than that from the  $\text{POCl}_3$  process (which was 5.51% after deposition of the ARC).

After ARC deposition, the wafers were subjected to screen printing and cofiring processes. Figure 7 illustrates a comparison of  $V_{\text{oc}}$  and  $I_{\text{sc}}$  between  $\text{POCl}_3$  diffusion and the implantation process for each condition and indicates that higher annealing temperatures resulted in lower  $V_{\text{oc}}$  and  $I_{\text{sc}}$ . The  $V_{\text{oc}}$  for the implantation process with an annealing temperature of  $900^\circ\text{C}$  was the lowest of all, likely because high-temperature annealing can degrade carrier lifetime and  $V_{\text{oc}}$ ; this is in accordance with the results of the WCT-120 measurements. Based on the heavy doping produced by high-temperature annealing,  $I_{\text{sc}}$  was lowest following high-temperature annealing at  $900^\circ\text{C}$ . When the annealing temperature was reduced to  $870^\circ\text{C}$ ,  $V_{\text{oc}}$  reached 0.623 V,

TABLE 3: Implied  $V_{oc}$  and lifetime.

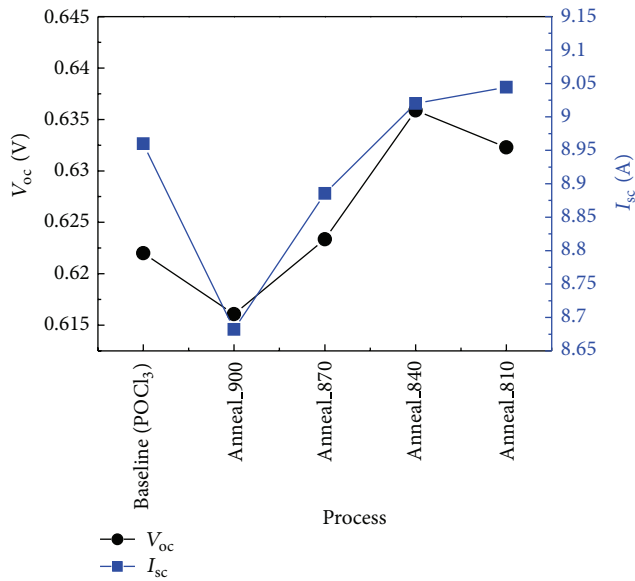
	POCl <sub>3</sub>	Anneal_900	Anneal_870	Anneal_840	Anneal_810
Implied $V_{oc}$ (V)	0.625	0.620	0.624	0.64	0.638
Lifetime ( $\mu$ s)	30.24	24.67	29.43	53.44	50.73

TABLE 4: The results of SiO<sub>2</sub> thickness and uniformity.

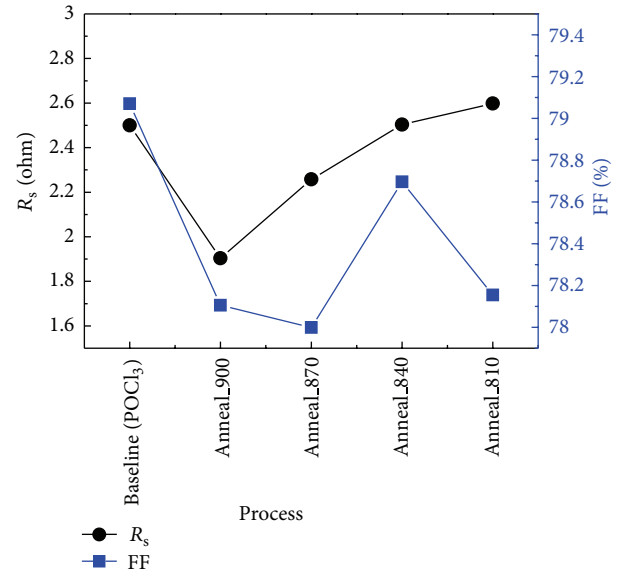
	POCl <sub>3</sub>	Anneal_900	Anneal_870	Anneal_840	Anneal_810
SiO <sub>2</sub> thickness (nm)	x	17.63	17.56	17.21	17.02
Uniformity (%)	x	0.81%	0.92%	1.05%	1.21%

TABLE 5: Comparison of  $R_w$  % between POCl<sub>3</sub> diffusion and implantation after ARC deposition.

	POCl <sub>3</sub>	Implant
$R_w$ %	5.51%	4.64%

FIGURE 7:  $V_{oc}$  and  $I_{sc}$  for the POCl<sub>3</sub> diffusion and implantation processes.

which was higher than that for the POCl<sub>3</sub> diffusion process. However,  $I_{sc}$  was still lower than that for POCl<sub>3</sub> diffusion owing to the lower  $R_{sheet}$  of 61.36  $\Omega$ /sq. As the annealing temperature reached 840°C,  $V_{oc}$  reached its highest value of 0.636 V. As shown in Figure 8,  $R_s$  was highest for the implantation process with an annealing temperature of 810°C, likely because the highest sheet resistance (70.02  $\Omega$ /sq) would have produced the worst metal contact. Besides the condition of annealing temperature at 810°C, the  $R_s$  of the implantation process is lower than that of POCl<sub>3</sub> diffusion process. This was likely due to good  $R_{sheet}$  uniformity caused by precise doping control by the ion implantation instrument. Moreover, higher annealing temperatures can achieve heavy doping and result in good contact with metal. As shown in Figure 9, the higher annealing temperature also caused a lower  $R_{shunt}$ , because a higher annealing temperature

FIGURE 8:  $R_s$  and FF for the POCl<sub>3</sub> diffusion and implantation processes.

degrades the bulk lifetime, which lowers  $R_{shunt}$ . The FF of the implantation process was highest for an annealing temperature of 840°C owing to the lower  $R_s$  and higher  $R_{shunt}$  performances. Moreover, the best average efficiency of 18.55% was found for the implantation process with an annealing temperature of 840°C (Figure 10). All electrical characteristics are presented in Table 6. In general, higher efficiency was found to result from higher  $V_{oc}$  and  $I_{sc}$ . Therefore, our results indicate that quasi-mono silicon wafer produced by ion implantation can improve photovoltaic cell efficiency. Table 7 presents the cell conversion cost per watt for traditional and implant processes for the quasi-mono wafer substrate. It is clear that the cost of the traditional process (0.1664 USD) was much higher than that of the implant process (0.1617 USD).

#### 4. Conclusions

In this study, we investigated a novel type of silicon material, the quasi-mono wafer, for use in high-efficiency solar cells. We produced this material by ion-implanted emitter formation and were able to raise the absolute cell efficiency of a

TABLE 6: Characteristics of  $\text{POCl}_3$  diffusion and implantation processes.

	$U_{oc}$	$I_{sc}$	$R_s$	$R_{sh}$	FF	$N_{Cell}$	$I_{rev1}$
Baseline ( $\text{POCl}_3$ )	0.622	8.96	2.50	756	79.07	18.08	0.03
Anneal_900	0.616	8.68	1.90	59.82	78.11	17.17	0.47
Anneal_870	0.623	8.89	2.26	42.71	78.00	17.76	0.65
Anneal_840	0.636	9.02	2.50	86.34	78.70	18.55	0.52
Anneal_810	0.632	9.04	2.60	83.43	78.15	18.37	0.55

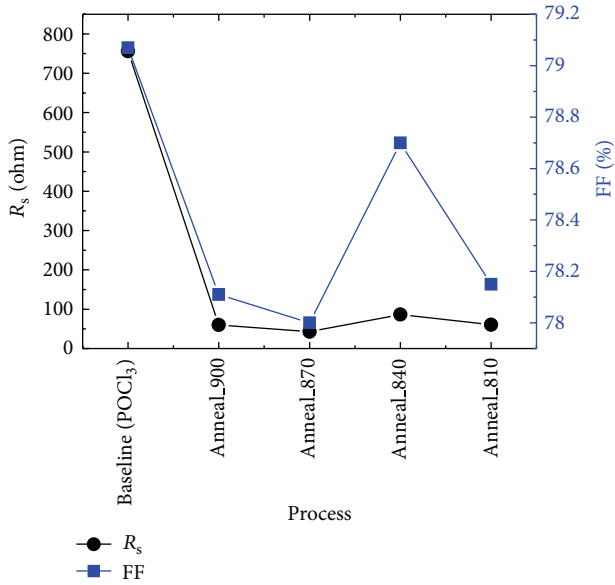
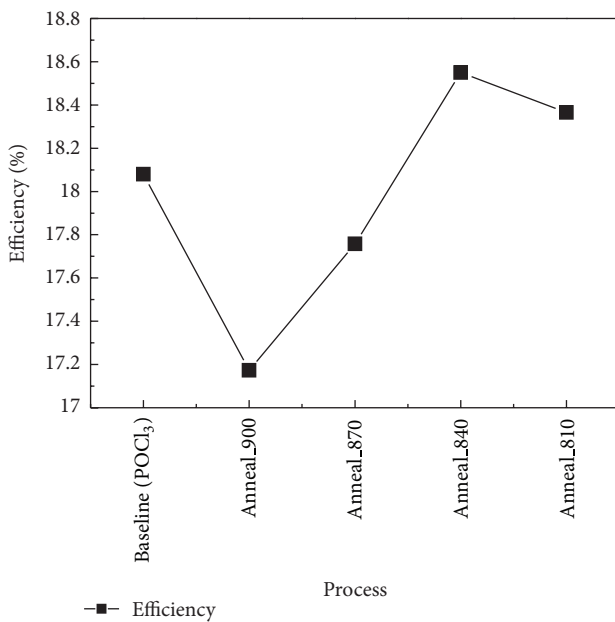
FIGURE 9:  $R_{shunt}$  and FF for the  $\text{POCl}_3$  diffusion and implantation processes.FIGURE 10: Efficiency for the  $\text{POCl}_3$  diffusion and implantation processes.

TABLE 7: The cell conversion cost per watt of traditional and implant processes on quasi-mono wafer substrate.

Station/process	Traditional process	Implant process
Texturing (USD)	0.07	0.07
Implant (USD)		0.08
Anneal (USD)		0.05
Diffusion (USD)	0.068	
PSG clean (USD)	0.033	
Wet isolation (USD)	0.036	
SiN (USD)	0.075	0.08
Screen printing (USD)	0.45	0.45
Conversion cost (USD)	0.732	0.73
Cell efficiency (%)	18.08%	18.55%
Wafer area ( $\text{m}^2$ )	0.024336	0.024336
Watts/wafer	4.40	4.51
Cell conversion cost		
Per watt (USD)	0.1664	0.1617

quasi-mono silicon wafer by 0.47% by following a simplified process flow that eliminates the PSG strip and junction isolation steps. The  $R_{sheet}$  uniformity from implantation was found to be better than that from the  $\text{POCl}_3$  diffusion process owing to the precise dopant control exercised by the ion implantation instrument. After activation by an annealing process, the implied  $V_{oc}$  from the implantation process with an annealing temperature less than  $900^\circ\text{C}$  was found to be better than that from the  $\text{POCl}_3$  diffusion process; this was likely due to the good surface passivation caused by the implantation and annealing processes. However, owing to the thinner  $\text{SiO}_2$  formed on the surface by the annealing process, the thickness of the silicon nitride should be modified to minimize  $R_w$ . After metallization, we achieved an average cell efficiency of 18.55%.

## Acknowledgments

This work was supported by the National Science Council under Contract n. NSC 101-2221-E-006-139. This work was also supported in part by the Center for Frontier Materials and Micro/Nano Science and Technology, National Cheng Kung University, Taiwan. This work was also supported in part by the Advanced Optoelectronic Technology Center, National Cheng Kung University, under projects from the Ministry of Education. The authors wish to thank Professor

S. J. Chang of National Cheng Kung University and Haw Yen, COO of Inventec Solar Energy Corporation, for their assistance in this study. This work is supported in part by Inventec Solar Energy Corporation.

## References

- [1] N. Stoddard, W. Bei, I. Witting et al., "Casting single crystal silicon: novel defect profiles from BP solar's Mono<sup>2</sup> wafers," *Solid State Phenomena*, vol. 131–133, pp. 1–8, 2008.
- [2] N. Stoddard, R. Sidhu, J. Creager et al., "Evaluating BP solar's Mono<sup>2</sup> material: lifetime and cell electrical data," in *Proceedings of the 34th IEEE Photovoltaic Specialists Conference (PVSC '09)*, pp. 001163–001168, June 2009.
- [3] E. Lohmüller, B. Thaidigsmann, M. Pospischil et al., "20% efficient passivated large-area metal wrap through solar cells on boron-doped Cz silicon," *IEEE Electron Device Letters*, vol. 32, no. 12, pp. 1719–1721, 2011.
- [4] B. Thaidigsmann, A. Drews, T. Fellmeth et al., "Synergistic effects of rear-surface passivation and the metal wrap through concept," *IEEE Journal of Photovoltaics*, vol. 2, no. 2, pp. 109–113, 2012.
- [5] F. Kiefer, C. Ulzhöfer, T. Brendemühl et al., "High efficiency N-type emitter-wrap-through silicon solar cells," *IEEE Journal of Photovoltaics*, vol. 1, no. 1, pp. 49–53, 2011.
- [6] D. Kray, J. Dicker, D. Osswald et al., "Progress in high-efficiency emitter-wrap-through cells on medium quality substrates," in *Proceedings of the 3rd World Conference on Photovoltaic Energy Conversion*, pp. 1340–1343, Osaka, Japan, May 2003.
- [7] J. Renshaw and A. Rohatgi, "Device optimization for screen printed interdigitated back contact solar cells," in *Proceedings of the 37th IEEE Photovoltaic Specialists Conference (PVSC '11)*, 2011.
- [8] F. J. Castaño, D. Morecroft, M. Cascant et al., "Industrially Feasible > 19% efficiency IBC cells for pilot line processing," in *Proceedings of the 37th IEEE Photovoltaic Specialists Conference (PVSC '11)*, 2011.
- [9] T. Böschke, R. Hellriegel, T. Wütherich et al., "Fully screen-printed PERC cells with laser-fired contacts an industrial cell concept with 19.5% efficiency," in *Proceedings of the 37th IEEE Photovoltaic Specialists Conference (PVSC '11)*, 2011.
- [10] P. Ortega, G. López, A. Orpella et al., "Crystalline silicon solar cells beyond 20% efficiency," in *Proceedings of the 8th Spanish Conference on Electron Devices (CDE '11)*, February 2011.
- [11] M. Jeon, J. Lee, S. Kim, W. Lee, and E. Cho, "Ion implanted crystalline silicon solar cells with blanket and selective emitter," *Materials Science and Engineering B*, vol. 176, no. 16, pp. 1285–1290, 2011.
- [12] T. Janssens, N. E. Posthuma, B. J. Pawlak, E. Rosseel, and J. Poortmans, "Implantation for an excellent definition of doping profiles in si solar cells," in *Proceedings of the 25th European Photovoltaic Solar Energy Conference and Exhibition 5th World Conference on Photovoltaic Energy Conversion*, Valencia, Spain, 2010.
- [13] H. F. Wolf, *Semiconductors*, John Wiley & Sons, 1971.
- [14] A. S. Grove, *Physics and Technology of Semiconductor Devices*, John Wiley & Sons, 1967.
- [15] D. V. Morgan, K. Board, and R. H. Cockrum, *An Introduction to Microelectronic Technology*, John Wiley & Sons, 1985.
- [16] S. M. Sze, *Semiconductor Device Physics and Technology*, John Wiley & Sons, 1969.
- [17] D. Redfield, "Method for evaluation of antireflection coatings," *Solar Cells*, vol. 3, no. 1, pp. 27–33, 1981.
- [18] G. E. Jellison and F. A. Modine, "Optical constants for silicon at 300 and 10 K determined from 1.64 to 4.73 eV by ellipsometry," *Journal of Applied Physics*, vol. 53, no. 5, pp. 3745–3753, 1982.
- [19] E. Palik, *Handbook of Optical Constants of Solids*, Academic Press, New York, NY, USA, 1985.
- [20] R. Low, A. Gupta, N. Bateman et al., "High efficiency selective emitter enabled through patterned ion implantation," in *Proceedings of the 35th IEEE Photovoltaic Specialists Conference (PVSC '10)*, pp. 001440–001445, Honolulu, Hawaii, USA, 2010.
- [21] J. Benick, N. Bateman, and M. Hermle, "Very low emitter saturation current densities on ion implanted boron emitters," in *Proceedings of the 25th European Photovoltaic Solar Energy Conference and Exhibition (EU-PVSEC '10)*, pp. 1169–1173, Valencia, Spain, September 2010.
- [22] T. Janssens, N. E. Posthuma, B. J. Pawlak, E. Rosseel, and J. Poortmans, "Implantation for an excellent definition of doping profiles in si solar cells," in *Proceedings of the 25th European Photovoltaic Solar Energy Conference and Exhibition (EUPVSEC '10)*, pp. 1179–1181, Valencia, Spain, September 2010.
- [23] R. A. Sinton, A. Cuevas, and M. Stuckings, "Quasi-steady-state photoconductance, a new method for solar cell material and device characterization," in *Proceedings of the 25th IEEE Photovoltaic Specialists Conference (PVSC '96)*, pp. 457–460, Washington, DC, USA, May 1996.
- [24] R. A. Sinton and A. Cuevas, "Contactless determination of current–voltage characteristics and minority-carrier lifetimes in semiconductors from quasi-steady-state photoconductance data," *Applied Physics Letters*, vol. 69, no. 17, article 2510, 3 pages, 1996.
- [25] B. A. Moys, "The theory of double-layer antireflection coatings," *Thin Solid Films*, vol. 21, no. 1, pp. 145–157, 1974.

## Research Article

# Realization of Colored Multicrystalline Silicon Solar Cells with $\text{SiO}_2/\text{SiN}_x\text{:H}$ Double Layer Antireflection Coatings

Minghua Li,<sup>1</sup> Libin Zeng,<sup>1</sup> Yifeng Chen,<sup>1,2</sup> Lin Zhuang,<sup>1</sup> Xuemeng Wang,<sup>3</sup> and Hui Shen<sup>1,3</sup>

<sup>1</sup> Institute for Solar Energy Systems, Guangdong Provincial Key Laboratory of Photovoltaic Technologies, State Key Laboratory of Optoelectronic Materials and Technologies, Sun Yat-sen University, Guangzhou 510006, China

<sup>2</sup> State Key Lab of PV Science and Technology, Trina Solar, Changzhou 213031, China

<sup>3</sup> Shunde SYSU Institute for Solar Energy, Shunde 528300, China

Correspondence should be addressed to Hui Shen; drshenhui@gmail.com

Received 24 January 2013; Revised 2 March 2013; Accepted 5 March 2013

Academic Editor: Sudhakar Shet

Copyright © 2013 Minghua Li et al. This is an open access article distributed under the Creative Commons Attribution License, which permits unrestricted use, distribution, and reproduction in any medium, provided the original work is properly cited.

We presented a method to use  $\text{SiO}_2/\text{SiN}_x\text{:H}$  double layer antireflection coatings (DARC) on acid textures to fabricate colored multicrystalline silicon (mc-Si) solar cells. Firstly, we modeled the perceived colors and short-circuit current density ( $J_{sc}$ ) as a function of  $\text{SiN}_x\text{:H}$  thickness for single layer  $\text{SiN}_x\text{:H}$ , and as a function of  $\text{SiO}_2$  thickness for the case of  $\text{SiO}_2/\text{SiN}_x\text{:H}$  (DARC) with fixed  $\text{SiN}_x\text{:H}$  (refractive index  $n = 2.1$  at 633 nm, and thickness = 80 nm). The simulation results show that it is possible to achieve various colors by adjusting the thickness of  $\text{SiO}_2$  to avoid significant optical losses. Therefore, we carried out the experiments by using electron beam (e-beam) evaporation to deposit a layer of  $\text{SiO}_2$  over the standard  $\text{SiN}_x\text{:H}$  for  $156 \times 156 \text{ mm}^2$  mc-Si solar cells which were fabricated by a conventional process. Semisphere reflectivity over 300 nm to 1100 nm and  $I$ - $V$  measurements were performed for grey yellow, purple, deep blue, and green cells. The efficiency of colored  $\text{SiO}_2/\text{SiN}_x\text{:H}$  DARC cells is comparable to that of standard  $\text{SiN}_x\text{:H}$  light blue cells, which shows the potential of colored cells in industrial applications.

## 1. Introduction

With the rapid development of photovoltaic (PV) industry, the decorative performance of solar modules gradually becomes an important issue, for instance, in building-integrated photovoltaics (BIPV) systems [1–3]. For industrial mass production multicrystalline silicon (mc-Si) solar cells, the front surface is usually covered by a layer of  $\text{SiN}_x\text{:H}$  deposited by plasma-enhanced chemical vapor deposition (PECVD), which serves for both passivation and antireflection [4]. When the thickness and refractive index of the  $\text{SiN}_x\text{:H}$  are optimized, the colors of solar cells look light blue. To realize colored solar cells, Tobias et al. reported a method by changing the thickness of the silicon nitride ( $n = 1.9$ ) or zinc sulfide ( $n = 2.3$ ), which acts as a single antireflection coating (ARC) on random pyramid textures [5]. However, this method results in significant  $J_{sc}$  losses. To improve the optical performance, multilayer ARC had been studied by simulation and experiments on polished surface

[6, 7]. For pyramid texture surface, we have showed that it is possible for DARC colored cells to achieve equal  $J_{sc}$  to standard blue cell [8]. For acid texture, simulations and experiments on  $3 \times 3 \text{ cm}^2$  mc-Si cells are under progress in our group [9]. Nevertheless, experimental reports on colored full dimensional industrial mc-Si cells with acid textures are still absent.

In this paper, we present our recent progress on simulations and experiments to fabricate colored mc-Si solar cells with a dimension of  $156 \times 156 \text{ mm}^2$ . In this study, we focus on using  $\text{SiO}_2/\text{SiN}_x\text{:H}$  DARC to replace the single  $\text{SiN}_x\text{:H}$  layer, and using electron beam (e-beam) evaporation technique to deposit a layer of  $\text{SiO}_2$  over the standard  $\text{SiN}_x\text{:H}$  after the conventional mc-Si cell fabrication. The solar cells with DARC stacks show various colors according to thickness of the  $\text{SiO}_2$  layer (top layer). Interestingly, the conversion efficiency of colored solar cells shows a little variation (+0.1% to -0.7%) compared to the reference cells with standard single  $\text{SiN}_x\text{:H}$  layer.

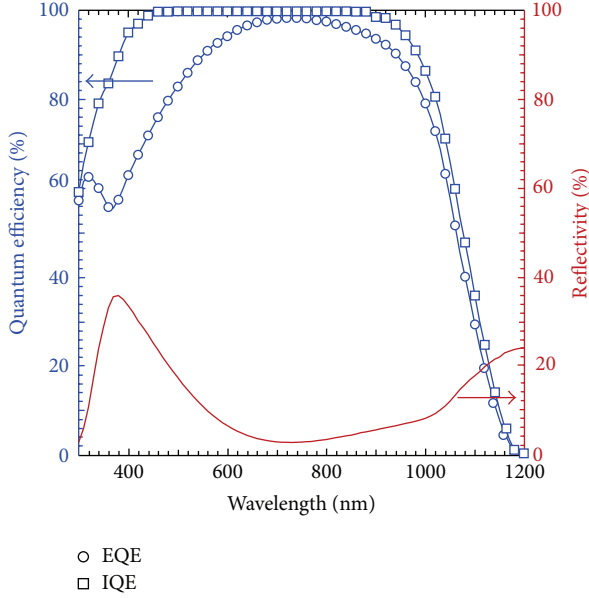


FIGURE 1: The quantum efficiency of solar cell with  $\text{SiN}_x\text{:H}$  SARC.

## 2. Optical Simulation

The typical acidic textured morphology of multicrystalline silicon is concave-like texture. We have simulated the morphology as three-dimensional ellipsoid by Monte Carlo ray tracing method [10], so we employed this model to calculate the reflectivity of the solar cells with both single  $\text{SiN}_x\text{:H}$  layer and  $\text{SiO}_2/\text{SiN}_x\text{:H}$  stacks. The simulations of colors are accomplished by calculating the tristimulus values  $X$ ,  $Y$ , and  $Z$  using the following equations:

$$\begin{aligned} X &= k \int \text{Flux}(\lambda) R(\lambda) x(\lambda) d\lambda, \\ Y &= k \int \text{Flux}(\lambda) R(\lambda) y(\lambda) d\lambda, \\ Z &= k \int \text{Flux}(\lambda) R(\lambda) z(\lambda) d\lambda, \end{aligned} \quad (1)$$

where  $\text{Flux}(\lambda)$  is the wavelength dependent photon flux under AM 1.5G spectrum;  $R(\lambda)$  is the reflectivity; and  $x(\lambda)$ ,  $y(\lambda)$ , and  $z(\lambda)$  are color matching functions defined by the International Commission on Illumination (CIE) [11, 12].

Furthermore, for better evaluation of the optical performance, we calculated the short-circuit current density ( $J_{sc}$ ) with

$$J_{sc} = \int_{300 \text{ nm}}^{1200 \text{ nm}} q \cdot \text{Flux}(\lambda) \cdot \text{IQE}(\lambda) \cdot [1 - R(\lambda)] d\lambda, \quad (2)$$

where  $q$  is the element charge,  $\text{IQE}(\lambda)$  the measured internal quantum efficiency of a conventional multicrystalline silicon solar cells (as shown in Figure 1), and  $R(\lambda)$  the simulated reflectivity.

Figure 2(a) shows the simulated color and the  $J_{sc}$  of multicrystalline silicon solar cells as a function of the thickness of single  $\text{SiN}_x\text{:H}$  ARC. As we can see, the peak of  $J_{sc}$

arrives with  $\text{SiN}_x\text{:H}$  thickness of 80 nm, but then  $J_{sc}$  drops significantly when the thickness deviates from 80 nm. To achieve yellow, purple, and green colors, single ARC will suffer  $2\sim 3 \text{ mA/cm}^2$   $J_{sc}$  losses. For comparison, we simulated the case of  $\text{SiO}_2/\text{SiN}_x\text{:H}$  DARC, with the bottom layer fixed to  $\text{SiN}_x\text{:H}$  (thickness = 80 nm,  $n = 2.1$ ) and with the thickness of  $\text{SiO}_2$  ( $n = 1.46$ ) varied from 0 nm to 300 nm as the top layer. Note that 0 nm  $\text{SiO}_2$  means the situation of optimal single layer  $\text{SiN}_x\text{:H}$ . As shown in Figure 2(b), a slight boost of  $J_{sc}$  can be observed when the  $\text{SiO}_2$  thickness varies from 0 nm to 150 nm, while the color changes from light blue, to grey yellow, red, and purple. On the other hand, when the  $\text{SiO}_2$  thickness continues to increase to 300 nm, deep blue and green colors will appear, with a small  $J_{sc}$  losses of up to  $0.5 \text{ mA/cm}^2$ . These indicate that the optical losses can be greatly suppressed with  $\text{SiO}_2/\text{SiN}_x\text{:H}$  DARC, comparing with the single  $\text{SiN}_x\text{:H}$  ARC in Figure 2(a).

## 3. Experiments

To further prove the simulations, experiments were carried out on industrial  $p$ -type mc-Si wafers with dimensions of  $156 \text{ mm} \times 156 \text{ mm}$ , and the wafer resistivity is between  $1\sim 3 \Omega\text{cm}$ . After acidic texturing and cleaning, a standard  $\text{POCl}_3$  diffusion is performed in a quartz tube to form an emitter with sheet resistivity of  $80 \Omega/\square$ . The samples were then coated with a  $\text{SiN}_x\text{:H}$  layer in a PECVD (Roth&Rau) system. The deposition of  $\text{SiN}_x\text{:H}$  was controlled to hold the refractive index of  $\text{SiN}_x\text{:H}$  ( $n = 2.1$ ) and its thickness of 80 nm. The metallizations are realized by screen printing to form the ‘‘H-pattern’’ front grid and full aluminum rear contact after firing. The  $I$ - $V$  measurements were carried out with Berger  $I$ - $V$  tester under calibration. To form the  $\text{SiO}_2/\text{SiN}_x\text{:H}$  DARC structure,  $\text{SiO}_2$  thin films were deposited by electron beam (e-beam) evaporation on the already fabricated solar cells. To avoid the deposition of  $\text{SiO}_2$  on the front side of the busbars, a steel mask was utilized as the shelter [13]. High purity  $\text{SiO}_2$  (99.99%) granules were used as the source material for evaporation and the source-to-substrate distance is 50 cm. E-type electron gun was employed for source evaporation. Ion bombardment was used to remove the dust on the substrate surface before deposition. The substrates were preheated and temperature was controlled at  $200^\circ\text{C}$  during the process. High purity oxygen (99.99%) was introduced into the chamber to maintain a pressure of  $3.0 \times 10^{-2} \text{ Pa}$  and used as reactive gas during the deposition. The deposition rate was controlled using a quartz crystal sensor placed near the substrate and was set to  $2 \text{ \AA/s}$ . The deposition time was adjusted to modulate the thicknesses of the  $\text{SiO}_2$  as the top layer of 84 nm, 136 nm, 190 nm, and 220 nm, respectively. Six samples were fabricated for each thickness. The structure of the solar cell with  $\text{SiO}_2/\text{SiN}_x\text{:H}$  DARC is schematically shown in Figure 3.

The Fourier transformed infrared spectroscopy (FTIR) measurement for the  $\text{SiO}_2$  thin film has been made at  $25^\circ\text{C}$  using a Thermo-Nicolet 6700 FTIR spectrometer. The chemical states of the  $\text{SiO}_2$  were investigated by X-ray photoelectron spectroscopy (XPS) using an ESCALab250 (U.K) spectrometer with monochromatic Al  $K\alpha$  radiation

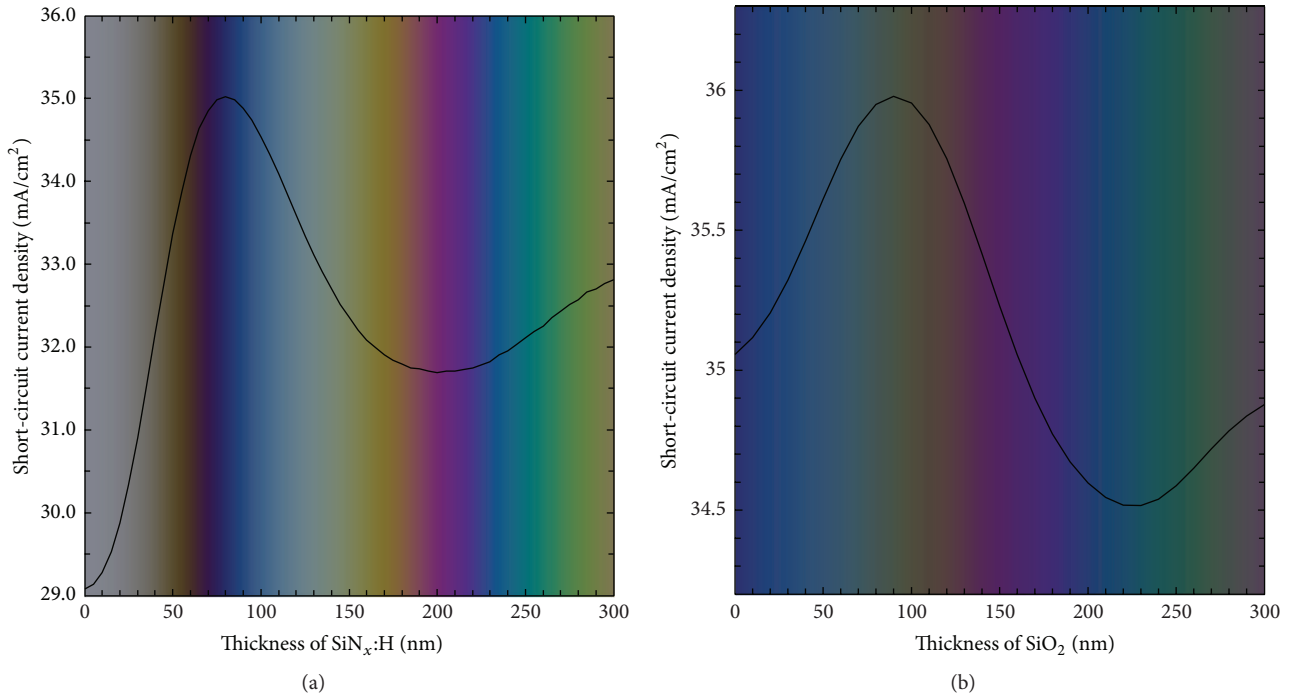


FIGURE 2: Calculated perceived color and short-circuit current density as a function of the thickness of (a) the standard single layer  $\text{SiN}_x\text{:H}$  (with  $n = 2.1$  at 633 nm) on a concave-like textured solar cell and (b)  $\text{SiO}_2$  on top of the standard  $\text{SiN}_x\text{:H}$  ( $n = 2.1$  at 633 nm, and thickness = 80 nm).

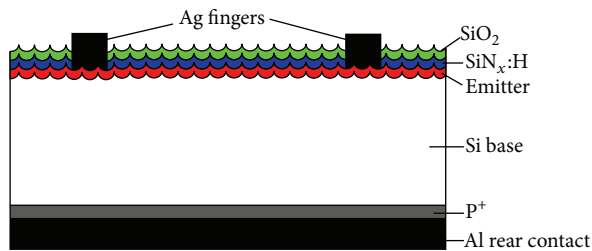


FIGURE 3: Schematic of solar cell with  $\text{SiO}_2/\text{SiN}_x\text{:H}$  DARC.

( $h\nu = 1486$  eV). All binding energies were calibrated with respect to C 1s spectral line at 284.8 eV. The morphology of the surface was characterized by field emission scanning electron microscope (JEOL, JSM-6330F). The refractive indexes of the  $\text{SiN}_x\text{:H}$  and  $\text{SiO}_2$  coatings were measured by a Sentech SE800 ellipsometer. The spectral reflectivity between 300 nm and 1100 nm was measured by a Hitachi U-4100 spectrophotometer. The quantum efficiency (QE) measurements were performed by a solar cell spectral response measurement system (PV measurement, QEX10). Finally, the  $I$ - $V$  characteristics of the DARC solar cells were measured using a Berger  $I$ - $V$  tester on a solar cell production line.

## 4. Results and Discussion

**4.1. Films Characterization and Potential Stability.** In order to get a qualitative spectra of  $\text{SiO}_2$  thin film compositions, we have performed Fourier transformed infrared spectroscopy

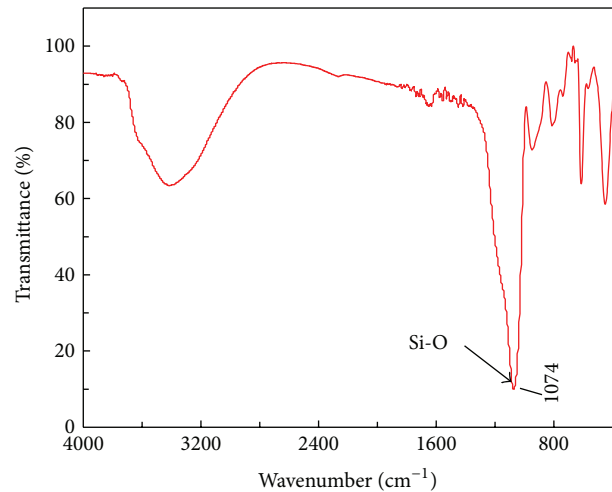


FIGURE 4: FTIR transmittance spectra of  $\text{SiO}_2$  thin film.

(FTIR) analysis. The samples were deposited bifacially with the same film thicknesses on the polished silicon wafer. The spectra are presented in Figure 4. The band in the 1040–1150  $\text{cm}^{-1}$  range is assigned to the stretching vibration mode Si–O [14, 15]. For the supplement of oxygen during the  $\text{SiO}_2$  deposition, a clear Si–O intensity peak (1074  $\text{cm}^{-1}$ ) is observed for the  $\text{SiO}_2$  layer, which is related to the high oxygen content in this layer. The SEM images are shown in Figure 5. A clear concave-like acid texture can be seen

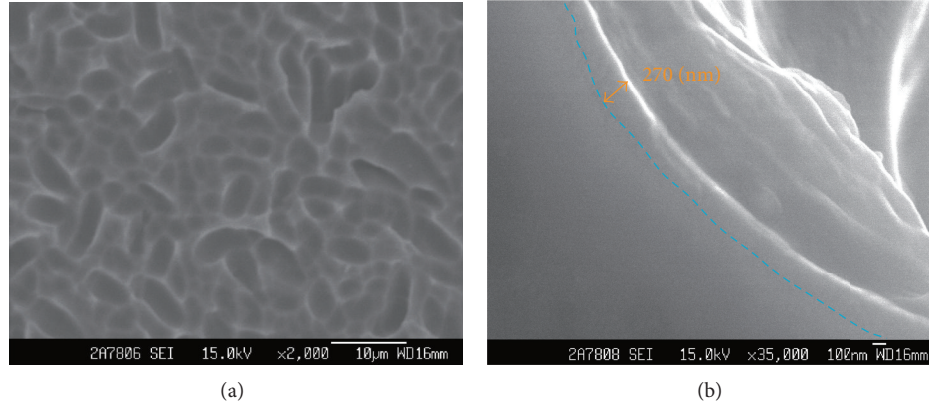


FIGURE 5: SEM images of (a) top view and (b) cross-section of multicrystalline silicon solar cell with  $\text{SiO}_2$  (190 nm)/ $\text{SiN}_x\text{:H}$  (80 nm) DARC.

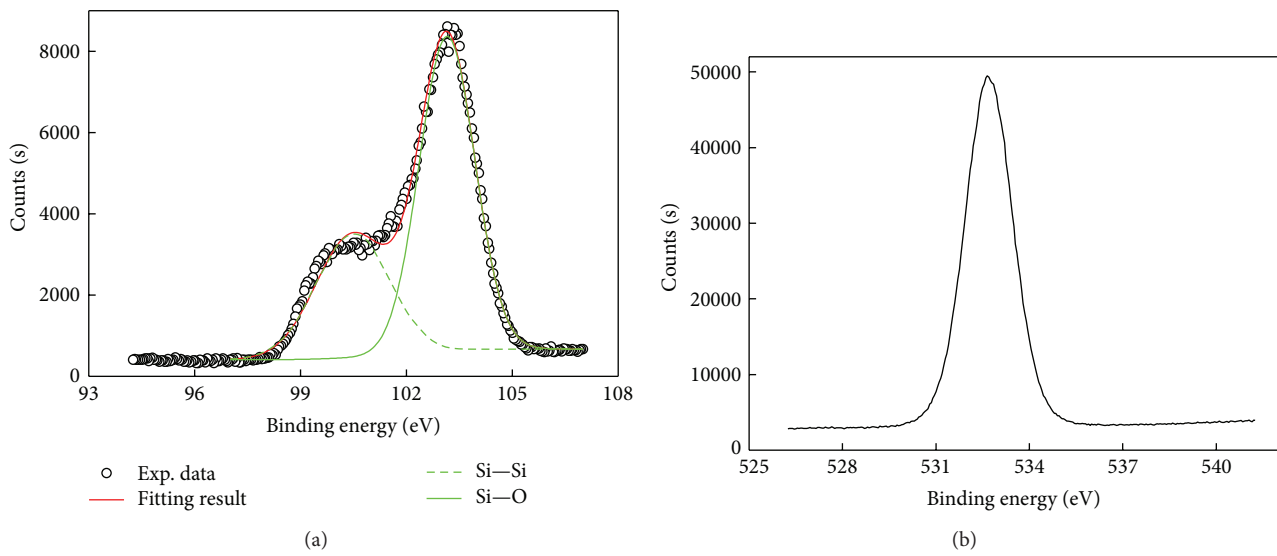


FIGURE 6: XPS spectra of  $\text{SiO}_2$ : (a) Si  $2p$  and (b) O  $1s$ .

in Figure 5(a), while the interface between silicon and  $\text{SiO}_2/\text{SiN}_x\text{:H}$  (deep blue color, with 80 nm  $\text{SiN}_x\text{:H}$  and 190 nm  $\text{SiO}_2$ ) is illustrated in Figure 5(b).

XPS was applied to determine the chemical state of the Si and O elements, which can confirm the presence of  $\text{SiO}_2$  layer in DARC. High-resolution spectra are shown in Figure 6(a) for Si  $2p$  and Figure 6(b) for O  $1s$ , respectively. The Si peaks were fitted using Gaussian curves. It is evident that two Si  $2p$  peaks are located at 100.5 eV and 103.2 eV, as seen in Figure 6(a), which can be attributed to the signal of  $\text{SiO}_2$ . It is recognized that the binding energy of Si  $2p$  related to  $\text{SiO}_2$  is dependent on the oxygen composition [16]. Then, the films prepared by electron beam evaporation in this study were nearly stoichiometric silicon dioxide.

It is important that the surface of the solar cell endures various kinds of physical conditions. Structural stability of the antireflection coating is a key issue.  $\text{SiN}_x\text{:H}$  films are widely used in photovoltaic industries due to their strong durability, excellent passivation properties, good dielectric characteristics, and resistance against corrosion by water.

In our work,  $\text{SiO}_2$  thin films were deposited on the conventional solar cells with pre-coated  $\text{SiN}_x\text{:H}$  single layer. The colored cells with  $\text{SiO}_2/\text{SiN}_x\text{:H}$  double layer antireflection coating do not need to suffer high temperature treatment again in the subsequent process, including encapsulation. For the  $\text{SiO}_2/\text{SiN}_x\text{:H}$  antireflection coating structure, due to different lattice spacing of substrate and silicon nitride layers, as well as stacking faults in the crystal structure, pin holes, or interstitial atoms, tension in deposited  $\text{SiN}_x\text{:H}$  layers can occur, while  $\text{SiO}_2$  film exhibits compressing force. The opposite mechanical property can lead to the lower stress in the double layers. In addition, the thermal expansion coefficient of  $\text{SiO}_2$  is smaller than that of silicon; thus the interface stress in  $\text{SiO}_2/\text{SiN}_x\text{:H}$  is smaller than that of  $\text{SiN}_x\text{:H}/\text{SiO}_2$  [17]. Consequently, such a good interface matching can avoid film cracks at the  $\text{SiO}_2/\text{SiN}_x\text{:H}$  interface. Besides, it has been confirmed that the  $\text{SiN}_x\text{:H}$  and  $\text{SiO}_2$  films also have good thermal stability [18]. Hence, all the factors shown above are the main reasons why  $\text{SiO}_2$  is the best candidate to form double layer antireflection coatings with  $\text{SiN}_x\text{:H}$ . On the other

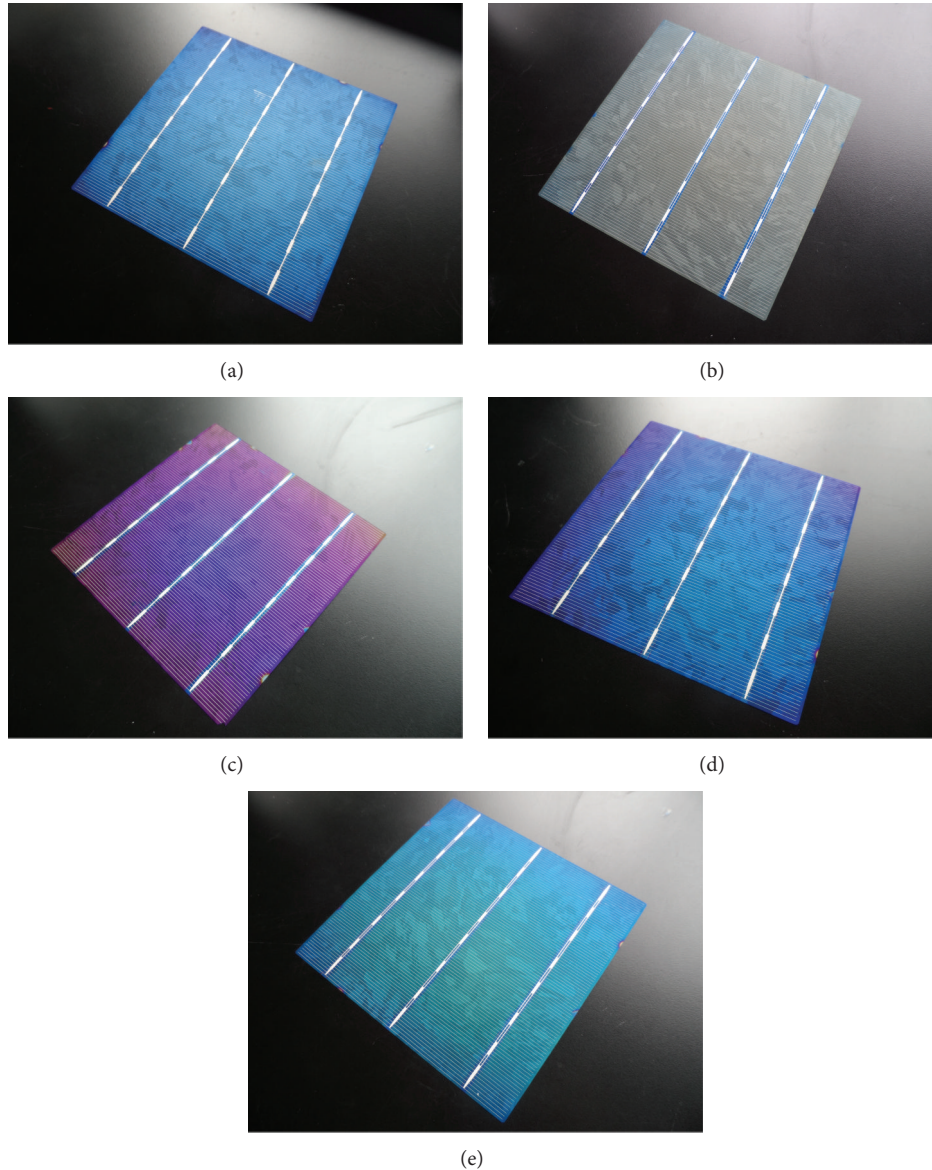


FIGURE 7: Photographs of the colored multicrystalline silicon solar cells with different layer stacks. (a)  $\text{SiN}_x\text{:H}$  (80 nm). (b)  $\text{SiO}_2$  (84 nm)/ $\text{SiN}_x\text{:H}$  (80 nm). (c)  $\text{SiO}_2$  (136 nm)/ $\text{SiN}_x\text{:H}$  (80 nm). (d)  $\text{SiO}_2$  (190 nm)/ $\text{SiN}_x\text{:H}$  (80 nm). (e)  $\text{SiO}_2$  (220 nm)/ $\text{SiN}_x\text{:H}$  (80 nm).

hand, for the deposition process of  $\text{SiO}_2$  on the conventional solar cells, the films properties are highly dependent upon both deposition parameters and subsequent processing. In order to obtain good thin film adhesion force on the substrate, we established the optimal process parameters to achieve high quality  $\text{SiO}_2$  films, which are transparent in the visible range and have less light absorption. The stability of  $\text{SiO}_2$  films,  $\text{SiN}_x\text{:H}$  films, and  $\text{SiO}_2/\text{SiN}_x\text{:H}$  double films has been well investigated by many groups before [19–21]. For the  $\text{SiO}_2/\text{SiN}_x\text{:H}$  double layers, postanneal treatment can not only improve the optical property, but also decrease residual stress. Based on above discussion, we believe the  $\text{SiO}_2/\text{SiN}_x\text{:H}$  structure has superior stability, which can be used in the colored solar cells.

**4.2. Optical Characterization.** Figure 7 presents the photographs of the fabricated DARC mc-Si solar cells ( $156 \text{ mm} \times 156 \text{ mm}$ ) samples with  $\text{SiO}_2$  thickness equal to 84 nm (grey yellow), 136 nm (purple), 190 nm (deep blue), and 220 nm (green) covering on 80 nm  $\text{SiN}_x\text{:H}$  (light blue). It is apparent that colored cells are achievable by varying the thickness of  $\text{SiO}_2$  (top layer) on the solar cell with  $\text{SiN}_x\text{:H}$  (bottom layer). For the whole cells, the color is basically uniform. However, small chromatic aberrations in the edges still can be observed, which indicated that higher spatial uniformity during the deposition is required for further improvements.

Figure 8 depicts the reflectivity of single layer  $\text{SiN}_x\text{:H}$  with optimized thickness of 80 nm, as well as with the reflectivity of  $\text{SiO}_2/\text{SiN}_x\text{:H}$  DARC for optimized grey yellow, purple,

TABLE 1: Performances of colored mc-Si cells with  $\text{SiO}_2/\text{SiN}_x$ :H ARC compared to single  $\text{SiN}_x$ :H cell (measurement conditions: AM 1.5 G,  $100 \text{ mW}/\text{cm}^2$ ,  $25^\circ\text{C}$ ).

Samples	Color	Eff. (%)	FF (%)	$J_{sc}$ ( $\text{mA}/\text{cm}^2$ )	$V_{oc}$ (mV)
$\text{SiN}_x$ :H (80 nm) (reference)	Light blue	16.87	76.89	35.18	623.6
$\text{SiO}_2$ (84 nm)/ $\text{SiN}_x$ :H (80 nm)	Grey yellow	16.97	76.66	35.77	618.6
$\text{SiO}_2$ (136 nm)/ $\text{SiN}_x$ :H (80 nm)	Purple	16.75	77.07	34.91	622.4
$\text{SiO}_2$ (190 nm)/ $\text{SiN}_x$ :H (80 nm)	Deep blue	16.13	76.93	33.86	619.2
$\text{SiO}_2$ (220 nm)/ $\text{SiN}_x$ :H (80 nm)	Green	16.43	77.05	34.30	621.6

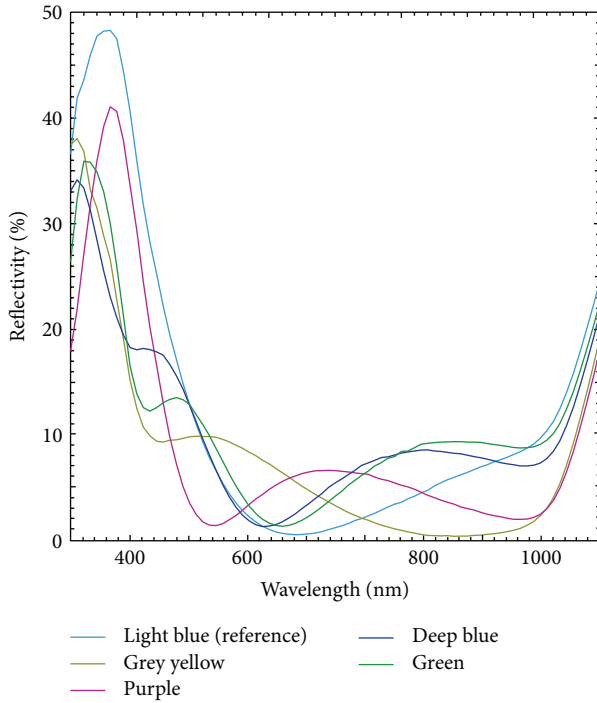


FIGURE 8: Reflectivity curves of the single  $\text{SiN}_x$ :H layer (light blue curve for  $\text{SiN}_x$ :H 80 nm) and double ARC with  $\text{SiO}_2$  thickness of 84 nm (grey yellow curve), 136 nm (purple curve), 190 nm (deep blue curve) and 220 nm (green curve) on top of 80 nm  $\text{SiN}_x$ :H.

deep blue, and green cells. As shown in Figure 8, the hunches of reflectivity move gradually from short wavelength to long wavelength, which explained the color switch by increasing the thickness of  $\text{SiO}_2$ .

**4.3. I-V Characteristics of Colored Solar Cells.** All I-V parameters presented in the study are averaged with six samples of each group. All measurements were conducted under the standard test conditions (AM 1.5G spectrum,  $100 \text{ mW}/\text{cm}^2$ ,  $25^\circ\text{C}$ ). Prior to the measurements, the simulator was calibrated with a reference multicrystalline silicon solar cell, which was calibrated by the Fraunhofer ISE. Table 1 summarizes the average performance parameters of colored mc-Si solar cells, compared to the standard light blue cells with 80 nm single  $\text{SiN}_x$ :H. As shown in Table 1, the FF of each group is nearly the same, while the  $V_{oc}$  shows small degradation for colored cells, which probably caused by the surface damages introduced during the e-beam evaporation.

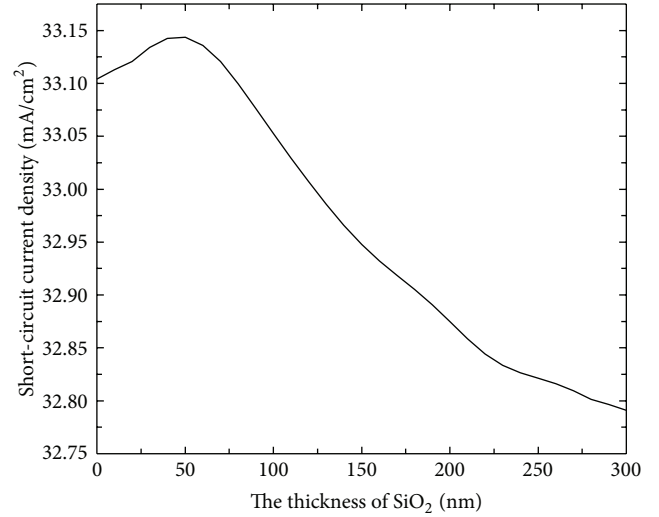


FIGURE 9: Calculated short-circuit current density of the colored solar cell module as a function of the thickness of  $\text{SiO}_2$  on top of the standard  $\text{SiN}_x$ :H ( $n = 2.1$  at 633 nm, and thickness = 80 nm).

The main power loss of colored cell comes from the  $J_{sc}$  losses, which reflects that the optical losses are still the dominating efficiency limit for colored solar cells. However, we demonstrate that comparable cell efficiency of colored solar cell is available, comparing to standard light blue cell, and 16.97% efficiency for grey yellow cell (abs. 0.1% higher than standard cell) with  $V_{oc}$  of 618.6 mV,  $J_{sc}$  of  $35.77 \text{ mA}/\text{cm}^2$ , and FF of 76.66% when  $\text{SiO}_2$  (84 nm)/ $\text{SiN}_x$ :H (80 nm) DARC is applied.

**4.4. Colored Solar Cell Module Simulation.** The matching ARC to refractive index of the cover materials in a module is one of the key factors that ultimately determine the optical properties of PV modules. To investigate the behaviors of solar cells with double layer antireflection coatings after encapsulation, we simulated the module  $J_{sc}$  by Monte Carlo ray tracing method. EVA was considered as the encapsulation material in the simulation since currently it is the most widely used with the refractive index of approximately 1.5 at 633 nm. Since the multiple total internal reflections between glass and air were neglected, the  $J_{sc}$  was underestimated slightly.

As shown in Figure 9, the  $J_{sc}$  is equal to  $33.11 \text{ mA}/\text{cm}^2$  when the thickness of  $\text{SiO}_2$  is 0 nm, which is the case of single

layer  $\text{SiN}_x\text{:H}$  ARC. As the  $\text{SiO}_2$  thickness increases from 0 nm to 50 nm,  $J_{sc}$  increases slightly and reaches the maximum value, and then the  $J_{sc}$  experienced a slow decrease; it drops to  $32.78 \text{ mA/cm}^2$  when the thickness of  $\text{SiO}_2$  is 300 nm. In overall, the advantages of DARCs are more limited in modules with EVA than in cells. This is mainly because the glass and EVA have a refractive index which is very close to  $\text{SiO}_2$ , and EVA has strong absorptivity in short wavelength. Therefore, the suppression of reflectivity in short wavelength via DARCs is not so notable anymore. Better encapsulation materials (such as PVB, silicone resin, and high transmittance glass) are needed to obtain high-performance module for the BIPV [22]. Additionally, the NICE (New Industrial Solar Cell Encapsulation) module concept [23, 24] seems to be a better option. Contrary to standard modules, NICE modules do not use EVA-like encapsulants. The use of nitrogen instead of EVA avoids any UV-cut from the incident spectrum that is typically observed with standard encapsulants. Further researches for this subject are now under investigation to optimize the module conversion efficiency.

## 5. Conclusions

We have successfully fabricated colored multicrystalline silicon solar cells by depositing an additional layer of  $\text{SiO}_2$  via e-beam evaporation on the standard  $\text{SiN}_x\text{:H}$  layer. By controlling the thickness of  $\text{SiO}_2$ , even better cell performances can be achieved; for example, grey yellow color cells have a higher  $J_{sc}$  than reference cells. With  $\text{SiO}_2/\text{SiN}_x\text{:H}$  DARC, the following benefits can be achieved.

- (1) Various colors can be achieved by adjusting the thickness of  $\text{SiO}_2$ .
- (2) The cells conversion efficiencies are very comparable, which indicates the potential of a smaller mismatch for colorful modules fabricated with cells of different colors.
- (3) Small degradations of  $V_{oc}$  are found after the deposition of  $\text{SiO}_2$ , which indicated that only little surface damage is caused by e-beam evaporation.

Therefore, more accurate e-beam evaporation process controls are needed for further works to improve the uniformity and reduce the surface damages. With  $\text{SiO}_2/\text{SiN}_x\text{:H}$  DRAC, colored mc-Si solar cells with comparable cell efficiencies are available for industrial applications, for instance, in architectural integration in buildings.

## Acknowledgments

The authors would like to thank the National Natural Science Foundation of China (Grant nos. 61076059 and 60906005) and National High-Tech Research and Development Program of China (863 Program, Grant no. 2012AA050302) and Guangdong Key Science & Technology Project 2010 (no. 2010A080805003) for financial support.

## References

- [1] T. J. N. Schoen, "Building-integrated PV installations in the Netherlands: examples and operational experiences," *Solar Energy*, vol. 70, no. 6, pp. 467–477, 2001.
- [2] R. Charron and A. K. Athienitis, "Optimization of the performance of double-façades with integrated photovoltaic panels and motorized blinds," *Solar Energy*, vol. 80, no. 5, pp. 482–491, 2006.
- [3] C. L. Cheng, C. S. S. Jimenez, and M. C. Lee, "Research of BIPV optimal tilted angle, use of latitude concept for south orientated plans," *Renewable Energy*, vol. 34, no. 6, pp. 1644–1650, 2009.
- [4] A. G. Aberle, "Overview on  $\text{SiN}$  surface passivation of crystalline silicon solar cells," *Solar Energy Materials and Solar Cells*, vol. 65, no. 1, pp. 239–248, 2001.
- [5] I. Tobias, A. El Moussaoui, and A. Luque, "Colored solar cells with minimal current mismatch," *IEEE Transactions on Electron Devices*, vol. 46, no. 9, pp. 1858–1865, 1999.
- [6] M. Spiegel, G. Willeke, P. Fath et al., "Colored solar cells with single, multiple and continuous layer antireflection coatings," in *Proceedings of the 13th European Photovoltaic Solar Energy Conference*, pp. 417–420, Nice, France, 1995.
- [7] J. H. Selj, T. T. Mongstad, R. Søndena, and E. S. Marstein, "Reduction of optical losses in colored solar cells with multi-layer antireflection coatings," *Solar Energy Materials and Solar Cells*, vol. 95, no. 9, pp. 2576–2582, 2011.
- [8] Y. F. Chen, P. P. Altermatt, Y. Yang, Z. Q. Feng, and H. Shen, "Color modulation of c-Si solar cells without significant current-loss by means of a double anti-reflective coating (DARC)," in *Proceedings of the 27th European Photovoltaic Solar Energy Conference and Exhibition*, pp. 2014–2016, September 2012.
- [9] L. B. Zeng, Y. F. Chen, S. M. Chen et al., "Simulation and fabrication to reduce optical losses in colored multi-crystalline silicon solar cells using double layer antireflection coatings," In press.
- [10] L. B. Zeng, Y. F. Chen, W. J. Ge et al., "Optimization of multi-layer antireflection coatings for multicrystalline silicon solar cells," in *Proceedings of the 27th European Photovoltaic Solar Energy Conference and Exhibition*, pp. 1299–1302, September 2012.
- [11] The CIE Central Bureau, "Colorimetric observers," ISO/CIE Standard 10527, The CIE Central Bureau, Vienna, Austria.
- [12] The CIE Central Bureau, "Colorimetric illuminants," ISO/CIE Standard 10526, The CIE Central Bureau, Vienna, Austria.
- [13] H. Shen, Y. Chen, X. Xu et al., "A structure to form colorful protective thin film via mask, granted, P.R. China patent, Application No. 201010168604. 9, Publish No. CN101834230A, 2010. 09. 15.
- [14] P. V. Bulkin, P. L. Swart, and B. M. Lacquet, "Effect of process parameters on the properties of electron cyclotron resonance plasma deposited silicon-oxynitride," *Journal of Non-Crystalline Solids*, vol. 187, pp. 403–408, 1995.
- [15] S. K. Ghosh and T. K. Hatwar, "Preparation and characterization of reactively sputtered silicon nitride thin films," *Thin Solid Films*, vol. 166, pp. 359–366, 1988.
- [16] A. Strass, P. Bieringer, W. Hansch et al., "Fabrication and characterization of thin low-temperature MBE-compatible silicon oxides of different stoichiometry," *Thin Solid Films*, vol. 349, no. 1–2, pp. 135–146, 1999.
- [17] J. Camassel and A. Tiberj, "Strain effects in device processing of silicon-on-insulator materials," *Applied Surface Science*, vol. 212–213, pp. 742–748, 2003.

- [18] B. Lenkeit, S. Steckemetz, F. Artuso, and R. Hezel, "Excellent thermal stability of remote plasma-enhanced chemical vapour deposited silicon nitride films for the rear of screen-printed bifacial silicon solar cells," *Solar Energy Materials and Solar Cells*, vol. 65, no. 1, pp. 317–323, 2001.
- [19] T. Minami, T. Utsubo, T. Yamatani, T. Miyata, and Y. Ohbayashi, "SiO<sub>2</sub> electret thin films prepared by various deposition methods," *Thin Solid Films*, vol. 426, no. 1-2, pp. 47–52, 2003.
- [20] A. El Amrani, I. Menous, L. Mahiou, R. Tadjine, A. Touati, and A. Lefgoum, "Silicon nitride film for solar cells," *Renewable Energy*, vol. 33, no. 10, pp. 2289–2293, 2008.
- [21] Z. Chen, Z. Lv, and J. Zhang, "PECVD SiO<sub>2</sub>/Si<sub>3</sub>N<sub>4</sub> double layers electrets on glass substrate," *IEEE Transactions on Dielectrics and Electrical Insulation*, vol. 15, no. 4, pp. 915–919, 2008.
- [22] I. Tobías, C. del Cañizo, and J. Alonso, "Chapter 7. Crystalline silicon solar cells and modules," in *Handbook of Photovoltaic Science and Engineering*, p. 293, John Wiley & Sons, New York, NY, USA, 2003.
- [23] R. Einhaus, K. Bamberg, R. D. Franclieu et al., "New industrial solar cell encapsulation (NICE) technology for PV module fabrication at drastically reduced costs," in *Proceedings of the 19th European Photovoltaic Solar Energy Conference and Exhibition*, pp. 2371–2374, August 2004.
- [24] J. Dupuis, E. Saint-Sernin, O. Nichiporuk et al., "NICE module technology—from the concept to mass production: a 10 years review," in *Proceedings of the 38th IEEE Photovoltaic Specialists Conference*, pp. 3183–3186, Austin, Tex, USA, 2012.

## Research Article

# A New Optimization Approach for Maximizing the Photovoltaic Panel Power Based on Genetic Algorithm and Lagrange Multiplier Algorithm

**Mahdi M. M. El-Arini, Ahmed M. Othman, and Ahmed Fathy**

*Electrical Power and Machine Department, Faculty of Engineering, Zagazig University, Zagazig 44519, Egypt*

Correspondence should be addressed to Ahmed Fathy; [ahmed\\_fathy\\_1984@yahoo.com](mailto:ahmed_fathy_1984@yahoo.com)

Received 27 October 2012; Revised 26 January 2013; Accepted 13 February 2013

Academic Editor: Peter Rupnowski

Copyright © 2013 Mahdi M. M. El-Arini et al. This is an open access article distributed under the Creative Commons Attribution License, which permits unrestricted use, distribution, and reproduction in any medium, provided the original work is properly cited.

In recent years, the solar energy has become one of the most important alternative sources of electric energy, so it is important to operate photovoltaic (PV) panel at the optimal point to obtain the possible maximum efficiency. This paper presents a new optimization approach to maximize the electrical power of a PV panel. The technique which is based on objective function represents the output power of the PV panel and constraints, equality and inequality. First the dummy variables that have effect on the output power are classified into two categories: dependent and independent. The proposed approach is a multistage one as the genetic algorithm, GA, is used to obtain the best initial population at optimal solution and this initial population is fed to Lagrange multiplier algorithm (LM), then a comparison between the two algorithms, GA and LM, is performed. The proposed technique is applied to solar radiation measured at Helwan city at latitude  $29.87^\circ$ , Egypt. The results showed that the proposed technique is applicable.

## 1. Introduction

In the last years, global warming and energy policies have become a hot topic on the international agenda as the developed countries are trying to reduce their greenhouse gas emissions. Renewable energy sources are considered as a technological option for generating clean energy. Among them, photovoltaic (PV) system has received a great attention as it appears to be one of the most promising renewable energy sources. PV power generation has an important role to play as it is a green source. The only emissions associated with PV power generation are those from the production of its components. However, the development for improving the efficiency of the PV system is still a challenging field of research. Maximum power point tracking (MPPT) algorithms are necessary in PV applications because the MPP of a solar module varies with the irradiation and temperature as shown in Figures 1 and 2. So, the use of MPPT is required to obtain the maximum output power from a module [1]. The optimization process can be defined as the finding values of variables that minimize or maximize the objective function

and satisfy the constraints. The optimization problems are centered on three main factors which are as follows:

- (1) *objective function* which is to be minimized or maximized;
- (2) *a set of unknown variables* that have effect on the objective function;
- (3) *A set of constraints* that allow the unknown to take on certain values but exclude others.

The most popular literature optimization techniques of the PV power are based on the usage of the MPPT. The MPPT control method uses one estimate processes between every two Perturb processes in search for the maximum PV output (EPP) which is proposed in [2].

An intelligent approach for MPPT DC-DC Boost converter focused on Perturb and Observe (P&O) algorithm and compared to a designed fuzzy logic controller which is presented in [3]. A comparative study of two types of MPPT which are P&O and incremental conductance method is introduced in [4]. The implementation of fuzzy logic

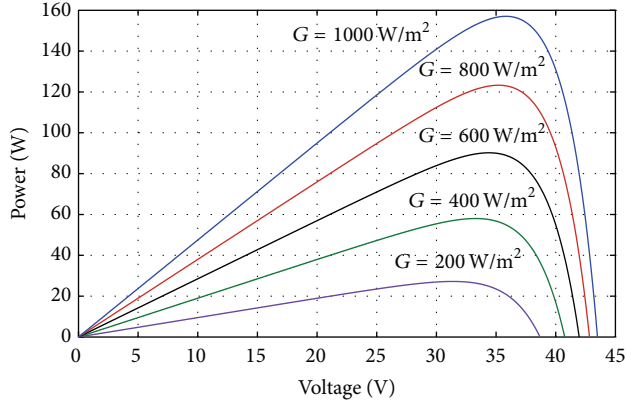


FIGURE 1: PV module voltage-power at different irradiance levels.

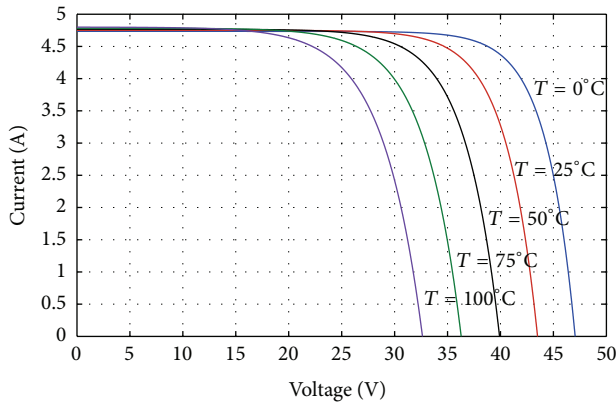


FIGURE 2: PV module voltage-current at different temperature levels.

controller based on the change of the PV module power,  $\Delta P_{pv}$ , and its change with respect to the module voltage,  $\Delta P_{pv}/\Delta V$  is studied in [5], the proposed fuzzy logic determines the size of the voltage then obtains the corresponding Power. The performance of fuzzy logic with various membership functions (MFs) is tested to optimize the MPPT. A novel intelligent fuzzy logic controller for MPPT based on boost converter and single-phase grid-connected inverter is introduced in [6]. An intelligent control method for MPPT of a photovoltaic system under variable temperature and insolation conditions which uses a fuzzy logic controller applied to a DC-DC converter device is proposed in [7]. A fuzzy logic control to control MPPT for a PV system is proposed in [8]. The analysis of the optimal operation of PV panels as a function of the weather conditions (solar irradiation, temperatures), and the design of a PV system provided with MPPT command ensuring instantaneously optimal operation of photovoltaic panels is presented in [9]. MPPT simulation based on using particle swarm optimization (PSO) algorithm is presented in [10]. The algorithm is employed on a buck-boost converter and tested experimentally using a PV array simulator. The design and implementation of an optimized stand-alone solar pumping system are presented in [11].

This paper presents a new optimization approach to maximize the electrical power of the PV panel. The technique

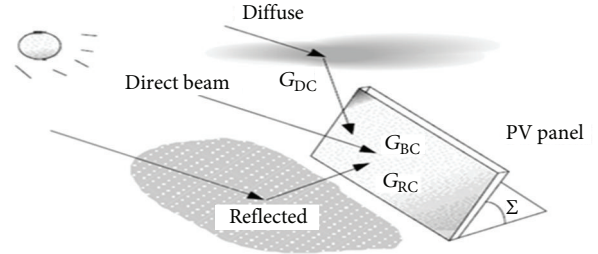


FIGURE 3: Direct, diffuse, and reflected beams that strike the PV panel.

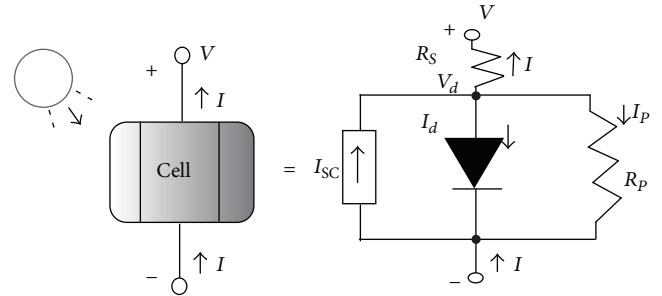


FIGURE 4: The equivalent circuit for a PV cell.

which is based on objective function represents the output power of the PV module and constraints, equality and inequality. First, the dummy variables that have effect on the output power are classified into two categories: dependent and independent. The proposed approach is a multistage one as GA is used to obtain the best initial population at optimal solution, and then the best initial population is fed to Lagrange multiplier algorithm (LM), then a comparison between two algorithms, GA and LM, is performed. The proposed technique is applied to solar radiation measured at Helwan city at latitude  $29.87^\circ$ , Egypt. The results showed that the proposed technique is applicable.

## 2. Mathematical Model of PV Module

The solar flux striking a PV panel can be resolved to three components; direct beam radiation that passes in a straight line through the atmosphere to the receiver, diffuse radiation that has been scattered by molecules in the atmosphere, and reflected radiation that has bounced off the ground or other surface in front of the collector as shown in Figure 3.

The total rate of radiation  $G_C$  strikes a collector on a clear day as follows [12]:

$$G_C = G_{BC} + G_{DC} + G_{RC},$$

$$G_C = Ae^{-km} \left[ \cos \beta \cos (\varphi_s - \varphi_C) \sin \Sigma + \sin \beta \cos \Sigma + C \left( \frac{1 + \cos \Sigma}{2} \right) + \rho (\sin \beta + C) \left( \frac{1 - \cos \Sigma}{2} \right) \right],$$

$$m = \frac{h_2}{h_1} = \frac{1}{\sin \beta},$$
(1)

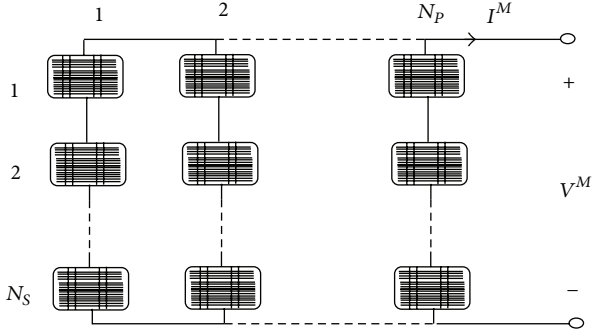


FIGURE 5: The equivalent circuit for a PV module.

where  $M$  is the air mass,  $\beta$  is the altitude angle,  $\varphi_S$  is the solar azimuth angle,  $\varphi_C$  is the PV module azimuth angle, positive for eastsouth and negative for westsouth,  $\Sigma$  is the PV module tilt angle,  $\rho$  is reflection factor, and  $C$  is sky diffuse factor and is given by the following equation [12]:

$$C = 0.095 + 0.04 \sin \left[ \frac{360}{365} (d - 100) \right], \quad (2)$$

where  $A$  and  $k$  are dependent on the day number and can be obtained by the following equations [1] and  $d$  is the day number:

$$A = 1160 + 75 \sin \left[ \frac{360}{365} (d - 275) \right] \quad (\text{W/m}^2), \quad (3)$$

$$k = 0.174 + 0.035 \sin \left[ \frac{360}{365} (d - 100) \right].$$

A PV cell can be simulated by a real diode in parallel with an ideal current source,  $I_{SC}$ , which depends on striking radiation. The generalized equivalent circuit of the PV cell is given in Figure 4 [13, 14].

One can derive the following equations for current and voltage:

$$I_{SC} = I + I_d + I_P,$$

$$I = I_{SC} - I_0 \left\{ \exp \left[ \frac{q(V^C + I \cdot R_s^C)}{nk_b T_C} \right] - 1 \right\} - \left( \frac{V^C + I \cdot R_s^C}{R_p^C} \right),$$

$$I_0 = \frac{I_{SC}}{(e^{qV/nk_b T_C} - 1)}. \quad (4)$$

The reverse saturation current,  $I_0$ , is dependent on the temperature and is given by the following equation:

$$I_0(T_C) = I_0(T_{ref}) * \left( \frac{T_C}{T_{ref}} \right)^3 * \exp \left( \frac{qE_G}{nK} \left( \frac{1}{T_{ref}} - \frac{1}{T_C} \right) \right). \quad (5)$$

The short circuit current,  $I_{SC}$ , depends on the solar radiation and cell temperature as follows:

$$I_{SC} = [I_{SCr} + K_i(T_C - T_{ref})] * G_C, \quad (6)$$

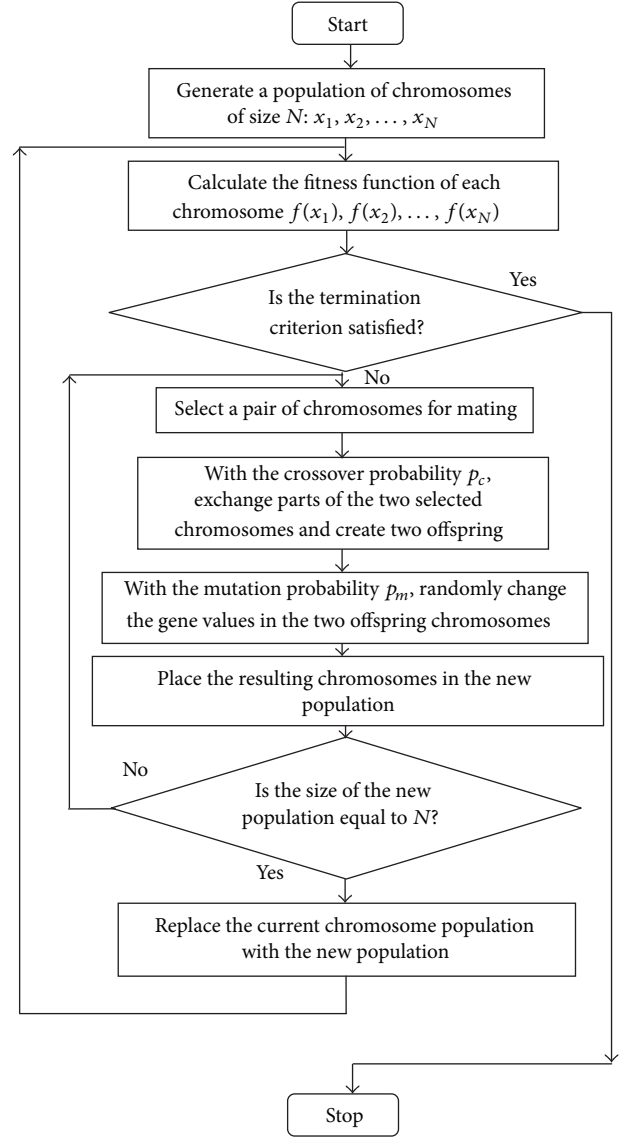


FIGURE 6: A simple GA flow chart.

where  $I$  is the cell output current,  $V$  is the cell output voltage, and  $R_S$  is the cell series resistance ( $\Omega$ ).

$R_P$  is the cell parallel resistance ( $\Omega$ ),  $n$  is the diode ideality factor,  $k_b$  is the Boltzmann constant ( $1.38e^{-23}$  J/K),  $T_C$  is the cell temperature ( $^{\circ}\text{C}$ ),  $T_{ref}$  is the reference temperature of the PV cell,  $I_0(T_{ref})$  is the cell reverse saturation current at reference temperature,  $E_G$  is the band gap of semiconductor used in the cell,  $I_{SCr}$  is the cell short circuit current at reference temperature and radiation,  $K_i$  is the short circuit current temperature coefficient, and  $G_C$  is the solar radiation strikes a tilted module in  $\text{W/m}^2$ .

The cell temperature is calculated as follows:

$$T_C = T_{ambient} + \left( \frac{\text{NOCT} - 20^{\circ}}{0.8} \right) * G_C, \quad (7)$$

where  $T_{ambient}$  is ambient temperature and NOCT is cell temperature in a module when ambient is  $20^{\circ}\text{C}$ .

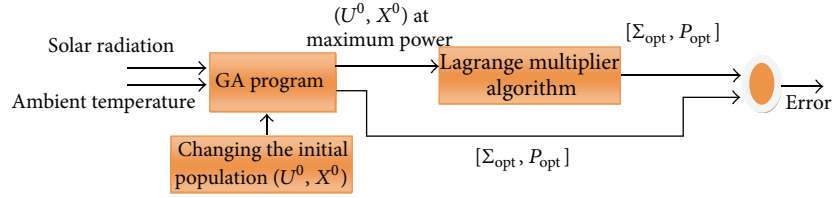


FIGURE 7: The proposed analysis steps.

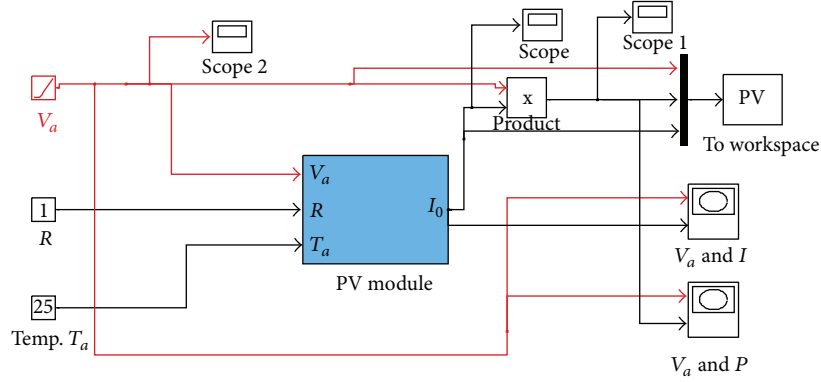


FIGURE 8: Simulink model of the PV module.

A PV module consists of series cells,  $N_S$ , and parallel branches,  $N_P$ , which are given in Figure 5.

The PV module's current  $I^M$  under variable operating conditions can be described as follows [15]:

$$I^M = N_P I_{SC} - N_P I_0 \left\{ \exp \left[ \frac{q \left( V^M / N_S + I^M \cdot R_S^M \right)}{nk_b T} \right] - 1 \right\} - \left( \frac{V^M / N_S + I^M \cdot R_S^M}{R_P^M} \right),$$

$$R_S^M = \frac{N_S}{N_P} R_s, \quad R_P^M = \frac{N_P}{N_S} R_p, \quad V^M = N_S V.$$
(8)

### 3. Proposed Technique

**3.1. The Proposed Optimization Problem.** The mathematical model of any continuous optimization problem can be described as follows:

$$\text{minimize or maximize } f(X, U), \quad (9)$$

where  $f(X, U)$  is an objective function to be minimized or maximized subjected to equality and inequality constraints as follows:

(1) *equality constraint*

$$q_i(X, U) = 0, \quad i = 1, 2, \dots, l, \quad (10)$$

TABLE 1: Electrical characteristic of bpsx150 PV module.

Maximum power ( $P_{\max}$ )	150 W
Voltage at $P_{\max}$ ( $V_{P_{\max}}$ )	34.5 V
Current at $P_{\max}$ ( $I_{P_{\max}}$ )	4.35 A
Warranted minimum $P_{\max}$	140 W
Short-circuit current ( $I_{sc}$ )	4.75 A
Open-circuit voltage ( $V_{oc}$ )	43.5 V
Maximum system voltage	600 V
Temperature coefficient of $I_{sc}$	$(0.065 \pm 0.015) \% / ^\circ C$
Temperature coefficient of $V_{oc}$	$-(160 \pm 20) \text{ mV} / ^\circ C$
Temperature coefficient of power	$-(0.5 \pm 0.05) \% / ^\circ C$
NOCT	$47 \pm 2 ^\circ C$

(2) *parametric inequality constraint*

$$X_j^{\min} \leq X_j \leq X_j^{\max}, \quad j = 1, 2, \dots, f, \quad (11a)$$

$$U_k^{\min} \leq U_k \leq U_k^{\max}, \quad k = 1, 2, \dots, r, \quad (11b)$$

(3) *functional inequality constraint*

$$h_y(X, U) \leq 0, \quad y = 1, 2, \dots, p, \quad (12)$$

where  $X$  is a vector of state, dependant, variables and  $U$  is a vector of control (independent) variables. First the dummy variables that have effect on the PV module power are classified into two categories: independent ( $U$ ) and dependent variables ( $X$ )— $U = [N_S, N_P, d, \Sigma, \varphi_C]$  and  $X = [\beta, m, \varphi_S, G_C, I_{SC}, I_0, T_C]$ .

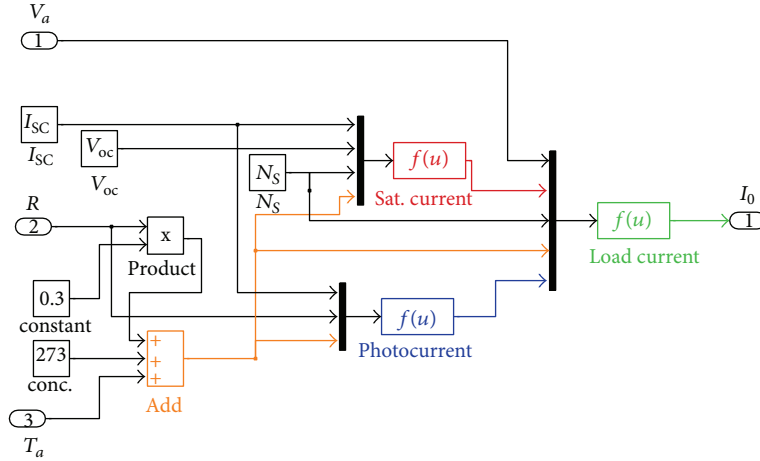


FIGURE 9: Detailed configuration of PV module subsystem.

The proposed objective function is expressed in the following form:

$$\begin{aligned}
 & \text{maximize } P_{pv}(X, U) \\
 & = f(T_C, V^M, m, \Sigma, \varphi_C, \beta, L, \omega, G_C, I_0) \\
 & = (N_s V^C) * I_{n+1}^M \\
 & = V^M * (I_n^M * (1 - (1 + \psi(T_C) \\
 & \quad * (1 - \mu(V^M, T_C, I^M)) \\
 & \quad * \partial(T_C))^{-1})) \\
 & + ((\psi(T_C) * \epsilon(m, \varphi_s, \beta, \Sigma, \varphi_C) \\
 & \quad * \mu(V^M, T_C, I^M) + \gamma(V^M)) \\
 & \quad \times (1 + \psi(T_C) * (1 - \mu(V^M, T_C, I^M)) \\
 & \quad * \partial(T_C))^{-1})). \tag{13}
 \end{aligned}$$

Subjected to the following proposed parametric constrained:

$$\begin{aligned}
 & N_s^{\min} < N_s < N_s^{\max}, \\
 & N_p^{\min} < N_p < N_p^{\max}, \\
 & d^{\min} < d < d^{\max} \rightarrow 1 \leq d \leq 365, \\
 & \Sigma^{\min} < \Sigma < \Sigma^{\max} \rightarrow 0 \leq \Sigma \leq 80, \\
 & \varphi_C^{\min} < \varphi_C < \varphi_C^{\max} \rightarrow -45 \leq \varphi_C \leq 45,
 \end{aligned} \tag{14}$$

the proposed equality constraint is given as

$$g(U, X) = V_{oc} - 184.0293 * \frac{N_s V^C}{T} = 0. \tag{15}$$

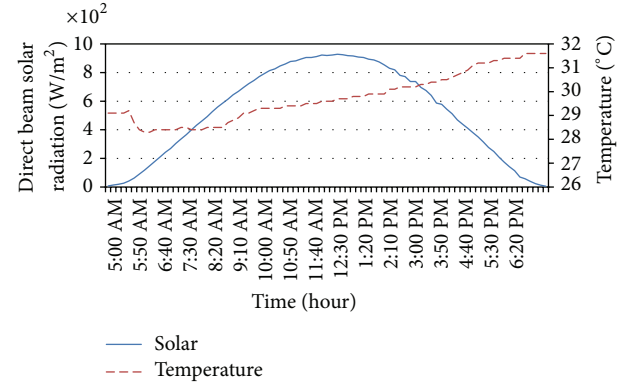


FIGURE 10: Direct beam solar radiation and ambient temperature for Helwan city, Egypt.

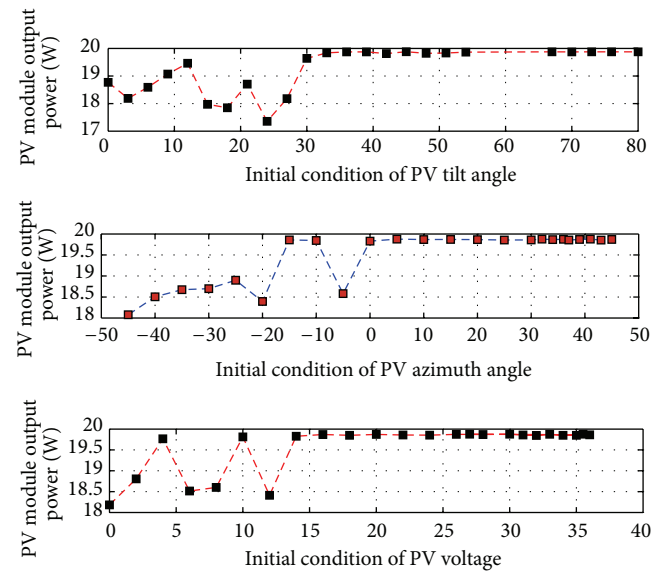


FIGURE 11: The optimal PV module power at changing the initial population in GA at 6:10 AM.

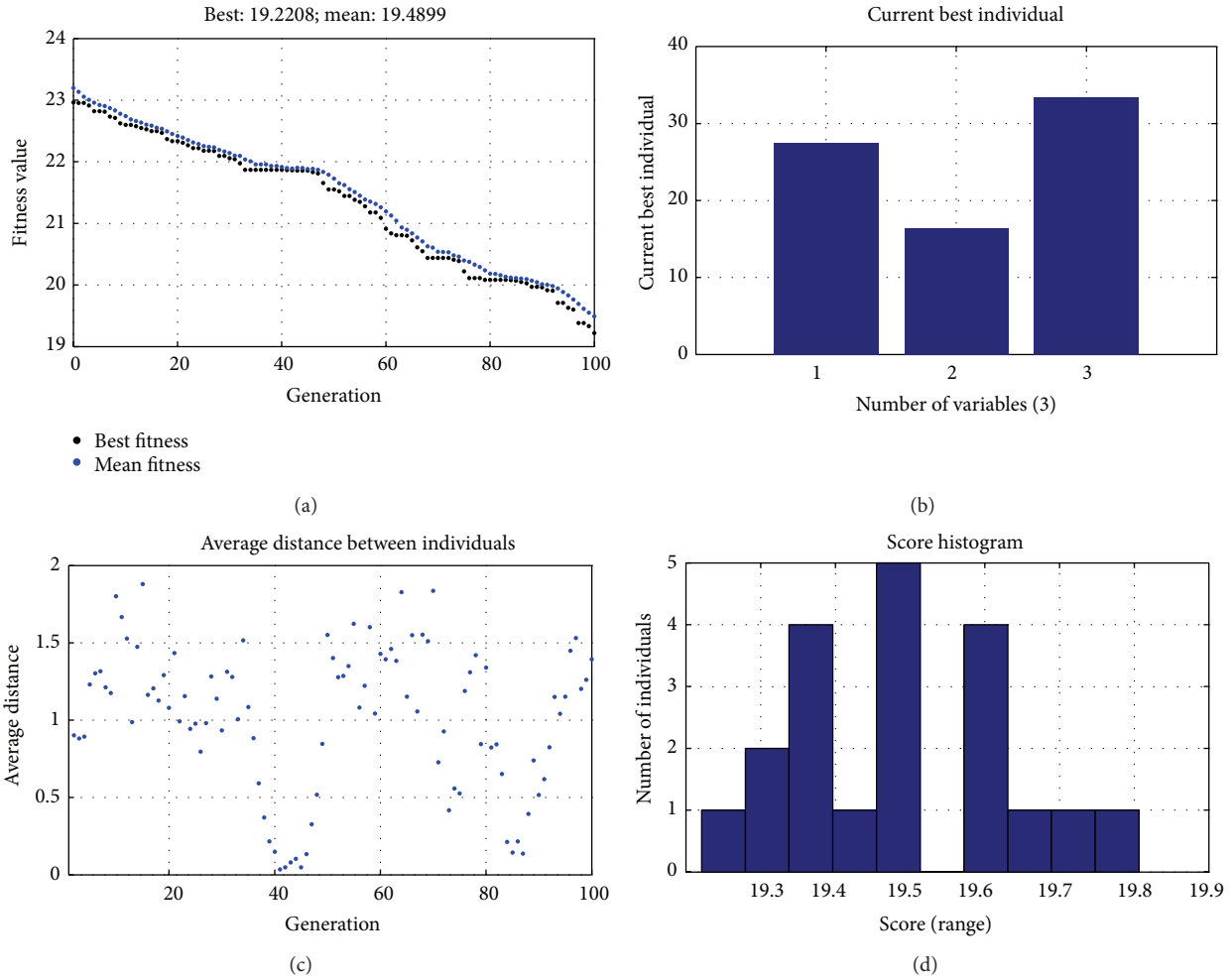


FIGURE 12: The optimal PV module power at changing the initial population in GA at 6:10 AM.

The limits of independent variables are selected according to the following aspects.

- (1) When  $\Sigma = 0^\circ$ , the PV module becomes horizontal and produces power, while for  $\Sigma = 90^\circ$ , the PV module becomes vertical and produces zero power; so, the selected limits are assumed between  $0^\circ$  and  $80^\circ$ .
- (2) The PV module azimuth angle is positive for east of south and becomes negative for west of south; so, the limits are selected as  $\pm 45^\circ$ .

3.2. *Genetic Algorithm.* Genetic algorithm, GA, is gradient free, parallel optimization algorithms that use a performance criterion for evaluation and a population of possible solutions to the search for a global optimum. GA is capable of handling complex and irregular solution spaces and has been applied to various difficult optimization problems [16]. It is inspired by the biological process of Darwinian evolution where selection, mutation, and crossover play a major role. The manipulation is done by the *genetic operators* that work on the *chromosomes* in which the parameters of possible solutions are encoded. In each generation of the GA, the new solutions

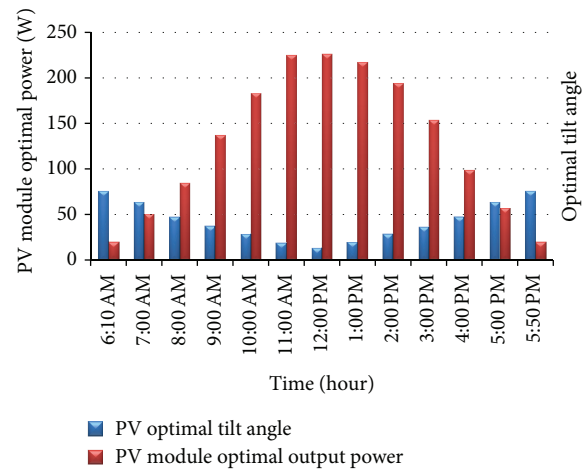


FIGURE 13: The optimal power and the corresponding tilt angle for June 10, 2012.

replace the solutions in the population that is selected for removal. The main elements of GA are populations of chromosomes, selection according to fitness, crossover to produce

TABLE 2: Effect of changing the initial tilt angle on the module power at 6:10 AM.

Initial solution [ $\Sigma_0^\circ, \varphi_{C0}^\circ, V_0^M$ ]	Independent variables			Dependant variables			$I^M$ (A)	$P_{pv}$ (W)
	$\Sigma^\circ$	$\varphi_C^\circ$	$V^M$ (V)	$G_C$ (Kw/m <sup>2</sup> )	$I_0$ (A)	$T$ (°C)		
$U_0 = [0, 5, 30]$	56.5384	44.4320	43.4848	0.0887	$4.5125 * 10^{-6}$	31.8929	0.4231	18.7692
$U_0 = [3, 5, 30]$	51.2944	44.7359	43.4484	0.0877	$4.4992 * 10^{-6}$	31.8609	0.4186	18.1864
$U_0 = [6, 5, 30]$	54.6782	44.8905	43.3716	0.0887	$4.5131 * 10^{-6}$	31.8944	0.4233	18.5889
$U_0 = [9, 5, 30]$	58.7500	45.0000	43.4777	0.0915	$4.5519 * 10^{-6}$	31.9871	0.4365	19.0712
$U_0 = [12, 5, 30]$	63.5000	45.0000	43.5000	0.0932	$4.5768 * 10^{-6}$	32.0463	0.4448	19.4612
$U_0 = [15, 5, 30]$	49.6782	44.9171	43.3964	0.0843	$4.4509 * 10^{-6}$	31.7443	0.4021	17.9730
$U_0 = [18, 5, 30]$	49.2228	44.5000	43.3857	0.0833	$4.4368 * 10^{-6}$	31.7098	0.3972	17.8469
$U_0 = [21, 5, 30]$	56.2744	44.8397	43.2505	0.0887	$4.5122 * 10^{-6}$	31.8921	0.4230	18.7031
$U_0 = [24, 5, 30]$	47.3468	42.7325	43.4541	0.0816	$4.4142 * 10^{-6}$	31.6547	0.3894	17.3567
$U_0 = [27, 5, 30]$	51.5620	44.9079	43.2911	0.0862	$4.4777 * 10^{-6}$	31.8091	0.4112	18.1797
$U_0 = [30, 5, 30]$	67.2500	44.9020	43.4535	0.0941	$4.5888 * 10^{-6}$	32.0746	0.4489	19.6382
$U_0 = [33, 5, 30]$	73.7500	45.0000	43.4414	0.0956	$4.6110 * 10^{-6}$	32.1269	0.4563	19.8390
$U_0 = [36, 5, 30]$	74.7500	45.0000	43.4958	0.0957	$4.6129 * 10^{-6}$	32.1313	0.4569	19.8724
$U_0 = [39, 5, 30]$	75.7500	45.0000	43.4894	0.0957	$4.6126 * 10^{-6}$	32.1307	0.4568	19.8726
$U_0 = [42, 5, 30]$	76.0000	45.0000	43.3601	0.0953	$4.6063 * 10^{-6}$	32.1160	0.4547	19.8134
<b><math>U_0 = [45, 5, 30]</math></b>	<b>75.8125</b>	<b>45.0000</b>	<b>43.4999</b>	<b>0.0958</b>	<b><math>4.6131 * 10^{-6}</math></b>	<b>32.1318</b>	<b>0.4570</b>	<b>19.8774</b>
$U_0 = [48, 5, 30]$	75.7500	45.0000	43.3796	0.0953	$4.6069 * 10^{-6}$	32.1173	0.4549	19.8224
$U_0 = [51, 5, 30]$	76.0000	45.0000	43.3997	0.0958	$4.6130 * 10^{-6}$	32.1317	0.4569	19.8315
$U_0 = [54, 5, 30]$	75.7500	45.0000	43.4689	0.0958	$4.6131 * 10^{-6}$	32.1318	0.4569	19.8632
$U_0 = [67, 5, 30]$	75.8125	45.0000	43.4989	0.0957	$4.6129 * 10^{-6}$	32.1313	0.4569	19.8769
$U_0 = [70, 5, 30]$	75.8125	45.0000	43.4903	0.0958	$4.6131 * 10^{-6}$	32.1318	0.4570	19.8730
$U_0 = [73, 5, 30]$	75.8125	45.0000	43.4989	0.0958	$4.6131 * 10^{-6}$	32.1318	0.4570	19.8769
$U_0 = [76, 5, 30]$	75.7500	45.0000	43.4963	0.0955	$4.6099 * 10^{-6}$	32.1243	0.4559	19.8757
$U_0 = [80, 5, 30]$	75.7813	45.0000	43.4966	0.0958	$4.6130 * 10^{-6}$	32.1317	0.4569	19.8759

new offspring, and random mutation of new offspring. A simple GA flow chart is shown in Figure 6.

The simplest form of genetic algorithm involves three types of operators: selection, crossover (single point), and mutation.

*Selection.* It selects chromosomes in the population for reproduction.

*Crossover.* It randomly chooses a locus and exchanges the subsequences before and after that locus between two chromosomes to create two offsprings.

*Mutation.* It randomly flips some of the bits in a chromosome.

**3.3. The Method of Lagrange Multipliers.** Lagrange multipliers, LM, play a vital role in the study of constrained optimization. It can be interpreted as the rate of change in the objective function with respect to changes in the associated constraint function [16]. The main formula of this method can be described as follows:

$$\nabla_{U,X} f(U, X) = -\lambda \nabla_{U,X} g, \quad (16)$$

where  $\nabla_{U,X} f = (\partial f / \partial U, \partial f / \partial X)$  and  $\nabla_{U,X} g = (\partial g / \partial U, \partial g / \partial X)$  are the respective gradients. Constant  $\lambda$  in (16) are called the *Lagrange multipliers* of the constrained problem.

By solving (15) one can get the value of  $\lambda$  and then obtain the value of  $U$  vector and  $X$  vector at optimal solution and the optimal power extracted from the PV module. The proposed analysis uses a real data for solar radiation and ambient temperature measured by solar radiation and meteorological station located at National Research Institute of Astronomy and Geophysics Helwan, Cairo, Egypt, which is located at latitude 29.87°N and longitude 31.30°E. The station is over a hill top of about 114 m height above sea level.

The initial condition of any optimization problem plays an important role in finding the optimal solution so GA program is performed under varying the initial condition of the independent variables until the optimal, maximum, power is obtained then Lagrange multiplier algorithm program is used and compared with GA to investigate the validity and quality of our proposed method.

The main steps of the proposed technique can be summarized as follows.

- (1) Using the real data for solar radiation and ambient temperature as an input to genetic algorithm program that obtain the optimal output power from the PV module.
- (2) Studying the effect of changing the initial population on the value of fitness function in order to obtain the optimal (maximum) possible power from the PV module.

TABLE 3: Effect of changing the initial collector azimuth angle on the module power at 6:10 AM.

Initial solution [ $\Sigma_0, \varphi_{C0}, V_0^M$ ]	Independent variables			Dependant variables			$I^M$ (A)	$P_{pv}$ (W)
	$\Sigma^\circ$	$\varphi_C^\circ$	$V^M$ (V)	$G_C$ (Kw/m <sup>2</sup> )	$I_0$ (A)	$T$ (°C)		
$U_0 = [45, -45, 30]$	50.6146	44.5382	43.4679	0.0867	$4.4841 * 10^{-6}$	31.8246	0.4134	18.0765
$U_0 = [45, -40, 30]$	53.9220	44.9146	43.3693	0.0880	$4.5023 * 10^{-6}$	31.8683	0.4196	18.5043
$U_0 = [45, -35, 30]$	56.1325	44.2593	43.4265	0.0888	$4.5140 * 10^{-6}$	31.8966	0.4236	18.6752
$U_0 = [45, -30, 30]$	55.7048	44.9776	43.3350	0.0874	$4.4944 * 10^{-6}$	31.8495	0.4170	18.6999
$U_0 = [45, -25, 30]$	57.7381	44.7576	43.3907	0.0870	$4.4883 * 10^{-6}$	31.8348	0.4149	18.8992
$U_0 = [45, -20, 30]$	53.4386	44.7737	43.2897	0.0877	$4.4994 * 10^{-6}$	31.8615	0.4187	18.3925
$U_0 = [45, -15, 30]$	75.7500	44.9988	43.4602	0.0957	$4.6130 * 10^{-6}$	32.1316	0.4569	19.8591
$U_0 = [45, -10, 30]$	75.7500	44.8301	43.4955	0.0956	$4.6102 * 10^{-6}$	32.1250	0.4560	19.8452
$U_0 = [45, -5, 30]$	54.9162	44.5165	43.4248	0.0891	$4.5189 * 10^{-6}$	31.9083	0.4253	18.5822
$U_0 = [45, 0, 30]$	76.0000	44.7835	43.4785	0.0956	$4.6104 * 10^{-6}$	32.1255	0.4561	19.8290
$U_0 = [45, 5, 30]$	75.7500	45.0000	43.4714	0.0955	$4.6100 * 10^{-6}$	32.1246	0.4559	19.8774
$U_0 = [45, 10, 30]$	75.7500	45.0000	43.4771	0.0953	$4.6062 * 10^{-6}$	32.1155	0.4547	19.8670
$U_0 = [45, 15, 30]$	75.7500	45.0000	43.4837	0.0953	$4.6069 * 10^{-6}$	32.1173	0.4549	19.8700
$U_0 = [45, 20, 30]$	75.7500	45.0000	43.4731	0.0958	$4.6131 * 10^{-6}$	32.1318	0.4570	19.8651
$U_0 = [45, 25, 30]$	75.7500	45.0000	43.4553	0.0957	$4.6122 * 10^{-6}$	32.1298	0.4567	19.8570
$U_0 = [45, 30, 30]$	76.0000	45.0000	43.4579	0.0952	$4.6052 * 10^{-6}$	32.1133	0.4543	19.8581
$U_0 = [45, 32, 30]$	75.7500	45.0000	43.4983	0.0953	$4.6068 * 10^{-6}$	32.1171	0.4549	19.8767
$U_0 = [45, 34, 30]$	76.0000	45.0000	43.4766	0.0957	$4.6124 * 10^{-6}$	32.1303	0.4567	19.8667
$U_0 = [45, 36, 30]$	75.7500	45.0000	43.4935	0.0958	$4.6130 * 10^{-6}$	32.1317	0.4569	19.8744
$U_0 = [45, 37, 30]$	76.0000	45.0000	43.4558	0.0944	$4.5943 * 10^{-6}$	32.0877	0.4507	19.8572
$U_0 = [45, 39, 30]$	75.7500	45.0000	43.4837	0.0958	$4.6130 * 10^{-6}$	32.1317	0.4569	19.8700
$U_0 = [45, 41, 30]$	<b>75.7500</b>	<b>45.0000</b>	<b>43.4997</b>	<b>0.0957</b>	<b><math>4.6126 * 10^{-6}</math></b>	<b>32.1307</b>	<b>0.4568</b>	<b>19.8776</b>
$U_0 = [45, 43, 30]$	75.7500	45.0000	43.4516	0.0957	$4.6118 * 10^{-6}$	32.1289	0.4565	19.8553
$U_0 = [45, 45, 30]$	75.7500	45.0000	43.4834	0.0953	$4.6063 * 10^{-6}$	32.1160	0.4547	19.8698

- (3) The initial population at the optimal PV output power is fed to the Lagrange multiplier algorithm and comparing the results with those obtained by GA. Figure 7 shows these proposed technique steps.

#### 4. Numerical Analysis

The analysis uses bpsx150 PV module which has 72 cells connected in series and its electrical characteristic is shown in Table 1 [17].

The bpsx150 PV module is simulated by MATLAB/Simulink toolbox as shown in Figure 8. Referring to Figure 8, there are three main inputs which are the module voltage, the solar radiation, and the ambient temperature; these items are labeled in Figure 9 with numbers 1, 2, and 3. Simulink is a software package of MATLAB program for modeling, simulating, and analyzing dynamical systems. It supports linear and nonlinear systems, modeled in continuous time, sampled time, or a hybrid of the two. For modeling, Simulink provides a graphical user interface, GUI, for building models as block diagrams, using click and drag mouse operations. The detailed configuration of the PV module is given in Figure 9. The analysis of the proposed algorithm is performed on measured solar radiation and ambient temperature as inputs to GA program. These data are measured at Helwan city, for the sunny day of June 10, 2012, and start from

6:10 AM to 5:50 PM. The direct beam solar radiation and the corresponding ambient temperature, Helwan city, at latitude 29.87°, Egypt, are given in Figure 10.

The initial population of GA program which contains ( $\Sigma_0, \varphi_{C0}, V_0^M$ ) plays an important role in finding the optimal power, so they are changed as follows.

- (1) The initial tilt angle,  $\Sigma_0$ , is changed at acceptable limits, fixing both  $\varphi_{C0}$  and  $V_0^M$  at acceptable values until the maximum power is obtained as shown in Table 2.

The optimal output power for this case is equal to 19.8774 W at  $\Sigma_0 = 45^\circ$  which is fixed at this value.

- (2) Changing the initial PV module azimuth angle,  $\varphi_{C0}$ , at acceptable limits with fixed acceptable initial module voltage until the optimal power is obtained as shown in Table 3.

The optimal output power for this case is equal to 19.8776 W at  $\varphi_{C0} = 41$  which is fixed at this value.

- (3) Changing the initial PV module voltage until the optimal power is obtained as shown in Table 4.

The final optimal output power is equal to 19.8778 W at  $V_0^M = 42$  V.

TABLE 4: Effect of changing the initial module voltage on the module power at 6:10 AM.

Initial solution [ $\Sigma_0^\circ, \varphi_{C0}^\circ, V_0^M$ ]	Independent variables			Dependant variables			$I^M$ (A)	$P_{pv}$ (W)
	$\Sigma^\circ$	$\varphi_C^\circ$	$V^M$ (V)	$G_C$ (Kw/m <sup>2</sup> )	$I_0$ (A)	$T$ (°C)		
$U_0 = [45, 41, 0]$	51.8224	44.5636	43.3348	0.0872	$4.4921 * 10^{-6}$	31.8439	0.4162	18.1819
$U_0 = [45, 41, 2]$	56.3961	45.0000	43.4018	0.0899	$4.5301 * 10^{-6}$	31.9350	0.4291	18.8057
$U_0 = [45, 41, 4]$	76.0000	44.9427	43.2811	0.0957	$4.6123 * 10^{-6}$	32.1299	0.4567	19.7672
$U_0 = [45, 41, 6]$	53.7614	44.8565	43.4569	0.0859	$4.4740 * 10^{-6}$	31.8003	0.4100	18.5142
$U_0 = [45, 41, 8]$	54.9695	44.5616	43.4382	0.0889	$4.5158 * 10^{-6}$	31.9008	0.4242	18.6007
$U_0 = [45, 41, 10]$	76.0000	45.0000	43.3597	0.0958	$4.6131 * 10^{-6}$	32.1318	0.4570	19.8132
$U_0 = [45, 41, 12]$	53.1965	44.7522	43.4134	0.0875	$4.4960 * 10^{-6}$	31.8533	0.4175	18.4128
$U_0 = [45, 41, 14]$	76.0000	44.9767	43.3995	0.0957	$4.6127 * 10^{-6}$	32.1308	0.4568	19.8273
$U_0 = [45, 41, 16]$	75.7500	45.0000	43.4834	0.0957	$4.6129 * 10^{-6}$	32.1313	0.4569	19.8698
$U_0 = [45, 41, 18]$	75.8750	45.0000	43.4408	0.0949	$4.6006 * 10^{-6}$	32.1023	0.4528	19.8504
$U_0 = [45, 41, 20]$	75.7500	45.0000	43.4871	0.0958	$4.6131 * 10^{-6}$	32.1318	0.4570	19.8716
$U_0 = [45, 41, 22]$	76.0000	45.0000	43.4579	0.0958	$4.6131 * 10^{-6}$	32.1318	0.4569	19.8581
$U_0 = [45, 41, 24]$	75.7500	45.0000	43.4499	0.0955	$4.6092 * 10^{-6}$	32.1227	0.4557	19.8545
$U_0 = [45, 41, 26]$	75.7500	45.0000	43.4741	0.0949	$4.6003 * 10^{-6}$	32.1017	0.4527	19.8728
$U_0 = [45, 41, 28]$	75.7500	45.0000	43.4839	0.0958	$4.6131 * 10^{-6}$	32.1318	0.4569	19.8701
$U_0 = [45, 41, 30]$	76.0000	45.0000	43.4818	0.0958	$4.6130 * 10^{-6}$	32.1316	0.4569	19.8776
$U_0 = [45, 41, 32]$	75.7500	45.0000	43.4565	0.0956	$4.6115 * 10^{-6}$	32.1281	0.4564	19.8575
$U_0 = [45, 41, 34]$	75.7500	45.0000	43.4324	0.0957	$4.6129 * 10^{-6}$	32.1313	0.4569	19.8466
$U_0 = [45, 41, 36]$	75.6875	45.0000	43.4969	0.0958	$4.6131 * 10^{-6}$	32.1318	0.4570	19.8760
$U_0 = [45, 41, 38]$	75.7500	45.0000	43.4403	0.0958	$4.6130 * 10^{-6}$	32.1317	0.4569	19.8501
$U_0 = [45, 41, 40]$	75.7500	45.0000	43.4393	0.0958	$4.6131 * 10^{-6}$	32.1318	0.4569	19.8497
$U_0 = [45, 41, 42]$	<b>76.0000</b>	<b>45.0000</b>	<b>43.5000</b>	<b>0.0957</b>	<b><math>4.6129 * 10^{-6}</math></b>	<b>32.1315</b>	<b>0.4569</b>	<b>19.8778</b>
$U_0 = [45, 41, 43]$	75.5625	45.0000	43.4655	0.0955	$4.6098 * 10^{-6}$	32.1241	0.4559	19.8615
$U_0 = [45, 41, 43.5]$	75.5000	45.0000	43.5000	0.0958	$4.6130 * 10^{-6}$	32.1317	0.4564	19.8772

TABLE 5: The optimal power and the corresponding tilt angle by GA for June 10, 2012.

Hour	Initial condition at optimal solution [ $\Sigma_0^\circ, \varphi_{C0}^\circ, V_0^M$ ]	Tilt angle at optimal power	Optimal power (W)
6:10 AM	[45, 41, 42]	75.7500	19.8773
7:00 AM	[54, 32, 26]	63.4998	50.0546
8:00 AM	[27, 30, 42]	47.2500	84.8483
9:00 AM	[42, 36, 14]	36.9459	137.1025
10:00 AM	[21, 32, 42]	28.2500	182.8460
11:00 AM	[70, 0, 36]	19.2309	225.0597
12:00 PM	[18, 30, 42]	13.0219	226.6207
1:00 PM	[30, 10, 43.5]	19.3121	217.1806
2:00 PM	[54, 30, 43.5]	28.2298	194.0017
3:00 PM	[3, 5, 32]	36.7493	153.7899
4:00 PM	[73, -40, 43.5]	47.7500	98.8123
5:00 PM	[24, -35, 43.5]	63.5000	56.5923
5:50 PM	[70, -45, 16]	75.8125	20.2942

Finally, one can derive that the optimal obtained power by GA at 6:10 AM is equal to 19.8778 W and is occurred at initial population which is equal to  $(\Sigma_0^\circ, \varphi_{C0}^\circ, V_0^M) = (45^\circ, 41^\circ, 42 \text{ V})$ . The curve shows the change of PV module power with

changing the initial population is shown in Figure 11. GA program response is shown in Figure 12 that contains the fitness function, the current best individuals, the average distance between individuals and the number of individuals for each iteration. The constant dependant values at optimal power are  $\delta = 17.5165$ ,  $\beta = 10.7181$ ,  $m = 5.3770$ ,  $\varphi_s = 75.8452$ , and  $\omega = 60$ .

The final population at optimal solution is equal to  $\Sigma = 75.7500$ ,  $\varphi_C = 45.0000$ , and  $V^M = 43.5000$ .

The optimal power and the corresponding tilt angle for 24 hours of the day are shown in Figure 13 and Table 5.

Once the bpsx150 PV module has a fixed number of series cells,  $N_S = 72$ , and a fixed number of parallel branches,  $N_P = 1$ , then they are not be considered as variables.

The initial condition at optimal power obtained from the GA is fed to the Lagrange multiplier algorithm to find the optimal power. The MATLAB function `fmincon` is used to perform the Lagrange multiplier analysis.

The Lagrange multiplier algorithm response is shown in Figure 14. A comparison between the GA and Lagrange multiplier algorithm is performed and is shown in Figure 15 and Table 6.

A comparison between the GA and Lagrange multiplier algorithm is performed and is shown in Figure 14 and Table 6.

It is clear that the difference between two proposed solution methods is very small as the initial condition of them is the same; the operating conditions of the PV module do

TABLE 6: A comparison between the GA and Lagrange multiplier algorithm.

Hour	Genetic algorithm solution		Lagrange multiplier algorithm results		Error in optimal tilt angle	Error in optimal power
	$\Sigma_{opt}$	$P_{opt}$	$\Sigma_{opt}$	$P_{opt}$		
6:10 AM	75.7500	19.8773	75.8114	19.8774	-0.0614	-1E - 04
7:00 AM	63.4998	50.0546	63.4993	50.0486	0.0005	0.006
8:00 AM	47.2500	84.8483	47.3668	84.8485	-0.1168	-0.0002
9:00 AM	36.9459	137.1025	36.8401	137.1174	0.1058	-0.0149
10:00 AM	28.2500	182.8460	28.2483	182.8456	0.0017	0.0004
11:00 AM	19.2309	225.0597	19.2598	225.0807	-0.0289	-0.021
12:00 PM	13.0219	226.6207	13.0221	226.6537	-0.0002	-0.033
1:00 PM	19.3121	217.1806	19.2598	217.1956	0.0523	-0.015
2:00 PM	28.2298	194.0017	28.2483	194.0071	-0.0185	-0.0054
3:00 PM	36.7493	153.7899	36.8401	153.8525	-0.0908	-0.0626
4:00 PM	47.7500	98.8123	47.3668	98.8142	0.3832	-0.0019
5:00 PM	63.5000	56.5923	63.4993	56.5563	0.0007	0.036
5:50 PM	75.8125	20.2942	75.8114	20.2752	0.0011	0.019

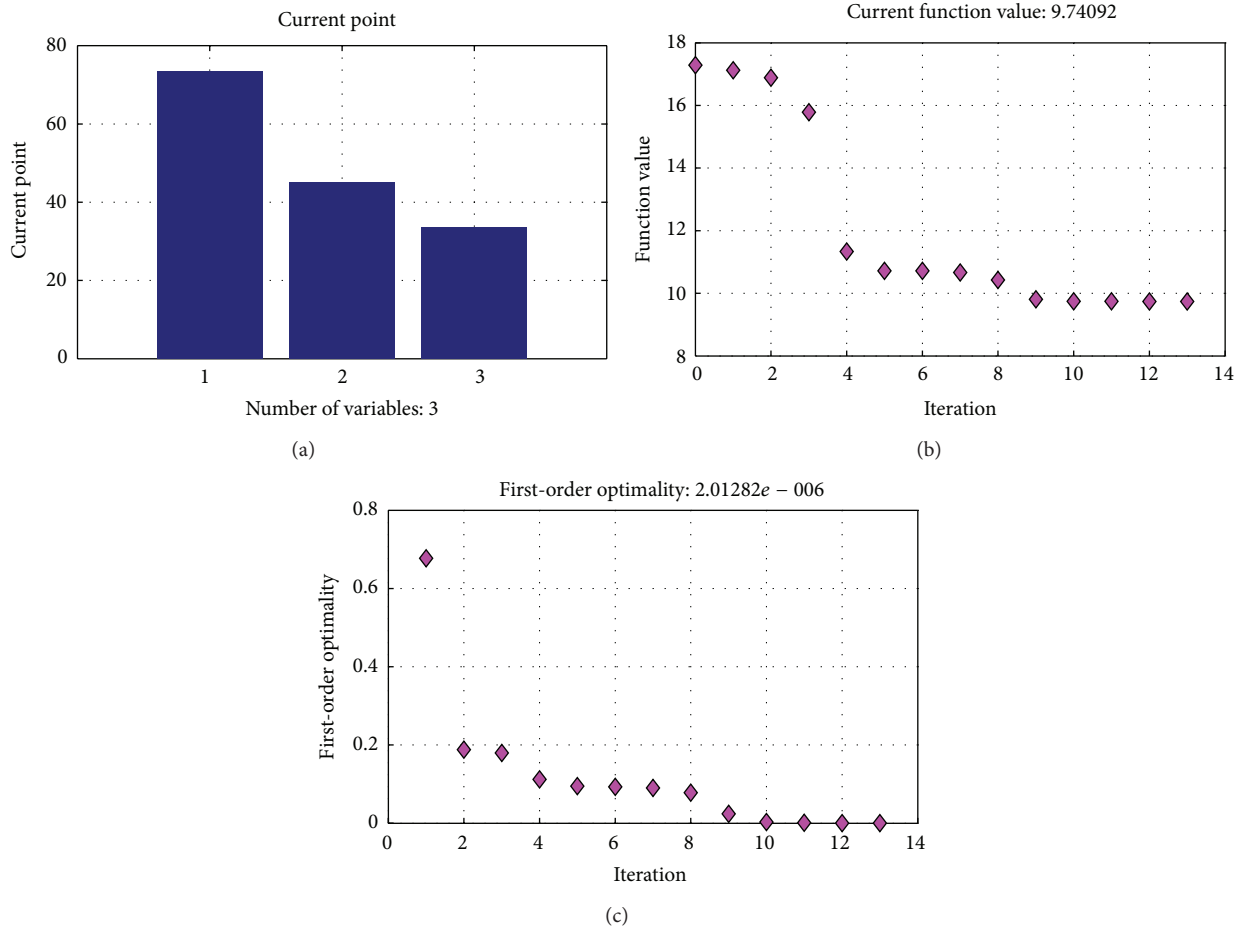


FIGURE 14: The Lagrange multiplier response.

not change. So, one can derive that the error between two methods is acceptable and the proposed method is applicable.

The benefits of this proposed approach are as follows.

- (i) A new objective function of the PV module output power subjected to constraints is presented.
- (ii) A simple optimization methodology to obtain the optimal power extracted from the PV module and corresponding tilt angle based on real data is formulated.
- (iii) Two suggested solution techniques are manipulated and the error between them is very small.

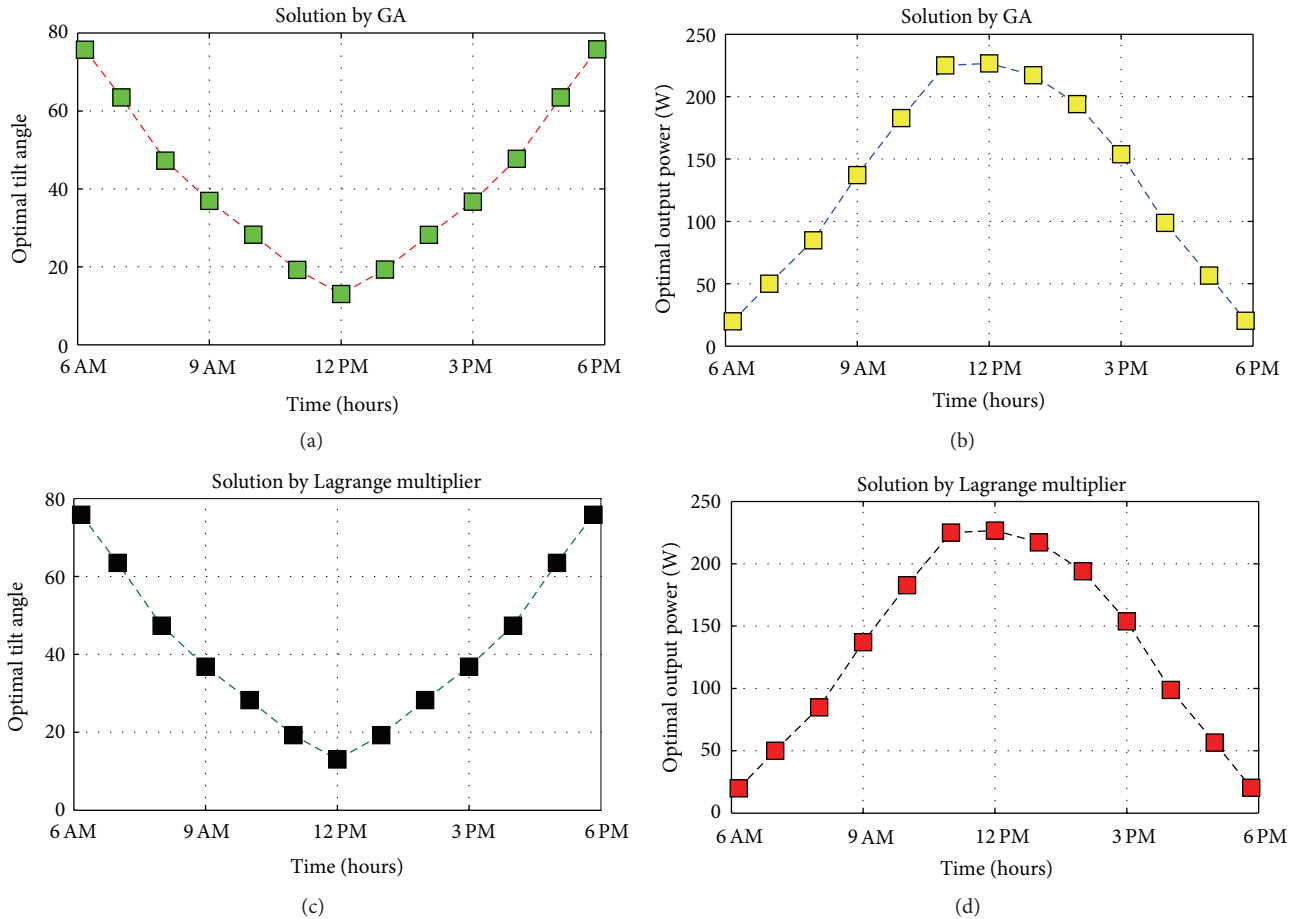


FIGURE 15: A comparison between the GA and Lagrange multiplier algorithm responses.

## 5. Conclusion

In this work a new optimization approach to maximize the PV module output power is presented. A new proposed objective function of PV module power and constraints is also presented. Genetic algorithm is performed under varying the initial population of independent variables, then Lagrange multiplier algorithm is simulated. The optimal PV module power obtained from both algorithms is compared. The analysis is based on real measured data of solar radiation and ambient temperature at Helwan city at latitude  $29.87^\circ$ , Egypt. The analysis is done in complete sunny day and the results showed that the error between two proposed solution techniques is acceptable and the proposed constrained optimization method is applicable.

## Acknowledgment

Cordial thanks and deep respect are offered to the Solar and Space Research Department, National Research Institute of Astronomy and Geophysics, Helwan, Egypt, for supporting this work and providing the authors with the required real data.

## References

- [1] G. M. Masters, *Renewable and Efficient Electric Power Systems*, John Wiley & Sons, Hoboken, NJ, USA, 2004.
- [2] C. Liu, B. Wu, and R. Cheung, "Advanced algorithm for MPPT control of photovoltaic systems," in *Proceedings of the Canadian Solar Buildings Conference*, Montreal, Canada, 2004.
- [3] M. Farhat and L. Sbita, "Advanced fuzzy MPPT control algorithm for photovoltaic systems," *Science Academy Transactions on Renewable Energy Systems Engineering and Technology*, vol. 1, no. 1, 2011.
- [4] B. Amrouche, M. Belhame, and A. Guessoum, "Artificial intelligence based P&O MPPT method for photovoltaic systems," *Review of Renewable Energy ICRES-07 Tlemcen*, pp. 11–16, 2007.
- [5] C. S. Chin, P. Neelakantan, H. P. Yoong, and K. T. K. Teo, "Optimisation of fuzzy based maximum power point tracking in PV system for rapidly changing solar irradiance," *Transaction on Solar Energy and Planning*, vol. 2, 2011.
- [6] G. Zeng, X. Zhang, J. Ying, and C. Ji, "A novel intelligent fuzzy controller for MPPT in grid-connected photovoltaic systems," in *Proceedings of the 5th WSEAS/IASME International Conference on Electric Power Systems, High Voltages, Electric Machines*, pp. 515–519, Tenerife, Spain, 2005.

- [7] M. S. Aït Cheikh, C. Larbes, G. F. Tchoketch Kebir, and A. Zerguerras, "Maximum power point tracking using a fuzzy logic control scheme," *Revue Des Energies Renouvelables*, vol. 10, no. 3, pp. 387–395, 2007.
- [8] P. Takun, S. Kaitwanidvilai, and C. Jettanasen, "Maximum power point tracking using fuzzy logic control for photovoltaic systems," in *Proceedings of the International Multi Conference of Engineers and Computer Scientists (IMECS '11)*, vol. 2, pp. 986–990, March 2011.
- [9] M. El Ouariachi, T. Mrabti, M. F. Yaden, K. Kassmi, and K. Kassmi, "Analysis, optimization and modeling of electrical energies produced by the photovoltaic panels and systems," *Revue Des Energies Renouvelables*, vol. 14, no. 4, pp. 707–716, 2011.
- [10] K. Ishaque, Z. Salam, A. Shamsudin, and M. Amjad, "A direct control based maximum power point tracking method for photovoltaic system under partial shading conditions using particle swarm optimization algorithm," *Applied Energy Journal*, vol. 99, pp. 414–422, 2012.
- [11] T. Perpétuo Corrêa, S. Isaac Seleme Jr., and S. Rocha Silva, "Efficiency optimization in stand-alone photovoltaic pumping system," *Renewable Energy Journal*, vol. 41, pp. 220–226, 2012.
- [12] G. M. Masters, *Renewable and Efficient Electric Power Systems*, John Wiley & Sons, Hoboken, NJ, USA, 2004.
- [13] N. Hidouri and L. sbita, "Water photovoltaic pumping system based on DTC SPMSM drives," *Journal of Electric Engineering*, vol. 1, no. 2, pp. 111–119, 2010.
- [14] B. Krishna Kumar, "Matlab based modelling of photovoltaic panels and their efficient, utilization for maximum power generation," in *Proceedings of the 1st National Conference on Intelligent Electrical Systems (NCIES '09)*, pp. 125–130, Salem, India, 2009.
- [15] A. M. Othman, M. M. M. El-Arini, A. Ghitas, and A. Fathy, "Realworld maximum power point tracking simulation of PV system based on fuzzy logic control," in *Proceedings of the 3rd Arab Conference on Astronomy and Geophysics ( ACAG '12)*, Helwan, Cairo, Egypt, 2012.
- [16] Z. Michalewicz, *Genetic Algorithms + Data Structures = Evolution Programs*, Springer, New York, NY, USA, 2nd edition, 1994.
- [17] <http://abcsolar.com/pdf/bpsx150.pdf>.

## Research Article

# Investigation of Solar Hybrid Electric/Thermal System with Radiation Concentrator and Thermoelectric Generator

**Edgar Arturo Chávez Urbiola and Yuri Vorobiev**

*CINVESTAV del IPN, Unidad Querétaro, Libramiento Norponiente 2000, 76230 Querétaro, QRO, Mexico*

Correspondence should be addressed to Edgar Arturo Chávez Urbiola; [echavez@qro.cinvestav.mx](mailto:echavez@qro.cinvestav.mx)

Received 16 October 2012; Revised 8 January 2013; Accepted 1 February 2013

Academic Editor: Keith Emery

Copyright © 2013 E. A. Chávez Urbiola and Y. Vorobiev. This is an open access article distributed under the Creative Commons Attribution License, which permits unrestricted use, distribution, and reproduction in any medium, provided the original work is properly cited.

An experimental study of a solar-concentrating system based on thermoelectric generators (TEGs) was performed. The system included an electrical generating unit with 6 serially connected TEGs using a traditional semiconductor material,  $\text{Bi}_2\text{Te}_3$ , which was illuminated by concentrated solar radiation on one side and cooled by running water on the other side. A sun-tracking concentrator with a mosaic set of mirrors was used; its orientation towards the sun was achieved with two pairs of radiation sensors, a differential amplifier, and two servomotors. The hot side of the TEGs at midday has a temperature of around  $200^\circ\text{C}$ , and the cold side is approximately  $50^\circ\text{C}$ . The thermosiphon cooling system was designed to absorb the heat passing through the TEGs and provide optimal working conditions. The system generates 20 W of electrical energy and 200 W of thermal energy stored in water with a temperature of around  $50^\circ\text{C}$ . The hybrid system studied can be considered as an alternative to photovoltaic/thermal systems, especially in countries with abundant solar radiation, such as Mexico, China, and India.

## 1. Introduction

Solar hybrid electric/thermal systems using photovoltaic (PV) panels combined with a water/air-filled heat extracting unit were designed and studied in many laboratories during the last three decades [1–10] and now are widely used throughout the world (England, Canada, China, Greece, India, and so forth). Some investigations were made [11–16] into the possibilities of using thermoelectric generators (TEGs) in solar hybrid systems, with the conclusion that TEGs can be successfully used in these systems instead of PV panels or together with them. An essential increase in thermoelectric conversion efficiency was achieved during the last decade [17–19], which is quite favorable for this kind of TEG's applications. With the traditional thermoelectric material  $\text{Bi}_2\text{Te}_3$ , the peak electric efficiency that could be obtained in such a system is 5% [16].

Chávez-Urbiola et al. [14] investigated different options of the construction of hybrid solar energy conversion systems using TEGs. They showed that these systems can be efficient (and economic in case of industrial production) even with the use of material and devices that are already available on

the market, especially in countries with high solar insolation (Mexico, China, India, etc.). Below we describe the construction and detailed experimental investigation of one of the hybrid systems analyzed in the above-mentioned paper [14], namely, the system with a solar radiation concentrator, TEG, and water-filled heat extracting unit. Circulation of water was achieved by thermosiphon effect. The experiments were performed in Querétaro, Mexico, at  $20^\circ$  of northern latitude, in March 2012.

## 2. Description of the Hybrid System

A schematic of the system is shown in Figure 1 where the solar radiation flux (1) is concentrated by the mosaic mirror (2) onto the electric/thermal generating unit (3) (details of the TEG are shown in Figure 2) consisting of a radiation absorber (hot plate), TEG array, and a cooling plate that is in direct contact with water-circulating copper tubes. The thermosiphon water loop includes a water storage thermal tank (4) with tubes for water entrance and output.

The radiation-concentrating block consisted of 55 plane mirrors each having a size equal to that of the TEG array

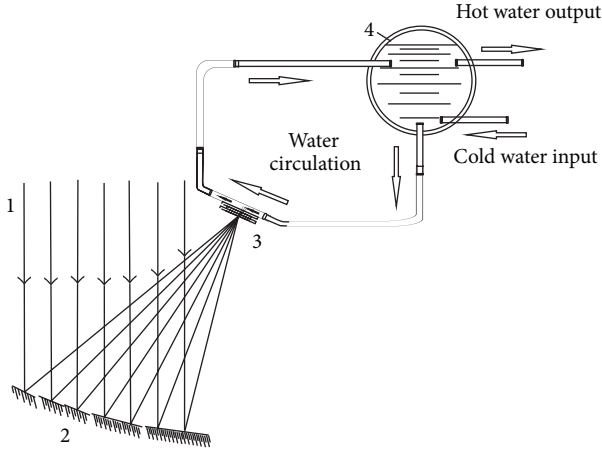


FIGURE 1: A schematic of the hybrid system.

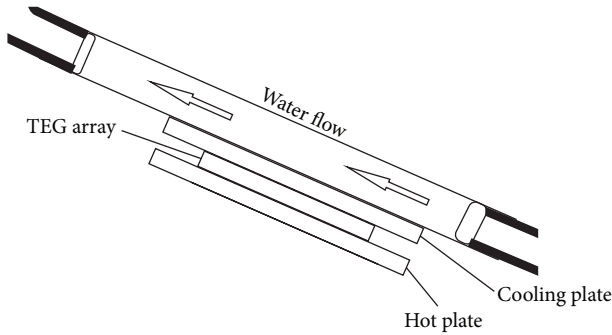


FIGURE 2: Thermoelectric generating (TEG) unit.

( $8 \times 12 \text{ cm}^2$ ), providing a concentration ratio (the number of mirrors focused on the heating plate multiplied by the mirror reflecting efficiency) of  $\sim 52$ , and considering a reflection efficiency of 0.95. The mirrors were positioned in a parabolic curve, with the focal point over the heating plate of the TEG assembly; the angle of the inclination of each mirror was calculated to achieve this effect. The block (mirror holder) was attached to the 2-axis sun-tracking system (see [20] for details) equipped with 2 pairs of radiation sensors positioned in such a way that the difference in photo response in each couple is zero if the mirror holder is orientated towards the sun, giving the highest illumination of the absorber hot plate. The difference in photo response increases with disorientation (disorientation signal). This difference signal is applied to a PIC16F877 microcontroller, which monitors the system using two geared servomotors.

The TEG array includes 6 generating elements of the type TGM-127-1.4-2.5 based on  $\text{Bi}_2\text{Te}_3$  (made by Kryotherm, Saint Petersburg, Russia; each element is  $4 \times 4 \times 0.5 \text{ cm}^3$ ). The electrical characteristics of the elements at different temperatures of the operation were given in a previous publication [14].

### 3. Calculation of Thermosiphon Loop

For the thermosiphon solar water heaters, the flow rate of the circulating water is conventionally calculated by equating the

pressure head and the friction head. Pressure head is caused by density gradients in the loop, and the friction head is caused by friction in the plumbing arrangement.

The pressure head in the thermosiphon causes flow to occur. This flow in the collector is driven by the weight difference between the hot water column in the return pipe passing through the collector and the cold fluid column in the inlet pipe. The temperature conditions are given by the inlet temperature of the fluid  $T_i = 25^\circ\text{C}$  and the inner surface temperature of the hot pipe  $T_s = 40^\circ\text{C}$ ; the density variations in the water along the collector are assumed to be linear for the calculations [21]. The desired maximum temperature in the cooling plate should be around  $50^\circ\text{C}$ .

Imagine an opened thermosiphon loop as a U-tube containing a fluid with one column filled with hot fluid and the other with cold fluid. A height difference,  $dh$ , results due to the density differences. If instead of U-tube one has a closed loop, this  $dh$  leads to a driving force that produces the flow in the loop.

The continuity equations under static equilibrium in case of U-tube can be expressed by

$$h_c \rho_c = h_h \rho_h \quad (1)$$

and the corresponding pressure head

$$dh = h_h - h_c, \quad (2)$$

which is a function of the temperature and the total height of the columns. We can rewrite (2) as a function of the cold- and hot-side densities and considering a total length  $L$ :

$$dh = L \left( 2 \frac{\rho_c}{\rho_c + \rho_h} - 1 \right). \quad (3)$$

To determine the thermal driving forces, it is necessary to take into account the values of  $T_i$  and  $T_s$ . Using the desired values of  $T_i = 25^\circ\text{C}$  and  $T_s = 40^\circ\text{C}$ ,  $dh = 2.51 \text{ mm}$  is obtained.

The friction head, flow rate, and convective coefficient are interrelated, but they also depend on several physical parameters that must be defined, such as piping type, materials, and pipe length, among others.

Using the Bernoulli equation, an energy conservation analysis can be made. For a pipe system [21] where  $p_1$  and  $p_2$  are inlet and outlet pressures,  $z_1$  and  $z_2$  are heights, and  $v_1$  and  $v_2$  are the corresponding flow velocities, the following can be written in terms of energy:

$$\frac{p_1}{\gamma} + z_1 + \frac{v_1^2}{2g} + h_A - h_R - h_L = \frac{p_2}{\gamma} + z_2 + \frac{v_2^2}{2g} v_2, \quad (4)$$

where  $h_A$  is the added energy,  $h_R$  is the subtracted energy,  $h_L$  is the energy loss (friction head),  $g$  is the acceleration of gravity, and  $\gamma$  is the specific weight of the fluid.

On the other hand, it is necessary to include the Darcy equation for friction head  $h_L$ :

$$h_L = f \frac{L}{D} \frac{v^2}{2g}, \quad (5)$$

where  $L$  is the piping length and  $D$  is its diameter that depends on the flow rate  $v$ . As the friction factor  $f$  depends on the Reynolds number  $Re$  for the laminar flow [21]

$$f = \frac{64}{Re} = \frac{64\mu}{v_s D \rho}, \quad (6)$$

for a thermosiphon system, the pressure head is equalized to friction head causing the energy loss

$$dh = h_L. \quad (7)$$

As a consequence, it is necessary to take into account the energy losses due to friction (major losses due to friction and minor losses due to changes in the size and direction of the flow path) in the loop.

The friction head can then be expressed for this case in terms of the friction factor and the flow rate

$$h_L = 1.5 \frac{v_s^2}{2g} + 351.7 \frac{v_s^2}{2g} f. \quad (8)$$

The first term corresponds to the sum of losses in the inlet and outlet, where it is common to use the estimation friction coefficient  $k_f = f(L_{eq}/D) = 1.5$  for systems of this kind [21]. Taking in consideration the laminar flow and equalizing the thermal driving head with the friction head, we get

$$dh = 1.5 \frac{v_s^2}{2g} + 351.7 \frac{v_s}{2g} \frac{64\mu}{D\rho}. \quad (9)$$

Solving (9) for  $dh = 2.51$  mm, a flow rate of  $v_s = 0.0436$  m/s is obtained.

Once the flow rate is defined, the convective coefficient can be calculated [21]. For the laminar region in the circular pipe and the temperature of 25°C, the corresponding Nusselt average number is

$$\overline{Nu} = 3.66 + \frac{0.065 (D/L) Re Pr}{1 + [(D/L) Re Pr]^{2/3}} = 5.051, \quad L_t < L. \quad (10)$$

For a thermal length  $L_t \approx 0.05 Re Pr D = 5.047$  m, the condition  $L_t < L$  is satisfied, and the convection coefficient can be calculated as

$$\overline{h}_c = \frac{\overline{Nu} k}{D} = \frac{5.051 \cdot 0.597 \text{ (W/mK)}}{0.01892 \text{ m}} = 154.84 \text{ (W/m}^2\text{K)}. \quad (11)$$

Once  $\overline{h}_c$  and  $v_s$  are determined, we can take them as initial values for the design of the heat exchanger, which starts with computer simulations.

#### 4. Design of the Heat Exchanger for Electric/Thermal Generating Unit

In order to determine the optimal configuration of the heat exchanger, several configurations were proposed and evaluated using commercial finite element method (FEM) software

(COMSOL Multiphysics 4.2a). For the flow rate, the value obtained earlier was used:  $v_s = 0.0436$  (m/s). The cooling plate temperature must not exceed 50°C, and the hot plate must be around 200°C. The solar power transformed into heat in the hot plate is around 200 W in an area of  $0.08 \times 0.12$  m<sup>2</sup>, in correspondence with the  $2 \times 3$  array of TEG elements.

The heat exchanger was designed to be as simple as possible, a flat plate attached to the commercial pipes. In Figure 3, the modeling results for several configurations are presented, changing parameters like hot plate location, pipe diameter, piping array, and welding material, among others. In this same figure, simulations from Figure 3(a) to 3(c) are for 1-inch-diameter and from Figure 3(d) to 3(f) are for 3/4-inch-diameter type K copper pipe according to ASTM B-88 standard. The red areas are the hottest and the blue ones the coldest, in accordance with the reference bar in the right side of each model.

After evaluating a wide range of configurations, two options that best meet the conditions were selected and evaluated, and the results are shown in Figure 4. One-inch type K copper pipe [21] was used in (a), obtaining a maximum value of 42.4°C in the center of the surface (red zone). 3/4-inch type K pipe was chosen for case (b), leading to a maximum value of 39.4°C distributed in a more uniform way along the center of the surface. Thus, option (b) was chosen for the experiment.

## 5. Experimental Results

The actual system studied is shown in the photograph in Figure 5. The positions of the thermocouples are indicated by the red and blue points. The red points also indicate the location of the ink injection, used to give idea of the actual water flow rate. As can be seen in the image, the thermoelectric assembly is illuminated by the concentration block.

The results of the system's electrical and thermal characterization are presented in Figures 6 and 7. To estimate the system's efficiency (both electrical and thermal), the intensity of solar radiation was taken as 950 W/m, which corresponds to the direct normal irradiance (DNI) in Queretaro, Mexico, at 20° of northern latitude, at the equinox time of the year. First, the electric power generated by the system during daytime is shown in Figure 6. The measurements were taken with a matched load, so the data shown gives the maximum power available. One can see that the average power was 20 W, thus producing 120 Wh of electric energy between 10 am and 4 pm (the total energy obtained during the day was 175 Wh). These results correspond to a maximum electric efficiency of the system of 5%, which agrees well with the estimations made in [14] and with the results of modeling [16].

Figure 7 presents the thermal characteristics of the hybrid system. The average hot water tank temperature was approximately 45°C, which is sufficient for domestic applications. The variations in the thermic efficiency,  $\eta_{\text{therm}} = (Q_{\text{therm}}/Q_{\text{sol}}) \times 100$ , observed during the time of the experiment give in average of 50%, which is higher than that an traditional PV/thermal systems. The corresponding thermal power is 200 W, giving the 1.2 kWh of energy in the 6 h between 10 am

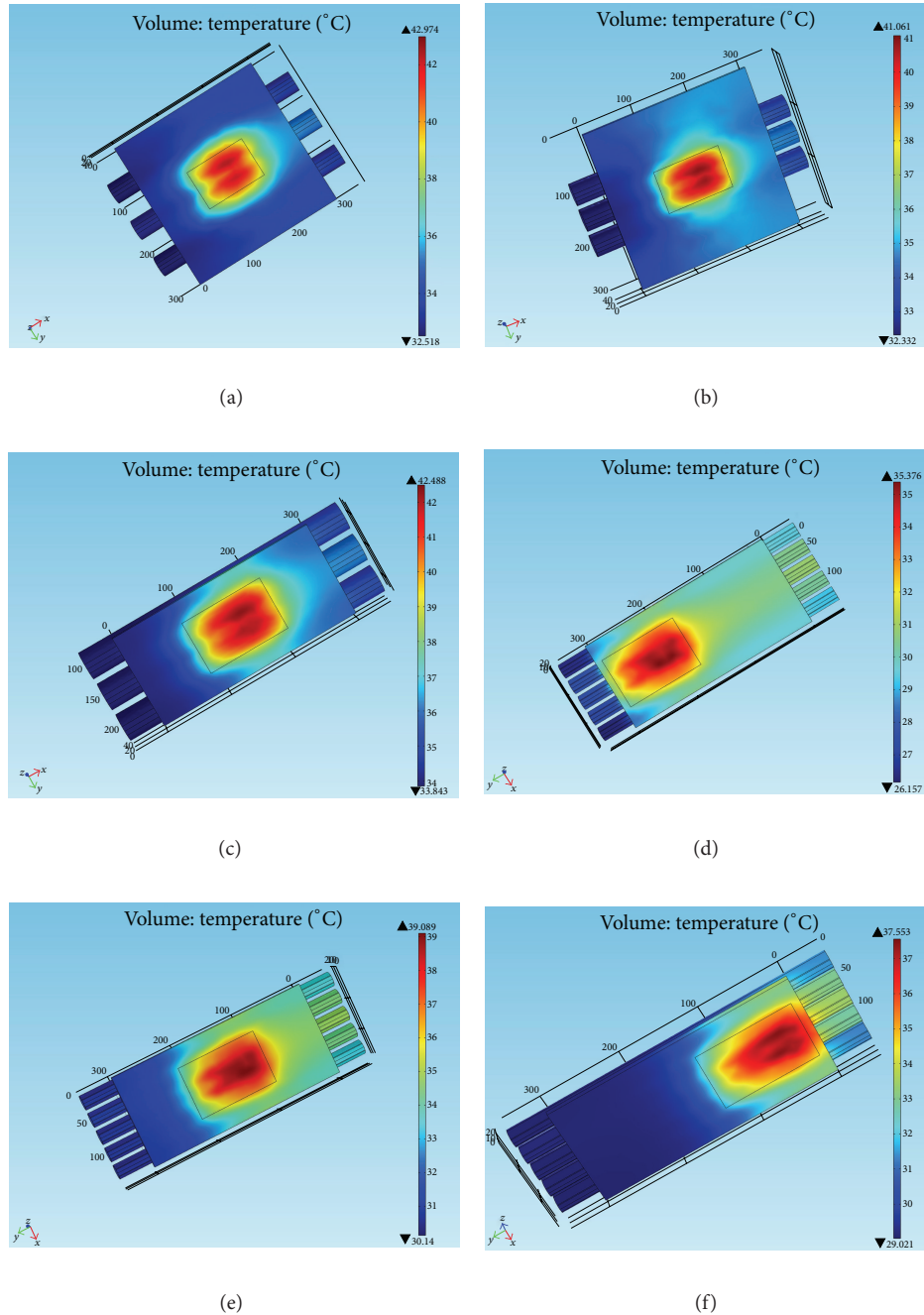


FIGURE 3: Computer simulations for different configurations (see text); the colors show the temperature distribution.

and 4 pm. It can also be seen that the flow rate correlates with the thermal efficiency—higher flow is accompanied by higher efficiency—although the water temperature in the tank is lower.

The cost-efficiency estimation made in our previous publication for the hybrid system studied [14] showed that at industrial production (in quantities of hundreds of systems), the cost of the electric energy generation could be 3-4 US dollars per watt peak, which is almost the same as the cost of the energy generated by PV panels. This is in contrast with the typical case where the cost of energy production

in hybrid systems is usually 50% higher than that in the individual devices. The cost of thermal energy in our system with TEGs is lower than that in the traditional PV/thermal systems because of the larger thermal power.

## 6. Conclusions

Performance of the designed hybrid system in the conditions at Queretaro, Mexico at the equinox time of the year has revealed that a systems electrical efficiency of 5% and thermal efficiency of 50% with the estimated cost of the electric

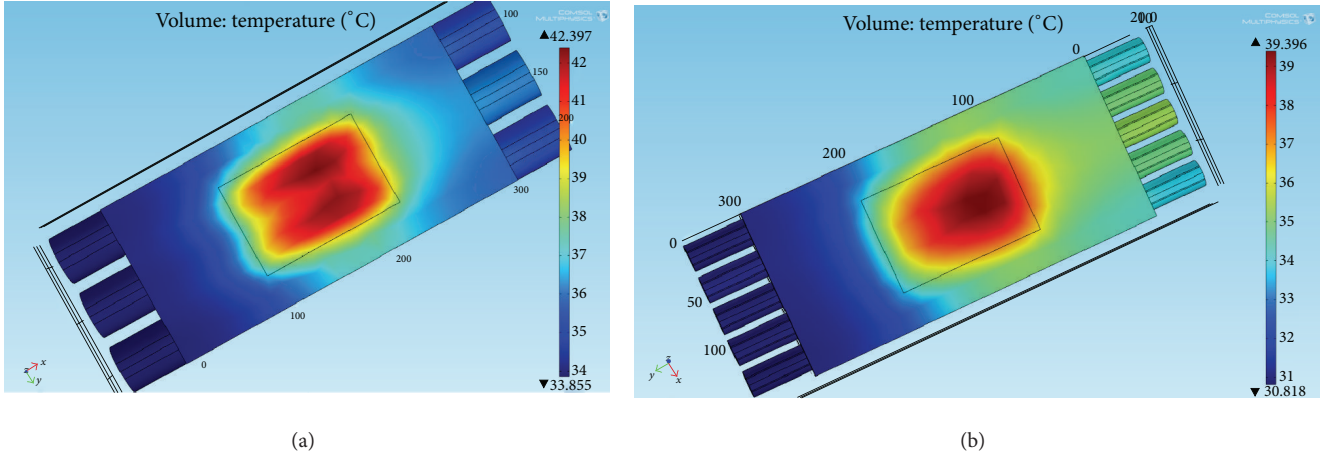


FIGURE 4: Computer simulations results for (a) 1" pipes and (b) 3/4" pipes.



FIGURE 5: Photograph of the system.

energy production are practically equal to those of the traditional photovoltaic/thermal systems. Thus, we conclude that the solar hybrid system with the concentrator and the thermoelectric generator, even with the existing components, can be considered as a reasonable alternative to the traditional electric/thermal solar hybrid system. Taking into account the rapid progress in the development of new nanostructured and highly efficient thermoelectric materials, we can expect that in the near future performance of the TEG-based systems can surpass that of the traditional solar hybrid systems, in particular, in the solar-rich regions having relatively low latitude.

**Nomenclature**

- $A_s$ : Effective flow area of the piping, m
- $C_p$ : Specific heat capacity, J/Kg $^{\circ}$ C
- $D$ : Piping diameter, m
- $dh$ : Pressure head (thermal driving head), m

- $f$ : Friction factor
- $g$ : Gravity, m/s
- $h$ : Height, m
- $h_A$ : Energy added to the fluid, J
- $h_c$ : Cold fluid column height, m
- $\bar{h}_c$ : Average convection coefficient, W/m $^{\circ}$ C
- $h_h$ : Hot fluid column height, m
- $h_L$ : Friction head inside the piping, m
- $h_R$ : Energy removed to the fluid, J
- $k_f$ : Friction coefficient
- $k$ : Thermal conductivity, W/mK
- $L$ : Piping length, m
- $L_{eq}$ : Equivalent piping length of the minor losses, m
- $L_t$ : Thermic inlet length, m
- $\dot{m}$ : Mass flow, Kg/s
- $\bar{Nu}$ : Average Nusselt number
- $p_1$ : Inlet pressure, N/m
- $p_2$ : Outlet pressure, N/m
- $Pr$ : Prandtl number
- $\dot{Q}$ : Heat flux, W
- $Q_{sun}$ : Solar heat input W
- $Q_{out}$ : Bottoming heat transfer W
- $Q_{therm}$ : Heat transfer to running water W
- $Re$ : Reynolds number
- $T_e$ : Outlet temperature in the fluid of the heating pipe,  $^{\circ}$ C
- $T_i$ : Inlet temperature in the fluid of the heating pipe,  $^{\circ}$ C
- $T_s$ : Inner surface temperature of the hot pipe,  $^{\circ}$ C
- $v$ : Flow velocity inside the piping, m/s
- $v_1$ : Inlet velocity of the fluid, m/s
- $v_2$ : Outlet velocity of the fluid, m/s
- $z_1$ : Height at the inlet point, m
- $z_2$ : Height at the outlet point, m
- $\eta_{therm}$ : Thermic efficiency
- $\rho$ : Fluid density, kg/m
- $\rho_c$ : Cold fluid density, kg/m
- $\rho_h$ : Hot fluid density, kg/m
- $\gamma$ : Specific weight of the fluid, N/m
- $\mu$ : Dynamic viscosity, Kg/m $\cdot$ s.

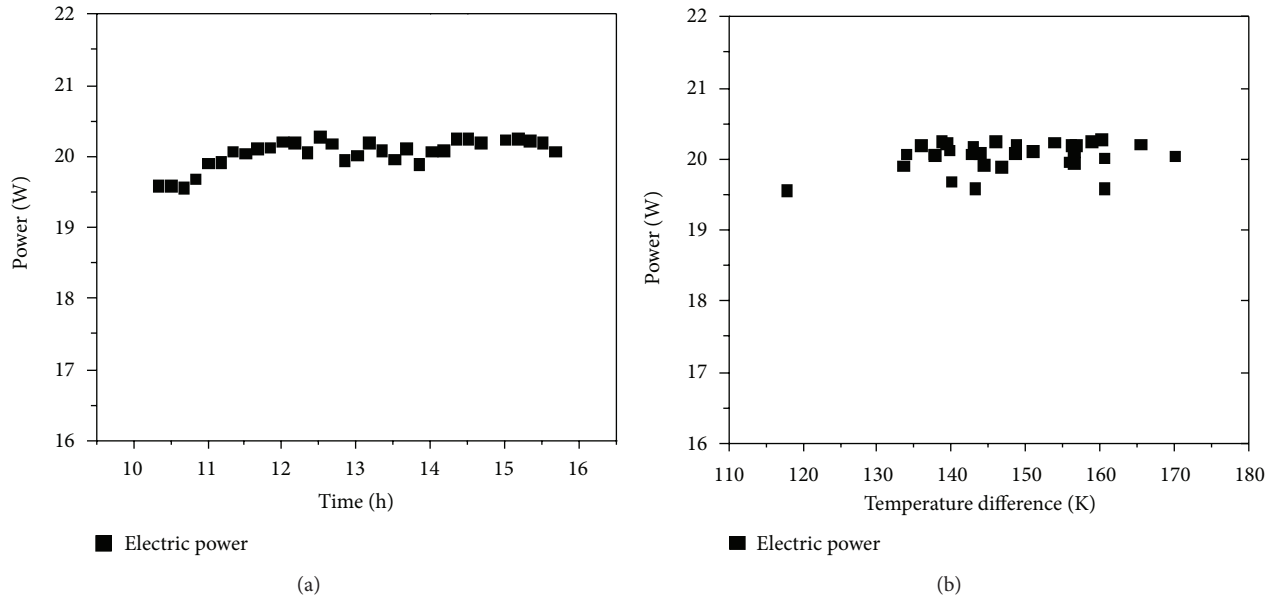


FIGURE 6: Electric power generation as a function of time of day (a) and as a function of the temperature difference between the TEG plates (b).

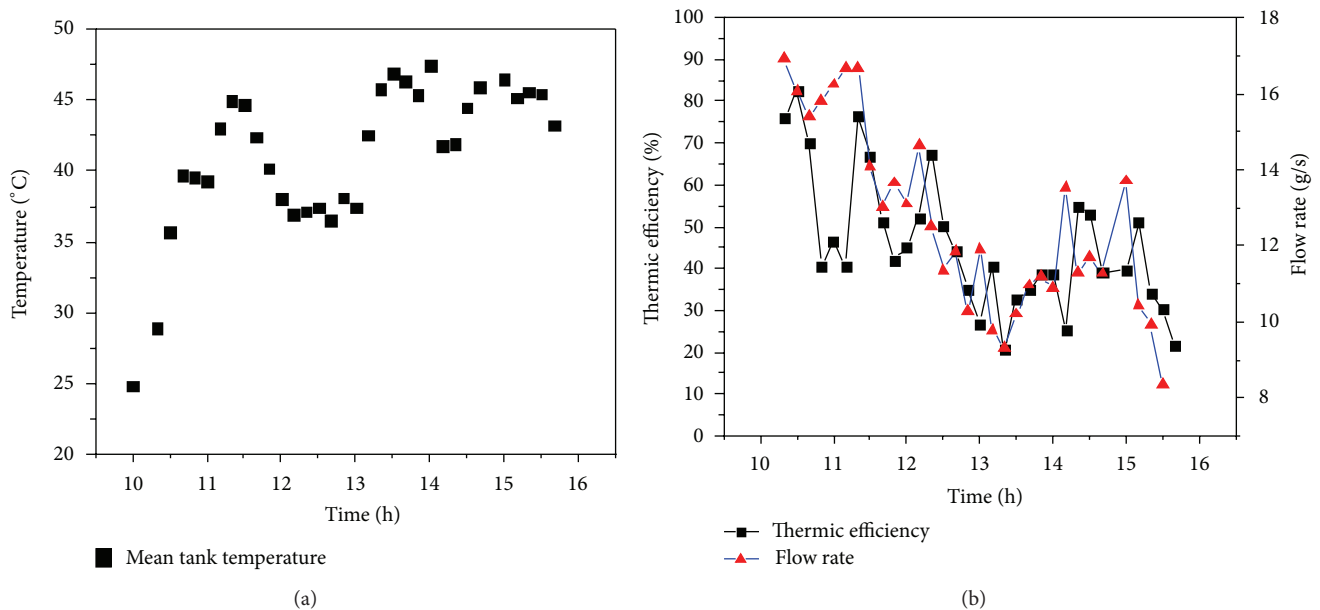


FIGURE 7: Hot water tank temperature (a) and calculated thermal efficiency of the system and the flow rate in the thermosiphon (b).

## Conflict of Interests

None of the authors of the present work have direct or indirect financial relation with the commercial identity “COMSOL Multiphysics 4.2a” that might lead to a conflict of interests of any kind for any of the authors.

## Acknowledgments

The authors are grateful to CONACYT for financial support of the project and for the Ph.D. scholarship of E. A. Chávez-Urbiola. They would also like to thank Dr. Mike Boldrick of the US Peace Corps for his review of the paper.

## References

- [1] E. C. Kern Jr. and M. C. Russell, “Combined photovoltaic and thermal hybrid collector systems,” in *Proceedings of the 13th ISES Photovoltaic Specialists*, pp. 1153–1115, Washington, DC, USA, June 1978.
- [2] P. Raghuraman, “Analytical predictions of liquid and air photovoltaic/thermal, flat-plate collector performance,” *Journal of Solar Energy Engineering*, vol. 103, no. 4, pp. 291–298, 1981.
- [3] H. P. Thomas, S. J. Hayter, R. L. Martin, and L. K. Pierce, “PV and PV/Hybrid products for buildings,” in *Proceedings of the 16th European Photovoltaic Solar Energy Conference and Exhibition*, vol. 2, pp. 1894–1897, Glasgow, UK, May 2000.

- [4] H. A. Zondag, D. W. De Vries, W. G. J. Van Helden, R. J. C. Van Zolingen, and A. A. Van Steenhoven, "The thermal and electrical yield of a PV-thermal collector," *Solar Energy*, vol. 72, no. 2, pp. 113–128, 2002.
- [5] J. Aschaber, C. Hebling, and J. Luther, "Realistic modelling of TPV systems," *Semiconductor Science and Technology*, vol. 18, no. 5, pp. S158–S164, 2003.
- [6] Y. Tripanagnostopoulos, "Aspects and improvements of hybrid photovoltaic/thermal solar energy systems," *Solar Energy*, vol. 81, no. 9, pp. 1117–1131, 2007.
- [7] H. A. Zondag, "Flat-plate PV-Thermal collectors and systems: a review," *Renewable and Sustainable Energy Reviews*, vol. 12, no. 4, pp. 891–959, 2008.
- [8] S. Dubey and G. N. Tiwari, "Thermal modeling of a combined system of photovoltaic thermal (PV/T) solar water heater," *Solar Energy*, vol. 82, no. 7, pp. 602–612, 2008.
- [9] A. Ibrahim, M. Y. Othman, M. H. Ruslan, S. Mat, and K. Sopian, "Recent advances in flat plate photovoltaic/thermal (PV/T) solar collectors," *Renewable and Sustainable Energy Reviews*, vol. 15, no. 1, pp. 352–365, 2011.
- [10] Y. Vorobiev, J. González-Hernández, P. Vorobiev, and L. Bulat, "Thermal-photovoltaic solar hybrid system for efficient solar energy conversion," *Solar Energy*, vol. 80, no. 2, pp. 170–176, 2006.
- [11] S. A. Omer and D. G. Infield, "Design optimization of thermoelectric devices for solar power generation," *Solar Energy Materials and Solar Cells*, vol. 53, no. 1-2, pp. 67–82, 1998.
- [12] P. Li, L. Cai, P. Zhai, X. Tang, Q. Zhang, and M. Niino, "Design of a concentration solar thermoelectric generator," *Journal of Electronic Materials*, vol. 39, no. 9, pp. 1522–1530, 2010.
- [13] D. Kraemer, L. Hu, A. Muto, X. Chen, G. Chen, and M. Chiesa, "Photovoltaic-thermoelectric hybrid systems: a general optimization methodology," *Applied Physics Letters*, vol. 92, no. 24, Article ID 243503, 2008.
- [14] E. A. Chávez-Urbiola, Y. Vorobiev, and L. P. Bulat, "Solar hybrid systems with thermoelectric generators," *Solar Energy*, vol. 86, no. 1, pp. 369–378, 2012.
- [15] W. G. J. H. M. V. Sark, "Feasibility of photovoltaic-thermoelectric hybrid modules," *Applied Energy*, vol. 88, no. 8, pp. 2785–2790, 2011.
- [16] D. Kraemer, K. McEnaney, M. Chiesa, and G. Chen, "Modeling and optimization of solar thermoelectric generators for terrestrial applications," *Solar Energy*, vol. 86, no. 5, pp. 1338–1350, 2012.
- [17] R. Venkatasubramanian, E. Siivola, T. Colpitts, and B. O'Quinn, "Thin-film thermoelectric devices with high room-temperature figures of merit," *Nature*, vol. 413, no. 6856, pp. 597–602, 2001.
- [18] A. Tavkhelidze, G. Skhiladze, A. Bibilashvili et al., "Thermionic converter with quantum tunneling," in *Proceedings of the IEEE 22th International Conference on Thermoelectrics*, pp. 435–438, August 2002.
- [19] L. P. Bulat, V. T. Bublik, I. A. Drabkin et al., "Bulk nanostructured polycrystalline p-Bi-Sb-Te thermoelectrics obtained by mechanical activation method with hot pressing," *Journal of Electronic Materials*, vol. 39, no. 9, pp. 1650–1653, 2010.
- [20] P. Vorobiev and Y. Vorobiev, "Automatic Sun tracking solar electric systems for applications on transport," in *Proceedings of 7th International Conference on Electrical Engineering, Computing Science and Automatic Control (CCE '10)*, pp. 66–70, Chiapas, Mexico, September 2010.
- [21] R. L. Mott, *Applied Fluid Mechanics*, Macmillan, New York, NY, USA, 4th edition, 1994.

## Review Article

# Key Success Factors and Future Perspective of Silicon-Based Solar Cells

S. Binetti,<sup>1</sup> M. Acciarri,<sup>1</sup> A. Le Donne,<sup>1</sup> M. Morgano,<sup>1</sup> and Y. Jestin<sup>2</sup>

<sup>1</sup> *Milano-Bicocca Solar Energy Research Center (MIB-SOLAR), Department of Materials Science, University of Milano-Bicocca, Via Cozzi 53, 20126 Milano, Italy*

<sup>2</sup> *Centre for Materials and Microsystems, Fondazione Bruno Kessler, Via Sommarive 18, 38123 Trento, Italy*

Correspondence should be addressed to S. Binetti; [simona.binetti@unimib.it](mailto:simona.binetti@unimib.it)

Received 18 January 2013; Accepted 6 February 2013

Academic Editor: Sudhakar Shet

Copyright © 2013 S. Binetti et al. This is an open access article distributed under the Creative Commons Attribution License, which permits unrestricted use, distribution, and reproduction in any medium, provided the original work is properly cited.

Today, after more than 70 years of continued progress on silicon technology, about 85% of cumulative installed photovoltaic (PV) modules are based on crystalline silicon (c-Si). PV devices based on silicon are the most common solar cells currently being produced, and it is mainly due to silicon technology that the PV has grown by 40% per year over the last decade. An additional step in the silicon solar cell development is ongoing, and it is related to a further efficiency improvement through defect control, device optimization, surface modification, and nanotechnology approaches. This paper attempts to briefly review the most important advances and current technologies used to produce crystalline silicon solar devices and in the meantime the most challenging and promising strategies acting to increase the efficiency to cost/ratio of silicon solar cells. Eventually, the impact and the potentiality of using a nanotechnology approach in a silicon-based solar cell are also described.

## 1. Introduction

Photovoltaic (PV) devices based on silicon are the most common solar cells currently being produced, and it is mainly due to silicon technology that the PV has grown by 40% per year over the last decade. Cost, sustainability, and environmental issues are at the core of actual PV industry activities. Competitors other than silicon have emerged in the last ten years. Organic PV is a fast growing research topic with the first companies producing products for consumers. Apart from efficiency, different open problems of DSC and organic solar cells still remain, such as scaled-up module prototypes, solar efficiencies fall up to 5% in outdoor, low lifetime and durability (less than 1 year), and a lack of standardized stability data. All these considerations will make it very difficult for organic solar cells to be competitive with respect to silicon solar cells in the next decades.

In the frame of inorganic thin film, Cu(In,Ga)Se<sub>2</sub> (CIGS) solar cells are one of the most promising in terms of both efficiency record (20.3%), nearly reaching the one of Si solar cell [1], and stability. Despite the promise of CIGS thin film and also of CdTe photovoltaic technologies with respect to

reducing cost per watt of solar energy conversion, these approaches rely on elements that are either costly and/or rare in the earth's crust (e.g., In, Ga, and Te) or that present toxicity issues (e.g., Cd), thereby potentially limiting these technologies in terms of future cost reduction and production growth. The new material (CZTS) in which indium and gallium from CIGS are replaced by the readily available elements zinc and tin [2, 3] is far to be applied or to be on the market rapidly. Furthermore, thin film technology still remains a smaller (albeit growing) part of the overall PV production.

On the other hand, the silicon solar cells technological improvements resulted in the achievement of the 25% record efficiency on lab scale and of 22% in production [4], very close to the theoretical maximum efficiency for a single junction PV device of 31%. This record is the latest step in more than 70 years history of silicon cell development. An additional step in the silicon solar cell development is ongoing, and it is related to further efficiency improvements through defect control, device optimization, surface modification, and nanotechnology approaches, these researches being aimed at increasing or at overcoming the classical efficiency limit.

This paper firstly attempts to point out the most important advances and current technologies used to produce crystalline silicon solar devices and in the meantime the most challenging and promising strategies acting to increase the ratio between the efficiency and the cost of silicon solar cells. Furthermore, recent results of our group on silicon-based device are reported.

## 2. Multicrystalline Silicon Solar Cells

Within c-Si, multicrystalline-(mc-) Si technology is the more commonly used material. This trend is growing and mc-Si modules will continue to retain a large portion of the market in the future. All this is strictly related to the fact that multicrystalline silicon is able to increase the ratio between efficiency and cost most effectively than monocrystalline one. Advanced mc-Si solar cells use new concepts for the technology of crystalline silicon in order to boost the efficiency of industrial cells and modules above 20%, for example, by laser technologies, fine line metallization, and improved front and back contacts. Details on the processing techniques as well as the most important milestones and breakthroughs for mc-Si solar cells are reported in [5]. A better understanding of defects and their influence on mc solar cells properties has been having a very relevant role in reducing the gap in the efficiency with respect to monocrystalline one. Gettering and passivation procedures have been studied for many years and used effectively to increase the efficiency of mc-Si. In any case, considerable efforts are still needed to approach the theoretical efficiency limit in multicrystalline silicon solar cells due to higher defect content, especially grain boundaries (GBs) and dislocations known to be harmful for the final cell performances. Reducing this harmful effect could be achieved by controlling the crystal growth in order to produce large grains in preferred orientations in such a way that the resulting grain boundaries do not generate, or generate less, dislocations. Dislocations have been identified as one of the main killer defects in mc-Si. In order to further increase the efficiency of mc-Si solar cell, a still crucial point is to understand the properties of dislocation-related deep levels as well as possible effects of interaction of impurities with dislocations. As matter of fact, in spite of many years of investigations, many aspects related to the influence of impurities on the electrical activity of dislocations are still open. Its electrical activity arises from intrinsic structural disorder at dislocation cores [6] shallow defect bands due to long-range strain fields and extrinsic impurity decoration [7, 8]. Nevertheless, it appears clear that dislocations do not have simple and regular influence on electrical properties of the material or on those of the devices.

All that considered, a lot of experimental and theoretical work should still be done also in this fundamental field. The control of defects density and the so-called defect engineering have become recently even more important, considering the potential of metallurgical grade silicon feedstock. During the Si feedstock crisis that started in 2005, the metallurgical purification routes taken by different companies (i.e., Dow Corning, Elkem, and others) attracted much attention due to

the scalability and fast setup time for factories. Solar grade from metallurgical grade (MG) silicon of reduced purity is currently being explored with the goal to further reduce material cost. Besides the cost, many are the advantages of using metallurgical silicon. The investment cost for an industrial scale feedstock production plant is expected to be significantly reduced compared to the investment for a comparable production plant based on trichlorosilane technology. Likewise, the energy payback of a silicon solar cell, nowadays mainly affected by the energy used to purify and crystallize the base silicon, can be reduced to 1 year or less using MG-Si. But due to the higher concentrations of deleterious impurities in MG-Si, new approaches are necessary and have been developed to make cost-effective solar cells from low-cost, but impurity-rich, feedstock. Some approaches deal, for instance, with metal nanodefects engineering to recover minority carrier diffusion length in heavily contaminated materials by proper thermal annealing [9, 10] or with developing new gettering process. To this date, the phosphorus diffusion at high temperature is the best and well-known gettering process, due to the enhanced solubility of gettered species in the phosphorus diffused layer.

Despite the higher level of metal contaminations, many works report that similar solar efficiency to those obtained with electronic grade feedstock can be achieved [11].

Furthermore, MG or solar grade silicon generated by refining processes often contains a large amount of doping elements (i.e., boron and phosphorus). In order to use this silicon besides controlling the maximum concentrations of different metallic impurities, the research is focusing also on the maximum acceptable concentrations of the doping elements and its effect on material and cell parameters [12, 13] Recently, the Hall majority carrier mobility of p-type, compensated multicrystalline solar grade silicon wafers for solar cells in the temperature range 70–373 K has been investigated. In the range of interest for silicon solar cells (above room temperature), the trend in carrier mobility is similar for all samples, and the measured value for the sample with low compensation ratio ( $R_C$ ) and low doping density is comparable to the uncompensated references (Figure 1). With decreasing temperature below approximately 150 K, the difference between samples with low  $R_C$  and samples with high  $R_C$  becomes higher [14].

The work carried out up to now seems to indicate that MG silicon can be used to produce effectively solar cells if impurities are below a well-defined limit indicated as solar grade specifications. In the case of higher impurities concentration, it is clear that the silicon supply could be much larger and or at lower cost or more sustainable. All these points can contribute to reduce the silicon solar cells cost. It is also clear that this material requires strong modification in crystallization process and in device realization, like new gettering or passivation process or postgrowth annealing step.

## 3. Light Harvesting Approach: The Down-Shifting Process

It is widely known that in a silicon solar cell a large portion of the energy loss can be ascribed to thermalization process.

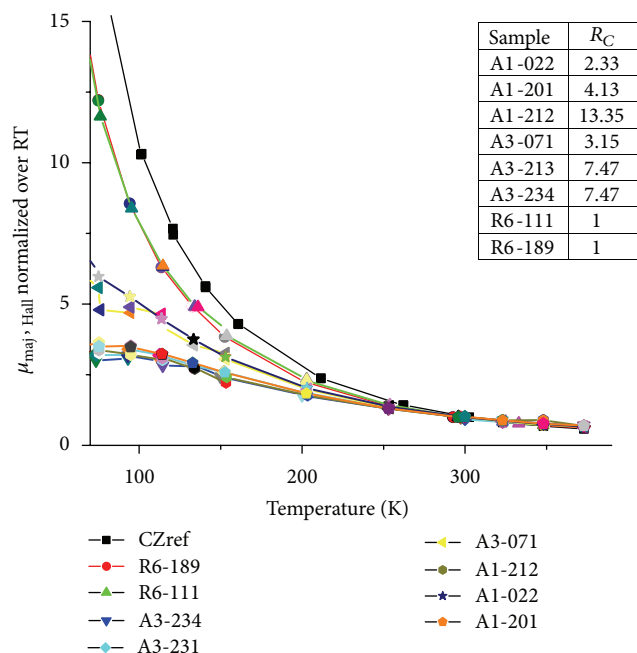


FIGURE 1: Temperature-dependent majority carrier mobility,  $\mu_{\text{maj, Hall}}$ , as measured by the Hall-effect setup, normalized values (ratio of the measured value at the given temperature over the measured value at room temperature). The compensation ratios ( $R_C$ ) of the different samples are reported in the table on the right. Adapted from [14].

A modification of the incident solar spectrum which allows a better exploitation of the high energy region is therefore expected to increase the efficiency of such a single junction cell. A possible approach to modify the high energy side of the solar spectrum is down-shifting [15]. In this process, one low energy photon is created by one high energy photon absorbed into a proper molecular system emitting around the maximum quantum efficiency value of the photovoltaic (PV) device. Molecular systems strongly absorbing in the high energy range and showing a consistent Stokes shift of their emission towards the region of the maximum conversion efficiency of the PV device are good candidates for down-shifting of the absorbed light. Rare-earth organic complexes constituted by a conjugated molecule acting as antenna and by an emitting lanthanide ion are good candidates as down-shifter (DSs). They possess also the separation between the absorption and the emission bands required to obtain large Stokes shift and to avoid self-absorption losses. In recent years, we have been working on inorganic DSs complexes to realize down-shifting of photons with wavelength lower than 400 nm without introducing strong modifications of the industrial process leading to the fabrication of the PV modules. Organolanthanide-based DSs have been included in polymeric layers suitable as PV modules encapsulating matrix. Relative enhancements of the total delivered power up to 2.9% have been reported for Si solar cells coated with 1  $\mu\text{m}$  thick  $\text{Eu}(\text{tfc})_3/4,4'$ bis(diethylamino) benzophenone-doped EVA [16] (see Figure 2).

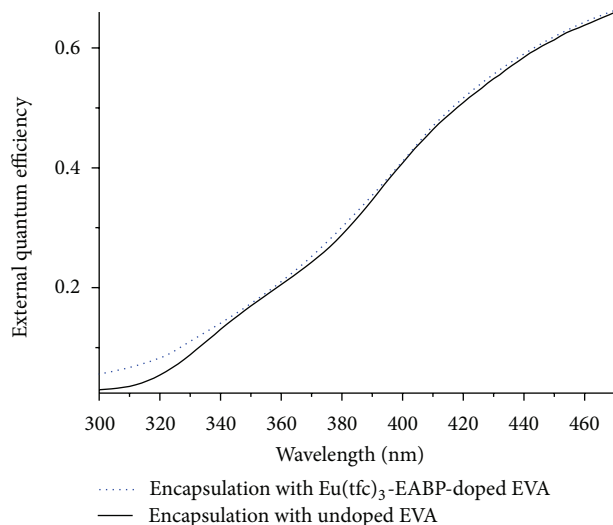


FIGURE 2: EQE measurements recorded on c-Si-based test modules encapsulated with undoped (solid line) and  $\text{Eu}(\text{tfc})_3/4,4'$ bis(diethylamino) benzophenone-( $\text{Eu}(\text{tfc})_3$ -EABP-) doped EVA (dots). The only down-shifting spectral region has been showed for better clarity.

Beside organolanthanide complexes, quantum dots (QDs) materials are also promising solution for the modification of the high energy side of the solar spectrum [17], considering also their higher stability. Due to the reduced dimensionality, QDs exhibit quantization of their electronic energy levels, with a consequent blue-shift of the optical absorption edge. The QDs electronic energy levels and optical absorption being dependent on their size, the effective bandgap can be easily tuned for solar spectrum modification purposes. In the last few years, QDs systems showing the potentialities for effective solar spectrum modification have been investigated [18, 19]. However, most of them contain toxic elements such as Cd, Pb, and Se (e.g., CdSe, PbSe, and PbS QDs). In order to focus the attention on nontoxic systems, we have tested ZnS nanoparticles (NPs) [20], already known as low cost, largely available luminescent materials [21]. ZnS:  $\text{Mn}^{2+}$  NPs have been prepared by wet chemical synthesis, a quite inexpensive and scalable method matching the requirements for photovoltaics. In particular, the  $\text{Mn}^{2+}$  related emission centered at 597 nm observed for ZnS:  $\text{Mn}^{2+}$  NPs size higher than 3.5 nm is really close to the maximum quantum efficiency of crystalline silicon-(c-Si-) based solar cells. The effect on the EQE of the deposition of ZnS:  $\text{Mn}^{2+}$  NPs on a commercial c-Si solar cell is showed in Figure 3, where the relative enhancement of the EQE is reported. The incident UV radiation is absorbed by the ZnS:  $\text{Mn}^{2+}$  NPs, generating photons emitted at longer wavelengths where Si is more efficient. A sharp peak of the relative EQE enhancement ( $\sim 6\%$ ) is present around 350 nm which is consistent with the absorption edge of the QDs (shown in the inset in Figure 3).

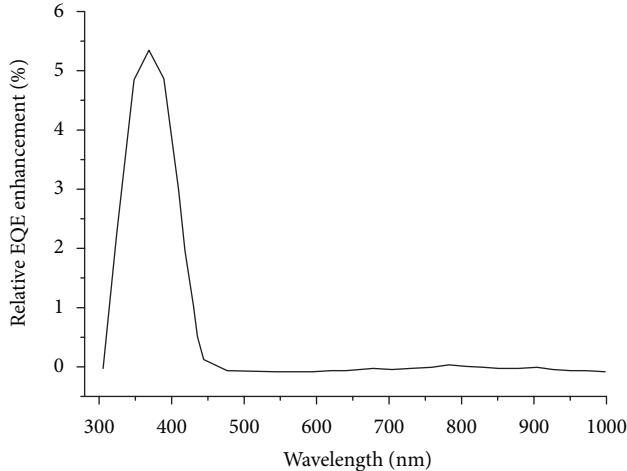


FIGURE 3: Relative EQE enhancement for a commercial monocrystalline Si solar cell after the deposition of ZnS:Mn<sup>2+</sup> NPs.

#### 4. Nanotechnology Approach

Among the different ways of exploiting nanotechnologies and typical nanoscale concepts, the band gap engineering of a silicon-based material is the most attractive. Silicon-rich oxide (SRO) and silicon-rich nitride (SRN) are the materials currently object of research for the realization of an all-silicon tandem solar cell. This material consists of nonstoichiometric silicon oxide or silicon nitride layers that, upon annealing at high temperature, can form quantum dots (QDs) after precipitation of the excess silicon. The quantum confinement effect of carriers induced by this nanostructure might allow the optical band gap of the SRO to be tuned, increasing it from the bulk silicon value, allowing the realization of all silicon based tandem solar cells [22, 23]. Moreover, there are no concerns about the toxicity of SRO or SRN, they are already widely available and widespread, and their realization process is fully compatible with the microelectronic industry and so with a large scale production.

Prototype devices have been already realized [24], but the efficiency obtained is still very low (less than 0.1%). Of the main issues to be still solved, and probably the research bottlenecks, are the doping of such nanostructures and the electrical transport processes [25].

It is clear that the extraction of photogenerated current is crucial, and it is made even more difficult by the presence of the insulating materials embedding the nanodots. In order to understand the transport mechanism in the configuration of QDs-based solar cell (i.e., from top to bottom), we performed *IV* scans on supposedly nanodoped as well as on intrinsic SRO samples.

Plasma-enhanced chemical vapor deposition (PECVD) was used to deposit 10 bilayers (nominal thickness 1.5 nm of each layer) of alternative layer of Si-rich SiO<sub>2</sub> (SRO) and SiO<sub>2</sub> on <100> 10 ohm cm p-type silicon wafer. Technical details are in [26].

All the samples have been annealed at 1050°C for one hour to nucleate the dots and to drive excess hydrogen away. To

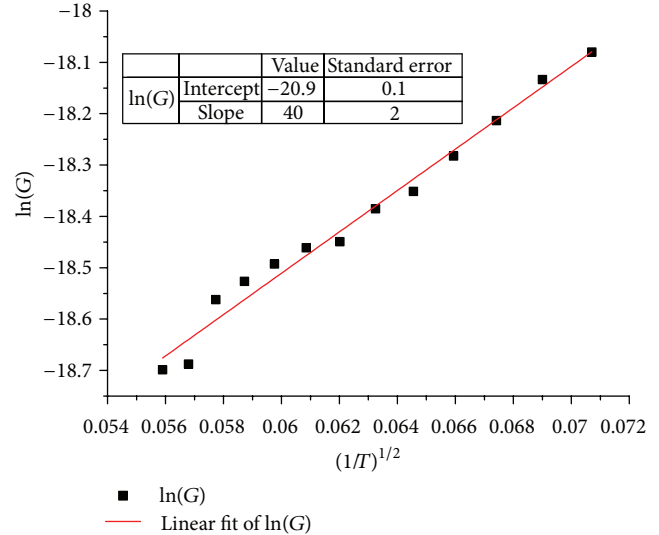


FIGURE 4: Plot of the log of the conductance versus the inverse square root of the temperature used for the fit demonstrating percolation mechanism.

to identify the transport mechanism, we performed *I/V* scans at different temperatures. By fitting with a straight line the region around the origin ( $\pm 0.5$  V, where the shape of the *IV* can be linearly approximated), we can obtain the temperature dependence of the conductance (*G*) versus the temperature. As can be seen in Figure 4, the values show a pretty good agreement with a linear relationship between the logarithm of the conductance and the inverse square root of the temperature, compatible with a hopping-percolation model as in [27], not completely suitable for a solar cell applications.

On the same samples, a feeble effect of light has been observed. From Figure 5, we can see that the conduction is diode-like in the dark but symmetric under illumination. This behavior can be explained by the generation of electron-hole pairs promoted by the photons. When there is no light, the sample acts as an MIS diode with an insulator layer made by the SRO even if this layer does not act as a full 200 nm thick layer of oxide. Nanostructuring and its composition play a crucial role in reducing the effective thickness of this layer, since a 200 nm thick stoichiometric layer of SiO<sub>2</sub> would prevent the conduction at this voltage. In this condition, the nanodots probably act as filled traps where carriers can have a good mobility and they do not participate at the conduction. When light is on, the dots might act as electron-hole couples generator (as they are intrinsic) and the conduction can be symmetric in the two directions.

A requirement for a tandem solar cell is the presence of a junction, and another crucial point is the doping of the Si QDs material. Although the doping mechanism is not clearly understood, homo- and heterojunction devices have been fabricated based on Si QD [24]. In any case, a strong improvement in understanding carrier transport and in doping mechanism is still needed.

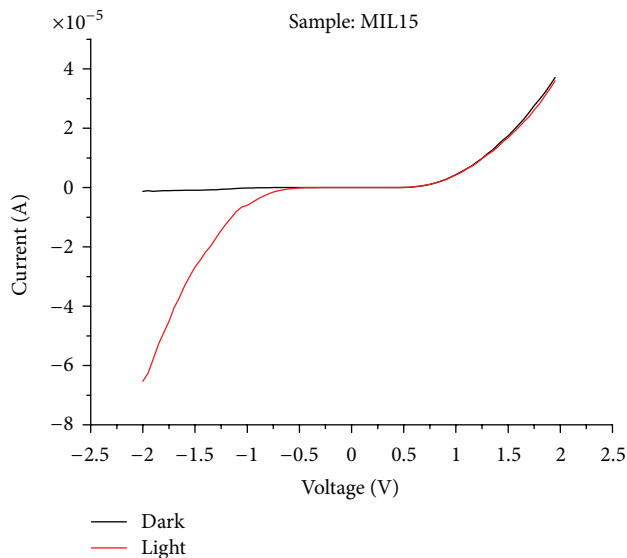


FIGURE 5:  $I/V$  scans of the samples in dark and under illumination.

## 5. Conclusions

Although new materials are coming and opening new outlook on the future of solar energy, silicon should be the leading material also in the next future. If we consider its peculiar properties and unique advantages: availability, no toxicity, long lifetime, and sustainability, no competitors are on the market. Development, innovation, and new devices concepts in silicon solar cells are taking place to bring down the cost of solar technologies and make them even more cost competitive with conventional sources. The reduction of cost-per-Watt towards grid parity and the grow of global installed power towards the Terawatt level can be achieved by silicon solar cells. However, an intense R&D activity is still needed to reach the target of a 40% efficiency silicon-based 9 solar cells will not be a dream.

## Acknowledgment

The authors would like to thank Professor Lorenzo Pavesi for many fruitful discussions.

## References

- [1] P. Jackson, D. Hariskos, E. Lotter et al., "New world record efficiency for Cu(In,Ga)Se<sub>2</sub> thin-film solar cells beyond 20%," *Progress in Photovoltaics: Research and Application*, vol. 19, no. 7, pp. 894–897, 2011.
- [2] T. K. Todorov, K. B. Reuter, and D. B. Mitzi, "High-efficiency solar cell with earth-abundant liquid-processed absorber," *Advanced Materials*, vol. 22, no. 20, pp. E156–E159, 2010.
- [3] H. Katagiri, K. Jimbo, S. Yamada et al., "Enhanced conversion efficiencies of Cu<sub>2</sub>ZnSnS<sub>4</sub>-based thin film solar cells by using preferential etching technique," *Applied Physics Express*, vol. 1, no. 4, 2008.
- [4] M. A. Green, K. Emery, Y. Hishikawa, W. Warta, and E. D. Dunlop, "Solar cell efficiency tables (version 39)," *Progress in Photovoltaics: Research and Applications*, vol. 20, no. 2, pp. 12–20, 2012.
- [5] R. Kopecek and M. McCann, "Multicrystalline silicon solar cells: standard processes and trends," in *Handbook of Silicon Photonics*, CRC Press, Taylor & Francis Group, 2013.
- [6] A. Castaldini, D. Cavalcoli, A. Cavallini, and S. Pizzini, "Experimental evidence of dislocation related shallow states in p-type Si," *Physical Review Letters*, vol. 95, no. 7, Article ID 076401, pp. 1–4, 2005.
- [7] M. Kittler, C. Ulhaq-Bouillet, and V. Higgs, "Influence of copper contamination on recombination activity of misfit dislocations in SiGe/Si epilayers: temperature dependence of activity as a marker characterizing the contamination level," *Journal of Applied Physics*, vol. 78, no. 7, pp. 4573–4583, 1995.
- [8] S. Acerboni, S. Pizzini, S. Binetti, M. Acciarri, and B. Pichaud, "Effect of oxygen aggregation processes on the recombining activity of 60° dislocations in Czochralski grown silicon," *Journal of Applied Physics*, vol. 76, no. 5, pp. 2703–2710, 1994.
- [9] M. D. Pickett and T. Buonassisi, "Iron point defect reduction in multicrystalline silicon solar cells," *Applied Physics Letters*, vol. 92, no. 12, Article ID 122103, 2008.
- [10] J. Hofstetter, D. P. Fenning, J. F. Lelievre, C. del Canizo, and T. Buonassisi, "Engineering metal precipitate size distributions to enhance gettering in multicrystalline silicon," *Physica Status Solidi A*, vol. 209, no. 10, pp. 1861–1865, 2012.
- [11] G. Coletti, P. C. Bronsveld, G. Hahn et al., "Impact of metal contamination in silicon solar cells," *Advanced Functional Materials*, vol. 21, no. 5, pp. 879–890, 2011.
- [12] J. Libal, S. Novaglia, M. Acciarri et al., "Effect of compensation and of metallic impurities on the electrical properties of Cz-grown solar grade silicon," *Journal of Applied Physics*, vol. 104, no. 10, Article ID 104507, 2008.
- [13] J. Veirman, S. Dubois, N. Enjalbert, J. P. Garandet, and M. Lemi, "Electronic properties of highly-doped and compensated solar-grade silicon wafers and solar cells," *Journal of Applied Physics*, vol. 109, no. 10, Article ID 103711, 2011.
- [14] C. Modanese, M. Acciarri, S. Binetti, A. Søiland, M. Acciarri, and S. Binetti, "Temperature-dependent Hall-effect measurements of p-type multicrystalline compensated solar grade silicon," *Progress in Photovoltaics: Research and Applications*, 2012.
- [15] E. Klampaftis, D. Ross, K. R. McIntosh, and B. S. Richards, "Enhancing the performance of solar cells via luminescent down-shifting of the incident spectrum: a review," *Solar Energy Materials & Solar Cells*, vol. 93, no. 8, pp. 1182–1194, 2009.
- [16] A. Le Donne, M. Dilda, M. Crippa, M. Acciarri, and S. Binetti, "Rare earth organic complexes as down-shifters to improve Si-based solar cell efficiency," *Optical Material*, vol. 33, no. 7, pp. 1012–1014, 2011.
- [17] C. Y. Huang, D. Y. Wang, C. H. Wang et al., "Efficient light harvesting by photon downconversion and light trapping in hybrid ZnS nanoparticles/Si nanotips solar cells," *ACS Nano*, vol. 4, no. 10, pp. 5849–5854, 2010.
- [18] A. J. Nozik, "Quantum dot solar cells," *Physica E*, vol. 14, pp. 115–120, 2002.
- [19] V. I. Klimov, S. A. Ivanov, J. Nanda et al., "Single-exciton optical gain in semiconductor nanocrystals," *Nature*, vol. 447, no. 7143, pp. 441–446, 2007.
- [20] A. Le Donne, S. K. Jana, S. Banerjee, S. Basu, and S. Binetti, "Optimized luminescence properties of Mn doped ZnS nanoparticles for photovoltaic applications," *Journal of Applied Physics*, vol. 113, no. 1, Article ID 014903, 5 pages, 2013.

- [21] J. Cao, J. Yang, Y. Zhang et al., "Optimized doping concentration of manganese in zinc sulfide nanoparticles for yellow-orange light emission," *Journal of Alloys and Compounds*, vol. 486, no. 1-2, pp. 890–894, 2009.
- [22] E. C. Cho, S. Park, X. Hao et al., "Silicon quantum dot/crystalline silicon solar cells," *Nanotechnology*, vol. 19, no. 24, Article ID 245201, 2008.
- [23] D. Di, I. Perez-Wurfl, G. Conibeer, and M. A. Green, "Formation and photoluminescence of Si quantum dots in SiO<sub>2</sub>/Si<sub>3</sub>N<sub>4</sub> hybrid matrix for all-Si tandem solar cells," *Solar Energy Materials and Solar Cells*, vol. 94, no. 12, pp. 2238–2243, 2010.
- [24] I. Perez-Wurfl, L. Ma, D. Lin, X. Hao, M. A. Green, and G. Conibeer, "Silicon nanocrystals in an oxide matrix for thin film solar cells with 492 mV open circuit voltage," *Solar Energy Materials and Solar Cells*, vol. 100, pp. 65–68, 2012.
- [25] M. Morgano, I. Perez-Wurfl, and S. Binetti, "Nanostructured silicon-based films for photovoltaics: recent progresses and perspectives," *Science of Advanced Materials*, vol. 3, no. 3, pp. 388–400, 2011.
- [26] M. Wang, A. Anopchenko, A. Marconi et al., "Light emitting devices based on nanocrystalline-silicon multilayer structure," *Physica E*, vol. 41, no. 6, pp. 912–915, 2009.
- [27] E. Šimánek, "The temperature dependence of the electrical resistivity of granular metals," *Solid State Communications*, vol. 40, no. 11, pp. 1021–1023, 1981.

## Review Article

# Reduction of Oxygen Impurity in Multicrystalline Silicon Production

**Bing Gao, Satoshi Nakano, and Koichi Kakimoto**

*Research Institute for Applied Mechanics, Kyushu University, Kasuga, Fukuoka 816-8580, Japan*

Correspondence should be addressed to Bing Gao; [gaobing@riam.kyushu-u.ac.jp](mailto:gaobing@riam.kyushu-u.ac.jp)

Received 7 December 2012; Accepted 17 January 2013

Academic Editor: Bhushan Sopori

Copyright © 2013 Bing Gao et al. This is an open access article distributed under the Creative Commons Attribution License, which permits unrestricted use, distribution, and reproduction in any medium, provided the original work is properly cited.

Effective control of oxygen impurity in multicrystalline silicon is required for the production of a high-quality crystal. The basic principle and some techniques for reducing oxygen impurity in multicrystalline silicon during the unidirectional solidification process are described in this paper. The oxygen impurity in multicrystalline silicon mainly originates from the silica crucible. To effectively reduce the oxygen impurity, it is essential to reduce the oxygen generation and enhance oxygen evaporation. For reduction of oxygen generation, it is necessary to prevent or weaken any chemical reaction with the crucible, and for the enhancement of oxygen evaporation, it is necessary to control convection direction of the melt and strengthen gas flow above the melt. Global numerical simulation, which includes heat transfer in global furnace, argon gas convection inside furnace, and impurity transport in both melt and gas regions, has been implemented to validate the above methods.

## 1. Introduction

Multicrystalline silicon has now become the main material in the photovoltaic market because of its low production cost and because of the high conversion efficiency of solar cells made from this material. The unidirectional solidification method is a cost-effective technique for large-scale production of multicrystalline silicon material. Similar to the Czochralski method for crystal growth, the unidirectional solidification method is also related to transport of impurities [1]. Oxygen impurity is one of the main impurities in the crystal. The oxygen impurity can cause  $\text{SiO}_2$  precipitation [2], dislocation [3], and stacking faults [4] and can cause significant deterioration of the conversion efficiency of solar cells. The degradation of the solar cell performance caused by oxygen has been reported in papers [5–8]. Oxygen precipitation is known to act as intrinsic gettering sites for impurities and to affect mechanical strength of the wafer [9, 10]. Oxygen can form a variety of inhomogeneous defects: such as thermal donors [11, 12] due to clusters of a few oxygen atoms [13], and some other donors due to  $\text{SiO}_2$  precipitates [11, 12]. Except for those inhomogeneous defects, there is another kind of uniform distributed defect: boron-oxygen complexes, which

is responsible for an asymptotic degradation of solar cell performance by up to 10% relative when the time scale of illumination is close to hours [14, 15].

Effective control of oxygen concentrations in a crystal is required for the production of a high-quality crystal. Some papers about carbon and oxygen impurities [1, 16–24] have been written by authors; however, until now, there is no review paper to systematically introduce the basic methods to reduce oxygen impurity during multicrystalline silicon production. Therefore, this paper provides a basic framework for oxygen reduction in multicrystalline silicon during the unidirectional solidification process from the view of control of chemical reaction, melt convection, and gas flow. Furthermore, the control of melt convection for oxygen reduction is first reported by the present paper.

## 2. Mechanism of Oxygen Incorporation

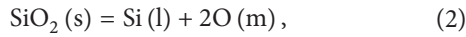
Incorporation of oxygen impurity into multicrystalline silicon occurs during the global unidirectional solidification process. To effectively illuminate the mechanism of oxygen incorporation, the global solidification process is divided into several substeps: melting process, solidification process,

and cooling process. During these processes, there are some differences in the main mechanism of oxygen incorporation into silicon.

**2.1. Melting Process.** During the melting process, there are two reactions occurring. The first is rapid reaction of the melt silicon with the silica crucible:

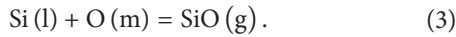


where the symbols (l), (s), and (g) denote liquid phase, solid phase, and gas phase, respectively. The second is decomposition of the silica crucible at a high temperature:



where the symbol (m) means the concentration inside the melt.

The silicon and oxygen atoms are transported onto the melt surface and react with each other to produce SiO gas:



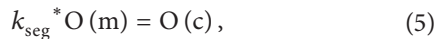
The resultant SiO gas evaporates from the melt surface. Reaction (2) is usually treated as a main source of oxygen impurity during the global solidification process and reaction (3) is treated as a main mechanism for oxygen reduction.

During the melting process, there is another chemical reaction that can contribute to oxygen incorporation. The graphite susceptor of the crucible can react with the crucible [16]:



Experimental results [25] have shown that SiO gas is most likely to be rapidly formed when carbon and silica particles are in contact, and reaction (4) is favorable over the entire temperature range from 1500 to 2500 K. The resultant SiO gas can diffuse back into melt from the carried gas.

**2.2. Solidification Process.** During the solidification process, besides reactions (1)–(4), there is another segregation reaction, that is, segregation of oxygen atoms into the crystal:



where the symbol (c) means the concentration in the crystal and  $k_{\text{seg}}$  is the segregation coefficient of oxygen, which is taken to be 0.85 [26].

**2.3. Cooling Process.** During the cooling process, the increase of oxygen impurity in solid phase is mainly due to diffusion from the crucible wall into the crystal. This contribution is very small due to small diffusion coefficient of oxygen in crystal, which is close to  $10^{-8} \text{ m}^2/\text{s}$  [27]. The diffusion depth of oxygen from the crucible wall is small and can be negligible.

### 3. Techniques for Oxygen Reduction and Numerical Models

The above analysis of oxygen incorporation indicates that oxygen impurity in multicrystalline silicon mainly originates

from the silica crucible. To effectively reduce oxygen impurity, it is essential to prevent or reduce any reaction with the crucible, such as reaction between the crucible and silicon and reaction between the crucible and its graphite susceptor. Meanwhile, it is also important to enhance the evaporation of SiO gas by controlling the melt and gas convection. Therefore, the basic principle for oxygen reduction is to reduce oxygen generation and to increase oxygen evaporation.

Global numerical modeling, which includes heat transfer in global furnace, argon gas convection inside furnace, and impurity transport in both melt and gas regions, has been implemented to validate the above methods.

**3.1. Numerical Methodology.** Our simulation implementation involves three steps: first, the temperature distribution of furnace components, due to heat transfer and heat radiation, is computed without gas flow; second, the flow field and temperature field of the cooling argon gas are computed using the temperature boundary conditions from the first step; and third, carbon and oxygen impurities in the gas and melt are computed using the flow field and temperature field from the second step.

The modeling of heat transfer in the furnace involves convective heat transfer of the melt in the crucible, conductive heat transfer in all solid components, and radiation heat transfer in all enclosures of the furnace. The melt flow in the crucible is assumed to be an incompressible laminar flow. The radiative heat exchange in all radiative enclosures is modeled on the basis of the assumption of diffuse-gray surface radiation.

The flow of argon gas through the furnace is considered to be a compressible and axisymmetric flow. The compressible flow solver can accurately simulate the buoyancy-driven flow due to the large density variation in the furnace. Although the flow velocity in this furnace is low, yet the density variation is significant for this buoyancy-driven flow, which is similar to the combustion problem.

The concentration of oxygen impurity is calculated by coupling the calculation of carbon impurity inside the global furnace. The SiO and CO concentrations inside gas and the C and O atom concentrations inside melt are calculated by a set of fully coupled program [1]. The boundary condition of SiO concentration at the melt surface is obtained from a dynamic update of SiO concentration [1]. The carbon flux from the gas into the melt is obtained from a local nonequilibrium consideration [1]. The carbon flux at the gas/melt interface is calculated locally and thus carbon accumulation in the melt is included. For details, refer to the paper [1].

#### 3.2. Techniques for Oxygen Reduction

**3.2.1. Reduction of Oxygen Generation.** Since an important source of oxygen impurity in the crystal is the reaction between the crucible and silicon, an effective method to weaken that reaction is to use  $\text{Si}_3\text{N}_4$  liner along the inner wall of the crucible. This liner can prevent direct contact between the crucible and silicon and thus reduce the intensity of chemical reaction between them. One simulation has been implemented to test the effect of the liner on oxygen impurity

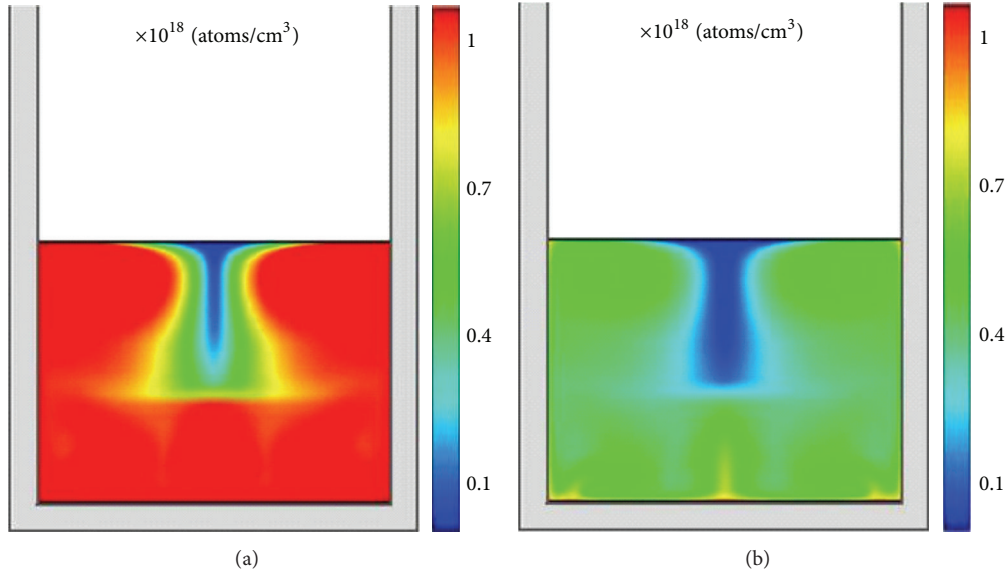


FIGURE 1: Oxygen concentration distributions inside a silicon crystal for different crucible conditions: (a) without  $\text{Si}_3\text{N}_4$  liner, (b) with  $\text{Si}_3\text{N}_4$  liner.

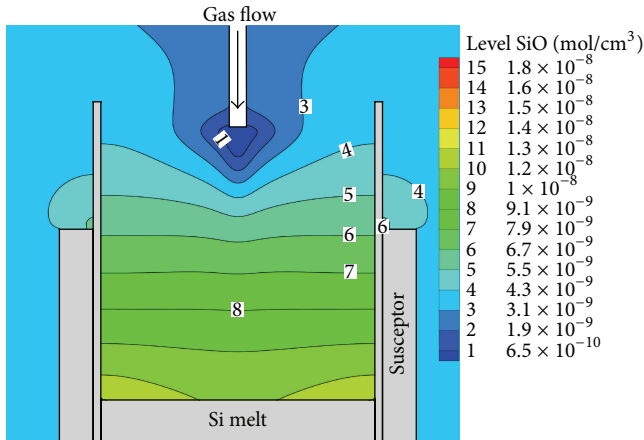
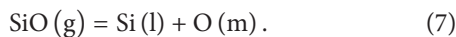


FIGURE 2: SiO gas distribution inside the gas space after considering the reaction between the silica crucible and the susceptor.

in a crystal [28]. The calculated oxygen concentrations in crystal without  $\text{Si}_3\text{N}_4$  liner (Figure 1(a)) and with  $\text{Si}_3\text{N}_4$  liner (Figure 1(b)) are shown in Figure 1. It can be seen that the oxygen concentration with  $\text{Si}_3\text{N}_4$  liner is obviously reduced. The paper [28] has pointed out the possible mechanism of oxygen reduction due to the  $\text{Si}_3\text{N}_4$  liner. Between the liner and the crucible, one chemical reaction occurs:



Between the liner and silicon melt, another reaction occurs:



The equilibrium oxygen concentration given from the reactions (6) and (7) at interfaces is about half of that in the case of reaction between a quartz crucible and silicon melt. The

equilibrium precondition of the reaction (7) is that the SiO gas can quickly pass through the  $\text{Si}_3\text{N}_4$  liner. We can derive that the thickness of  $\text{Si}_3\text{N}_4$  liner has a direction effect on oxygen reduction, since thicker liner can effectively impede the SiO gas passing through the liner. Therefore, from the view of point of oxygen reduction, it is more preferable to use thick  $\text{Si}_3\text{N}_4$  liner.

Oxygen impurity measures at different solidified fraction with  $\text{Si}_3\text{N}_4$  liner have been implemented in our group [28]. The comparison between the measured data and simulated data shows good agreement under  $\text{Si}_3\text{N}_4$  liner [28].

Another important source of oxygen impurity is the reaction between the crucible and its graphite susceptor. Numerical simulations have been implemented to test the effect of that reaction on oxygen impurity [16]. The chemical reaction is only considered at triple-phase points, that is, the crossing point among the crucible, susceptor, and gas space. The SiO distribution inside the gas space is shown in Figure 2. It can be seen that there is a large SiO concentration at the crossing point, which is  $6.7 \times 10^{-9}$  mol/cm<sup>3</sup>. The large concentration can cause SiO gas to diffuse back into the silicon melt from that triple-phase point and thus cause large oxygen impurity in the melt.

Figure 3 shows the variation of oxygen concentration in the melt with variation of carbon activity at the  $\text{SiO}_2$  surface [16]. When the carbon activity increases, oxygen impurity in the melt rapidly increases.

The increase of oxygen impurity in melt is due to the rapid generation of SiO and CO in gas phase:  $\text{C}(s) + \text{SiO}_2(s) = \text{SiO}(g) + \text{CO}(g)$ . The resultant SiO and CO gases can diffuse back into the melt from the carried gas. Therefore, when carbon activity increases, more SiO and CO gases result in and diffuse into melt.

Therefore, an effective method for reducing oxygen impurities in the crystal is to prevent reaction between the silica

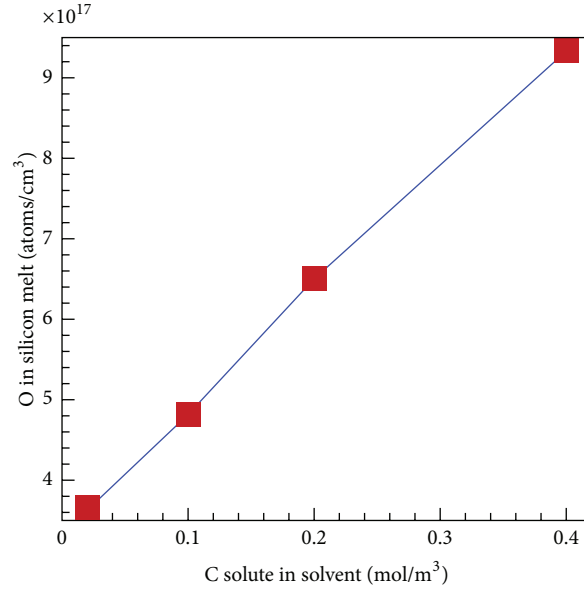


FIGURE 3: Oxygen concentrations in silicon melt with different carbon activities at the SiO<sub>2</sub> surface.

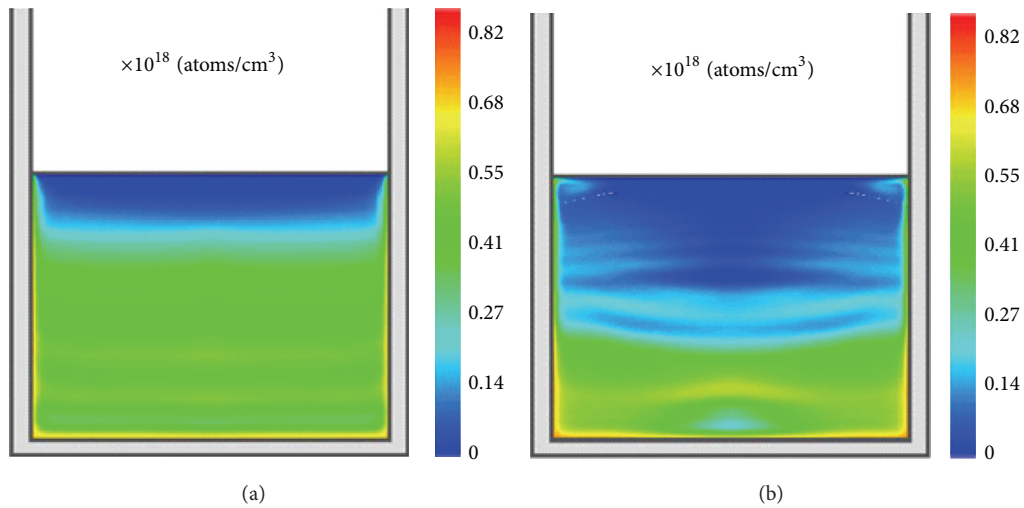


FIGURE 4: Oxygen concentration distributions inside silicon melt for different convection directions: (a) first from the crucible wall to the bottom and then to the surface, (b) first from the crucible wall to the surface and then to the bottom.

crucible and the graphite susceptor by setting a free space between them or by depositing a layer of SiC film on the surface of the susceptor.

**3.2.2. Enhancement of Oxygen Evaporation.** Since reaction (3) is a main source for oxygen evaporation, an effective method for oxygen reduction is to promote evaporation reaction (3). The evaporation speed is determined by the oxygen flux inside the melt and inside the gas. Therefore, it is essential to increase flux in both sides for effective reduction of oxygen impurity.

Inside the melt, the oxygen concentration at the melt surface is always minimal due to evaporation. Thus, the flux

along the surface is determined by the concentration just beneath the surface, denoted by  $C_m$ . If  $C_m$  is large, oxygen flux is definitely large. Therefore, it is essential to increase  $C_m$  as much as possible to enhance oxygen flux toward the surface. Figure 4 shows oxygen concentration in the melt with different convection patterns. In Figure 4(a), the melt flows first from the crucible wall to the bottom and then to the surface, and in Figure 4(b), the melt flows first from the crucible wall to the surface and then to the bottom. It can be seen that when the melt directly flows from the crucible wall to the surface, the oxygen concentration inside the global melt is obviously small. The main reason is that  $C_m$  near the surface is larger when the melt directly carries the oxygen

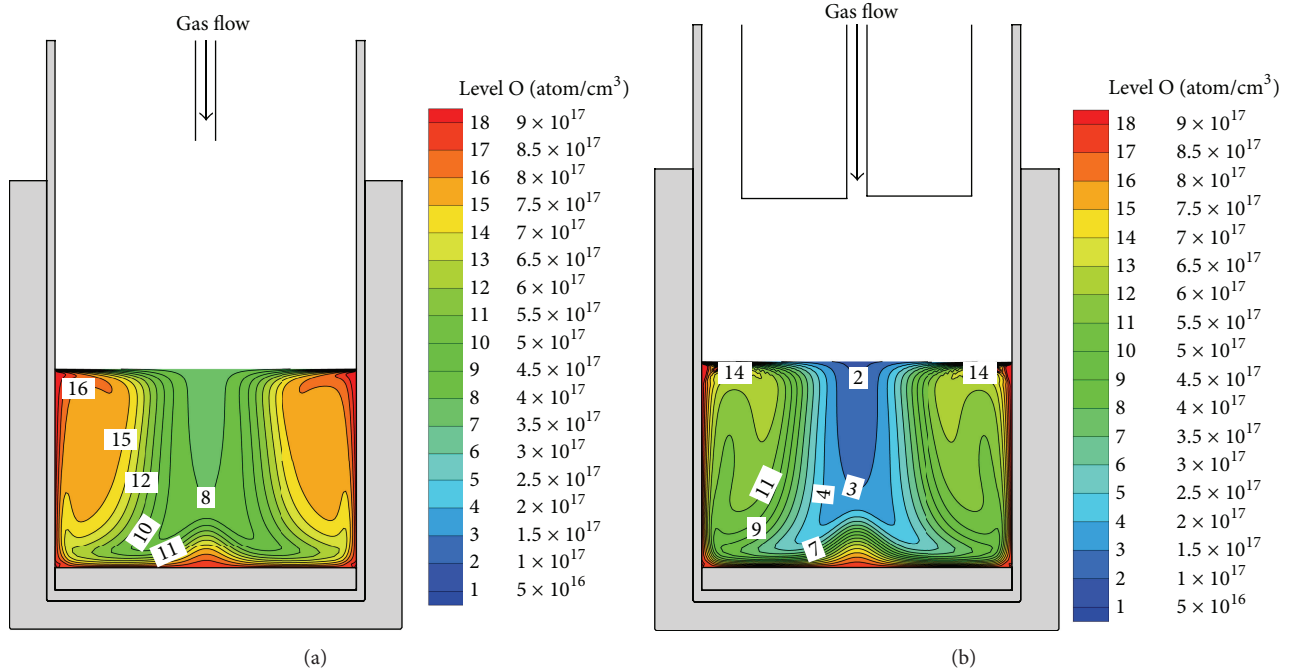


FIGURE 5: Oxygen concentration distributions inside silicon melt: (a) without a crucible cover, (b) with a crucible cover.

from the crucible wall to the surface. Therefore, the oxygen impurity can be effectively reduced by controlling the flow pattern of the melt.

Inside the gas space, the oxygen concentration at the gas/melt interface is always maximal. Thus, the oxygen flux along the interface is determined by the concentration just above the interface, denoted by  $C_g$ . If  $C_g$  is small, the flux is definitely large. Therefore, it is essential to reduce that value as much as possible to enhance the evaporation flux. Two numerical simulations have been done with a fixed flow rate of argon gas and temperature boundary conditions. The shape of the gas tube has some difference for the two cases. Figure 5 shows a comparison of oxygen distributions inside the melt without a cover (Figure 5(a)) and with a cover (Figure 5(b)) [18]. It can be seen that the oxygen concentration is obviously small with a cover. The main reason is that the cover strengthens the flow above the melt, which reduces  $C_g$  above the interface and causes a large SiO flux out from the surface. Therefore, the oxygen impurity can be effectively reduced by strengthening the gas flow above the melt.

To indicate the validation of our calculation, some measurements and numerical simulations have been done for the effect of strengthening the gas flow on impurities [1]. The comparison between numerical and experimental results showed good agreement for impurities if the gas flow is strengthened by increasing the gas flow rate [1].

#### 4. Conclusions

The oxygen impurity inside multicrystalline silicon mainly originates from the silica crucible. To effectively reduce the oxygen impurity, it is essential to reduce the oxygen generation and enhance oxygen evaporation. For the reduction of

oxygen generation, it is necessary to weaken the chemical reaction between the crucible and silicon by using a layer of  $\text{Si}_3\text{N}_4$  liner and to prevent the reaction between the crucible and the graphite susceptor by setting a free space between them or by depositing a layer of SiC film on the surface of the susceptor. For the enhancement of oxygen evaporation, it is necessary to increase the oxygen concentration value beneath the melt surface as much as possible by adjusting the convection direction and to reduce the oxygen concentration just above the melt-gas interface as much as possible by strengthening gas flow. The feasibility of the above methods has been validated by the global numerical simulation.

#### Acknowledgments

This work was partly supported by the New Energy and Industrial Technology Development Organization (NEDO) under the Ministry of Economy, Trade and Industry (METI).

#### References

- [1] B. Gao, S. Nakano, and K. Kakimoto, "Global simulation of coupled carbon and oxygen transport in a unidirectional solidification furnace for solar cells," *Journal of the Electrochemical Society*, vol. 157, no. 2, pp. H153–H159, 2010.
- [2] H. J. Möller, L. Long, M. Werner, and D. Yang, "Oxygen and carbon precipitation in multicrystalline solar silicon," *Physica Status Solidi*, vol. 171, no. 1, pp. 175–189, 1999.
- [3] H. J. Möller, C. Funke, A. Lawrenz, S. Riedel, and M. Werner, "Oxygen and lattice distortions in multicrystalline silicon," *Solar Energy Materials and Solar Cells*, vol. 72, no. 1–4, pp. 403–416, 2002.
- [4] V. V. Bolotov, M. D. Efremov, I. Babanskaya, and K. Schmalz, "Raman study of mechanical stresses in processes of oxygen

- precipitation in silicon," *Materials Science and Engineering B*, vol. 21, no. 1, pp. 49–54, 1993.
- [5] D. Yang, L. Li, X. Ma, R. Fan, D. Que, and H. J. Moeller, "Oxygen-related centers in multicrystalline silicon," *Solar Energy Materials and Solar Cells*, vol. 62, no. 1–2, pp. 37–42, 2000.
  - [6] S. Martinuzzi and I. Perichaud, "Influence of oxygen on external phosphorus gettering in disordered silicon wafers," *Materials Science Forum*, vol. 143, pp. 1629–1634, 1994.
  - [7] K. Tempelhoff, F. Spiegelberg, R. Gleichmann, and D. Wruck, "Precipitation of oxygen in dislocation-free silicon," *Physica Status Solidi A*, vol. 56, no. 1, pp. 213–223, 1979.
  - [8] K. Nauka, H. C. Gatos, and J. Lagowski, "Oxygen-induced recombination centers in as-grown Czochralski silicon crystals," *Applied Physics Letters*, vol. 43, no. 3, pp. 241–243, 1983.
  - [9] D. E. Bornside, R. A. Brown, T. Fujiwara, H. Fujiwara, and T. Kubo, "Effects of gas-phase convection on carbon contamination of Czochralski-grown silicon," *Journal of the Electrochemical Society*, vol. 142, no. 8, pp. 2790–2804, 1995.
  - [10] U. Gösele and T. Y. Tan, "Oxygen diffusion and thermal donor formation in silicon," *Applied Physics A*, vol. 28, no. 2, pp. 79–92, 1982.
  - [11] W. Bergholz, "Chapter 12 grown-in and process-induced defects," *Semiconductors and Semimetals*, vol. 42, no. C, pp. 513–575, 1994.
  - [12] A. Borghesi, B. Pivac, A. Sassella, and A. Stella, "Oxygen precipitation in silicon," *Journal of Applied Physics*, vol. 77, no. 9, pp. 4169–4244, 1995.
  - [13] J. Michel and L. C. Kimerling, "Electrical properties of oxygen in silicon," *Semiconductors and Semimetals*, vol. 42, no. C, pp. 251–287, 1994.
  - [14] J. Schmidt, "Light-induced degradation in crystalline silicon solar cells," *Solid State Phenomena*, vol. 95, pp. 187–196, 2004.
  - [15] J. Schmidt and K. Bothe, "Structure and transformation of the metastable boron- and oxygen-related defect center in crystalline silicon," *Physical Review B*, vol. 69, no. 2, Article ID 024107, pp. 241071–241078, 2004.
  - [16] B. Gao, S. Nakano, and K. Kakimoto, "Influence of reaction between silica crucible and graphite susceptor on impurities of multicrystalline silicon in a unidirectional solidification furnace," *Journal of Crystal Growth*, vol. 314, no. 1, pp. 239–245, 2011.
  - [17] B. Gao, S. Nakano, and K. Kakimoto, "Effect of crucible cover material on impurities of multicrystalline silicon in a unidirectional solidification furnace," *Journal of Crystal Growth*, vol. 318, no. 1, pp. 255–258, 2011.
  - [18] B. Gao, X. J. Chen, S. Nakano, and K. Kakimoto, "Crystal growth of high-purity multicrystalline silicon using a unidirectional solidification furnace for solar cells," *Journal of Crystal Growth*, vol. 312, no. 9, pp. 1572–1576, 2010.
  - [19] B. Gao and K. Kakimoto, "Global simulation of coupled carbon and oxygen transport in a Czochralski furnace for silicon crystal growth," *Journal of Crystal Growth*, vol. 312, no. 20, pp. 2972–2976, 2010.
  - [20] Y. Y. Teng, J. C. Chen, C. W. Lu, and C. Y. Chen, "Numerical investigation of oxygen impurity distribution during multicrystalline silicon crystal growth using a gas flow guidance device," *Journal of Crystal Growth*, vol. 360, no. 1, pp. 12–17, 2012.
  - [21] A. D. Smirnov and V. V. Kalaev, "Development of oxygen transport model in Czochralski growth of silicon crystals," *Journal of Crystal Growth*, vol. 310, no. 12, pp. 2970–2976, 2008.
  - [22] C. Reimann, M. Trempa, T. Jung, J. Friedrich, and G. Müller, "Modeling of incorporation of O, N, C and formation of related precipitates during directional solidification of silicon under consideration of variable processing parameters," *Journal of Crystal Growth*, vol. 312, no. 7, pp. 878–885, 2010.
  - [23] T. Carlberg, T. B. King, and A. F. Witt, "Dynamic oxygen equilibrium in silicon melts during crystal growth by the czochralski technique," *Journal of the Electrochemical Society*, vol. 129, no. 1, pp. 189–193, 1982.
  - [24] D. E. Bornside, R. A. Brown, T. Fujiwara, H. Fujiwara, and T. Kubo, "Effects of gas-phase convection on carbon contamination of Czochralski-grown silicon," *Journal of the Electrochemical Society*, vol. 142, no. 8, pp. 2790–2804, 1995.
  - [25] A. W. Weimer, K. J. Nilsen, G. A. Cochran, and R. P. Roach, "Kinetics of carbothermal reduction synthesis of beta silicon carbide," *AIChE Journal*, vol. 39, no. 3, pp. 493–503, 1993.
  - [26] K. Hoshikawa and X. Huang, "Oxygen transportation during Czochralski silicon crystal growth," *Materials Science and Engineering B*, vol. 72, pp. 73–79, 2000.
  - [27] S. Hisamatsu, H. Matsuo, S. Nakano, and K. Kakimoto, "Numerical analysis of the formation of  $\text{Si}_3\text{N}_4$  and  $\text{Si}_2\text{N}_2\text{O}$  during a directional solidification process in multicrystalline silicon for solar cells," *Journal of Crystal Growth*, vol. 311, no. 9, pp. 2615–2620, 2009.
  - [28] H. Matsuo, R. B. Ganesh, S. Nakano et al., "Thermodynamical analysis of oxygen incorporation from a quartz crucible during solidification of multicrystalline silicon for solar cell," *Journal of Crystal Growth*, vol. 310, no. 22, pp. 4666–4671, 2008.

## Research Article

# Effect of Annealing Temperature on CuInSe<sub>2</sub>/ZnS Thin-Film Solar Cells Fabricated by Using Electron Beam Evaporation

**H. Abdullah and S. Habibi**

*Department of Electrical, Electronics, and Systems Engineering, Faculty of Engineering and Built Environment, Universiti Kebangsaan Malaysia, 43600 Bangi, Selangor, Malaysia*

Correspondence should be addressed to H. Abdullah; [huda@eng.ukm.my](mailto:huda@eng.ukm.my)

Received 17 October 2012; Accepted 10 December 2012

Academic Editor: Sudhakar Shet

Copyright © 2013 H. Abdullah and S. Habibi. This is an open access article distributed under the Creative Commons Attribution License, which permits unrestricted use, distribution, and reproduction in any medium, provided the original work is properly cited.

CuInSe<sub>2</sub> (CIS) thin films are successfully prepared by electron beam evaporation. Pure Cu, In, and Se powders were mixed and ground in a grinder and made into a pellet. The pellets were deposited via electron beam evaporation on FTO substrates and were varied by varying the annealing temperatures, at room temperature, 250°C, 300°C, and 350°C. Samples were analysed by X-ray diffractometry (XRD) for crystallinity and field-emission scanning electron microscopy (FESEM) for grain size and thickness. I-V measurements were used to measure the efficiency of the CuInSe<sub>2</sub>/ZnS solar cells. XRD results show that the crystallinity of the films improved as the temperature was increased. The temperature dependence of crystallinity indicates polycrystalline behaviour in the CuInSe<sub>2</sub> films with (1 1 1), (2 2 0)/(2 0 4), and (3 1 2)/(1 1 6) planes at 27°, 45°, and 53°, respectively. FESEM images show the homogeneity of the CuInSe<sub>2</sub> formed. I-V measurements indicated that higher annealing temperatures increase the efficiency of CuInSe<sub>2</sub> solar cells from approximately 0.99% for the as-deposited films to 1.12% for the annealed films. Hence, we can conclude that the overall cell performance is strongly dependent on the annealing temperature.

## 1. Introduction

Among various materials for thin film solar cells, copper indium diselenide (CuInSe<sub>2</sub>) has emerged as a promising material due to its use as a solar radiation absorber. In recent years, interest has increased regarding the use of copper indium selenide (CIS) compounds, which are elements of the I-III-VI<sub>2</sub> group, as materials for thin film photovoltaic solar cells because of their high theoretical efficiency of approximately 24.8% [1]. CuInSe<sub>2</sub> is a promising material for thin film solar cells because of its extraordinary radiation stability [2]. CuInSe<sub>2</sub> films possess certain exceptional material characteristics including a band-gap, absorption coefficient and minority carrier diffusion length which are particularly suitable for photovoltaic applications. Because these films can be prepared with n- and p-type conductivity, there is potential for both a homo- and heterojunction [3]. CuInSe<sub>2</sub> is also favoured because it is more environmentally benign than CIS. These materials have remarkably stable electrical properties over a wide range of stoichiometries [4]. Recently, CIS solar cells have been produced with efficiencies as high

as 15.4%, and have demonstrated good long-term stability and stable device performance [5]. To achieve further commercial success for CuInSe<sub>2</sub>-based photovoltaics and to reduce the cost of these solar cells, it is necessary to mass-produce quality CuInSe<sub>2</sub> films via a low-cost, eco-friendly, and easily scalable process [6]. Evaporation techniques are typically used to produce good film stoichiometry for elements and simple compounds [7]. Among II-VI compounds, zinc sulfide (ZnS) and zinc selenide (ZnSe) are suitable for many applications [8]. ZnS has a large band gap of approximately 3.7 eV, high refractive index, high precision dielectric constant, and broad band of wavelengths [9]. At certain temperatures, ZnS can change phase from cubic to wurtzite [10]. ZnS can be used in the fabrication of optoelectronic devices, photoconductors and window materials for thin film heterojunction solar cells [11]. The aim of this research is to study the dependence of CuInSe<sub>2</sub>:ZnS solar cell efficiencies, structures, and morphologies on the annealing temperature of the CuInSe<sub>2</sub> films. In this study, CuInSe<sub>2</sub> films with an annealing temperature of room temperature (27°C), 250°C, 300°C, or 350°C were examined for changes in morphology and structure by

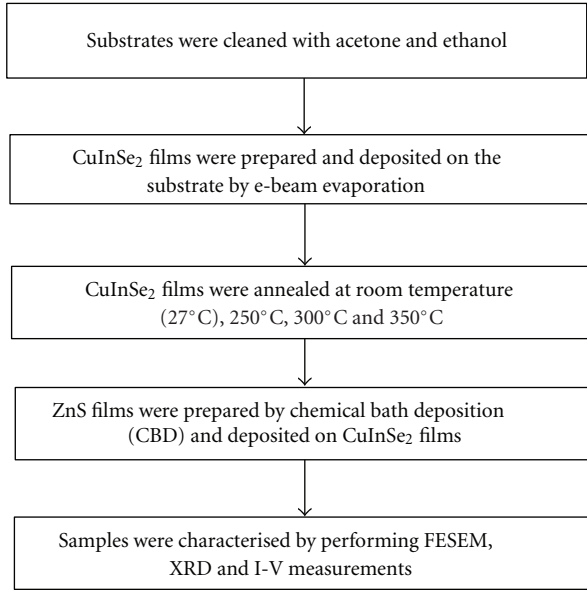


FIGURE 1: Flow chart of overall process in fabrication of  $\text{CuInSe}_2$ :ZnS solar cell by electron beam evaporation and chemical bath deposition (CBD) method.

FESEM and XRD analysis. To study the effects of the annealing temperature on the overall  $\text{CuInSe}_2$ :ZnS solar cell efficiency, I-V measurements were performed for thin films with annealing temperatures of 27°C and 100°C.

## 2. Experimental Details

$\text{CuInSe}_2$  layers were produced by annealing  $\text{CuInSe}_2$  pellets onto FTO glass substrates via electron beam evaporation. ZnS layers were made using the chemical bath deposition (CBD) technique with a 3 h deposition time. The  $\text{CuInSe}_2$  pellets were made from a mixture of Cu, In and Se powders, while ZnS films were fabricated from a  $\text{Zn}(\text{CH}_3\text{COO})_2$ , TEA,  $\text{NH}_3$ ,  $\text{C}_6\text{H}_5\text{Na}_3\text{O}_7$  and thiourea solution.  $\text{CuInSe}_2$  films were varied by using annealing temperatures of room temperature, 250°C, 300°C, and 350°C to study the effect of the annealing temperature on the morphology, structure and the efficiency of the solar cells. The flow of the cell fabrication is outlined in Figure 1. The surface morphology was studied with field-emission scanning electron microscopy (FESEM) while the crystallinity of the  $\text{CuInSe}_2$  films was determined by X-ray diffraction (XRD). I-V data were collected by Gamry Instruments G300 with a light intensity of  $110 \text{ mW/cm}^2$ . Figure 2 shows a diagram of the prepared samples with ZnS and  $\text{CuInSe}_2$  films on top of a glass substrate with an FTO layer.

## 3. Results and Discussions

Figure 2 shows the cross-section of prepared samples with ZnS and  $\text{CuInSe}_2$  films on top of glass substrate and FTO layer while Figure 3 shows FE-SEM images of  $\text{CuInSe}_2$  films deposited with an annealing temperature of 27°C, 250°C,

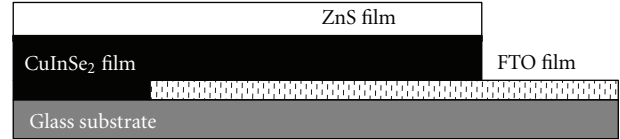


FIGURE 2: Cross-section of prepared samples with ZnS and  $\text{CuInSe}_2$  films.

TABLE 1: Particle size of  $\text{CuInSe}_2$  for each annealing temperature.

Annealing temperature (°C)	Particle size (nm)
27	113.90
250	27.90
300	21.66
350	24.03

300°C, or 350°C. From the results obtained,  $\text{CuInSe}_2$  films were deposited uniformly over the substrate. These layers covered the entire surface of the substrate even without annealing, but the nonannealed films resulted in grains having less homogeneity. The grains became smaller and more densely arranged when temperature increased from 300°C to 350°C than when the temperature was increased from 250°C to 300°C. FE-SEM also shows an increase in grain size due to the roughness that developed when the growth rate was increased with an increase in annealing temperature [12]. The average particle size and film thicknesses are shown in Table 1.

As shown in Table 1, the average particle sizes were 156.33 nm, 137.70 nm, 139.53 nm, and 163.77 nm for annealing temperatures of 27°C, 250°C, 300°C, and 350°C, respectively. After the heat treatment, single grains of  $\text{CuInSe}_2$  were developed and the morphology of the films became denser. The thicknesses measured 172.67 nm, 109.76 nm, 121.33 nm, and 133.23 nm for the annealing temperatures of 27°C, 250°C, 300°C, and 350°C, respectively. These show that at room temperature,  $\text{CuInSe}_2$  films have the greatest thickness, and after annealing, the thickness decreases from 172.67 nm to 109.76 nm. This thickness change occurs because the smaller grains deposited on the film upon thermal treatment have less energy and have lost some of the weak binding between the grains and the substrate. These grains leave the substrate after annealing, but with increased annealing temperatures up to 300°C and 350°C, the denser grains become larger serve to increase the thickness of the film. The average size of the grains measured was approximately 100 nm. The similar phenomenon has also been studied by Zhang et al. 2010 [13]. We can conclude from these results that annealing temperature, particle size and film morphology are all proportionally related.

The diffraction patterns for  $\text{CuInSe}_2$  samples annealed at temperatures of 27°C, 250°C, 300°C, and 350°C are shown in Figure 4. From analysis of the XRD patterns, it was observed that the  $\text{CuInSe}_2$  crystallinity increased from amorphous structure to a polycrystalline structure as the annealing temperature increased. As shown in Figure 4, the  $\text{CuInSe}_2$  films are amorphous at room temperature. There are three

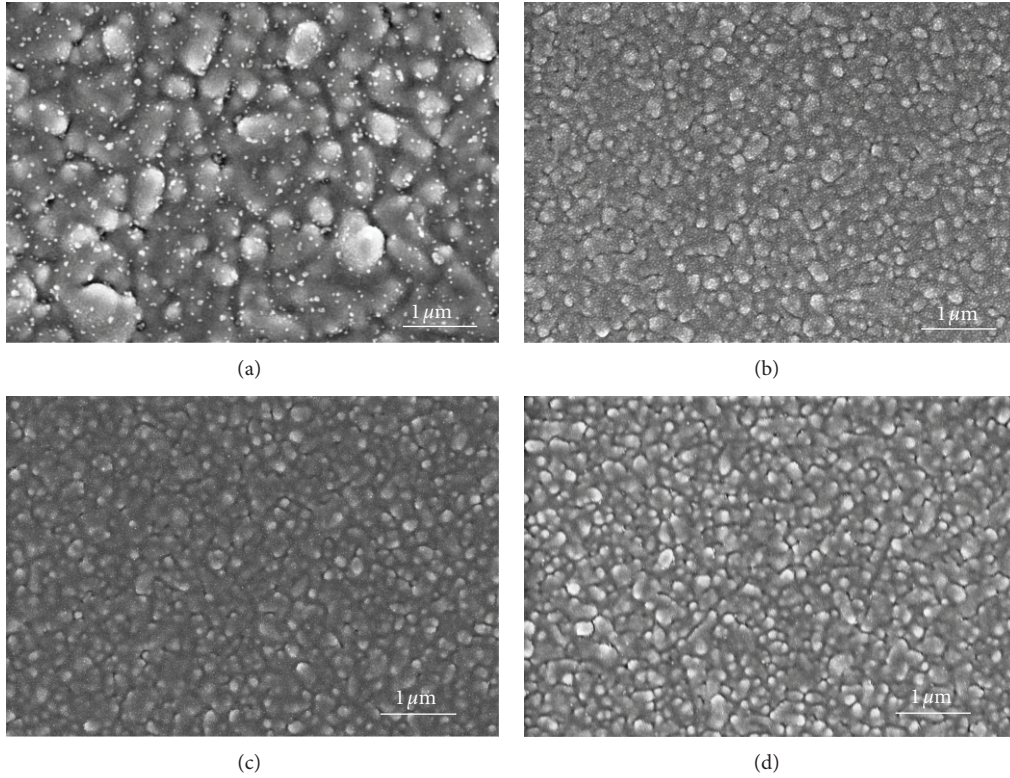


FIGURE 3: FESEM images of CIS samples prepared at temperature (a) room temperature, (b) 250°C, (c) 300°C, and (d) 350°C.

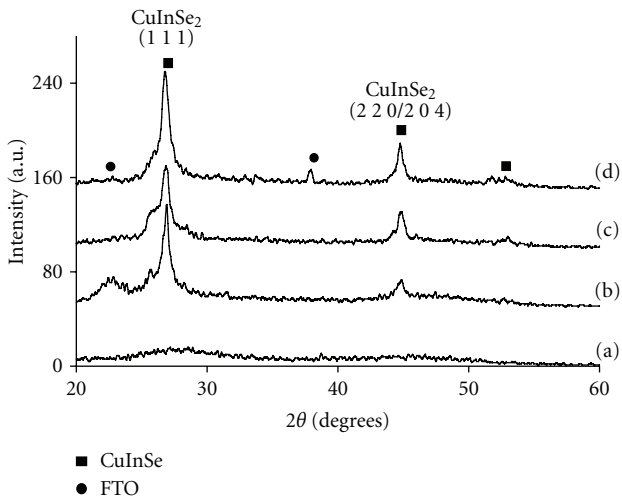


FIGURE 4: XRD results of CIS films prepared at temperature (a) room temperature, (b) 250°C, (c) 300°C, and (d) 350°C.

dominant peaks corresponding to (1 1 2), (2 2 0)/(2 0 4), and (3 1 2)/(1 1 6) orientations at a  $2\theta$  of 27°, 45°, and 53°, respectively. These peaks have also been studied by Bindu et al. [6], Soon et al. [14], Yang and Chen [12], and Jeong et al. [15]. At an annealing temperature of 250°C, three peaks, which contained both CuInSe<sub>2</sub> and FTO, could be observed with (1 1 2) and (2 2 0)/(2 0 4) orientations, as reported by Bernéde and Assmann [16]. At a temperature of 300°C,

CuInSe<sub>2</sub> peaks were dominant and the FTO peaks slowly disappeared. When the temperature was increased to 350°C, CuInSe<sub>2</sub> peaks appeared at three locations ( $2\theta$ ) of 27°, 45°, and 53°. The peaks became sharper after the annealing temperature was increased, showing that the crystal sizes were larger than 1 nm [17]. The intensity of the peaks decreased with increasing annealing temperature, showing that the amount of the binary compound CuSe decreases during the annealing process. Higher and sharper peaks also appeared, showing that the primary crystal structure was successfully increased after the annealing process.

Figure 4 also shows that the main phase of the deposited CuInSe<sub>2</sub> film has a chalcopyrite structure [18].

A qualitative estimation of the crystal size was obtained from Scherrer's formula:

$$D = \frac{k\lambda}{B \cos \theta}, \quad (1)$$

where  $k$  is the shape factor,  $\lambda$  is the wavelength (0.154 nm),  $B$  is the full-width at half-maximum of the main peak, and  $\theta$  is the main peak position [19]. The crystal size was calculated and is shown in Table 2. The average crystal size of CuInSe<sub>2</sub> was 2.63 nm, 2.55 nm, and 3.05 nm for CuInSe<sub>2</sub> (1 1 1), 8.99 nm, 7.49 nm, and 7.05 nm for the (2 2 0)/(2 0 4) plane, and 3.70 nm for the (3 1 2)/(1 1 6) plane. The grain size increased in the (1 1 1) plane and decreased in the (2 2 0)/(2 0 4) plane proportionally with the increasing annealing temperature. At the higher temperatures of 300°C

TABLE 2: Crystal size and diffraction angle for each of annealing temperature.

Samples	Annealing temperature (°C)	2 $\theta$ (degrees)	Crystal size, $d$ (nm)	( $h k l$ )
CuInSe <sub>2</sub> _27	25	Amorphous	Amorphous	Amorphous
CuInSe <sub>2</sub> _250	250	26.9	2.63	111
		45.0	8.99	2 2 0/2 0 4
CuInSe <sub>2</sub> _300	300	26.9	2.55	111
		44.9	7.49	2 2 0/2 0 4
CuInSe <sub>2</sub> _350	350	26.8	3.05	112
		44.8	7.05	2 2 0/2 0 4
		52.7	3.70	3 1 2/1 1 6

TABLE 3: Efficiency of CuInSe<sub>2</sub>:ZnS solar cell at produced room temperature and annealing temperature of 100°C.

Sample	Annealing temperature (°C)	Current density, $J$ (mA/cm <sup>2</sup> )	Open-circuit voltage (V)	Fill factor FF	Efficiency (%)
4000_room temperature	27	8.65	0.20	0.36	0.99
4000_100	100	1.92	1.96	0.33	1.12

and 350°C, the FTO peak disappeared and a peak corresponding to the (3 1 2)/(1 1 6) plane is observed, showing that the growth of the ternary compound CuInSe<sub>2</sub>. This analysis shows that the crystalline structure of CuInSe<sub>2</sub> films can be changed from an amorphous to a polycrystalline phase with heat treatment.

CuInSe<sub>2</sub>:ZnS solar cells were fabricated by depositing ZnS thin films on top of CuInSe<sub>2</sub> films via the chemical bath deposition (CBD) method with a deposition time of 3 h. Figure 5 shows the I-V curves for CuInSe<sub>2</sub>:ZnS solar cells for the CuInSe<sub>2</sub> films annealed at temperatures of 27°C and 100°C. These temperatures have been chosen for the I-V measurements and are merely included to study the effect of annealing treatments on the overall solar cell efficiency. As shown in Figure 5, the effect of the changes in annealing temperature on the solar cell efficiencies was analysed and the results indicate that there was a difference in current density ( $J_{sc}$ ) and open-circuit voltage ( $V_{oc}$ ) of the samples before and after annealing. After annealing,  $J_{sc}$ , decreased from 8.65 mA/cm<sup>2</sup> to 1.92 mA/cm<sup>2</sup> while  $V_{oc}$ , increased from 0.20 V to 1.96 V. This could be due to the surface morphology of the samples prior to annealing as was shown by FESEM. This condition enhanced the electron-hole pair recombination rate in the film which affected the overall cell performance. The cell with the thicker layer had a lower efficiency, despite having greater photon absorption due to a simultaneous decrease in internal quantum efficiency [20]. As shown in Table 3, which presents the calculated efficiency along with  $J_{sc}$ , the fill factor, FF and  $V_{oc}$ , annealing increases the efficiency of CuInSe<sub>2</sub>:ZnS solar cells from 0.99% to 1.12%.

#### 4. Conclusions

This study used electron beam evaporation, with annealing temperatures of 27°C, 250°C, 300°C, and 350°C, and the

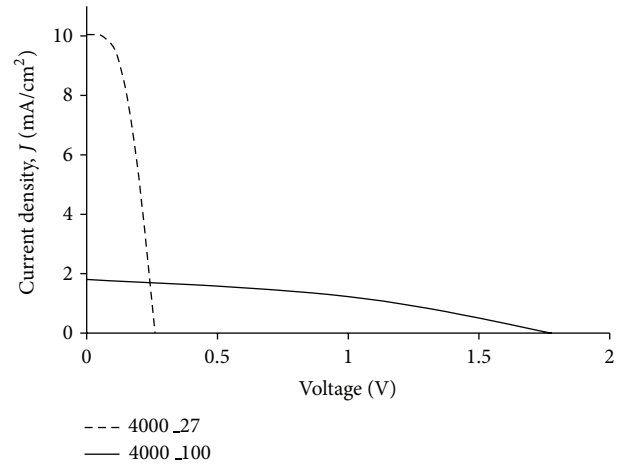


FIGURE 5: I-V measurement CIS:ZnS solar cell with room temperature (27°C) and 100°C.

chemical bath deposition (CBD) method, with a 3 h deposition time, to produce CuInSe<sub>2</sub>:ZnS solar cells. XRD analysis suggested that the diffraction of CuInSe<sub>2</sub> films changed from an amorphous to a polycrystalline phase after annealing at 27°, 45° and 53° at (1 1 2), (2 2 0)/(2 0 4), and (3 1 2)/(1 1 6) orientations, respectively. FESEM results showed that the CuInSe<sub>2</sub> particles were in better arrays after annealing and had sizes of 156.33 nm, 137.70 nm, 139.53 nm, and 163.77 nm. The thicknesses measured were 172.67 nm, 109.76 nm, 121.33 nm, and 133.23 nm for annealing temperatures of 27°C, 250°C, 300°C, and 350°C, respectively. From these data, we conclude that as the annealing temperature increases, the particle size and thickness also increase. I-V measurements indicated that annealing increases the efficiency of solar cells from 0.99% to 1.12%. These results show the dependence of both the efficiency and the structural and

morphological characteristics of CuInSe<sub>2</sub> layers on annealing temperature.

## References

- [1] O. Tesson, M. Morsli, A. Bonnet, V. Jousseau, L. Cattin, and G. Massé, "Electrical characterisation of CuInSe<sub>2</sub> thin films for solar cells applications," *Optical Materials*, vol. 9, no. 1–4, pp. 511–515, 1998.
- [2] A. V. Postnikov and M. V. Yakushev, "Lattice dynamics and stability of CuInSe<sub>2</sub>," *Thin Solid Films*, vol. 451–452, pp. 141–144, 2004.
- [3] K. L. Chopra and S. R. Das, *Thin Film Solar Cells*, Plenum Press, New York, NY, USA, 1983.
- [4] M. Altosaar, M. Danilson, M. Kauk et al., "Further developments in CIS monograin layer solar cells technology," *Solar Energy Materials and Solar Cells*, vol. 87, no. 1–4, pp. 25–32, 2005.
- [5] T. Markvart and L. Castaner, *Practical Handbook of Photovoltaics: Fundamentals and Applications*, Elsevier, 2003.
- [6] K. Bindu, C. S. Kartha, K. P. Vijayakumar, T. Abe, and Y. Kashiwaba, "CuInSe<sub>2</sub> thin film preparation through a new selenisation process using chemical bath deposited selenium," *Solar Energy Materials and Solar Cells*, vol. 79, no. 1, pp. 67–79, 2003.
- [7] A. Y. Ono, *Electroluminescent Displays*, World Scientific, Technology & Engineering, 1995.
- [8] P. Roy, J. R. Ota, and S. K. Srivastava, "Crystalline ZnS thin films by chemical bath deposition method and its characterization," *Thin Solid Films*, vol. 515, no. 4, pp. 1912–1917, 2006.
- [9] A. U. Ubale, V. S. Sangawar, and D. K. Kulkarni, "Size dependent optical characteristics of chemically deposited nanostructured ZnS thin films," *Bulletin of Materials Science*, vol. 30, no. 2, pp. 147–151, 2007.
- [10] D. Moore and W. L. Zhong, "Growth of anisotropic one-dimensional ZnS nanostructures," *Journal of Materials Chemistry*, vol. 16, pp. 3898–3905, 2006.
- [11] X. D. Gao, X. M. Li, and W. D. Yu, "Morphology and optical properties of amorphous ZnS films deposited by ultrasonic-assisted successive ionic layer adsorption and reaction method," *Thin Solid Films*, vol. 468, no. 1–2, pp. 43–47, 2004.
- [12] Y. H. Yang and Y. T. Chen, "Solvochemical preparation and spectroscopic characterization of copper indium diselenide nanorods," *Journal of Physical Chemistry B*, vol. 110, no. 35, pp. 17370–17374, 2006.
- [13] Z. Zhang, J. Li, M. Wang, M. Wei, G. Jiang, and C. Zhu, "Influence of annealing conditions on the structure and compositions of electrodeposited CuInSe<sub>2</sub> films," *Solid State Communications*, vol. 150, no. 47–48, pp. 2346–2349, 2010.
- [14] S. H. Kang, Y. K. Kim, D. S. Choi, and Y. E. Sung, "Characterization of electrodeposited CuInSe<sub>2</sub> (CIS) film," *Electrochimica Acta*, vol. 51, no. 21, pp. 4433–4438, 2006.
- [15] W. J. Jeong, H. G. Ahn, Y. J. Kim, H. H. Yang, and G. C. Park, "The properties of CuInSe<sub>2</sub> by DC/RF magnetron sputtering and thermal evaporation method," *Transactions on Electrical and Electronic Materials*, vol. 8, no. 2, pp. 89–92, 2007.
- [16] J. C. Bernède and L. Assmann, "Polycrystalline CuInSe<sub>2</sub> thin films synthesized by microwave irradiation," *Vacuum*, vol. 59, no. 4, pp. 885–893, 2000.
- [17] E. Tzvetkova, N. Stratieva, M. Ganchev, I. Tomov, K. Ivanova, and K. Kochev, "Preparation and structure of annealed CuInSe<sub>2</sub> electrodeposited films," *Thin Solid Films*, vol. 311, no. 1–2, pp. 101–106, 1997.
- [18] Z. W. Zhang, J. Li, J. L. Liu, and C. F. Zhu, "Synthesis and characterization of supported CuInSe<sub>2</sub> nanorod arrays on rigid substrates," *Chinese Journal of Chemical Physics*, vol. 24, no. 1, pp. 115–120, 2011.
- [19] Z. H. Li, E. S. Cho, and S. J. Kwon, "Properties of the Cu(In,Ga)Se<sub>2</sub> absorbers deposited by electron-beam evaporation method for solar cells," *Current Applied Physics*, vol. 11, no. 1, pp. 28–33, 2011.
- [20] V. A. Akhavan, M. G. Panthani, B. W. Goodfellow, D. K. Reid, and B. A. Korgel, "Thickness-limited performance of CuInSe<sub>2</sub> nanocrystal photovoltaic devices," *Optics Express*, vol. 18, no. 19, pp. A411–A420, 2010.

## Research Article

# Interface Study of ITO/ZnO and ITO/SnO<sub>2</sub> Complex Transparent Conductive Layers and Their Effect on CdTe Solar Cells

**Tingliang Liu, Xing Zhang, Jingquan Zhang, Wenwu Wang, Lianghuan Feng, Lili Wu, Wei Li, Guanggen Zeng, and Bing Li**

*College of Materials Science and Engineering, Sichuan University, Chengdu 610064, China*

Correspondence should be addressed to Guanggen Zeng; [yigezeng@sina.com](mailto:yigezeng@sina.com)

Received 28 September 2012; Accepted 18 December 2012

Academic Editor: Sudhakar Shet

Copyright © 2013 Tingliang Liu et al. This is an open access article distributed under the Creative Commons Attribution License, which permits unrestricted use, distribution, and reproduction in any medium, provided the original work is properly cited.

Transparent ITO/ZnO and ITO/SnO<sub>2</sub> complex conductive layers were prepared by DC- and RF-magnetron sputtering. Their structure and optical and electronic performances were studied by XRD, UV/Vis Spectroscopy, and four-probe technology. The interface characteristic and band offset of the ITO/ZnO, ITO/SnO<sub>2</sub>, and ITO/CdS were investigated by Ultraviolet Photoelectron Spectroscopy (UPS) and X-ray Photoelectron Spectroscopy (XPS), and the energy band diagrams have also been determined. The results show that ITO/ZnO and ITO/SnO<sub>2</sub> films have good optical and electrical properties. The energy barrier those at the interface of ITO/ZnO and ITO/SnO<sub>2</sub> layers are almost 0.4 and 0.44 eV, which are lower than in ITO/CdS heterojunctions (0.9 eV), which is beneficial for the transfer and collection of electrons in CdTe solar cells and reduces the minority carrier recombination at the interface, compared to CdS/ITO. The effects of their use in CdTe solar cells were studied by AMPS-1D software simulation using experiment values obtained from ZnO, ITO, and SnO<sub>2</sub>. From the simulation, we confirmed the increase of  $E_{ff}$ , FF,  $V_{oc}$ , and  $I_{sc}$  by the introduction of ITO/ZnO and ITO/SnO<sub>2</sub> layers in CdTe solar cells.

## 1. Introduction

Transparent conducting oxide (TCO) layers have been extensively studied because of their use as transparent electrodes in displays and in photovoltaic devices [1]. By incorporating a high resistance layer, the thickness of a conducting cadmium sulfide (CdS) layer can be reduced, which significantly improves the blue response of CdTe devices [2] and makes CdTe thin-film solar cells more competitive [3]. Wu has reported the efficiency of 16.5% with <100 nm CdS thickness [4]. However, as the thickness of CdS is decreased, the films would become discontinuous leading to the formation of localized CdTe/TCO junction, which leads to excessive shunting and therefore lowers the solar cell efficiency [5]. Using complex transparent conductive layers is known as a feasible method to improve the characteristics of CdTe thin films solar cells. Indium-tin oxide (ITO) systems, SnO<sub>2</sub>, and ZnO have been used as the high resistance layer because of their excellent electrical and optical properties [6, 7] and the improvement of device performance [8].

The complex transparent conductive layers are always heterojunction structure, which are rather complicated

systems for their different electron affinities, band gaps. The band offset and interface properties of a heterostructure are some of the most important properties. Sheng et al. have studied the n-layer/transparent conducting oxide (n/TCO) interfaces in amorphous silicon (a-Si:H) and microcrystalline silicon (mc-Si:H) materials by XPS [9]. Liu et al. studied the interface properties and band alignment of Cu<sub>2</sub>S/CdS heterojunction, and the band offsets are obtained [10]. Horn studied electronic structure at the interface, relating to band bending and the evolution of transport barriers such as the Schottky barrier and the heterojunction band offset [11]. Bernède and Marsillac. have measured the band offsets of SnO<sub>2</sub>/γ-In<sub>2</sub>Se<sub>3</sub> heterojunction by XPS and estimated the conduction band discontinuity  $\Delta E_c$  to be  $-0.3 \pm 0.3$  eV [12]. Mönch discussed the electronic properties and chemical interactions at GaAs (110) and InP (110) surfaces [13].

In this present work, ITO, ZnO, and SnO<sub>2</sub> films have been successfully prepared on ITO coated glass substrate by DC- and RF-magnetron sputtering and characterized by XRD, UV/Vis spectra, and four-probe apparatus. UPS and XPS were used to characterize the band offset of ITO/CdS,

TABLE 1: The parameters used in the AMPS-1D simulation.

	ITO	ZnO	SnO <sub>2</sub>	CdS	CdTe
E <sub>g</sub> (eV)	3.72	3.27	4.11	2.42	1.46
EPS	9.4	9	9	9	9.4
Electron mobility (cm <sup>2</sup> /V/s)	30	100	3.6	340	500
Hole mobility (cm <sup>2</sup> /V/s)	5	25	1	50	60
Carrier density (cm <sup>-3</sup> )	4.3 * 10 <sup>20</sup>	10 <sup>19</sup>	2.4 * 10 <sup>18</sup>	10 <sup>17</sup>	2 * 10 <sup>15</sup>
Density of state, CB (cm <sup>-3</sup> )	4 * 10 <sup>19</sup>	1.8 * 10 <sup>19</sup>	1.8 * 10 <sup>19</sup>	1.8 * 10 <sup>19</sup>	7.5 * 10 <sup>17</sup>
Density of state, VB (cm <sup>-3</sup> )	10 <sup>18</sup>	2.4 * 10 <sup>18</sup>	2.4 * 10 <sup>18</sup>	2.4 * 10 <sup>18</sup>	1.8 * 10 <sup>18</sup>
Electron affinity	3.6	4	3.44	4.5	4.28
Thickness (μm)	0.4	0.15	0.15	0.15	6

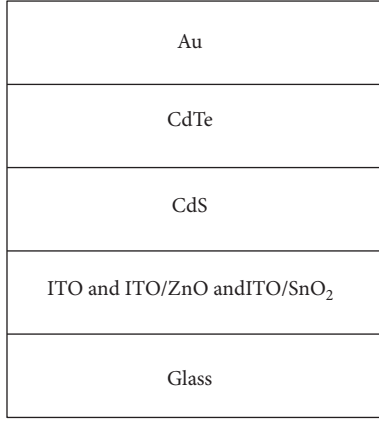


FIGURE 1: Structural view of CdTe solar cells with different configuration.

ITO/ZnO, and ITO/SnO<sub>2</sub> layers and the influence on the transfer of electrons in CdTe thin film solar cells. AMPS-1D simulations, based on the Poisson equation and the hole-electron continuity equations in one dimension [14], were used to study the device performance of the CdTe solar cells with these different transparent conductive layers.

## 2. Experiment

DC magnetron was used to sputter the ITO and ZnO films in this paper. The targets were ceramic ITO (In<sub>2</sub>O<sub>3</sub> : Sn<sub>2</sub>O<sub>3</sub> = 90 : 10) and metallic Zn (99.999%). The substrate was held at 300 °C while the sputtering pressure was 1.0 Pa for ITO and 2.4 Pa for Zn, of high purity argon (99.999%) mixed with 10% oxygen. The SnO<sub>2</sub> films were prepared on an ITO substrate by RF-magnetron sputtering. Sputtering was conducted at 267 °C and 1.0 Pa of argon (99.999%) mixed with 1% oxygen. The ITO layers were about 400 nm and the ZnO (SnO<sub>2</sub>) were about 150 nm. The CdS layers were deposited by chemical bath deposition (CBD) and were about 150 nm thick.

The TCO/CdS structure was analyzed by X-ray diffraction (DX-2500, Dandong Fangyuan Instrument LLC) using Cu Ka radiation ( $\lambda = 0.15405$  nm). The sheet resistance was measured with a Digital Four-Probe Tester (SZT-2, Suzhou Tongchuan Electronics). The thickness of each film was measured with a stylus profiler (XP-2, Ambios Technology

Inc.). The optical transmission was measured by UV/Vis spectrometer (Perkin Elmer Inc., Lambda-950). The XPS and UPS were measured by the multifunctional X-ray Photoelectron Spectroscopy (AXIS Ultra<sup>DLD</sup>, Kratos Analytical Inc.) with the base pressure  $\sim 5.0 \times 10^{-9}$  Torr, the X-ray of Al K $\alpha$ , and the X-ray tube power of 130 W. The samples were etched by 21.2 eV He<sup>+</sup> beam and were biased with 7.36 volts to obtain reproducible cut-off results. The work functions were determined from the low-kinetic energy cut-off in the UPS spectra; that is, the intersection of the linear extrapolation with the baseline. In this experiment, samples were cleaned and thinned by sputtering with He<sup>+</sup> ions in HUV.

AMPS-1D has been employed to model and analyze the CdTe solar cells, and the different cells configuration is shown in Figure 1. The parameters used in the simulation are shown in Table 1. The electron affinity energies and mobility were obtained from [15–17]. The thickness of CdTe film was set as 6 μm.

## 3. Results and Discussion

**3.1. XRD.** Figure 2 shows XRD patterns of ZnO and SnO<sub>2</sub> films deposited on ITO films. The main diffraction peaks (400), (440), and (222) and so on come from the ITO films. Only one weak peak of ZnO was observed in the spectra labeled as (101), and one weak peak of SnO<sub>2</sub> was observed labeled as (200) at 36.10° diffraction angle. This indicates that the ZnO and SnO<sub>2</sub> films have been deposited successfully onto the ITO films.

**3.2. Transmittance.** The optical and electrical properties of ITO, ITO/ZnO, and ITO/SnO<sub>2</sub> films were measured. The thickness was 400 nm for ITO films and 150 nm for ZnO and SnO<sub>2</sub> films. Figure 3 shows the optical transmission of the as-deposited ITO/ZnO and ITO/SnO<sub>2</sub> films. At the wavelength from 500 nm to 850 nm, the average transmittance is 82% for ITO/ZnO and 81.64% for ITO/SnO<sub>2</sub> films, respectively, which are not lower than ITO films (85%) too much. On the other hand, in the blue region, the red shifts of the effective absorption edge of ITO/ZnO and ITO/SnO<sub>2</sub> films are clearly observable. The sheet resistance of the ZnO was obtained as 108 Ω/□ while 104 Ω/□ for the SnO<sub>2</sub> films, which are higher than ITO (13.2 Ω/□). The deposition of ZnO or SnO<sub>2</sub> films as high resistance transparent (HRT) on ITO

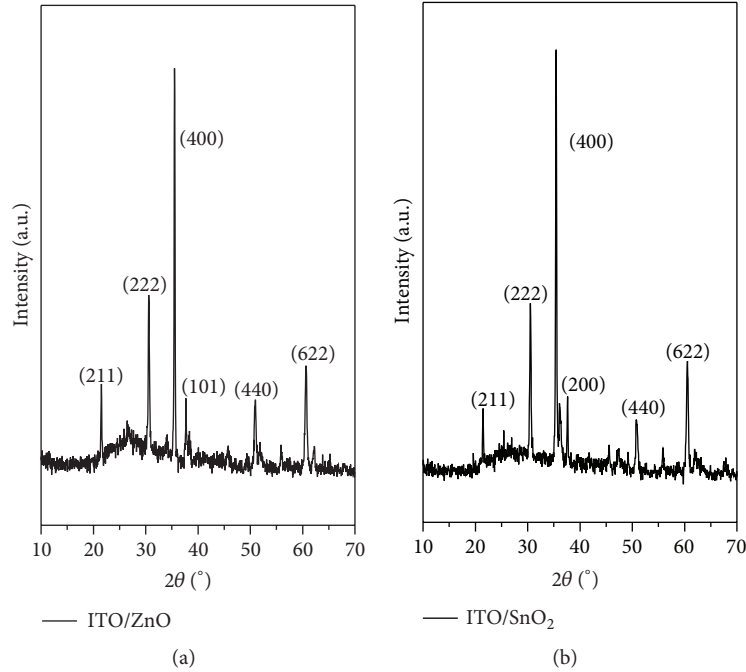


FIGURE 2: XRD spectrum of ITO/ZnO and ITO/SnO<sub>2</sub> films.

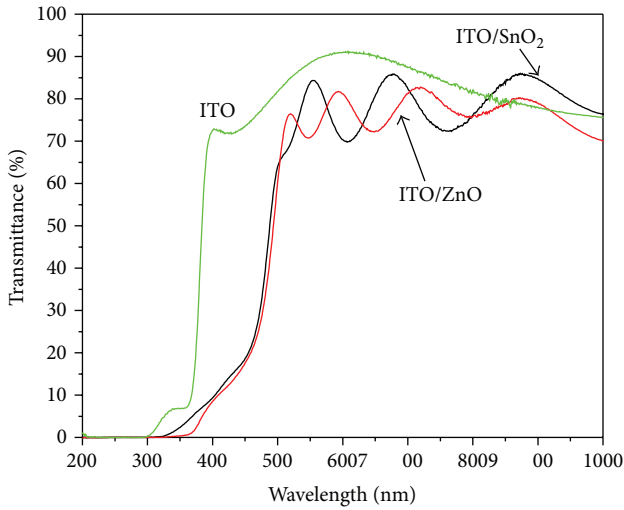


FIGURE 3: Transmittance spectra of the ITO, ITO/ZnO, and ITO/SnO<sub>2</sub> films.

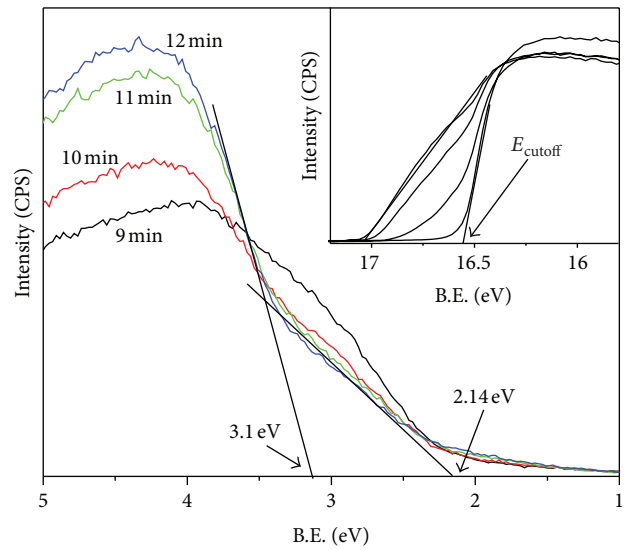


FIGURE 4: UPS profiling spectra of ITO/CdS films.

films can passivate the CdS surface than ITO, which could eliminate the leakage current caused by the pinhole effects of CdS [15] and thus improves the short circuit current remarkably.

3.3. XPS/UPS. Before analysis with XPS/UPS, all of the samples were cleaned by sputtering with He<sup>+</sup> ions for 1 minute in HUV to eliminate surface effects. The layers were profiled using XPS and UPS by taking spectra after every profiling time intervals until it revealed to the ITO film by He<sup>+</sup> sputtering.

3.3.1. ITO/CdS System. Figure 4 shows the UPS of ITO/CdS structure at different times (9–12 min). The “valence band offset” corresponds to be  $(E_F - E_{VBM})$  and provides a direct measure of the Fermi level at the sample surface. The results show that the valence band maximum (VBM) in the interface of ITO/CdS films increases from 2.14 eV to 3.10 eV. The  $E_{cutoff}$  (secondary electron onset) is the abscissa value on the left side when the intensity is 0 in the later UPS, so the work function can be obtained by

$$\Phi = h\nu - (E_{cutoff} - E_{Fermi}). \quad (1)$$

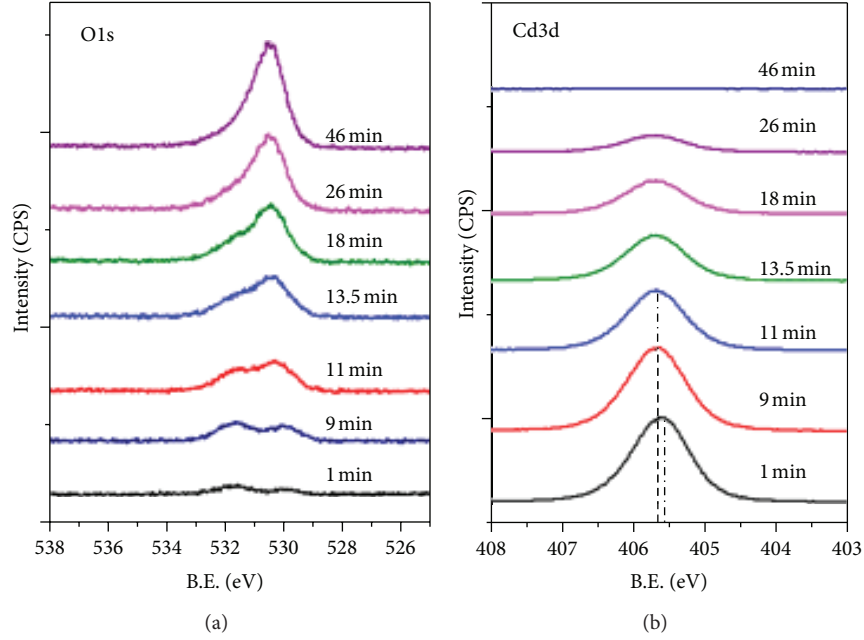


FIGURE 5: XPS spectrum of the O1s and Cd3d regions for n-ITO/n-CdS isotype heterojunction at various profiling times.

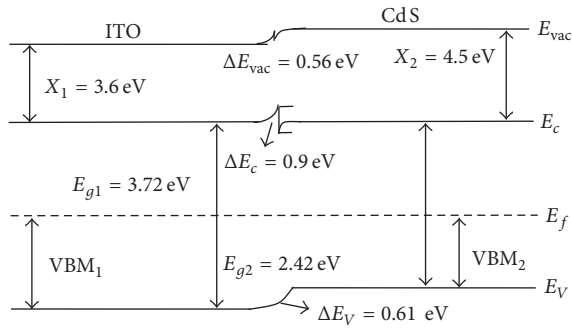


FIGURE 6: Energy band diagram of the ITO/CdS isotype heterojunction.

The  $h\nu$  is the excitation energy of Helium (21.2 eV), and the  $E_{\text{Fermi}}$  is set to be 0, so the  $\Phi$  would be concluded to be 4.7 eV for CdS and 4.2 eV for ITO. And the interface dipole  $\delta$  of ITO and CdS films can be obtained as 0.41 eV and 0.28 eV by

$$\delta = E_g - \text{VBM}. \quad (2)$$

The XPS at various times in Figure 5 shows the band energy variation at the interface of the ITO/CdS films. The profiling of samples starts CdS films and ends at 46 min, when the intensity peak of Cd3d is zero. The O1s emission gradually increases in intensity and the Cd3d decreases during the profiling process. At 1–9 min the intensity of O1s is weak and the B.E. is of no change because the content of oxygen atoms is very lower when the CdS films have been etched for 1 min. At 9–11 min, the intensity of O1s increases while the Cd3d decreases and the B.E. of Cd3d increases about 0.14 eV. That is to say, that the surface profiling occurs

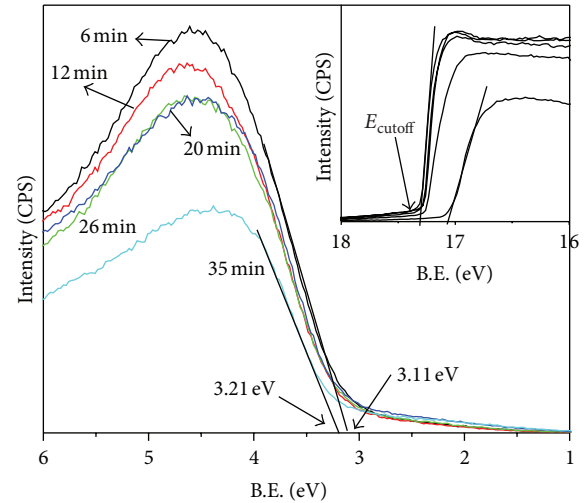


FIGURE 7: The UPS spectra of ITO/ZnO thin films.

at 9–11 min. The thickness of CdS films is 150 nm, so the profiling speed is estimated as 15 nm/min. The intensity of Cd3d decreases gradually and passes off at 46 min. The results show a shift in all the core level lines to larger binding energies, which indicates the formation of a space charge layer (band bending) in the substrate.

In order to construct the band energy diagram, the position of  $E_F$  within the bulk must be known. The difference between the vacuum level  $\Delta E_{\text{vac}}$  can be obtained by subtracting the overall band bending from the difference of the work functions by ( $x$  is electron affinity)

$$\Delta E_{\text{vac}} = (\chi_2 + \delta_2) - (\chi_1 + \delta_1) = 0.56 \text{ eV}. \quad (3)$$

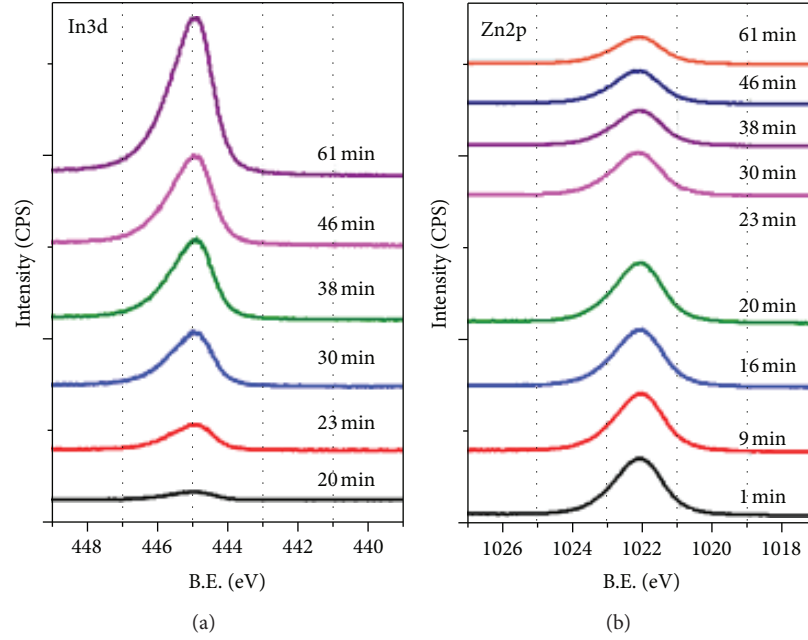


FIGURE 8: XPS spectrum in the In3d and Zn2p regions for n-ITO/n-ZnO isotype heterojunction under various profiling time.

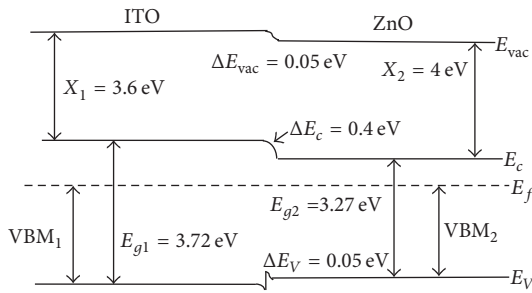


FIGURE 9: Energy band diagram of the ITO/ZnO isotype heterojunction.

Then the valence band offset  $\Delta E_V$  can be determined by using the band energy difference between the O1s and Cd3d at intermediate coverage and the binding energies of the core levels with respect to the valence band. One has

$$\Delta E_V = (\text{VBM}_1 - \text{VBM}_2) - \Delta E_{\text{vac}} = 0.61 \text{ eV}. \quad (4)$$

Using the  $\Delta E_V$  and the band gaps given before, the conduction band offset  $\Delta E_c$  was calculated to be

$$\Delta E_c = \Delta E_{\text{vac}} + (\delta_1 - \delta_2) = 0.9 \text{ eV}. \quad (5)$$

Having determined band bending, band offset, and interface dipole, the final band alignment at the interface ITO/CdS heterojunction is presented in Figure 6. The conduction band bends upward in the ITO layer at the surface while the CdS layer bends downward. The electrons need to overcome a huge energy barrier (about 0.9 eV) when transferring from the CdS to ITO films.

**3.3.2. ITO/ZnO System.** The characterization of the layer at different profiling times is illustrated in Figure 7. The VBM

increases from 3.11 eV to 3.21 eV at the interface of the ITO/ZnO films. And the  $\Phi$  would be calculated to be 3.8 eV for ZnO and 4.1 eV for ITO. And the interface dipole  $\delta$  of ITO and ZnO films can be obtained as 0.51 eV and 0.16 eV.

The XPS at various profiling times in Figure 8 shows the variations in the band energy of the ITO/ZnO films at the interface (20–23 min). The profiling of samples starts ZnO films and ends at 61 min. The In3d (ITO) emission gradually increases in intensity and the Zn2p (ZnO) intensity decreases along the profiling progress. The thickness of ZnO films is 150 nm, so the profiling speed is estimated as 7 nm/min, which is obviously lower than CdS. And  $\Delta E_{\text{vac}} = 0.05 \text{ eV}$  was obtained and the valence band offset  $\Delta E_V$  and conduction band offset  $\Delta E_c$  were calculated to be 0.4 eV and 0.05 eV, respectively.

The final band alignment at the interface ITO/ZnO heterojunction is presented in Figure 9. The conduction band bends downward in the ITO layer while ZnO layer bends upward at the interface. The barrier energy is about 0.4 eV, which is lower than ITO/CdS heterojunction potential barrier. That is to say the introducing ZnO film is beneficial for the transfer and collection of electrons.

**3.3.3. ITO/SnO<sub>2</sub> System.** The interface profiling from 9 to 20 min is presented in Figure 10. At the interface of ITO/SnO<sub>2</sub>, the VBM value decreases from 3.38 eV to 3.28 eV. The  $\Phi$  of SnO<sub>2</sub> films would be calculated to be 4.14 eV and 4.06 eV for ITO films. And the interface dipole  $\delta$  of ITO and SnO<sub>2</sub> films can be obtained as 0.44 eV and 0.73 eV.

The XPS at various profiling times is showed in Figure 11. The profiling of samples starts SnO<sub>2</sub> films and ends at 42 min, when the intensity of Sn3d passes off. It confirms that the In3d (ITO) emission increases in intensity and the Sn3d

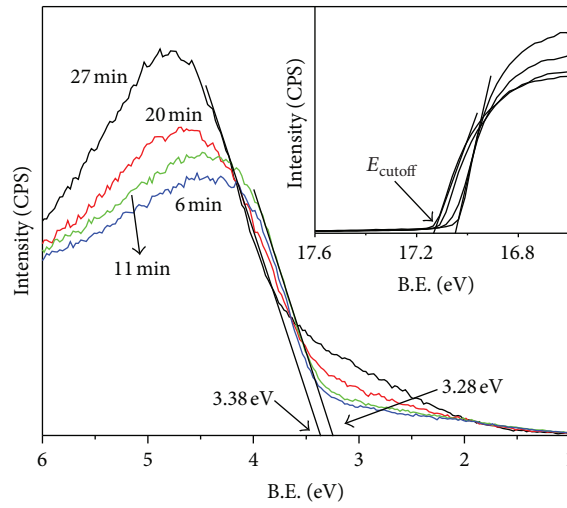


FIGURE 10: The UPS spectra of ITO/SnO<sub>2</sub> complex layers.

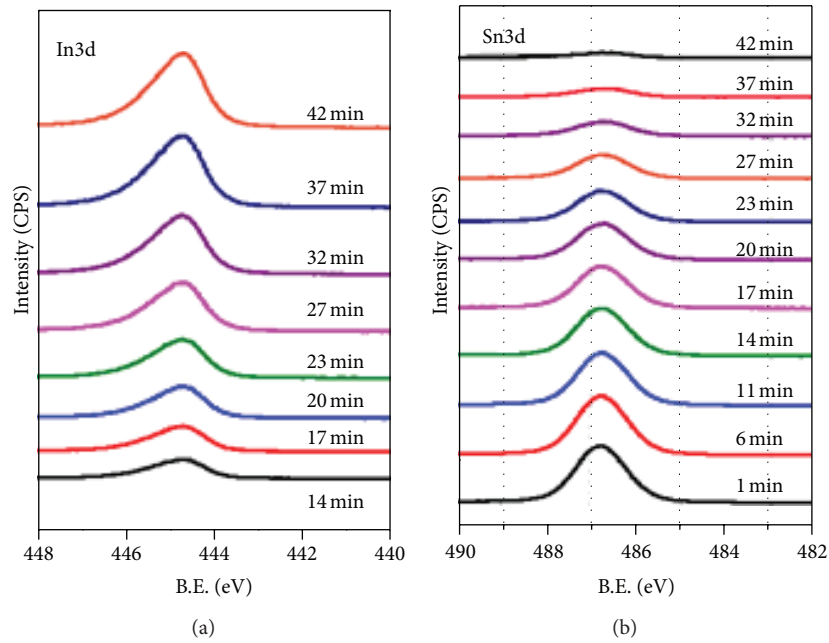


FIGURE 11: XPS spectrum in the In3d and Sn3d regions of an n-ITO/n-SnO<sub>2</sub> isotype heterojunction at various profiling times.

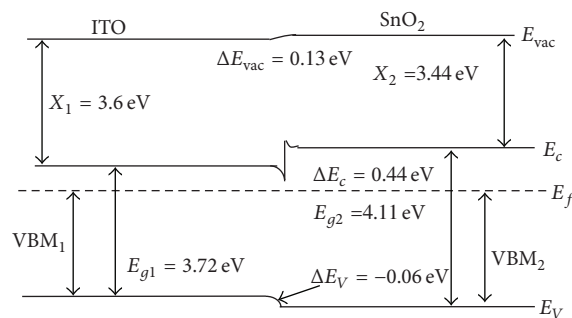


FIGURE 12: Energy band diagram of the ITO/SnO<sub>2</sub> isotype heterojunction.

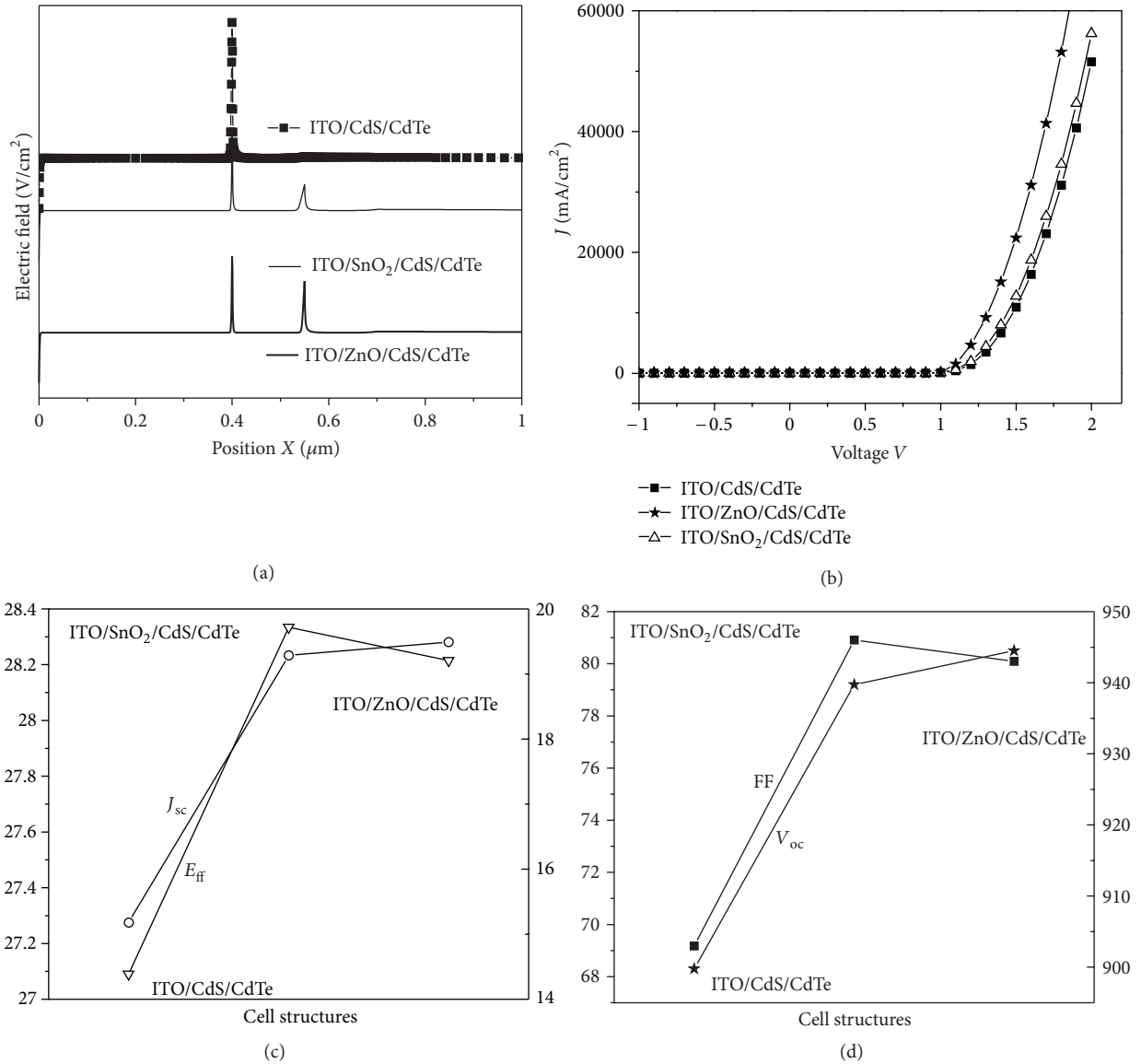


FIGURE 13: The simulated output performance for different structure: the electric field distribution (a), the dark  $I-V$  curve (b),  $J_{sc}$  and  $E_{ff}$ , (c) and FF &  $V_{oc}$  (d).

(SnO<sub>2</sub>) decreases during the profiling process. At 20–23 min, the profiling came to the interface, and the profiling speed is estimated as 7 nm/min and the thickness of SnO<sub>2</sub> film is 150 nm. The adding of SnO<sub>2</sub> films between ITO and CdS films also changes the energy structure. The  $\Delta E_{vac} = 0.13$  eV,  $\Delta E_C = 0.44$  eV, and  $\Delta E_V = -0.06$  eV were also obtained.

The energy band diagram is presented in Figure 12. The conduction band bends downward in the ITO layer at the surface while SnO<sub>2</sub> layer bends upward. The results shows that electrons must overcome an energy barrier (0.44 eV) when transferring from the SnO<sub>2</sub> to ITO films, which is also less than that in the ITO/CdS heterojunction. Thus adding SnO<sub>2</sub> layer is also beneficial for the transfer and collection of electrons.

**3.4. Device Simulation.** Based on the previous analysis, we have simulated the effect of ITO/ZnO and ITO/SnO<sub>2</sub> films in CdTe cells by AMPS-1D. Figure 13 shows the electric fields, dark  $I-V$  curves, and simulated output performance of different cells. The results show that inserting of ZnO or SnO<sub>2</sub> films changes the electric field distribution, with the electric field strength decreasing at the ITO/CdS interface and a new electric field appearing at the ZnO (or SnO<sub>2</sub>)/CdS interface. These electric field distributions are beneficial for the transfer and collection of electrons in CdTe cells. The introduction of ITO/ZnO or ITO/SnO<sub>2</sub> films in CdTe solar cells improves the efficiency ( $E_{ff}$ ), open voltage ( $V_{oc}$ ), and short circuit current ( $I_{sc}$ ) significantly.

Also, we fabricated CdTe solar cells with or without HRT films. The cells with ZnO films have the efficiency of 12.17%

( $V_{oc} = 742$  mV,  $J_{sc} = 26$  mA/cm<sup>2</sup>, FF = 62.6%, and area = 0.5 cm<sup>2</sup>) and the sample with SnO<sub>2</sub> films has the efficiency of 11.4% ( $V_{oc} = 724$  mV,  $J_{sc} = 25.8$  mA/cm<sup>2</sup>, FF = 61.2%, and area = 0.5 cm<sup>2</sup>), while the sample without HRT layers has a much lower efficiency of 8.7% ( $V_{oc} = 689$  mV,  $J_{sc} = 23.55$  mA/cm<sup>2</sup>, FF = 53.6%, and area = 0.5 cm<sup>2</sup>). The results also show that the introduction of HRT layers decreases the series resistance, which was partly attributed to good interface properties between HRT and CdS layers.

#### 4. Conclusion

The ITO/ZnO and ITO/SnO<sub>2</sub> films were successfully deposited on a glass substrate by DC- and RF-magnetron sputtering. The optical transmittance of the ITO/ZnO and ITO/SnO<sub>2</sub> as complex TCO layers was 82% and 81.64% from 500 nm–850 nm, respectively. The measured sheet resistances of ITO/ZnO and ITO/SnO<sub>2</sub> layers were 10<sup>5</sup> Ω/□ and 37.5 Ω/□, respectively. The interface compositions of the TCO layers were characterized by UPS and XPS, and the energy band diagrams were determined. The energy barriers at the interface of ITO/ZnO and ITO/SnO<sub>2</sub> layers are almost 0.4 and 0.44 eV, which are lower than those at ITO/CdS heterojunctions (0.9 eV). The ITO/ZnO and ITO/SnO<sub>2</sub> as complex transparent conductive benefit the transfer and collection of electrons in CdTe solar cells and reduce the minority carriers recombination at the interface, compared to CdS/ITO.

Furthermore, we have also simulated and analyzed the effects of the ITO/ZnO and ITO/SnO<sub>2</sub> films on CdTe cells by AMPS-1D. The results show that the electric field distribution changes a lot by the introduction of ZnO and SnO<sub>2</sub> films between ITO and CdS. The  $E_{ff}$ , FF,  $V_{oc}$ , and  $I_{sc}$  are improved significantly, that is to say, the ITO/ZnO and ITO/SnO<sub>2</sub> complex transparent conductive layers are beneficial for the performance of CdTe solar cells.

#### Acknowledgments

This research was supported by the National Basic Research Program (973 Program) of China under Grant no. 2011 CBA00708.

#### References

- [1] J. Herrero, M. T. Gutiérrez, C. Guillén et al., "Photovoltaic windows by chemical bath deposition," *Thin Solid Films*, vol. 361-362, pp. 28–33, 2000.
- [2] K. L. Chopra, P. D. Paulson, and V. Dutta, "Thin-film solar cells: an overview," *Progress in Photovoltaics*, vol. 12, no. 2-3, pp. 69–92, 2004.
- [3] Z. Fang, X. C. Wang, H. C. Wu, and C. Z. Zhao, "Achievements and challenges of CdS/CdTe solar cells," *International Journal of Photoenergy*, vol. 2011, Article ID 297350, 8 pages, 2011.
- [4] X. Wu, "High-efficiency polycrystalline CdTe thin-film solar cells," *Solar Energy*, vol. 77, no. 6, pp. 803–814, 2004.
- [5] C. S. Ferekides, D. Marinsky, V. Viswanathan et al., "High efficiency CSS CdTe solar cells," *Thin Solid Films*, vol. 361, pp. 520–526, 2000.
- [6] T. Minami, "Present status of transparent conducting oxide thin-film development for Indium-Tin-Oxide (ITO) substitutes," *Thin Solid Films*, vol. 516, no. 17, pp. 5822–5828, 2008.
- [7] X. Wu, J. Keane, R. Dhere et al., "16.5%-efficient CdS/CdTe Polycrystalline thin film solar cell," in *Proceedings of the 17th European Photovoltaic Solar Energy Conference*, pp. 995–1000, Germany, 2001.
- [8] C. S. Ferekides, R. Mamazza, U. Balasubramanian, and D. L. Morel, "Transparent conductors and buffer layers for CdTe solar cells," *Thin Solid Films*, vol. 480-481, pp. 224–229, 2005.
- [9] S. Sheng, H. Hao, H. Diao et al., "XPS depth profiling study of n/TCO interfaces for p-i-n amorphous silicon solar cells," *Applied Surface Science*, vol. 253, no. 3, pp. 1677–1682, 2006.
- [10] G. Liu, T. Schulmeyer, J. Brötz, A. Klein, and W. Jaegermann, "Interface properties and band alignment of Cu<sub>2</sub>S/CdS thin film solar cells," *Thin Solid Films*, vol. 431-432, pp. 477–482, 2003.
- [11] K. Horn, "Photoemission studies of barrier heights in metal-semiconductor interfaces and heterojunctions," *Applied Surface Science*, vol. 166, no. 1, pp. 1–11, 2000.
- [12] J. C. Bernède and S. Marsillac, "Band alignment at the interface of a SnO<sub>2</sub>/γ-In<sub>2</sub>Se<sub>3</sub> heterojunction," *Materials Research Bulletin*, vol. 32, no. 9, pp. 1193–1200, 1997.
- [13] W. Mönch, "Electronic properties and chemical interactions at III-V compound semiconductor surfaces: germanium and oxygen on GaAs(110) and InP(110) cleaved surfaces," *Applied Surface Science*, vol. 22-23, no. 2, pp. 705–723, 1985.
- [14] A. Bouloufa, K. Djessas, and A. Zegadi, "Numerical simulation of CuIn<sub>x</sub>Ga<sub>1-x</sub>Se<sub>2</sub> solar cells by AMPS-1D," *Thin Solid Films*, vol. 515, no. 15, pp. 6285–6287, 2007.
- [15] M. A. Matin, M. Mannir Aliyu, A. H. Quadery, and N. Amin, "Prospects of novel front and back contacts for high efficiency cadmium telluride thin film solar cells from numerical analysis," *Solar Energy Materials and Solar Cells*, vol. 94, no. 9, pp. 1496–1500, 2010.
- [16] M. A. Contreras, M. J. Romero, B. To et al., "Optimization of CBD CdS process in high-efficiency Cu(In,Ga)Se<sub>2</sub>-based solar cells," *Thin Solid Films*, vol. 403-404, pp. 204–211, 2002.
- [17] S. J. Fonash, *Solar Cell Device Physics*, Academic Press, New York, NY, USA, 1981.

## Research Article

# Forecasting the Development of Different Solar Cell Technologies

**Arturo Morales-Acevedo and Gaspar Casados-Cruz**

*Electrical Engineering Department, CINVESTAV-IPN, Avenida IPN No. 2508, 07360 Mexico City, DF, Mexico*

Correspondence should be addressed to Arturo Morales-Acevedo; [amorales@solar.cinvestav.mx](mailto:amorales@solar.cinvestav.mx)

Received 3 October 2012; Accepted 25 November 2012

Academic Editor: Bhushan Sopori

Copyright © 2013 A. Morales-Acevedo and G. Casados-Cruz. This is an open access article distributed under the Creative Commons Attribution License, which permits unrestricted use, distribution, and reproduction in any medium, provided the original work is properly cited.

Solar cells are made of several materials and device structures with the main goal of having maximum efficiency at low cost. Some types of solar cells have shown a rapid efficiency progress whereas others seem to remain constant as a consequence of different factors such as the technological and economic ones. Using information published by the National Renewable Energy Laboratory (NREL) about the increase of solar cells record efficiency, we apply a simple mathematical model to estimate the evolution in the near future for the different cell technologies. Here, as an example, we use data for solar cells made with representative materials and structures of each of the three “PV generations.”

## 1. Introduction

The photovoltaic effect was discovered by Becquerel in 1839, but it was until the 1950s that a semiconductor device for converting sunlight energy into electrical energy was developed. Since then, such devices have evolved, and nowadays solar cells are made of different materials and structures. Although most of the semiconductor materials exhibit the photovoltaic effect, they should have a bandgap greater than 1.0 eV to be suitable for practical solar cells. The most important parameter of any solar cell is its efficiency, that is, how much of the sunlight energy is converted into electrical energy. Shockley and Queisser established that a single-junction solar cell can reach a maximum efficiency of 30% [1]. Every year NREL publishes the Best Research-Cell efficiencies data (Figure 1). It contains information about the time evolution of solar cells made of several materials and structures. In this plot we can observe that some types of solar cells have a progressive development (CuInGaSe<sub>2</sub>), while for others it seems that their evolution has stopped (dye-sensitized TiO<sub>2</sub>).

It is important to have a tool for efficiency forecasting since it can help for taking decisions on investment for each developed technology. We think that it is possible to have a single model for predicting the efficiency evolution for all the different solar cells.

For our purposes in this work, we have chosen representative materials of the known three “PV generations.”

The first generation corresponds to crystalline silicon (c-Si) solar cells. The second generation refers to cells made from thin films of polycrystalline materials: Cadmium Telluride (CdTe) and Copper-Indium-Gallium-Selenide (CuInGaSe<sub>2</sub> or CIGS). For the third generation we have chosen the multijunction or tandem solar cells to be operated under concentrated sunlight. This is a very promising technology since the reported maximum efficiency is currently above 43%, although they are very sophisticated. In the following sections, first we shall give a brief description of these types of solar cells, and then we will establish the forecasting model and the results obtained for each of the selected technologies.

*1.1. c-Si.* Silicon is one of the more abundant elements in the Earth's crust. The first successful solar cells were made of c-Si, and at first they had efficiencies between 6% and 10%, and they were used for powering spatial equipments in satellites. The basic structure of this solar cell type is shown in Figure 2. It consists of a single p-n junction. The p-type silicon base is around 300  $\mu\text{m}$  thick whereas the n-type emitter is around 100 nm thick. An antireflection coating layer is deposited over the emitter in order to minimize reflection losses. Metal contacts are placed at the bottom of the cell as a whole layer and at the top as fingers. Approaches for increasing the efficiency include making inverted pyramids at the surface [2], buried contacts, and selective emitters, and so forth. At

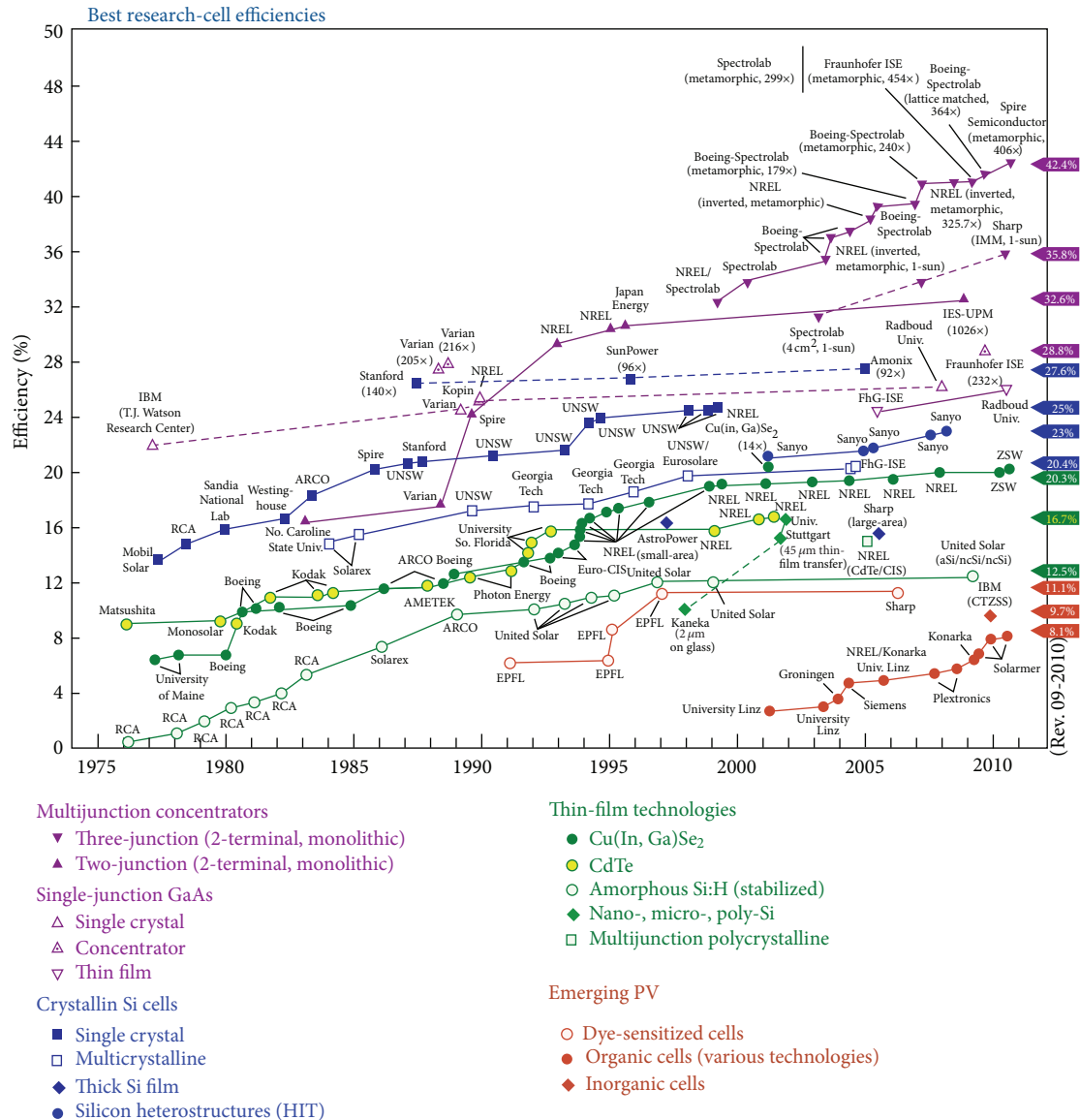


FIGURE 1: NREL's data about record of solar cells efficiencies.

present, c-Si solar cells have reached record efficiencies near 25%, for which the top and bottom surfaces have been well passivated [3].

**1.2. CdTe.** Cadmium Telluride was synthesized for the first time in 1947; both conductivities p and n can be obtained using dopants or by varying the Cd-Te stoichiometry. There are many methods to deposit CdTe for solar cells, and some of them, like spray pyrolysis and screen printing, are very inexpensive. This is the main reason this material became important for the photovoltaic industry. The first CdTe solar cell having a 6% efficiency was reported in 1963 [4]. The typical structure of a CdTe solar cell is depicted in Figure 3. The efficiency for this solar cell remained unchanged since 2001 (16.5%) [5], until 2011 when a solar cell manufacturer obtained 17.3% solar cells [6]. Morales-Acevedo has

explained before that the maximum efficiency expected with the current technology for CdTe solar cells is around 18%, unless new structures are developed based on this material [7].

**1.3. CuInGaSe<sub>2</sub>.** Solar cells of this material first were made from CuInSe<sub>2</sub> (CIS) because it exhibits interesting properties for solar cells. The first thin film solar cell made of CIS was reported in 1976, and it had an efficiency of 4% to 5% [8]. Due to its low bandgap (1.08 eV), indium was replaced by an alloy of indium and gallium which allows varying the material bandgap from 1.08 to 1.68 eV depending upon the [Ga]/[In + Ga] ratio. CIGS thin films can be prepared by coevaporation or by selenization of CuInGa layers previously deposited by sputtering. The typical structure of this type of solar cells is shown in Figure 4. The substrate can be rigid glass, or flexible

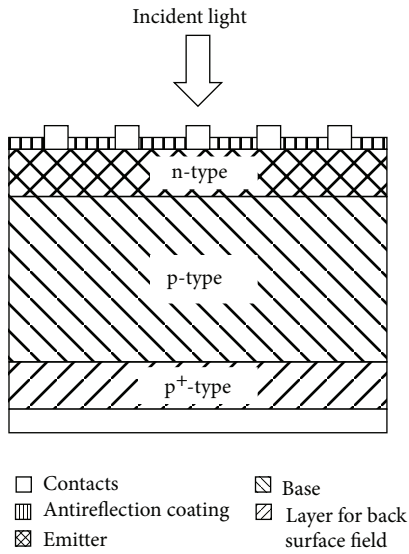


FIGURE 2: Typical silicon solar cell structure.

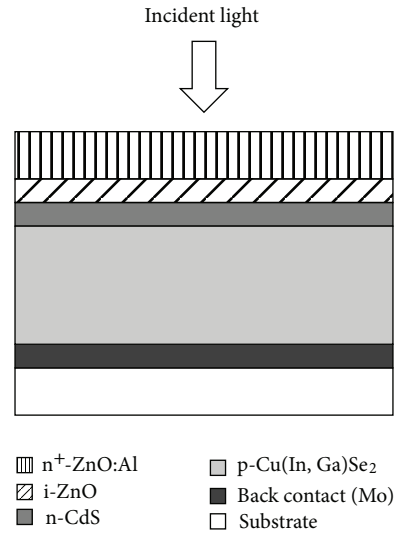


FIGURE 4: CIGS solar cell structure.

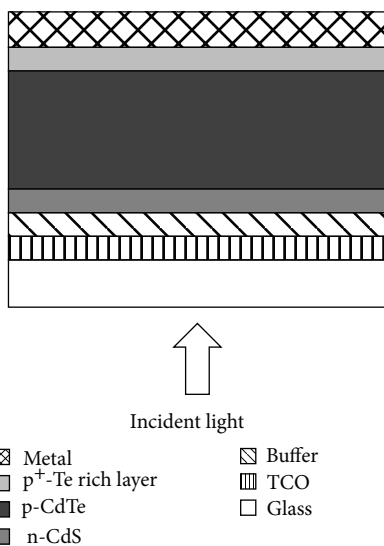


FIGURE 3: Cadmium Telluride solar cell structure.

like metal foils or plastics. The achieved efficiency depends on the deposition conditions, and improvements have been made changing some of the procedures in the film growth process. This cell has reached a record efficiency of 20.3% [9].

**1.4. Multijunction Solar Cells.** The solar cells previously described are single junction, and their maximum efficiency is limited, theoretically, by the material with which they are made, remembering that the bandgap of the absorber layer limits which part of the solar spectrum is absorbed by the device. To overcome this limitation multijunction solar cells have been proposed. Basically it consist of a stack of two or more single junction solar cells with different materials, with the larger bandgap material at the top of the structure and the lower bandgap material at the bottom. These cells are used in space applications, but they represent a promising

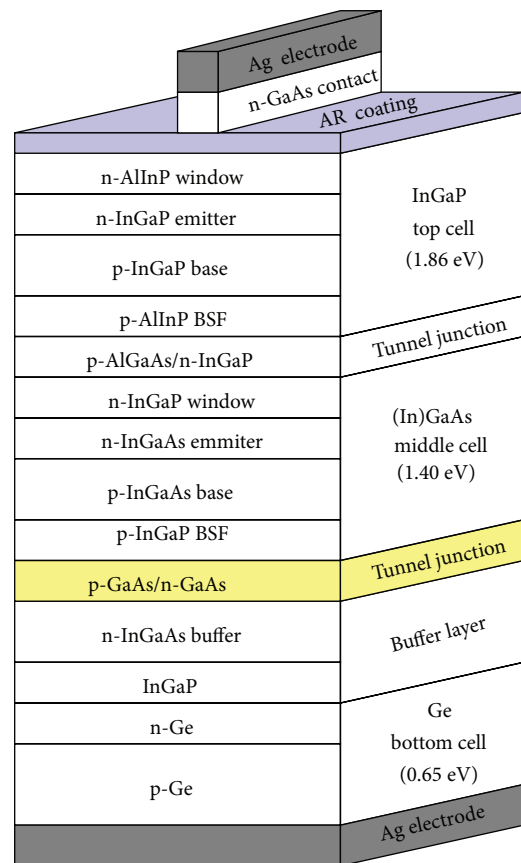


FIGURE 5: Typical multijunction solar cell.

technology for terrestrial applications when combined with solar radiation concentration. The first multijunction solar cell that could overcome the limit for a single junction was reported in 1985 with a value of 34% [10]. A sketch of a triple junction monolithic solar cell is shown in Figure 5. This particular structure has reached an efficiency of 34.1% at one

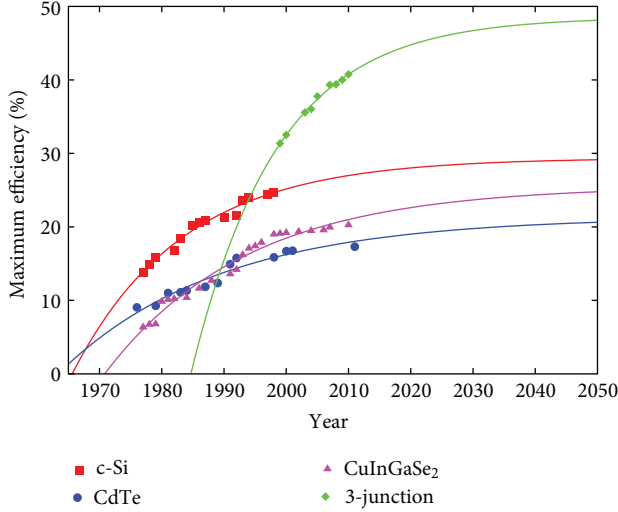


FIGURE 6: NREL's data fitted to proposed forecasting model.

sun and 41.6% at 364 suns [11], whereas the record efficiency (43.5% at 418 suns) is held by a slightly different structure [12].

## 2. The Forecasting Model

In Figure 1 the NREL plot of the record efficiencies for different solar cells along time is shown. Notice that some types of solar cells change its record efficiency in a relatively short time (e.g., the three-junction solar cell technology). Others, like c-Si and CIGS, currently exhibit a slower record efficiency growth. CIGS solar cells are still under development, but c-Si solar cells seem to have stopped its progress since the year 2000. The slowest development rate for the chosen technologies described previously corresponds to CdTe solar cells which recently (2011) improved their record efficiency from 16.5% [5] to 17.3% [6], after 10 years without variation. This behavior suggests a “bound efficiency growth” limited by the open-circuit voltage [7]. First, the increase of short-circuit current density would cause a rapid (linear) efficiency growth, and then further improvement due to the (logarithmic) open-circuit voltage increase would determine the record efficiency. Therefore, we shall use the following function proposed by Goetzberger et al. [13]:

$$\eta = \eta_{\max} \left( 1 - \exp\left(\frac{y - y_0}{\tau}\right) \right), \quad (1)$$

where  $\eta$  is the cell efficiency (%) at a given year  $y$ ;  $y_0$  is the year for which significant development began,  $\eta_{\max}$  is the maximum efficiency a given solar cell technology would achieve, and  $\tau$  is a characteristic time parameter (years) related to the rate of development.

## 3. Results and Discussion

We extracted the data for the selected solar cell types from Figure 1. The reported maximum efficiency every year was taken into account. A least-squares fitting to the proposed

TABLE 1: Model parameters fitting.

Cell type	Parameter		
	$\eta_{\max}$ (%)	$y_0$ (year)	$\tau$ (years)
c-Si	$29.4 \pm 2.8$	$1965 \pm 2.2$	$17.7 \pm 5.4$
CdTe	$21.4 \pm 3.4$	$1963 \pm 4.1$	$25.6 \pm 11.7$
CIGS	$25.6 \pm 2.4$	$1970 \pm 1.2$	$22.8 \pm 5.2$
Triple junction	$48.5 \pm 3.9$	$1984 \pm 2.6$	$13.8 \pm 4.5$

model was performed using this data. A plot of the fitted function along with the data for the chosen technologies is shown in Figure 6, and the corresponding fitted parameters are summarized in Table 1. These parameters were not restricted for the fitting process, and therefore the results we obtained are related to the information contained implicitly in the data selected for each technology. This is the main reason for having  $y_0$  different than the real starting year for each technology. For example, it is well known that silicon solar cells began their development around 1954, but the  $y_0$  year given in Table 1 for these cells is 1965. This is not wrong since the value obtained for  $y_0$  here can be understood as the year for which development began to be really significant and for which the basic technology for the high efficiencies presently achieved was established. In this regard, the invention of the back surface field, as depicted in Figure 2, was very important and the real silicon solar cell development began after this improvement around 1965.

Other interesting observations can be obtained from the results shown in Table 1. First of all, we can notice that triple-junction solar cells are having a rapid development as compared to the other three technologies. This difference in the evolution velocity is a consequence of both the physical and technological limitations for each kind of solar cell, in addition to the total investment for their research and development. We can notice that solar cells made on polycrystalline materials will reach their maximum (limiting) efficiencies more slowly than those made with crystalline materials since the characteristic time ( $\tau$ ) is shorter in the latter case.

Notice also that the maximum efficiency predicted for polycrystalline solar cells is far from the 30% theoretically predicted by Shockley and Queisser [1]. Furthermore, Silicon, CdTe, and CIGS solar cell efficiencies are already very close to their own predicted limit ( $\eta_{\max}$ ), and then their future evolution will be very slow. Meanwhile, triple-junction solar cells can still be improved towards the 50% limit. However, in order to have these (space) kind of solar cells ready for terrestrial applications a great effort is needed in order to develop low-cost solar concentration systems.

Of the technologies considered here, Cds/CdTe solar cells are those for which the minimum efficiency is expected, while the triple junction technology promises the highest efficiency, close to 50%. Then, in the short term, CdTe will keep some market share, but in the long term it might be replaced, first by CIGS solar cells and then by the third generation triple-junction solar cells under concentrated sunlight, when these new technologies become mature enough at production

level. Silicon solar cells, in the midterm, will maintain an important share of the PV market since their efficiency/cost ratio is still competitive and since this technology continues to be improved due to high production volume and the new developments that are reducing the silicon solar cell cost at industry, despite their efficiency record saturation.

#### 4. Conclusion

In this work we have shown that it is possible to use a simple model for solar cell development forecasting. This model allows both the prediction of the maximum expected efficiency and the rate of development. Among the many technologies under development today we have chosen three with great potential for replacing silicon solar cells which is currently the dominant technology in the commercial market. CdTe is the technology for which the minimum efficiency is expected, while the triple-junction technology promises the highest efficiency, close to 50%. Then, in the short term, CdTe will keep some market share, but in the long term it might be replaced, first by CIGS solar cells and then by the third-generation triple-junction solar cells under concentrated sunlight, when these new technologies become mature enough at production level.

#### Acknowledgment

This work was supported by CONACyT Project no. 83042 and ICyTDF Project no. 117/2012.

#### References

- [1] W. Shockley and H. J. Queisser, "Detailed balance limit of efficiency of  $p$ - $n$  junction solar cells," *Journal of Applied Physics*, vol. 32, no. 3, pp. 510–519, 1961.
- [2] J. Zhao, A. Wang, P. Altermatt, and M. A. Green, "Twenty-four percent efficient silicon solar cells with double layer antireflection coatings and reduced resistance loss," *Applied Physics Letters*, vol. 66, pp. 3636–3638, 1995.
- [3] T. M. Razykov, C. S. Ferekides, D. Morel, E. Stefanakos, H. S. Ullal, and H. M. Upadhyaya, "Solar photovoltaic electricity: current status and future prospects," *Solar Energy*, vol. 85, no. 8, pp. 1580–1608, 2011.
- [4] D. A. Cusano, "CdTe solar cells and photovoltaic heterojunctions in ii-vi compounds," *Solid-State Electronics*, vol. 6, no. 3, pp. 217–232, 1963.
- [5] X. Wu, J. C. Keane, C. DeHart et al., "16.5% efficient CdS/CdTe polycrystalline thin film solar cell," in *Proceedings of the 17th European Photovoltaic Solar Energy Conference*, pp. 995–999, Munich, Germany, 2001.
- [6] First Solar News Releases, 2011, <http://www.firstsolar.com/>.
- [7] A. Morales-Acevedo, "Thin film CdS/CdTe solar cells: research perspectives," *Solar Energy*, vol. 80, no. 6, pp. 675–681, 2006.
- [8] L. L. Kazmerski, F. R. White, and G. K. Morgan, "Thin-film CuInSe<sub>2</sub>/CdS heterojunction solar cells," *Applied Physics Letters*, vol. 29, no. 4, pp. 268–270, 1976.
- [9] P. Jackson, D. Hariskos, E. Lotter et al., "New world record efficiency for Cu(In, Ga)Se<sub>2</sub> thin-film solar cells beyond 20%," *Progress in Photovoltaics*, vol. 19, pp. 894–897, 2011.
- [10] J. M. Olson, T. Gessert, and M. M. Al-Jassim, "GaInP<sub>2</sub>/GaAs: a current-and lattice-matched tandem cell with a high theoretical efficiency," in *Proceedings of the 18th Photovoltaic Specialist Conference*, pp. 552–555, Las Vegas, Nev, USA, 1985.
- [11] R. R. King, A. Boca, W. Hong et al., "Band-gap-engineered architectures for high-efficiency multijunction concentrator solar cells," in *Proceedings of the 24th European Photovoltaic Solar Energy Conference and Exhibition*, Hamburg, Germany, 2009.
- [12] Solar Junction Latest News, 2011, <http://www.sj-solar.com/>.
- [13] A. Goetzberger, J. Luther, and G. Willeke, "Solar cells: past, present, future," *Solar Energy Materials and Solar Cells*, vol. 74, no. 1–4, pp. 1–11, 2002.

## Research Article

# Alumina and Hafnia ALD Layers for a Niobium-Doped Titanium Oxide Photoanode

Naji Al Dahoudi,<sup>1,2</sup> Qifeng Zhang,<sup>1</sup> and Guozhong Cao<sup>1</sup>

<sup>1</sup>Department of Materials Science and Engineering, University of Washington, Seattle, WA 98195, USA

<sup>2</sup>Physics Department, Al-Azhar University-Gaza, P.O. Box 1277, Gaza, Palestine

Correspondence should be addressed to Naji Al Dahoudi, naji@alazhar.edu.ps

Received 13 November 2012; Accepted 18 December 2012

Academic Editor: Sudhakar Shet

Copyright © 2012 Naji Al Dahoudi et al. This is an open access article distributed under the Creative Commons Attribution License, which permits unrestricted use, distribution, and reproduction in any medium, provided the original work is properly cited.

Niobium-doped titanium dioxide (TiO<sub>2</sub>) nanoparticles were used as a photoanode in dye-sensitized solar cells (DSCs). They showed a high photocurrent density due to their higher conductivity; however, a low open-circuit voltage was exhibited due to the back-reaction of photogenerated electrons. Atomic layer deposition is a useful technique to form a conformal ultrathin layer of Al<sub>2</sub>O<sub>3</sub> and HfO, which act as an energy barrier to suppress the back electrons from reaching the redox medium. This resulted in an increase of the open-circuit voltage and therefore led to higher performance. HfO showed an improvement of the light-to-current conversion efficiency by 74%, higher than the 21% enhancement obtained by utilizing Al<sub>2</sub>O<sub>3</sub> layers.

## 1. Introduction

The world is in urgent quest of seeking alternative renewable energy resources. Because of their low-cost materials and their simple elaboration of manufacturing, dye-sensitized solar cells [1–5] are considered as a promising candidate to replace the commercial silicon solar cells [6–8]. Titanium oxide is one of the extremely favorable materials [9] for the working electrode (photoanode) of DSCs. The control of their morphological properties, structure, and the kinetic transport of the charge carriers have a significant impact of their performance in the DSSCs. Using metal ions as dopants has a significant effect on the electrical properties of TiO<sub>2</sub>. This doping leads to significant changes of electrical conductivity, shifting of Fermi level potential, particle aggregation, charge transfer kinetics, and dye absorption characteristics of TiO<sub>2</sub> [10]. Ko et al. [11] have found remarkable enhancement by doping the TiO<sub>2</sub> with aluminum and tungsten.

However, many reports have suggested that the performance of DSCs at the optimized level of metal ions doping into TiO<sub>2</sub> relates mainly the tuning of the flat band of TiO<sub>2</sub>. Lü et al. [12] synthesized a well-crystalline niobium (Nb) doped anatase TiO<sub>2</sub> (Nb : TiO<sub>2</sub>) and investigated its effect on the performance of DSSCs. It was revealed that Nb doping

had positive effect on the short-circuit current with positive shift of the flat band potential. Doping of titanium oxide by metal ions may elevate the electron hole pair production, however, may create more trapping sites that affect the performance of dye-sensitized solar cells. Charge recombination occurs at the interface between the working electrode and the dye/electrolyte interfaces, where photogenerated electrons in the porous electrode tend to recombine with either the oxidized dye or the oxidized species in electrolyte, thereby reducing the open-circuit voltage. One effective approach for impeding charge recombination is to apply the porous electrode/dye interface with a thin insulating metal oxide layer, which impedes charge recombination by forming an energy barrier for charge transport at the interface. Since the insulating layer impedes both charge recombination and electron injection, the thickness of the insulating layer should be optimized that does not affect the electron injection through the photoanode. So, atomic layer deposition (ALD) is an effective technique to deposit ultrathin layer with controllable thickness, where no other deposition technique can achieve the conformality as that done by the ALD on high-aspect structures [13].

In this work niobium doped titanium oxide nanoparticles were employed to fabricate a photoanode film of DSCs.

To increase the open circuit voltage of the cell, atomic deposited layers of  $\text{Al}_2\text{O}_3$  and  $\text{HfO}$  were utilized to form conformal insulating layers to suppress the charge recombination. The thickness of the coating layers was optimized to achieve the best performance.

## 2. Experimental Work

Nanoparticles of undoped  $\text{TiO}_2$  for preparing the photoanode film were obtained through hydrothermal treatment of  $\text{TiO}_2$  sol, as previously reported. The Nb-doped  $\text{TiO}_2$  was obtained by a cohydrolysis of Ti and Nb precursors (e.g., titanium isopropoxide and niobium ethoxide, resp.) in an atomic ratio of 95:5. The precursor solution underwent a hydrothermal growth at  $200^\circ\text{C}$  for 5 h. The resultant precipitate was washed with water and ethanol for several times, dried at  $90^\circ\text{C}$ , and ground to fine powder for use.

Typically, 0.1 g of Nb:TiO<sub>2</sub> nanopowder is wetted and grinded by using 0.3 g of 15 wt.% aqueous polyethylene glycol (PEG20T) in a mortar for 5 minutes until a homogeneous viscous paste was formed. The Nb:TiO<sub>2</sub> paste was deposited onto FTO glass substrates using the doctor blading technique to form a  $(14\text{--}16) \pm 2 \mu\text{m}$  thick film. The obtained films were dried for 30 min at  $100^\circ\text{C}$  and then heated in air up to  $450^\circ\text{C}$  for 60 min.

## 3. ALD of Alumina and Hafnia

The Nb:TiO<sub>2</sub> films were then treated by atomic layer deposition (Oxford OpAL System) of  $\text{Al}_2\text{O}_3$  and  $\text{HfO}$  for 0, 5, 10, 15, and 20 cycles, respectively. The deposition temperature was kept at  $25^\circ\text{C}$  for the precursor and an argon gas was used as a carrier gas to deliver the precursor effectively. The substrate temperature was kept at  $180^\circ\text{C}$  during the ALD process. The deposition rate was 0.8 and  $0.5 \text{ \AA}$  per cycle for  $\text{Al}_2\text{O}_3$  and  $\text{HfO}$ , respectively. After the ALD process, the coated film was reannealed at  $450^\circ\text{C}$ .

## 4. Cell Assembly and Characterization

All the films were sensitized by immersing in a 0.5 mM ruthenium-based N719 dye solution for 24 h, then rinsed with ethanol and dried in air at RT. A Pt-coated silicon substrate was used as the counter electrode, and an iodide-based solution, consisting of 0.6 M tetrabutylammonium iodide, 0.1 M lithium iodide, 0.1 M iodine, and 0.5 M 4-*tert*-butylpyridine in acetonitrile, was used as the liquid electrolyte. Photovoltaic properties of each solar cell were characterized using simulated AM 1.5 sunlight illumination with an output power of  $100 \text{ mW/cm}^2$ . An ultraviolet solar simulator (Model 16S, Solar Light Co., Philadelphia, PA, USA) with a 200 W xenon lamp power supply (Model XPS 200, Solar Light Co., Philadelphia, PA, USA) was used as the light source, and a semiconductor parameter analyzer (4155A, Hewlett-Packard, Japan) was used to measure the current and voltage. The  $J$ - $V$  measurement was repeated three times and the average results were reported. The electrochemical impedance spectroscopy (EIS) was carried

out through the Solartron 1287A coupling with the Solartron 1260 FRA/impedance analyzer to investigate electronic and ionic processes in DSCs.

The morphology of the photoanode surfaces was characterized by scanning electron microscopy (SEM, JEOL JSM-7000).

To measure the adsorbed N3 dye amount on the films, the dye was desorbed by immersing dye-sensitized films in a solution containing 0.1 M NaOH in water and ethanol (1:1, v/v). An ultraviolet-visible-near infrared spectrophotometer (UV-VIS-NIR, Perkin Elmer Lambda 900) was employed to measure the dye concentration of the desorbed-dye solution.

## 5. Results and Discussions

The  $J$ - $V$  curves and the performance characteristic values ( $J_{sc}$ ,  $V_{oc}$ ,  $\eta$ , and  $ff$ ) for the DSCs based on the Nb-TiO<sub>2</sub> photoanode before and after the atomic deposition of alumina and hafnia layers are depicted on Figures 1(a) and 1(b) and summarized in Table 1. The niobium-doped titanium oxide photoanode showed a relatively high photocurrent density ( $14.25 \text{ mA/cm}^2$ ) corresponding to relatively high dye loading ( $2.22 \times 10^{-7} \text{ mol/cm}^2$ ), but a low open-circuit voltage (547 mV) which result in an efficiency of 2.93%. The low open circuit voltage is explained as a result of the high rate of charge recombination, where photogenerated electrons in the porous electrode tend to recombine with either the oxidized dye or the oxidized species in the electrolyte, thereby reducing the open-circuit voltage [14]. The deposition of atomic layers of alumina resulted in an increase of the open-circuit voltage up to 623 mV after 20 cycles and an increase of the photocurrent density up to  $18.53 \text{ mA/cm}^2$  after 15 cycles. The increase in photocurrent, and hence efficiency, is likely to arise from the improved connectivity of the nanoparticles composed the photoanode, where no perceptible change can be observed in the dye loading, but presents a reduction in carrier recombination. The alumina layers showed a more effective suppression of the charge recombination by increasing the thickness of the layers which resulted in an increase of the open circuit voltage up to 14% and the overall efficiency up to 21%. Beyond 15 cycles of ALD of alumina, a decrease in the photocurrent density was founded, which is attributed to the low efficiency of the electron transport due to too much thickness of the coating layer.

On the other hand, using hafnium oxide as a passivation layer of the Nb-doped titania nanoparticles exhibited much more enhancement compared with the utilization of alumina layer as shown in Figure 1(b). The open-circuit voltage increased gradually from 547 mV to 675 mV by increasing the number of the ALD hafnia layers up to 15 cycles. The photocurrent density increased up to  $16.43 \text{ mA/cm}^2$  after 5 cycles followed by minimal drop for the 10 cycles sample and further drop down to  $14.4 \text{ mA/cm}^2$  for the 15 cycles sample. This behavior is correlated with the dye loading as shown in Table 1. So, by incorporating 10 cycles of ultrathin hafnia layers, the best performance with overall efficiency of 5.12% was achieved, which exemplifies an improvement of

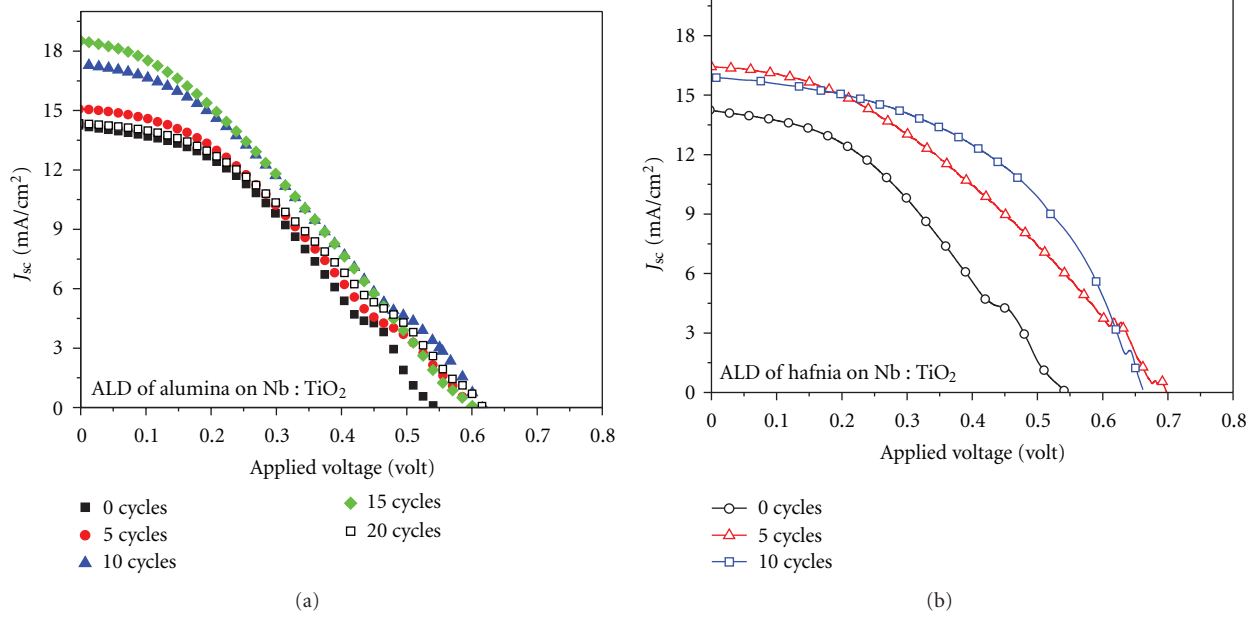


FIGURE 1: The  $J$ - $V$  curves for DSCs composed of ALD of alumina on Nb:TiO<sub>2</sub> photoanode (a) and of hafnia-coated one (b) treated with different cycles.

TABLE 1: The DSC performance parameters for alumina and hafnia ALD Nb:TiO<sub>2</sub> photoanode coated with different cycles.

	$J_{sc}$ (mA/cm <sup>2</sup> )		$V_{oc}$ ( $<\pm 0.01$ Volt)		$\eta$ (%)		FF ( $<\pm 0.01$ )		Dye loading $\times 10^{-7}$ (mol/cm <sup>2</sup> )	
	Al <sub>2</sub> O <sub>3</sub>	HfO	Al <sub>2</sub> O <sub>3</sub>	HfO	Al <sub>2</sub> O <sub>3</sub>	HfO	Al <sub>2</sub> O <sub>3</sub>	HfO	Al <sub>2</sub> O <sub>3</sub>	HfO
0 cycles	14.25 $\pm$ 0.15	14.25 $\pm$ 0.11	547	547	2.93 $\pm$ 0.04	2.93 $\pm$ 0.04	0.38	0.38	2.20	2.20
5 cycles	15.1 $\pm$ 0.17	16.43 $\pm$ 0.08	600	698	3.06 $\pm$ 0.05	4.16 $\pm$ 0.03	0.34	0.36	2.29	2.35
10 cycles	17.3 $\pm$ 0.14	15.9 $\pm$ 0.15	616	663	3.5 $\pm$ 0.07	5.12 $\pm$ 0.06	0.33	0.45	2.26	2.27
15 cycles	18.53 $\pm$ 0.16	14.4 $\pm$ 0.11	610	675	3.55 $\pm$ 0.03	3.72 $\pm$ 0.04	0.31	0.38	2.16	1.77
20 cycles	14.4 $\pm$ 0.2	—	623	—	3.1 $\pm$ 0.06	—	0.35	—	1.89	—

74%. Such an enhancement of the performance explained the improvement of the fill factor. This is attributed to better electron transport via the interfaces, which means that the diffuse of the hafnia phase through the photoanode network is efficient and can be demonstrated as a conformal buffering coating to suppress the leakage current. Both alumina and hafnia layers have a higher conduction band edge from niobium-doped titanium oxide, which act as a blocking layer of the back electrons [15].

## 6. Structural Properties

XRD pattern for the layers did not show any traces for alumina or hafnia, as the expected XRD is not sensitive for this ultrathin layer. It is very likely that we have an amorphous ALD coating, or with very poor crystallinity. The surface morphology of the niobium-doped titanium oxide is depicted in Figure 2(a) using different magnification. The film exhibited a mesoporous structure, which led to better dye loading. Figures 2(b) and 2(c)

exhibited the surface morphology of the niobium-doped titanium oxide layer after 10 cycles of ALD of alumina and hafnia, respectively. The ALD layers of alumina and hafnia formed a homogenous conformal coverage on the surface of Nb:TiO<sub>2</sub> nanoparticles and inside the mesoporous structure enhancing the coalescence between the nanocrystalline nanoparticles making them closer, which may introduce favorable path for electron transport through the photoanode layer. In addition, the porous structure of the layer is still retained as shown in Figure 2(c), which preserves the high dye loading ability. So, the ALD hafnia improved the connectivity of the emerged nanoparticles with enhanced blocking layer against the leakage current, while retaining the high dye loading of the photoanode as shown in Table 1. The composition of the surface of the layer, which was determined by the EDX, exhibited the existence of the elements K-lines of aluminum, niobium, and titanium referred to the L-spectrum (see the inset in Figure 2(b)). However, it is difficult to argue that a doping of aluminum or hafnium is expected to

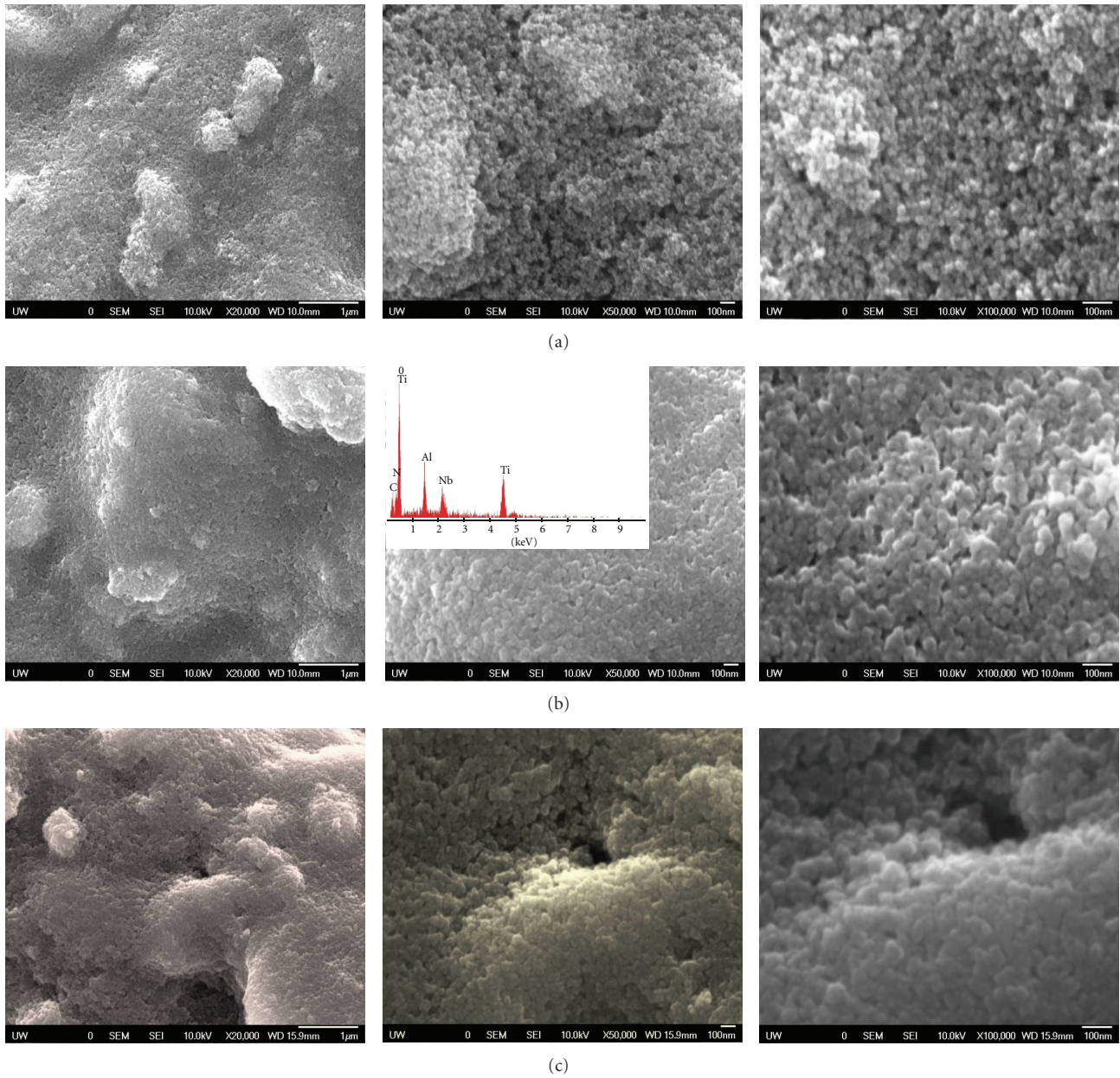


FIGURE 2: SEM images of the surface of (a) uncoated Nb : TiO<sub>2</sub> films, for Nb : TiO<sub>2</sub> layer treated with 10 cycle of ALD of (b) alumina and (c) hafnia. The index of (b) showed the EDX spectrum of the layer.

take place. The SEM images revealed a coverage effect more likely.

## 7. Electrochemical Impedance Spectroscopy (EIS)

Figures 3(a) and 3(b) exhibit the typical electrochemical impedance spectroscopy (EIS) Nyquist plots for the assembled DSCs made of ALD alumina and hafnia photoanode, respectively. Two semicircles is appeared, where the smallest one in the high-frequency range represents the

electrochemical reaction at the counter electrode and the largest one represents the charge transfer resistance at the electrolyte/dye/metal oxide interfaces. The diameter of the semicircle of the ALD alumina and hafnia photoanode is larger than that of the uncoated one, which means that the charge transfer resistance increased by the deposition of alumina and hafnia layers over the surface of the nanoparticles. The charge transfer resistance increased by increasing the number of cycles, where the different thickness of the blocking layers may be the major factor of such behavior. The peak of the semicircle in the midfrequency range in the Nyquist plot is correlated with the reaction rate

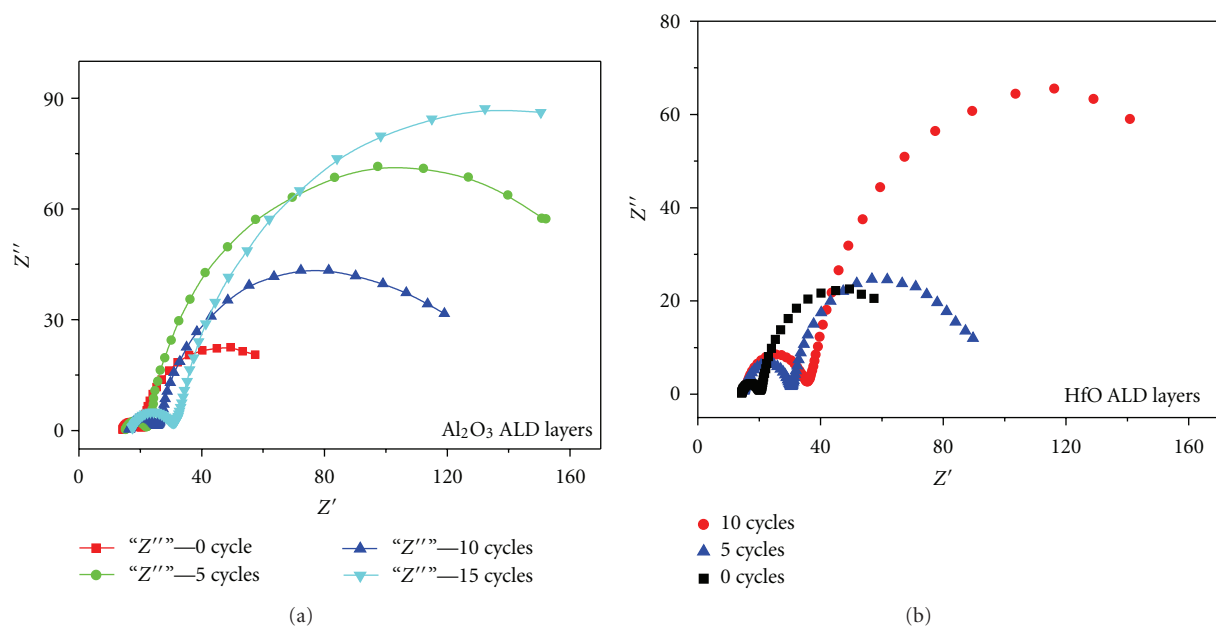


FIGURE 3: EIS spectra showing the Nyquist plots of the alumina ALD layers on Nb:TiO<sub>2</sub> DSC (a) and hafnia ALD layers on Nb:TiO<sub>2</sub> (b) for different cycles.

constant for the recombination process. The shift to higher frequency means a longer life-time is obtained, which results in higher performance of the DSCs.

## 8. Conclusion

Niobium-doped titanium oxide nanoparticulate photoanode in DSC showed a high photocurrent density due to its higher conductivity; however, a low open-circuit voltage is exhibited due to the higher recombination rate. Depositing conformal ultrathin atomic layers of Al<sub>2</sub>O<sub>3</sub> and HfO can suppress the back electrons from reaching the redox medium, which results in an increase of the open-circuit voltage and therefore lead to higher performance. HfO showed an improvement of the light-to-current conversion efficiency by 74%, higher than the 21% enhancement obtained by utilizing Al<sub>2</sub>O<sub>3</sub> layer.

## Conflict of Interests

The authors declare that they have no conflict of interests to disclose. Potential conflicts do not exist.

## Acknowledgments

N. Al Dahoudi would like to acknowledge the Council for International Exchange of Scholars (CIES) for their Fulbright Scholarship. This work is supported in part by the US Department of Energy, Office of Basic Energy Sciences, Division of Materials Sciences, under Award no. DE-FG02-07ER46467 (Q. Zhang), the National Science Foundation (DMR 1035196, DMR-0605159, and CMMI-1030048), and

the Royalty Research Fund (RRF) from the Office of Research at the University of Washington.

## References

- [1] R. D. McConnell, "Assessment of the dye-sensitized solar cell," *Renewable and Sustainable Energy Reviews*, vol. 6, no. 3, pp. 273–295, 2002.
- [2] B. O'Regan and M. Grätzel, "A low-cost, high-efficiency solar cell based on dye-sensitized colloidal TiO<sub>2</sub> films," *Nature*, vol. 353, no. 6346, pp. 737–740, 1991.
- [3] Y. Chiba, A. Islam, Y. Atanabe, R. Komiya, N. Koide, and L.Y. Han, "Dye-sensitized solar cells with conversion efficiency of 11.1%," *Japanese Journal of Applied Physics*, vol. 45, supplement 2, pp. L638–L640, 2006.
- [4] A. Yella, H.-W. Lee, H. N. Tsao et al., "Porphyrin-sensitized solar cells with cobalt (II/III)-based redox electrolyte exceed 12 percent efficiency," *Science*, vol. 334, no. 6056, pp. 629–634, 2011.
- [5] Q. Zhang and G. Cao, "Nanostructured photoelectrodes for dye-sensitized solar cells," *Nano Today*, vol. 6, no. 1, pp. 91–109, 2011.
- [6] A. G. Aberla, T. Lauinger, and R. Hezel, "Remote PECVD silicon—a key technology for the crystalline silicon PV industry of the 21st century?" in *Proceedings of the 14th European Photovoltaic Solar Energy Conference*, pp. 684–689, H. S. Stephens & Associates, 1997.
- [7] T. Saga, "Advances in crystalline silicon solar cell technology for industrial mass production," *NPG Asia Materials*, vol. 2, pp. 96–102, 2010.
- [8] B. Lim, S. Hermann, K. Bothe, J. Schmidt, and R. Brendel, "Permanent deactivation of the boron-oxygen recombination center in silicon solar cells," in *Proceedings of the 23rd European Photovoltaic Solar Energy Conference*, p. 1018, 2008.
- [9] U. Diebold, "The surface science of titanium dioxide," *Surface Science Reports*, vol. 48, no. 5–8, pp. 53–229, 2003.

- [10] J.-J. Lee, M. Rahman, S. Sarker et al., *Metal Oxides and Their Composites for the Photoelectrode of Dye Sensitized Solar Cells*, *Advances in Composite Materials for Medicine and Nanotechnology*, InTech, 2011.
- [11] K. H. Ko, Y. C. Lee, and Y. J. Jung, "Enhanced efficiency of dye-sensitized TiO<sub>2</sub> solar cells (DSSC) by doping of metal ions," *Journal of Colloid and Interface Science*, vol. 283, no. 2, pp. 482–487, 2005.
- [12] X. Lü, X. Mou, J. Wu et al., "Improved-Performance Dye-Sensitized solar cells using Nb-Doped TiO<sub>2</sub> electrodes: efficient electron Injection and transfer," *Advanced Functional Materials*, vol. 20, no. 3, pp. 509–515, 2010.
- [13] S. M. George, "Atomic layer deposition: an overview," *Chemical Reviews*, vol. 110, no. 1, pp. 111–131, 2010.
- [14] C. Lin, F.-Y. Tsai, M.-H. Lee, C.-H. Lee, T.-C. Tien, and L.-P. Wang, "Enhanced performance of dye-sensitized solar cells by an Al<sub>2</sub>O<sub>3</sub> charge-recombination barrier formed by low-temperature atomic layer deposition," *Journal of Materials Chemistry*, vol. 19, no. 19, pp. 2999–3003, 2009.
- [15] V. Ganapathy, B. Karunakaran, and S.-W. Rhee, "Improved performance of dye-sensitized solar cells with TiO<sub>2</sub>/alumina core-shell formation using atomic layer deposition," *Journal of Power Sources*, vol. 195, no. 15, pp. 5138–5143, 2010.